Electromagnetic Properties of Light Neutron-Rich Nuclei - Lifetime Measurements of ^{16}C and ^{23}Ne

Elektromagnetische Eigenschaften von leichten neutronenreichen Kernen - Messungen von Lebensdauern in ^{16}C und ^{23}Ne

Vom Fachbereich Physik der Technischen Universität Darmstadt
zur Erlangung des Grades eines Doktors der Naturwissenschaften (Dr. rer. nat.)
genehmigte Dissertation von Michael Bernhard Mathy aus Dieburg
Darmstadt 2020 — D17

1. Gutachten: Marina Petri, PhD
2. Gutachten: Prof. Dr. Robert Roth

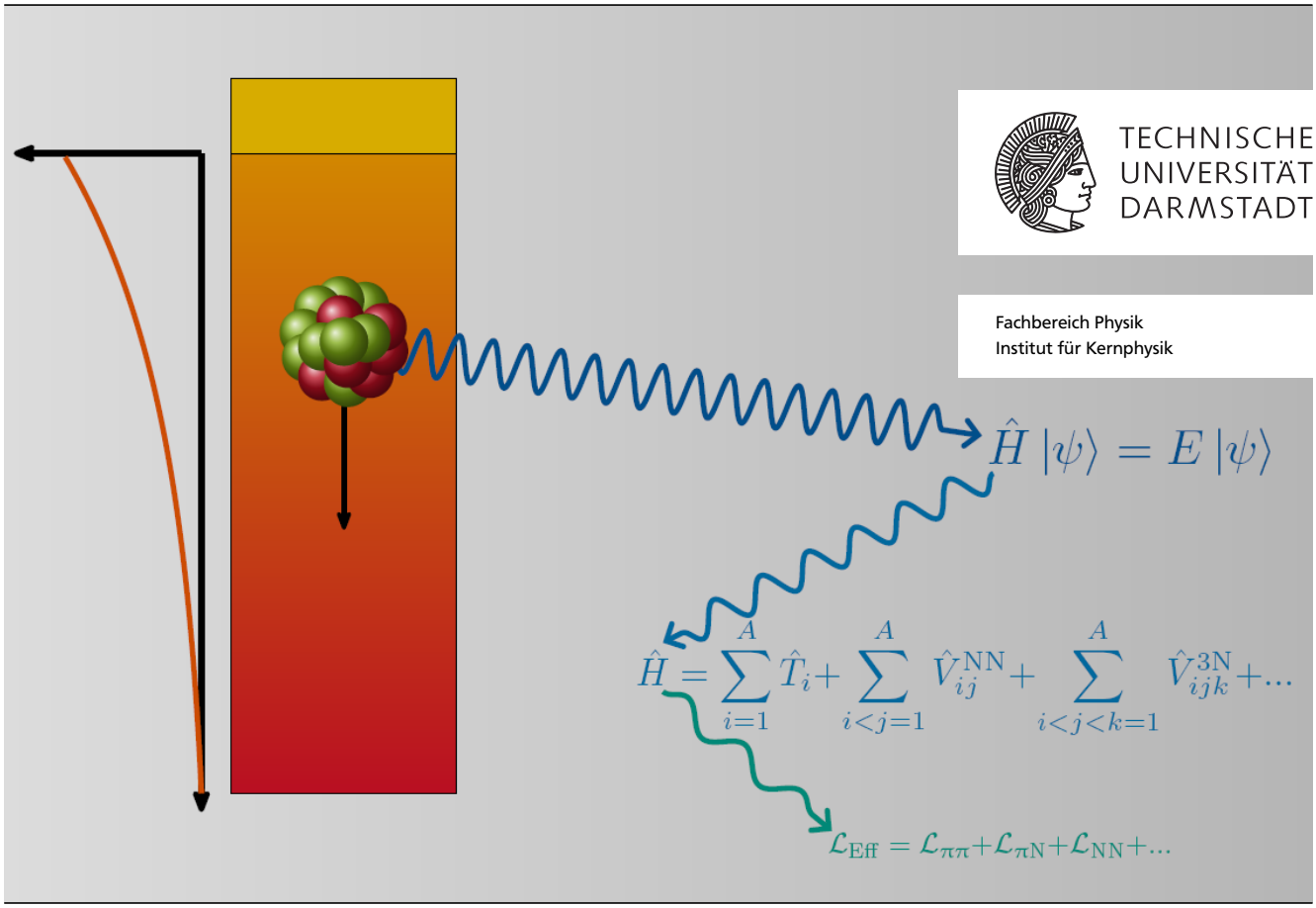

Argonne NATIONAL LABORATORY · THE ROYAL SOCIETY · UNIVERSITY of York · DFG · SFB 1245

Electromagnetic Properties of Light Neutron-Rich Nuclei - Lifetime Measurements of ^{16}C and ^{23}Ne
Elektromagnetische Eigenschaften von leichten neutronenreichen Kernen - Messungen von Lebensdauern in ^{16}C und ^{23}Ne

Genehmigte Dissertation von Michael Bernhard Mathy aus Dieburg

1. Gutachten: Marina Petri, PhD
2. Gutachten: Prof. Dr. Robert Roth

Tag der Prüfung: 14. Dezember 2020
Veröffentlichung auf TUprints: 2021

Darmstadt, Technischen Universität Darmstadt — D17

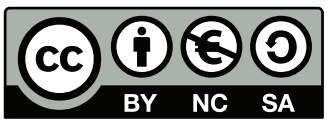

Für meinen Großvater Josef Mathy

The paradox is only a conflict between reality and your feeling of what reality ought to be.

—

Richard Feynman

This work was funded by the Deutsche Forschungsgemeinschaft (DFG, German Research Foundation) under Grant No. SFB 1245 (project ID 279384907).

Abstract

The lifetimes of higher-lying excited states were measured for ^{16}C and ^{23}Ne using a target and degrader setup made of beryllium and gold to apply the Doppler-shift attenuation method. The experiment was performed at the Argonne National Laboratory exploiting the reaction ^{9}Be(^{9}Be,2p)^{16}C* as well as ^{9}Be(^{16}O,2p)^{23}Ne*, which was available due to oxidation of the target. The emitted gamma rays were measured with Gammasphere while the charged particles were detected with Microball. By comparing the measured gamma-ray spectra for different detection angles and 2p events with Geant4 simulations, lifetimes can be obtained. An elaborated explanation of the used analysis method and potential uncertainties is given in this work. The simulations were carried out for two different sets of stopping powers to check their influence on the results.

For ^{23}Ne the lifetimes of two higher-lying states could be measured for the first time. The lifetime of the $(5/2^{+},7/2^{+})_{2}$ state (2517 keV) was obtained to $641(79)\,\mathrm{fs}^{+16\,\mathrm{fs}}_{-6\,\mathrm{fs}}\left(\mathrm{syst}_{\mathrm{target}}\right)$, while the lifetime of the $(5/2^{+},7/2^{+})_{1}$ state (1702 keV) was obtained to $168(55)\,\mathrm{fs}^{+8\,\mathrm{fs}}_{-1\,\mathrm{fs}}\left(\mathrm{syst}_{\mathrm{target}}\right)$ $^{+72\,\mathrm{fs}}_{-80\,\mathrm{fs}}\left(\mathrm{syst}_{\mathrm{feeding}}\right)$. To consider the feeding for the lower state it was assumed that the angular distributions are the same for both observed transitions. Theoretical USDB calculations were able to reproduce the level energies well, while they significantly underestimate the experimental lifetimes.

For ^{16}C the lifetime of the 4^{+}_{1} state could be constrained between $\tau_{\mathrm{Min}}=1.9^{+0.0}_{-0.1}\left(\mathrm{syst}_{\mathrm{target}}\right)$ ps and 4 ps. This results in $2.74\,\mathrm{e}^{2}\mathrm{fm}^{4}\leq B\left(E2;4^{+}_{1}\rightarrow 2^{+}_{1}\right)\leq 5.78^{+0.32}_{-0.00}\left(\mathrm{syst}_{\mathrm{target}}\right)\mathrm{e}^{2}\mathrm{fm}^{4}$ as a transition strength limit for the 4^{+}_{1} state. Theoretical predictions from no-core shell model calculations with NN+NNN interactions and p–sd shell model calculations for several effective two body interactions fulfill this constraint. The most likely lifetime range for the 2^{+}_{2} state was obtained to be 244 fs to 376 fs. Together with branching ratio limits for this state, which are known from previous measurements, the transition strengths for the 2^{+}_{2} state could be constrained. No-core shell model, recent in-medium no-core shell model, and p–sd shell model calculations are compared to these results.

In the second part of this work a conceptual design of a ^{14}C electron scattering experiment at the QCLAM Spectrometer at the S-DALINAC is presented.

Zusammenfassung

In dieser Arbeit wurden die Lebensdauern von höherliegenden angeregten Zuständen in ^{16}C and ^{23}Ne gemessen. Dazu wurde mithilfe eines Beryllium-Targets sowie Gold-Degraders die Doppler-Shift Attenuation Method verwendet. Das Experiment wurde am Argonne National Laboratory durchgeführt und die Reaktionen ^{9}Be(^{9}Be,2p)^{16}C* und ^{9}Be(^{16}O,2p)^{23}Ne* verwendet. Letztere Reaktion wurde durch eine Oxidation des Targets ermöglicht. Die emittierten Gammastrahlen wurden mit dem Gammasphere-Detektor gemessen, während geladene Teilchen mit dem Microball-Detektor erfasst wurden. Durch einen Vergleich der gemessenen Gammaspektren für verschiedene Winkel und 2p Ereignissen mit Geant4 Simulationen, kann die Lebensdauer der Zustände bestimmt werden. Eine ausführliche Diskussion über die verwendeten Analysemethoden und die sich daraus ergebenden möglichen Unsicherheiten wird in der vorliegenden Arbeit dargelegt. Die Simulationen wurden für zwei verschneidene Datensätze für Teilchen-Bremsvermögen durchgeführt, um deren Einfluss auf die Ergebnisse zu testen.

Für ^{23}Ne konnten die Lebensdauern von zwei höherliegenden Zuständen zum ersten Mal gemessen werden. Die Messung ergab Lebensdauern von $641(79)\,\mathrm{fs}^{+16\,\mathrm{fs}}_{-6\,\mathrm{fs}}\left(\mathrm{syst}_{\mathrm{target}}\right)$ für den $(5/2^{+},7/2^{+})_{2}$ Zustand (2517 keV) und $168(55)\,\mathrm{fs}^{+8\,\mathrm{fs}}_{-1\,\mathrm{fs}}\left(\mathrm{syst}_{\mathrm{target}}\right)^{+72\,\mathrm{fs}}_{-80\,\mathrm{fs}}\left(\mathrm{syst}_{\mathrm{feeding}}\right)$ für den $(5/2^{+},7/2^{+})_{1}$ Zustand (1702 keV). Um das Feeding in dem niedrigeren Zustand zu berücksichtigen, wurde angenommen, dass die Winkelverteilung für die beiden beobachteten Übergänge gleich ist. Theoretische USDB Berechnungen waren in der Lage die Zustandsenergien gut wiederzugeben, während sie die experimentellen Lebensdauern unterschätzten.

Für ^{16}C konnte die Lebensdauer des 4^{+}_{1} Zustandes zwischen $\tau_{\mathrm{Min}}{=}1.9^{+0.0}_{-0.1}\left(\mathrm{syst}_{\mathrm{target}}\right)\,\mathrm{ps}$ und 4 ps limitiert werden. Dies liefert $2.74\,\mathrm{e}^{2}\mathrm{fm}^{4}{\leq}B\left(E2;4^{+}_{1}\rightarrow 2^{+}_{1}\right){\leq}5.78^{+0.32}_{-0.00}\left(\mathrm{syst}_{\mathrm{target}}\right)\,\mathrm{e}^{2}\mathrm{fm}^{4}$ für die dazugehörige Übergangsstärkenlimitierung. Theoretische Vorhersagen von No-Core Shell Model Berechnungen mit $NN{+}NNN$ Wechselwirkungen und $p{-}sd$ Schalenmodell Rechnungen für effektive Zwei-Körper Wechselwirkungen erfüllen diese Limitierung. Der wahrscheinlichste Bereich für die Lebensdauer des 2^{+}_{2} Zustandes wurde zu 244 fs bis 376 fs bestimmt. Unter der Verwendung der Verzweigungsverhältnisse, welche aus früheren Messungen bekannt sind, können die beteiligten Übergangsstärken des 2^{+}_{2} Zustandes beschränkt werden. Die Berechnungen für No-Core Shell Modelle, ein kürzlich entwickeltes In-Medium No-Core Shell Model und ein $p{-}sd$ Schalenmodell werden mit diesen Ergebnissen verglichen.

Im zweiten Teil der Arbeit wird ein konzeptionelles Design für ein ^{14}C Elektronenstreuungsexperiment an dem S-DALINAC unter der Verwendung des QCLAM Spektrometers vorgestellt.

Contents

Part I

In-Flight Lifetime Measurements in Carbon-16 and Neon-23

1 Introduction

Since hundreds of years one of the biggest questions for which humanity seeks a satisfying answer can be phrased by “So that I may perceive whatever holds // The world together in its inmost folds.” [†]. This question not only drove Goethe’s main character “Faust” into madness, it is until today one of the most complex challenges for modern science, especially for modern particle and nuclear physics. Although, many elaborated theories were developed and enhanced in the last century, there are still many unsolved problems which occur when we try to understand the fundamental interactions which set up the rules of the universe we live in.

For now, the quantum-mechanical standard model of particle physics explains the innermost of the world very successfully to a large extend [PRS+14]. This model uses a set of elemental particles which interact via four different fundamental interactions. One of these interactions is the strong interaction described very successfully by Quantum Chromodynamics [ME11]. The strong interaction generates a force which acts on elemental particles which are from the quark family. The combination of three light quarks can form a nucleon. The so created nucleon is either a proton (up-, up-, down-quarks) or neutron (up-, down-, down-quarks). Here, the range of the strong interaction, which glues the three quarks together, does not end sharply at the end of a nucleon. The interaction reaches outside the boundaries of each nucleon, e.g. as a pion exchange, and so a residual interaction is created. This residual interaction is the so-called nuclear force. This force is the reason that many different stable and unstable nuclei consisting of several nucleons can be formed. These nuclei themselves can form atoms which can create many different complex types of matter which our world is made of. Although, the nuclear force plays such an important role and is investigated elaborately in the last decades, its overall form and properties are not understood yet. This goes hand in hand with the fact that also the strong interaction is not completely described so far. Additionally, the mathematical evolution going from the strong interaction to the nuclear force is quite challenging and strongly limited due to the properties of the strong interaction. It turns out that Quantum Chromodynamics is non-perturbative in its low energy region and hence it is arduous to apply appropriate mathematical approximations which describe the interactions between nucleons. Hence, learning more about the nuclear force helps to understand the strong interaction and vice versa [PRS+14].

Due to this, many different approaches and models which try to describe the nuclear force were developed until today. It is one main goal of modern nuclear physics to test these different models and to constrain their ranges of validity. To do so, measurements which get access to the

[†] “Dass ich erkenne, was die Welt // Im Innersten zusammenhält.” - From “Faust. Eine Tragödie” by Johann W. v. Goethe

structure of the nuclei are compared to theory predictions. Here, one very important approach is the classification of the electromagnetic properties of nuclei and their excited states. Especially the lifetime determination of gamma-decays of excited nuclear states are a good benchmark for modern nuclear theories. The lifetime measurements of such decays are a model-independent way to get an insight in the nuclear structure. In fact, these lifetimes are strongly related to the transition strengths between two nuclear states. The transition strength itself depends on the wavefunctions of the involved states and the transition operator. While the transition operator for electromagnetic transition is known precisely, the wavefunctions will differ for different theoretical approaches. Hence, lifetime measurements are a perfect way to probe different nuclear models [NSS79, Sri06, MK92]. Today, lifetime measurements are carried out for exotic nuclei which have extraordinary N/Z ratios close to the proton or neutron drip lines [ES08]. For these cases much more unexpected behaviours can be found as for stable nuclei near shell closures. Exotic nuclei are even more challenging to be described by theory. For them, details of the used interaction (e.g. adding three body forces) suddenly can have a huge influence on the electromagnetic properties, which did not play a big role for stable nuclei. Hence, exotic nuclei are interesting cases to test state of the art nuclear models.

In the last years the electromagnetic properties in the neutron-rich carbon isotopic chain were found to be an interesting candidate to test modern theories. While a large number of different neutron-rich carbon isotopes are accessible with modern experiment techniques, a variety of unexpected behaviours could be measured, which challenge the theoretical models. So for example, a disappearance of the N=14 sub-shell gap could be observed in the neutron-rich carbon isotopic chain which is uncommon for nuclei in that region such as neutron-rich oxygen isotopes [SSS$^+$08]. Focusing on the unstable neutron-rich ^{16}C nucleus, the transition strengths and hence the lifetimes of the excited states are of big interest. Here, the first excited 2^+_1 state at 1.76 MeV was mainly analysed in the past. While two complex measurements using the recoil shadow methods done by Imai et al. [IOA$^+$04] and Ong et al. [OIS$^+$08] came to inconsistent results for the lifetime of the 2^+_1 state, the two more recent measurements performed by Wiedeking et al. [WFM$^+$08] and Petri et al. [PPC$^+$12] obtained consistent results among each other. In their works four excited states could be observed in ^{16}C. Wiedeking et al. used a ^{9}Be(^{9}Be,2p)^{16}C* reaction while Petri et al. used a ^{9}Be(^{17}N,^{16}C*)X reaction to investigate lifetimes of the excited states applying the recoil distance method. The results can be seen in Figure 1.1. The figure shows a level scheme which is created by combining the results from both works using uncertainty weighted means. For the 2^+_1 state the lifetime could be determined to 11.5(1.4) ps which correspond to an $E2$ transition strengths of $B(E2;2^+_1\rightarrow 0^+)$=4.18(53) e^{2}fm^4. This strength is very similar to $B(E2;2^+_1\rightarrow 0^+)$ strengths which are obtained for ^{14}C and ^{18}C isotopes, whereas e.g. the $B(E2;2^+_1\rightarrow 0^+)$ strength in ^{20}C is significantly enhanced [RMM$^+$87, OIS$^+$08, VBB$^+$12, PFM$^+$11].

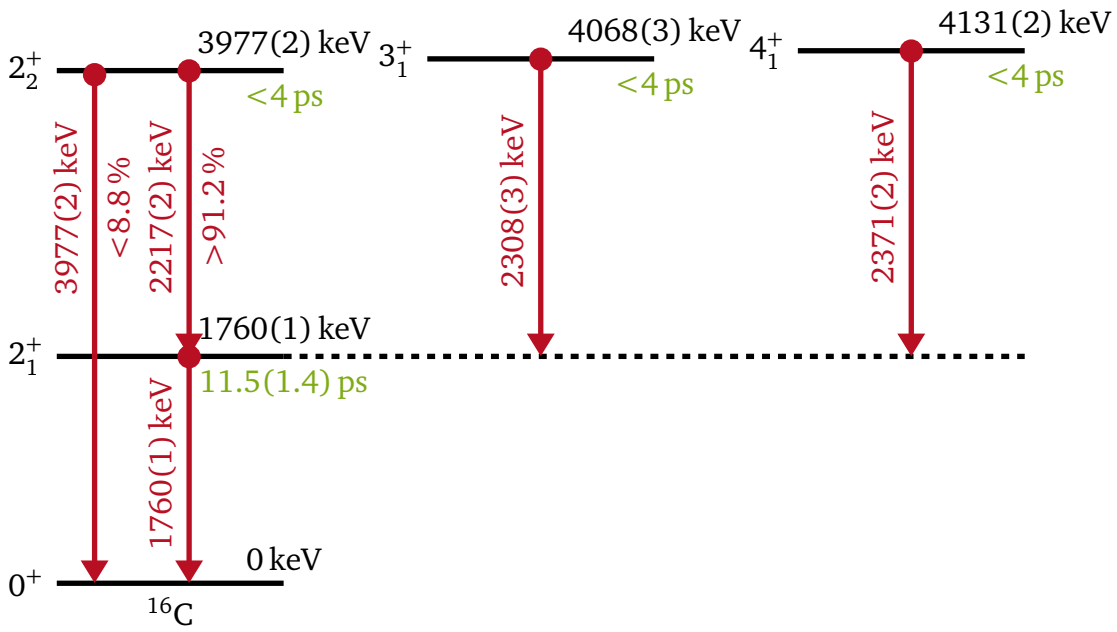

Figure 1.1: Level scheme of ^{16}C. The energies printed in black are the energies of the states while the energies printed in red are the transition energies of the gamma rays. These energies are an uncertainty weighted mean using the results from [WFM$^+$08, PPC$^+$12]. The lifetime of the 2_1^+ state and the lifetime limits for the three higher-lying states are printed in green. The lifetime of the 2_1^+ state is also an uncertainty weighted mean using the results and statistical uncertainties from [WFM$^+$08, PPC$^+$12]. The branching ratio limit for the transitions from the 2_2^+ state is taken from [PPC$^+$12].

A comparison between the experimental results and theoretical predictions for the $B(E2; 2_1^+ \rightarrow 0^+)$ strength is given in Figure 1.2. The figure summarize the results from Wiedeking et al. [WFM$^+$08] and Petri et al. [PPC$^+$12]. The $B(E2; 2_1^+ \rightarrow 0^+)$ strength in ^{16}C can be reproduced well by *p*–*sd* shell model calculations using three different empirically derived effective two-body interactions (WBP, WBT, WBT*) in combination with effective charges. Ab initio No-Core Shell Model (NCSM) calculations with CD-Bonn 2000 (CDB2k) *NN* interactions predict a transition strength which is too small by a factor of two [PPC$^+$12, FRN13]. This is a special characteristic of ^{16}C, where for neighbouring carbon isotopes the predictions from ab initio NCSM calculations produced better results in terms of $B(E2; 2_1^+ \rightarrow 0^+)$ [PPC$^+$12, FRN13]. Advanced NCSM calculations using chiral *NN*+*NNN* interactions showed large changes in the results for the transition strengths, but they do not fully converge to a final value for the $B(E2; 2_1^+ \rightarrow 0^+)$ strength [PPC$^+$12, FRN13].

Additionally, the branching ratio for the $2_2^+ \rightarrow 2_1^+$ and $2_2^+ \rightarrow 0^+$ transitions could be constrained in the work from Petri et al. [PPC$^+$12]. The 2_2^+ state mainly decays via the 2_1^+ state. Only in less than 8.8 % of the cases, the state decays directly into the 0^+ ground state. These properties are again well reproduced by the *p*–*sd* shell model calculations. But the ab initio NCSM

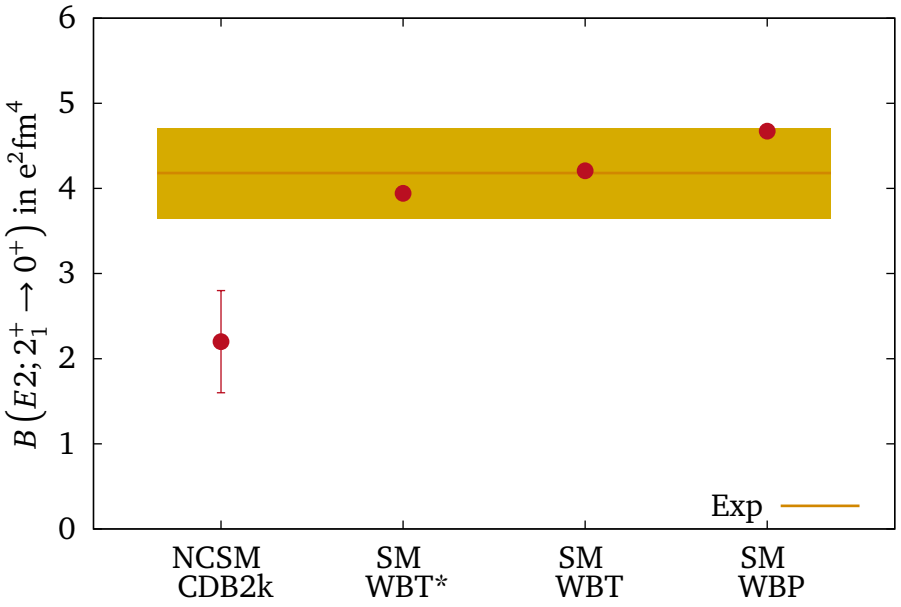

Figure 1.2: Comparison of $B\left(E2; 2_1^+ \rightarrow 0^+\right)$ strengths in ^{16}C. The experimental vaule of 4.18(53) e^2fm^4 is the uncertainty weighted mean using the results from [WFM$^+$08, PPC$^+$12]. The theoretical predictions for NCSM calculations with CDB2k NN interactions and p–sd shell model calculations for several effective two-body interactions (WBP, WBT, WBT*) are taken from [PPC$^+$12]. For details see also Section 2.9.

calculations with CDB2k NN interactions favour the $2_2^+ \rightarrow 0^+$ transition instead of the $2_2^+ \rightarrow 2_1^+$ transition, which stands in clear contradiction with the measurements [PPC$^+$12, FRN13]. This problem can be revised if chiral three body interactions are added to the interactions of the NCSM calculations. Then the NCSM calculations predict a branching ratio of only 2.4 % for the $2_2^+ \rightarrow 0^+$ transition which agrees with the experiment again. Also the predicted dominant transition strengths, which mainly define the lifetimes of the 2_2^+ and the 3_1^+ state, depend strongly on the used interactions. They change by a multiple when three body interactions are added. So for example the transition strength $B(E2; 3_1^+ \rightarrow 2_1^+)$ becomes strongly suppressed by a factor of $\approx$18 for the NN+NNN interactions compared to CDB2k NN interactions [FRN13]. Hence, the electromagnetic properties of the higher-lying states in ^{16}C are very sensitive to the details of the underlying Hamiltonian and key observables to benchmark ab initio calculations. But as it can be seen in Figure 1.1 just an upper limit of 4 ps for the lifetimes of the three higher-lying states could be obtained in [WFM$^+$08, PPC$^+$12]. So it is important to measure the lifetimes of these states as precisely as possible.

Most recent measurements from Ciemała et al. could constrain the lifetime for the 2_2^+ state [CZC$^+$20]. Here, the lifetimes were obtained by analysing the Doppler-shifted gamma-transition line shapes from in-flight decays. For these results the obtained lifetime of the 2_2^+ state depends strongly on the exact $2_2^+ \rightarrow 2_1^+$ transition energy, which is not known precisely enough so far. Their results cover an energy range from 2214 keV to 2218 keV. If the transition energy is assumed as

2218 keV, the lifetime is given by ≈50(20) fs, while it is $\approx 100^{+100}_{-50}$ fs for 2216 keV. If the transition energy is assumed as 2214 keV, only a lower limit of 210 fs can be given. A more precise constraint of the lifetime could not be achieved, because the number of counts were too low.

Due to the situation mentioned above, it is the goal of this thesis to measure the unknown lifetimes of the three higher-lying states in ^{16}C and compare them to *p*—*sd* shell model calculations as well as NCSM calculations and to new state of the art in-medium similarity renormalization group NCSM calculations [GVHR17] for effective chiral two-nucleon plus three-nucleon interactions [HVH$^+$20]. The expected lifetimes are in the femtoseconds range and due to this a Doppler-Shift Attenuation Method measurement was realized at the Argonne National Laboratory in 2016. For this experiment a ^{9}Be beam bombarded a ^{9}Be target which enables the fusion-evaporation process ^{9}Be(^{9}Be,2p)^{16}C* [WFM$^+$08]. At the downstream end of the target a gold degrader was mounted which slows the excited ^{16}C isotopes down until they are fully stopped. While the isotopes are slowed down they can emit Doppler shifted gamma rays. The emitted gamma rays were measured using the Gammasphere detector array which can detect the gamma rays under 17 different angles using HPGe detectors [Lee90]. To select events for which ^{16}C isotopes are created the Microball particle detector was placed inside the scattering chamber [SHD$^+$96]. With this detector it was possible to identify the evaporated protons and sort for events for which two protons were detected in coincidence with gamma rays in the Gammasphere detectors. By comparing the so achieved experimental gamma-ray spectra to gamma-ray spectra from Geant4 Monte Carlo simulations one gets access to the lifetimes of the higher-lying states. In the later analysis it was found that in the data also transitions from ^{22}Ne and ^{23}Ne isotopes can be found due to the oxidation of the ^{9}Be target. The former case could be used as a benchmark for the experiment and the analysis method because for ^{22}Ne the lifetimes of the two lowest excited states are known very precisely [SB15]. For ^{23}Ne lifetimes of two higher-lying states could be measured for the first time. They will be compared to USDB *sd*-shell model calculations [BW88, BR06, RMB08, Bro19].

The first part of this thesis discusses the lifetime measurements for ^{16}C and ^{23}Ne. Therefore, Chapter 2 explains the physical basics and concepts which are necessary to understand the importance of lifetimes in nuclear physics and how they can be measured. Additionally, nuclear models which are used to calculate the lifetimes theoretically are introduced. In Chapter 3 the experimental method, the setup and the used detectors are explained in detail. Then Chapter 4 discusses the Geant4 simulations whose results will be compared to the experimental data. Here the main focus lies on the procedure which creates the excited isotopes of interest in the simulation and how their energy loss in the degrader is treated. Next, Chapter 5 explains the overall analysis procedure which is applied to the experimental data. Here, it is explained how both detectors were calibrated and how the proton cuts were set. Then it is explained how events were created between coincidence Gammasphere and Microball entries. Furthermore, the proton

energy and angular distributions are discussed with focus on possible artificial biases to the lifetime measurements stemming from biases in the proton detection. Finally, Chapter 6 shows the results which were obtained in this work. First a benchmark test using the known lifetimes from the states in ^{22}Ne is presented. It confirms the accuracy of the here applied methods. Then the results for ^{23}Ne as well as ^{16}C are discussed in detail. For ^{16}C the focus is set on the lifetime of the 2^+_2 state and a lower lifetime limit for the 4^+_1 state. The lifetime for the 3^+_1 state could not be determined due to contaminations stemming from gamma rays emitted by ^{15}N. Also, the results for ^{23}Ne and ^{16}C are compared to several theoretical models.

The second part of this thesis will focus on the development of an electron scattering experiment on ^{14}C. An elaborate introduction to this topic is given in the beginning of the second part.

2 Theory and Physical Background

This chapter contains the physical background that is important to understand the analysis and interpretation of the experiment discussed in this thesis. First, the gamma decay of excited nuclear states will be discussed. Afterwards, the measurement of gamma rays and the determination of lifetimes of excited nuclear states is explained in detail. In the end, the nuclear structure and theoretical descriptions will be discussed for ^{16}C and ^{23}Ne.

2.1 Lifetimes of Nuclear States and Gamma Decay

This section, which follows [Mat16] and is oriented by [Sri06, MK92, Sta11], will give an overview about the lifetimes of excited nuclear states and the gamma decay of those. It will motivate the importance and advantages of lifetime measurements for nuclear structure physics.

During the gamma decay, a nucleus de-excites with a certain probability from an excited state to a state with lower energy. These states are specified by their quantum numbers and their energy whereat the total energy of the ground state is the lowest. Every state is described by a particular wave function $|\psi\rangle$, which depends on quantum numbers and fixes the energy of the state E via the time-independent Schrödinger equation

$$\hat{H}\,|\psi\rangle = E\,|\psi\rangle \tag{2.1}$$

with the Hamiltonian $\hat{H}$. Due to this, $|\psi\rangle$ is also called the eigenstate of the nucleus.

The main quantum numbers for a nucleus' eigenstate are given by the total angular momentum J and the parity π. In this way, an eigenstate can be identified by J^π. The quantum numbers of a particular state are generated by coupling the quantum numbers of the nucleons in the nucleus and their orbit properties. When a nucleus de-excites from a state $|J_\mathrm{i}^\pi\rangle$ with E_i to a state $|J_\mathrm{f}^\pi\rangle$ with E_f, the nucleus emits a gamma ray with an energy of

$$E_\gamma = h\nu = E_\mathrm{i} - E_\mathrm{f}, \tag{2.2}$$

where the recoil of the nucleus is neglected and ν is the frequency of the photon (see Fig. 2.1). During this de-excitation, the quantum numbers of the nucleus are also changing, and because of the angular momentum conservation, the gamma-quantum needs to carry an angular momentum

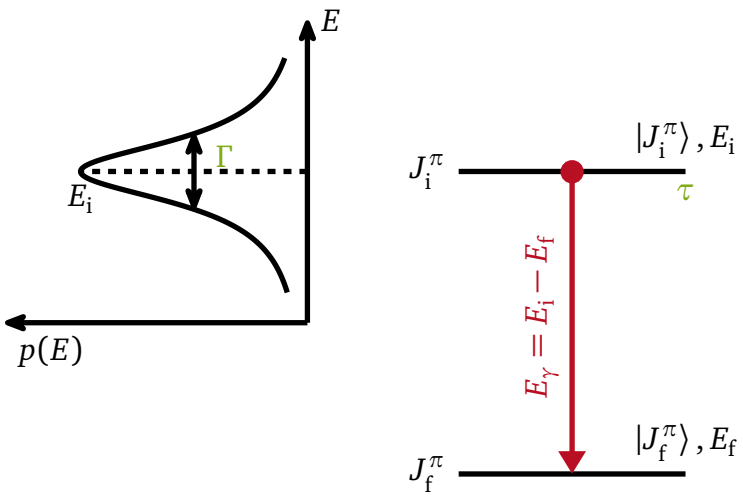

Figure 2.1: This diagram shows a gamma decay between the initial state $|J_i^\pi\rangle$ and the final state $|J_f^\pi\rangle$, where the initial state has the lifetime τ and the level width Γ. The figure is modified and reprinted from [NSS79] with permission from IOPScience.

l as well. The radiation character of the gamma ray is fixed by the conservation of the momentum and the quantum-mechanical selection rules to:

$$|J_i - J_f| \leq l \leq J_i + J_f \tag{2.3}$$

$$\pi_i \cdot \pi_f = \begin{cases} (-1)^l & \Rightarrow \text{ electric character (E)} \\ (-1)^{l+1} & \Rightarrow \text{ magnetic character (M)} \end{cases} \tag{2.4}$$

Here, the radiation character is often named by its multipolarity 2^l instead of using the angular momentum l. Trainsitions with l=1 are called dipole (2^1=2) transitions, l=2 are called quadrupole (2^2=4) transitions, l=3 are called octupole (2^3=8) transitions and so forth. Also, the short nomenclature (σl) is used where σ is replaced by "E" for electric or by "M" for magnetic transitions. For example, the de-excitation J_i^π=1^-→J_f^π=0^+ is called electric dipole transition or shortly $E1$ transition and J_i^π=1^+→J_f^π=0^+ is called magnetic dipole transition or shortly $M1$ transition. The radiation character also determines the angular distribution of the gamma radiation. For more information, see e.g. [MK92].

For the gamma decay, the temporal change of the number of nuclei $\dot{N}_i$ in the excited state $|J_i^\pi\rangle$ is proportional to the total number of nuclei $N_i(t)$ in this excited state $|J_i^\pi\rangle$ at the time t. Hence, the relation

$$\dot{N}_i(t) = -\lambda N_i(t) \tag{2.5}$$

applies, which is known as the radioactive decay law. There, λ is the decay constant and denotes the probability for a transition per unit time. Under the assumption that N_0 nuclei are excited in state $|J_i^\pi\rangle$ at t=0, this differential equation is solved to

$$N_i(t) = N_0 \cdot \mathrm{e}^{-\lambda t} = N_0 \cdot \mathrm{e}^{-\frac{t}{\tau}}. \tag{2.6}$$

On the right hand side of this equation, the lifetime $\tau{=}1/\lambda$ is introduced. The lifetime τ equals the elapsed time in which the number of excited nuclei is dropped down to N_0/e.

To calculate the gamma decay constant λ theoretically, *Fermi's golden rule*

$$\lambda = \frac{2\pi}{\hbar} \left|\langle \psi_\mathrm{f}| V_\mathrm{int} |\psi_\mathrm{i}\rangle\right|^2 \rho(E_\mathrm{f}) \tag{2.7}$$

is used. There, V_int is the electromagnetic interaction potential, $\rho(E_\mathrm{f})$ is the level density of states with energy E_f, $|\psi_\mathrm{i}\rangle$ is the nucleus wave function before the decay, and $|\psi_\mathrm{f}\rangle$ is the nucleus wave function after the decay. Under the assumption that the decay $J_\mathrm{i}^\pi \rightarrow J_\mathrm{f}^\pi$ has only one radiation character given by (σl), *Fermi's golden rule* is evaluated to

$$\lambda(\sigma l) = \frac{2(l+1)}{\epsilon_0 l \hbar[(2l+1)!!]^2} \cdot \left[\frac{E_\gamma}{\hbar c}\right]^{2l+1} \cdot B(\sigma l; J_\mathrm{i}^\pi \rightarrow J_\mathrm{f}^\pi), \tag{2.8}$$

which can be also written as

$$B(\sigma l; J_\mathrm{i}^\pi \rightarrow J_\mathrm{f}^\pi) = \frac{\epsilon_0 l \hbar[(2l+1)!!]^2}{2(l+1)} \cdot \left[\frac{\hbar c}{E_\gamma}\right]^{2l+1} \cdot \frac{1}{\tau}. \tag{2.9}$$

Here, $B(\sigma l; J_\mathrm{i}^\pi \rightarrow J_\mathrm{f}^\pi)$ is the reduced transition strength. A detailed derivation of this equation is for example given in [Sri06]. The reduced transition strength is calculated via

$$B(\sigma l; J_\mathrm{i}^\pi \rightarrow J_\mathrm{f}^\pi) = \frac{1}{2J_\mathrm{i}+1} \cdot \sum_{m_\mathrm{i}, m_\mathrm{f}} \left|\langle J_\mathrm{f}^\pi| \mathcal{O}_{\sigma l} |J_\mathrm{i}^\pi\rangle\right|^2, \tag{2.10}$$

with $\mathcal{O}_{\sigma l}$ as radiation transition operator. It can be seen that this transition strength is directly sensitive to the wave functions of the nucleus.

As a result of Equation 2.9, lifetime measurements are a model-independent way to access the reduced transition strength $B(\sigma l; J_\mathrm{i}^\pi \rightarrow J_\mathrm{f}^\pi)$. By also theoretically calculating the transition strength with Equation 2.10, it is possible to test the accuracy of different nuclear wave functions. For that reason, lifetime measurements are a great tool to check the accuracy of nuclear models and to get a better insight into the nuclear structure.

Further, it has to be mentioned that due to the finite lifetime of the excited state the energy E_i of the state is not a discrete value. Following Heisenberg's uncertainty principle, the energy level has a certain energy width Γ_Total and is distributed as a Lorentz function around E_i (see Fig. 2.1 left). Here Γ_Total corresponds to the Full Width at Half Maximum (FWHM) of the Lorentz peak. Furthermore, the equation

$$\Gamma_\mathrm{Total}\tau = \hbar \tag{2.11}$$

holds [NSS79]. This shows that the lifetime is directly related to the total energy width of the state. While a state has one fixed lifetime, the decay width Γ_{Total} is the sum of the partial widths Γ_j of all possible decay modes a state has and hence

$$\Gamma_{\text{Total}} = \sum_j \Gamma_j(\sigma l) \tag{2.12}$$

as well as

$$\lambda_{\text{Total}} = \sum_j \lambda_j(\sigma l). \tag{2.13}$$

So if more than one decay mode is available for a state, the theoretical reduced transition strengths $B(\sigma l; J_{\text{i}}^{\pi} \rightarrow J_{\text{f}}^{\pi})$ have to be calculated for all available decay modes and then the decay constants $\lambda_j(\sigma l)$ have to be summed up to the total decay constant λ_{Total}. The total decay constant λ_{Total} then defines the lifetime τ of the considered state.

If Equation 2.8 is evaluated for the three lowest possible l values following [BM69], one obtains

$$\begin{aligned}
\lambda(E1) =& 1.59 \cdot 10^{15} \frac{1}{\text{s}} \cdot \left(\frac{E_\gamma}{\text{MeV}}\right)^3 \cdot \frac{B(E1)}{e^2\text{fm}^2} \\
\lambda(E2) =& 1.22 \cdot 10^{9} \frac{1}{\text{s}} \cdot \left(\frac{E_\gamma}{\text{MeV}}\right)^5 \cdot \frac{B(E2)}{e^2\text{fm}^4} \\
\lambda(E3) =& 5.67 \cdot 10^{2} \frac{1}{\text{s}} \cdot \left(\frac{E_\gamma}{\text{MeV}}\right)^7 \cdot \frac{B(E3)}{e^2\text{fm}^6} \\
\lambda(M1) =& 1.76 \cdot 10^{13} \frac{1}{\text{s}} \cdot \left(\frac{E_\gamma}{\text{MeV}}\right)^3 \cdot \frac{B(M1)}{\mu_{\text{N}}^2\text{fm}^0} \\
\lambda(M2) =& 1.35 \cdot 10^{7} \frac{1}{\text{s}} \cdot \left(\frac{E_\gamma}{\text{MeV}}\right)^5 \cdot \frac{B(M2)}{\mu_{\text{N}}^2\text{fm}^2} \\
\lambda(M3) =& 6.28 \cdot 10^{0} \frac{1}{\text{s}} \cdot \left(\frac{E_\gamma}{\text{MeV}}\right)^7 \cdot \frac{B(M3)}{\mu_{\text{N}}^2\text{fm}^4}
\end{aligned} \tag{2.14}$$

Comparing these equations reveals that electric transitions are in general about two orders of magnitude stronger than magnetic transitions of equal multipole orders. For one radiation character the decay probability reduces drastically if l is increased. Due to this, the most important transition types are an $E1$ transition or an $E2$ transition or a $M1$ transition. If $E1$, $E2$ or $M1$ transitions are allowed, higher transition orders are unlikely and rarely observed. If $E1$, $E2$ or $M1$ transitions are forbidden, the next higher transition order is dominant.

In the following work different theoretical shell model calculations will be compared to the

experimental results for excited states in ^{16}C and ^{23}Ne (cf. Sec. 2.6 and 2.9). For these cases often $E2$ transitions are dominant. In shell model calculations Equation 2.10 can be expressed as

$$B(E2; J_{\mathrm{i}}^{\pi} \rightarrow J_{\mathrm{f}}^{\pi}) = \frac{1}{2J_{\mathrm{i}}+1} \left| M_{\mathrm{p}} e_{\mathrm{p}} + M_{\mathrm{n}} e_{\mathrm{n}} \right|^2 \tag{2.15}$$

for $E2$ transitions [SZZS04, dS59]. Here M_{p} and M_{n} are shell model proton and neutron quadrupole matrix elements connecting the J_{i}^{π} and J_{f}^{π} states. The parameters e_{p} and e_{n} are the effective proton and neutron charge. The effective charges can be used to compensate truncation of the model space which is used in the theoretical calculations. They simulate virtual excitations of particles from closed shells to higher shells which are normally forbidden due to the model space truncation [dS59]. Their exact value depends on the shell configuration of the investigated nucleus. Standard values to reproduce transition strengths for a wide range of medium mass nuclei with a symmetrical number of protons and neutrons are e_{p}=1.3 and e_{n}=0.5. If a neutron-rich isotope as ^{16}C is investigated the excitations are dominated by the excessive valence neutrons. Here, the neutrons are less bound which means that their wave function is more spread out and hence the core polarization becomes smaller [BM69, BM75]. In such cases the effective neutron charge and the $E2$ transition strength decrease significantly [SZZS04].

2.2 Gamma-Ray Spectroscopy and Semiconductor Detectors

To measure the lifetime of excited states it is typically necessary to detect the emitted gamma rays. Gamma rays can interact via several mechanisms with matter. For spectroscopy, the main important interactions are the *photo effect*, the *Compton scattering*, and the *pair production*. Which interaction dominates is determined by the atomic number Z of the detector material and the energy of the gamma ray. For small energies around 0.1 MeV, the *photo effect* is the main important one. Here the gamma ray is fully absorbed by an atom from the detector material and an electron is ejected. The total energy of the gamma ray is transferred to the electron. As a result the electron overcomes the binding energy of the atom and gains some kinetic energy which is equal to the gamma-ray energy minus the binding energy of the electron. This electron can create an electrical signal which can be measured. The signal has to be proportional to the kinetic energy of the electron and so the signal is proportional to the energy of the gamma ray. For energies between a few hundred keV up to a few MeV, the *Compton scattering* dominates. During the *Compton scattering*, the gamma ray scatters inelastically on a loosely bound electron from the detector material. Hence, the gamma ray changes its energy and direction while the electron is kicked out of the atom and gains some kinetic energy. If *Compton scattering* happens inside a detector, it is possible that the gamma ray just deposits a part of its energy (the kinetic energy the electron takes) and then leaves the detector material again. Above 5 MeV, the *pair production* dominates. During the *pair production*, the energy of the gamma ray is transferred into the creation of

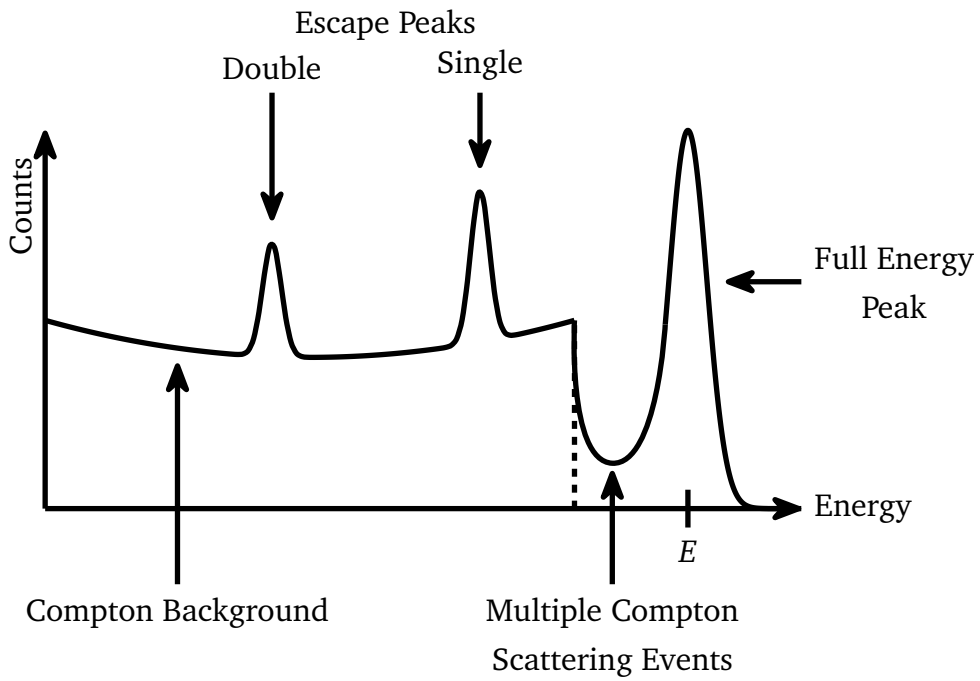

Figure 2.2: Qualitative spectrum obtained from a gamma-ray detector with a realistic size for a single gamma-ray energy E (cf. [Mat16, Gil08, Kno00]). The gamma-ray energy E was larger than $1.022\,\mathrm{MeV}$.

an electron-positron pair. The gamma ray needs an energy of at least $E{=}2m_\mathrm{e}c^2{\approx}1.022\,\mathrm{MeV}$ to enable this process. The electron and positron create a measurable signal. Here, the positron annihilates again with an electron from the material. During the annihilation, two additional photons are created which have an energy of 511 keV each. These can now deposit their energy inside the detector material as well or leave it. The cross section that an interaction happens in a material with the atomic number Z scales with $Z^{4..5}$ for the *photo effect*, with Z for the *Compton scattering* and with Z^2 for the *pair production* [ES08].

To measure the full energy of a gamma ray, it is important that the whole energy is deposited inside the detector. This means that inside the detector a sequence of interactions has to happen which ends with the *photo effect* for the main gamma ray and all secondary created photons. In reality, this does not happen for all gamma rays and a complex spectrum like the one shown in Fig. 2.2 is obtained. The figure shows a qualitative spectrum obtained from a gamma-ray detector for a single gamma-ray energy $E{>}1.022\,\mathrm{MeV}$. On the right end of the spectrum, we see the so-called full energy peak at the energy E. This peak corresponds to interactions which ended with a *photo effect* and the whole energy is deposited inside the detector. Left from this peak, we have a section which stems from a scattering sequence of multiple Compton events in the detector before the gamma ray left the detector. Left from this, we have the so-called Compton edge. It is a sharp edge in the spectrum. Here the gamma ray interacted once with the detector via one *Compton scattering* while the maximum possible energy was transferred to

the electron (the gamma ray was scattered by 180°). Left from the Compton edge, we have a continuous Compton background which corresponds to a single *Compton scattering* for which not the maximum possible energy was transferred to the electron. If the gamma-ray energy E was larger than 1.022 MeV, two so-called escape peaks can be seen on top of the Compton background. The reason for this peak is the *pair production*. There, one (single escape) or two (double escape) photons of the annihilation process left the detector and were not measured. The peaks are located at $E-511\,\text{keV}$ and $E-2{\cdot}511\,\text{keV}$.

One main goal of gamma-ray spectroscopy is to increase the ratio between counts in the full energy peak and the counts in the complete spectrum. This ratio is called the peak-to-total-ratio. To increase the peak-to-total-ratio the easiest way is to build a large detector. Increasing the size of the detector faces two problems. First of all, the size of the detector is limited due to technical reasons. Second, it is not always an advantage to have large detectors. As it can be read in the next Sections 2.3 and 2.5, it is important to measure the gamma-ray energy and the radiation angle of the gamma ray at the same time to correct the Doppler shift or to exploit the Doppler shift for lifetime measurements. This is not possible with a large detector. To use small detectors, but still get a large peak-to-total-ratio, one uses solid state detectors with large Z (the *photo effect* cross section scales faster with Z than the *Compton scattering* cross section). Another method to achieve an even better peak-to-total-ratio is the so-called Compton suppression. Here the actual gamma-ray detector material, which has good detector properties e.g. energy resolution, is surrounded by an active shielding. This shielding is chosen so that it has a very large total cross section for any kind of gamma interaction. Other detector properties do not matter for the shielding. Every time a gamma ray scatters out of the detector, it most probably will interact in the shielding. Then the active shielding can send a veto to suppress the signal from the actual detector. Hence, events for which not the total energy is deposited in the detector will be ignored and the peak-to-total-ratio rises.

Today, semiconductor detectors are often the favourite choice to be used in gamma-ray spectroscopy. The reason for this is the combination of good detector properties semiconductor detectors have. Semiconductors in general are solids with a fixed crystalline structure with a small energy gap of $\approx$1 eV between the conduction band and the valence band. To increase the conductivity, it is possible to dope the semiconductors by implanting impurity atoms into the crystal lattice. Here, two types are possible. On the one hand, it is possible to implant atoms which have one valence electron more than the lattice atoms. As a result additional electrons are added to the system which are energetically just below the conduction band. Here electrons form the majority of the charge carriers and this type of semiconductor is called n-type semiconductor. On the other hand, it is possible to implant atoms which are missing one valence electron compared to the lattice atoms. Then electron-holes are created just above the valence band. So

the majority of charge carriers are positive holes and these semiconductors are called p-type semiconductors.

To build a semiconductor detector, a n-type and a p-type semiconductor are brought in contact. Because of the different charge carrier concentrations, a concentration gradient arises. Hence, the excess electrons of the n-type are moving towards the p-type and the excessive positive holes of the p-type are moving towards the n-type. This leads to a zone in which the holes and electrons can recombine and a depletion layer is generated. The depletion layer can have a thickness of a few µm and no free charge carriers are available for conduction. This area can be increased by applying a bias voltage. The depletion layer can now be used as an active detector area. When the area is hit by a gamma ray, it transfers its energy to an electron which then interacts with the surrounding electrons. Hence, the electron-hole pairs are separated again and a measurable current is created. For this process the number of separated electron-hole pairs is proportional to the deposited energy. While the deposited gamma-ray energy is in the range of a few hundred keV up to a few MeV, the energy to separate an electron-hole pair is in the range of electron-volts. One interaction can separate millions of electron-hole pairs. Due to this, statistical fluctuations are small and so the achieved energy resolution is very good. Today e.g. High Purity Germanium (HPGe) detectors are widely used. With a band gap of only 0.7 eV at ≈90 K, an energy resolution of FWHM/E_0≈0.2 % at E_γ=1.33 MeV is achievable [ES08]. Additionally, with an atomic number of Z=32, germanium has a large proton number compared to other elements which are available for semiconductor manufacturing. This large charge number increases the probability for an interaction of a gamma ray and thus leads to an increase of the peak-to-total-ratio. Also, HPGe can be manufactured in a very large size in the range of ≈10 cm. All in all, semiconductor detectors and especially HPGe detectors are a good choice for gamma-ray detection. This section was adopted from [Mat16, Kno00, ES08, Gil08].

2.3 Relativistic Doppler Shift

This thesis investigates an experiment in which the nuclei of interest are moving while they are emitting gamma rays. In this case, the relativistic Doppler effect needs to be considered for energy measurements. Let's assume that a nucleus is moving in the laboratory frame along the vector $\boldsymbol{x}$ with the velocity v=$|v|$. During the flight, the nucleus de-excites by emitting a gamma ray with the energy E_{cm} in the rest frame of the nucleus. Then an observer in the laboratory frame will measure the Doppler shifted energy

$$E_{\mathrm{Lab}}(\beta, \theta_{\mathrm{Lab}}) = \frac{E_{\mathrm{cm}}}{\gamma\,(1-\beta\cos\theta_{\mathrm{Lab}})} = E_{\mathrm{cm}}\frac{\sqrt{1-\beta^2}}{1-\beta\cos\theta_{\mathrm{Lab}}}, \tag{2.16}$$

where θ_{Lab} is the so-called radiation angle between the direction of the emitted gamma ray and $\boldsymbol{x}$ [Sta15, Jac62]. The coefficient β is defined as β=v/c with the speed of light c and

$\gamma = 1/\sqrt{1-\beta^2}$ is the Lorentz factor. For a velocity much smaller the speed of light, Equation 2.16 can be approximated via

$$E_{\mathrm{Lab}}(\beta, \theta_{\mathrm{Lab}}) \underset{\beta \ll 1}{\approx} E_{\mathrm{cm}} \frac{1}{1-\beta\cos\theta_{\mathrm{Lab}}}. \tag{2.17}$$

So for a small β the Doppler shift vanishes if the radiation angle θ_{Lab} is 90°. Due to the fact that the center of mass radiation angle θ_{cm} will never play a role in the following analysis, θ_{Lab} will also be written as θ for simplification.

2.4 Lifetime Measuring Techniques

The main goal of this work is to measure the lifetimes of excited nuclear states in ^{16}C. Many different lifetime measuring techniques have been developed in the past. First of all, one has to distinguish between direct and indirect methods. Direct methods use a technique to directly get access to the lifetime of the state. Indirect methods are techniques which measure the energy width of the excited state and then calculate the lifetime using Equation 2.11. The expected lifetimes in this thesis are in the range of a few hundred femtoseconds up to a few picoseconds, which means $\approx 10^{-13}\,\mathrm{s} - 10^{-12}\,\mathrm{s}$ [PPC+12, WFM+08]. Using this as an input in Equation 2.11, the expected line width would be $\Gamma \approx 10^{-2}\,\mathrm{eV} - 10^{-3}\,\mathrm{eV}$, which is not measurable with common gamma-ray detectors. Therefore, a direct technique has to be used. An overview over all classical direct lifetime measuring techniques is illustrated in Figure 2.3. Here the lifetime ranges for which a technique obtains suitable results are shown.

If the lifetime is longer than $10^{-11}\,\mathrm{s}$, electron timing methods become available. Here the exponential decay of the states is measured to extract the lifetime directly. To do so, the experiment has to be designed in a way that there is the possibility to know at which time the state of interest was populated. These methods are strongly limited by the time resolution of the used electronics. For shorter lifetimes it is just not possible to measure the exponential decay because the electronics can not resolve decays at different times any more. Down to $10^{-12}\,\mathrm{s}$, the so-called Recoil Distance Method (RDM) is available. In this method, the particle of interest is shot on a thin target where the nucleus gets excited. Afterwards, it travels a known distance before it enters a degrader which slows the particle down. The gamma rays are emitted in-flight. Due to the relativistic Doppler shift (cf. Sec. 2.3), one can distinguish between gamma rays which were emitted before (particle is fast during decay) and after (particle is slowed down before decay) the degrader. By looking at the ratio of decays which happened before and after the degrader, the lifetime can be accessed. This method is limited by the smallest finite distance between target and degrader which can be measured safely. A detailed overview about the RDM can be found in e.g. [DMP12]. If the lifetime is even shorter ($5 \cdot 10^{-13}\,\mathrm{s} - 10^{-10}\,\mathrm{s}$), the Doppler-Shift Attenuation Method (DSAM) is available. Here the degrader is directly mounted behind the target. Hence, the nuclei of interest are continuously slowed down in the degrader while they are emitting the

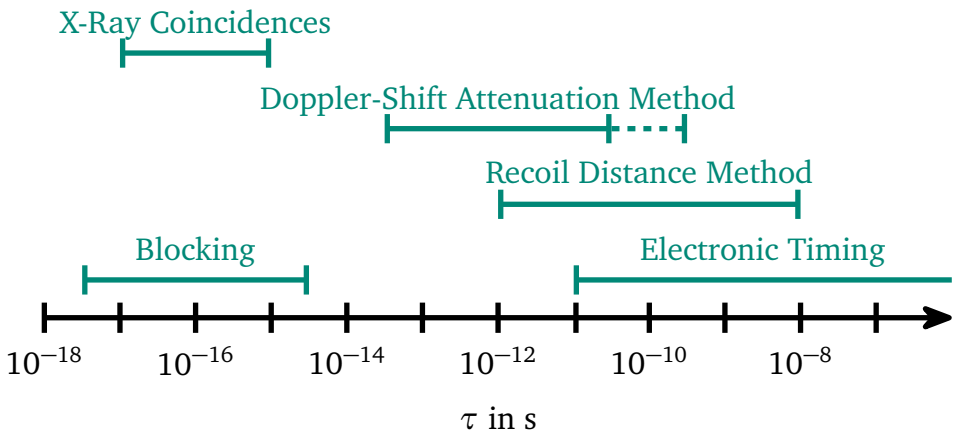

Figure 2.3: Ranges for different direct lifetime measuring techniques. Figure modified and reprinted from [NSS79] with permission from IOPScience.

gamma rays. Then, the lifetime can be accessed by looking at the influence of the Doppler effect on the gamma-ray spectra (cf. Sec. 2.5). To access lifetimes in the range of $5 \cdot 10^{-17}\,\mathrm{s} - 5 \cdot 10^{-14}\,\mathrm{s}$ the so-called blocking method is used. This method is similar to the RDM but now the travel time of the excited nuclei of interest is measured between two lattice atoms in a crystal. So on one hand, the blocking method is sensitive for much smaller lifetimes than the RDM, but on the other hand, it is much more difficult to realise this method. There are also a few other so-called exotic techniques like the X-ray coincidences method ($10^{-17}\,\mathrm{s} - 10^{-15}\,\mathrm{s}$) which will be not discussed in this thesis. A much more detailed discussion about all the methods mentioned so far can be found in [NSS79].

Furthermore, a new generation of gamma-ray detectors is available nowadays. These position sensitive gamma-ray detectors, such as GRETA/GRETINA [DLV+99, LCC+04, PLM+13, ES08] or AGATA [AAA+12, ES08] also allow new lifetime measuring techniques. The heart of these new devices are electronically segmented Ge detectors, which make it possible to measure the interaction position of the gamma rays inside the detectors. This additional information allows the tracking of the interaction path of a gamma ray inside the detectors. This process is called gamma-ray tracking. With this tracking, the radiation angle of the gamma ray can be determined much more precisely as a continuous quantity. Exploiting this information, the new continuous-angle Doppler-Shift Attenuation Method is available [Sta15]. This method is based on the DSAM but can compare measured line-shapes between simulation and experimental much more precisely and in a wider lifetime range. This stems from the fact that the line shape can now be analysed also as a function of the polar angle as a continuous quantity instead of discrete radiation angles. Another new method is the lifetime measurement via decay position reconstruction, which was investigated in [Mat16]. Here the information of the gamma-ray tracking is used to reproduce the decay positions of the nuclei which decay in-flight after passing a thin target. With this a decay position distribution can be achieved, which is directly sensitive to the lifetime of

the excited state. The range of lifetimes for which this method is feasible depends strongly on the beam velocity because the beam velocity strongly influences the width of the decay position distribution. For a beam velocity of $\beta \approx 0.4$, the measurable lifetime range is in the order of hundreds of picoseconds [Mat16].

2.5 Doppler-Shift Attenuation Method

In this work, the expected lifetimes are in the range of $\approx 10^{-13}\,\mathrm{s} - 10^{-12}\,\mathrm{s}$ [PPC+12, WFM+08]. Also, the gamma-ray detector Gammasphere [Lee90] was used during the experiment which can measure the emitted gamma rays under 17 different angles covering ≈46 % of the total solid angle (cf. Sec. 3.3). Because of these reasons, the DSAM is the method of choice for the experiment discussed here. The DSAM was first applied in 1948 by Elliott and Bell [EB48, NSS79]. Since then, it was widely used to measure the lifetimes of excited states for many different (exotic) nuclei.

The basic idea of the DSAM is illustrated in Figure 2.4 top. Here an incoming particle beam with velocity β_B hits a thin reaction target. Inside this target some kind of reaction happens between the beam nuclei and the target nuclei. After the reaction, the residual nuclei can be excited in the state of interest and have the velocity β_0. Those excited nuclei enter the so-called degrader, which is placed directly behind the target. Its material is chosen so that the probability of further reactions is small while the nuclei are slowed down sufficiently. This leads to materials with a large Z. In most cases, the thickness of the degrader is scaled so that all nuclei are stopped inside the degrader. While the excited nuclei travel through the degrader they can emit gamma rays.

The number of emitted gammas, $N(x)$, which decay at position x, depends on the lifetime τ of the excited state and follows the exponential decay law

$$N(x) \propto \mathrm{e}^{-\frac{t(x)}{\tau}}. \tag{2.18}$$

This equation uses the fact that the elapsed time $t(x)$ corresponds to the position x at which the decay happens (cf. Fig. 2.4 bottom). How many gamma rays are emitted for stopped particles depends strongly on the lifetime of the state. If the lifetime exceeds a certain value, decays can happen while the excited nuclei is already at rest in the degrader.

Additionally, the velocity $\beta(x)$ of the nuclei at position x decreases while the covered distance in the degrader grows. Because of this, the Doppler shifted energy $E_\mathrm{Lab}(\beta(x), \theta)$, which is measured in the laboratory frame, also depends on the position x of the decay. A schematic visualisation of this behaviour is illustrated in the bottom part of Figure 2.4.

So, the longer the lifetime of a state, the more excited nuclei will travel further in the degrader before they decay and will have a smaller velocity during the decay. This means that the mean

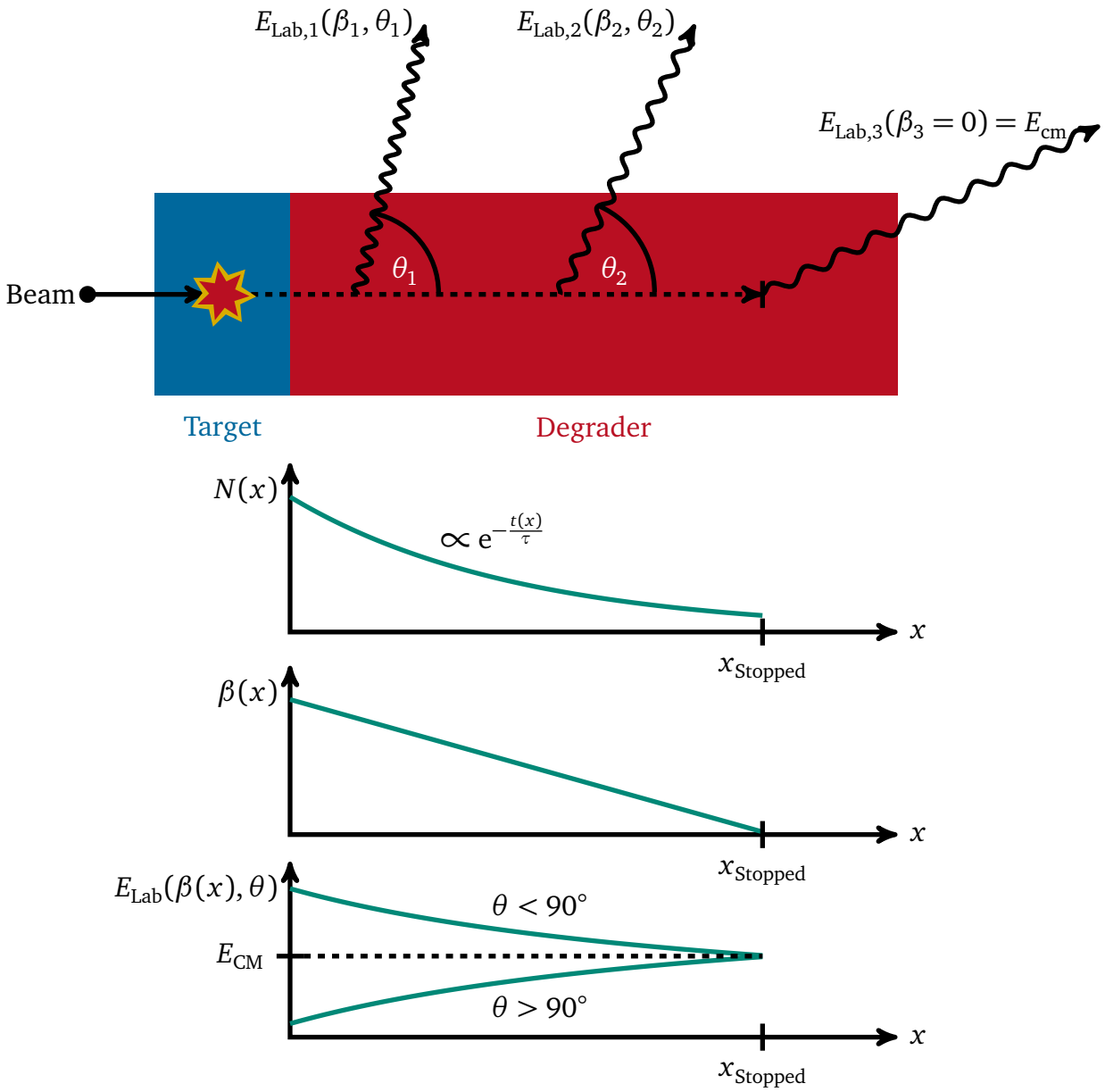

Figure 2.4: Principle of the DSAM. Top: A particle beam hits a target where the reaction of interest (marked by the star) happens. Afterwards, the excited particles (dashed line) pass through the degrader which slows them down until they are stopped. During this process gamma rays can be emitted at all positions (three examples are shown). The energy $E_{\mathrm{Lab}}(\beta, \theta)$ of the gamma rays which is measured in the laboratory frame can be calculated with Equation 2.16. Bottom: Schematic drawing of the number of de-exciting nuclei $N(x)$, the velocity of the nuclei $\beta(x)$, and the measured energy $E_{\mathrm{Lab}}(\beta(x), \theta)$ in respect to the position x in the degrader. Due to the fact that the measured gamma-ray energy depends on the position x of the decay and that the number of decays at a given position x depends on the lifetime, the measurement of $E_{\mathrm{Lab}}(\beta(x), \theta)$ is sensitive to the lifetime of the excited state.

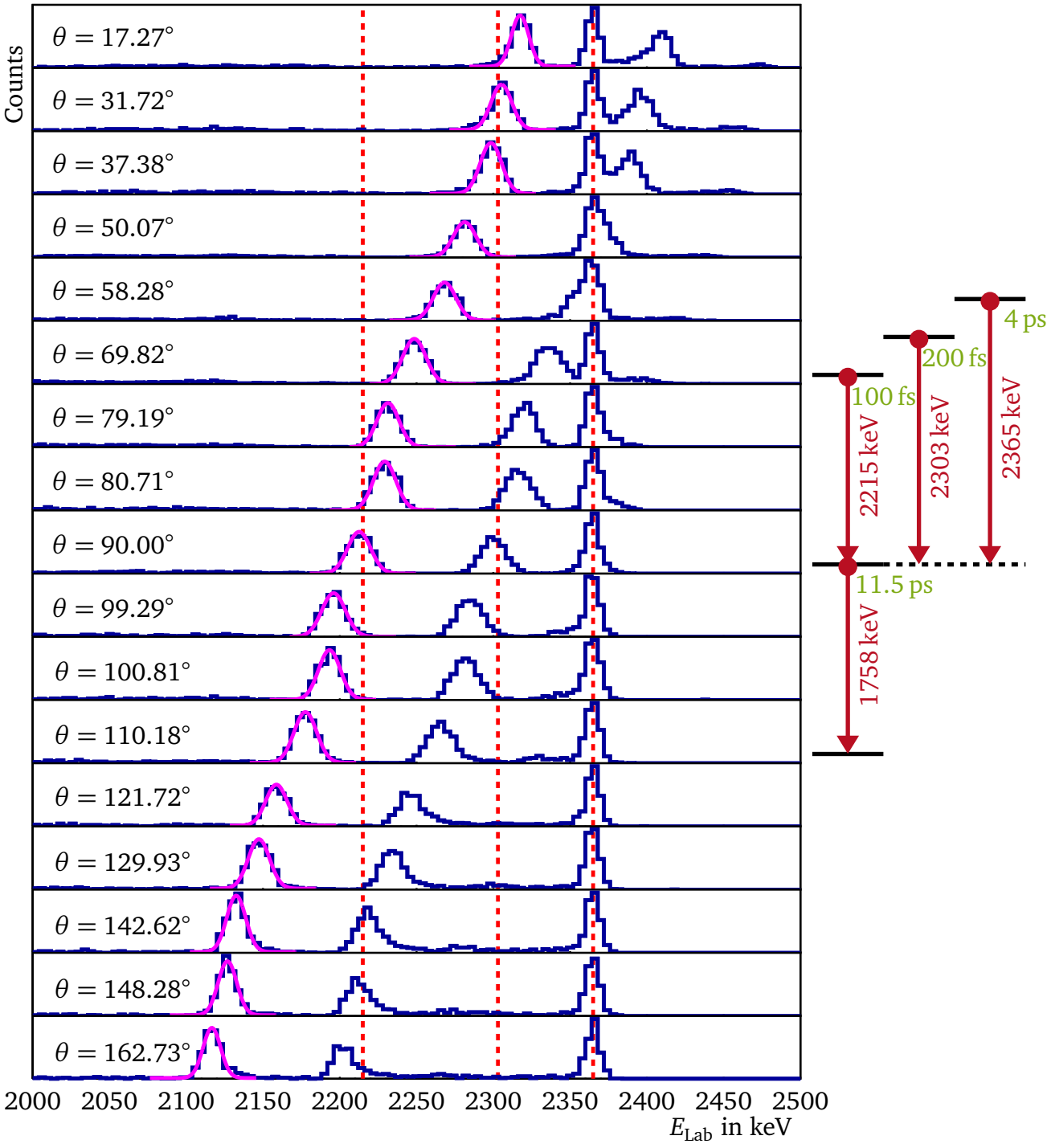

Figure 2.5: This figure shows simulated spectra of a DSAM measurement. In the Geant4 simulation, the excited nuclei of interest were randomly spawned inside a Be target with β_0=0.05 along the beam axis and slowed down in an Au degrader. For excitation, three different levels could be populated (cf. level scheme to the right). Each level decays via one possible gamma-ray transition. The center-of-mass gamma-ray energies are 2215 keV, 2303 keV and 2365 keV. The lifetimes of the state are 100 fs (left peak), 200 fs (middle peak) and 4 ps (right peak). The purple function is a Gaussian fit to obtain the shift of the centroid $\overline{E}_{\mathrm{Lab}}$ as a function of θ.

decay velocity $\overline{\beta}$ gets smaller for longer lifetimes and thus the Doppler shift has a smaller influence on the gamma-ray energy in the laboratory frame. As a conclusion of these facts, the mean decay velocity $\overline{\beta}$ is directly sensitive to the lifetime of the excited state. To get access to $\overline{\beta}$,one exploits Equation 2.16 and modifies it to

$$E_{\mathrm{Lab}}(\overline{\beta},\theta) = E_{\mathrm{cm}}\frac{\sqrt{1-\overline{\beta}^2}}{1-\overline{\beta}\cos\theta}. \tag{2.19}$$

By measuring the centroid shift of the energy E_{Lab} as a function of θ, it is possible to determine the mean decay velocity $\overline{\beta}$ of the excited state. By comparing the experimental measured $\overline{\beta}$ to different assumed theoretical values for $\overline{\beta}$, one gets access to the lifetime of the excited state. In this work, the theoretical $\overline{\beta}$ will be obtained using Geometry and Tracking Toolkit (Geant4) simulations which are discussed in Chapter 4. If the lifetime is too long, nearly all or all excited nuclei will decay at rest and no Doppler effect occurs. Then the method can not be applied any more. This sets an upper lifetime limit for this method.

To define θ, the mounting angles at which the detectors are placed are used. The angles θ are always measured relative to the beam axis. But these are not the real radiation angles of the gamma rays. The excited nuclei suffer lateral straggling while they pass the degrader. Hence, the direction of movement does not align with the beam axis anymore and so the mounting angle of a detector is not the same as the radiation angle. But due to the fact that the straggling is uniformly distributed in all directions around the beam axis, these effects cancel on the average. As a result, the mounting angle can still be used and can be seen as a mean radiation angle θ. The straggling just adds an additional peak broadening to the energy spectra.

A simulation of a DSAM measurement can be seen in Figure 2.5. The figure shows the measured laboratory energy E_{Lab} for several different θ for three different states with three different lifetimes; namely 100 fs, 200 fs and 4 ps (cf. level scheme at the right side of Fig. 2.5). The excited nuclei were randomly spawned inside a Be target with β_0=0.05 and are slowed down in an Au degrader. The three gamma-ray energies in the center-of-mass system E_{cm} (2215 keV, 2303 keV and 2365 keV) are marked by the red dashed lines. One can see that the centroid energy $\overline{E}_{\mathrm{Lab}}$ which belongs to the state with 4 ps is not moving in the different spectra because for this state all decays happen when the nuclei are already fully stopped. For this state, the mean decay velocity $\overline{\beta}$ is zero and hence no lifetime could be obtained in an experiment with the DSAM. For the two other states, the centroid energy E_{Lab} is moving around E_{cm} as a function of θ. At θ=90° the effect of the Doppler shift vanishes due to the fact that β is small and $E_{\mathrm{Lab}}\approx E_{\mathrm{cm}}$. For the 100 fs state, the centroid energy is moving in a wider range compared to the movement of the centroid energy for the 200 fs state. This is due to the fact that a smaller lifetime has a larger $\overline{\beta}$ and the Doppler effect has a larger influence. Another representation of the simulated data can be seen in the 2D plot of Figure 2.6. Here, the radiation angle is plotted versus the laboratory energy of the measured gamma rays. For this the discrete angles of Gammasphere were randomized

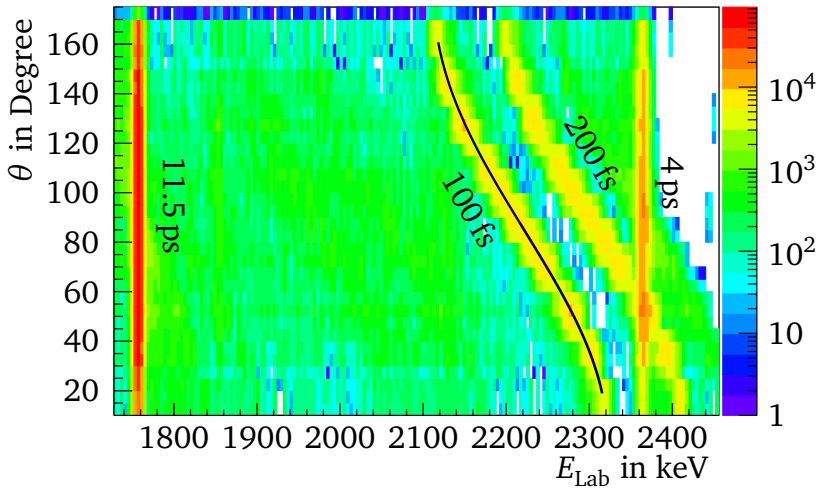

Figure 2.6: Radiation angle versus laboratory energy for a simulated DSAM measurement. The plot is a different representation of the data from Figure 2.5. In the Geant4 simulation, the excited nuclei of interest were randomly spawned inside a Be target with β_0=0.05 along the beam axis and slowed down in an Au degrader. For excitation, three different levels could be populated. Each level decays via one possible gamma-ray transition and all populate one long-living state which decays after 11.5 ps. The level scheme can be seen in Figure 2.5 to the right. The lifetimes of the states are labelled in the figure. The black function is obtained with the fit which is shown in Figure 2.7 (a).

around their center value. This representation will be later used to show the experimental results because it is more clearly and more compact compared to the representation in Figure 2.5. But the values for E_{Lab} are always obtained by Gaussian fits to the discrete spectra from Figure 2.5.

If, for the here shown example, the lifetime of the state is somewhere between 200 fs and 4 ps it is possible that one transition produces two peaks, for which one peak is moving for different detection angles and one peak is not moving. This is explained with the fact that for such lifetimes a part of the nuclei decay in-flight and a part decay while the nuclei are already fully stopped. The non-moving peak corresponds to the part of nuclei which are already in rest when the gamma decay happen. The longer the lifetime, the larger the stopped component will be until only a stopped component is available (e.g. for 4 ps). This behaviour can also be used for a lifetime estimation as explained and applied in Section 6.5.1.

Furthermore, Figure 2.7 shows E_{Lab} as a function of $\cos\theta$ for the two states with the shorter lifetime. The centroid energy E_{Lab} was obtained by fitting a Gauss-function to the corresponding peak in Figure 2.5 (purple line). To these data points Equation 2.19 is fitted to obtain the mean decay velocity. In this example, the results are $\overline{\beta}$=0.0472(1) for the 100 fs state and $\overline{\beta}$=0.0459(1) for the 200 fs state, which shows that the lifetime of these two states would be resolvable in an experiment.

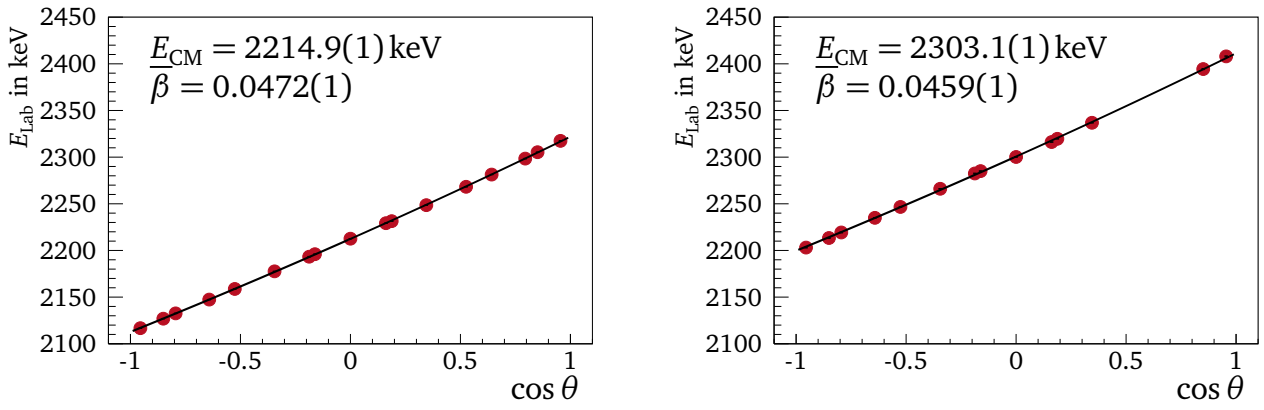

(a) τ=100 fs (b) τ=200 fs

Figure 2.7: E_{Lab} as a function of $\cos\theta$ for β_0=0.05 and τ=100 fs (left) as well as for τ=200 fs (right) created with simulated data. For the τ=100 fs state, 17 data points are available which are obtained from the purple fits in Figure 2.5. For the τ=200 fs state, only 14 data points are available because for some forward angles the moving peak interferes with the peak from the τ=4 ps state (cf. Fig. 2.5 top).

The time scale for the DSAM and the mean decay beta $\overline{\beta}$ for a given τ is defined by the slowing down time of the excited nucleus in the degrader material. Following [NSS79], the attenuation factor F is introduced. It is defined as the ratio between the mean decay velocity $\overline{\beta}$ and the initial velocity β_0 and hence $0 \leq F \leq 1$. The factor can be expressed as

$$F = \frac{\overline{\beta}}{\beta_0} = \frac{1}{\beta_0 \tau} \int_0^\infty \beta(t) e^{-\frac{t}{\tau}} dt \tag{2.20}$$

where $\beta(t)$ describes how the excited nuclei are slowed down in the degrader. It is quite difficult to get an analytical form for $\beta(t)$. A first rough approximation, which is a good description for the electronic stopping process, assumes that the rate of energy loss is proportional to the velocity which can be written as

$$\frac{dE}{dx} \propto v. \tag{2.21}$$

This fact can also be expressed as

$$\beta(t) = \beta_0 e^{-\frac{t}{\kappa}} \tag{2.22}$$

where κ is the slowing down time constant depending on the properties of the degrader material. This leads to

$$x(t) = \int c\beta(t) dt \quad \Rightarrow \quad t = -\kappa \ln\left(-\frac{x}{c\beta_0\kappa}\right) \underset{t \text{ in Eq. 2.22}}{\Rightarrow} \beta(x) \propto -\frac{x}{\kappa} \tag{2.23}$$

(cf. Fig. 2.4 bottom). Furthermore, using Equation 2.22 as input for Equation 2.20 gives

$$F = \frac{1}{1 + \tau/\kappa} \tag{2.24}$$

for the attenuation factor. By calculating κ theoretically and measuring F, it would be possible to get the lifetime τ. Thereby two problems occur: first of all, the derivation of Equation 2.24 uses a simple approximation which is only roughly valid for electronic stopping processes. In a realistic process, interactions with the nuclei of the degrader also happen. Secondly, it is not simple to calculate the constant κ theoretically. Due to this, Monte Carlo simulations are used to model the slowing down process in the degrader. For these simulations the Geant4 framework is used [Gea14]. More about the Geant4 simulations and the here used implementation can be found in Chapter 4. A crucial point of these simulations is of course the stopping mechanism for nuclei in matter. Therefore, the here used stopping powers and the stopping mechanisms of the simulation are discussed elaborately in Section 4.4.

2.6 The Nuclear Shell Model

To calculate the lifetime of an excited state theoretically, the reduced transition strengths have to be calculated via Equation 2.10 for all possible transitions starting at this state. To do so, the wave functions of the involved states have to be known. To obtain the wave functions the Schrödinger Equation 2.1 has to be solved. Here, the Hamiltonian $\hat{H}$ contains the complete nuclear interaction between all nucleons. The Hamiltonian for a nucleus with A nucleons can be expressed as

$$\hat{H} = \sum_{i=1}^{A} \hat{T}_i + \hat{V}\left(\boldsymbol{r}_1, \boldsymbol{r}_2, ..., \boldsymbol{r}_A\right) \tag{2.25}$$

where $\hat{T}_i$ is the kinetic energy operator for each nucleon i and $\hat{V}$ is the operator for total nuclear potential which depends on the positions $\boldsymbol{r}_i$ of all nucleons. While for nucleons with the mass m the kinetic energy operator $\hat{T}_i$ can be simply expressed as

$$\hat{T}_i = -\frac{\hbar^2}{2m_i}\nabla_i^2, \tag{2.26}$$

a global analytical form for the total nuclear potential $\hat{V}$ is not derived yet. Till today many models were developed which try to approximate $\hat{V}$ in such a way that it is possible to solve the Schrödinger equation and to get reasonable results at the same time. Especially for exotic nuclei with an unequal ratio of protons and neutrons it becomes very hard to solve the Schrödinger equation with reasonable effort and hence various approximations have been developed [SH15]. Here two complementary approaches are possible: On one hand semi-empirical methods are

available which use phenomenological equations deduced from experimental data and observations concerning nuclei. On the other hand ab initio calculations are available for which $\hat{V}$ is deduced by using fundamental physical properties and constants of the strong force which results in the nuclear force. While the ab initio approach is discussed in Section 2.7 the empirical approach is discussed in this section focusing on the simple nuclear shell model and follows the descriptions from [Ber07, SP08, Hei19].

In the first step towards the nuclear shell model the short range of the nuclear force is exploited and so only two-body interactions are considered in the potential $\hat{V}$. With this assumption the Hamiltonian from Equation 2.25 can be changed to

$$\hat{H} = \sum_{i=1}^{A} \hat{T}_i + \sum_{i<j=1}^{A} \hat{V}_{ij}\left(\boldsymbol{r}_i, \boldsymbol{r}_j\right). \tag{2.27}$$

In this new Hamiltonian the operator $\hat{V}_{ij}$ represents the two-body potential between the nucleons i and j. By defining $\hat{V}_{ij}$ via simple semi-empirical expressions it is in principle possible to solve the Schrödinger equation using Slater determinants which are derived from a given basis (cf. beginning of Sec. 2.8). This procedure is equivalent to diagonalizing the respective matrix of the Hamiltonian $\hat{H}$ from Equation 2.27 to obtain its eigenvalues. Here it has to be taken into account that for an exact solution an infinite set of bases has to be used, which is not feasible for real calculations. Hence, the basis range has to be truncated which can influence the obtained results. Although only two-body potentials are used in this method and the basis is truncated strongly, it still becomes quickly impossible to apply this method to larger nuclei. The dimensionality of this problem rises too fast when A is increased and even with modern computers this approach is not feasible. To overcome this problem a central potential $\hat{U}_i$ is introduced to the shell model. The central potential should represent a mean potential which interacts with nucleon i and is created from the average interaction between nucleon i and all remaining nucleons. By adding $0 = \sum_i \left[\hat{U}_i - \hat{U}_i\right]$ to Equation 2.27 one obtains the relation

$$\hat{H} = \underbrace{\sum_{i=1}^{A}\left[\hat{T}_i + \hat{U}_i(\boldsymbol{r}_i)\right]}_{\hat{H}_{\text{Cen}}} + \underbrace{\sum_{i<j=1}^{A} \hat{V}_{ij}\left(\boldsymbol{r}_i, \boldsymbol{r}_j\right) - \sum_{i=1}^{A} \hat{U}_i(\boldsymbol{r}_i)}_{\hat{H}_{\text{Res}}}. \tag{2.28}$$

Here, $\hat{H}_{\text{Res}}$ marks the residual interaction which is the difference between the central potential and the real two-body interaction. If the central potential is chosen correctly this term should be small and can be neglected at first order. Hence, the Schrödinger equation has to be only solved for $\hat{H}_{\text{Cen}}$ which describes A independent particles in a central potential. This problem can be solved rather easily and results in the famous simple nuclear shell model first derived by M. Goeppert-Mayer, E. P. Wigner, and J. H. D. Jensen in 1949 independently from each other.

They used a Wood-Saxon potential in combination with a spin-orbit interaction for the central potential. With this model it was for the first time possible to describe systematics in nuclei over a large range, such as the magic numbers or ground state spins by assigning the nucleons to fixed discrete energy levels. The lowest energy levels according to the simple shell model are shown in Figure 2.8 for protons and neutrons separately. One energy level is also called an orbit which is defined by a given angular momentum l ($l \widehat{=} s, p, d, f, ...$) and the total angular momentum $J = l + s$ stemming from the spin-orbit term. The number of nucleons per orbit is limited due to the Pauli principle. If the separation energy between two orbits is large a new shell starts. With the shell closures the magic numbers can be explained. The angular momentum of a state is now defined by the angular momenta of the orbits which are occupied by an odd number of nucleons. Orbits which are full or occupied by an even number of nucleons will not contribute to the properties of the state because the spins of a pair of nucleons couple to zero. When it comes to higher excited states or to exotic nuclei with an extreme proton to neutron ratio or nuclei far away from closed shells, the simple shell model loses its validation very quickly.

Then the residual interaction has to be considered as well. Assuming that nucleons from low lying fully occupied orbitals will not contribute to the behaviour of the nucleus, the Hamiltonian can be divided into a core with $A-N$ nucleons and N valence nucleons orbiting the core. This leads to

$$\hat{H} = \hat{H}_{\text{Core}} + \hat{H}_{\text{Val}} \tag{2.29}$$

with

$$\hat{H}_{\text{Core}} = \sum_{i=N+1}^{A} \left[\hat{T}_i + \hat{U}_i(\boldsymbol{r}_i)\right] \quad + \sum_{i<j=N+1}^{A} \hat{V}_{ij}(\boldsymbol{r}_i, \boldsymbol{r}_j) - \sum_{i=N+1}^{A} \hat{U}_i(\boldsymbol{r}_i) \tag{2.30}$$

$$\hat{H}_{\text{Val}} = \sum_{i=1}^{N} \left[\hat{T}_i + \hat{U}_i(\boldsymbol{r}_i)\right] \quad + \sum_{i=1}^{N} \sum_{j=N+1}^{A} \hat{V}_{ij}(\boldsymbol{r}_i, \boldsymbol{r}_j) + \sum_{i<j=1}^{N} \hat{V}_{ij}(\boldsymbol{r}_i, \boldsymbol{r}_j) - \sum_{i=1}^{N} \hat{U}_i(\boldsymbol{r}_i) \tag{2.31}$$

for the Hamiltonians. If one considers again just two-body interactions the same trick can be applied a second time by interpreting the second part as residual interactions which are small. This changes the equations to

$$\hat{H}_{\text{Core}} = \sum_{i=N+1}^{A} \left[\hat{T}_i + \hat{U}_i^{\text{Core}}(\boldsymbol{r}_i)\right] \tag{2.32}$$

$$\hat{H}_{\text{Val}} = \sum_{i=1}^{N} \left[\hat{T}_i + \hat{U}_i^{\text{Core}}(\boldsymbol{r}_i)\right] + \sum_{i<j=1}^{N} \hat{V}_{ij}(\boldsymbol{r}_i, \boldsymbol{r}_j) \tag{2.33}$$

with

$$\hat{U}_i^{\text{Core}} = \sum_{j=N+1}^{A} \hat{V}_{ij}(\boldsymbol{r}_i, \boldsymbol{r}_j) \tag{2.34}$$

as a mean potential produced by the two-body forces of the nucleons of the inner core. Hence, the residual interaction which plays a significant role is limited to the valence nucleons. This approach truncated the dimensionality of the problem drastically, but still considers residual interactions in terms of two-body forces. For the mean potential different sorts of semi-empirical effective interactions were tested in the past successfully. Their parametrization and the types of considered shells define the range for which the shell model gives reasonable results.

The description of ^{16}C in the framework of the shell model is shown in Figure 2.8 and is discussed in more detail in Section 2.9. On the proton side the two lowest orbits $1s_{1/2}$ and $1p_{3/2}$ are filled, while for the neutrons the three lowest orbits are fully occupied. Hence, the two remaning valence neutrons should mainly determine the behaviour of excited ^{16}C isotopes. They can occupy the s and d orbits in the third shell. But also the excitation of protons into the $1p_{1/2}$ orbit can influence the results. Hence, p—sd shell model calculations were performed by A. Brown [Bro20, PPC$^+$12] using the `OXBASH` shell model code [BERGed] to describe the properties of ^{16}C. In the calculations harmonic oscillator wave functions were calculated for protons in the p shell model space and neutrons in the sd shell model space. This was done for three different sets of empirically two-body nucleon-nucleon effective interactions, namely WBP [WB92], WBT [WB92], and WBT* [SSS$^+$08]. The interactions are defined by least-squares fits to 51 0p-shell and 165 cross-shell binding energies. While for WBP and WBT the set of experimental data which are included to the fit is varied, the WBT* interaction is based on the WBT interaction, but here the neutron-neutron two-body matrix elements are reduced to 75 %. This was introduced to compensate that the experimental excitation spectra for several carbon isotopes are systematically compressed compared to the WBT results [SSS$^+$08]. The results of these shell model calculations are discussed in Section 6.5.4.

In the later analysis also excited states from ^{23}Ne are investigated. To describe them theoretically Universal sd Shell (USD) calculations were performed by A. Brown [Bro19]. Here only sd shells are considered in the calculations because lower orbits are fully occupied for protons as well as neutrons and so they are treated as an inert core. The interaction is derived from free nucleon-nucleon interactions and modified to fit to various experimental data [BW88]. Later the interaction was redefined to reproduce even better results for neutron-rich nuclei ending in the here used USDB interactions [BR06, RMB08]. The results of the USDB calculations are discussed in Section 6.4.

2.7 Ab Initio Approaches

In the previous section the shell model, which is based on empirical effective interactions, was introduced. By using such empirical approaches one loses the insight to the underlying physics which forms the mean nucleon interactions. To get rid of this problem the so-called ab initio

approach is introduced in this section. It is the goal of such ab initio methods to describe the nuclear force by using deeper fundamental and microscopical physical principles, while the input of experimental data should be kept at a minimum.

A possible ab initio method is the No-Core Shell Model (NCSM) which will be discussed in the next section. It is the basic idea of the ab initio NCSM to expand the Hamiltonian from Equation 2.25 in terms of many-body interactions to

$$\hat{H} = \sum_{i=1}^{A} \hat{T}_i + \sum_{i<j=1}^{A} \hat{V}_{ij}^{\mathrm{NN}}\left(\boldsymbol{r}_i, \boldsymbol{r}_j\right) + \sum_{i<j<k=1}^{A} \hat{V}_{ijk}^{\mathrm{3N}}\left(\boldsymbol{r}_i, \boldsymbol{r}_j, \boldsymbol{r}_k\right) + ... \tag{2.35}$$

Here, $\hat{V}_{ij}^{\mathrm{NN}}$ expresses the two-body interaction which can be compared to the two-body interaction from the simple shell model as introduced in the section before and $\hat{V}_{ijk}^{\mathrm{3N}}$ represents a three-body interaction [BNV13]. In principle this Hamiltonian can be expanded up to any order, but due to the limitation of computation power the expansion is for most cases stopped at the three-body forces. The two-body interactions are still dominant due to the short range of the nuclear force and thus this method can lead to similar behaviours as the shell model. Nevertheless, adding three-body forces is often sufficient enough to see significant changes in the results compared to results for which only two-body interactions are considered. This is particularly pronounced for exotic nuclei for which the number of protons differs strongly from the number of neutrons. Another important advantage of this approach is that the different interactions can now be systematically deduced from more fundamental physics. For this the Quantum Chromodynamics (QCD) is used.

The QCD describes the strong interaction between coloured quarks. These quarks form nucleons which themselves form the nuclei. Hence, the interaction between the nucleons is a residual interaction originating from the strong force [ME11]. To describe the nuclear interactions as a residual force stemming from the strong interaction, the QCD has to be applied in its low energy region. This is highly non-trivial due to the fact that the QCD is non-perturbative in the low energy region because the strong interaction gets more powerful for long distances ($\gtrsim$1 fm). To overcome this problem the chiral Effective Field Theory (EFT) was derived. An elaborate description of the chiral EFT and its development can be found e.g. in [ME11]. Next, a short summary of the idea of the chiral EFT is given following [ME11, Hei19].

The chiral EFT underlies all symmetries of the QCD and the interactions are described by the exchange of hadrons or contact terms. Here, a suitable separation of scales has to be defined which limits the amount of possible hadrons in the calculations to limit the model space and the computational requirements. For the separation of scales the large gap between the masses of the pions (m_{p}=140 MeV/c^2) and the masses of vector mesons like $\rho(770)$ (m_{ρ}=775 MeV/c^2) is appropriate. Hence, the pion mass defines the so-called soft scale $Q{\sim}m_{\mathrm{p}}$ and the rho mass sets a range for the hard scale $\Lambda_{\chi}{\sim}m_{\rho}$, which is also called the chiral symmetry breaking scale.

Using these separation scales the interaction in the chiral EFT can be expanded in terms of the soft scale divided by the hard scale, i.e. Q/Λ_χ. Due to this it is enough to consider pions and of course the nucleons themselves to describe the nuclear interaction in the chiral EFT framework.

As a result from the considerations above, an effective Lagrangian $\mathscr{L}_{\mathrm{Eff}}$ can be expressed as

$$\mathscr{L}_{\mathrm{Eff}} = \mathscr{L}_{\pi\pi} + \mathscr{L}_{\pi\mathrm{N}} + \mathscr{L}_{\mathrm{NN}} + \ldots \tag{2.36}$$

using individual Lagrangians for the pion-pion interaction $\mathscr{L}_{\pi\pi}$, for the interaction between pions and nucleons $\mathscr{L}_{\pi\mathrm{N}}$, and for the contact term of the nucleon-nucleon interaction $\mathscr{L}_{\mathrm{NN}}$. Each individual Lagrangian can be expanded by increasing orders following

$$\mathscr{L}_{\pi\pi} = \mathscr{L}^{(2)}_{\pi\pi} + \mathscr{L}^{(4)}_{\pi\pi} + \ldots \tag{2.37}$$

$$\mathscr{L}_{\pi\mathrm{N}} = \mathscr{L}^{(1)}_{\pi\mathrm{N}} + \mathscr{L}^{(2)}_{\pi\mathrm{N}} + \mathscr{L}^{(3)}_{\pi\mathrm{N}} + \ldots \tag{2.38}$$

$$\mathscr{L}_{\mathrm{NN}} = \mathscr{L}^{(0)}_{\mathrm{NN}} + \mathscr{L}^{(2)}_{\mathrm{NN}} + \mathscr{L}^{(4)}_{\mathrm{NN}} + \ldots \tag{2.39}$$

$$\ldots = \ldots \tag{2.40}$$

for which the superscript reflects the number of derivatives or pion-mass insertions (also referred as the chiral dimension). Intermediate missing orders would be zero due to symmetry reasons and therefore they are left out right from the beginning. Detailed mathematical definitions of those Lagrangians are given in [ME11]. In the next step the chiral perturbation theory is applied to distinguish between large and small contributions to the total effective Lagrangian. There, the different contributions are analysed concerning $\left(Q/\Lambda_\chi\right)^\nu$ to define for which power ν the terms are relevant. This so-called power counting revealed that for a given ν just a finite number of terms contributes to the effective Lagrangian and that these terms underlie a strict hierarchy while creating the nuclear forces.

Starting with the leading order (LO, ν=0), the Lagrangian consists of two momentum-independent contact terms ($\sim Q^0$), defined by a nucleon contact term and the static one-pion exchange leading to a Yukawa potential. Although this is a very limited approximation, already important features as the tensor force or NN scattering in peripheral partial waves of very high orbital angular momentum are described well. For the next power ν=1, all contributions vanish due to parity and time-reversal invariance. The next leading order (NLO, ν=2) includes additional higher contact terms with two-pion exchanges. The leading order for the two-pion exchanges is rather weak, but higher orders of the two-pion exchanges include now a spin-orbit term as well as central, spin-spin, and tensor terms. In the next-to-next leading order (NNLO, ν=3) the first non-vanishing three-nucleon forces (NNN) appear, the intermediate-range attraction is improved strongly and first relativistic corrections are considered in the Lagrangian. Going even higher to the next-to-next-to-next leading order (N^{3}LO, ν=4) also four-nucleon forces are available, whereat the four-nucleon forces are considerably weaker than the NNN interactions. This power counting goes on forever. Due to limited computing power today's calculations are often truncated to the N^{3}LO ignoring the four-body forces which is a good compromise between computation time and level of detail represented in the effective Lagrangian.

2.8 No-Core Shell Model and Similarity Renormalization Group Methods

In the next step the ab initio NCSM is introduced shortly following the explanations of [BNV13, Hei19]. The Hamiltonian which has to be solved is given by Equation 2.35. The NN and NNN interactions can be derived from chiral EFT as explained in the section before. In contrast to the simple shell model, the NCSM does not define an inert core and all nucleons can contribute to the properties of the nucleus. A main feature of the NCSM is the choice of the basis and its truncation. As a basis, the Harmonic-Oscillator (HO) bases are used which are truncated by a maximal total HO energy. The HO basis is able to deal with single-nucleon coordinates, which allows the use of the second quantization framework without violating the translational invariance of the system. This has also the advantage that all tools which have been developed for the HO basis and the second quantization framework can be transferred straightforward to the NCSM.

Because the NN and NNN interactions describe a many body system, relative coordinates and momenta are used in the equations. Due to this, the HO basis can be constructed in Jacobi coordinates. Furthermore, the HO basis has to be antisymmetric because the nucleons are fermions. In principle it is possible to antisymmetrize the Jacobi-coordinate HO basis, but if more than four nucleons are considered this is rather impractical and the effort increases dramatically. Hence, a more systematic way is chosen to create an antisymmetric HO basis for an A body problem. For this, one starts with the well-known single-nucleon HO wave function for a nucleon i given by

$$|\alpha_i\rangle = |nlm_\mathrm{l}\rangle \otimes |\tfrac{1}{2}m_\mathrm{s}\rangle \otimes |\tfrac{1}{2}m_\mathrm{t}\rangle\,, \tag{2.41}$$

which is defined by the principal quantum number n, the angular momentum l, the spin $s{=}1/2$, the isospin $t{=}1/2$, and their respective projections m_x. The energy eigenvalues for a HO wave function depend on the HO frequency, which is defined by $\hbar\Omega$. Then the antisymmetric Slater determinant is constructed via

$$|\alpha_1, \alpha_2, ...\alpha_A\rangle_\mathrm{S} = \frac{1}{\sqrt{A!}} \sum_\pi (-1)^{N_\mathrm{T}(\pi)} \cdot \hat{P}_\pi \left(\alpha_1 \otimes \alpha_2 \otimes ... \otimes \alpha_A\right) \tag{2.42}$$

as a basis. Here, the sum includes all $A!$ possible permutations π of the indices. $\hat{P}_\pi$ represents the permutation-operator, while $N_\mathrm{T}(\pi)$ defines the number of transpositions for a given permutation π. Now, the total wave function $|\Psi\rangle$ can be written as a linear combination of Salter determinants leading to

$$|\Psi\rangle = \sum_{\alpha_1<\alpha_2<...<\alpha_A} C_{\alpha_1,\alpha_2,...\alpha_A} |\alpha_1, \alpha_2, ...\alpha_A\rangle_\mathrm{S}\,. \tag{2.43}$$

Until now the basis is infinite and hence it has to be truncated in a sophisticated way to perform actual calculations. This truncation is defined by deciding which combinations of the quantum

numbers n and l are allowed. To do so, the maximum possible sum of all HO excitations is limited to

$$\sum_{i=1}^{A}(2n_i + l_i) \leq N_{\text{Totmax}}. \tag{2.44}$$

The truncation parameter N_{Totmax} defines how large the model space will be and so it defines the complexity of the calculations. Here, the dimension of the problem increases combinatorially with N_{Totmax} and A. Hence, N_{Totmax} should be chosen as small as possible without losing too much possible excitation configurations. Due to this, the calculations can be performed for a increasing number of N_{Totmax} and then the convergences of the observable as a function of N_{Totmax} can be studied to find a optimal N_{Totmax} or a proper extrapolation of the observables. Often, the truncation parameter is defined as N_{Max} which limits the maximal allowed HO excitation energy above the unperturbed ground state. So for small nuclei N_{Totmax}=N_{Max} holds, but for nuclei with A>4 the truncation parameter N_{Max} gets smaller than N_{Totmax} because an unperturbed ground state becomes available. If the model space is truncated and the observables are not fully converged, the results will also depend on the HO frequency $\hbar\Omega$. To eliminated a dependency on $\hbar\Omega$ the observables can be calculated for different combinations of N_{Max} and $\hbar\Omega$. Then the observables are extrapolated towards $N_{\text{Max}}\rightarrow\infty$ for the different sets of $\hbar\Omega$. This has to result in one final value for the observable, which is independent of $\hbar\Omega$ (cf. end of Sec. 6.5.4).

A disadvantage of the HO basis is an incorrect asymptotic behaviour and often the model space needs to be very large to achieve accurate results, which exceeds today's available computing power quickly. So for the case of ^{16}C, NCSM calculations have problems to converge in an appropriate way for NN plus NNN interactions [FRN13]. Furthermore, the truncated many-nucleon HO bases cannot accommodate strong short-range correlations which are often required for realistic effective interactions. To overcome these problems and to speed up the convergence at the same time, various renormalization procedures can be applied. Instead of solving the eigenvalue problem directly by a direct NCSM-type diagonalization, these methods decouple a reference state from all possible particle-hole excitations to shrink the required model space. To do so, the renormalization procedures use similarity transformations which soften the interactions and generate effective operators for all observables. The so derived interactions avoid the before mentioned problems, while at the same time they still act among all nucleons and preserve all the symmetries of the initial NN and NNN interactions. One possible renormalization procedure is the so-called Similarity Renormalization Group (SRG) [BFP07].

In the SRG the idea is to diagonalize the Hamiltonian with a continuous unitary transformation $\hat{U}(s)$ which is applied via

$$\hat{H}(s) = \hat{U}(s)\hat{H}(0)\hat{U}^{\dagger}(s), \tag{2.45}$$

where $\hat{H}(0)$ represents the starting Hamiltonian (e.g. defined by Equation 2.35) and s is the so-called flow parameter [HBM+16]. Defining the generator

$$\hat{\eta}(s) := \frac{\mathrm{d}\hat{U}(s)}{\mathrm{d}s}\hat{U}^{\dagger}(s), \tag{2.46}$$

Equation 2.45 can be derived to the operator flow equation

$$\frac{\mathrm{d}}{\mathrm{d}s}\hat{H}(s) = \left[\hat{\eta}(s), \hat{H}(s)\right] \tag{2.47}$$

exploiting the fact that $\hat{\eta}(s) = -\hat{\eta}^{\dagger}(s)$. With the operator flow equation it is now possible to transform the Hamiltonian smoothly by integrating over the flow parameter s from 0 to ∞. By rearranging the equation of the generator one obtains a differential equation for $\hat{U}(s)$, which can be solved to

$$\hat{U}(s) = \varsigma \cdot \exp \int_0^s \mathrm{d}s' \hat{\eta}(s'). \tag{2.48}$$

With this equation the unitary transformation is well-defined for a given generator. The choice of the generator $\hat{\eta}(s)$ regulates how the Hamiltonian will be transformed. For the choice of $\hat{\eta}(s)$ many different approaches are possible, which are listed and discussed elaborately in [HBM+16].

A possible way to define $\hat{\eta}(s)$ is the use of the second quantization by applying a normal ordering and Wick's theorem. This approach leads to the In-Medium (IM)-SRG framework [TBS11, TBS12]. Here, the A—body operators are approximated by two-body methods which need less computational power. Additionally, the fact is used that low-lying excitation spectra are dominated by excitations of particles which are close to the Fermi level. This fact suppresses the coupling between the ground state and excitations strongly if their energies differ to a large amount compared to the nuclear interaction's resolution scale. For such a case the ground state of the system can be fairly approximated by a single Slater determinant $|\Phi\rangle$ instead of using a state which is constructed from the vacuum state $|0\rangle$. This approximated ground state $|\Phi\rangle$ can be used as a reference state to construct a complete many-body basis. Hence, the ground state is decoupled from the excitations and the model space is decreased without losing significant information of the system. Due to the fact that the reference state uses a single Slater determinant, the IM-SRG framework is only appropriate for the description of nuclei around shell closures.

By replacing the normal ordering with the multi-reference normal ordering the IM-SRG method is further improved to the multi-reference IM-SRG [HBM+16, GVHR17]. Here, the reference state can be arbitrary correlated and the single-particle states are no longer of pure particle or hole character. Furthermore, correlations which are difficult to be described as few-body excitations of the reference state can be built directly into the reference state [HBM+16]. Due to these facts, the multi-reference IM-SRG can also describe open-shell nuclei such as exotic neutron-rich nuclei [HBM+16].

Finally, the multi-reference IM-SRG can be combined with the NCSM, to exploit the advantages of both frameworks. This method, which was first derived by Gebrerufael et al. [GVHR17], is called In-Medium No-Core Shell Model (IM-NCSM), because the key point is the use of an in-medium decoupled Hamiltonian inside the framework of the NCSM. To combine both methods Gebrerufael et al. first performed a NCSM calculation with a truncation parameter $N_{\mathrm{Max}}^{\mathrm{Ref}}$ to obtain a reference state $|\Phi\rangle_{\mathrm{Ref}}$ which has a multidimensional model space for open-shell nuclei. Then they performed a multi-reference IM-SRG calculation using $|\Phi\rangle_{\mathrm{Ref}}$ and an imaginary-time generator which are a compromise between efficiency and robustness [HBM$^+$16]. Next, the IM-SRG-evolved Hamiltonians are used in NCSM calculations to obtain the eigenvectors as well as the eigenenergies for ground- and excited-states. To obtain observables the eigenvectors are evaluated using operators which have been transformed to be consistent with the IM-SRG framework. This allows the IM-NCSM to describe arbitrary open-shell nuclei, while the complexity of $|\Phi\rangle_{\mathrm{Ref}}$ is well controlled by $N_{\mathrm{Max}}^{\mathrm{Ref}}$. Furthermore, the convergence is accelerated considerably due to the decoupling. The results of these IM-NCSM calculations using NN+NNN interactions from chiral EFT [HVH$^+$20] are presented and discussed in Section 6.5.4.

2.9 The Neutron-Rich Carbon-16 Isotope

The properties and theoretical descriptions of the exotic neutron-rich nucleus ^{16}C, which consists of six protons and ten neutrons and has a half-life of 0.75 s [AW76], are discussed in this section, following [Syn18]. The level scheme of ^{16}C can be seen in Figure 1.1. The properties of the four excited states are defined by uncertainty weighted means from the work by Wiedeking et al. [WFM$^+$08] and Petri et al. [PPC$^+$12]. In the framework of the simple shell model, the nucleons of ^{16}C are arranged as shown in Figure 2.8. On the proton side the two lowest orbits $1s_{1/2}$ and $1p_{3/2}$ are filled. Due to the relative large gap between the $1p_{3/2}$ and the $1p_{1/2}$ orbit, protons should mainly occupy the $1s_{1/2}$ and $1p_{3/2}$ orbit. The probability to excited protons from the $1p_{3/2}$ to the $1p_{1/2}$ orbit should be small. Excitations to higher orbits inside the sd-shell should be completely negligible. Hence, they are normally not considered in the used model spaces and nothing is known about their structure. Overall, the contribution of the protons to the properties of excited ^{16}C isotopes should be small but they are not insignificant. On the neutron side the s- and the p-shells are fully occupied and the contribution of these nucleons to the properties of ^{16}C is rather insignificant. Hence, the behaviour of ^{16}C will be dominated by the two valence neutrons in the sd-shell. Here, the $1d_{5/2}$ and the $2s_{1/2}$ orbits are degenerated in terms of single particle energies and a strong mixing of those orbits occurs for ^{16}C and neutron-rich carbon isotopes in general [SSS$^+$08]. Due to this, the N=14 sub-shell gap between the $1d_{5/2}$ and the $2s_{1/2}$ orbit disappears for neutron-rich carbon isotopes, while for other nuclei in that region such as neutron-rich oxygen isotopes a N=14 sub-shell gap is strongly pronounced [SSS$^+$08]. This

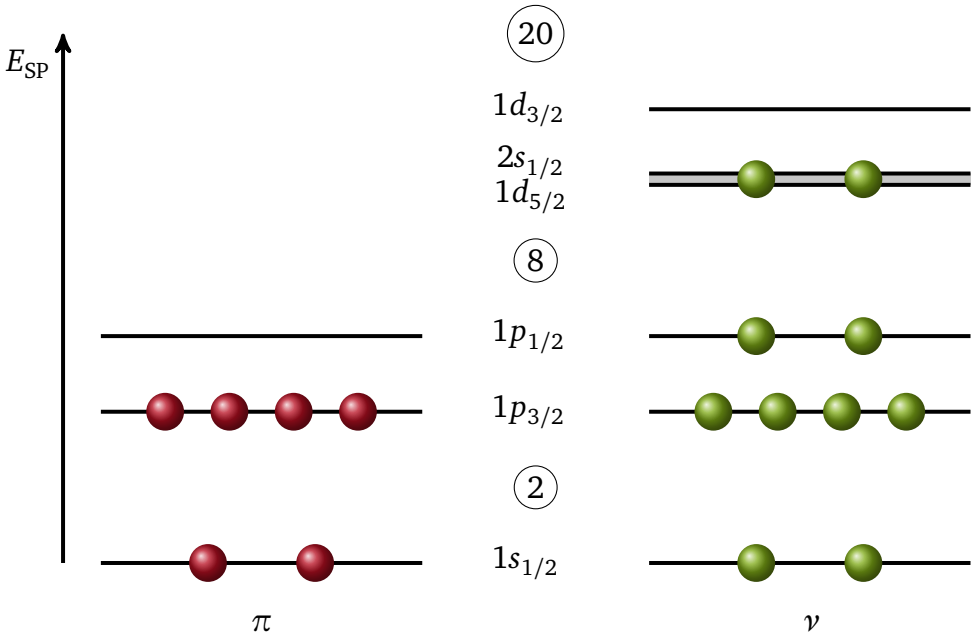

Figure 2.8: The shell structure and nucleons occupation for ^{16}C according to the simple shell model (cf. Sec. 2.6). The orbits are filled with protons (red) and neutrons (green) independently. The numbers inside the circles indicate the magic numbers for a given shell closure. The orbitals are sorted by the increasing single particle energy E_{SP}. The neutron $1d_{5/2}$ and the $2s_{1/2}$ orbits are degenerated and a strong mixing of those orbits occurs for ^{16}C and neutron-rich carbon isotopes in general [SSS$^+$08]. For the protons nothing is known about the structure of the sd-shell. Also the probability to excite protons to a sd-shell orbit should be completely negligible and hence the proton sd-shell is not considered in the model spaces.

can be explained with a reduction in the proton-neutron tensor force and the neutron-neutron interaction for neutron-rich carbon isotopes [SSS$^+$08]. Evidence for the degeneracy of the sd-shell in neutron-rich carbon isotopes and especially for ^{16}C were found in several measurements and theoretical calculations e.g. in [HS07, FMO$^+$07]. So for example, Wuosmaa et al. [WBB$^+$10] measured the neutron-transfer reaction ^{15}C(d,p)^{16}C to extract relative spectroscopic factors by comparing the measured cross-section with theoretical distorted-wave Born approximation calculations. To describe the spectroscopic factors with shell model calculations a strong mixing of the $1d_{5/2}$ and the $2s_{1/2}$ orbit is necessary. Furthermore, Horiuchi et al. were able to describe ^{16}C rather successfully by using a three-body model of ^{14}C+n+n [HS06]. To describe the ^{14}C+n+n case analytically, they applied the sum of two single n-^{14}C potentials which were determined to reproduce level energies in ^{15}C well. The total ^{14}C+n+n potential generates almost the same single particle wave function for both $1d_{5/2}$ and $2s_{1/2}$ orbits. Hence, they assumed a strong mixing of the two orbits.

Due to the before mentioned facts, shell model predictions should be calculated by allowing protons in the p-shell model space and neutrons in the sd-shell model space (cf. Sec. 2.6). Neutron holes in the p-shell can be ignored because excitations of neutrons from the p to the sd-shell are mainly Pauli blocked by the neutrons from the sd-shell [PPC+12]. Such shell-model calculations were successfully applied in the work from Petri et al. [PPC+12] by using the `OXBASH` shell model code [BERGed], to describe the excited level energies of the four low-lying excited states as well as the $E2$ transition strength of the $2_1^+ \rightarrow 0^+$ transition and branching ratio limits in ^{16}C (cf. Fig. 1.1). They tested three different sets of empirically two-body nucleon-nucleon effective interactions, namely WBP [WB92], WBT [WB92], and WBT* [SSS+08] (cf. Sec. 2.6). Here, the WBT* potential leads to a very good agreement with the experimental results. To reproduce the experimental $B(E2; 2_1^+ \rightarrow 0^+)$ strength, effective charges were applied (cf. Sec. 2.1) following the $\propto 1/A$ parametrisation from [SZZS04]. This confirmed the $\propto 1/A$ dependency of the effective charges, which can be explained with core polarization as introduced by Bohr and Mottelson [BM69, BM75]. Hence, in Section 6.5.4 the results of these shell model calculations in combination with effective charges will be compared to the results of this work.

Furthermore, in the work from Frossén et al. [FRN13], first large scale ab initio NCSM calculations for neutron-rich carbon isotopes were performed. They used NN interactions such as the CDB2k NN interactions [Mac01] as well as chiral N^{3}LO two-body forces [EM03] and chiral N^{2}LO three-body forces [GQN09]. While they were able to reproduce the experimental $B(E2; 2_1^+ \rightarrow 0^+)$ strengths well for several neutron-rich carbon isotopes using CDB2k NN interactions, the theoretical prediction is suppressed by a factor of two in the case of ^{16}C. In these calculations the 2_1^+ state excitation of ^{16}C is dominated by a re-arrangement of the neutrons in the sd-shell. Also the experimental branching ratio limit for the $2_2^+ \rightarrow 2_1^+$ (>91.2 %) and $2_2^+ \rightarrow 0^+$ (<8.8 %) transitions can not be reproduced by the CDB2k NN calculations [PPC+12]. Here the calculations favour the $2_2^+ \rightarrow 0^+$ transition instead of the $2_2^+ \rightarrow 2_1^+$ transition. Additionally, the quadrupole moment of ^{16}C is a special case. For all even neutron-rich carbon isotopes the predicted quadrupole moments of the 2_1^+ state are negative except for ^{16}C. Hence, it would be very interesting to check this fact experimentally, whereat it is rather difficult to get experimental access to the quadrupole moments of exotic nuclei. Further, Frossén et al. could show that their results in terms of branching ratios are strongly improved if the chiral three-body forces are included. For these NN+NNN calculations the convergence speed is reduced drastically and hence only relative $B(E2)$ strengths could be obtained for the higher-lying states. Nevertheless, interesting and strong pronounced changes could be observed when the NNN interactions were added. So the $2_2^+ \rightarrow 0^+$ transition is suppressed by a factor of $\approx$7 for chiral NN+NNN interactions compared to chiral NN interactions only, and it is suppressed by a factor of $\approx$20 compared to calculations with CDB2k NN interactions. Also the transition strengths of the other higher-lying states are influenced strongly by NNN forces. So for example the transition strength

$B(E2; 3_1^+ \rightarrow 2_1^+)$ becomes strongly suppressed by a factor of ≈18 for the chiral NN+NNN interactions compared to CDB2k NN interactions [FRN13]. To speed up the convergence for the chrial NN+NNN interactions, IM-NCSM calculations (cf. Sec. 2.8) have been recently carried out by Roth et al. [Rot20, GVHR17]. In the course of this work the NCSM calculations from Frossén et al. [FRN13] and more recent advanced approaches such as the IM-NCSM calculations will be compared to the experimental results in Section 6.5.4.

Another approach to describe the first excited 2_1^+ state of ^{16}C is the simple picture of a two states mixing as it was investigated in [WFM$^+$08, PPC$^+$12, MPF$^+$14, SPM$^+$20, Syn18]. Here, the first state is represented by the 2_1^+ state of ^{18}O at 1.982(1) MeV [AS87]. The state can be described by the re-arrangement of the two neutrons outside the ^{16}O core inside the sd-shell. The second state is represented by the 2_1^+ state of ^{14}C at 7.012(4) MeV [AS91a]. This state is interpreted as a pure proton excitation at which the protons are excited from the $1p_{3/2}$ orbit to the $1p_{1/2}$ orbit. Hence, the first excited 2_1^+ state of ^{16}C is described as a superposition of a pure proton excitation in the p-shell and a pure neutron excitation in the sd-shell as pictured in Figure 2.9. In the mathematical description of the simple shell model the ground state of ^{16}C is approximated by

$$|^{16}\mathrm{C}; 0^+\rangle \approx |\nu(sd)^2; J{=}0\rangle \otimes |\pi(1p_{3/2})^4(1p_{1/2})^0; J{=}0\rangle\,, \tag{2.49}$$

while the 2_1^+ state is described by

$$\begin{aligned} |^{16}\mathrm{C}; 2_1^+\rangle = \alpha\,|\nu(sd)^2; J{=}2\rangle \otimes |\pi(1p_{3/2})^4(1p_{1/2})^0; J{=}0\rangle \\ + \beta\,|\nu(sd)^2; J{=}0\rangle \otimes |\pi(1p_{3/2})^3(1p_{1/2})^1; J{=}2\rangle\,, \end{aligned} \tag{2.50}$$

where ν represents the neutrons and π the protons single particle wave functions and sd represents the combined $(1d_{5/2}+2s_{1/2})$ neutron orbit due to the orbit degeneration. The parameters α and β define the mixing of the pure proton and the pure neutron excitation character and so they are called mixing amplitudes. The proton mixing amplitude β can be accessed via one-proton knockout reactions from nitrogen isotopes. This was measured in the past by Syndikus et al. [SPM$^+$20, Syn18] and Petri et al. [PPC$^+$12]. Their results were in agreement among each other and the uncertainty weighted mean of both works leads to β^2=10.7(8) %. Hence, the excitation of ^{16}C into to 2_1^+ state is dominated by the behaviour of the neutrons inside the sd-shell and the protons play a minor role as it is expected in the framework of the simple shell model.

A different framework for the description of neutron-rich carbon isotopes are Antisymmetrized Molecular Dynamics (AMD) calculations which were performed by Kanada-En'yo et al. [KE05, KEKS13]. The AMD calculations are a useful approach for the description of the deformation and clustering aspects in light nuclei. In a naive picture for the AMD calculations, different subgroups

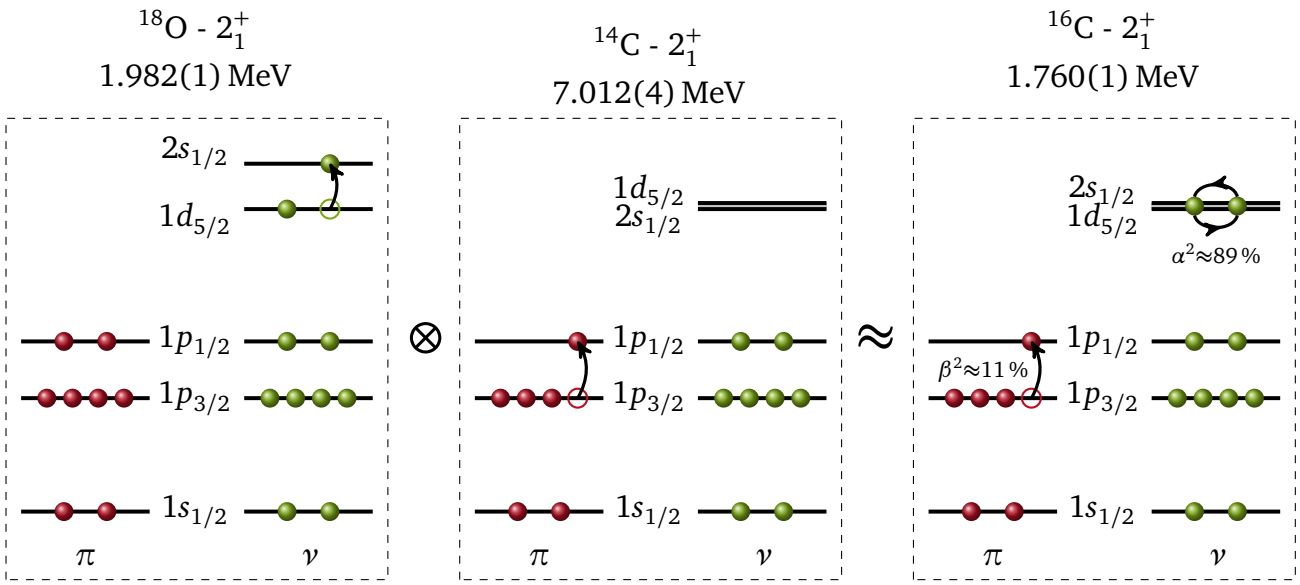

Figure 2.9: Naive interpretation of the first excited 2^+_1 state in ^{16}C using the idea of a two states mixing in the framework of the simple shell model [WFM+08, PPC+12, MPF+14, SPM+20, Syn18]. The picture is motivated by the 2^+_1 state of ^{18}O, which can be described by a dominant neutron excitation and the 2^+_1 state of ^{14}C, which can be described by a dominant proton excitation. The total wave function of the 2^+_1 state for ^{16}C is described as a superposition of such proton and neutron excitations as defined by Equation 2.50. The proton mixing amplitude is given by β^2=10.7(8) % [SPM+20, Syn18, PPC+12]. The relative energy gaps of the $1d_{5/2}$ and the $2s_{1/2}$ orbit are taken from [SSS+08].

of nucleons can form sub-nuclei which themselves form the total nucleus by a molecule-like arrangement. In the scope of these calculations Kanada-En'yo et al. could describe neutron-rich carbon isotopes (including ^{16}C) well in terms of level energies and $B(E2; 2^+_1 \rightarrow 0^+)$ strengths [KE05, KEKS13]. For ^{16}C they found a prolate deformation of the neutron distribution and an oblate deformation of the proton distribution, for which the symmetry axes are perpendicular. In this framework the excitation into the 2^+_1 state can be described as a collective rotation of the nucleons. Due to the fact that in the AMD calculations the rotational axis and the symmetry axis of the proton distribution are aligned for ^{16}C, the proton-contribution to the $B(E2; 2^+_1 \rightarrow 0^+)$ strength is small and the behaviour of the 2^+_1 state is dominated by the neutrons. Also the neutron and proton motions are sort of decoupled, because they underlay different deformation types. Hence, the $B(E2; 2^+_1 \rightarrow 0^+)$ strength for ^{16}C is reduced compared to other neutron-rich carbon isotopes e.g. ^{20}C. For ^{20}C the proton and the neutron distributions follow both an oblate deformation. Due to this, the neutron and proton motions are strongly coupled. Further, the symmetry axis and the principal axis are aligned and so the $B(E2; 2^+_1 \rightarrow 0^+)$ strength strongly increases. This behaviour could be confirmed experimentally, where Petri et al. [PFM+11] measured a strength of $B(E2; 2^+_1 \rightarrow 0^+) = 7.5^{+3.0}_{-1.7}\,\mathrm{e^2fm^2}$ which is ≈1.8 times larger than for ^{16}C. This behaviour is also

supported by shell model calculations using isospin-dependent effective charges [PFM+11]. Furthermore, AMD calculations can also be used to describe the nucleus ^{14}C rather successfully. A description of ^{14}C in terms of such AMD calculations is given in the second part of this thesis in Section 9.1.

3 Experiment

In this section the reaction which should provide excited ^{16}C isotopes, the experimental setup, the corresponding detectors, and the measurement principle are explained, which are needed to measure the lifetime of excited states in ^{16}C.

3.1 Reaction Channel of Interest

To investigate excited states in ^{16}C, first an experimental access to ^{16}C* has to be chosen. In this work, the fusion-evaporation reaction

$$^{9}\mathrm{Be} + {}^{9}\mathrm{Be} \;\rightarrow\; {}^{18}\mathrm{O}^* \;\rightarrow\; {}^{A}Z^* + N_\mathrm{p}\cdot\mathrm{p} + N_\mathrm{n}\cdot\mathrm{n} \tag{3.1}$$

was used to create excited ^{16}C* isotopes: ^{9}Be is bombareded on ^{9}Be and they fuse to highly excited ^{18}O* with a Q-value of Q=23.477 MeV. Here ^{18}O* is called an intermediate isotope. The ^{18}O* decays immediately via many different evaporation channels to a residual isotope ^{A}Z and residual particles N_pp+N_nn where N_p is the number of protons and N_n is the number of neutrons. A list of all decay channels can be seen in Table A.1. As a result, 18 different reaction channels are possible. The given relative cross sections for each reaction channel are calculated with the statistical model estimates from PACE4 [TB08, Gav80]. It can be seen that the channel of interest with

$$^{9}\mathrm{Be} + {}^{9}\mathrm{Be} \;\rightarrow\; {}^{18}\mathrm{O}^* \;\rightarrow\; {}^{16}\mathrm{C}^* + 2\cdot\mathrm{p} \tag{3.2}$$

happens in approximately 0.04 % of the cases. As a result it is very unlikely that ^{16}C* is produced and hence a good filter for the reaction channel of interest needs to be applied during the experiment. For this filter, the two evaporated protons will be used. The fact that this fusion-evaporation leads to the reaction of interest, with excited ^{16}C* as a residual isotope, was already shown in the work of Wiedeking et al. [WFM$^+$08].

3.2 Measurement Principle and Experimental Setup

To measure the lifetimes of the excited states in ^{16}C a DSAM experiment (cf. Sec. 2.5) was performed at the Argonne National Laboratory (ANL). For this the Argonne Tandem Linac Accelerator System (ATLAS) was used to get a ^{9}Be Beam [ATL19]. ATLAS ran for the first time in 1977 and was the world's first superconducting accelerator for projectiles heavier than electrons.

In the following the ATLAS will be explained briefly, whereby the information are taken from [Dav13]. At ATLAS, any stable isotope of any element from hydrogen up to uranium can be accelerated. Thereby, energies up to 17 MeV/A are possible. For this, two preliminary accelerators are available at the facility. They inject the isotopes in the main ATLAS Linear Accelerator (linac). In this experiment the Positive Ion Injector (PII) was used as preliminary accelerator. The first stage of the PII is the electron cyclotron resonance plasma ion source. This source provides the ions for the preliminary beam. To do so a neutral gas is fed into a plasma chamber, which is magnetically confined. This chamber is heated by microwaves. These microwaves also provide a rapidly varying E-field. If the microwave frequency matches the electron gyration frequency $\omega_g = eB/m_e$ (where B is the magnetic field strength, e is the charge of an electron and m_e is its mass), the free electrons in the chamber gain a large amount of energy. With these energies, it is likely that the free electrons start to ionize the neutral gas atoms inside the source. This increases the amount of free electrons and so an electron avalanche is created which causes a quick complete ionization of the gas atoms. The charge state for the used ^{9}Be isotopes was $4e$ after the ionization. These ions are extracted from the chamber with a 350 kV capacitor plate. From all ions in the chamber, roughly 60-70 % are successfully extracted towards the second stage, the bunching system. This system prevents a too big energy spread of the ions. The beam bunches now have a width of ≈96 ns. Afterwards, the isotopes are injected into the PII-linac. The PII-linac has 18 resonators to accelerate the particles and 11 superconducting solenoids to focus the beam particles. In the PII-linac, the ^{9}Be beam was accelerated to a kinetic energy of 16 MeV which leads to a velocity of $v = 0.062c$.

In the next step, the beam is injected into the main linac. The main linac consists of two parts, namely the 20 MeV booster linac and the 20 MeV ATLAS linac. In each linac the isotopes can gain up to 20 MeV. In total, 32 splint-ring resonators are used. They can be phased independently, which allows a broad range of beam velocities. In this experiment, the ^{9}Be beam is accelerated to 39.8 MeV, which means $v = 0.097c$ in terms of velocity. The drift tubes are made of niobium, which has excellent superconducting properties. In the final step, the beam is guided via ion optics to an experimental hall where the target device is placed inside Gammasphere.

In the experimental hall the actual DSAM measurement takes place. Here, the measurement principle, which is sketched in Figure 3.1, is realised: the ^{9}Be beam hits a ^{9}Be target with a kinetic energy of 39.8 MeV. The target thickness along the beam direction is 7.5 µm (1.3875 $^{mg}/_{cm^2}$). Due to the fact that projectile (^{9}Be) and the target (^{9}Be) have the same mass the maximum possible compound nucleus excitation energy is the Q-value of the reaction plus the half of the incoming kinetic energy of the projectile. The kinetic beam energy is 39.8 MeV and the Q-value is $Q = 23.477$ MeV so the maximum possible compound nucleus excitation energy for the ^{18}O* is 43.377 MeV. As discussed earlier, an evaporation of ^{18}O* happens, which can create, amongst many others, excited ^{16}C* isotopes in combination with two protons. After the reaction, the ^{16}C*

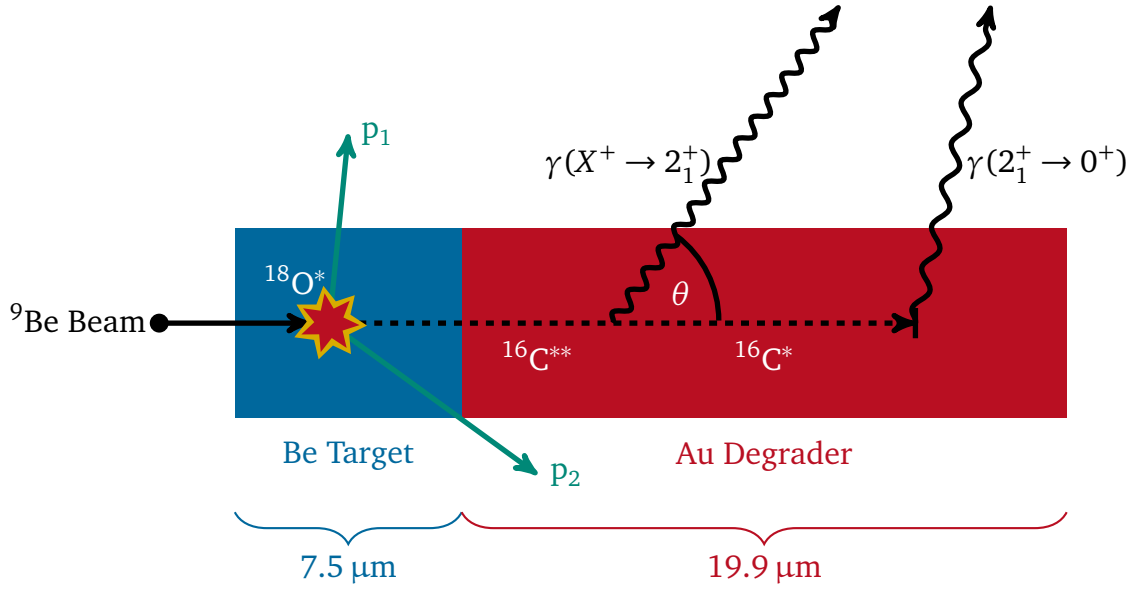

Figure 3.1: Sketch of the measurement principle: A ^{9}Be beam hits a ^{9}Be target. In the target, a fusion-evaporation (marked with a star) creates an highly excited ^{16}C** isotope and two protons. The ^{16}C** isotope travels through the Au degrader and de-excites in flight from a higher-lying state to the 2^+_1 state. After the ^{16}C* isotope is stopped it de-excites at some point from the 2^+_1 to the ground state. The two protons can leave the target in all directions. They are measured with Microball while the gammas are measured with Gammasphere (cf. Fig. 3.2).

residuals will travel through the degrader. The degrader is backed on the back of the Be target and consists of Au with a thickness of 19.9 µm (38.42 $^{mg}/_{cm^2}$). In this degrader, the ^{16}C* isotopes are slowed down until they are fully stopped. During the stopping process, the ^{16}C* isotopes can de-excite in flight from a higher-lying state to the 2^+_1 state. After the ^{16}C isotopes are stopped, they de-excite from the 2^+_1 state to the ground state. The decay from the 2^+_1 to the ground state can not happen in-flight because the lifetime of this state is with 11.5 ps and the isotopes are fully stopped before the decay happens. Hence, no Doppler-shift will be observed later for the 2^+_1 state in the spectra.

To get an insight into the beta distribution of the ^{16}C isotopes directly after their production, also target-only-runs have been performed. To get the beta distribution of the ^{16}C isotopes directly after their production in an experimental way is important for the applied Geant4 simulations (cf. Sec. 4.3). These results can be used to have more realistic initial settings for the simulations which already include experimental biases. For the target-only-runs the target and degrader device was replaced by a thin Be target with a thickness of 0.5 µm (92.5 $^{µg}/_{cm^2}$). For this thin target energy loss effects which could influence the kinematic of the ^{16}C isotopes and evaporated protons are neglectable. A more detailed explanation of the usage of the target-only-runs can be found in Section 5.8.

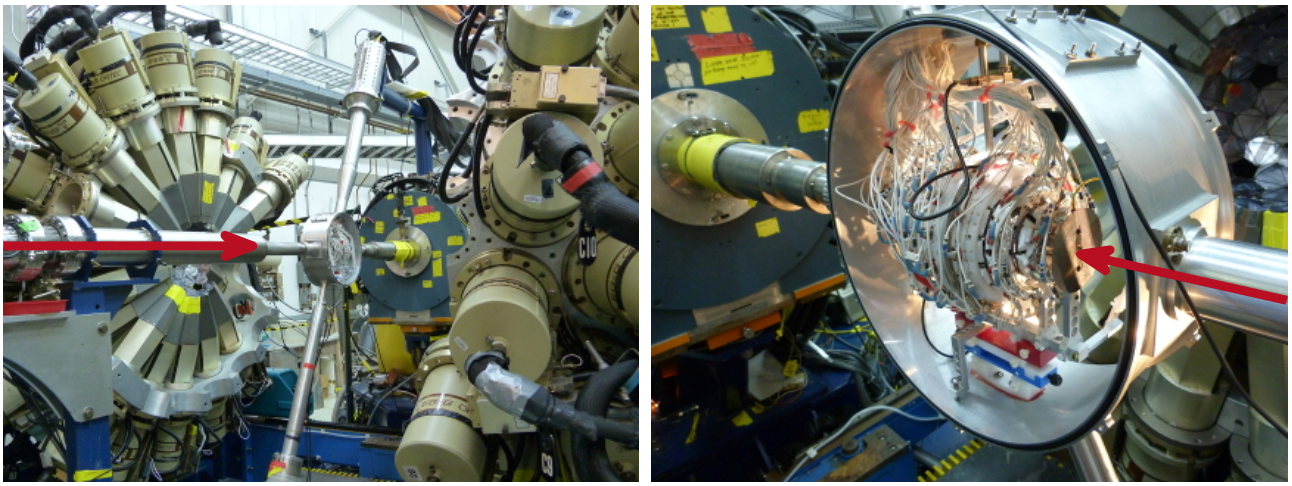

(a) Open Gammasphere with μ-Ball inside (b) Zoom on μ-Ball while the target chamber is opened.

Figure 3.2: Picture of Gammasphere and μ-Ball. The red arrow indicates the beam direction.

The whole target and degrader device is mounted in the center of a spherical target chamber. Inside the target chamber, as a sphere around the target, the Microball (μ-Ball) particle detector is mounted (cf. Sec. 3.4). This detector, which can be seen in Figure 3.2 (b), measures and identifies particles which are emitted during the fusion-evaporation process. With this, it is possible to gate on two protons to select the ^{16}C reaction channel for the gamma-ray spectra. The emitted gamma rays are measured with Gammasphere (cf. Sec. 3.3). This gamma detector consists of 110 Compton suppressed HPGe detectors and can be seen in Figure 3.2 (a) in an open setting. During the experiment, both Gammasphere halves are moved towards the center so that the 110 Compton suppressed germanium detectors form a closed ball around the spherical target chamber.

The total beam-time of the experiment was roughly 132 hours. Thereof, 106 hours were used for target-and-degrader-runs. There the beam current was varying between 0.25 enA and 1.50 enA with an average of roughly 1.1 enA. The remaining 26 hours were used for the target-only-runs. During this measurement the beam current was varying between 1.0 enA to 1.5 enA. At the end, a short proton beam run of ≈40 minutes at about 100 epA was shot on a ^{12}C target. With this data μ-Ball can be energy calibrated. During the whole experiment the data recording was divided into many runs. Each run was about one hour long.

3.3 Gammasphere

The heart of the experimental setup is Gammasphere, which is a large gamma-ray detector array [Lee90]. Gammasphere, shown in Figure 3.2 (a), started its operation in 1993. Today it consists of 110 Compton suppressed HPGe detectors. The detector array of Gammasphere is

designed to maximize the covered solid angle while the angular segmentation is limited to a reasonable value. This led to an icosahedron symmetry consisting of 122 polyhedral elements namely 110 hexagons and 12 pentagons. The 12 pentagon elements are used for support structures as well as entrance and exit holes for the beam line, while the 110 hexagons are filled with the detector modules. A detector module, which can be seen in Fig 3.3, consists of a HPGe crystal as active volume, which is surrounded by a Bismuth Germanate (BGO) shield. Behind the shield, photo multipliers are placed to read out the BGO shield and behind that sits the detector electronics connected to a liquid nitrogen dewar vessel for cooling. The cooling reduces the thermal electronic noise drastically. To allow a compact arrangement of the detectors, the modules are tapered with an angle of 7.45°. The distance between the target position and the beginning of HPGe crystal is 25.25 cm. A HPGe crystal of one module covers 0.418 % from the total solid angle 4π. Over all, 46 % of 4π are covered by the 110 HPGe crystals. This advanced setting leads to a full energy peak efficiency close to 10 % for gamma rays with an energy of 1.3 MeV [Sta15]. The opening angle of one HPGe detector is 7.4°. With this, a total energy resolution (detector resolution plus Doppler broadening) of ≈5.5 keV for β=0.02 can be achieved. Figure 3.2 (a) shows Gammasphere in the open position. This position is used for maintenance work at the target chamber as for example placing μ-Ball inside. During an experiment, Gammasphere is closed and it forms one complete ball where no space is left between Gammasphere and the target chamber.

The BGO shield is used for Compton suppression (cf. Sec. 2.2) of gamma rays which are scattered out of a HPGe crystal. BGO scintillators are a preferred choice for the Compton suppression because while their energy resolution is for the most tasks unsatisfying, the efficiency is high compared to HPGe crystals. At Gammasphere, each HPGe crystal is surrounded by six BGO shield elements. Additionally, a BGO suppression plug is placed between the back of the HPGe crystal and the electronics. It allows the suppression of Compton events which scattered under forward angles out of the HPGe crystals. This improves the low-energy background in the spectra. The total arrangement is an ideal compromise to have as much active volume as possible while at the same time the Compton suppression probability is maximised.

When the BGO shield is hit, a veto signal is sent which can be used to ignore the events registered in the corresponding HPGe crystal. To reduce the number of false vetos created by gamma rays which directly hit the front of a BGO shield, the so-called hevimet shields are placed in front of the BGO scintillators. The hevimet shields consist of different heavy metals to achieve a large absorption coefficient. With this elaborated suppression technique a full energy peak to total ratio of 68 % can be reached for gamma rays in the range of 1.3 MeV. For comparison the full energy peak to total ratio for a typical HPGe crystal without Compton suppression would be ≈25 %.

The detector modules are arranged into 17 rings. Each ring is mounted so that it covers one specific radiation angle θ while the polar angle ϕ of the detectors rotates around the beam

Figure 3.3: Sketch of four Gammasphere detector modules. Figure reprinted from [ES08] with permission from Elsevier.

axis. The radiation angle θ of each ring, the number of detectors per ring, and the number of during the experiment available detectors is listed in Table A.3. The module rings are arranged symmetrically to 90°, so for every ring at θ=90°+X° there is a ring at θ=90°−X°. Hence, for a DSAM measurement up to 17 different angles are available. A simulation of such a DSAM measurement at Gammasphere can be seen in Figure 2.5 (cf. Sec. 2.5). As can be read in Table A.3, the smallest angle at θ=17.27° was not available during this experiment. In total 87 HPGe detectors have been used during this experiment. All the information in this section is taken from [ES08, Dav13].

3.4 Particle Detector Microball

As explained in Section 3.2, a Particle Identification (PID) is needed to have the possibility to cut on the 2p reaction channel. For this task, the μ-Ball particle detector was used [SHD+96]. μ-Ball was developed in the 1990s at Washington University. A picture of μ-Ball is illustrated in Figure 3.2 (b). As it can be seen, μ-Balls compact design allows that it is placed inside the target

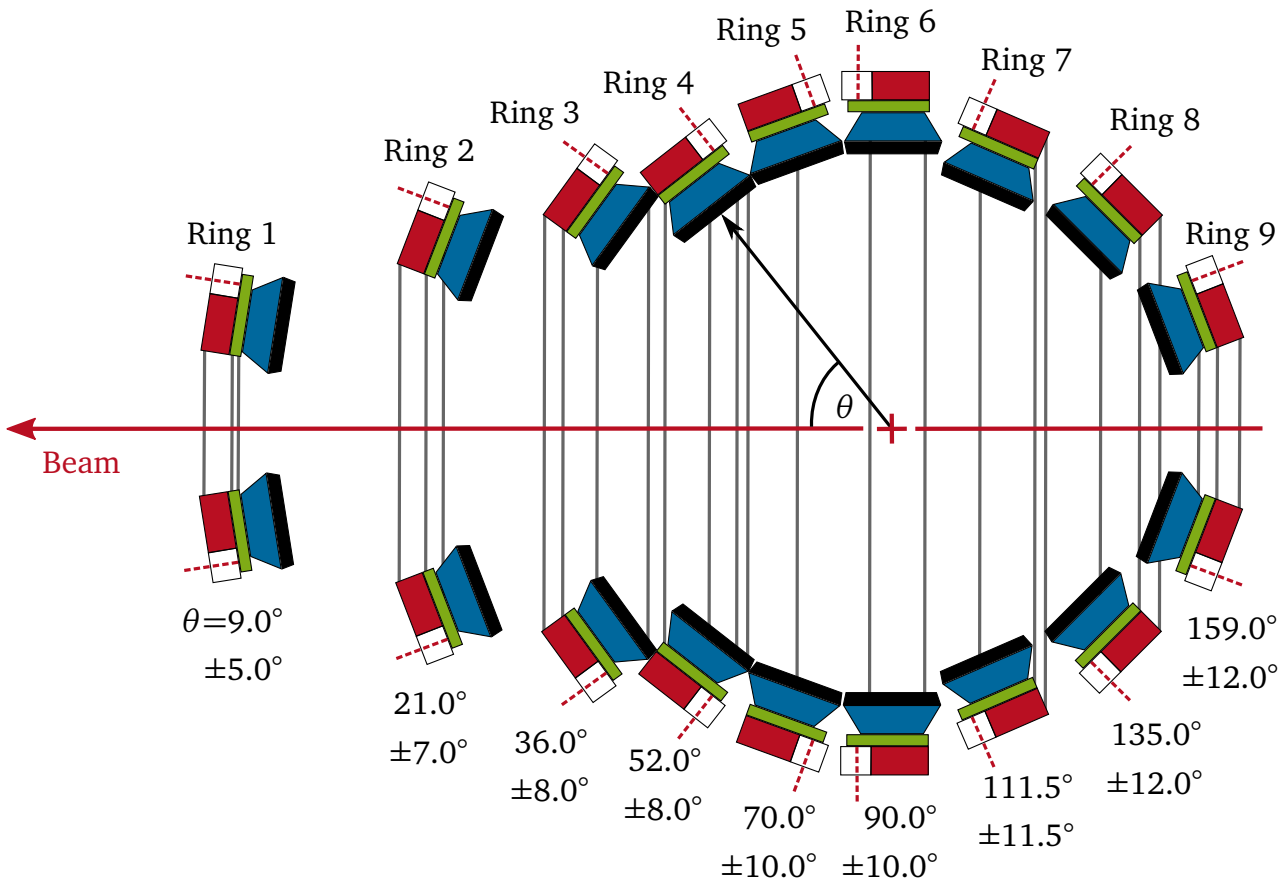

Figure 3.4: Sketch of μ-Ball showing a vertical section. The CsI(Tl) detectors are shown in black, the light guides are shown in blue, the Si photodiodes are shown in green, and the supporting rings are shown in red. A projection of the support structure is illustrated in light grey. The target position is marked by the red cross in the center of the detector. Figure modified and reprinted from [SHD+96] with permission from Elsevier.

chamber of Gammasphere. This is needed since charged particles can not travel far outside the vacuum and around the target chamber the Gammasphere detector modules start immediately.

There are two versions of μ-Ball available. One is the *spectroscopy* μ-Ball, which was constructed with the minimum possible mass for optimal particle channel selection and a smaller influence on the gamma rays. The other one is the so-called *reaction* μ-Ball which has detectors with a larger mass to measure more energetic particles. The proton range for *spectroscopy* μ-Ball is between 14.3 MeV for backward angles and up to 24.5 MeV for forward angles (cf. Tab. A.6). This is sufficient for the experiment of this thesis and so *spectroscopy* μ-Ball was used.

The μ-Ball consists of 96 CsI(Tl) scintillator detectors which are arranged in 9 rings around the beam axis as it can be seen in Figure 3.4. There the detectors are shown in black, facing the target position. The technical data and angles of each ring can be found in Table A.6. It should be mentioned that only 95 detectors were installed in this experiment because one detector had to be removed for the target mounting. The chosen arrangement of the detectors and the use

of the CsI(Tl) detectors has many advantages. First of all, μ-Ball achieves an excellent PID for charged particles using CsI(Tl) scintillators with a high thallium concentration of 1200 ppm. Secondly, this arrangement covers a large solid angle. The μ-Ball detectors are planar and each detector is arranged relative to its neighbours so that no detector is shadowed by its neighbour ring. The gap between two rings is 0.10 mm while the gap between two neighbouring detectors is 0.12 mm. The loss of solid angles due to gaps is only 1.8 % of 4π. The lost space for the target mounting is 0.9 % of 4π and the gaps for the beam entrance and exit is 0.74 % of 4π. Due to this the total covered solid angle is 96.5 % of 4π. Additionally, this arrangement helps for an adequate segmentation of the detector. Hence, the count rate can be nearly equally distributed among the rings if the emission characteristics of the particle is uniformly. This allows μ-Ball to measure around 4500 counts/s and so μ-Ball can keep up with Gammasphere which is important for coincidence experiments. Although μ-Ball fills out most of the target chamber, the interaction probability for the gamma rays is quite low. Measurements with ^{60}Co show that the peak-to-total-ratio of Gammasphere is 0.57(1) without μ-Ball and 0.52(1) with μ-Ball inside [SHD^{+}96]. This is a reduction of just 9 %.

For the particle detection, the properties of the CsI(Tl) scintillator are exploited. If a charged particle hits the CsI(Tl) scintillators, the atoms in the CsI(Tl) are excited and emit photons which are in the visible range. The number of emitted photons is for light particles proportional to the energy of the charged particle. Due to the fact that the CsI(Tl) is a monocrystalline solid, i.e. the crystal lattice of the entire solid is continuous and unbroken to the edges of the sample, it is transparent for its own emitted photons. Hence, the total emitted light can be extracted at the end of a CsI(Tl) scintillator. At μ-Ball, Si photodiodes are coupled to the end of a CsI(Tl) scintillator to convert the light output into an electrical signal which is proportional to the number of emitted photons. Hence, the maximum of the produced electrical signal is proportional to the energy of the charged light particle. With this, it is possible to achieve an energy resolution of 2.7 % for α-particles at 8.78 MeV. For an energy calibration it has to be considered that every single μ-Ball detector is protected by thin absorbers. These absorbers shield the detectors against low energy or heavy particles as well as x-rays. Therefore, the surfaces of all detectors are covered with a thin aluminium foil. On top on these foils additional Pb or Ta absorbers are installed. The thickness of the aluminium foils and the absorbers varies from detector to detector. The thickness of the aluminium foils reaches from 0.15 $^{mg}/_{cm^2}$ to 0.58 $^{mg}/_{cm^2}$. The thickness of the Pb absorbers reaches from 20.2 $^{mg}/_{cm^2}$ to 34.4 $^{mg}/_{cm^2}$ while the thickness of the Ta absorbers reaches from 3.6 $^{mg}/_{cm^2}$ to 14.2 $^{mg}/_{cm^2}$. More information about the energy calibration of μ-Ball can be found in Section 5.6.

To do the PID, the fact that the CsI(Tl) has two decay components for its emitted light is used. The first component is the longer one with a mean decay time of τ=7 µs. This decay time is independent of the particle type and presents the main limitation of the count rate. The second decay component is the shorter one and has a mean decay time of τ=0.4-1.0 µs. Here, the

decay time depends on the particle type. The lighter the particle is, the longer the decay time of the shorter decay component. Hence, by looking at the maximum and the tail of the signal at the same time, a PID is possible. In Figure 3.5 schematic signal responses are illustrated. The response for two α-particles (continuous lines) and two protons (dashed lines) is shown. Two cases for two different energies are shown whereat for one case the α-particle and the proton should have the same energy. To distinguish between the two particles, one has to measure the signal height at two different times, namely t_B and t_C. At t_B the maximum of the signal B is detected while at t_C the signal height C during the drop of the signal is measured. The value B at t_B is in first order proportional to the particle energy. By comparing B and C one can now identify the particles. An example for such a measurement can be seen in Figure 3.6 (a) and Figure 5.5 (a). Figure 5.5 (a) shows the PID for one target-and-degrader-run of the experiment. Figure 3.6 (a) shows the measurement of ^{249}Cf$\rightarrow\alpha+^{234}$Cm which was carried out before the main lifetime experiment was started. This measurement was used to set up the electronics of μ-Ball and to find proper values for t_B and t_C. During the experiment, values around t_B=1 µs and t_C=8 µs were used. Another representation of this PID is illustrated in Figure 3.6 (b). Here B is plotted versus B/C: the y-axis corresponds to the energy of the particles while the different particles appear as straight lines along the x-axis. This representation is used later to set the particle cuts as can be seen in Section 5.4 and Figure 5.5.

During this process a problem appears in the detector read-out. The charge sensitive pre-amplifiers used for the Si photodiode have a rise time of 1 µs and a decay time of ≈300 µs. To recover the two components of the CsI(Tl), a low and a high frequency filtering two-stage shaper has to be used. With these devices, an aperiodic pulse with a shape proportional to x^4e^{-4x} with $x=t/\tau_0$ was applied. Simulation of the signal behaviour showed that a setting with τ_0=1.3 µs and a pole zero correction give the best results. The pole zero correction is used to reduce the pile up.

If the detector read-out is set like this, it is possible to set the time gate t_B at the position of the signal maximum at around 1 µs and the time gate for the tail t_C at around 9 µs. The time gates were set for each detector separately. To find good values, the source measurement ^{249}Cf was used.

More details of μ-Ball and the electronics used can be found in the work from D.G. Sarantites et al. [SHD+96].

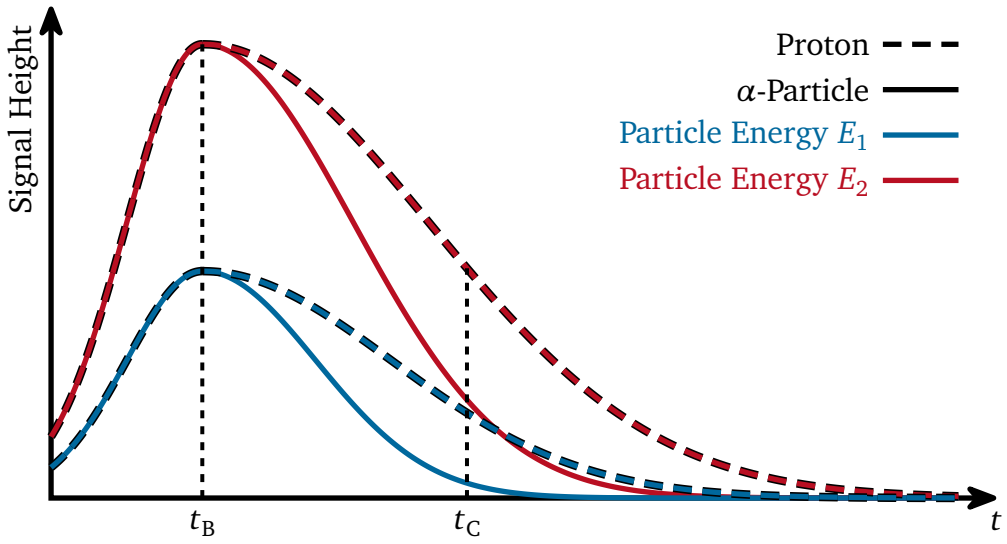

Figure 3.5: Principle of the PID for μ-Ball. This plot illustrates the signal response of one CsI(Tl) detector of μ-Ball. The response is shown for two α-particles (continuous line) and two protons (dashed line). Two cases for two different energies ($E_1 < E_2$) are shown whereat for one case the α-particle and the proton have the same energy. The signal is detected at t_B (maximum of the signal) and at t_C (tail of the signal). During the experiment the detection times were set to $t_B \approx 1$ µs and $t_C \approx 8$ µs.

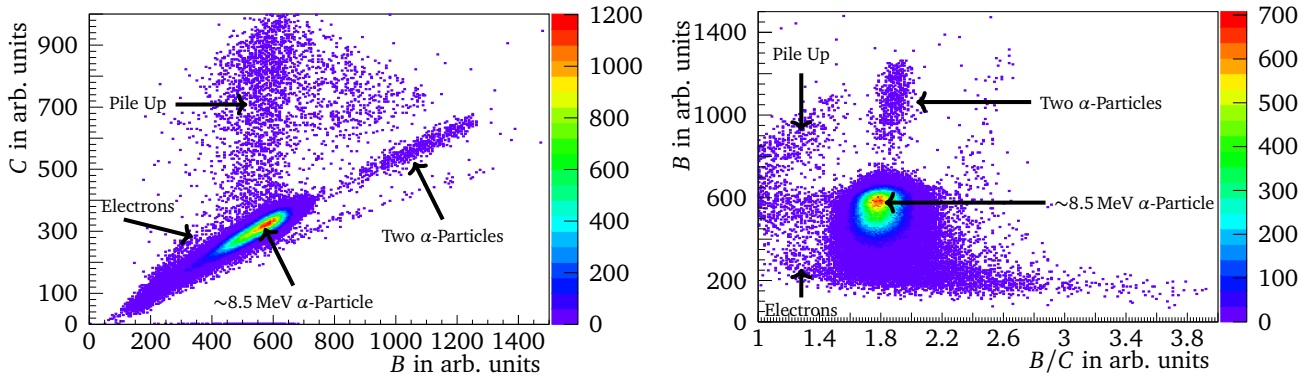

(a) PID: C vs. B

(b) PID: B vs. B/C

Figure 3.6: PID for ^{249}Cf$\rightarrow\alpha+^{234}$Cm using μ-Ball: The left plot shows the signal height B (signal amplitude) versus the signal height C (signal tail) while the right plot shows B versus B/C. The second representation is later used to set the PID cuts. For the definition of the values of B and C see Figure 3.5.

4 Geant4 Simulations

To get access to the lifetime, the experimental mean decay beta is compared to simulated mean decay betas (cf. Sec. 2.5). For the simulation, the framework of Geant4 is used in this thesis [Gea14]. Geant4 was developed by the *Geant Collaboration* at CERN. It is a C++ based Monte-Carlo simulation code for nuclear and fundamental particle physics experiments. In Geant4 the user has the possibility to implement user-defined code into the classes of Geant4. In these classes all necessary conditions for the simulation are fixed, the used physical models are loaded, and it is managed what kind of data and how the data is extracted from the simulation. All fundamental, important classes and their call sequences of the simulation used here can be found in [Mat16]. In the following, a short summary of the classes and their tasks in the context of the simulation here used is given. This explanation is orientated by [Mat16].

An entire simulation process in Geant4 is called a `Run`, which is controlled by the `RunManager`. For accessing the simulation before a `Run` is started and after the `Run` is finished, the `G4UserRunAction` class can be used. When the Geant4 simulation is started, first the `Properties` method is loaded, which contains information and settings for the simulation. Also at the beginning, the `G4UserDetectorConstruction` class, the `G4PhysicsList` class, and the `G4ActionInitialiser` class are built. The `G4UserDetectorConstruction` class constructs the world and detector geometries. The `G4PhysicsList` contains all physical models which are used in the simulation. In the `G4PhysicsList` the model `G4EmStandardPhysics_option4` is loaded to describe the electro-magnetic interaction of the simulated gamma rays. The `G4ActionInitialiser` class will start the `G4UserPrimaryGenerator` and the `G4UserEventAction` class. These two classes are responsible for the `Events`. A `Run` can consist of many `Events`. Every `Event` includes the `Tracks` of the primary particle and the `Tracks` of all particles which are generated by the primary particle by interactions with matter. All required properties of the primary particle are given by the `G4UserPrimaryGenerator` class. An `Event` starts with the generation of the primary particle and ends when all tracks are finished. This means that all particles (primary and secondary) have reached an exit condition, e.g. the particles have left the simulation volume or the energy has dropped below a certain threshold. For accessing the simulation before an `Event` has started or after an `Event` is finished, the `G4UserEventAction` class can be used. During one `Event` the particle `Tracks` contain all momentary information about the particles like the particle species, the energy, the momentum vector or the internal quantum state of the particle. The `Tracks` are continuously updated by `Steps`. In one `Step` some kind of an interaction can take place. This can be any interaction which is listed in the `G4PhysicsList` and is allowed in the current material in which the particle stays in

the moment of evaluation. During a `Step` the properties of a particle can be changed. Possible interactions are e.g. ionization, excitation, scattering, and so on. Also during this, secondary particles can be generated. The distance, which a particle covers in a material between two `Steps`, is sampled by using the mean free path of the particle in consideration of the possible physical processes. The mean free paths are calculated from cross sections, which are taken from databases and/or calculated analytically using phenomenological equations. To access the simulation before or after a `Step` is performed, the `G4UserSteppingAction` class can be used. Also the `G4UserSteppingAction` class is linked with the `Hit` class and the `G4UserSensitiveDetector` class. The `Hit` class and the `G4UserSensitiveDetector` class are responsible for the data acquisition. If an interaction takes place in a volume which is listed as a sensitive detector in the `G4UserSensitiveDetector` class, then the information can be accessed via the `Hit` class.

The Geant4 code which is used in this work is based on a simulation used in [Hei15, Mat16]. A detailed description of the here used simulation would be go beyond the scope of this thesis. In [Mat16] a more detailed explanation of how the simulation code is arranged can be found.

For the simulation, the Geant4 version 4.10.3.p02 is used. For further analysis of the simulated and experimental data, The Data Analysis Framework `ROOT` version 5.34.36 is used [Bru97].

4.1 Geometries

The geometry of the Geant4 simulation is illustrated in Figure 4.1. All geometries are created in the `G4UserDetectorConstruction` class while the Ge and the BGO detectors are also added to the `G4UserSensitiveDetector` class. The target (not visible) is a rectangular box whose origin is placed in the center of the simulation at (0,0,0). The target has a dimension of 5 mm x 5 mm x 7.5 µm and reaches from (-2.5 mm, -2.5 mm, -3.75 µm) to (2.5 mm, 2.5 mm, 3.75 µm). In the beam direction directly behind the target, the degrader is placed with dimensions of 5 mm x 5 mm x 19.89 µm. For later analysis, the target-only-run has also to be simulated. For this the target and degrader setup can be replaced by a thin Be target with the dimension of 5 mm x 5 mm x 0.5 µm, which is also centred at (0,0,0).

Around the center of the simulation, the Ge crystals are placed on a sphere with a radius of 25.25 cm. The crystals are simulated as a cylinder with a radius of 3.5 cm and a height of 7.5 cm. Every Ge crystal is surrounded by a BGO box. The rest of the experimental setup is not simulated. This is sufficient because the only property which is important to extract from the simulation is the mean decay beta of the residual particle. As discussed in Section 4.3 the whole fusion-evaporation process is not of interest and also no efficiency has to be deduced from the simulation. Hence, the interaction of the particles with the beam pipe or μ-Ball has not to be taken into account.

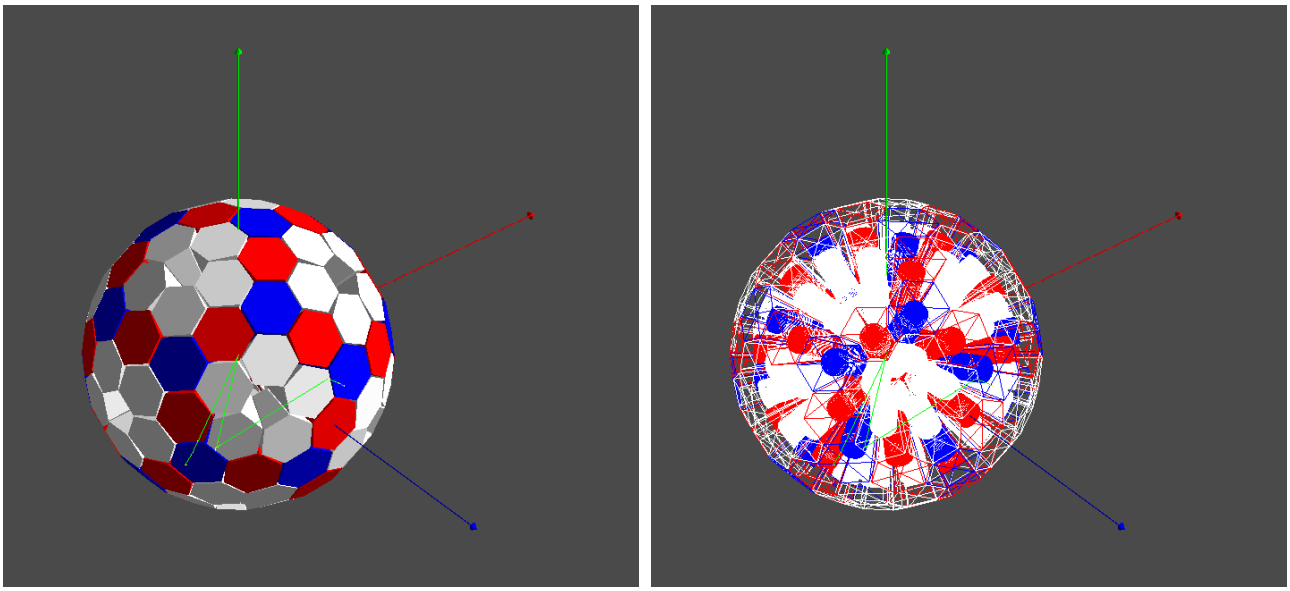

(a) Sketch of the Geant4 simulation (b) Wired sketch of the Geant4 simulation

Figure 4.1: Sketch of the Geant4 simulation. The white, red, and blue boxes are the BGO shielding for the Compton suppression. The cylinders inside the BGO shielding are the Ge crystals which represent the active detector volume. They can be seen in the right picture. The thin green line shows an example of a gamma-ray track which interacted with the detector. The arrows represent the used Cartesian coordinate system. The blue arrow indicates the x-axis, the green arrow indicates the y-axis, while the red arrow indicates the z-axis which is the beam axis. An arrow has the length of 1 m.

4.2 Lifetimes

For the analysis of this work different lifetimes for excited states have to be simulated. To set the lifetime of an excited state the `GeantUserData` have to be changed. Inside the `GeantUserData`, the `ENSDFSTAT` data can be found. Here, all nuclear levels and lifetimes of all nuclei, which are listed in the `Evaluated Nuclear Structure Data File` (ENSDF), are included. Before a simulation starts, the corresponding lifetime is changed in the `ENSDFSTAT` table. Also in the `PhysicsList` class, the following options have to be set:

```
G4NuclideTable::GetInstance()->SetThresholdOfHalfLife(-1.0*s);
G4NuclideTable::GetInstance()->SetLevelTolerance(10.0*eV);
```

The first line ensures that all lifetimes are simulated whatever the lifetime is. Otherwise, short lifetimes in the femtosecond range might be ignored by the simulation. The second line secures that the excitation levels are found in the `ENSDFSTAT` data even when there are some rounding errors.

4.3 Creation of the Excited Ions

A crucial part of the simulation is the creation of the excited isotopes of interest, which happens inside the `PrimaryGeneratorAction` class. One way to do so would be the simulation of the incoming Be beam and the whole fusion-evaporation process (cf. Sec 3.1). Here, the problem occurs that the kinematic and the energy distribution of the residual protons after the evaporation is not known. This kinematic influences the kinematic of the residual isotopes (e.g. ^{16}C) strongly and so the mean decay beta of the residual isotope. But the mean decay beta is the main value which will be extracted from the simulation. Hence, another approach has to be chosen: In the used simulation the residual particle (e.g. ^{16}C) is directly created in an excited state inside the target material and the whole fusion-evaporation process is skipped. To get the correct initial kinematics for the residual isotope, the initial beta β_{ini} of the residual isotope has to be estimated. For this the measured mean beta $\overline{\beta}_{\mathrm{TO}}$ for the residual isotopes from the target-only-runs is used. An elaborated description of the $\overline{\beta}_{\mathrm{TO}}$ estimation is given in the Section 5.8. In the following explanation, it is only focused on the creation process of the excited isotopes in the simulation assuming a realistic $\overline{\beta}_{\mathrm{TO}}$ is already known.

In the first step, the starting position for the residual isotope is chosen. The isotope will be spawned inside the target. The target itself is a rectangular box, which is centred at (0,0,0). Along the z-axis, which is the beam axis, the thick target reaches from -3.75 µm to +3.75 µm (thickness of the thick Be target: 7.5 µm). First, the x and y component of the position of the isotope are chosen. These components are orthogonal in respect to the beam axis. After the experiment, the beam spot on the target had the shape of a circle with a diameter of roughly 2.5 mm. Due to this the isotopes in the simulation are spawned uniformly distributed on a disc with a diameter of 2.5 mm in the x,y-plane. The center of this disc is placed in the center of the target x,y-plane. In the second part of step one, the z coordinate has to be chosen. The z coordinate has to be inside the target which reaches from z=-3.75 µm to z=+3.75 µm. But the probability to create the residual isotope (e.g. ^{16}C) is not uniformly distributed along the target. This is due to the fact that the incoming ^{9}Be beam loses energy while it passes the ^{9}Be target and so the cross section changes. To take this into account, the code of LISE^{++} [TB08] is used to calculate the energy loss of the ^{9}Be beam for a given travelled distance in ^{9}Be. With this, the new kinetic energy of the ^{9}Be particle at a given travelled distance is calculated. This energy is then plugged in the PACE4 code to provide a cross section distribution for the fusion-evaporation [TB08, Gav80]. As an example, Figure 4.2 (a) shows the so derived cross section distribution for ^{16}C if the incoming ^{9}Be beam has an energy of 39.8 MeV. To the data points the function

$$\mathrm{C.S.}(z) = a \cdot z + b \tag{4.1}$$

is fitted with a=$-0.00716\,^{\mathrm{mb}}/_{\mu\mathrm{m}}$ and b=0.27243 mb for ^{16}C. It can be seen that the cross section decreases by 21.8 % going from 0 µm to 7.5 µm travelled distance. This confirms the fact that

a uniform distribution along the z-axis would not be a good approximation. To obtain a proper distribution along the z-axis, first the C.S.(z) function is normalized in the interval from 0 µm to 7.5 µm with

$$N = \int_{0\,\mu\mathrm{m}}^{7.5\,\mu\mathrm{m}} \mathrm{C.S.}(z)\mathrm{d}z \quad \Rightarrow \quad \mathrm{C.S.}^{\mathrm{N}}(z) = \frac{a}{N} \cdot z + \frac{b}{N} \tag{4.2}$$

where N=1.65282 mbµm for ^{16}C. Then the so-called “inversion-method” is applied. Therefore, the cumulative distribution function $F(z)$ is calculated via

$$U := F(z) = \int_0^z \mathrm{C.S.}^{\mathrm{N}}(t)\mathrm{d}t = -\frac{a}{2N}z^2 + \frac{b}{N}z, \tag{4.3}$$

which is then inverted to

$$z = \frac{a}{b} \pm \sqrt{\left(\frac{b}{a}\right)^2 - \frac{2N}{a}U}. \tag{4.4}$$

Taking the negative part of this equation and subtracting 3.75 µm (because the target is centred at z=0) leads to the position calculation equation

$$z(U) = \frac{a}{b} - \sqrt{\left(\frac{b}{a}\right)^2 - \frac{2N}{a}U} - 3.75\,\mu\mathrm{m}. \tag{4.5}$$

If U is now replaced by a uniformly distributed value between 0 and 1, this function gives the correct start position distribution.

In the second step, the starting beta β_{ini} of the isotope has to be defined. The direction will be set to (0,0,1) because the experiment is only sensitive to the beta component along the beam direction. To get a proper beta the target-only-runs are used to extract a decay beta from there. Because the target-only-runs use a much thinner target (0.5 µm), it can be assumed that most decays happen outside the target and the energy loss in the target is negligible. Hence, the target-only-runs give an insight to the mean beta the residual isotope (e.g. ^{16}C) has directly after the creation. More information of the target-only-run and the extraction of the decay beta can be found in Section 5.8. The beta $\overline{\beta}_{\mathrm{TO}}$, which stems from the target-only-run will have a statistical uncertainty $u\left(\overline{\beta}_{\mathrm{TO}}\right)$. Due to this a random beta $\beta_{\mathrm{TO,Rand}}$ is sampled for every event using a Gaussian distribution which has the mean value of $\overline{\beta}_{\mathrm{TO}}$ and a sigma of $u\left(\overline{\beta}_{\mathrm{TO}}\right)$. The randomized beta $\beta_{\mathrm{TO,Rand}}$ is then decreased according to the distance Δz between the beginning of the target and the position at which the isotope is created. Hence, Δz reaches from 0 µm to 7.5 µm. To get the decreasing slope again, results from LISE++ for the intermediate isotope are used. For example Figure 4.2 (b) shows the beta the ^{18}O has after the fusion when the ^{9}Be beam reacted after it travelled the distance Δz in the target. To this data, the function

$$\beta_{\mathrm{O16}}(\Delta z) = g \cdot \Delta z + h \tag{4.6}$$

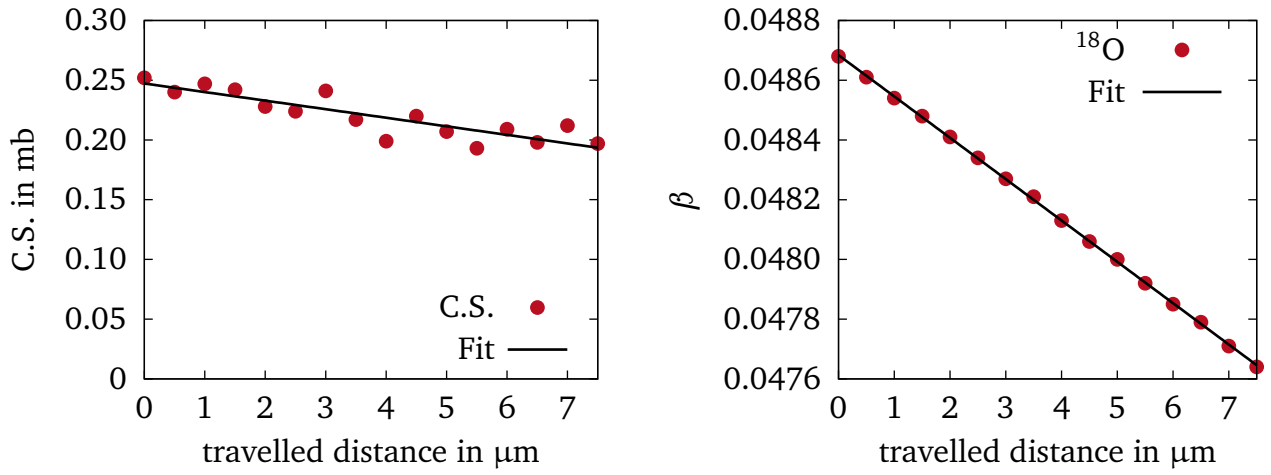

(a) Cross section distribution for ^{16}C (b) Beta loss for ^{18}O

Figure 4.2: Cross section distribution and velocity loss for the isotope creation. The left plot shows the cross section distribution to create the residual ^{16}C isotopes along a ^{9}Be target if the incoming ^{9}Be beam has an energy of 39.8 MeV. The right plot shows the beta loss of the intermediate ^{18}O, if it is created along a ^{9}Be target and the incoming ^{9}Be energy is 39.8 MeV. The values are obtained using LISE^{++} and PACE4 [TB08, Gav80].

is fitted, which resulted in $g = -1.384(6)\,^{10^{-4}}/_{\mu m}$ and h=0.048684(3) (for ^{18}O). If, in the first step, the starting position z was chosen according to Equation 4.5, then the initial beta for the event is given by

$$\beta_{\text{ini}}(z) = \beta_{\text{TO,Rand}} \frac{h + g \cdot (z + 3.75\,\mu\text{m})}{h}. \tag{4.7}$$

This approximation is roughly valid because the energy and beta loss is linear in the region of interest.

In the last step, the isotope is excited randomly via an excitation vector into one of the possible excited states. The excitation vector contains all levels in which the isotope should be excited combined with a given probability that this level is chosen.

4.4 Stopping Theory and Ion Ranges

To get access to the lifetime with DSAM, it is essential to have a good description for the slowing down process of the nuclei in the target and degrader. In Section 2.5, it was already mentioned that it is very difficult to calculate this complete process analytically. The slowing down process of nuclei in matter consists basically of two parts, namely (I) the interactions with atomic electrons and (II) the interactions with nuclei [NSS79]. Hence, the total energy loss $\mathrm{d}E(E)$ per distance $\mathrm{d}x$ can be written as

$$\frac{\mathrm{d}E(E)}{\mathrm{d}x} = \left(\frac{\mathrm{d}E(E)}{\mathrm{d}x}\right)_{\text{e}} + \left(\frac{\mathrm{d}E(E)}{\mathrm{d}x}\right)_{\text{n}} \tag{4.8}$$

where “e” refers to the electronic part and “n” to the nuclear part. For part (I), the nuclei of interest collide with the electrons from the material via the Coulomb forces. Due to the fact that the nuclei are much heavier than the electrons, it will take many collisions to slow them down. The maximum energy an A=30 nucleus with 1 MeV can lose in one interaction with an electron is about 70 eV. Because of this, the slowing down process can be considered with no significant change in direction of the nuclei. Additionally, it can be seen as a continuous process in which the first approximation is described by Equation 2.21 and Equation 2.22, as well as by

$$\left(\frac{\mathrm{d}E(E)}{\mathrm{d}x}\right)_{\mathrm{e}} = k(A_1, A_2, Z_1, Z_2)\epsilon^{1/2}. \tag{4.9}$$

In this equation, ϵ is the dimensionless kinetic energy of the nucleus of interest and k is a constant which depends on A, Z of the nucleus of interest and the material in which the slowing down process happens. The interaction with electrons dominates for velocities $\beta \geq 2\,\%$. For part (II), the moving nuclei of interest interact with nuclei from the material they pass. Here the masses of both participants are in the same order of magnitude. As a result of this the nuclei of interest will lose energy in a few discrete steps and it is also likely that they change their direction of movement. This effect dominates for velocities $\beta \leq 0.3\,\%$ and is much harder to be described analytically. More about these issues can be found e.g. in [NSS79].

To avoid these problems, one applies the advantage of the Monte Carlo Geant4 simulation. In Geant4 every simulation step an interaction can take place. During the interaction, the nuclei can change their direction and/or a small energy loss $\mathrm{d}E(E)$ is applied. Here $\mathrm{d}E(E)$ depends on the current energy of the particle, the travelled distance since the last step, and of course the material in which the slow down process happens. In Geant4 the energy loss $\mathrm{d}E(E)$ as a function of the current energy of the particle can be looked up in a database. The standard database of Geant4 uses the dataset ICRU73 from the International Commission on Radiation Units and measurements (ICRU). The ICRU73 data are a mixture of calculated and measured stopping powers for ions heavier than helium [ICR05].

In this context, it is very important to mention that Geant4 is developed and optimized for high energy physics, which means particle energies above 100 AMeV. But the experiment evaluated here deals with particle energies of ≈4.4 AMeV. Following the investigations from [Hei15], two changes in the simulation process are applied to get a more accurate slowing down behaviour for the low energy regions.

First of all, the ICRU73 stopping powers are replaced by stopping powers which are calculated with the program SRIM (The Stopping and Range of Ions in Matter). SRIM is a software-package concerning the stopping and range of ions in matter. It was introduced in 1985 and is still being upgraded today. The SRIM software-package is able to reproduce the stopping behaviour of ions quite well for many different materials over a wide energy range [ZZB10]. Figure A.1 shows comparisons between SRIM calculations and experimental results for the stopping power of

carbon in many different materials [Zie19, ZZB10]. It can be seen that SRIM reproduces the stopping quite well for a large range. The mean deviation is only 5.3 %. In Figure A.2, one can see a zoom in the range of interest. Here it can be seen that the data points for carbons stopping power in Gold differs around 5 % from the SRIM predictions. To achieve this accuracy while the needed computation power is inside realistic limitations, SRIM uses a combination of different models. The heart of these calculations is the so-called *magic formula* which analytically describes atom-atom collisions and the concept of a *free-flight-path*, which helps that only significant collisions are evaluated. These models are able to predict the stopping and range of ions based on experimental data and expanding this data to unmeasured regions [Zie19]. A detailed explanation about the fundamental physics the SRIM software-package uses can be found in [JFZ15].

Additionally, the so-called *forced stepping* method is added to the simulation code. Geant4 approximates a stepping length for every simulation step. The stepping length depends on the type and energy of the simulated particle as well as on the material the particle travels through. After the particle covered the distance of the current stepping length, the behaviour of the particle is newly evaluated and after that a new step is started. In [Hei15] it was worked out that the normal stepping length Geant4 uses is too long for the low energy processes and short lifetimes investigated here. To avoid this problem, the *forced stepping* method forces the simulation to evaluate the next step not later than a given distance which can be set by the user. By setting the *forced stepping* distance to smaller values, the simulation gets more possibilities to change the behaviour of a particle in a given movement range, but as a disadvantage the simulation needs much longer to process. So a fair balance between sensitivity and computation time has to be found.

To test the influence of the stopping powers and the *forced stepping* the range of ions in different materials is analysed. Figure 4.3 shows the range of ^{16}C ions with an incoming kinetic energy of 20 MeV in beryllium (left side) and in gold (right side) for different settings. The red curve shows the range behaviour SRIM predicts, the other curves are the results from the used Geant4 simulation. The behaviour of the Geant4 simulation was analysed for the ICRU73 stopping powers with a *forced stepping* of 0.1 µm (black curve), for the SRIM stopping powers with a *forced stepping* of 0.1 µm (purple curve) and for the SRIM stopping powers without *forced stepping* (green curve). For ^{16}C→Be, the stopping behaviour between the SRIM results and the Geant4 simulations is very similar if the *forced stepping* is set to 0.1 µm. If the *forced stepping* is turned off, then the peak shape from the Geant4 simulation differs significantly from the SRIM results even using the SRIM stopping powers (green curve). Here the ions can travel further than for a *forced stepping* of 0.1 µm because fewer slowing down processes are evaluated by the simulation. For ^{16}C→Au, the influence of the stopping power database used is much larger. The standard ICRU73 dataset overestimates the energy loss compared to the SRIM calculations. If the Geant4 simulation uses the ICRU73 dataset, the ion range is much smaller (black curve)

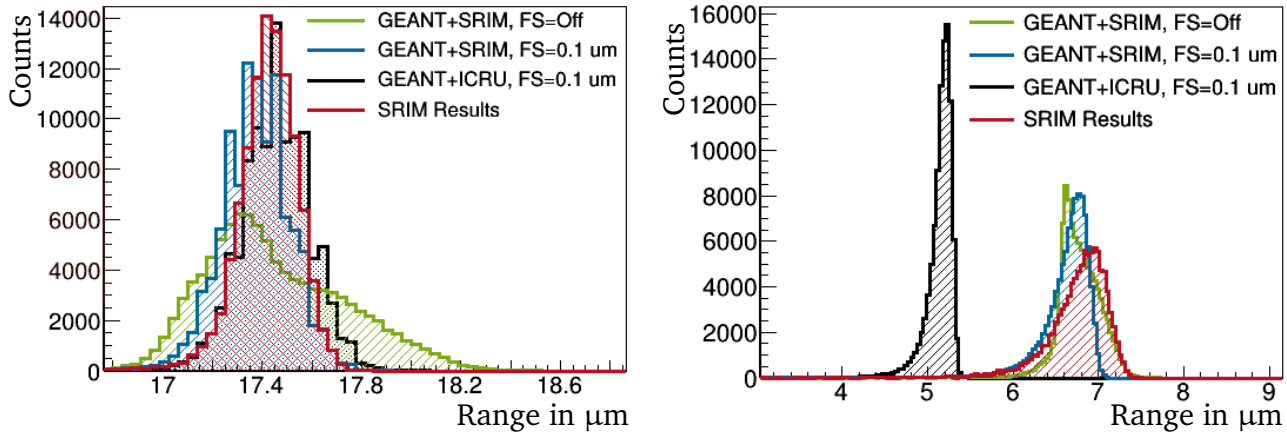

(a) ^{16}C in Be (b) ^{16}C in Au

Figure 4.3: Range of ^{16}C ions in Be and Au for different simulation settings. The incoming kinetic energy of the ^{16}C ions was 20 MeV. The red curve shows the results from SRIM calculations. The other curves are the results from the used Geant4 simulations for different combinations of the used stopping powers (ICRU73 or SRIM) and the *forced stepping* (FS).

compared to the SRIM calculations (red curve). If the SRIM dataset is used in the Geant4 simulations the results are similar to the SRIM results. Here, turning the *forced stepping* on or off has no large influence.

Furthermore, for an even finer *forced stepping* than 0.1 µm no significant change could be observed for the ion ranges for both cases. Due to this facts a *forced stepping* of 0.1 µm will be used for all simulations which are carried out in this work. Most of the time the analysis will be done for the ICRU73 dataset as well as for the SRIM dataset as stopping powers. The results can than be compared whereat the results for the SRIM stopping powers should be more reliable.

4.5 Energy Resolution

To get a realistic simulation, the energy resolution of the gamma-ray detectors also has to be taken into account. The detector resolution is applied in the analysis script after the simulation is finished. To do so the energy with perfect resolution stemming from the simulation is set as a mean value μ of a Gaussian probability distribution given by

$$f(E;\mu,\sigma) = \frac{1}{\sigma\sqrt{2\pi}} e^{-\frac{(E-\mu)^2}{2\sigma^2}}. \tag{4.10}$$

Then a new energy value is sampled randomly following this distribution. Here, the parameter σ is the standard deviation of the distribution. It is connected to the FWHM of the Gaussian peak by

$$\text{FWHM} = 2\sqrt{2\ln 2}\sigma \approx 2.355\sigma. \tag{4.11}$$

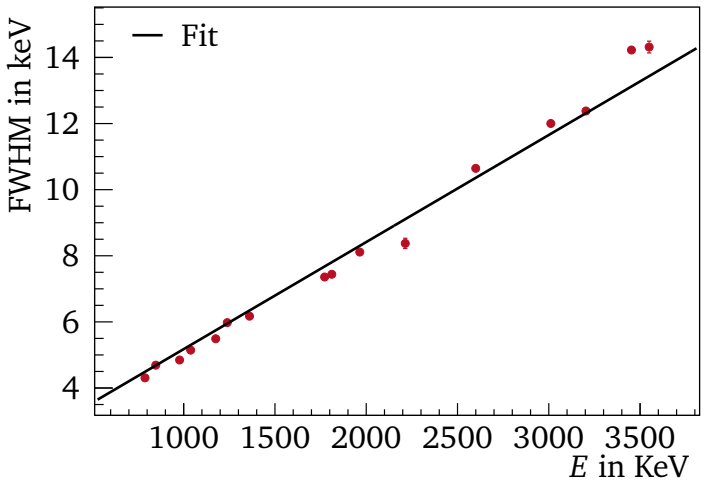

Figure 4.4: Energy resolution in terms of FWHM as a function of the gamma-ray energy E. The data points are obtained with a ^{56}Co source. The most error bars are too small to be visible but they are considered for the fit. The fit function is given by Equation 4.12.

The FWHM value of the detectors depends on the measured gamma-ray energy E. To get a realistic behaviour of FWHM(E) experimental values are taken. Therefore, the ^{56}Co source measurement is used. Here Gaussian fits are applied to 16 different peaks between 790 keV and 3550 keV. Then the FWHM value is extracted for every peak and plotted against the energy E of the peak. The result is shown in Figure 4.4. Using the function

$$\mathrm{FWHM}(E) = 3.23952 \cdot 10^{-3} \cdot E[\mathrm{keV}] + 1.93613\,\mathrm{keV} \tag{4.12}$$

the data points could be fitted. In the analysis scripts, Equation 4.12 is used to calculate the FWHM value for a given detected energy E and afterwards the energy with realistic resolution is sampled following the Gaussian distribution from Equation 4.10 with σ=0.425 · FWHM(E).

5 Analysis

This section explains the basic analysis steps which have been applied to all data. First the raw Gammasphere energy is calculated. Then, this energy is calibrated and the efficiency of Gammasphere is calculated. Later, the proton cuts are introduced and the event builder, which searches for coincidence between Gammasphere and μ-Ball, is explained. Then the calibration of μ-Ball and the calculation of the proton energy is explained. Afterwards it can be looked at the measured proton distribution for the different settings. In the last part, the idea and analysis of the target-only-runs is explained, which is used to extract the initial beta for the Geant4 simulations.

5.1 Raw Energy Calculation of Gammasphere

In the first step of the analysis, the raw gamma-ray energy has to be calculated from the data which is provided from Gammasphere. Recently the read-out electronics of Gammasphere were changed to a digital version, the so-called Digital Gammasphere (DGS). There is not only one signal height recorded, but also additional information about the signal shape. A typical measured signal for one event of DGS can be seen in Figure 5.1 [Zhu16]. Here the so-called signal trace is shown. This means that the signal height $V(i)$ for each sample i is shown. One sample corresponds to one discrete read-out period of DGS. For the example shown here, the signal is first dropping from a previous event. Then, at around the sample $i+M$, an event takes place and the signal rises proportional to the deposited energy. After the sample $i+M+K$, the signal starts to drop again. To get a raw energy value, one has to determine, as precisely as possible, the increase in the signal going from sample $i+M$ to sample $i+M+K$. Here, the problem occurs that the signal coming from the read-out electronics does not have to be zero, when an event is registered. The signal can be higher due to pile up from an event before, or it can be lower than the baseline due to an undershoot from an event before. For that reason, the signal behaviour has to be investigated at a larger sample size before and after the event happens. But, if a larger sample size is investigated, then the correction for the exponential decay, which the signal always underlies, becomes more and more important. Additionally, it has to be taken into account that every detector has its own signal baseline height, which can vary during the experiment, which also then induces some kind of exponential decay in the signal. To correct these problems, a so-called pole-zero correction and a baseline correction are applied to the raw gamma-ray energy calculation. In the following, the whole procedure of calculating and correcting the raw energy is explained.

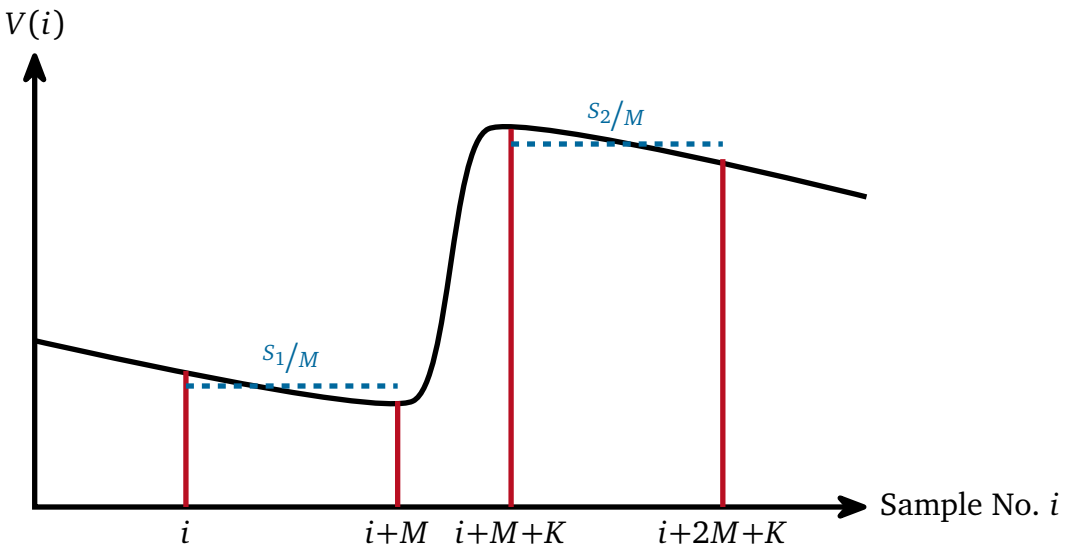

Figure 5.1: Signal shape and information provided by DGS [Zhu16]: The plot shows the signal height $V(i)$ at different samples i for a typical DGS event. The red lines mark the samples for which DGS reads out the signal height. Also the mean signal height S_i/M is indicated by the blue dashed lines. For more explanations see the text from Section 5.1.

In general, the signal decay follows the sum of different exponential decays stemming from the pre-amplifier electronics. If no event happens, the signal height for sample $i+1$ is given by

$$V(i+1) = V(i)\sum_j \mathrm{e}^{-\lambda_j} + B \tag{5.1}$$

where λ_j are the unit decay constants per sample for the different exponential decays, $V(i)$ is the signal height at sample i and B is the height of the baseline the detector signal has on average. Following the red lines in Figure 5.1, DGS provides the following values

$$m_2^{\text{begin}} := V(i) \tag{5.2}$$
$$m_2^{\text{end}} := V(i+M) \tag{5.3}$$
$$m_3^{\text{begin}} := V(i+M+K) \tag{5.4}$$
$$m_3^{\text{end}} := V(i+2M+k) \tag{5.5}$$
$$S_1 := \sum_{n=i}^{i+M} V(n) \tag{5.6}$$
$$S_2 := \sum_{n=i+M+K}^{i+2M+k} V(n) \tag{5.7}$$

where S_1 is called pre-rise energy and S_2 is called post-rise energy. During the experiment, M was set to 350 samples and k to 116 samples.

To calculate the raw energy in a simple way without corrections, one has to apply

$$E_{\text{Simple}} = \frac{S_2}{M} - \frac{S_1}{M}, \tag{5.8}$$

where S_1/M is the mean signal height between sample i and $i+M$, as well as S_2/M is the mean signal height between sample $i+M+K$ and $i+2M+k$ (cf. Fig. 5.1 blue dashed lines). This easy approach is not sufficient enough, which is proven in Figure 5.2 (a). Here, the value S_1 is plotted versus E_{Simple} for an ^{88}Y source measurement. It can be seen that for different given energies, E_{Simple}, tilted lines are visible (an example is marked by the black arrow) in the 2D plot. This indicates that the calculated energy E_{Simple} depends on the pre-rise signal height, which should not be the case. To correct this, a pole-zero factor P and a baseline term B is applied to Equation 5.8, which leads to

$$E_{\text{Advanced}} = \frac{S_2}{M} - \frac{S_1}{M}P - (1-P)B. \tag{5.9}$$

The pole-zero factor corrects the relative exponential signal drop, which happens in the time window between the signal rise and the time when the post signal height is measured, i.e. the time passed between sample $i+M$ and sample $i+2M+K$. This signal drop always superposes the increasing signal part induced by the event. P can be expressed as

$$P = \sum_j \mathrm{e}^{-\lambda_j(M+K)} \tag{5.10}$$

which corresponds to a factor between 0 and 1. Hence, the term $S_1/M \cdot P$ in Equation 5.9 corrects the pre-rise signal by the amount of height which is missing in the rising and the post-rise part due to the exponential decay of the detector signal.

Assuming that the different exponential decays can be re-written into one effective exponential decay with the unit decay constant λ, the pole-zero factor can be approximated by

$$P \approx \mathrm{e}^{-\lambda(M+K)} = \left(\mathrm{e}^{-\lambda M}\right)^{\frac{M+K}{M}}. \tag{5.11}$$

The factor $\mathrm{e}^{-\lambda M}$ describes the relative signal drop, while M samples are processed without a signal increase due to an event. This factor can be accessed by the DGS data via

$$\mathrm{e}^{-\lambda M} = \frac{m_3^{\text{end}} - m_2^{\text{end}}}{m_3^{\text{begin}} - m_2^{\text{begin}}}. \tag{5.12}$$

This means that the pole-zero factor can be calculated with the expression

$$P = \left(\frac{m_3^{\text{end}} - m_2^{\text{end}}}{m_3^{\text{begin}} - m_2^{\text{begin}}}\right)^{\frac{M+K}{M}}. \tag{5.13}$$

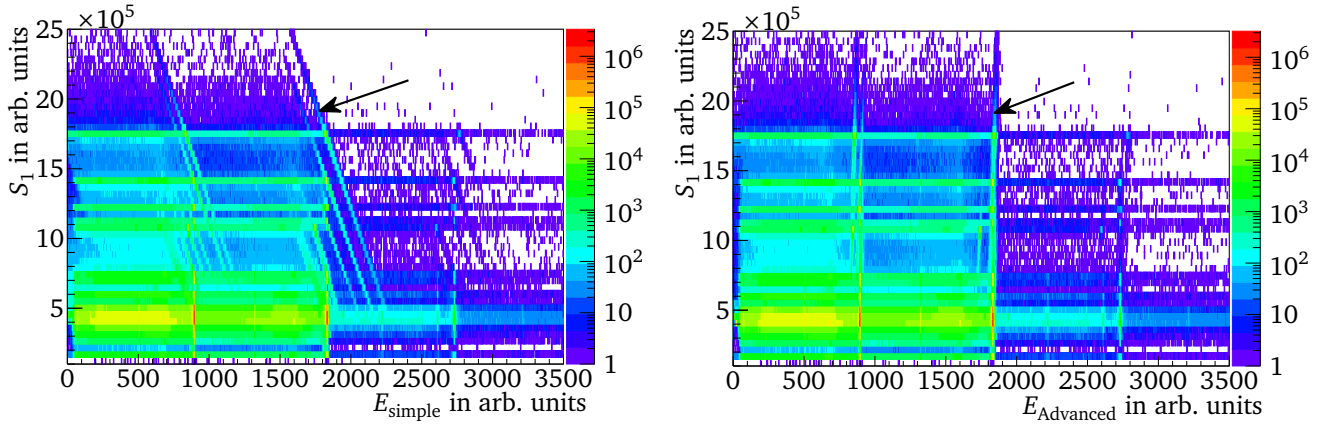

(a) S_1 over E_{Simple} (b) S_1 over E_{Advanced}

Figure 5.2: Pre-rise signal height over raw energy for a ^{88}Y source measurement. For S_1 over E_{Simple} (left plot) tilted structures can be seen (marked with arrow). This means that the calculated energy depends on the pre-rise signal height. For S_1 over E_{Advanced} this effect is compensated.

The baseline corresponds to the mean signal height without an event peak. It also has to be corrected with the pole-zero factor P because changes in the baseline height also follow an exponential decay. The baseline B can be approximated via the two following equations:

$$B_1 = \frac{\frac{S_2}{M} m_2^{\text{begin}} - \frac{S_1}{M} m_3^{\text{begin}}}{(\frac{S_2}{M} - \frac{S_1}{M}) - (m_3^{\text{begin}} - m_2^{\text{begin}})} = \frac{S_2 m_2^{\text{begin}} - S_1 m_3^{\text{begin}}}{(S_2 - S_1) - M(m_3^{\text{begin}} - m_2^{\text{begin}})} \tag{5.14}$$

$$B_2 = \frac{m_2^{\text{end}} m_3^{\text{begin}} - m_2^{\text{begin}} m_3^{\text{end}}}{(m_3^{\text{begin}} - m_3^{\text{end}}) - (m_2^{\text{begin}} - m_2^{\text{end}})} \tag{5.15}$$

For a real physics event, B_1 and B_2 should be approximately equal. To decide if an event is physical or not, it has to be checked if the ratio $r = B_1/B_2$ is close to 1.

In Figure 5.2 (b) it can be seen that the correction applied from Equation 5.9 worked properly. Here, the value S_1 is plotted versus E_{Advanced} for an ^{88}Y source measurement. Now for a given energy E_{Advanced}, only vertical straight lines can be seen. This means that the calculated raw energy does not depend on the pre-rise signal behaviour anymore.

In total, the raw energy calculation works for every detector separately with the following steps:

1. Loop over all events of a source run and calculate B_1 and B_2 following Equation 5.14 and 5.15 respectively. If the ratio $r = B_1/B_2$ is between 0.95 and 1.05, calculate the factor $e^{-\lambda M}$ following Equation 5.12 and store them.

2. When the loop is finished, calculate the mean value for all stored $e^{-\lambda M}$ and use this mean value in Equation 5.13 to obtain the pole-zero value P. Store the P value for each detector.

This value is used later for all further calculations since P should not change during an experiment.

3. Loop over the part of the data which should be analysed and calculate B_1 and B_2 following Equation 5.14 and 5.15 respectively. If the ratio $r = {}^{B_1}/_{B_2}$ is between 0.95 and 1.05, store the baseline value B_1.

4. Calculate the mean value of B using the stored B_1 values (the running average).

5. Loop over the same part of the data and calculate the raw energy following Equation 5.9 using P from step 2 and B from step 4.

During the analysis in this thesis, it is looped each time over one run-file for step 3 and 5. One run-file corresponds to a beam time of roughly 1 hour. The pole-zero values used for all detectors can be seen in Table A.4 and A.5.

5.2 Energy Calibration of Gammasphere

In the next step, the raw energy is calibrated to get a proper energy spectrum. For this, four source measurements have been performed before and after the experiment. For each source, all clearly visible and separated peaks were used for calibration. The gamma-ray energies of these standard sources are known very precisely. The following gamma-ray energies were used:

- ^{56}Co: 511.006, 846.771, 1037.840, 1238.282, 1771.351, and 2598.459 keV
- ^{152}Eu: 244.697, 344.279, 778.904, 867.373, 964.079, and 1408.006 keV
- ^{88}Y: 898.042 and 1836.063 keV
- ^{16}O: 6128.63 keV

In total, 15 different gamma-ray energies between 235 keV and 6130 keV have been used to calibrate the detectors. To obtain the excited ^{16}O, which decays via a gamma ray with an energy of 6128.63 keV, a combined source has been used. The combined source consists of ^{238}Pu and ^{13}C. The ^{238}Pu makes an α decay with $\tau \approx 127$ a, which allows the reaction $^{13}\mathrm{C}(\alpha{+}\mathrm{n})^{16}\mathrm{O}^*$ to happen inside the combined source.

For the calibration, first the raw advanced energy E_{Advanced} using Equation 5.9 is calculated as explained in Section 5.1. Then each peak is identified and the position of the peak is defined by Gaussian fits to the spectra. Then these positions are set in relation to the actual energy of the peak using the linear relationship

$$E[\mathrm{keV}] = \mathrm{Gain}[\mathrm{keV/Channel}] \cdot E_{\mathrm{Advanced}}[\mathrm{Channel}] + \mathrm{Offset}[\mathrm{keV}]. \tag{5.16}$$

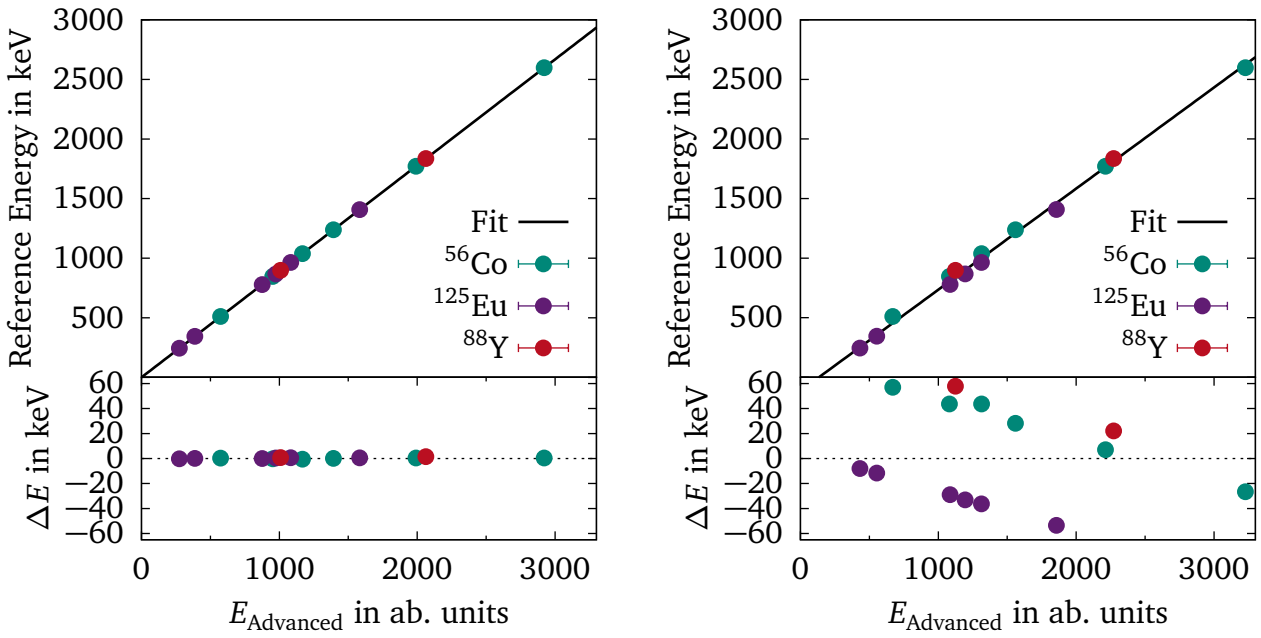

(a) Detector 55

(b) Detector 79

Figure 5.3: Energy calibration of the Gammasphere detectors 55 and 79 between 245 keV and 2600 keV for the source measurement of ^{56}Co, ^{152}Eu, and ^{88}Y. The ^{16}O data points are not shown here, but they were used for the calibration fits. The error bars are too small to be visible but they are considered for the fit. In the lower part of the plot, the residual for the calibrated energy E is shown.

The linear calibration went well for most of the detectors. The values for gain and offset can be found for all detectors in Table A.4 and A.5. An example of a successful calibration can be seen in Figure 5.3 (a) for detector 55. But for three detectors, namely number 19, 40, and 79, some problems occurred. For the detectors 19 and 79, it was not possible to achieve a consistent linear calibration for all of the source peaks. As an example, Figure 5.3 (b) shows the calibration that did not work for detector 79. Detector 40 did not produce useful spectra at all. Here, for each physical gamma-ray energy two peaks arise in the spectrum. Hence, the spectra for detector 19, 40, and 79 were declared unreliable and are not used in any further analysis.

5.3 Efficiency Calibration of Gammasphere

For later count rates and branching ratio estimations, the efficiencies of the Gammasphere detectors have to be known. To obtain the efficiencies for the different detectors and the whole setup again, the source measurements are used.

In the first step, the total efficiency for two energies is calculated using the ^{88}Y source measurement. For this, the so-called “counting method” is used following the approach from [Thi11, Wam11]. Here a decay which features the emission of two successive gamma rays is

exploited. As it can be seen in the decay scheme in Figure A.5, this is always the case for ^{88}Y. When the gamma ray γ_A with E_a=898 keV is emitted, the gamma ray γ_B with E_b=1836 keV has always to be emitted too. To get the absolute efficiency, it is looped over all events of the ^{88}Y measurement and the following quantities are evaluated for each event:

- If γ_A or γ_B is recorded more than one time the event is disregarded in order to suppress random coincidences.
- If only γ_A was measured, the quantity A_{tot} is increased by one.
- If only γ_B was measured, the quantity B_{tot} is increased by one.
- If the gamma ray γ_A was recorded in detector k and in the same event gamma ray γ_B was recorded in detector l, the quantities A_{tot}, B_{tot}, A_k, and B_l are increased by one.

Afterwards, the total efficiency for the detector i and for the two energies E_a and E_b is given by

$$\epsilon_i(E_a) = \frac{A_i}{B_{tot}} \cdot \frac{4\pi}{\Omega_D} \cdot \frac{I_B}{I_A} \text{ and} \tag{5.17}$$

$$\epsilon_i(E_B) = \frac{B_i}{A_{tot}} \cdot \frac{4\pi}{\Omega_D} \cdot \frac{I_A}{I_B}. \tag{5.18}$$

Here Ω_D is the solid angle of one detector which is 0.418 % of 4π (cf. Sec. 3.3). The relative intensities for the two gammas are given by I_A=93.7(3) % and I_B=99.2(3) % [MS14]. Afterwards, the mean efficiency (mean value over all detectors) is calculated to $\epsilon(E_A)$=6.561(30) % and $\epsilon(E_B)$=3.965(19) %.

In the second step, the relative efficiency $\epsilon_{rel}(E)$ depending on the gamma-ray energy E is calculated for a larger energy range using the ^{56}Co source. The known relative gamma-ray intensities $I_{rel}(E)$ are taken from [JSD11]. With this data, it is possible to calculate the relative efficiency of the detector for energy E_i using the relation

$$\epsilon_{rel}(E) = \frac{C(E_i)}{C(E_0)} \cdot \frac{I_{rel}(E_0)}{I_{rel}(E_i)} \tag{5.19}$$

where $C(E_i)$ and $C(E_0)$ are the total number of counts for the transition with the energy E_i and E_0, respectively. The number of counts is achieved by applying Gaussian fits to the spectrum at the corresponding peaks. The relative efficiency is normalized to the efficiency at E_0 for which any transition can be chosen. Here, the transition with 846.77 keV was used for E_0. All used energies and relative gamma-ray intensities can be found in Table A.9. The results are plotted in Figure 5.4 (a). The data as fitted using the function

$$\epsilon_{rel}(E) = \frac{p_0}{E - p_1} + p_2 \tag{5.20}$$

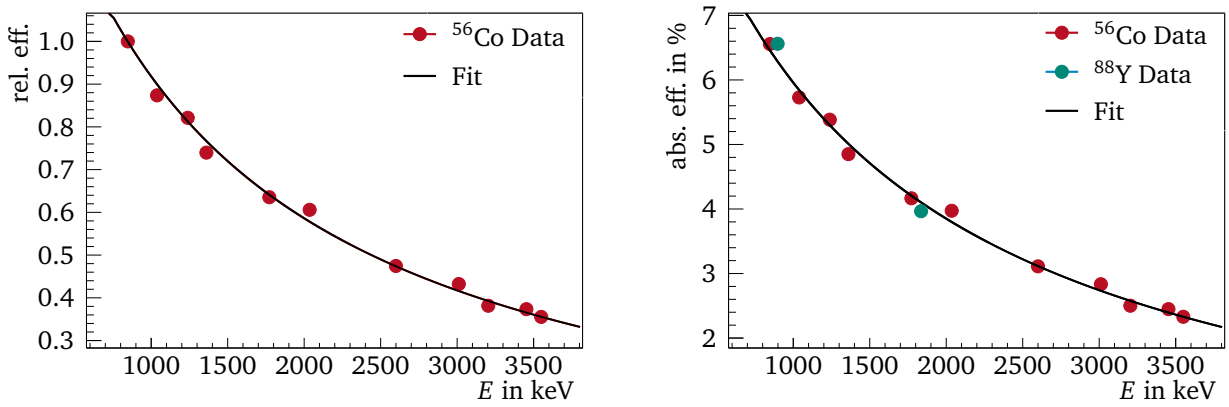

(a) Relative efficiency

(b) Absolute efficiency

Figure 5.4: Efficiency calibration of Gammasphere: The left plot shows the relative efficiency calibration normalized to the transition at 846.77 keV. The right plot shows the absolute efficiency calibration. The fit function is given by Equation 5.20. The error bars are too small to be visible but they are considered for the fit.

and so the uncertainty is given by

$$u^2(\epsilon_{\mathrm{rel}}(E)) = \left(\frac{1}{E-p_1}\Delta p_0\right)^2 + \left(\frac{p_0}{(E-p_1)^2}\Delta p_1\right)^2 + (\Delta p_2)^2 \\ + 2\frac{p_0}{(E-p_1)^3}\mathrm{cov}(p_0,p_1) + 2\frac{p_0}{(E-p_1)^2}\mathrm{cov}(p_1,p_2) + 2\frac{1}{E-p_1}\mathrm{cov}(p_0,p_2) \tag{5.21}$$

where $\mathrm{cov}(p_k,p_l)$ is the covariance between p_k and p_l. The fit parameters are determined to be p_0=2109(62) keV, p_1=−1070(37) keV and p_2=−0.101(1).

In the last step, the data points and the Function 5.20 are scaled so that they conform to the mean value of the absolute efficiency, which were obtained for the ^{88}Y source in the first step. The result of this can be seen in Figure 5.4 (b). The scaled parameters are determined to be p_0'=15080(1199) keV%, p_1'=−1221(119) keV and p_2'=−0.83(19) %. With this scaled Function 5.20, it is now possible to calculate the absolute mean efficiency for a given gamma-ray energy. So for example at 1 MeV the total efficiency is 5.95(2) %.

5.4 Proton Cuts

To select the ^{16}C reaction channel, it is necessary to gate on events at which two protons were emitted. To do so, the PID of μ-Ball is used (cf. Sec. 3.4). A typical measurement of one μ-Ball detector can be seen in Figure 5.5 (a) and (b). In this figure, the data points from approximately one hour of beam time for μ-Ball detector 21 (θ=36°) are plotted. In Part (a), the height of the signal tail C versus the signal height B is plotted. One can clearly identify the different residual

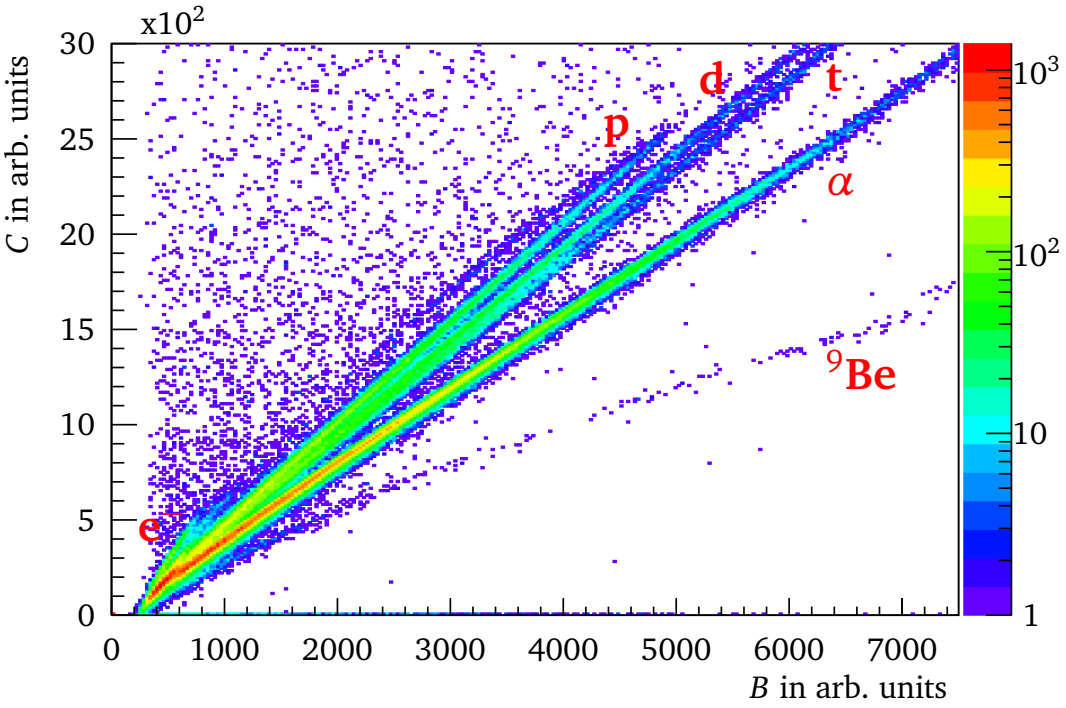

(a) PID: C vs. B

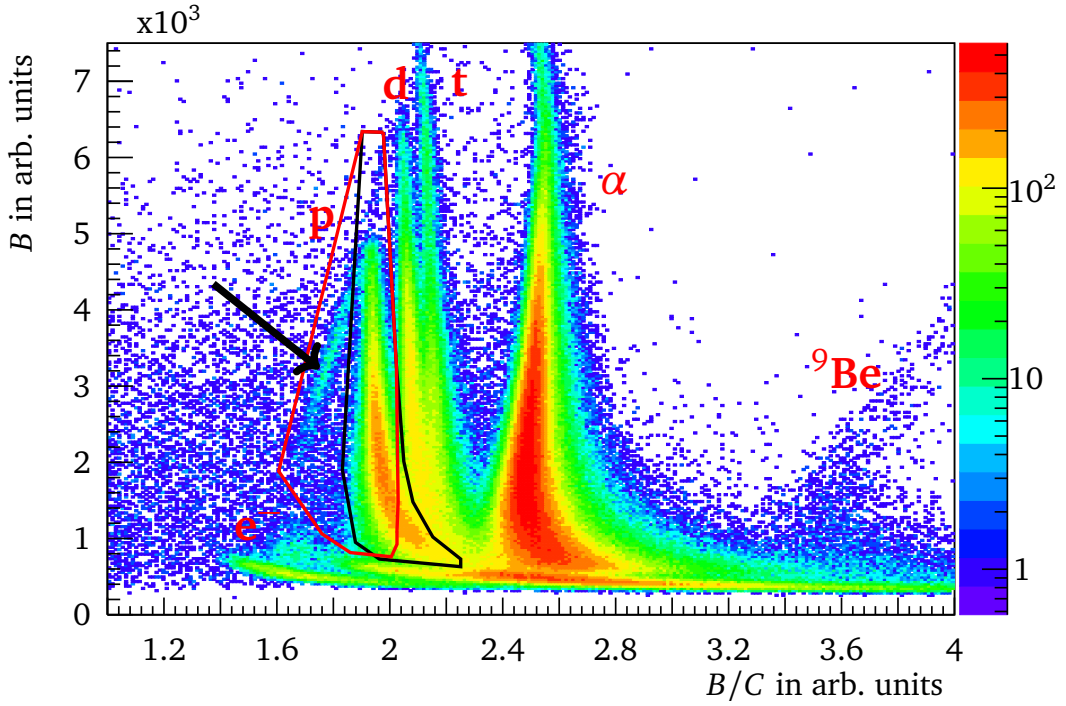

(b) PID: B vs. B/C

Figure 5.5: Particle identification for one target-and-degrader-run using μ-Ball: The data are shown for detector No. 21 (θ=36°). One can identify the different particles, namely electrons (e^-), protons (p), deuteron (d), tritium (t), α-particles (α), and ^{9}Be particles. The normal proton cut is shown in black and the clean proton cut is shown in red in Part (b). The black arrow marks the location of the proton punch-through events.

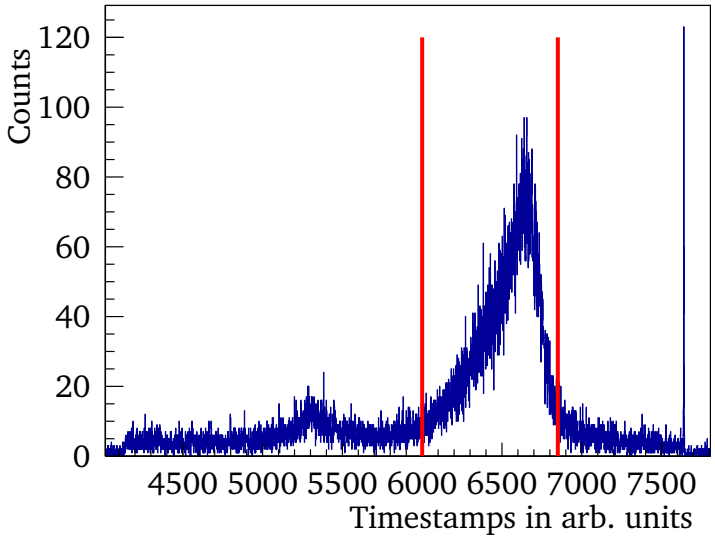

Figure 5.6: Internal μ-Ball timestamps and time cuts for detector 43 and for one run. The time cuts are at 6000 and 6859 (cf. Tab. A.7). They are illustrated by the red lines.

particles, namely electrons (e^-), protons (p), deuteron (d), tritium (t), α-particles (α), and some elastically scattered ^{9}Be beam particles. In Part (b) of Figure 5.5, the signal height is plotted versus the ratio B/C. In this representation, the proton cuts have been applied. Here two kinds of cuts have been applied. The cut marked in black is the so-called normal proton cut. This cut was chosen to maximize the statistics in the two proton channel. But here contaminations from the deuteron and tritium channel are possible. The cut shown in red is the so-called clean proton cut. For this cut the risk of a possible contamination from the deuteron and tritium channel is minimized. But here the statistic in the two proton channel will be smaller. Furthermore, the black arrow shows the positions of proton punch-through events. For these events the proton energy was so high that the protons could leave the CsI detectors before they deposited their complete energy in the detector. For these events the particles can also be identified as protons but a proper energy can not be obtained for these protons. Due to the fact that the proton energy (cf. Sec. 5.6) is later used for the analysis, these events are not included into the clean proton cuts. Events for which two particles are detected in the proton cuts will be from now on called 2p events. Also the cut will be shorty called p cut or 2p cut.

All these cuts have been created for all used μ-Ball detectors. Here it was noticeable that the position of the data points sometimes moved when run files were changed. This can be explained by a slight drift in the electronics during the experiment due to rising temperature. To correct this, the proton cuts were checked for each detector and run file and were adjusted if necessary.

Furthermore, it should be mentioned that nine detectors of μ-Ball were not available during this experiment. All six detectors in ring number 1 were disabled and an additional shielding was mounted to save these detectors from radiation damage due to elastically scattered beam

particles. Three detectors, namely detector No. 55 (θ=90°), 57 (θ=90°) and 93 (θ=159°) had a malfunction and their data could not be used. In total, 86 μ-Ball detectors were available during the experiment.

Additionally to the PID information, μ-Ball provides its own internal timestamps for every entry. To achieve a proper PID and proper coincidences between μ-Ball and Gammasphere (cf. Sec. 5.5), a time gate onto the prompt peak in the time spectra has to be set for each detector. The time gates for all detectors can be found in Table A.7. An example for detector 43 is shown in Figure 5.6.

5.5 Event Builder and Time Cut

In the next step of the analysis, a coincidence between Gammasphere and μ-Ball entries has to be applied. An entry was written whenever Gammasphere or μ-Ball detected something. For the coincidence, the global timestamps of the recorded entries are used. The timestamps are an up-counting integer which increased continuously during the experiment. The timestamp difference of two consecutive entries can be seen in Figure 5.7. Here the left peak (marked by I) stems from the prompt gamma rays which were measured by Gammasphere. These are gammas which can be assumed as coincident. The peak width is going from 0 to 4 channels. One channel corresponds approximately to 12 ns. The entries in the middle of the plot are produced by random coincidences. The wiggling structure, which can be seen, stems from the radio frequency of the cyclotron. The width of the wiggling is approximately 8 channels, which is around 96 ns. The peak on the right side (marked by II) corresponds to the μ-Ball entries which are in coincidence with the Gammasphere entries. The red lines indicate the applied time cut. They are located by channel 650 and 665. So the coincident μ-Ball entries were recorded roughly 8.2 µs after the corresponding Gammasphere entries. The Gammasphere entries are all separated in terms of the timestamps, which means that every entry has its own timestamp and the raw multiplicity of one Gammasphere entry is always one. The μ-Ball entries are already combined for the different μ-Ball detectors, which means that one μ-Ball entry can have a μ-Ball multiplicity larger than one. Also the Gammasphere entries come first because the μ-Ball readout was delayed. Now an event building algorithm has to be developed which reads all entries and creates events for which the chosen Gammasphere entries and possible μ-Ball entries are in coincidence.

For this algorithm three major loops over the data are executed. In the first loop all data are read from the files and so it is looped over every entry available. During this loop it is checked whether the signals from the μ-Ball entries fulfil the proton-cuts and the μ-Ball time gates (cf. Sec. 5.4). If the multiplicity of a μ-Ball entry is two and both signals fulfil the proton-cuts as well as the μ-Ball time gates, this entry is saved as a valid μ-Ball event. So every μ-Ball entry is either refused or saved as one single μ-Ball event. At the same time all Gammasphere entries are saved to Gammasphere events. Thereby it is checked, if the timestamp difference between the

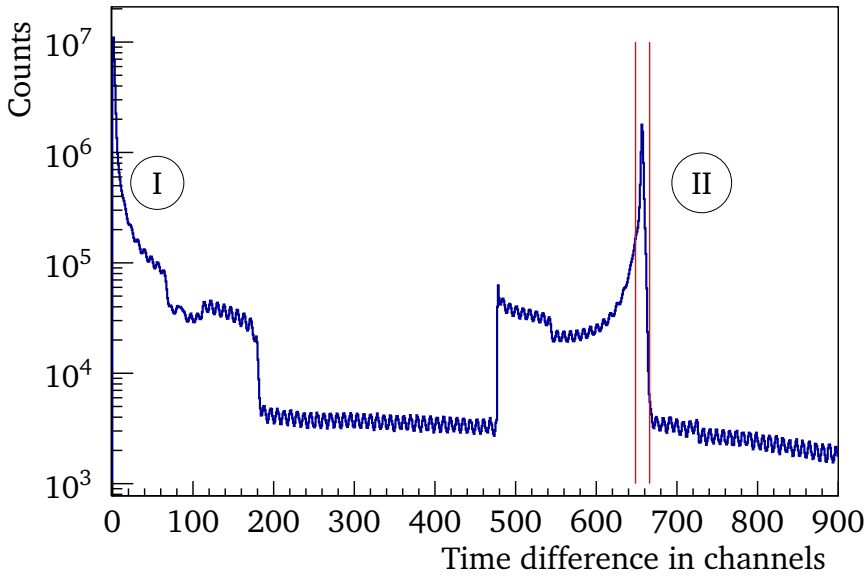

Figure 5.7: Time difference of two consecutive entries. The red lines show the time gate which is applied for the μ-Ball entries. The peak marked with I corresponds to the prompt gamma-ray entries, while the peak marked with II corresponds to μ-Ball entries. The wiggling structure stems from the radio-frequency of the accelerator.

first entry of a Gammasphere event and consecutive entries is smaller or equal than 4 channels. If this is the case all these entries are added to one Gammasphere event. If this is not the case, the current Gammasphere event is finished and the current read Gammasphere entry is set to the first entry of a new Gammasphere event. The second loop looks through all so far saved Gammasphere events and applies the BGO suppression for each event. Afterwards, the third loop loads all remaining Gammasphere events. The loop checks for each Gammasphere event if a μ-Ball event exists for which the timestamp came 650 up to 665 channels later than the Gammasphere timestamp. If this is the case a two proton event (2p event) is saved using the data from the current Gammasphere event and the corresponding μ-Ball event. All other events are ignored. The so created 2p events can be then used for the following analysis.

5.6 Energy Calibration of Microball

For later analysis the kinetic energies of the protons in the target-only-runs have to be known. Therefore, the energy calibration for μ-Ball is explained in this section. For the calibration a proton beam with 12.24(11) MeV was shot on a ^{12}C target for a few hours. The target had a thickness of 100 $\mu g/cm^2$. The scattered protons were measured by μ-Ball. The energy calibration for μ-Ball consists of two steps. First, the detector output of channel B is converted into an energy value E_{CsI} the protons deposited in the given CsI(Tl) detector. Afterwards, these energies have to be corrected for the energy loss the protons suffered while passing the different absorbers

which are mounted in front of the μ-Ball detectors (cf. Sec. 3.4). Applying this correction one gets access to the kinetic energy the protons had after they left the target in the target-only-runs. Assuming the energy loss in the thin target of the target-only-runs is neglectable, the so obtained proton energy represents the energy the protons had directly after their evaporation.

The first step of the energy calibration was performed by the group of D.G. Sarantites et al. [Sar16]. They identified three prominent peaks in the proton energy spectrum for each detector and got their positions in terms of the signal height from channel B. The three different peaks belong to the three possible reactions the protons can have with the ^{12}C target: The protons can scatter elastically at a ^{12}C nucleus or the protons excited the ^{12}C to the 2^+_1 state (at 4439 keV) or the protons excited the ^{12}C to the 0^+_1 state (at 7654 keV, Hoyle state). Then they calculated for these three cases the expected energy E_{CsI} the protons should have deposited in the CsI(Tl) of a μ-Ball detector. These calculations include the full scattering kinematic, the energy loss in the target and the energy loss due to the different absorbers in front of the CsI(Tl) detectors. The results of this calculations can be found in Figure A.3. Finally, they could assign the three peak positions in terms of the signal height from channel B to the energy E_{CsI} in MeV which the protons should have deposited in the CsI(Tl) detectors. With this data, calibration-functions of the form

$$E_{\mathrm{CsI}}[\mathrm{MeV}] = \mathrm{Gain}[\mathrm{MeV/Channel}] \cdot B[\mathrm{Channel}] + \mathrm{Offset}[\mathrm{MeV}] \tag{5.22}$$

could be fitted for every detector. The gain and the offset for all μ-Ball detectors are listed in Table A.8. So it is now possible to calculate E_{CsI} according to Eq. 5.22 for all proton events.

In the second step of the energy calibration the energy E_{CsI} has to be corrected for the energy loss the protons suffer in the absorbers. As stated in Section 3.4 each detector surface is covered by two layers. A thin aluminium foil is directly attached to the CsI(Tl) detectors. On top of this a Pb or Ta absorber is mounted, where the type of the absorber and the thickness varies from detector to detector. Hence, the energy will be corrected first for the aluminium foil and then for the Pb or Ta layer depending on which detector was hit. To correct for the energy loss, incoming proton energies E are plotted over the total proton range R in the given material. The proton range data for all materials were obtained using SRIM [Zie19, JFZ15]. Figure 5.8 illustrates the principle idea of the energy loss correction for an aluminium foil. The black curve shows the relation between the proton energy E[MeV] and the range R[µm] in aluminium. It was found out that this relation can be described very well by the function

$$E(R) = p_{\mathrm{Al},1} \cdot \sqrt[3]{R} + p_{\mathrm{Al},2} \cdot \sqrt[2]{R} + p_{\mathrm{Al},3} \cdot R, \tag{5.23}$$

where $p_{\mathrm{Al},1}$, $p_{\mathrm{Al},2}$, $p_{\mathrm{Al},3}$ are fit parameters. The fit to the proton range data from SRIM leads to $p_{\mathrm{Al},1}$=$-0.4336\,\mathrm{MeV}/\mu\mathrm{m}^{1/3}$, $p_{\mathrm{Al},2}$=$0.54019\,\mathrm{MeV}/\mu\mathrm{m}^{1/2}$ and $p_{\mathrm{Al},3}$=$0.000356\,\mathrm{MeV}/\mu\mathrm{m}$ for aluminium. To apply the energy loss correction, first the already known energy E_{CsI} is taken and the intersection $E(R_1)$=E_{CsI} is numerically calculated. Then the value R_2=R_1+d_{Al} is calculated, where d_{Al} is the

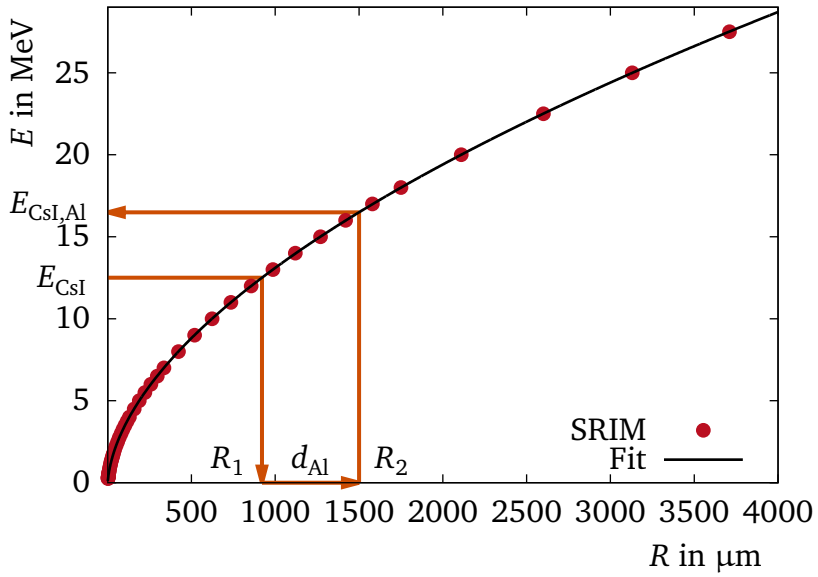

Figure 5.8: The idea of the energy loss correction for μ-Ball detectors is shown for aluminium foils. The proton range data are obtained from SRIM [Zie19, JFZ15]. The proton energy E in MeV is plotted over the corresponding range R in the material. The parameter E_{CsI} is the proton energy which the protons deposited in the detector, while d_{Al} is the foil thickness. The goal variable is the proton energy before they passed the foil marked by $E_{CsI,Al}$. The shown function $E(R)$ can be described by Equation 5.23.

thickness of the current aluminium foil. Finally, one gets the energy the protons had before they entered the aluminium foil defined by $E_{CsI,Al}=E(R_2)$. With these results the energy E_{CsI} can be converted to the energy $E_{CsI,Al}$ the proton had before entering the aluminium foil for every event.

After this is done one applies the same method for the Pb or Ta absorbers. Here, one starts with $E_{CsI,Al}$ as an input to find the intersection $E(R_1)=E_{CsI,Al}$. Then $R_2=R_1+d_{Pb/Ta}$ is calculated, which finally leads to $E_{CsI,Al,Pb/Ta}=E(R_2)$. The value $E_{CsI,Al,Pb/Ta}$ gives now the energy in MeV the protons had before they hit an absorber and so this is the energy which will be used in the following analysis. The fits to the SRIM range data for Pb and Ta can be seen in Figure A.4 (a) and (b), respectively. The fit parameters were obtained as $P_{Pb,1}=-0.730\,\mathrm{MeV}/\mu\mathrm{m}^{1/3}$, $p_{Pb,2}=0.8237\,\mathrm{MeV}/\mu\mathrm{m}^{1/2}$ and $p_{Pb,3}=0.00212\,\mathrm{MeV}/\mu\mathrm{m}$ for Pb as well as $p_{Ta,1}=-0.903\,\mathrm{MeV}/\mu\mathrm{m}^{1/3}$, $p_{Ta,2}=1.0517\,\mathrm{MeV}/\mu\mathrm{m}^{1/2}$ and $p_{Ta,3}=0.00274\,\mathrm{MeV}/\mu\mathrm{m}$ for Ta.

The results of this energy calibration and corrections are shown in Figure 5.9. The data are obtained for 2p events which are taken from target-and-degrader-runs. In the figures the energy of one proton is plotted against the energy of the other proton for each 2p event. In Part (a) the uncalibrated energy distribution given by the signal height B is shown. These values are converted to E_{CsI} in MeV following Equation 5.22. The result of this is shown in Figure 5.9 Part (b). It can be seen that the proton energies which were deposited in the CsI(Tl) detectors are spread in a range from 1 MeV to 28 MeV, whereat the mean is around 6.15 MeV. Part (c) and

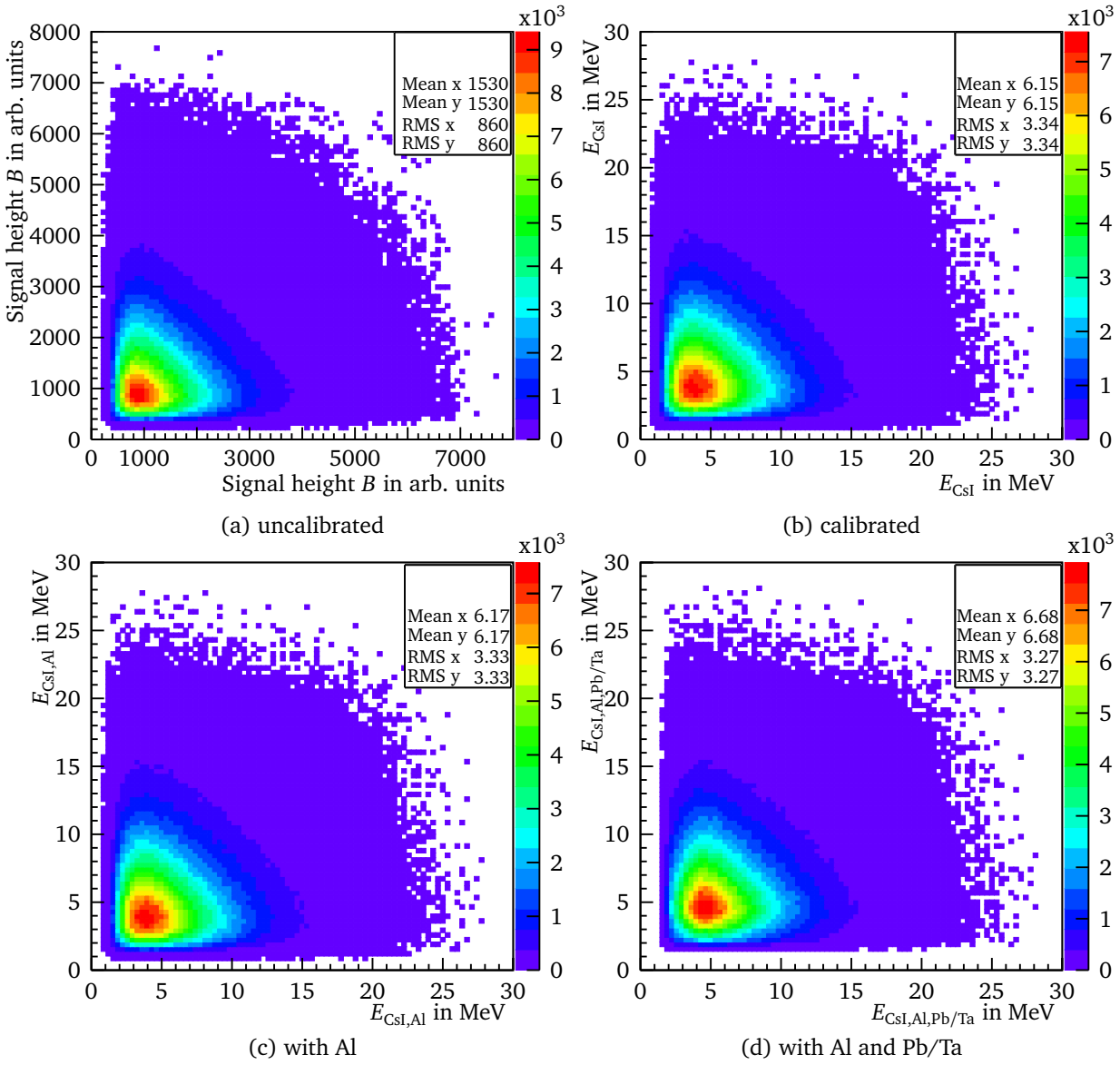

Figure 5.9: Proton energy distributions for dirty 2p events which are taken from target-and-degrader-runs.

(d) of Figure 5.9 show the proton energies corrected for the absorbers. The mean value of the energy distribution for the aluminium correction $E_{CsI,Al}$ (Part (b)) did not change compared to the E_{CsI} energies. This can be explained with the fact that the aluminium foils were very thin. Their thickness reached from 0.15 $^{mg}/_{cm^2}$ to 0.58 $^{mg}/_{cm^2}$. Also the stopping power of aluminium is much smaller compared to the stopping power of Pb or Ta. The distribution of the energies $E_{CsI,Al,Pb/Ta}$, which are corrected for aluminium and the Pb/Ta absorbers, has a mean value which is 0.5 MeV larger than the mean value for E_{CsI} or $E_{CsI,Al}$. This confirms that the energy loss in the Pb/Ta absorbers can not be ignored if the proton kinematic is used in later analysis. Furthermore, the spread in the energy distributions (cf. Root Mean Square (RMS) in Figure 5.9) is smaller for the full corrected energy $E_{CsI,Al,Pb/Ta}$ compared to the distribution of E_{CsI}. This behaviour can be

explained with the fact that the absorber correction eliminates artificially induced offsets in the measured proton energy E_{CsI} due to the different absorber thicknesses for the different detectors. The proton energies from Figure 5.9 Part (d) can now be used for further analysis.

5.7 Proton Distributions

In this section the proton energy and angular distributions for 2p events are investigated. The distributions for target-only-runs and target-and-degrader-runs are compared in respect of artificial changes in the proton kinematics. Changes in the detected proton kinematics lead to changes in the kinematic of the residual isotopes (e.g. ^{16}C) which are used for analysis as well. This can influence the extraction of mean decay betas in later analysis.

Figure 5.10 shows the 2p events energy distributions for target-only-runs (a) and target-and-degrader-runs (b) with a gamma gate on the 2_1^+ of ^{16}C. Hence, mainly protons which are in coincidence with ^{16}C events are shown. This is done to get rid of uncorrelated random protons from other reactions. The same analysis was also done for a ^{23}Ne channel (cf. Sec. 6.1) as well as all 2p events which lead to very similar results. Thus, the proton angular distributions are mainly dominated by the kinematic of the beam and the energy loss in the target and degrader. Hence, only the case of ^{16}C is discussed in the following.

The plotted energies in Figure 5.10 are the absorber corrected proton energies $E_{\mathrm{CsI,Al,Pb/Ta}}$ calculated as stated in Section 5.6. It can be seen that the mean value of the distribution is smaller for the target-and-degrader-runs than for the target-only-runs. This can be explained with the fact that the protons lost some energy in the degrader before they are registered by the μ-Ball detector. But as stated in Section 5.8 the detected proton energy distribution directly influences the mean decay beta which can be extracted from the gamma-ray spectra. This has to be considered in the target-only-run analysis which is discussed in Section 5.8.

Furthermore, not only the proton energy distribution is important for the mean decay beta analysis but also the proton angular distribution. The angles of the protons define their momentum direction and due to conservation of momentum, the momentum of the protons after the evaporation influences directly the momentum of the residual particle (e.g. ^{16}C). Because only the momentum part along the beam axis is relevant the θ_{p} distributions are analysed.

Figure 5.11 shows the 2p events θ_{p} distributions for target-only-runs (a) and target-and-degrader-runs (b) with a gamma gate on the 2_1^+ of ^{16}C. The θ_{p} angles are the angles of the μ-Ball ring which detected the protons (cf. Sec. 3.4 and Fig. 3.4). In the Figure 5.11 a trend can be seen that for both settings more protons are detected under forward angles compared to backward angles. This can be explained with the high beam velocity along the beam axis, which boost the protons more in forward directions. The ring at 90° detected fewer protons as its neighbour rings. This is expected because protons have to travel a very long way through the target and/or degrader if they travel towards a detector under 90°. If they are emitted under nearly 90° they

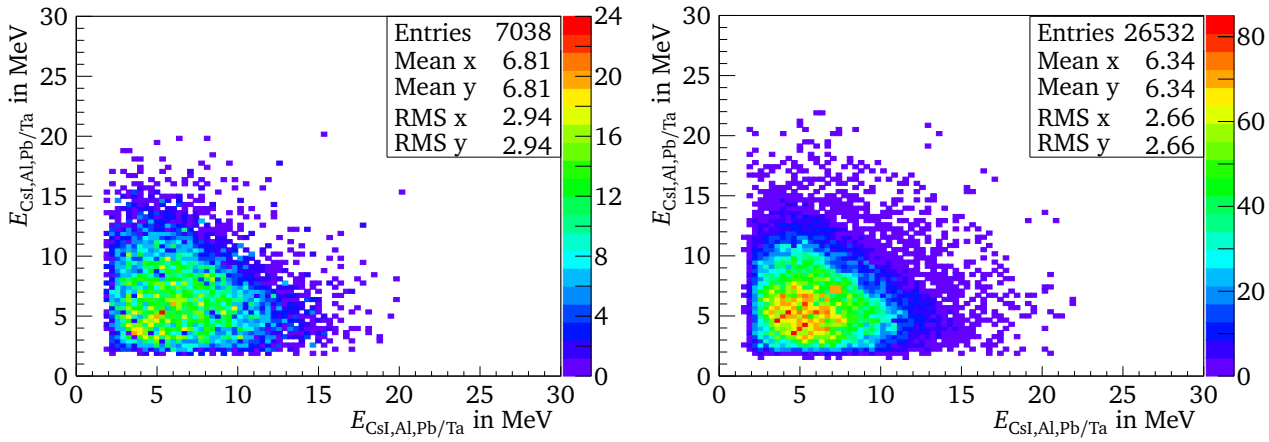

(a) target-only-runs (b) target-and-degrader-runs

Figure 5.10: Proton energy distribution of $E_{CsI,Al,Pb/Ta}$ for dirty 2p events with a gamma gate on the 2_1^+ of ^{16}C.

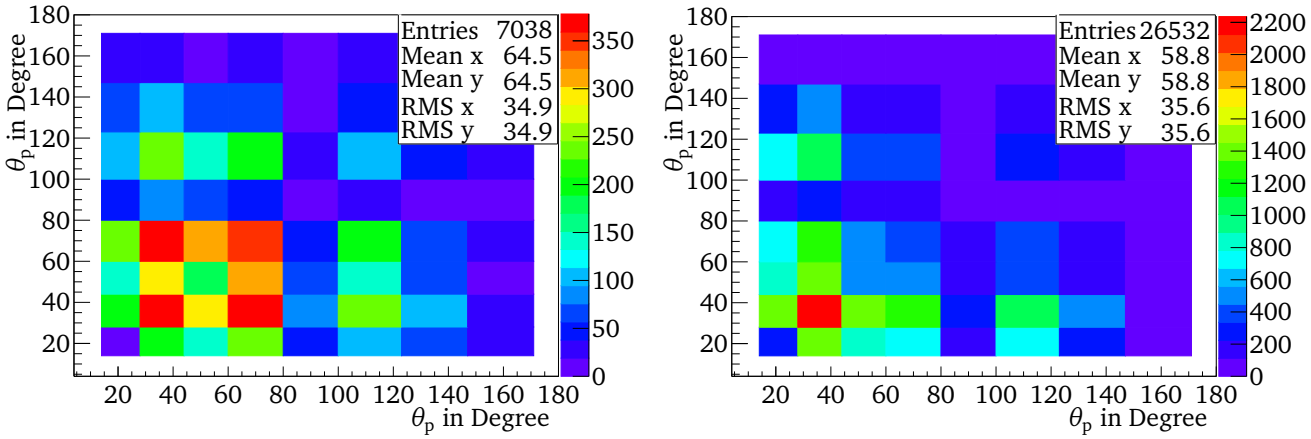

(a) target-only-runs (b) target-and-degrader-runs

Figure 5.11: Proton θ_p distribution for dirty 2p events with a gamma gate on the 2_1^+ of ^{16}C. The irregular binning of the 2D-histograms is matched to the opening angles of the μ-Ball rings (cf. Fig. 3.4).

have to travel perpendicular to the beam axis which means that they have to pass half of the target width, which is in the range of mm. Hence, these protons will stuck in the target and/or degrader material and will not be measured.

Looking further at Figure 5.11 one can see that especially under forward angles the θ_p distributions differ a lot comparing target-only-runs to target-and-degrader-runs. For the target-only-runs a larger ratio of protons is detected under forward angles (<90°) compared to the target-and-degrader-runs. This is expected, because it is likely that protons with smaller energies will get stuck in the degrader and are not able to reach the detectors. This fact also influences the mean and the RMS of the distributions, which differ significantly comparing the two settings. Hence,

the presence of a degrader influences the angular distribution very strongly. It seems that this effect is even more pronounced than for the energy distributions. Hence, the absence of the degrader in the target-only-runs will have a significant influence on the extracted mean decay beta. Due to this, a correction has to be applied to the target-only-runs. This will be the main topic of the next section.

5.8 Target-Only-Runs

As stated in Section 4.3, it is necessary to obtain a value for the initial beta with which the residual isotopes are spawned in the Geant4 simulation. For this, the target-only-runs are analysed. In the target-only-runs, a thin ^{9}Be target is used without a degrader. The target thickness was 0.5 µm. In the target the excited residual isotopes of interest (e.g. ^{16}C) are created. Afterwards, they left the target and de-excited by emitting a gamma ray in-flight. Because the slow down effect in the thin target is negligible, the velocity of the particle during the decay is approximately the same as the velocity the particle has directly after its creation. This means that the average influence of the fusion-evaporation kinematics is already included in the mean decay beta. By extracting the mean decay beta from the target-only-runs, one gets a good starting point for the initial beta which is used in the Geant4 simulations. This method also has the additional advantage that all systematics of the experimental setup are already included in the extracted mean decay beta. If the beta is extracted from the target-only-run, only gamma rays are taken into account which were measured in coincidence with two protons in μ-Ball. Due to this, the data themselves include systematic effects of proton loss in the target, the sensitivity of the μ-Ball detectors, and the sensitivity of the Gammasphere detectors. The sensitivity of the μ-Ball detectors can have an especially large influence onto the results. Here, the sensitivity is strongly angle dependent because the shielding at the μ-Ball detectors is not the same for all angles. Also, the most forward angle was not used at all. This creates an unsymmetrical bias whether a proton is recorded or not. But this directly influences the extracted mean decay beta, because the mean decay beta of the residual isotope depends on the emitting direction of the two protons. Further, it is nothing known about the fusion-evaporation kinematics, especially in terms of the proton energy distributions. Hence, it is a huge advantage to use the results from the target-only-run as an input into the simulations.

As shown in Section 5.7, the angular and energy distributions of the protons change systematically comparing the target-only-runs with the target-and-degrader-runs. This behaviour is quite obvious, because protons under forward angles with low energies can get stuck in the degrader. These protons will not reach a μ-Ball detector and so this event is skipped in the 2p cut. This effect is not symmetrical along the beam axis and hence this leads to a change in the measured beta. Hence, for target-and-degrader-runs the mean decay beta will be only measured for events for which no slow protons were evaporated under forward angles. Assuming the 2p events from the

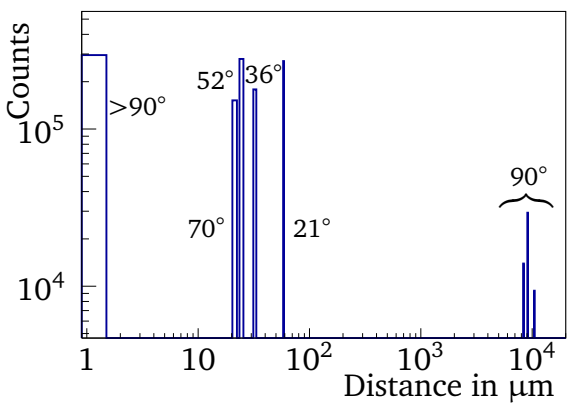

(a) Proton distance in degrader

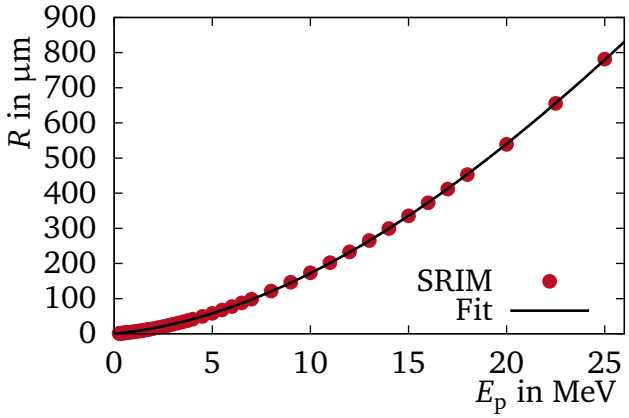

(b) Proton range in gold

Figure 5.12: Proton distance distribution (a) and range in a fictive gold degrader (b). The data in Part (a) are for a fictive gold degrader with 19.9 µm thickness and 16.43 mm width for the target-only-runs. The shown angles indicate the angles of the μ-Ball rings. Part (b) shows the range R for protons in gold according to SRIM calculations [Zie19, JFZ15]. The shown fit function is given by Equation 5.24.

target-and-degrader-runs are sensitive to a "goal" proton distribution without slow protons, then the 2p events proton distribution from the target-only-runs have to be modified to reproduce the same systematic proton loss. This modification is explained in the following.

For this modification the loss of protons due to a fictive gold degrader is simulated during the analysis of the target-only-runs. In the first step, the distance the protons have to cover in such a fictive gold degrader is calculated. For this it is assumed that protons are created at the center of the thin target (which is justified due to the small size of the target compared to μ-Ball) and that the angle of the protons matches the angle of the μ-Ball detector which detects the particular proton. Due to the opening angles of the μ-Ball detectors this is not really true but it is the best approach which can be done for this setup. With these assumptions it is possible to create a vector of direction for each proton. Then the distance each proton would travel inside a fictive gold degrader is calculated. The fictive gold degrader has the same dimension as the real degrader in the target-and-degrader-runs. Therefore, the thickness of the fictive gold degrader along the beam axis is 19.9 µm and the width perpendicular to the beam axis is given by 16.43 mm each. If protons are emitted under backward angles the covered distance in the fictive degrader is set to zero because the degrader sits downstream relative to the target.

The distribution of the distance the protons have covered in such a fictive gold degrader is shown in Figure 5.12 (a) for all target-only-runs. The peaks are assigned to the angles of the corresponding μ-Ball detector rings. As stated earlier protons which are detected under backward angels (θ_p>90°) do not pass the fictive degrader and so their distance is set to zero. The protons which are detected under forward angels (70° to 21°) cover distances in the range

of several 10 µm. If the protons are detected under 90° the covered distance increases by a factor of thousand according to the calculations. This can be explained with the fact that protons which travel perfectly perpendicular to the beam axis have to pass the fictive degrader along its width. The width is in the range of 10 mm and so is the distance the protons would travel in the fictive degrader. The 90° protons appear in the distribution as three separate peaks because now the angle φ of the proton directions has a significant influence on the calculated distances. But these huge distances are not realistic because protons with the here expected energy can not pass such a long distance in gold (cf. Fig. 5.12 (b)). Following these calculations, protons which are detected under 90° should also not appear in the target-and-degrader-runs. But as seen in Figure 5.11 (b) protons are detected under 90° for the target-and-degrader-runs. This reveals a problem of the here applied modification. Protons which were detected under 90° in the experiment did not necessarily have an exact emission angle of 90°. Their angles can be in the range from 80° to 100° due to the opening angle for the μ-Ball detector ring at 90° (cf. Fig. 3.4), or they hit an detector under 90° due to angular strangling in the degrader. Hence, the distance such protons had to cover in gold can be much smaller in reality. But in the target-only-runs modification all these protons are treated as if they travelled perfectly perpendicular to the beam axis and so their calculated distance in the degrader is much too large. To avoid this problem in the further analysis, events for which at least one proton was detected under 90° will be ignored. As seen in Section 5.7 the number of events with one or two protons under 90° is small compared to other angle combinations. Hence, the number of counts lost due this restriction should be not too problematic.

After the covered distance in the fictive gold degrader is calculated for the detected protons, also the maximum range in gold is calculated for the protons. For this SRIM was used again to calculate the range of protons in gold [Zie19, JFZ15]. Figure 5.12 (b) shows the results of this calculations. Here, the range R in µm is plotted over the proton energy E_p in MeV. The SRIM data can be well described by the fit function

$$R(E_\mathrm{p}) = p_1 \cdot E_\mathrm{p}^3 + p_2 \cdot E_\mathrm{p}^2 + p_3 \cdot E_\mathrm{p}, \tag{5.24}$$

where p_1, p_2 and p_3 are fit parameters. They were determined to $p_1 = -0.01002\,\mu\mathrm{m}/\mathrm{MeV}^3$, $p_2 = 1.282\,\mu\mathrm{m}/\mathrm{MeV}^2$ and $p_3 = 5.410\,\mu\mathrm{m}/\mathrm{MeV}$. Furthermore, it can be seen that protons with an energy of 25 MeV have a range of about 800 µm. This shows that no protons are able to pass the total width of the gold degrader of 16.43 mm. Hence, protons detected under 90° can not be used for this modification as stated earlier.

Finally, with this framework the complete modification can be applied to the target-only-runs: First, the angles of the protons for each event are checked. If the angle is 90°, the event is ignored. If not, the covered distance in the fictive gold degrader is calculated. Then the maximum range the proton can pass in gold is calculated. For this the calibrated and absorber corrected proton energy $E_{\mathrm{CsI,Al,Pb/Ta}}$ is fed into Equation 5.24. If the maximum range of a proton is smaller than the

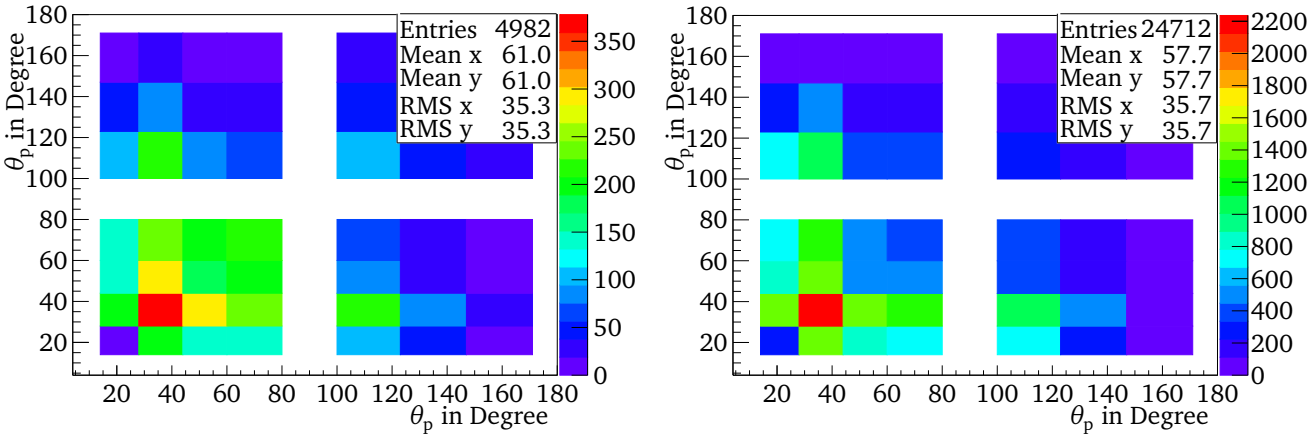

(a) target-only-runs (b) target-and-degrader-runs

Figure 5.13: Proton θ_p distribution for dirty 2p events with a gamma gate on the 2_1^+ of ^{16}C. For the target-and-degrader-runs all events with protons detected under 90° are ignored. For the target-only-runs the degrader-passed check was applied. The irregular binning of the 2D-histograms is matched to the opening angles of the μ-Ball rings (cf. Fig. 3.4).

distance it has to pass in the fictive gold degrader, it is assumed that this proton will get stuck in the degrader. Then this proton is not included in the analysis and the event is ignored. With this modification the influence of a gold degrader on the proton kinematics can be approximately transferred to the target-only-runs. In the following analysis these modifications will also be labelled as *degrader-passed check*.

To test the degrader-passed check, Figure 5.13 shows again proton angular distributions for target-only-runs (a) and target-and-degrader-runs (b) with a gamma gate on the 2_1^+ of ^{16}C. But now the degrader-passed check is applied to the target-only-runs and for better comparison, events with protons detected under 90° are ignored for the target-and-degrader-runs. It can be seen that the two angular distributions are not perfectly identical. While the mean of the distribution is 61.0° for the target-only-runs, the mean for the target-and-degrader-runs is 57.7°. This remaining deviation can be mainly explained with the fact that the calculated proton distance is only available for a few discrete values due to the limited amount of μ-Ball rings. As a result of this the real proton kinematic can not be completely represented by the calculations during the degrader-passed check. Nevertheless, the proton angular distribution for the degrader-passed check (cf. Fig.5.13 (a)) is much closer to the goal distribution of the target-and-degrader-runs (cf. Fig.5.13 (b)) compared to the unmodified proton angular distribution for the target-only-runs as seen in the last section and Figure 5.11 (a). This is also reflected in the mean values of the distributions. The mean of the unmodified proton angular distribution for the target-only-runs is 64.5°. Hence, the difference to the goal distribution of the target-and-degrader-runs is larger than

for the modified target-only-runs. All in all it can be concluded that the degrader-passed check helps to reduce the influence of the bias due to the missing degrader in the target-only-runs.

Hence, the mean decay beta extracted from the target-only-run using the degrader-passed check includes only the parts of the mean decay beta this experiment is sensitive for. It also only represents the part of the velocity parallel to the beam direction. But as stated earlier, this is not a problem because the further analysis is only sensitive to velocities in beam direction. To extract the beta of an isotope, a clearly visible peak of the isotopes of interest (e.g. the 2_1^+ of ^{16}C) is chosen in the spectra of the target-only-run. Then the target-only beta $\overline{\beta}_{\mathrm{TO}}$ is extracted as explained in Section 2.5. This $\overline{\beta}_{\mathrm{TO}}$ can then be fed into the Geant4 simulations (cf. Sec. 4.3).

5.9 Target Position Correction for the Target-Only-Runs

The target for the target-only-run was mounted on a different structure than the target-and-degrader-run setup. The thin target was located roughly d=0.2 cm upstream compared to the center of Gammasphere. For this, the θ which is assigned to the Gammasphere detectors has to be corrected to a new θ'. The geometry of this correction is shown in Figure 5.14. At z=0 the center of Gammasphere is given and the new target position for the target-only-run is moved with the amount d into negative z direction. Then one can find the following relations

$$x = r\cos(\theta), \tag{5.25}$$

$$y = r\sin(\theta)\,\text{and} \tag{5.26}$$

$$\tan(\theta') = \frac{y}{d+x}, \tag{5.27}$$

where r=25.25 cm+$l/2$=29 cm. Finally, the theta correction is described by

$$\theta' = \arctan\left(\frac{\sin(\theta)}{\cos(\theta) + d/r}\right). \tag{5.28}$$

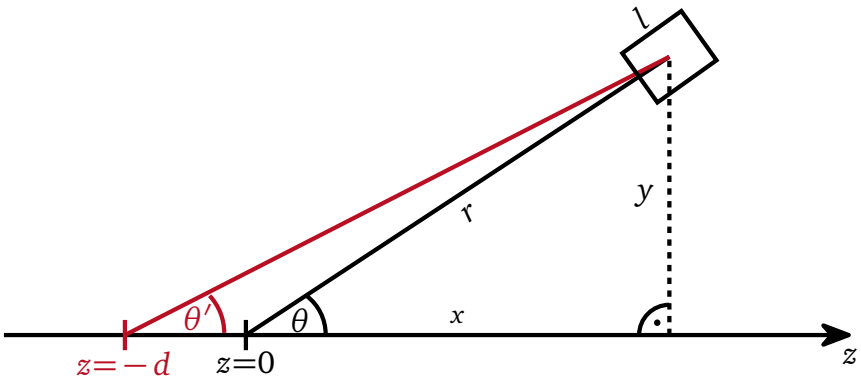

Figure 5.14: Sketch of the target position correction. For the target-only-run, the target is shifted d=0.2 cm upstream compared to the center of Gammasphere at z=0. The black rectangle represents one Ge crystal which is located under the angle θ and has a length of l=7.5 cm.

5.10 Target-And-Degrader-Runs

To get the lifetimes of excited states, the mean decay beta of the excited isotopes has to be measured using the target-and-degrader-runs. The runs are again evaluated for 2p events. The bias induced due to missing protons which got stuck inside the degrader is already corrected in the analysis of the target-only-runs. But as stated in Section 5.8 this modification can not be applied for events for which at least one proton was measured under 90°. Hence, during the analysis of the target-and-degrader-runs all events have to be ignored for which at least one proton was measured under 90°. Otherwise no further modifications have to be applied.

To extract the mean decay beta, the peak of interest (e.g. the 2_2^+ of ^{16}C) is chosen in the spectra of the target-and-degrader-runs. Then the mean decay beta $\overline{\beta}$ is extracted as explained in Section 2.5. This $\overline{\beta}$ can then be compared to the Geant4 simulation results to extract a proper lifetime.

5.11 Multiplicity of Gammasphere and Microball

Another characteristic, which has to be checked, is the multiplicity of Gammasphere and μ-Ball. Figure 5.15 (a) shows the multiplicity for Gammasphere in coincidence with protons and Figure 5.15 (b) shows the multiplicity for μ-Ball for detected protons. It can be seen that for both detectors the number of counts decreases strongly exponentially for increasing multiplicity. This is as expected. For Gammasphere, the number of counts drops by a factor of 0.231 when going from a multiplicity of 1 to a multiplicity of 2. For μ-Ball, where the 2 proton efficiency is crucial for the experiment, the number of counts drops by a factor of 0.007 when going from a multiplicity of 1 to a multiplicity of 2. This shows the importance of the two proton cut to extract the channel of interest. Otherwise, the spectra are dominated by reactions with other residual particle configurations.

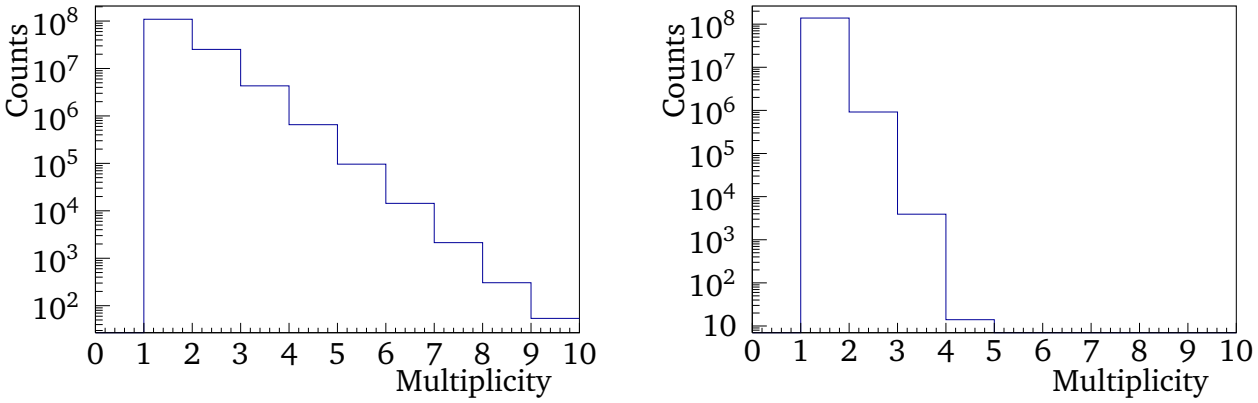

(a) Gammasphere multiplicity

(b) μ-Ball multiplicity

Figure 5.15: Multiplicity distribution of Gammasphere and μ-Ball. The Gammasphere multiplicity distribution is given for events which were coincident with protons. The μ-Ball multiplicity is given for detected protons.

6 Results

In this chapter all results are discussed in detail. First the spectra for the two proton cuts are described to give an overview about the measured data. Then the results of the lifetime measurements for ^{22}Ne, ^{23}Ne, and ^{16}C are given.

6.1 Two Proton Cut Spectra

At the beginning the results for the two proton cuts are presented. Figure 6.1 and Figure 6.2 show the spectrum for 2p cuts for the target-and-degrader-runs. While Figure 6.1 shows the complete detected gamma spectrum, Figure 6.2 shows a zoom on the region from 100 keV to 2500 keV. In both spectra many transitions can be seen. Transitions which could be identified are marked with arrows and named in the spectra. The transitions which are marked in black are neutron induced reactions. They happen with the germanium inside the Gammasphere detectors or with the aluminium of the beam pipe and target chamber. These are background reactions which always appear when neutrons are emitted. These transitions have also been stated e.g. in [LS69, EDQ$^+$89, Loe17, Hei19].

The transitions from the 2_1^+ and the 4_1^+ state of ^{16}C are clearly visible at the expected energy as stopped peak. Hence, the 2p cuts are successfully applied to the gamma-ray spectra. The analysis of the lifetimes of these states is discussed in detail in Section 6.5. Besides the background reactions and the ^{16}C transitions, some other residual isotopes could be identified. They are marked with red and green arrows. For these transitions, the initial state of the transition and the lifetimes are given. Marked in red, one can see transitions from ^{14}C, ^{15}C, ^{15}N, and ^{16}N. These isotopes stem from reactions of the ^{9}Be beam with the ^{9}Be target (cf. Tab. A.1). For ^{14}C and ^{15}C the residual particles contain two protons as well as two neutrons and one neutron, respectively. Hence, it is expected to see them in the 2p cut spectra. For ^{15}N and ^{16}N only one proton is emitted. But the production probability for these two isotopes is much larger than for the ^{16}C isotopes. For ^{15}N the cross section is 410 times larger than for ^{16}C and for ^{16}N the cross section is 10.7 times larger than for ^{16}C according to the PACE4 calculations (cf. Tab. A.1). This enables the possibility for random coincidences between two independent protons from two independent reactions.

Furthermore, transitions from ^{22}Ne, ^{23}Ne, and ^{23}Na are visible. They are marked with green arrows. These isotopes stemmed from reactions of the ^{9}Be beam with ^{16}O isotopes. It was

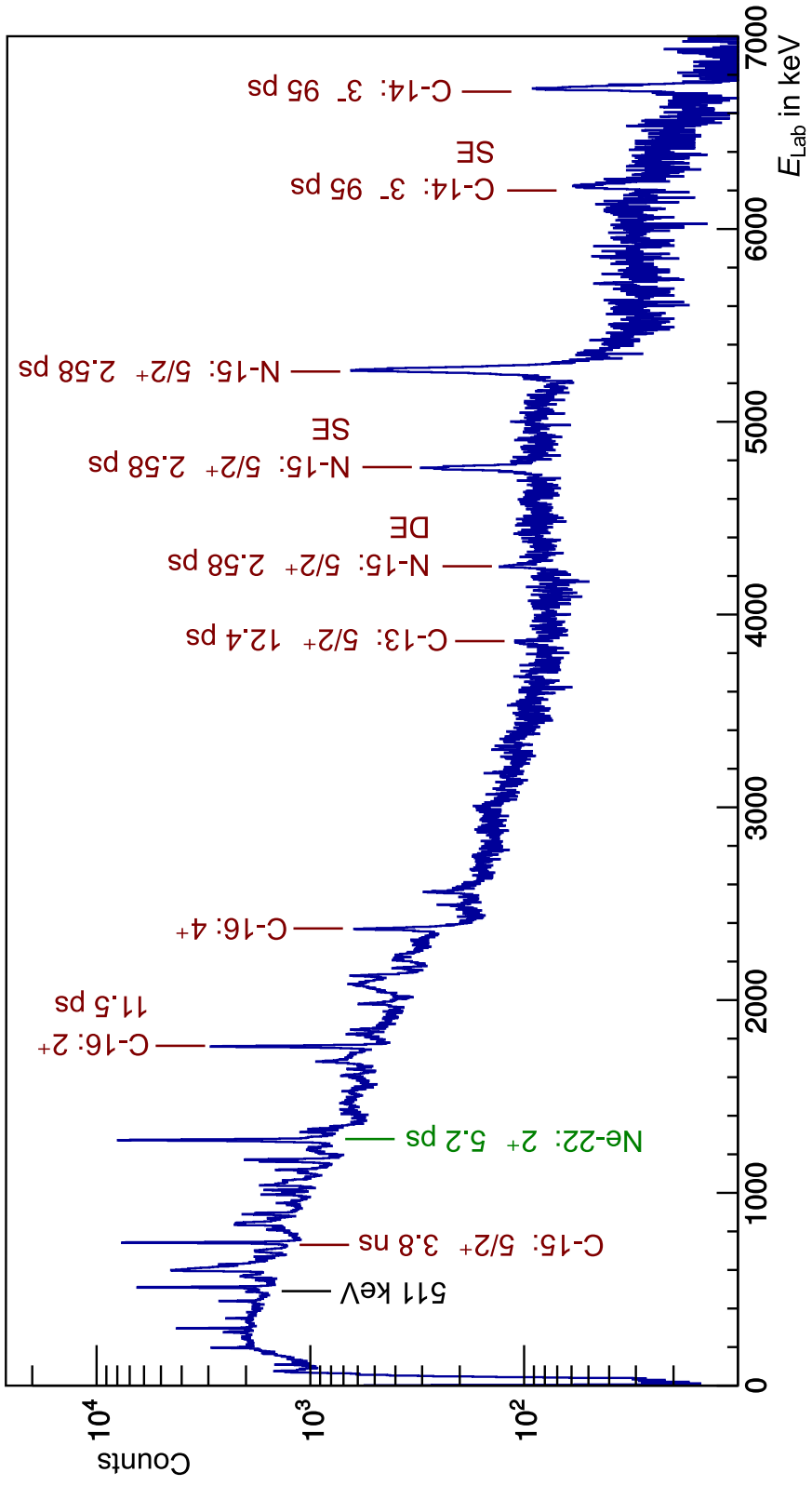

Figure 6.1: Gamma spectrum with normal 2p cuts applied for target-and-degrader-runs. The most pronounced peaks are marked. The given numbers are the lifetimes of the states which are taken from [AS90a, AS90c, ASKN91, AS90b, SB15, PPC$^+$12, WFM$^+$08]. If a peak is marked in red, it stems from the reaction ^{9}Be $+^9$ Be. If a peak is marked in green, it stems from the reaction ^{9}Be $+^{16}$ O. The aberration "DE" stands for double escape peak and "SE" stands for single escape peak.

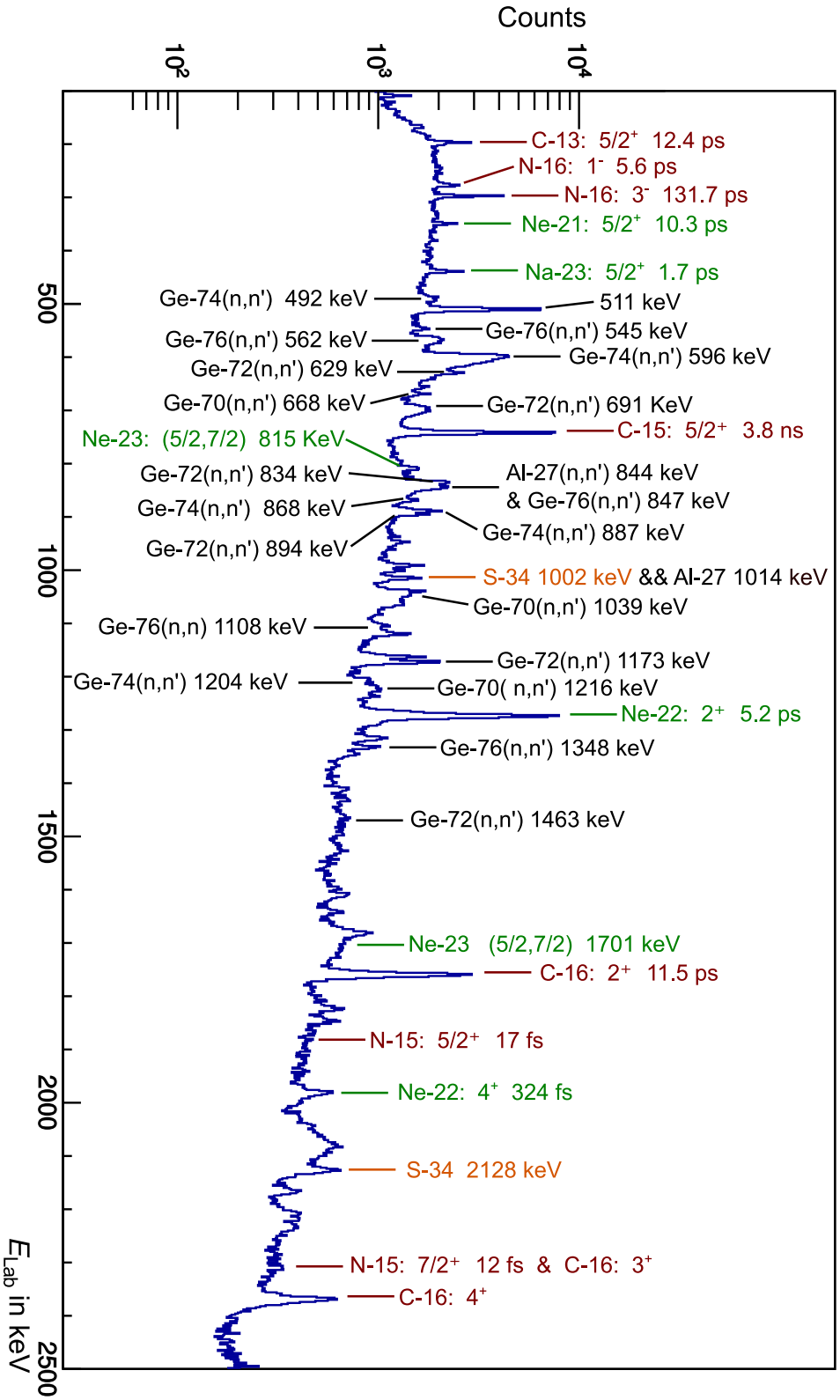

Figure 6.2: Gamma spectrum with normal 2p cuts applied for target-and-degrader-runs from 100 keV to 2500 keV. The most relevant peaks are marked. The given numbers are the quantum-numbers and lifetimes of the states. Also sometimes the energies of the corresponding transitions are given. The data are taken from [AS90a, JKC90, ASKN91, AS90b, Fir06, Fir07, Fir15, SB15, NS12, PPC+12, WFM+08]. If a peak is marked in red, it stems from the reaction $^{9}\mathrm{Be} + ^{16}\mathrm{O}$. If a peak is marked in green, it stems from the reaction $^{9}\mathrm{Be} + ^{9}\mathrm{Be}$. If a peak is marked in orange, the peaks marked in black are neutron induced reactions. The peaks marked in orange stem from other contaminations.

discovered that the target was oxidized on its outside layers. These oxidation layers provide ^{16}O isotopes for additional reactions. Due to this the reactions

$$^{9}\mathrm{Be} + ^{16}\mathrm{O} \;\rightarrow\; ^{25}\mathrm{Mg}^{*} \;\rightarrow\; ^{A}Z^{*} + N_{\mathrm{p}} \cdot \mathrm{p} + N_{\mathrm{n}} \cdot \mathrm{n} \tag{6.1}$$

are possible, where N_{p} is the number of protons and N_{n} is the number of neutrons.

A list of all reaction channels, which can be accessed with the reaction ^{9}Be+^{16}O, is found in Table A.2. For ^{22}Ne and ^{23}Ne also two protons are emitted and hence they appear in the 2p cut spectra. For ^{23}Na only one proton is emitted but again the probability that ^{23}Na is produced is very high. According to PACE4, the cross section of ^{23}Na is 430 times larger than for ^{16}C.

Looking at the Tables A.1 and A.2 it can be seen that the isotopes ^{12}C, ^{16}O and ^{20}Ne also have a large cross section and two or more protons could be emitted during the creation process. But in the 2p cut spectra no transitions could be found which can belong to ^{12}C, ^{16}O or ^{20}Ne. To investigate this further also cuts on the detected alpha particles were created. Analysing the gamma spectra for the alpha cuts revealed that transitions of all three isotopes could be found. In detail one could see transitions from the 2_1^+ state of ^{12}C, the 3_1^- state of ^{16}O, and the 2_1^+ as well as the 4_1^+ state from ^{20}Ne. This implies that ^{12}C, ^{16}O, and ^{20}Ne isotopes are created mainly via the alpha evaporation channel and will not appear in the 2p cut spectra.

Additionally, two ^{34}S transitions can be seen in Figure 6.2. The sulphur stems from an unknown contamination. To prove that the peaks belong to ^{34}S a gamma spectrum with a gate on the dominant transition from the 5_1^- state (at 5690.7 keV and E_γ=1001.6 keV) is shown in Figure 6.3. The spectrum is obtained from the target-only-runs. There ^{34}S decays in-flight and hence, the gamma energies are Doppler corrected before the energy gate is applied. In the spectrum, the prominent decay chain 5_1^- (at 5690.7 keV)$\rightarrow 4_1^+$ (at 4688.9 keV)$\rightarrow 2_1^+$ (at 2127.6 keV)$\rightarrow 0_1^+$ (at 0 keV) from ^{34}S can be clearly seen without any significant background.

If a transition produces a sharp Gaussian peak in Figure 6.1 and Figure 6.2, then the decay happened at rest which means that the lifetime is in the range of picoseconds or longer. If the lifetime is much shorter the decay happened in-flight and the peak in the figures is smeared out due to the Doppler effect. To get a better overview of decays which happened in-flight and which happened at rest, a 2D plot, as can be seen in Figure 6.4, is used in the following sections. The figure shows the measured radiation angle over the laboratory energy for the target-and-degrader-runs with normal 2p cuts. Thereby, the plotted radiation angle was randomized around the discrete value stemming from the angle of the Gammasphere detectors. The limits of the randomized angle are defined by the opening angle of one Gammasphere ring which is ±7.5°. The figure covers an energy range from 1200 keV to 2600 keV. It can be seen that transitions $2_1^+ \rightarrow 0^+$ of ^{22}Ne (E_γ=1275 keV) and ^{16}C (E_γ=1758 keV) appear as straight vertical lines, which means that there is no centroid shift. This is expected, because the lifetimes for these transitions are in the range of picoseconds and so the gamma decay happens at rest. For the transition

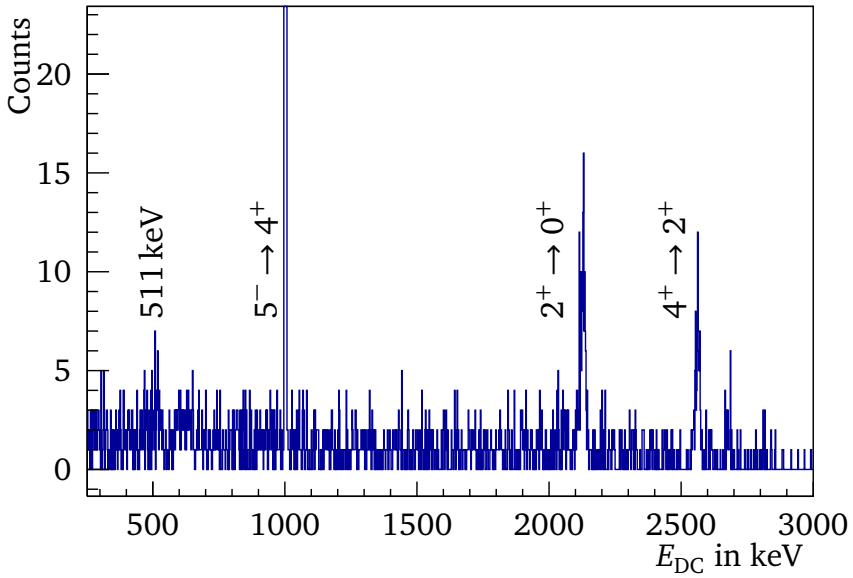

Figure 6.3: Gamma spectrum for normal 2p cuts for target-only-runs with a gamma gate on the 5^- state (at 5690.7 keV and E_γ=1001.6 keV) in ^{34}S. The gamma-ray energy is Doppler corrected using β_{DC}=0.02208. The prominent decay chain 5^-_1(at 5690.7 keV)→ 4^+_1(at 4688.9 keV)→ 2^+_1(at 2127.6 keV)→ 0^+_1(at 0 keV) from ^{34}S can be clearly seen.

$4^+_1 \rightarrow 2^+_1$ of ^{22}Ne (center of mass energy at 2083 keV) the centroid energy is shifting for different angles. Hence, the decay happened in-flight which is again expected, because the lifetime of the 4^+_1 state of ^{22}Ne is 324(6) fs [SB15]. This state will be used as a benchmark for the here applied evaluations. The benchmark test will be discussed in Section 6.3. The $4^+_1 \rightarrow 2^+_1$ transition of ^{16}C (E_γ=2365 keV) appears in a straight vertical line. Hence, the lifetime of this state has to be in the picosecond range as well. The $3^+_1 \rightarrow 2^+_1$ transition of ^{16}C (centroid energy at 2303 keV) shows a moving centroid. Hence, the lifetime is in the femtosecond range. But as stated later in Section 6.5 this transition is superimposed by the transition $7/1^+_2 \rightarrow 5/2^+_1$ of ^{15}N with a center of mass energy of 2297 keV. The transition $2^+_2 \rightarrow 2^+_1$ of ^{16}C is not visible for the here shown settings. For more information about the ^{16}C transitions and the lifetime estimations see Section 6.5.

Furthermore, the same analysis was done for the clean 2p cuts (cf. Sec. 5.4). For these gamma-ray spectra the overall number of counts decreased as expected. But by comparing the count loss for the channel of interests with the count loss for background channels it was found that they all scale the same. This showed that no extra advantage can be gained by using the clean 2p cuts. Also, as stated earlier, it is not possible to calculate a correct proton energy for all protons in the clean 2p cuts. Hence, in the following analysis every evaluation will be only done for the normal 2p cuts. For simplification they will be just called 2p cuts or 2p events.

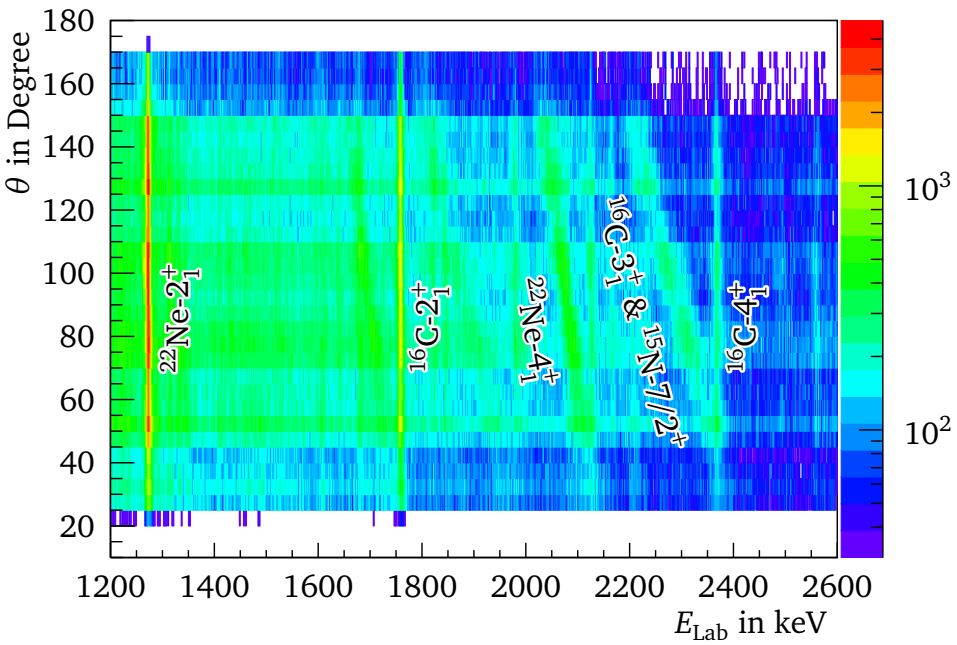

Figure 6.4: Radiation angle θ versus laboratory energy E_{Lab} for the normal 2p cuts for target-and-degrader-runs. Transitions of interest are labelled. The corresponding isotope and the initial state of the transition is given. The z-axis range was truncated to a minimum of 30 counts per bin for a better visualization of the smaller peaks.

6.2 Count Rate Estimations for the $2^+_1 \rightarrow 0^+_1$ Transition in Carbon-16

To check that the experiment and the event builder worked as expected, the counts of the $2^+_1 \rightarrow 0^+_1$ transition of ^{16}C are extracted and compared to count rate estimations which were performed in the experiment proposal [PHP+16]. These estimations are based on the measurement by Wiedeking et al. [WFM+08], who measured about 200 counts in the $2^+_1 \rightarrow 0^+_1$ transition in 36 hours with a beam intensity of 0.5 pnA. This corresponds to 11.1 counts per hour at 1 pnA. The production beam time of the target-and-degrader-runs in this experiment was about 106 hours and the average beam current was 1.1 enA=0.275 pnA (cf. Sec. 3.2). This would lead to 324 counts in total if the same setup was used. Following the proposal, the total γ-p-p efficiency should be 125 times larger for the here analysed experiment compared to the setup used by Wiedeking et al. This would result in 40,500 counts in the $2^+_1 \rightarrow 0^+_1$ transition. The proposal assumed a two proton efficiency of 25 % and a total Gammasphere efficiency of 10 % at 1 MeV. But this was not achieved during the experiment. Due to problems with the electronics and triggers of μ-Ball, the one proton efficiency was decreased to 30 % [SR16]. This leads to a two proton efficiency of 9 % which reduces the expected counts to $^{9}/_{25}$·40,500 counts=14,580 counts. The Gammasphere efficiency at 1 MeV was 5.96 % (cf. Sec. 5.3) due to missing detectors. As a result the expected total number of counts in the $2^+_1 \rightarrow 0^+_1$ transition should be $^{5.95}/_{10}$·14,580 counts=8,675 counts.

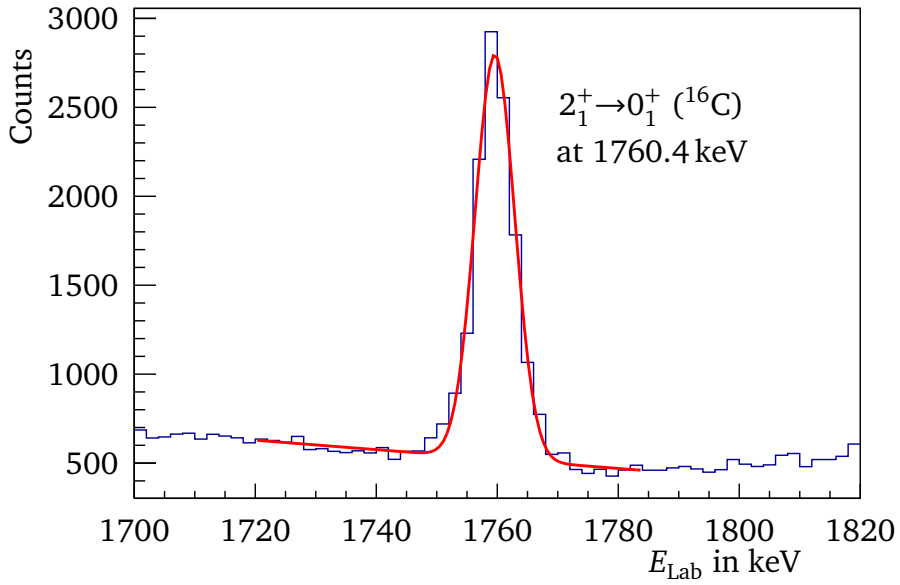

Figure 6.5: $2_1^+ \rightarrow 0_1^+$ transition of ^{16}C obtained in the 2p cut spectra for the target-and-degrader-runs. The shown fit-function is given by Equation 6.2.

To evaluate the experimental data, a Gaussian function is fitted to the $2_1^+ \rightarrow 0_1^+$ transition of ^{16}C in the target-and-degrader-runs. The result can be seen in Figure 6.5. The fit-function is described by

$$f(E) = p_0 \mathrm{e}^{-\frac{1}{2}\left(\frac{E-p_1}{p_2}\right)^2} + p_3 \cdot E + p_4 \tag{6.2}$$

and so the counts are given by

$$C = \frac{\sqrt{2\pi} p_0 p_2}{\mathrm{Binwidth}}, \tag{6.3}$$

which leads to 9346(171) counts. Here, the correlation between the fit-parameter p_0 and p_2 is considered in the calculation of the statistical uncertainty. This result is in good agreement with the corrected proposal estimations of 8,675 counts. Thereby, one has to consider that the average beam intensity could only be estimated very roughly because it was not measured continuously during the experiment.

6.3 Results for Neon-22

As mentioned in Section 6.1, two transitions from ^{22}Ne can be seen in the 2p cut spectra. The ^{22}Ne stems from reactions of the ^{9}Be beam with a thin oxidation layer at the target. If the ^{9}Be beam hits ^{16}O isotopes, the reaction channel

$$^{9}\mathrm{Be} + ^{16}\mathrm{O} \;\rightarrow\; ^{25}\mathrm{Mg}^{*} \;\rightarrow\; ^{22}\mathrm{Ne}^{*} + 2\cdot\mathrm{p} + 1\cdot\mathrm{n} \tag{6.4}$$

is available. Here, the residual particles are two protons and one neutron. The experimental setup was not able to detect the neutrons but the two protons will satisfy the 2p cut. Hence, the ^{22}Ne channel appears clearly in the 2p cut spectra. A level scheme with the two lowest excited states of ^{22}Ne is illustrated in Figure 6.6. In the level scheme, the two transitions $4_1^+ \rightarrow 2_1^+$ with 2082.6(5) keV and $2_1^+ \rightarrow 0^+$ with 1274.5 keV can be seen. For both states, the lifetimes are known very precisely. For the 2_1^+ state the lifetime is stated as 5.19(7) ps [SB15]. Transitions from this state should arise in the spectra when the particles are fully stopped in the degrader. For the 4_1^+ state the most recent value for the lifetime is given by 324(6) fs [SB15]. This is in a range the experiment is sensitive to. The value was obtained as an uncertainty weighted mean from eight different measurements. Due to this, the ^{22}Ne channel can be used as a good benchmark test for the analysis which is applied in this thesis. Next, the lifetime of the 4_1^+ state of ^{22}Ne will be extracted and compared to the results of the previous measurements.

First, it will be proofed that the two gamma-ray transitions really belong to ^{22}Ne. Then the transition $2_1^+ \rightarrow 0^+$ is analysed for the target-only-runs to extract the mean beta the ^{22}Ne isotopes had after their creation. This information is used as an input for the Geant4 simulation to get a proper correlation between the lifetime of the 4_1^+ state and the mean decay beta of the target-and-degrader-runs. Finally, the mean decay beta of the experimental target-and-degrader-runs is extracted and compared to the simulation results to achieve a proper lifetime for the 4_1^+ state.

To demonstrate that the investigated transitions belong to ^{22}Ne a gamma-gamma coincidence gate is used. Figure 6.7 (a) and (b) shows the radiation angle versus laboratory energy for the 2p cut for the target-and-degrader-runs in a range from 1400 keV to 2400 keV. For Part (a) no gamma gate was set. Besides the strong $2_1^+ \rightarrow 0^+$ transition of ^{16}C some other small transitions and a lot of background is visible. The $4_1^+ \rightarrow 2_1^+$ transition of ^{22}Ne is also slightly visible. In Figure 6.7 (b) a gamma gate is applied. The gate is reaching from 1271.7 keV to 1277.3 keV. Hence, the plot only shows gammas which are in coincidence with the $2_1^+ \rightarrow 0^+$ transition of ^{22}Ne. In this spectrum, the $2_1^+ \rightarrow 0^+$ transition of ^{16}C, the background, and all other weaker transitions vanished. Only the $4_1^+ \rightarrow 2_1^+$ transition of ^{22}Ne remains. This indicates the two investigated states should belong to ^{22}Ne.

In the next step, the mean decay beta $\overline{\beta}_{\mathrm{TO}}$ is extracted from the target-only-runs following the idea from Section 5.8. For this, the transition $2_1^+ \rightarrow 0^+$ is used because for this transition the

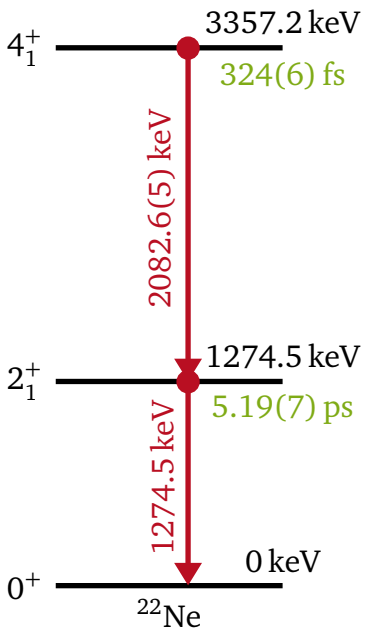

Figure 6.6: Level scheme of the two lowest excited states of ^{22}Ne. The energies printed in black are the energies of the states, while the energies printed in red are the transition energies emitted by gamma rays [SB15]. The lifetimes of the states are taken from [SB15] and shown in green.

number of counts is large enough to get a proper $\overline{\beta}_{\mathrm{TO}}$. The analysed data were obtained by applying the degrader-passed check to the target-only-runs as explained in Section 5.8. Figure 6.8 (a) shows the radiation angle θ versus laboratory energy E_{Lab} for these data. A moving peak structure for a transition which decayed in-flight can be clearly seen. The location of this peak structure is around the expected energy for the $2_1^+ \rightarrow 0^+$ transition (marked with the dashed line). For this transition all available angles of Gammasphere could be used to extract the centroid energies $E_{\mathrm{Lab}}(\overline{\beta}, \theta)$ for each angle θ. In Figure 6.8 (b) the centroid shift as a function of $\cos(\theta')$ is illustrated. For this, the Gammasphere angles θ were corrected to θ' according to the target position correction of 0.2 cm which is explained in Section 5.9. The shown data points were achieved by fitting Gaussian functions to the $2_1^+ \rightarrow 0^+$ peaks in the respective gamma-ray spectra for each discrete Gammasphere angle (cf. Sec. 2.5). The shown fit, described by Equation 2.19, leads to a result of E_{cm}=1274.0(1) keV which is close enough to the accepted value of 1274.537(7) keV [SB15]. Also the position and the shape of the fit-function reproduces the data well as can be seen in Figure 6.8 (a) and (b). The mean decay beta was obtained to $\overline{\beta}_{\mathrm{TO}}$=0.03229(14). The obtained value for $\overline{\beta}_{\mathrm{TO}}$ can then be fed into the Geant4 simulations to calculate the initial betas β_{ini} the isotopes get in the simulation (cf. Sec. 4.3).

Now the data from the target-and-degrader-runs are evaluated to get the experimental mean decay beta $\overline{\beta}_{\mathrm{Exp}}$ for the transition $4_1^+ \rightarrow 2_1^+$. As explained before, events with protons which were detected under 90° have to be ignored. Figure 6.9 (a) shows the radiation angle θ versus lab-

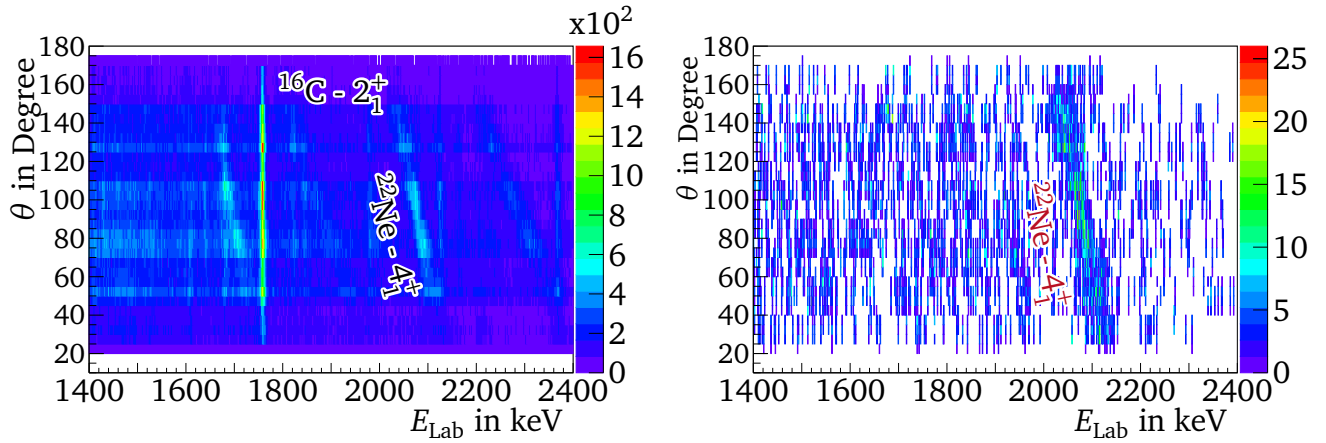

(a) No gamma gate

(b) Gamma gate on the $2_1^+ \rightarrow 0^+$ transition of ^{22}Ne

Figure 6.7: Radiation angle θ versus laboratory energy E_{Lab} for the 2p cut for target-and-degrader-runs in the range from 1400 keV to 2400 keV. In the right plot, a gamma-gamma coincidence gate is applied for the $2_1^+ \rightarrow 0^+$ transition of ^{22}Ne. The gate is reaching from 1271.7 keV to 1277.3 keV. This corresponds to a 2σ range around the mean value of 1274.5 keV.

oratory energy E_{Lab} for these data. A moving peak structure from a transition which decayed in-flight can be clearly seen. The locations of these peaks are around the expected energy for the $4_1^+ \rightarrow 2_1^+$ transition (marked with the dashed line). For this transition eleven angles of Gammasphere (namely 58.28°, 69.82°, 79.19°, 80.71°, 90.00°, 99.29°, 100.81°, 110.18°, 121.72°, 129.93° and 142.62°) could be used to extract the centroid energies $E_{\mathrm{Lab}}(\overline{\beta}, \theta)$. For the other angles no proper Gaussian fit to the peaks could be established. For the forward angles smaller than 58.28° the $4_1^+ \rightarrow 2_1^+$ transition peaks interfere with a stopped peak from an unidentifiable background source. For the backward angles larger than 142.62° the number of counts was too low to make a proper fit to the peaks stemming from the $4_1^+ \rightarrow 2_1^+$ transition. Nevertheless, these are enough data points to extract a proper mean decay beta with a small statistical uncertainty. In Figure 6.9 (b) the centroid shift as a function of $\cos(\theta)$ is illustrated. The data points were achieved by fitting Gaussian functions to the $4_1^+ \rightarrow 2_1^+$ peaks in the respective gamma-ray spectra for the eleven discrete Gammasphere angles (cf. Sec. 2.5). The shown fit, described by Equation 2.19, leads to the results of E_{cm}=2081.6(2) keV which is close to the accepted value of 2082.6(5) keV [SB15]. The mean decay beta was obtained to $\overline{\beta}_{\mathrm{Exp}}$=0.02262(34). The position and the shape of the fit-function reproduce the data well as can be seen in Figure 6.9 (a) and (b). Only the data point for θ=142.62° ($\cos(142.62°) \approx -0.79$) is not described well by the fit. A reason for this could not be found and the Gaussian fit to the particular gamma-ray spectrum seems trustworthy as well. Hence, the data point was still considered in the fit. Further, it should be noted that its influence is not large because it has one of the largest uncertainty of all used

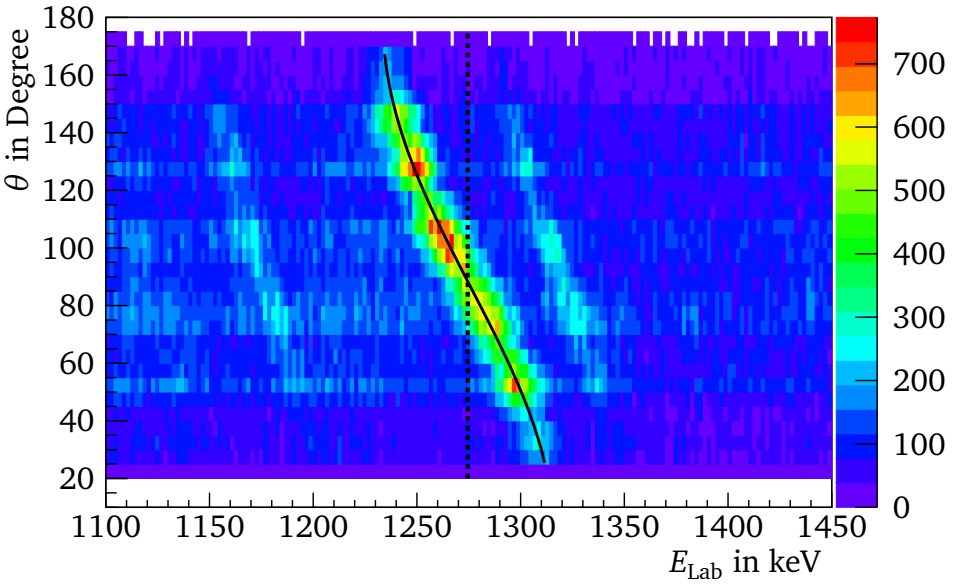

(a) Radiation angle θ versus laboratory energy E_{Lab}

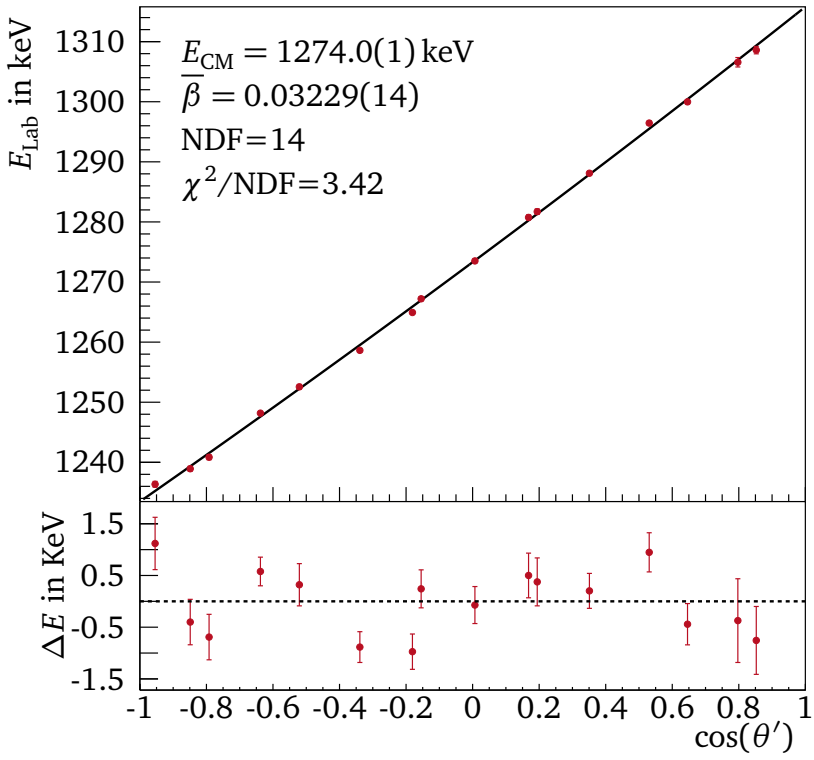

(b) E_{Lab} versus $\cos(\theta')$ fit

Figure 6.8: Analysis of the energy shift for target-only-runs, 2p cut and degrader-passed check focusing on the $2_1^+ \rightarrow 0^+$ transition of ^{22}Ne. The black fit-functions are described by Equation 2.19. The dashed line in Part (a) indicates the expected gamma-ray energy $E_{\mathrm{cm}} = 1274.5$ keV of the transition [SB15]. The lower plot in Part (b) shows the residuals ΔE of the fit which is shown in the upper plot of Part (b).

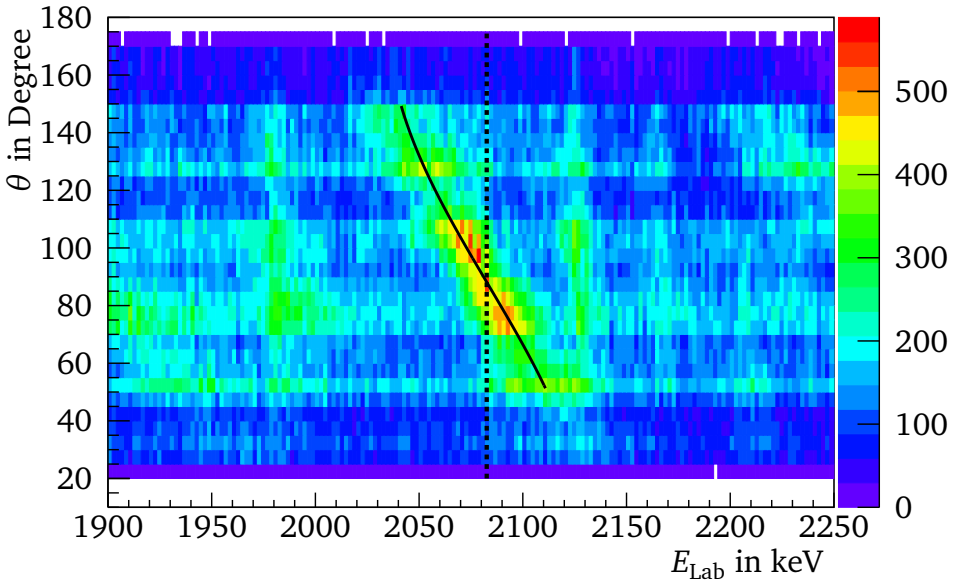

(a) Radiation angle θ versus laboratory energy E_{Lab}

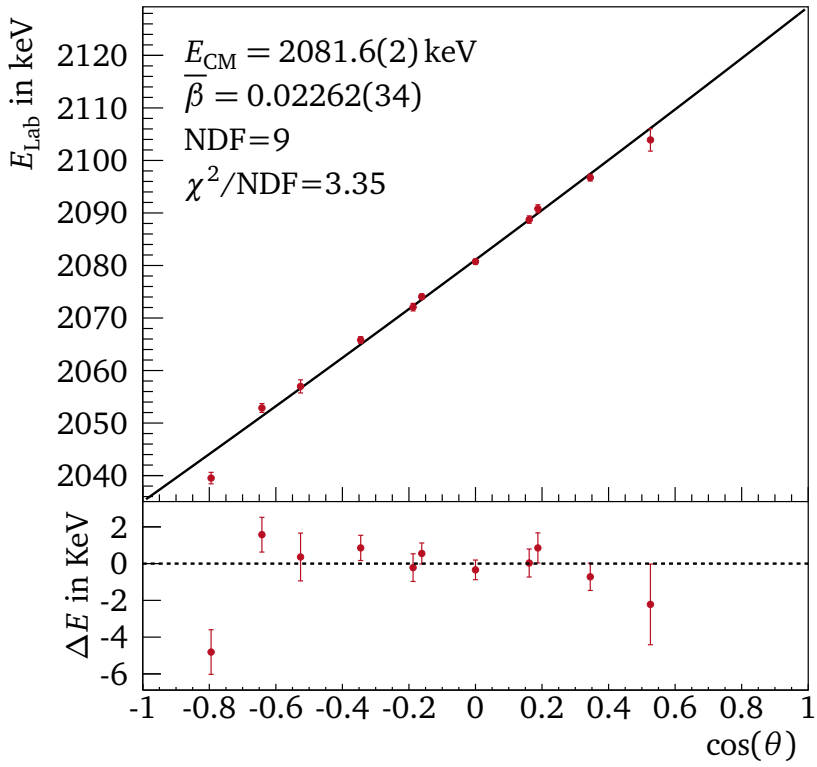

(b) E_{Lab} versus $\cos(\theta)$ fit

Figure 6.9: Analysis of the energy shift for target-and-degrader-runs and 2p cut focusing on the $4_1^+ \rightarrow 2_1^+$ transition of ^{22}Ne. Events with protons detected under 90° are ignored. The black fit-functions are described by Equation 2.19. The dashed line in Part (a) indicates the expected gamma-ray energy $E_{\mathrm{cm}} = 2082.6$ keV of the transition [SB15]. The lower plot in Part (b) shows the residuals ΔE of the fit which is shown in the upper part.

data points and so it is not weighted strongly in the fit.

In the final step the Geant4 simulations are used to obtain a relation between the lifetime of the 4_1^+ state and the measured mean decay beta $\overline{\beta}_{\mathrm{Exp}}$. For this, the Geant4 simulations are started for several different lifetimes using $\overline{\beta}_{\mathrm{TO}}$=0.03229(14) to calculate the initial betas. The simulation is run for the most parts as explained in Section 4.3. But for ^{22}Ne the starting position distribution in the Geant4 simulations has to be sampled in a different way as for ^{16}C. The ^{16}C isotopes can be created along the whole ^{9}Be target, while the ^{22}Ne isotopes can just be created in an area where a significant amount of ^{16}O can be found. Due to this the starting positions of the ^{22}Ne isotopes are not distributed along the whole target. Instead, the isotopes are created inside one thin oxidation layer at the beginning of the target because here the ^{16}O atoms stemming from the oxidation process should be found. The thickness of the oxidation layer is chosen to be 5 nm. This is a typical thickness of oxidation layers on beryllium according to the work from Hoover et al. [HCFR89]. With these settings the Geant4 simulations can be run for different lifetimes and the corresponding mean decay betas $\overline{\beta}_{\mathrm{Sim}}(\tau_{\mathrm{Sim}})$ can be extracted. For the extraction of the simulated mean decay betas $\overline{\beta}_{\mathrm{Sim}}(\tau_{\mathrm{Sim}})$ single Gaussian functions are fitted to the spectra for the same eleven Gammasphere angles which were used for the analysis of the target-and-degrader-runs and the fit settings as well as the fit range are chosen the same. This is done to match the experimental conditions as good as possible and to not introduce an artificial bias due to the truncation of used Gammasphere rings.

Figure 6.10 shows the here obtained results. Part (a) of the figure shows the results for simulations with ICRU73 stopping powers and Part (b) shows the results for SRIM stopping powers. Both results do not differ that much. This can be explained with the fact that the difference in the stopping powers is not that big for ^{22}Ne compared to the effect for ^{16}C. In both cases the linear function

$$\overline{\beta}_{\mathrm{Sim}}(\tau_{\mathrm{Sim}}) = a \cdot \tau_{\mathrm{Sim}} + b \tag{6.5}$$

was fitted to the simulated data, which describes the data well enough. To get the lifetime τ_{Exp} of the state, the intersection of the fit-function with the experimental mean decay beta $\overline{\beta}_{\mathrm{Exp}}$ has to be found. In the figure this is visualized by the intersection of the black fit-function and the orange line which represents the measured mean decay beta $\overline{\beta}_{\mathrm{Exp}}$. The yellow band around the line represents the statistical uncertainty of $\overline{\beta}_{\mathrm{Exp}}$. Analytically this is achieved via

$$\overline{\beta}_{\mathrm{Sim}}\left(\tau_{\mathrm{Exp}}\right) := \overline{\beta}_{\mathrm{Exp}} \quad \Rightarrow \quad \tau_{\mathrm{Exp}} = \frac{\overline{\beta}_{\mathrm{Exp}} - b}{a}, \tag{6.6}$$

using the fit-parameters from Equation 6.5. The statistical uncertainty $u\left(\tau_{\mathrm{Exp}}\right)$ of a such obtained lifetime is given by

$$u\left(\tau_{\mathrm{Exp}}\right) = \sqrt{\left(\frac{1}{a}\Delta\overline{\beta}_{\mathrm{Exp}}\right)^2 + \left(\frac{\overline{\beta}_{\mathrm{Exp}} - b}{a^2}\Delta a\right)^2 + \left(\frac{1}{a}\Delta b\right)^2 + 2\frac{\overline{\beta}_{\mathrm{Exp}} - b}{a^3}\mathrm{cov}(a,b)}, \tag{6.7}$$

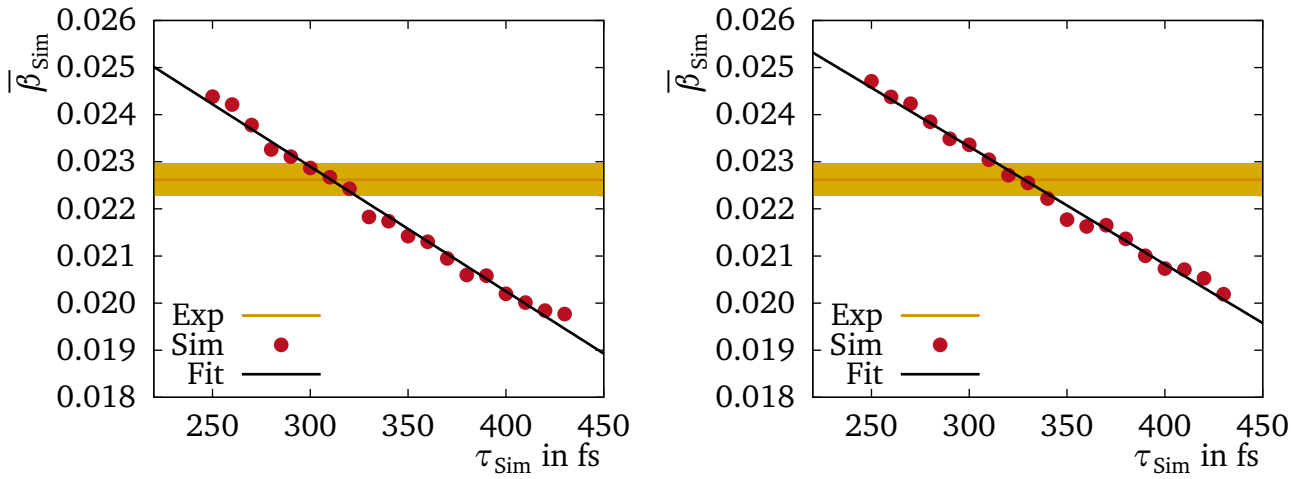

(a) For ICRU73 stopping powers

(b) For SRIM stopping powers

Figure 6.10: Simulated mean decay beta $\overline{\beta}_{\mathrm{Sim}}$ versus simulated lifetime τ_{Sim} for the $4_1^+ \rightarrow 2_1^+$ transition of ^{22}Ne. In the simulations the ^{22}Ne isotopes were created in a thin oxidation layer at the beginning of the target. The initial beta in the simulation was obtained with $\overline{\beta}_{\mathrm{TO}}$=0.03229(14). The yellow band illustrates the experimental mean decay beta value of $\overline{\beta}_{\mathrm{Exp}}$=0.02262(34) including its uncertainty. The shown fit-function is described by Equation 6.5.

where cov(a, b) is the covariance between a and b stemming from the fit. Applying this formalism leads to results of 311(13) fs for ICRU73 stopping powers and 328(14) fs for SRIM stopping powers for the lifetime of the 4_1^+ state in ^{22}Ne. Hence, both results are in agreement with the 324(6) fs, which is the most recent uncertainty weighted mean value from all accepted previous measurements as stated in [SB15]. For both results the one sigma uncertainty intervals are overlapping.

As a summary, Figure 6.11 shows the temporal development of the measured lifetimes for the 4_1^+ state in ^{22}Ne. In the left part of the figure, the results from the eight previous experiments (blue to orange data points) can be seen. Next to it, the most recent uncertainty weighted mean (324(6) fs [SB15]) is shown as a black data point and as a grey uncertainty band. This value was calculated using all results from the eight previous experiments. Finally, the figure shows the results which are obtained in this work (right part). The red data point shows the results for SRIM stopping powers and the purple data point shows the results for ICRU73 stopping powers. The figure emphasiz the good agreement of the different data among each other as well as with the uncertainty weighted mean in terms of the one sigma confidence interval. The precision and accuracy which are obtained with the method from this work are very satisfying. The precision is in the same range as for the most recent measurement [FAB$^+$79]. Overall, these results show that the DSAM method as it is performed in this work should lead to reasonable results for the following analysis.

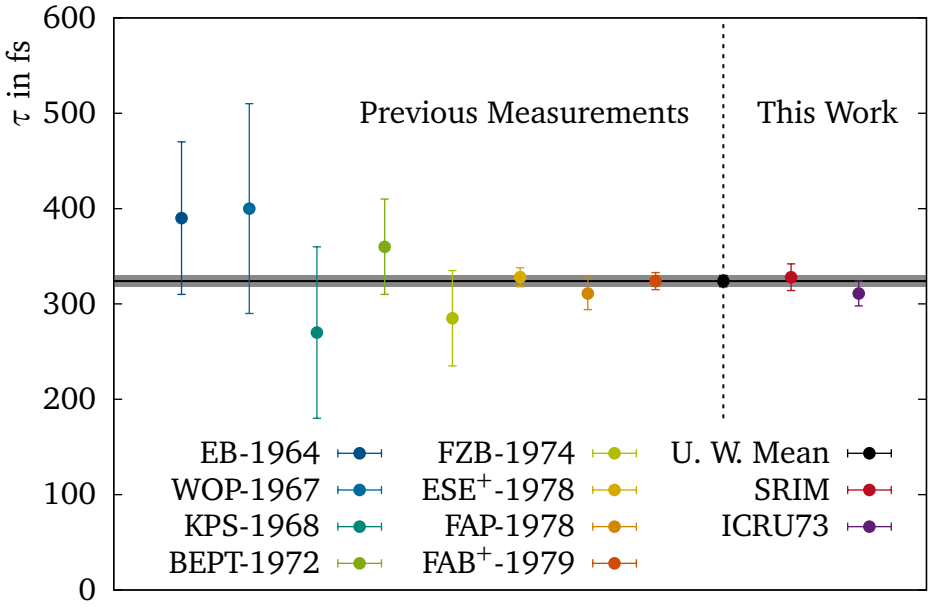

Figure 6.11: Temporal development of the measured lifetimes for the 4_1^+ state in ^{22}Ne. The results are arranged from old to new going from left to the right side of the plot. The eight values from the previous measurements are taken from [EB64, WOP67, KPS68, BEPT72, FZB74, ESE$^+$78, FAP78, FAB$^+$79] respectively. They lead to the uncertainty weighted mean of 324(6) fs [SB15], which is shown as a black point and as a grey uncertainty band. The results from this work, illustrated by the red (SRIM stopping powers) and purple (ICRU73 stopping powers) data points, are in good agreement with the previous measurements.

6.4 Results for Neon-23

Besides ^{22}Ne also transitions from ^{23}Ne could be observed in the 2p cut spectra (cf. Sec. 6.1). The ^{23}Ne isotopes were also created during reactions from ^{9}Be with ^{16}O isotopes in the oxidized target. If the ^{9}Be beam hits ^{16}O isotopes, the reaction channel

$$^{9}\mathrm{Be} + ^{16}\mathrm{O} \;\rightarrow\; ^{25}\mathrm{Mg}^{*} \;\rightarrow\; ^{23}\mathrm{Ne}^{*} + 2\cdot\mathrm{p} \tag{6.8}$$

is available. Here, the residual particles are two protons as for the ^{16}C reactions. Hence, the ^{23}Ne transitions are in the 2p event spectra. Figure 6.12 shows a level scheme of the five lowest excited states of ^{23}Ne. The lifetime is just known for the lowest $1/2^{+}$ state at 1017 keV. It is stated to 257(14) ps [FMC66, Fir06], which is not in the range this experiment is sensitive to. For all other states the lifetimes are expected in the femtosecond range. In the 2p cut spectra two transitions from ^{23}Ne could be observed, namely 1702 keV→0 keV and 2517 keV→1702 keV. They are marked with an asterisk in Figure 6.12 and they belong to the states $(5/2^{+},7/2^{+})_1$→$5/2^{+}$ and $(5/2^{+},7/2^{+})_2$→$(5/2^{+},7/2^{+})_1$ for which the quantum numbers are not finally known yet. Following the given level scheme, the two transitions 2517 keV→1702 keV and 1702 keV→0 keV should come in coincidence if a 2517 keV→1702 keV transition was present. This fact will now be used to check that the two transitions really belong to ^{23}Ne.

To demonstrate that the two mentioned transitions belong to ^{23}Ne a gamma-gamma coincidence gate is used. Figure 6.13 (a) and (b) show the 2p cut total gamma-ray spectra for all target-and-degrader-runs in the range from 1400 KeV to 2200 KeV. In this range the transition 1702 keV→0 keV should appear. In the figure the gamma-ray energy was Doppler corrected to suppress the centroid shift which the gammas from in-flight decays underlie. The beta for this correction was chosen to be β_{DC}=0.02518. This is the mean decay beta for the 1702 keV→0 keV transition for the target-and-degrader-runs as shown later in this section. Figure 6.13 (a) shows the spectrum without any gamma-gamma coincidence gate. Here, a complex peak structure appears in the spectrum. On the left a huge background is visible. It could stem from different transitions which decay in rest or in-flight. They are strongly smeared out by the Doppler correction which is obviously done with a wrong beta for them. In the middle of the spectrum the 1702 keV→0 keV transition from ^{23}Ne appears. It produces a sharp peak because a valid beta was chosen for the Doppler correction. Next to it the 2^{+}_{1}→0^{+} transition from ^{16}C can be seen. The transition is fractured into several peaks because the gammas were emitted in rest and hence the Doppler correction changes the gamma-ray energies wrongly, whereby the induced errors depend on the discrete detection angle. On the right side of the spectrum the 4^{+}_{1}→2^{+}_{1} transition from ^{22}Ne appears. The gammas produce a sharp peak although the state decays in-flight. This can be explained with the fact that the here chosen Doppler correction beta β_{DC} is very close to the mean decay beta for the 4^{+}_{1}→2^{+}_{1} transition of 0.02262 (cf. Sec. 6.4 and Fig. 6.9). Hence, the Doppler correction is roughly valid for this transition.

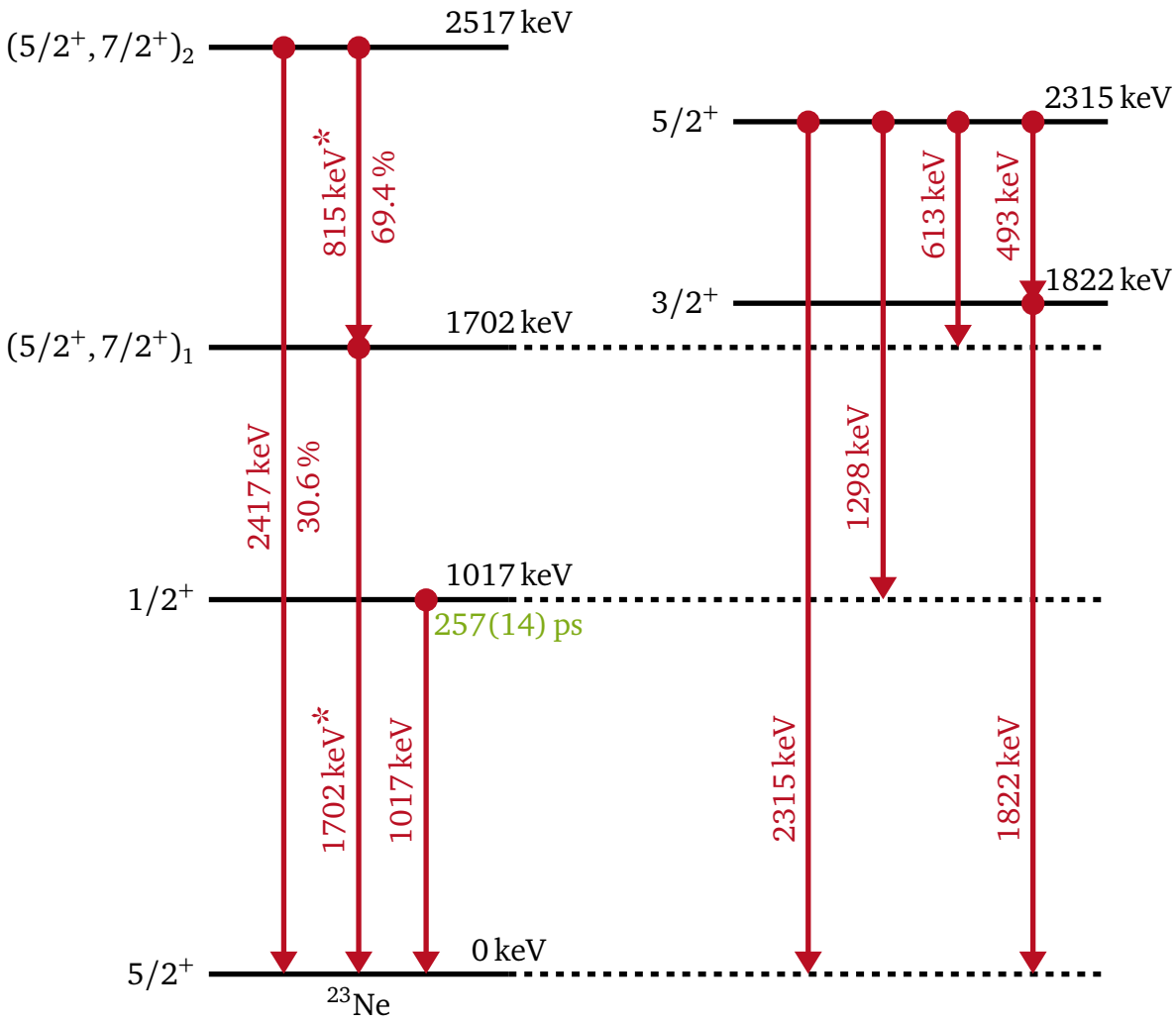

Figure 6.12: Level scheme of the five lowest excited states of ^{23}Ne. The energies printed in black are the energies of the states while the energies printed in red are the transition energies emitted by gamma rays [Fir06]. If a gamma-ray energy is marked with a star this transition was seen in the 2p cut spectrum. The lifetime of the $1/2^+$ state is taken from [FMC66, Fir06] and shown in green.

Figure 6.13 (b) on the other hand shows the spectrum with a gamma-gamma coincidence gate. The gate is defined by the peak from the 2517 keV→1702 keV transition of ^{23}Ne, which is located at 815 keV. Therefore, a Gaussian function was fitted to the peak at 815 keV using the Doppler corrected target-and-degrader-runs spectrum. This leads to a centroid energy of 814.7 KeV and a sigma of 6.5 keV. The gate was chosen to reach from the mean value plus/minus two sigma. Hence, the gate reaches from 801.7 keV to 827.7 keV. In the spectrum with the energy gate it can be seen that the background and the $2_1^+ \rightarrow 0^+$ transition from ^{16}C as well as the $4_1^+ \rightarrow 2_1^+$ transition from ^{22}Ne have vanished. Only one peak remains for which the mean could be determined via a Gaussian fit to 1700.4(1.1) KeV. This is in good agreement with the official accepted value of 1701.5(2) keV for the 1702 keV→0 keV transition from ^{23}Ne [Fir06]. Hence, these two peaks

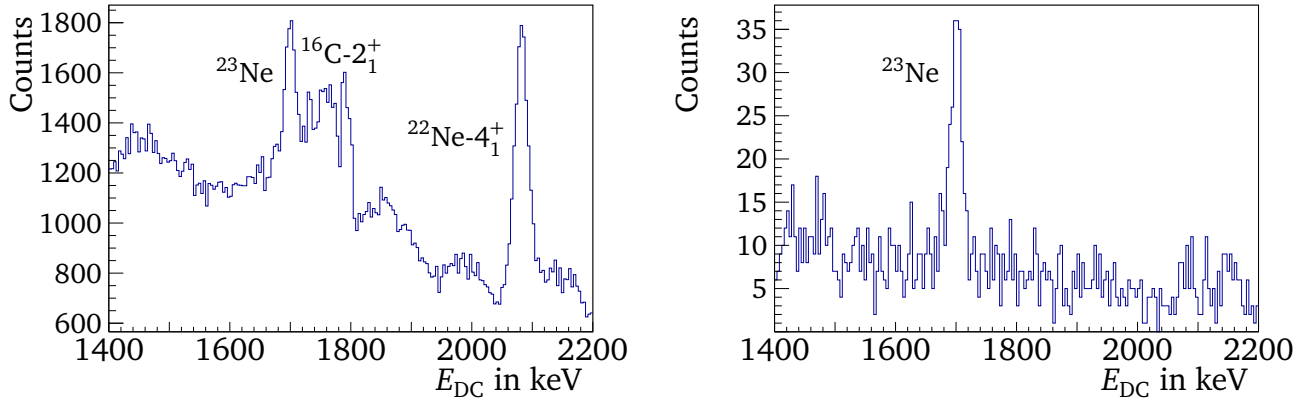

(a) No gamma gate

(b) Gamma gate on the 2517 keV→1702 keV transition of ^{23}Ne

Figure 6.13: Doppler corrected total gamma-ray spectra for all target-and-degrader-runs and 2p cuts in the range from 1400 KeV to 2200 KeV. The beta for the Doppler correction was set to β_{DC}=0.02518. In the right plot, a gamma-gamma coincidence gate is applied to the 2517 keV→1702 keV transition of ^{23}Ne. The gate is reaching from 801.7 keV to 827.7 keV. This corresponds to a 2σ range around the mean value of 814.7 KeV.

belong to ^{23}Ne transitions and in the following the lifetimes of the two corresponding peaks will be determinated.

In the next step, the mean decay beta $\overline{\beta}_{TO}$ is extracted from the target-only-runs following the idea from Section 5.8. For this, the transition 2517 keV→1702 keV is used because for this transition the number of counts was larger and it is not effect by feeding like the 1702 keV→0 keV transition. The analysed data were obtained by applying the degrader-passed check to the target-only-runs as explained in Section 5.8. Figure 6.14 (a) shows the gamma-ray spectra for four discreet chosen Gammasphere angles, namely 90.00°, 100.81°, 110.19°, and 142.62°. For these four angles the 2517 keV→1702 keV transition could be identified with an adequate certainty as a moving peak (right fitted peak in the figure). Using the centroid of these four peaks the fit in Figure 6.14 (b) can be obtained. Here, E_{Lab} is plotted versus cos(θ'). For this, the Gammasphere angles θ were corrected to θ' according to the target position correction of 0.2 cm which is explained in Section 5.9. To the four data points the function from Equation 2.19 is fitted to extract the mean decay beta $\overline{\beta}_{TO}$. In this case only four data points with a rather large uncertainty are available. This leads to large uncertainties for the results of the fit parameters, especially for the mean decay beta. Due to this, the E_{CM} was fixed to the most recent known value of 815.4 keV [Fir06], for which the uncertainty is only 0.5 keV. This is much smaller than the uncertainty which is expected from the fit which is performed in Figure 6.14 (b). The later analysis in this section of the higher-lying states will also show that the obtained results for E_{CM} from this

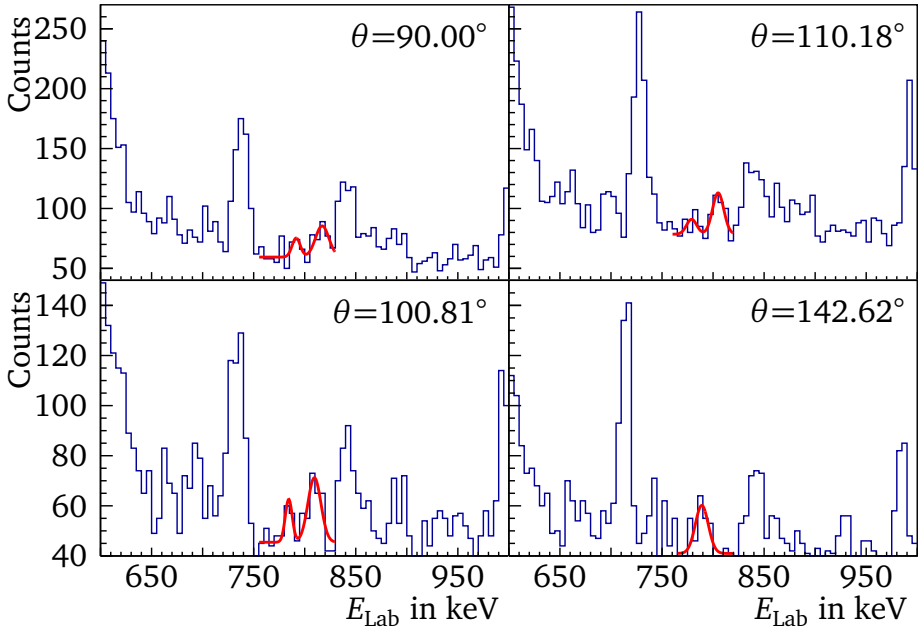

(a) Gamma-ray spectra for discreet angles

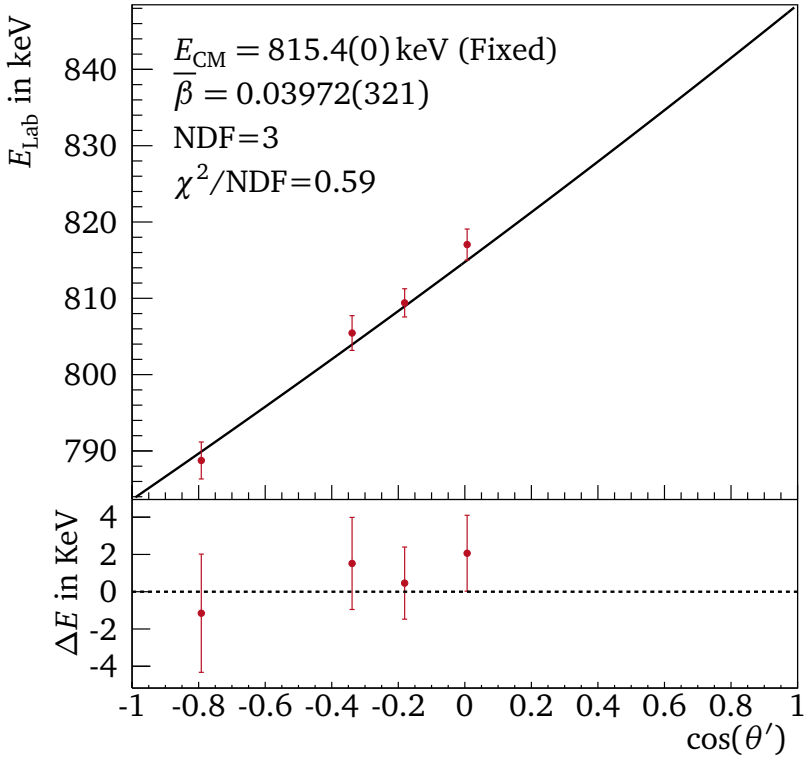

(b) E_{Lab} versus $\cos(\theta')$ fit

Figure 6.14: Analysis of the energy shift for target-only-runs, 2p cut and degrader-passed check focusing on the 2517 keV→1702 keV transition of ^{23}Ne. Part (a) shows the gamma-ray spectra for four discreet chosen Gammasphere angles. Part (b) shows the E_{Lab} versus $\cos(\theta')$ fit for these four angles. The black fit-function is described by Equation 2.19. The lower plot in Part (b) shows the residuals ΔE of the fit which is shown in the upper plot of Part (b).

work are in agreement with the accepted values from [Fir06]. Hence, it seems to be valid to fix E_{CM} to 815.4 keV [Fir06] for this fit, which leads to $\overline{\beta}_{TO}$=0.0397(32) for the mean decay beta. This obtained value can then be fed into the Geant4 simulations to calculate the initial betas β_{ini} the isotopes get (cf. Sec. 4.3). Further it should be emphasized again that the extracted lifetimes depend strongly on the chosen $\overline{\beta}_{TO}$ which is used in the simulations. Because only four small peaks close to the detection limit were available for the extraction of $\overline{\beta}_{TO}$, systematic biases (e.g. decision which angles are considered, definition of the fit range, considering additional peaks in the fit routine which interfere with the peak of interests or not, etc.) and random background fluctuations have a large influences on $\overline{\beta}_{TO}$. The systematic uncertainties are difficult to estimate and to propagate to the further results. So, the further results are just valid, assuming that the result $\overline{\beta}_{TO}$=0.0397(32) is not significantly influenced by unconsidered systematic uncertainties. Hence, a remeasurement of the lifetimes with this technique is recommended, for which the measurement should be designed in a way that the 2517 keV→1702 keV transition of ^{23}Ne is detected with much better statistics.

Now the data from the target-and-degrader-runs are evaluated to get the experimental mean decay beta $\overline{\beta}_{Exp}$ for the two transitions of ^{23}Ne. Events with protons which were detected under 90° are ignored. Figure 6.15 (a) shows the radiation angle θ versus laboratory energy E_{Lab} for these data focusing on the 2517 keV→1702 keV transition. Moving peaks for a transition which decayed in-flight can be seen. The locations of these peaks are around the expected energy for the 2517 keV→1702 keV transition of 815 KeV (marked with the dashed line). Right to the moving peak structures a wide stopped peak structure from the neutron induced reactions ^{72}Be(n,n') and ^{27}Al(n,n') is placed around 835 keV. This wide peak structure limits the amount of Gammasphere angles under forward direction for which the centroid shift for the 2517 keV→1702 keV transition could be extracted. In total the centroid shift for $E_{Lab}(\overline{\beta}, \theta)$ could be analysed for nine Gammasphere angles (namely 69.82°, 79.19°, 80.71°, 90.00°, 99.29°, 100.81°, 110.18°, 121.72°, and 129.93°). In Figure 6.15 (b) this centroid shift is illustrated as a function of cos(θ). The data points were achieved by fitting Gaussian functions to the 2517 keV→1702 keV transition peaks in the respective gamma-ray spectra for the nine discrete Gammasphere angles (cf. Sec. 2.5). The shown fit, described by Equation 2.19, leads to the results of E_{cm}=813.7(4) keV which is comparable to the international accepted value of 815.4(5) keV [Fir06]. The mean decay beta was obtained to $\overline{\beta}_{Exp,2517\,keV}$=0.02225(138). The position and the shape of the fit-function reproduce the data well as it can be seen in Figure 6.15 (a) and (b).

Figure 6.16 (a) shows the radiation angle θ versus laboratory energy E_{Lab} for the same data focusing on the 1702 keV→0 keV transition. Moving peaks for a transition which decayed in-flight can be seen. The locations of these peaks are around the expected energy for the 1702 keV→0 keV transition of 1701.5 keV (marked with the dashed line). Right from the moving peak structures a pronounced stopped peak structure can be seen which belongs to the $2_1^+ \rightarrow 0^+$ transition from

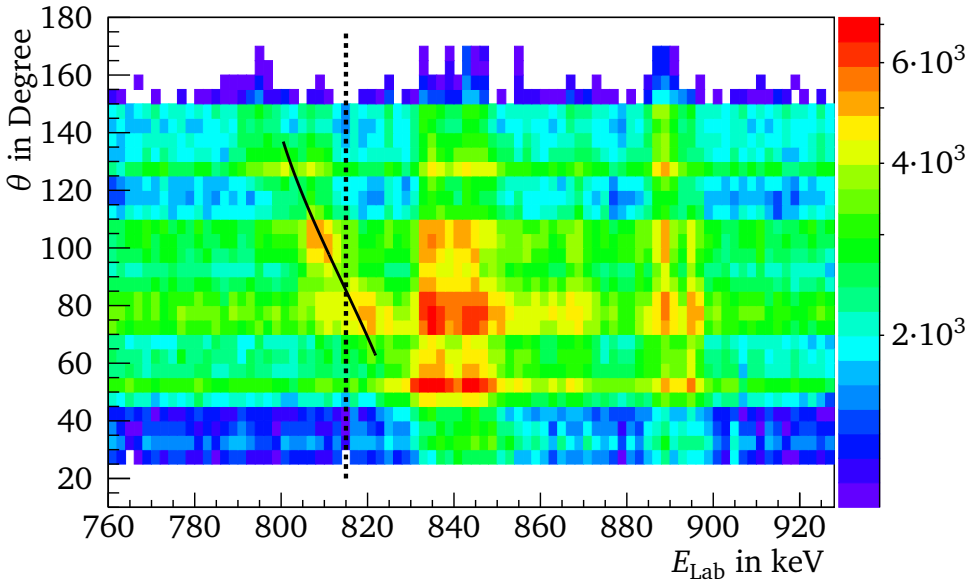

(a) Radiation angle θ versus laboratory energy E_{Lab}

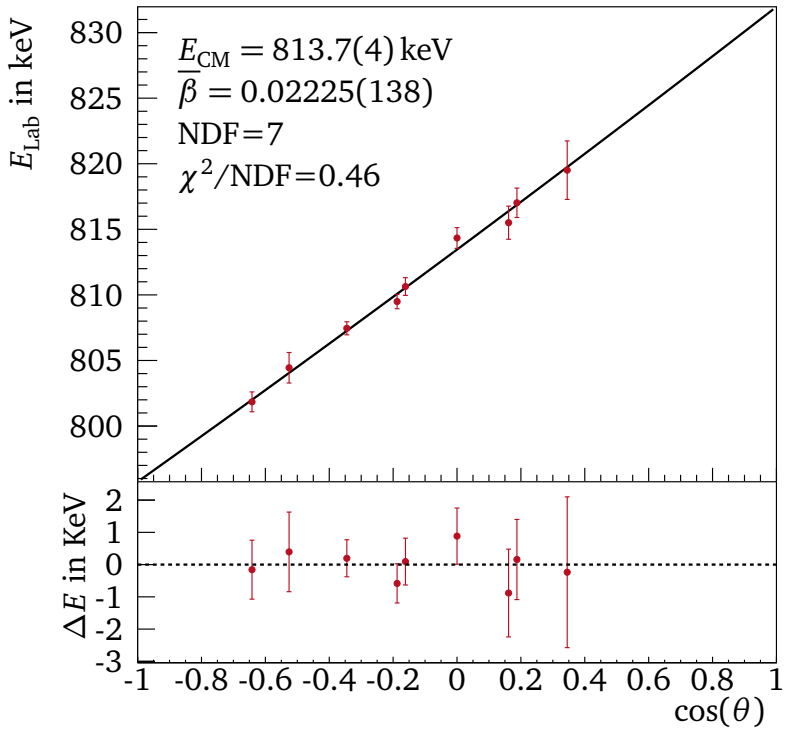

(b) E_{Lab} versus $\cos(\theta)$ fit

Figure 6.15: Analysis of the energy shift for target-and-degrader-runs and 2p cut focusing on the 2517 keV→1702 keV transition of ^{23}Ne. Events with protons detected under 90° are ignored. In part (a) the z-axis range was truncated to a minimum of 1000 counts per bin for a better visualization. The black fit-functions are described by Equation 2.19. The dashed line in Part (a) indicates the expected gamma-ray energy E_{cm}= 815.4 keV of the transition [Fir06]. The lower plot in Part (b) shows the residuals ΔE of the fit shown in the upper part.

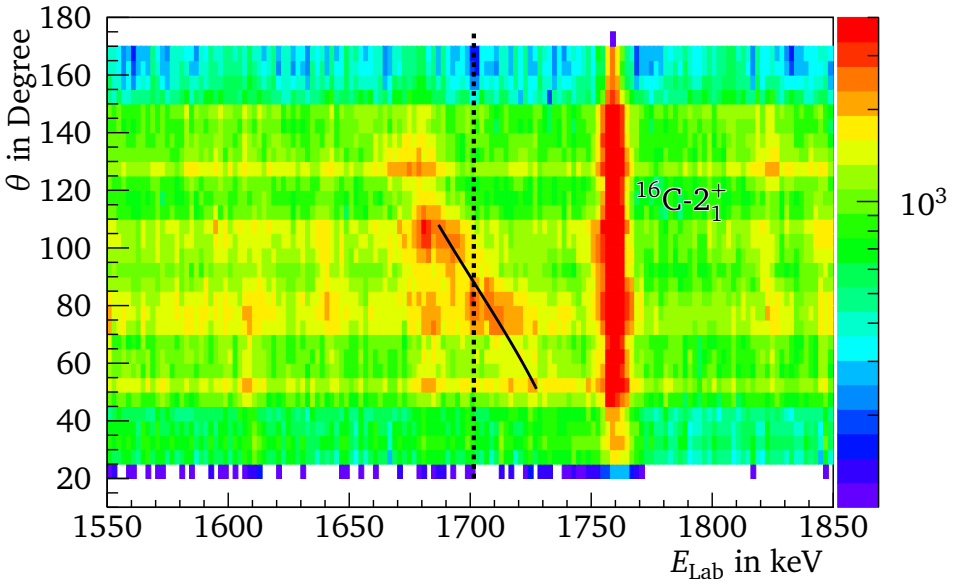

(a) Radiation angle θ versus laboratory energy E_{Lab}

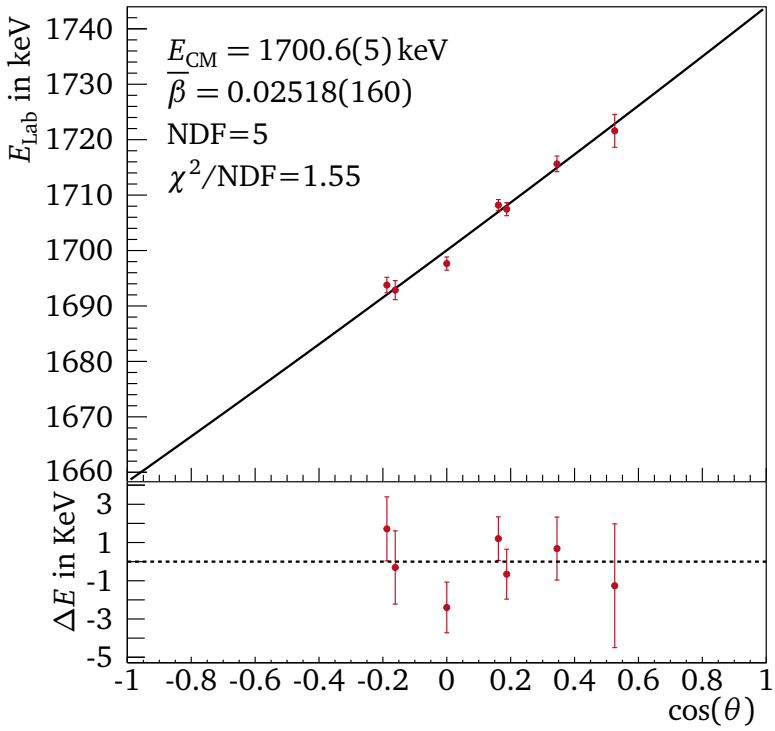

(b) E_{Lab} versus $\cos(\theta)$ fit

Figure 6.16: Analysis of the energy shift for target-and-degrader-runs and 2p cut focusing on the 1702 keV→0 keV transition of ^{23}Ne. Events with protons detected under 90° are ignored. In part (a) the z-axis range was truncated to a maximum of 4000 counts per bin for a better visualization. The black fit-functions are described by Equation 2.19. The dashed line in Part (a) indicates the expected gamma-ray energy E_{cm}= 1701.5 keV of the transition [Fir06]. The lower plot in Part (b) shows the residuals ΔE of the fit shown in the upper part.

^{16}C. Left from the moving peak structures a stopped background peak is visible around 1680 keV. The source for this peak could not be finally clarified. This peak limits the amount of Gammasphere angles under backward direction for which the centroid shift for the 1702 keV→0 keV transition could be extracted. In total the centroid shift of $E_{\mathrm{Lab}}(\overline{\beta}, \theta)$ could be analysed for seven Gammasphere angles (namely 58.28°, 69.82°, 79.19°, 80.71°, 90.00°, 99.29°, 100.81°). In Figure 6.16 (b) this centroid shift is illustrated as a function of $\cos(\theta)$. The data points were achieved by fitting Gaussian functions to the 1702 keV→0 keV transition peaks in the respective gamma-ray spectra for the seven discrete Gammasphere angles (cf. Sec. 2.5). The shown fit, described by Equation 2.19, leads to the result of E_{cm}=1700.6(5) keV, which is in agreement with the accepted value of 1701.5(2) keV [Fir06]. The mean decay beta was obtained to $\overline{\beta}_{\mathrm{Exp,1702\,keV}}$=0.02518(160). The position and the shape of the fit-function reproduce the data well as it can be seen in Figure 6.16 (a) and (b).

In the next step the lifetime can be extracted for the two transitions of ^{23}Ne by comparing the experimental mean decay betas with the mean decay betas from the simulation for the target-and-degrader-runs. Because the 2517 keV→1702 keV transition feeds into the 1702 keV→0 keV transition, this feeding effect has to be taken into account while simulating the 1702 keV→0 keV transition. Hence, the lifetime for the higher-lying state $(5/2^+, 7/2^+)_2$ at 2517 keV will be deduced first in the following. Therefore, the Geant4 simulations are applied with the same approach as for the analysis of the ^{22}Ne case: ^{23}Ne isotopes, which are excited in the $(5/2^+, 7/2^+)_2$ state, are spawned in a thin oxidation layer at the beginning of the target using $\overline{\beta}_{\mathrm{TO}}$=0.03972(321) to calculate the initial beta of the isotopes. This is done for a set of several different lifetimes and for each lifetime setting the corresponding mean decay betas $\overline{\beta}_{\mathrm{Sim}}(\tau_{\mathrm{Sim}})$ are extracted. For the extraction of $\overline{\beta}_{\mathrm{Sim}}(\tau_{\mathrm{Sim}})$ single Gaussian functions are fitted to the spectra of the same nine Gammasphere angles which were used for the analysis of the target-and-degrader-runs for the 2517 keV→1702 keV transition and approximately the same fit ranges are used. This is done to match the experimental conditions as good as possible and to not introduce an artificial bias due to the truncation of used Gammasphere rings. The simulations were performed in the range from 300 fs to 850 fs because here the experimental result was reflected (cf. Fig. 6.17). It should be noted that for the simulation results the moving peak is smeared out for the extreme angles far away from 90° and for large lifetimes ($\tau_{\mathrm{Sim}} \gtrsim$550 fs) due to interfering with an arising stopped peak component (cf. mid of Sec. 2.5). The stopped component is smaller than the moving component. In the experimental spectra no stopped peak component can be seen for any angle. But here the statistic is too small to see a stopped peak component, if the ratio between moving and stopped component is the same as for the simulations for $\tau_{\mathrm{Sim}} \approx$650 fs. Also the 2517 keV→1702 keV transition is only observed for angles close to 90°. For these spectra the stopped component is not separated from the moving component and a slightly broader peak appears. Hence, the simulated data are not in contradiction with the experimental spectra. A remeasurement with a higher statistic would be worthwhile.

Figure 6.17 shows the here obtained simulation results for $\overline{\beta}_{\mathrm{Sim}}(\tau_{\mathrm{Sim}})$ for different lifetimes. Part (a) of the figure shows the results for simulations with ICRU73 stopping powers and Part (b) shows the results for SRIM stopping powers. Both results do not differ much. This can be explained with the fact that the difference in the stopping powers is not that big for ^{23}Ne compared to the effect for ^{16}C. While for the analysis of ^{22}Ne a linear fit to the simulated data was sufficient, now an exponential function, which is defined by

$$\overline{\beta}_{\mathrm{Sim}}(\tau_{\mathrm{Sim}}) = a \cdot \mathrm{e}^{-b\tau_{\mathrm{Sim}}} + c, \tag{6.9}$$

has to be fitted to the simulated data points. This can be explained with the fact that now a much larger range in terms of lifetimes is covered. That was necessary due to the larger statistical uncertainty of the experimental mean decay beta $\overline{\beta}_{\mathrm{Exp,2517\,keV}}$. To get the lifetime τ_{Exp} of the state, the intersection of the fit-function with the experimental mean decay beta $\overline{\beta}_{\mathrm{Exp,2517\,keV}}$ has to be found. In the figure this is visualized by the intersection of the black fit-function and the orange line which represents the measured mean decay beta $\overline{\beta}_{\mathrm{Exp,2517\,keV}}$. The yellow band around the line represents its statistical uncertainty. Analytically this is achieved via

$$\overline{\beta}_{\mathrm{Sim}}\left(\tau_{\mathrm{Exp}}\right) := \overline{\beta}_{\mathrm{Exp}} \quad \Rightarrow \quad \tau_{\mathrm{Exp}} = -\frac{1}{b}\ln\left(\frac{\overline{\beta}_{\mathrm{Exp}} - c}{a}\right), \tag{6.10}$$

using the fit-parameters from Equation 6.9. The statistical uncertainty $u\left(\tau_{\mathrm{Exp}}\right)$ of a such obtained lifetime is given by

$$\begin{aligned} u^2\left(\tau_{\mathrm{Exp}}\right) = &\left(\frac{1}{b\left(c-\overline{\beta}_{\mathrm{Exp}}\right)} \cdot \Delta\overline{\beta}_{\mathrm{Exp}}\right)^2 + \left(\frac{1}{ab} \cdot \Delta a\right)^2 + \left(\frac{\ln\left(\overline{\beta}_{\mathrm{Exp}} - c\right) - \ln(a)}{b^2} \cdot \Delta b\right)^2 \\ &+ \left(\frac{1}{b\left(\overline{\beta}_{\mathrm{Exp}} - c\right)} \cdot \Delta c\right)^2 + 2 \cdot \frac{\ln\left(\overline{\beta}_{\mathrm{Exp}} - c\right) - \ln(a)}{ab^3} \cdot \mathrm{cov}(a,b) \\ &+ 2 \cdot \frac{1}{ab^2\left(\overline{\beta}_{\mathrm{Exp}} - c\right)} \cdot \mathrm{cov}(a,c) + 2 \cdot \frac{\ln\left(\overline{\beta}_{\mathrm{Exp}} - c\right) - \ln(a)}{b^3(\overline{\beta}_{\mathrm{Exp}} - c)} \cdot \mathrm{cov}(b,c), \end{aligned} \tag{6.11}$$

where $\mathrm{cov}(p_i, p_j)$ is the covariance between parameter p_i and p_j stemming from the fit. Applying this formalism leads to a result of 630(78) fs for ICRU73 stopping powers and 641(79) fs for SRIM stopping powers for the lifetime of the $(5/2^+, 7/2^+)_2$ state at 2517 keV in ^{23}Ne.

Additional to the statistical uncertainty stemming from the statistical uncertainty of the mean decay beta $\overline{\beta}_{\mathrm{Exp,2517\,keV}}$, also a systematic uncertainty due to the target thickness will be calculated for all further results. If the real target thickness is slightly different compared to the expected value, the excited isotopes would enter the degrader a bit earlier or later. This would

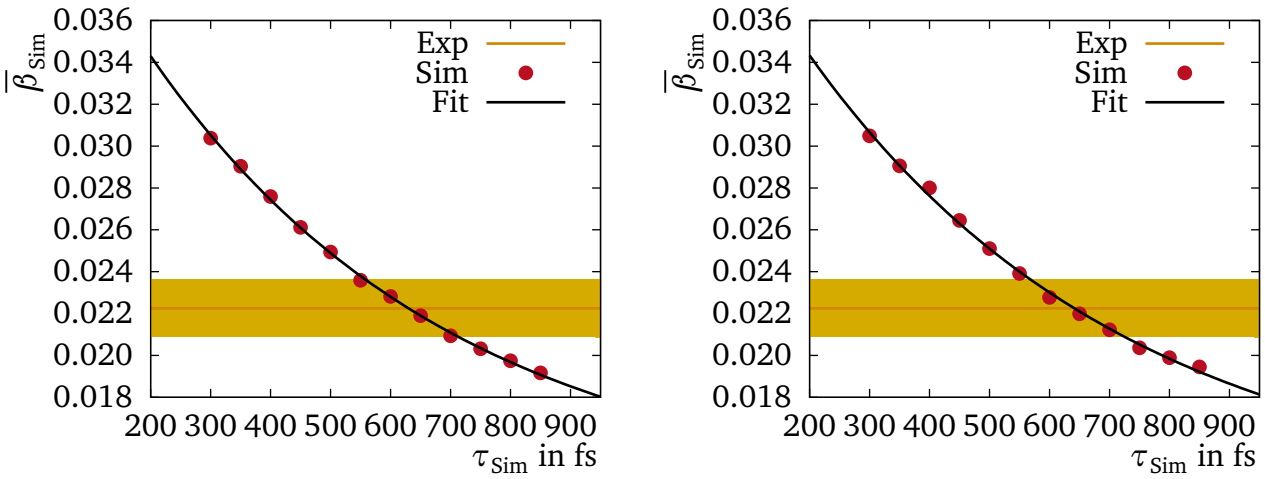

(a) For ICRU73 stopping powers

(b) For SRIM stopping powers

Figure 6.17: Simulated mean decay beta $\overline{\beta}_{\mathrm{Sim}}$ versus simulated lifetime τ_{Sim} for the 2517 keV→1702 keV transition of ^{23}Ne. In the simulations the ^{23}Ne isotopes were created in a thin oxidation layer at the beginning of the target. The initial beta in the simulation was obtained with $\overline{\beta}_{\mathrm{TO}}$=0.03972(321). The yellow band illustrates the experimental mean decay beta value of $\overline{\beta}_{\mathrm{Exp,2517\,keV}}$=0.02225(138) including its uncertainty. The shown fit-function is described by Equation 6.9.

change the time in which the isotopes are slowed down before they decay. Hence, this influences the mean decay betas and so the extracted lifetimes. The maximum range of the uncertainty of the target thickness could be estimated to be ±10 %. Due to this the Geant4 simulations are also carried out for the two extreme values of the target thickness and then the lifetime is extracted the same way as before. The differences between the lifetimes for the mean target thickness and the extreme target thicknesses give an insight into the systematic uncertainty due to the target thickness. This analysis leads to 630(78) $\mathrm{fs}^{+14\,\mathrm{fs}}_{-14\,\mathrm{fs}}\left(\mathrm{syst}_{\mathrm{target}}\right)$ for ICRU73 stopping powers and 641(79) $\mathrm{fs}^{+16\,\mathrm{fs}}_{-6\,\mathrm{fs}}\left(\mathrm{syst}_{\mathrm{target}}\right)$ for SRIM stopping powers as a lifetime for the $(5/2^+, 7/2^+)_2$ state.

Now, the lifetime for the lower lying state $(5/2^+, 7/2^+)_1$ at 1071 keV can be extracted. As stated earlier, feeding has to be taken into account for this case. To do so, the Geant4 simulation has to know the ratio $R_{1702\,\mathrm{keV}}$ for which the ^{23}Ne isotopes are excited directly into the $(5/2^+, 7/2^+)_1$ state and the ratio $R_{2517\,\mathrm{keV}}$ for which the ^{23}Ne isotopes are excited into the $(5/2^+, 7/2^+)_2$ state and feed into to the $(5/2^+, 7/2^+)_1$ state. To extract these ratios the peak areas of the two transitions for the target-and-degrader-runs are compared in the following. Because this can only be done for several discrete Gammasphere angles also the angular gamma-ray distribution for both transitions has to be considered in the analysis. The ratios themselves have to be angle independent. Unfortunately the quantum numbers of the two states, the dominant decay types of the two transitions and hence the angular gamma-ray distributions of the two

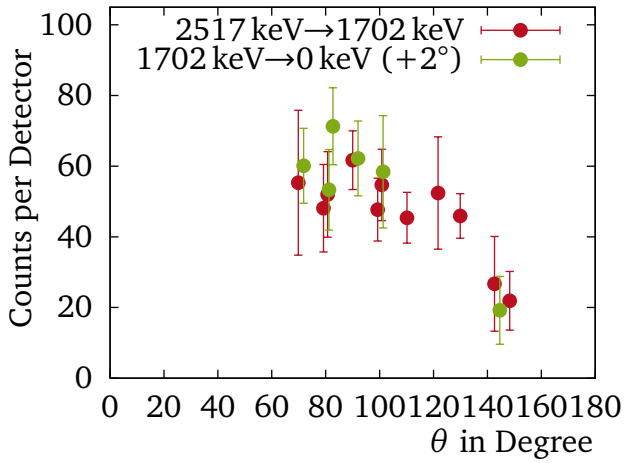

Figure 6.18: Angular distribution for the 2517 keV→1702 keV and 1702 keV→0 keV transition of ^{23}Ne. The counts for each angle were obtained by fitting Gaussian functions to the peaks in the gamma-ray spectra for the corresponding Gammasphere angle θ. The total number of counts was then divided by the number of detectors in the corresponding Gammasphere ring to make the distribution independent of the number of detectors. The data points for the 1702 keV→0 keV transition are shifted by 2° to the right for a better visualization.

transitions are not finally known. The statistics in the target-and-degrader-run data is too low to investigate the angular distribution of consecutive decays from ^{23}Ne with a proper certainty. So for the next analysis steps it will be assumed that both transitions follow the same angular distribution in the range of interest. This is for example legitimate if all three involved states are a $5/2^+$ state, which is possible with the knowledge so far.

If the number of excited isotopes in the $(5/2^+, 7/2^+)_2$ state which decay via the 2517 keV→1702 keV transition is given by $N_{2517\,\mathrm{keV}}$ and the number of excited isotopes in the $(5/2^+, 7/2^+)_1$ state is given by $N_{1702\,\mathrm{keV}}$ the relations

$$A_{815\,\mathrm{keV}} = \epsilon(815\,\mathrm{keV}) \cdot N_{2517\,\mathrm{keV}} \tag{6.12}$$

$$A_{1702\,\mathrm{keV}} = \epsilon(1702\,\mathrm{keV}) \cdot (N_{2517\,\mathrm{keV}} + N_{1702\,\mathrm{keV}}) \tag{6.13}$$

hold. In these relations $\epsilon(E)$ represents the corresponding Gammasphere efficiency as deduced in Section 5.3. These efficiencies were calculated to $\epsilon(815\,\mathrm{keV})$=6.58(4) % and $\epsilon(1702\,\mathrm{keV})$=4.33(1) %. The parameters $A_{815\,\mathrm{keV}}$ and $A_{1702\,\mathrm{keV}}$ represent the areas of the peaks at the transitions energies of 815 keV and 1702 keV respectively. With these relations the excitation ratios for the simulations can be expressed via

$$R_{2517\,\mathrm{keV}} = \frac{N_{2517\,\mathrm{keV}}}{N_{1702\,\mathrm{keV}} + N_{2517\,\mathrm{keV}}} = \frac{\epsilon(1702\,\mathrm{keV})}{\epsilon(815\,\mathrm{keV})} \cdot \frac{A_{815\,\mathrm{keV}}}{A_{1702\,\mathrm{keV}}} \tag{6.14}$$

$$R_{1702\,\mathrm{keV}} = \frac{N_{1702\,\mathrm{keV}}}{N_{1702\,\mathrm{keV}} + N_{2517\,\mathrm{keV}}} = 1 - R_{2517\,\mathrm{keV}}. \tag{6.15}$$

Table 6.1: Excitation ratio $R_{2517\,\mathrm{keV}}$ for the $(5/2^+, 7/2^+)_2$ state and $R_{1702\,\mathrm{keV}}$ for the $(5/2^+, 7/2^+)_1$ state of ^{23}Ne. The ratios were obtained with Equations 6.15. The parameters $A_{815\,\mathrm{keV}}$ and $A_{1702\,\mathrm{keV}}$ represent the areas of the peaks at the transition energies of 815 keV and 1702 keV respectively. The areas were obtained by fitting Gaussian functions to the peaks in the gamma-ray spectra for the corresponding Gammasphere angle θ.

θ	$A_{815\,\mathrm{keV}}$	$A_{1702\,\mathrm{keV}}$	$R_{2517\,\mathrm{keV}}$	$R_{1702\,\mathrm{keV}}$
69.8°	498(184)	481(84)	0.68(28)	0.32(28)
79.2°	192(50)	213(46)	0.59(20)	0.41(20)
80.7°	260(61)	357(55)	0.48(13)	0.54(13)
90.0°	432(58)	436(75)	0.65(14)	0.35(14)
99.3°	239(45)	292(80)	0.54(18)	0.46(18)
142.6°	133(67)	96(48)	0.91(65)	0.09(65)
uncertainty weighted mean:			0.58(8)	0.42(8)

These two ratios were calculated for the spectra of six different Gammasphere angles separately. For these angles a proper peak area could be deduced for both transitions. The number of counts per detector for these areas is also shown in Figure 6.18. The ratio results for all six available angles are listed in Table 6.1. These values are used to calculate an uncertainty weighted mean value for the excitation ratios which leads to $R_{1702\,\mathrm{keV}}$=0.42(8) and $R_{2517\,\mathrm{keV}}$=0.58(8). If one compares the individual ratio values in Table 6.1 with the uncertainty weighted mean values, they are all in agreement considering the one sigma uncertainty. This shows that for the here possible precision the extracted ratios are angle independent. Hence, the ignorance of different angular distributions for the two consecutive transitions seems to have a smaller influence than the uncertainties stemming from the low statistics. Hence, the assumption that both transitions follow the same angular distribution is justified considering the possible precision of this analysis.

With these information the lifetime $\tau_{1702\,\mathrm{keV}}$ for the lower lying state $(5/2^+, 7/2^+)_1$ at 1702 keV can be extracted using the Geant4 simulation. For this, the ^{23}Ne isotopes are excited randomly into the $(5/2^+, 7/2^+)_1$ state or the $(5/2^+, 7/2^+)_2$ state in such a way that the before obtained excitation ratios are reproduced for a large number of simulated isotopes. Further, the branching ratio for the 2517 keV→1702 keV transition of the $(5/2^+, 7/2^+)_2$ state is set to 100 % in the simulations, because a branching to other states was also not considered in the experimental analysis. Then the analysis of the lifetime follows the same idea as for the higher-lying state done before. It should be noted that for the simulation results also a stopped peak component was visible for the smallest used angle (58.28°) and longer lifetimes. This is a similar behaviour as for the higher-lying state discussed before. For the final obtained lifetime the stopped component is again smaller than the moving component and so it is possible that this stopped component is

not visible in the experimental data due to low statistics. To the smeared out peak for 58.28° also one single Gauss function was fitted over the same fit range as used for the experimental data. Hence, the Gaussian fit to the simulated describes the peak not very good any more. But it was stick to this method because this is the approach closest to the experimental evaluation. For the experimental evaluation also only one Gaussian function was fitted to the transition peak and it can not be certainly deduce whether there is stopped component included in the peak structure or not. A systematic uncertainty due to the improper Gaussian fit to the simulated spectra for the smallest used angle (58.28°) is not given analytical. But it was estimate that this uncertainty has a clearly smaller impact than the statistical uncertainty of the experimental beta values.

For the analysis of the $(5/2^+, 7/2^+)_1$ state at 1702 keV an additional uncertainty due to the feeding has to be considered. This uncertainty is defined by the fact that the lifetime of the higher-lying state has its own uncertainty and that the excitation vector has also an uncertainty. Due to this, for both stopping powers simulations with three different settings are carried out to deal with the feeding uncertainty. To get the mean lifetime, the lifetime of the higher-lying state is set to its mean value and the excitation ratios are set to their mean values. To get an upper limit for the lifetime due to the feeding, the lifetime of the higher-lying state is set to its mean value minus its uncertainty while the excitation ratio $R_{2517\,\mathrm{keV}}$ is set to its mean value minus its uncertainty. To get an lower limit for the lifetime, the lifetime of the higher-lying state is set to its mean value plus its uncertainty while the excitation ratio $R_{2517\,\mathrm{keV}}$ is set to its mean value plus its uncertainty. The ratio $R_{1702\,\mathrm{keV}}$ is always defined by $R_{1702\,\mathrm{keV}}=1-R_{2517\,\mathrm{keV}}$. To deal with the uncertainty due to the target thickness, again the two extreme target thicknesses are simulated. For these cases the lifetime of the higher-lying state is set to the value the previous analysis revealed as extreme lifetimes due to the changed thicknesses.

The results for all different combinations of stopping power, target thickness and feeding uncertainty are summarized in Table 6.2. By combining these data the final results for the lifetime of the lower lying state $(5/2^+, 7/2^+)_1$ can be expressed as $163(55)\,\mathrm{fs}^{+6\,\mathrm{fs}}_{-0\,\mathrm{fs}}\left(\mathrm{syst}_{\mathrm{target}}\right)^{+62\,\mathrm{fs}}_{-80\,\mathrm{fs}}\left(\mathrm{syst}_{\mathrm{feeding}}\right)$ for ICRU73 stopping powers and $168(55)\,\mathrm{fs}^{+8\,\mathrm{fs}}_{-1\,\mathrm{fs}}\left(\mathrm{syst}_{\mathrm{target}}\right)^{+72\,\mathrm{fs}}_{-80\,\mathrm{fs}}\left(\mathrm{syst}_{\mathrm{feeding}}\right)$ for SRIM stopping powers. It can be seen that the uncertainty due to the target thickness is negligible in this case and also that there is no difference between ICRU73 or SRIM stopping powers. The statistical uncertainty due to the uncertainty of the mean decay beta has the same magnitude of order as the uncertainty due to the feeding. Overall the uncertainties for these two lifetimes are much larger than the uncertainties which could be achieved during the analysis of ^{22}Ne. This was expected because the number of counts in the peaks from the ^{23}Ne transitions is much smaller and fewer Gammasphere angles were available for the analysis.

Table 6.2: Settings for the Geant4 simulations to extract the mean lifetime $\tau_{1702\,\mathrm{keV}}$ and its uncertainties for the $(5/2^+, 7/2^+)_1$ state of ^{23}Ne. The simulations are executed for both types of stopping powers. For each stopping power setting three different values for the target thickness d (d=7.50 µm, $0.9d$=6.75 µm, and $1.1d$=8.25 µm) are checked. Furthermore, the feeding uncertainty for $\tau_{1702\,\mathrm{keV}}$ is evaluated by changing the lifetime $\tau_{2516\,\mathrm{keV}}$ of the higher-lying state and by changing the excitation ratios ($R_{2517\,\mathrm{keV}}$, $R_{1702\,\mathrm{keV}}$) according to their statistical uncertainties. The ratio $R_{1702\,\mathrm{keV}}$ is not listed in the table because it is defined by $R_{1702\,\mathrm{keV}}=1-R_{2517\,\mathrm{keV}}$.

Stopping Power	Uncertainty Part	d in µm	$\tau_{2516\,\mathrm{keV}}$ in fs	$R_{2517\,\mathrm{keV}}$ unitless	$\tau_{1702\,\mathrm{keV}}$ in fs
ICRU73	mean value	7.50	630	0.58	**163(55)**
	feeding	7.50	552	0.50	225
	feeding	7.50	708	0.66	83
	target	6.75	616	0.58	168
	target	8.25	644	0.58	163
SRIM	mean value	7.50	641	0.58	**168(55)**
	feeding	7.50	562	0.50	240
	feeding	7.50	720	0.66	88
	target	6.75	635	0.58	176
	target	8.25	657	0.58	167

6.4.1 Comparison with Theory

Finally, the here obtained lifetimes for ^{23}Ne are compared to theoretical calculations. Due to the fact that the angular momentum and the branching ratios of the two investigated states are not finally known, it can not be decomposed to which part each transition strength type contributes to the total transition rate. Hence, in the theoretical calculations, $M1$ and $E2$ strengths are considered for the total transition rate, because they will clearly dominate the behaviour. Then only the lifetime can be compared with the experimental results. If the theory predictions differ from the experimental results it can not be figured out whether the deviation stems from the $M1$ part or the $E2$ part or both parts.

The theoretical calculations were done by A. Brown using the USDB framework, which was already introduced in Section 2.6. In the USDB calculations $E2$ transitions are dominant. Hence, the reduced transition strengths for these transitions are calculated with Equation 2.15 before these strengths are converted into decay rates. To apply Equation 2.15 the effective charges were set to e_p=1.224 and e_n=0.423 following the work from Sagawa et al. [SZZS04]. The transition rates were calculated for the theoretical transition energies. Figure 6.19 shows a level scheme of ^{23}Ne for the experimental results as well as for theoretical USDB calculations done by A. Brown [Bro19]. While the energies of the levels and the most quantum numbers are reproduced well by the USDB calculations, significant discrepancies for the lifetimes can be seen. For the $1/2^+_1$ state the experimental lifetime is twice as long as the theoretical prediction. For the higher-lying states the situation is worse. For the $(5/2^+, 7/2^+)_1$ state the experimental lifetime is larger by a factor of 6.8 and for the $(5/2^+, 7/2^+)_2$ state the experimental lifetime is larger by a factor of 4.5 compared to the USDB calculations. This can not be compensated by the experimental uncertainties. For the $(5/2^+, 7/2^+)_1$ state the theory value deviates by minus 2.5 sigma, while for the $(5/2^+, 7/2^+)_2$ state the discrepancy is even larger. Here, the theory value deviates by minus 6.3 sigma. This strong underestimation of the lifetime in sd-shell nuclei is no new phenomena. So for example in the work from Heil et al. it could be shown that also in the case of ^{21}O the lifetime of the $1/2^+_1$ state is strongly underestimated by USDB calculations [Hei19, HPV$^+$20]. Here the USDB predicts 176 ps while the experiment states the lifetime to 420^{+35}_{-32} ps.

Overall this reveals that no sufficient descriptions of the lifetimes in ^{23}Ne are possible using USDB calculations. Hence, it would be very interesting to apply other theoretical approaches such as the NCSM and check if they can reproduce the lifetimes in ^{23}Ne more accurately.

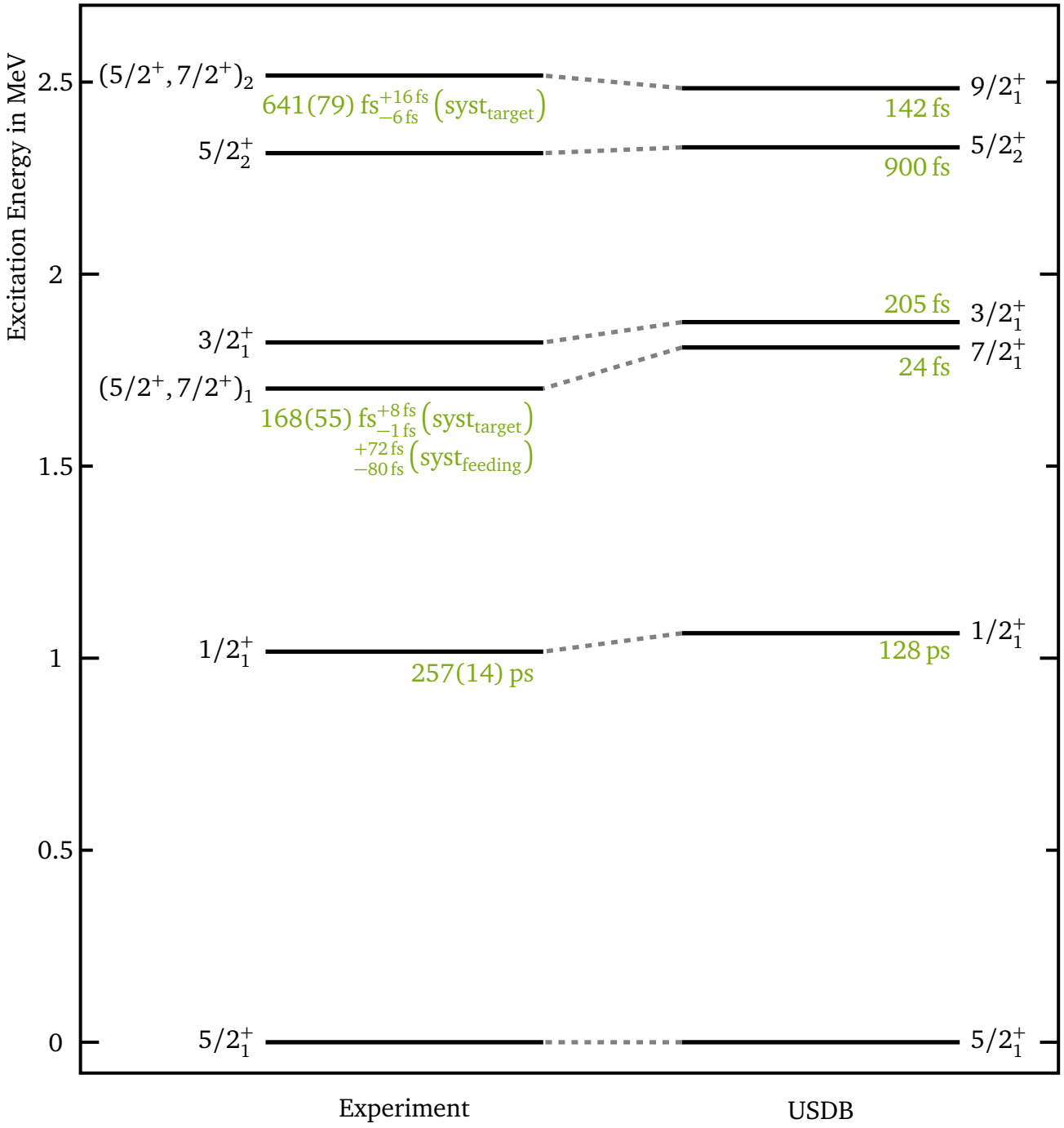

Figure 6.19: Level scheme of ^{23}Ne for the experimental results and for theoretical USDB calculations. The experimental lifetime of the $1/2^+_1$ state is taken from [FMC66] while the level energies are from [Fir06]. The new experimental lifetimes of the higher-lying states are the results from this work for SRIM stopping powers. The lifetimes predicted by theoretical USDB calculations are from A. Brown [Bro19] and calculated for theoretical transition energies. The used $B(E2)$ strengths were obtained for modified effective charges (e_{p}=1.224 and e_{n}=0.423) following the results from [SZZS04].

6.5 Results for Carbon-16

In this section the results for ^{16}C are discussed in detail. For ^{16}C the three higher-lying states 4_1^+, 3_1^+, and 2_2^+ will be investigated (cf. Sec. 2.9 and Fig. 1.1). First, the target-only-runs will be used to extract a beta which can be used as input for the simulations. Then each state is evaluated separately by looking at the target-and-degrader-runs and the corresponding lifetimes are extracted if possible. Finally, the experimental lifetimes are compared to various theoretical calculations.

To analyse the lifetime of the higher-lying states later, an initial beta has to be defined for the Geant4 simulations. For this, the target-only-runs are analysed and the mean decay beta for the $2_1^+ \rightarrow 0^+$ transition is extracted. This is the only transition from ^{16}C which is visible in the target-only-runs spectra for the 2p cuts. The mean decay beta $\overline{\beta}_{\mathrm{TO}}$ is extracted following the idea from Section 5.8. The analysed data were obtained by applying the degrader-passed check to the target-only-runs as explained in Section 5.8. Figure 6.20 (a) shows the radiation angle θ versus laboratory energy E_{Lab} for those data. A moving peak structure for a transition which decayed in-flight can be clearly seen. The location of this peak structure is around the expected energy of E_{cm}=1760 keV for the $2_1^+ \rightarrow 0^+$ transition (marked with the dashed line). For this transition all available angles of Gammasphere except 37.38° could be used to extract the centroid energies $E_{\mathrm{Lab}}(\overline{\beta}, \theta)$ for each angle θ. For the 37.38° spectrum the number of counts are too low to make a proper Gaussian fit to the transition peak. In Figure 6.20 (b) the centroid shift as a function of $\cos(\theta')$ is illustrated. For this, the Gammasphere angles θ were corrected to θ' according to the target position correction of 0.2 cm as explained in Section 5.9. The shown data points were achieved by fitting Gaussian functions to the $2_1^+ \rightarrow 0^+$ peaks in the respective gamma-ray spectra for each discrete Gammasphere angle (cf. Sec. 2.5). The shown fit, described by Equation 2.19, leads to a result of E_{cm}=1759.0(4) keV which is in agreement with the uncertainty weighted mean of 1760(1) keV from [WFM$^+$08, PPC$^+$12]. Also the position and the shape of the fit-function reproduce the data well as it can be seen in Figure 6.8 (a) and (b). Only the data point for θ=80.71° ($\cos(80.71°) \approx 0.16$) is not described well by the fit. A reason for this could not be found and the Gaussian fit to the particular gamma-ray spectrum seems confiding as well. Hence, the data point was still considered in the fit. With this fit the mean decay beta was obtained to $\overline{\beta}_{\mathrm{TO}}$=0.04527(44). The obtained value for $\overline{\beta}_{\mathrm{TO}}$ can then be fed into the Geant4 simulations to calculate the initial betas β_{ini} the isotopes get in the simulation. For all further analyses, the spawn procedure for the ^{16}C isotopes is exactly implemented as explained in Section 4.3. No additional adjustments as it was the case for ^{22}Ne or ^{23}Ne have to be made.

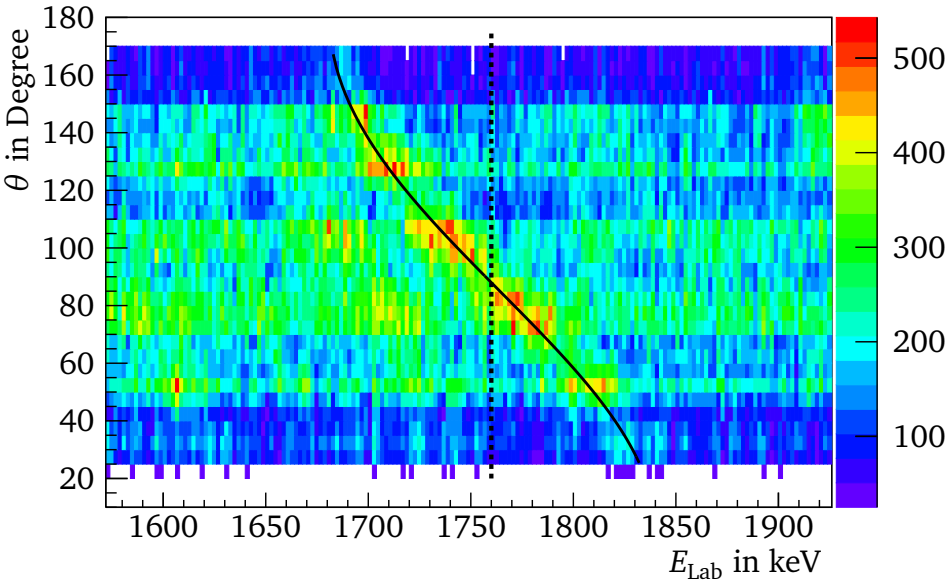

(a) Radiation angle θ versus laboratory energy E_{Lab}

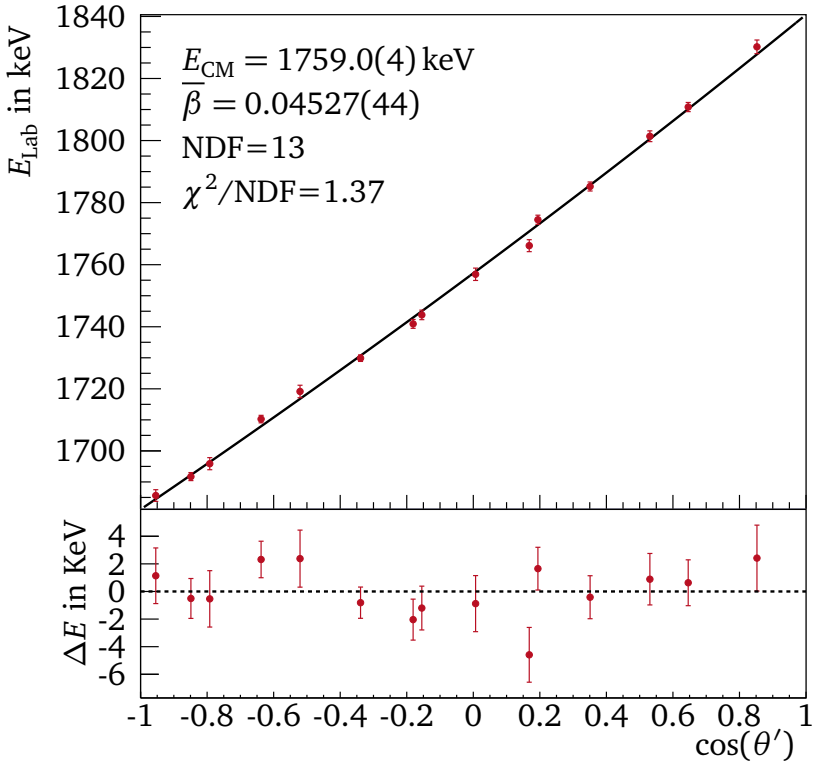

(b) E_{Lab} versus $\cos(\theta')$ fit

Figure 6.20: Analysis of the energy shift for target-only-runs, 2p cut and degrader-passed check focusing on the $2_1^+ \rightarrow 0^+$ transition of ^{16}C. The black fit-functions are described by Equation 2.19. The dashed line in Part (a) indicates the expected gamma-ray energy $E_{\mathrm{cm}} = 1760$ keV of the transition [WFM$^+$08, PPC$^+$12]. The lower plot in Part (b) shows the residuals ΔE of the fit which is shown in the upper plot of Part (b).

6.5.1 Results for the 4_1^+ State

In this section the results for the 4_1^+ state of ^{16}C are discussed. The 2p cut spectrum from Figure 6.4 shows that the $4_1^+ \rightarrow 2_1^+$ transition produced a stopped peak without a moving component. Hence, the lifetime should be in the picosecond range and the DSAM as explained in Section 2.5 can not be applied to the 4_1^+ state. Additionally, from [WFM$^+$08, PPC$^+$12] it is already known that the lifetime should be smaller than 4 ps. Therefore, a lower lifetime limit will be estimated for the 4_1^+ state in the following to give a narrow range for the value of the lifetime. To achieve a proper lower lifetime limit, the experimental gamma-ray spectra for discrete angles are used and compared to the results from the Geant4 simulations. Thereby, the fact is used that a transition of a state with a lifetime in a low picosecond range produces two peaks in the spectra: One bigger peak which is located at the center of mass energy of the transition. This peak is produced by the decay of stopped isotopes. Additionally, one smaller peak is produced which is Doppler shifted in terms of energy. This peak belongs to the remaining in-flight decays. The ratio of these two peaks depends strongly on the lifetime. The longer the lifetime, the more decays happen for stopped isotopes and so more and more counts appear in the non-Doppler-shifted peak. Due to this, it is now checked how long the lifetime has to be until a significant moving peak occurs in the simulated spectra, which also has to be visible in the experimental spectra. By comparing the simulation results with the experimental spectra one gets access to a lower lifetime limit. An other method, in which the line shape towards lower energies of the stopped peak is analysed and compared to simulations, was not carried out in this work, because the strong background fluctuations and contaminations from unknown sources would hinder the analysis and it assumed that the here applied method gives a maybe larger but more stable upper limit.

Focusing first on the experimental gamma-ray spectra, a condition has to be established which defines whether a significant moving peak exists or not. For this purpose it is defined that a peak on top of the background has to have a maximum which is larger than the two sigma uncertainty of the background. Everything else is considered as background fluctuations. The two sigma uncertainty of the background will be labelled as M_{BG} in the following. Additionally, the maximum height of the stopped peak M_{Stopped} from the $4_1^+ \rightarrow 2_1^+$ transition is extracted to calculate the ratio

$$R_{\mathrm{Exp}} = \frac{M_{\mathrm{BG}}}{M_{\mathrm{Stopped}}}. \tag{6.16}$$

This is done for all Gammasphere angles for which the $4_1^+ \rightarrow 2_1^+$ transition is resolved clearly in the spectrum. This was possible for five Gammasphere angles, namely 121.72°, 129.93°, 142.62°, 148.28°, and 162.73°. For smaller angles the $4_1^+ \rightarrow 2_1^+$ transition interferes with the $7/2_1^+ \rightarrow 5/2_1^+$ transition of ^{15}N and so these data can not be used. As an example the analysis is discussed for the spectra of 148.28° now. The analysis for the remaining angles followed the same scheme

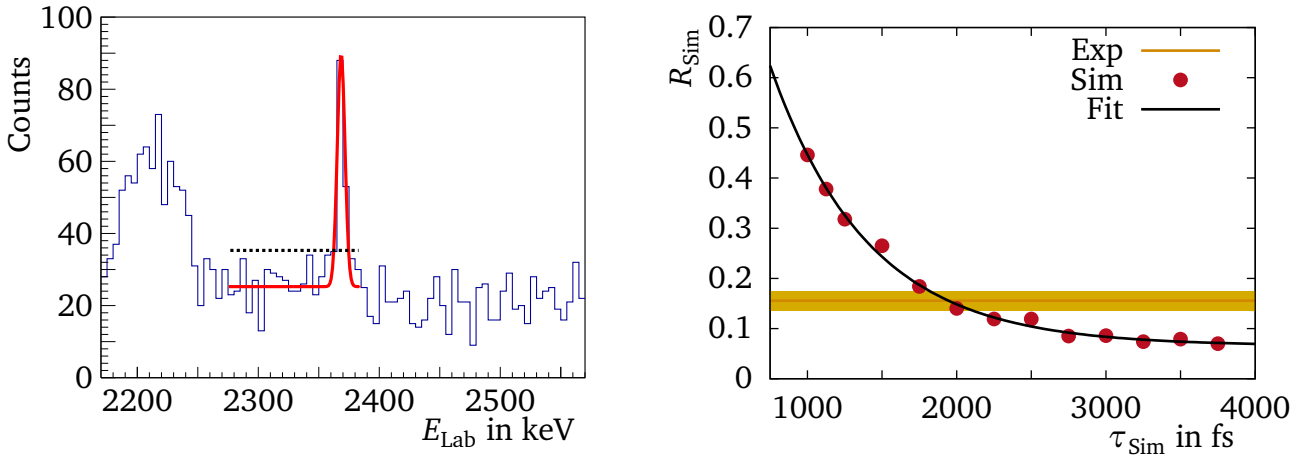

(a) Experimental data (b) Simulation results

Figure 6.21: Estimation of a lower lifetime limit for the 4_1^+ state of ^{16}C using the Gammasphere spectrum under 148.28°. The left part shows the 2p cuts gamma-ray spectrum under 148.28° for the target-and-degrader-runs. The red fit-function represents a Gaussian function plus a linear background. The black dashed line represents the background height plus its two sigma uncertainty. The right part shows the Geant4 simulation results for $R_{\mathrm{Sim}}(\tau_{\mathrm{Sim}})$ using SRIM stopping powers and $\overline{\beta}_{\mathrm{TO}}$=0.04527(44). The black fit-function is described by Equation 6.18. The yellow band illustrates the experimental ratio of R_{Exp}=0.156(19) including its uncertainty.

and no discrepancy occurred. Figure 6.21 (a) shows the 2p cuts gamma-ray spectrum under 148.28° for the target-and-degrader-runs. To the spectrum a Gaussian function plus a linear background was fitted. This results in a background height of 25.3 counts with a two sigma uncertainty of M_{BG}=2·5.0 counts. The two sigma uncertainty is visualized as a black dashed line. It can be seen that there is no moving peak component which is higher than this line. Hence, it is assumed that no moving peak is present. The maximum height of the stopped peak is given by M_{Stopped}=64.7(8.0) counts and so the ratio is calculated to R_{Exp}=0.156(19).

In the next step the Geant4 simulations are applied and the same five Gammasphere angles are investigated. Thereby, the $4_1^+ \rightarrow 2_1^+$ transition is simulated for different lifetimes of the 4_1^+ state in the low picosecond range. Then the ratio

$$R_{\mathrm{Sim}}(\tau_{\mathrm{Sim}}) = \frac{M_{\mathrm{Moving}}}{M_{\mathrm{Stopped}}} \tag{6.17}$$

is calculated for each simulated lifetime τ_{Sim}, where M_{Moving} is the peak maximum of the moving peak component and M_{Stopped} is the peak maximum of the stopped peak component. This is done for all Gammasphere angles separately. The results of this analysis are shown in Figure 6.21 (b) for SRIM stopping powers and the 148.28° spectrum. To the data the function

$$R_{\mathrm{Sim}}(\tau_{\mathrm{Sim}}) = a \cdot \mathrm{e}^{-b\tau_{\mathrm{Sim}}} + c \tag{6.18}$$

could be fitted well. To obtain an estimator τ_{Min} for the lower lifetime limit, the intersection of the fit-function with the experimental ratio R_{Exp} has to be found. In the figure this is visualized by the intersection of the black fit-function and the orange line which represents the experimental ratio R_{Exp}. The yellow band around the line represents its statistical uncertainty. Analytically this is achieved via

$$R_{\mathrm{Sim}}(\tau_{\mathrm{Sim}}) := R_{\mathrm{Exp}} \quad \Rightarrow \quad \tau_{\mathrm{Min}} = -\frac{1}{b}\ln\left(\frac{R_{\mathrm{Exp}} - c}{a}\right), \tag{6.19}$$

using the fit-parameters from Equation 6.18. The statistical uncertainty $u(\tau_{\mathrm{Min}})$ of a such obtained lifetime is given by Equation 6.11, by replacing $\overline{\beta}_{\mathrm{Exp}}$ with R_{Exp}. Applying this formalism leads to τ_{Min}=1.95(15) ps for the 148.28° spectrum.

To achieve the final result for the lower lifetime limit, this method was applied to all five Gammasphere angles and then the uncertainty weighted mean is calculated. The obtained values are shown in Figure 6.22 (a) for ICRU73 stopping powers and in part (b) for SRIM stopping powers. The yellow band illustrates the uncertainty weighted mean including its one sigma uncertainty. It can be seen that all data points are in agreement with the uncertainty weighted mean by considering their one sigma uncertainties. The uncertainty weighted means are given by 1.76(8) ps for ICRU73 stopping powers and by 1.95(9) ps for SRIM stopping powers. Because only a lower lifetime limit and no exact value for the lifetime can be given here, the lower limit is obtained by subtracting the mean value by its one sigma uncertainty. This leads to a lower lifetime limit of τ_{Min}=1.7 ps using ICRU73 stopping powers and τ_{Min}=1.9 ps using SRIM stopping powers.

Additionally, systematic uncertainties due to the target thickness are estimated. For this, the same analysis was done again for Geant4 simulations using the lower target thickness limit with a thickness of minus 10 %. For this setting the extracted lifetime limits were the shortest. Comparing the results for the mean target thickness from before with the results for the short target, the systematic uncertainty can be estimated by the subtraction of both values. This leads to the final results of $\tau_{\mathrm{Min}}=1.7^{+0.0}_{-0.1}\left(\mathrm{syst}_{\mathrm{target}}\right)$ ps using ICRU73 stopping powers and $\tau_{\mathrm{Min}}=1.9^{+0.0}_{-0.1}\left(\mathrm{syst}_{\mathrm{target}}\right)$ ps using SRIM stopping powers as a lower lifetime limit for the 4^+_1 state of ^{16}C.

Taking the SRIM stopping power results from this work and the upper lifetime limit from Wiedeking et al. [WFM+08], the lifetime of the 4^+_1 state has to be between $\tau_{\mathrm{Min}}=1.9^{+0.0}_{-0.1}\left(\mathrm{syst}_{\mathrm{target}}\right)$ ps and 4 ps which corresponds to transition rates of $\lambda_{\mathrm{Min}}\left(4^+_1\right)=2.50\cdot 10^{11}\,1/\mathrm{s}$ and $\lambda_{\mathrm{Max}}\left(4^+_1\right)=5.26^{+0.29}_{-0.00}\left(\mathrm{syst}_{\mathrm{target}}\right)\cdot 10^{11}\,1/\mathrm{s}$. As known so far the 4^+_1 state only decays via the $4^+_1\rightarrow 2^+_1$ transition. This enables the decay modes $E2$, $M3$, $E4$, $M5$, and $E6$. As explained earlier, decay modes higher than $E2$ are strongly suppressed and can be neglected if a $E2$ com-

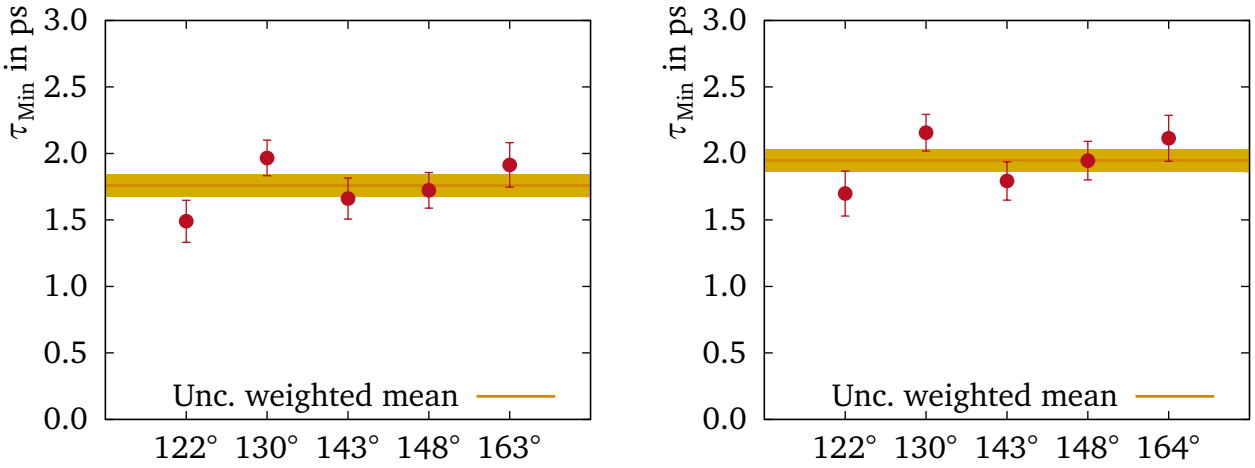

(a) For ICRU73 stopping powers

(b) For SRIM stopping powers

Figure 6.22: Results for a lower lifetime limit τ_{Min} for the 4_1^+ state of ^{16}C. The values are plotted for the five Gammasphere angles for which the analysis from Section 6.5.1 was possible. The Geant4 simulations were executed for $\overline{\beta}_{\mathrm{TO}}$=0.04527(44). The yellow band illustrates the uncertainty weighted mean including its one sigma uncertainty for these data points. The uncertainty weighted means were deduced to 1.76(8) ps for ICRU73 stopping powers and 1.95(9) ps for SRIM stopping powers.

ponent is part of the transition. Hence, following Equations 2.14 and using the experimental transition energy of 2369 KeV, the $E2$ transition strength of the 4_1^+ state is limited to

$$2.74\,\mathrm{e}^2\mathrm{fm}^4 \leq B\left(E2; 4_1^+ \rightarrow 2_1^+\right) \leq 5.78^{+0.32}_{-0.00}\left(\mathrm{syst}_{\mathrm{target}}\right)\,\mathrm{e}^2\mathrm{fm}^4. \tag{6.20}$$

This result will be compared to various theoretical predictions in Section 6.5.4.

6.5.2 Results for the 3_1^+ State

Now, the 3_1^+ state in ^{16}C will be investigated for the target-and-degrader-runs. In the Figure 6.4 one can clearly see a moving peak structure around 2308 keV which is the center of mass energy of the $3_1^+ \rightarrow 2_1^+$ transition of ^{16}C. But as already stated in Section 6.1, also transitions from ^{15}N could be observed in these spectra. Thereby the transition $7/2_1^+ \rightarrow 5/2_1^+$ with a center of mass energy of 2297 keV [AS90a] can interfere with the events from the $3_1^+ \rightarrow 2_1^+$ transition of ^{16}C. Also the lifetime for the $7/2_1^+$ state of ^{15}N is stated as 12 fs [AS90a]. Due to this, the $7/2_1^+ \rightarrow 5/2_1^+$ transition of ^{15}N should appear as a moving peak structure as it is observed in Figure 6.4. Hence, ^{15}N events can influence the analysis of the $3_1^+ \rightarrow 2_1^+$ transition of ^{16}C strongly and so they have to be investigated in detail first.

A level scheme of ^{15}N is shown in Figure A.6 in the appendix. If a gamma-ray energy is marked with an asterisk this transition is observed in the 2p cut spectra. In the following it

will be demonstrated that the transition chains $7/2^+_1 \rightarrow 5/2^+_1 \rightarrow 1/2^-$ and $5/2^+_2 \rightarrow 5/2^+_1 \rightarrow 1/2^-$ are present in the 2p cut spectra. Therefore, Figure 6.4 will be created again with the additional condition that all drawn events fulfill a gamma gate. The gamma gate is set on the $5/2^+_1 \rightarrow 1/2^-$ transition of ^{15}N. The range of the gate was obtained by fitting a Gaussian function plus a linear background to the peak of the $5/2^+_1 \rightarrow 1/2^-$ transition at 5270 keV for the target-and-degrader-runs (cf. Fig. 6.1). The fit results are given by E_{cm}=5269.0(2) keV with a sigma of 10.2(2) keV. The centroid energy is in agreement with the best known value for the $5/2^+_1 \rightarrow 1/2^-$ transition [AS90a]. Using these values, a gamma gate around E_{cm}=5269 keV with a plus/minus two sigma width can be applied to the 2p cut spectra for the target-and-degrader-runs. The result is shown in Figure 6.23. The figure shows the same setting as Figure 6.4 but now the gamma gate is applied. By comparing both figures one can clearly see that the background and almost all transitions are vanishing if the gamma gate is applied. Only two transitions are left in the spectrum with the gamma gate. They can be identified as the $7/2^+_1 \rightarrow 5/2^+_1$ and $5/2^+_2 \rightarrow 5/2^+_1$ transition of ^{15}N. Hence, the ^{15}N transition chains $7/2^+_1 \rightarrow 5/2^+_1 \rightarrow 1/2^-$ and $5/2^+_2 \rightarrow 5/2^+_1 \rightarrow 1/2^-$ are present in the 2p cut spectra.

This analysis revealed that the $7/2^+_1 \rightarrow 5/2^+_1$ transition of ^{15}N appears considerably in the 2p cut spectra. Hence, the mean decay beta for the $3^+_1 \rightarrow 2^+_1$ transition from ^{16}C can not simply be extracted from the target-and-degrader-runs data because the events from ^{15}N will influence the results. How strong this influence is pronounced will be checked now. Therefore, it will be estimated how many counts $C_{7/2^+_1 \rightarrow 5/2^+_1}$ in the 2p cut spectra belong to the $7/2^+_1 \rightarrow 5/2^+_1$ transition of ^{15}N and how many counts $C_{3^+_1 \rightarrow 2^+_1}$ in the 2p cut spectra belong to the $3^+_1 \rightarrow 2^+_1$ transition from ^{16}C.

For the case of ^{16}C the results from this work are combined with results from the work from Wiedeking et al. [WFM$^+$08]. As stated earlier, Wiedeking et al. also used the reaction ^{9}Be(^{9}Be,2p)^{16}C to investigate the excited states in ^{16}C. They observed the four transitions $4^+_1 \rightarrow 2^+_1$, $3^+_1 \rightarrow 2^+_1$, $2^+_2 \rightarrow 2^+_1$, and $2^+_1 \rightarrow 0^+$. Following their results, the number of counts for the $3^+_1 \rightarrow 2^+_1$ transition divided by the number of counts for the $4^+_1 \rightarrow 2^+_1$ transition is given by $R(3^+_1 \rightarrow 2^+_1 / 4^+_1 \rightarrow 2^+_1)$=1.00(19) [Fal08, WFM$^+$08]. This calculation assumes that in the results from Wiedeking et al. no counts from ^{15}N contaminated the peak from the $3^+_1 \rightarrow 2^+_1$ transition from ^{16}C. Such a contamination can not be excluded completely, because they used the same reaction and the same detection concept. But assuming no contamination in the Wiedeking et al. data and using $R(3^+_1 \rightarrow 2^+_1 / 4^+_1 \rightarrow 2^+_1)$=1.00(19) is the best approach which is feasible now. Next, the 2p cut target-and-degrader-runs spectrum from this work (cf. Fig. 6.2) is used to extract the number of counts for the $4^+_1 \rightarrow 2^+_1$ transition of ^{16}C. This transition appears as a fully stopped peak in the spectrum and hence the number of counts can be obtained very reliably. Therefore, a Gaussian function plus a linear background is fitted to the peak which results in 2385(136) Counts for the $4^+_1 \rightarrow 2^+_1$ transition. By multiplying this number with $R(3^+_1 \rightarrow 2^+_1 / 4^+_1 \rightarrow 2^+_1)$ one should expect for this work $C_{3^+_1 \rightarrow 2^+_1}$=2385(473) counts in the 2p cut spectra for the $3^+_1 \rightarrow 2^+_1$ transition of ^{16}C.

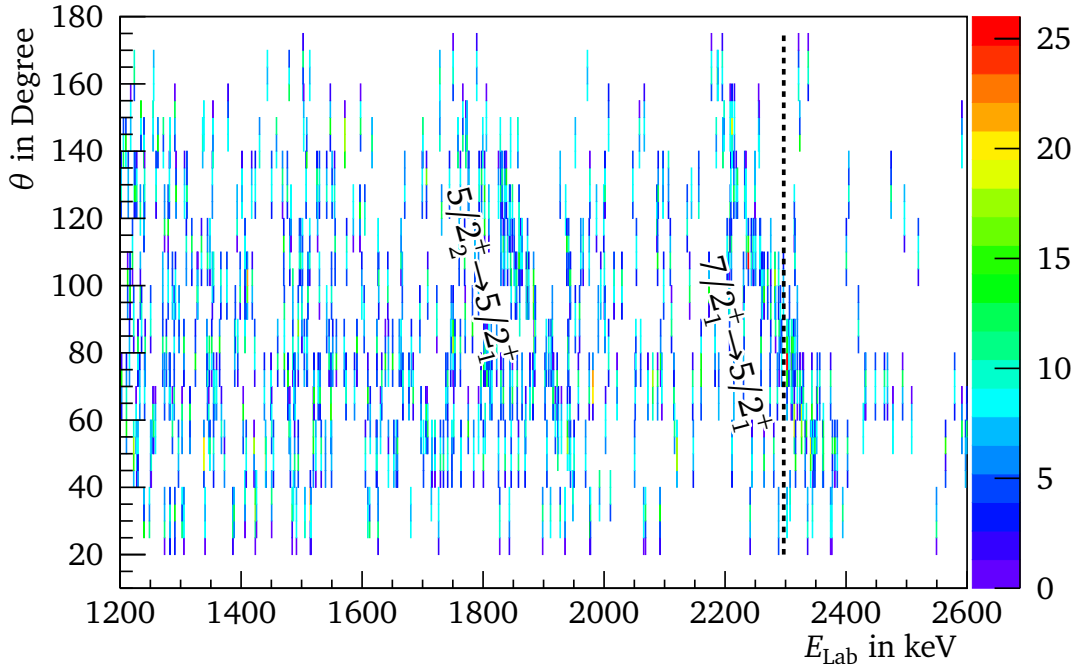

Figure 6.23: Radiation angle θ versus laboratory energy E_{Lab} for 2p cuts for target-and-degrader-runs with a gamma gate on the $5/2_1^+ \rightarrow 1/2^-$ transition of ^{15}N. The gamma gate limits are defined by 5269.0±20.4 keV which corresponds to a $\pm 2\sigma$ gate around the center of mass energy of the $5/2_1^+ \rightarrow 1/2^-$ transition. The black dashed line marks the center of mass energy of the $7/2_1^+ \rightarrow 5/2_1^+$ transition of ^{15}N. Two transitions from ^{15}N are labelled. The figure can be directly compared with Figure 6.4, which shows the same data without the gamma gate.

Now, the number of counts $C_{7/2_1^+ \rightarrow 5/2_1^+}$ for the $7/2_1^+ \rightarrow 5/2_1^+$ transition of ^{15}N are estimated. For this case no external data are available but the $5/2_1^+ \rightarrow 1/2^-$ transition at 5270 keV can be used. This transition also appears as a fully stopped peak in the spectrum for the 2p cut target-and-degrader-runs (cf. Fig. 6.1) and hence the number of counts can be obtained very reliably. For this, a Gaussian function plus a linear background is fitted to the peak which results in $C_{5/2_1^+ \rightarrow 1/2^-}$=6332(129) counts for the $5/2_1^+ \rightarrow 1/2^-$ transition. To deduce the number of counts for the $7/2_1^+ \rightarrow 5/2_1^+$ transition from this information, the fact is used that only one proton is evaporated in the reaction channel for ^{15}N. Due to this, the gamma-ray spectra were also obtained if at least one proton was detected in μ-Ball. For this at-least-1p setting, the number of counts for ^{15}N is much larger and dominates the events from ^{16}C considerably. As stated earlier the cross section to produce ^{15}N is around 410 times larger than for ^{16}C (cf. Sec. 6.1) and for the 1p case no ^{16}C events should appear at all. Hence, for the at-least-1p cut spectra the ratio $R(7/2_1^+ \rightarrow 5/2_1^+ \ / \ 5/2_1^+ \rightarrow 1/2^-)$ between counts from the $7/2_1^+ \rightarrow 5/2_1^+$ transition and the $5/2_1^+ \rightarrow 1/2^-$ transition can be extracted while neglecting an influence of ^{16}C

events. This leads to $R(7/2_1^+ \rightarrow 5/2_1^+ \ / \ 5/2_1^+ \rightarrow 1/2^-)$=0.976(2). This ratio should also be valid for the 2p cut spectra, because the numbers of counts for both ^{15}N transitions are truncated the same way. By multiplying $R(7/2_1^+ \rightarrow 5/2_1^+ \ / \ 5/2_1^+ \rightarrow 1/2^-)$ with $C_{5/2_1^+ \rightarrow 1/2^-}$ one should expect $C_{7/2_1^+ \rightarrow 5/2_1^+}$=6180(127) counts in the 2p cut spectra for the $7/2_1^+ \rightarrow 5/2_1^+$ transition of ^{15}N.

Combining the results for the case of ^{16}C with the results from ^{15}N, the ratio

$$\frac{C_{3_1^+ \rightarrow 2_1^+}}{C_{7/2_1^+ \rightarrow 5/2_1^+}} = 0.39(8) \tag{6.21}$$

is deduced. Hence, in the 2p cut spectra the number of counts for ^{15}N is approximately 2.6 times larger than the number of counts for ^{16}C around the energy of 2308 keV. Also this ratio was calculated under the assumption that in the results from Wiedeking et al. no counts from ^{15}N contaminated the peak from the $3_1^+ \rightarrow 2_1^+$ transition from ^{16}C. But if this was the case, the value for $R(3_1^+ \rightarrow 2_1^+ / 4_1^+ \rightarrow 2_1^+)$ would go down and so the number of counts $C_{3_1^+ \rightarrow 2_1^+}$ for ^{16}C would go down as well. Hence, the ratio from Equation 6.21 would decrease and so even fewer ^{16}C events would be observed around 2308 keV, which would result in the fact that events from ^{15}N would dominate even more.

Furthermore, in Section 6.5.3 the 2p cut spectra will be investigated for a gamma gate on the $2_1^+ \rightarrow 0^+$ transition of ^{16}C. Here the $3_1^+ \rightarrow 2_1^+$ transition could also not be identified, although the $4_1^+ \rightarrow 2_1^+$ transition appears weakly. This reveals a conflict with the ratio $R(3_1^+ \rightarrow 2_1^+ / 4_1^+ \rightarrow 2_1^+)$=1.00(19) from the Wiedeking et al. data. That circumstance suggests that maybe Wiedeking et al. also had undiscovered contaminations from ^{15}N events at the position of the $3_1^+ \rightarrow 2_1^+$ transition of ^{16}C.

All in all, it is not possible to extract a proper lifetime for the 3_1^+ state in ^{16}C with the data from this work, because events stemming from ^{15}N will always be dominating at the region of interest. Assuming that the $3_1^+ \rightarrow 2_1^+$ transition should be visible in the 2p cut spectra as shown in Figure 6.4, it can only be concluded that the lifetime has to be in the femtosecond range, because a stopped peak component can not be seen at all.

6.5.3 Results for the 2_2^+ State

In this section the results for the 2_2^+ state of ^{16}C are discussed. The 2_2^+ state decays via two transitions, namely $2_2^+ \rightarrow 0^+$ and $2_2^+ \rightarrow 2_1^+$ (cf. level scheme in Fig. 1.1). The $2_2^+ \rightarrow 2_1^+$ transition around 2217 keV is not visible in the 2p cut spectrum for the target-and-degrader-runs as it can be seen in Figure 6.4. It seems that the 2_2^+ state is not populated strongly enough to appear in this spectrum. Following the results from [Fal08, WFM$^+$08], the count ratio between the $4_1^+ \rightarrow 2_1^+$ and $2_2^+ \rightarrow 2_1^+$ transition is given by 0.45(11). By reducing the intensity of the $4_1^+ \rightarrow 2_1^+$ transition in Figure 6.4 by a factor of 0.45 and assuming that the 2_2^+ state has a lifetime in the femtosecond range, which means that the $2_2^+ \rightarrow 2_1^+$ transition produces a moving peak structure, it can be

accepted that the $2_2^+ \rightarrow 2_1^+$ transition is not visible because it is superposed by background fluctuations. Furthermore, the $2_2^+ \rightarrow 0^+$ transition is also not visible in the spectra, which is expected if the $2_2^+ \rightarrow 2_1^+$ transition is not visible. Here, Petri et al. already showed that the branching ratio for the $2_2^+ \rightarrow 0^+$ transition is smaller than 8.8 % [PPC+12].

To check whether the $2_2^+ \rightarrow 2_1^+$ transition vanishes in the background or if the 2_2^+ state was not populated at all, the gamma-ray spectra of the target-and-degrader-runs are produced again but now a gamma gate is set on the $2_1^+ \rightarrow 0^+$ transition. The used gate is a $\pm 2\sigma$ gate around the mean energy. A Gaussian fit to the $2_1^+ \rightarrow 0^+$ transition resulted in E_{cm}=1273.8 keV and σ=2.8 keV. Due to the fact that the $2_2^+ \rightarrow 2_1^+$ transition feeds into the 2_1^+ state, the background should vanish while $2_2^+ \rightarrow 2_1^+$ gammas can still appear in the spectrum. Figure 6.24 shows the gamma-ray spectra with such a gamma gate on the $2_1^+ \rightarrow 0^+$ transition for discreet Gammasphere angles from 69.82° to 162.73°. For smaller angles no transitions of ^{16}C could be observed with certainty. The three dashed lines in the spectra mark the expected center of mass energy for the three transitions $4_1^+ \rightarrow 2_1^+$, $3_1^+ \rightarrow 2_1^+$ and $2_2^+ \rightarrow 2_1^+$, which all feed in the 2_1^+ state and hence are in coincidence with the $2_1^+ \rightarrow 0^+$ transition. In the Figure 6.24 one clearly sees the $4_1^+ \rightarrow 2_1^+$ transition as a stopped peak for the most angles (counts around the right dashed line). The $2_2^+ \rightarrow 2_1^+$ transition could be observed as a moving peak for seven angles. But as it can be seen the statistic is for most angles very small and it can not for all cases certainly distinguished which count belongs to the $2_2^+ \rightarrow 2_1^+$ transition and which does not. By comparing the number of counts in the $4_1^+ \rightarrow 2_1^+$ transition peak with the number of counts in the $2_2^+ \rightarrow 2_1^+$ transition peak, the count ratio of 0.45(11) given by [Fal08, WFM+08] seems to be in the correct order of magnitude for the most angles. This confirms the assumption that the 2_2^+ state was populated but its transitions vanish in the spectra without a gamma gate due to the large background fluctuations. The $3_1^+ \rightarrow 2_1^+$ transition is again not visible in the spectra. Maybe the transition occurs in the 90.00° spectrum (around the middle dashed line), but no reasonable conclusion can be drawn with these low statistics. This is another hint that Wiedeking et al. also saw counts from the $7/2_1^+ \rightarrow 5/2_1^+$ transition of ^{15}N which interfere with the counts from the $3_1^+ \rightarrow 2_1^+$ transition of ^{16}C (cf Sec. 6.5.2). The red fit-functions at the $2_2^+ \rightarrow 2_1^+$ transition peaks in Figure 6.24 are defined by a single Gaussian function. The fits were obtained by using the binned-likelihood method due to the low statistics.

The results for the mean value of these fits are plotted against $\cos(\theta)$ in Figure 6.25. Thereby it could be shown that the mean value for the 69.82° spectrum is clearly too close to the value for 90° as compared to the value for 110.18°. It is assumed that one can trust the results from 90°, 110.18° and 129.93° most. For 110.18° and 129.93° the number of counts is the largest, while for 90° the Doppler-shift vanishes approximately. Assuming that these three data points are trustworthy, the value from 69.82° deviates too strongly compared to the expected shift, which is deduced from comparing the values from 90° with the values from 110.18°. Hence, the data point for the 69.82° spectrum is not considered in the fit. The fit, described by Equation 2.19,

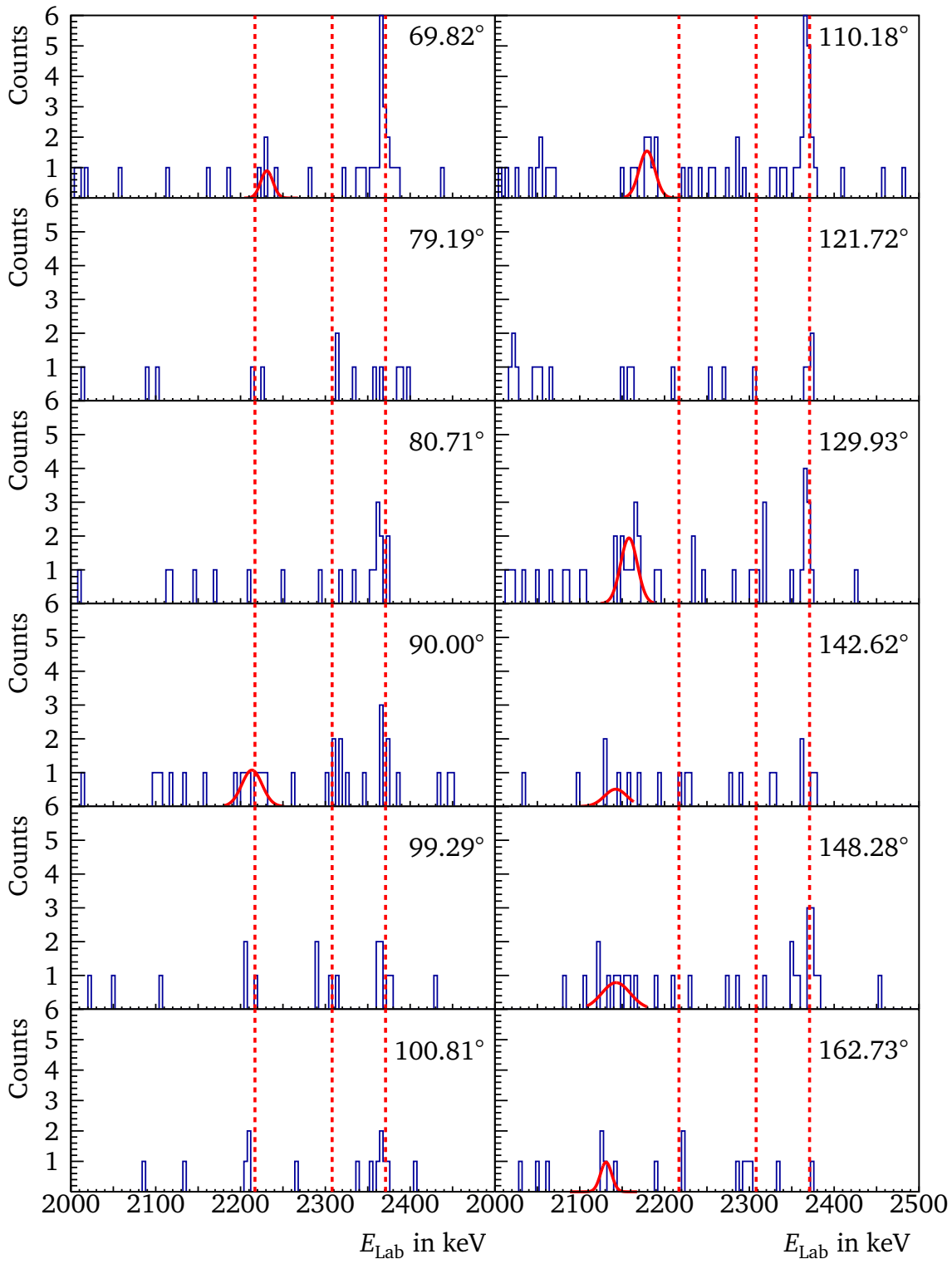

Figure 6.24: Analysis of the energy shift for target-and-degrader-runs and 2p cut focusing on the $2_2^+ \rightarrow 2_1^+$ transition of ^{16}C. The spectra for the discrete Gammasphere angles are obtained for a two sigma gamma gate on the $2_1^+ \rightarrow 0^+$ transition with E_{cm}=1273.8 keV and σ=2.8 keV. The red dashed lines mark the expected energies for the $4_1^+ \rightarrow 2_1^+$, $3_1^+ \rightarrow 2_1^+$ and $2_2^+ \rightarrow 2_1^+$ transitions [WFM$^+$08, PPC$^+$12]. The red fit-functions are defined by a single Gaussian function. The fits were obtained by using the binned-likelihood method due to the low statistics.

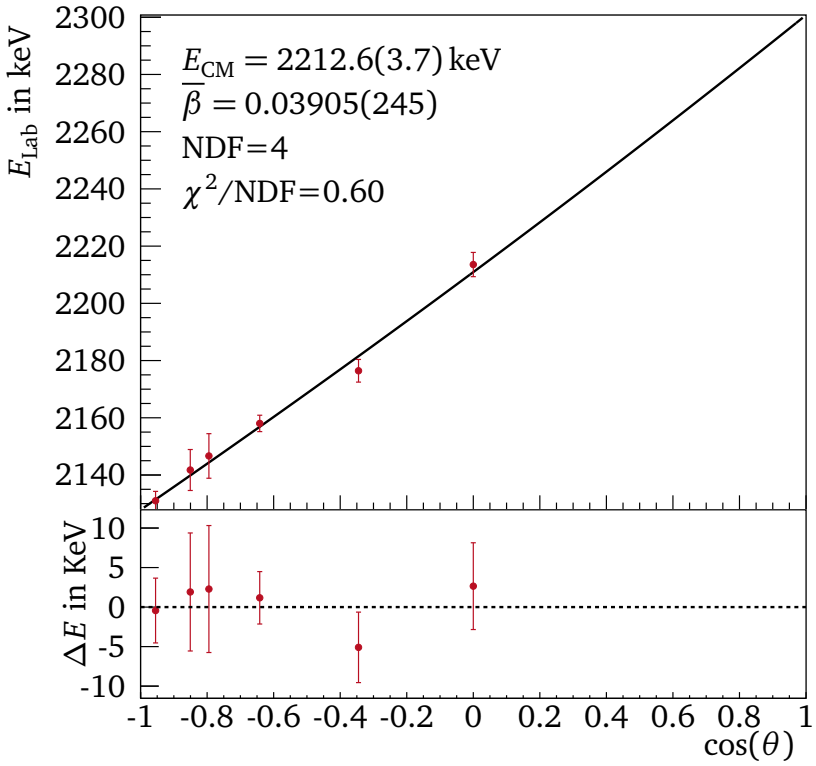

Figure 6.25: E_{Lab} versus cos(θ) fit for target-and-degrader-runs and 2p cut focusing on the $2_2^+ \rightarrow 2_1^+$ transition of ^{16}C. The E_{Lab} values are extracted from the Gaussian fits shown in Figure 6.24 except the value for 69.82°. The black fit-function is described by Equation 2.19. The lower plot shows the residuals ΔE of the fit which is shown in the upper part.

leads to the results of E_{cm}=2212.6(3.7) keV which is in agreement with the uncertainty weighted mean value of 2217(2) keV from [WFM$^+$08, PPC$^+$12], by considering the statistical uncertainties of both values. The mean decay beta was obtained to $\overline{\beta}_{Exp}$=0.03905(245) with a rather large relative statistical uncertainty. It should be highlighted that the small number of counts for the $2_2^+ \rightarrow 2_1^+$ transition (cf. Fig. 6.24) introduce the large uncertainty for the beta value. This uncertainty propagates to the further analysis and hence the following lifetime predictions are vague and an addition measurement with better statistics is recommended (cf. end of Sec. 6.5.4).

In the next step the Geant4 simulations are used to obtain a relation between the lifetime of the 2_2^+ state and the measured mean decay beta $\overline{\beta}_{Exp}$. For this, the Geant4 simulations are started for several different lifetimes in the femtosecond range as explained in Section 4.3. The simulated mean decay beta is extracted using the same angles as for the experimental analysis. For this, a single Gaussian function is fitted to the peaks for each spectra. Because the here covered lifetime range from 25 fs to 700 fs is large and for higher lifetimes the stopped peak component dominants, the fit range is truncated so that the Gaussian fits reflects mainly the moving peak component. Looking at the experimental data (cf. Fig. 6.24) and focusing on the

distance between the Gaussian fit and the position of the stopped peak (left red dashed line), it can be assumed that these fits only contain counts from the moving part, especially for the larger angles. A final and safe conclusion whether the experimental fit contains counts from the stopped component or not can not be drawn for all used angle due to the low statistics. Hence, the possibility for a unconsidered systematic uncertainty is given. But as stated next anyhow only an estimation can be made with the data available here and no mean value is given.

Figure 6.26 shows the obtained simulation results. Part (a) of the figure shows the results for ICRU73 stopping powers and Part (b) shows the results for SRIM stopping powers. Again an exponential function as described by Equation 6.9 suits the data well enough. To get the lifetime τ_{Exp} of the state, the intersection of the fit-function with the experimental mean decay beta $\overline{\beta}_{\mathrm{Exp}}$=0.03905(245) has to be found. But as it can be seen in both plots, this is not possible because the experimental mean decay beta is too small. Furthermore, the plot reveals that the statistical uncertainty of the experimental mean decay beta is much too large for the here applied method. Even if the experimental mean decay beta would be larger, the uncertainty band would cover the whole analysed range from 25 fs to 700 fs. Above ≈550 fs the method breaks down because the largest part of the transitions already decayed in rest. Using the uncertainty band only an estimation for a lower lifetime limit can be given for the 2_2^+ state by finding the intersection between the experimental mean decay beta and the upper limit of the uncertainty band. This results in $\tau \gtrsim 319$ fs for ICRU73 stopping powers and $\tau \gtrsim 244$ fs for SRIM stopping powers for the 2_2^+ state. These results should not be interpreted as a hard limit for the lifetime towards smaller values but combined with the results discussed next they define a most likely range for the lifetime.

To constrain the lifetime of the 2_2^+ state further, an additional evaluation method is applied to the data. Following the main idea from the evaluation of the 4_1^+ state, now the number of counts C_{Moving} in the moving peak component are compared to the number of counts C_{Stopped} in the stopped peak component. Here it holds again: The longer the lifetime, the more counts will be in the stopped peak component. For the evaluation of the 2_2^+ state, the Geant4 simulations are executed for different lifetimes and then the count ratio

$$R_{\mathrm{Sim}}(\tau_{\mathrm{sim}}) = \frac{C_{\mathrm{Stopped}}(\tau_{\mathrm{sim}})}{C_{\mathrm{Moving}}(\tau_{\mathrm{sim}})} \tag{6.22}$$

is calculated for each lifetime and each Gammasphere angle separately. In the next step it is checked how many counts $C_{\mathrm{Moving,Exp}}$ in the moving peak component can be found in the experimental data. With

$$C_{\mathrm{Stopped,Sim}}(\tau_{\mathrm{sim}}) = C_{\mathrm{Moving,Exp}} \cdot R_{\mathrm{Sim}}(\tau_{\mathrm{sim}}) \tag{6.23}$$

it can be deduced how many counts $C_{\mathrm{Stopped,Sim}}$ should appear in the stopped peak component for a given lifetime according to the simulations. Next, the experimental number of counts

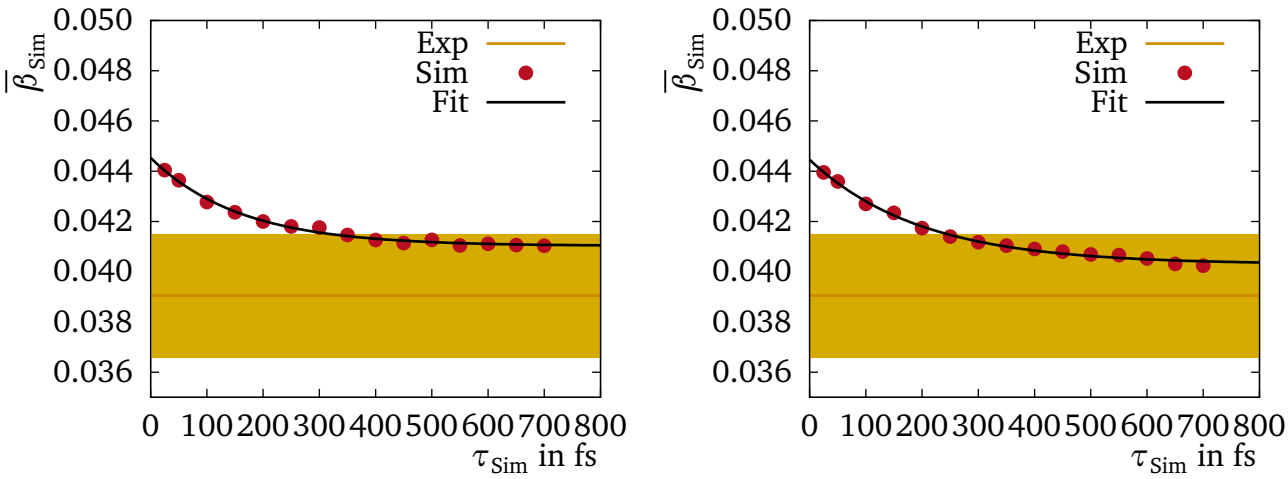

(a) For ICRU73 stopping powers

(b) For SRIM stopping powers

Figure 6.26: Simulated mean decay beta $\overline{\beta}_{\mathrm{Sim}}$ versus simulated lifetime τ_{Sim} for the $2_2^+ \rightarrow 2_1^+$ transition of ^{16}C. The initial beta in the simulation was obtained with $\overline{\beta}_{\mathrm{TO}}$=0.04527(44). The yellow band illustrates the experimental mean decay beta value of $\overline{\beta}_{\mathrm{Exp}}$=0.03905(245) including its uncertainty. The shown fit-function is described by Equation 6.9.

$C_{\mathrm{Stopped,Exp}}$ for the stopped peak component is estimated. Finally, the lifetime can be constrained by comparing $C_{\mathrm{Stopped,Sim}}(\tau_{\mathrm{sim}})$ with $C_{\mathrm{Stopped,Exp}}$. For this analysis only the spectra for 110.18° and 129.93° can be used. These are the only spectra for which we have a significant number of counts in the moving peak component and the moving and stopped peak component are safely separated in the spectra which are obtained from the simulation. The clear separation is important to minimize the probability that counts from both peaks are mixed up in the experimental data, for which this is hard to distinguish due to the low statistics. The analysis in the following is done separately for the 110.18° and 129.93° data and then the mean value is calculated for these two results.

The counts in the moving peak component for the experimental data are deduced by summing up the bins in the given fit range, which can be seen in the Figure 6.24. This results in $C^{110^\circ}_{\mathrm{Moving,Exp}}$=9.0(3.0) counts for 110.18° and $C^{130^\circ}_{\mathrm{Moving,Exp}}$=12.0(3.5) counts for 129.93°. To obtain the experimental counts $C_{\mathrm{Stopped,Exp}}$ for the stopped peak one has to be even more careful. The position and the width of the peak is not exactly known. To get a reasonable width, a Gaussian function is fitted to the $4_1^+ \rightarrow 2_1^+$ transition peak in the target-and-degrader-runs without a gamma gate. This peak can be used as a good width approximation due to several reasons. This peak stems from the same reaction, it is roughly at the same energy and it is also a fully stopped peak. The use of the $4_1^+ \rightarrow 2_1^+$ transition peaks leads to a sigma of σ_{R}=5 keV for 110.18° and σ_{R}=6 keV for 129.93°. The index "R" indicates that these sigmas are later used to pin down the range in which counts will be considered. Next, the fit result from Figure 6.25 is used to define the

Table 6.3: Experimental counts in the stopped peak component for target-and-degrader-runs and 2p cut focusing on the $2_2^+ \rightarrow 2_1^+$ transition of ^{16}C. The values are obtained for a two sigma gamma gate on the $2_1^+ \rightarrow 0^+$ transition with E_{cm}=1273.8 keV and σ=2.8 keV. They are extracted from the spectra which are seen in Figure 6.24. The possible peak positions are deduced from the fit result from Figure 6.25.

	Angle: 110.18°		Angle: 129.93°	
Peak Position in keV	Range in keV	$C_{Exp,Stopped}$ in Counts	Range in keV	$C_{Exp,Stopped}$ in Counts
2209	2199-2219	0(1)	2197-2221	0(1)
2210	2200-2220	0(1)	2198-2222	0(1)
2211	2201-2221	0(1)	2199-2223	0(1)
2212	2202-2222	0(1)	2200-2224	0(1)
2213	2203-2223	0(1)	2201-2225	0(1)
2214	2204-2224	1(1)	2202-2226	0(1)
2215	2205-2225	1(1)	2203-2227	0(1)
2216	2206-2226	1(1)	2204-2228	0(1)
2217	2207-2227	1(1)	2205-2229	0(1)

position of the stopped peak component to be E_{cm}=2212.6(3.7) keV. To reflect the uncertainty of the energy in the results, the lifetime will be calculated with respect to the chosen center of mass energy. Therefore, the peak position is varied to all values which are located inside $E_{cm} \pm \sigma$=2213±4 keV. The step-size is set to 1 keV. Hence, the position for the stopped peak is set to nine different values from 2209 KeV to 2217 keV. Then for each position a range of $\pm 2\sigma_R$ is set around this current position. In this range all bin contents are summed up and treated as counts which belong to the stopped peak component. The results for this analysis are summarised in Table 6.3. To take the low statistic into account the uncertainty is set to at least one count even if zero counts were observed. As already discussed the lifetime depends on the real center of mass energy of the transition. As it could be seen in Table 6.3 the analysed energy range has to be separated into two domains namely 2209.0 keV to 2213.5 keV and 2213.5 keV to 2217.0 keV for which the lifetime is obtained separately.

As an example the results of this analysis method are shown in Figure 6.27 for the 110.18° case with $C_{Stopped,Exp}$=1(1) counts in the stopped peak component (cf. Tab. 6.3). Part (a) shows the results for ICRU73 stopping powers and Part (b) for SRIM stopping powers. The top plot shows the simulation results for $R_{Sim}(\tau_{sim})$. To the data the function

$$R_{Sim}(\tau_{sim}) = a \cdot \tau_{sim}^2 + b \cdot \tau_{sim} \tag{6.24}$$

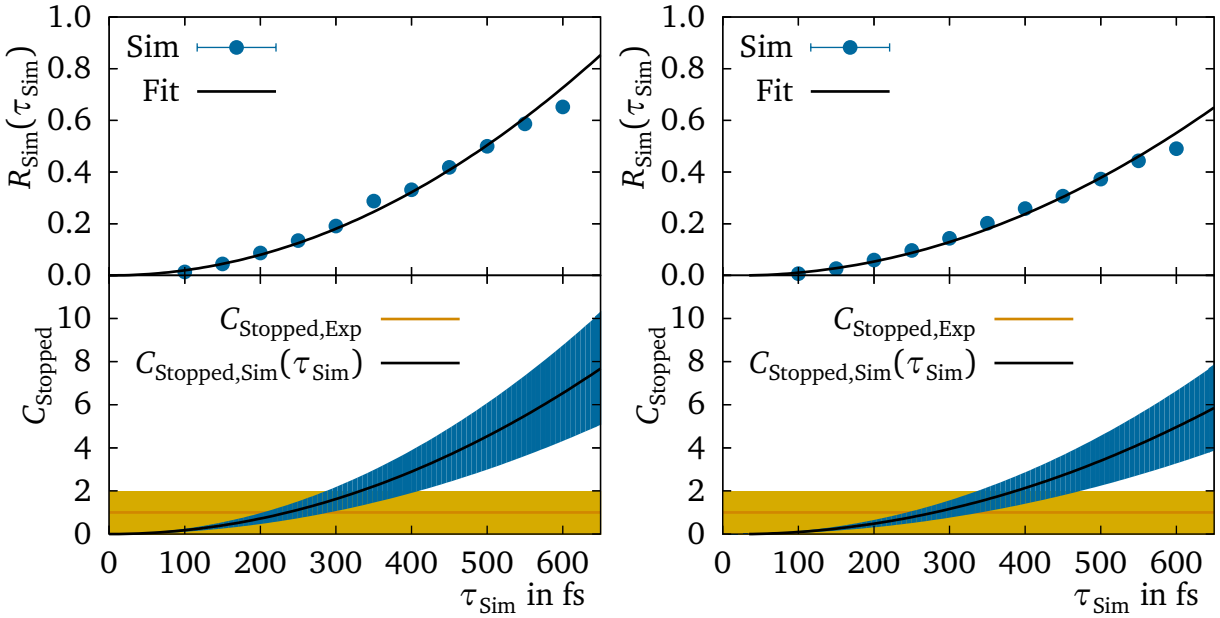

(a) For ICRU73 stopping powers

(b) For SRIM stopping powers

Figure 6.27: Count ratios between the moving and stopped peak component for the $2_2^+ \rightarrow 2_1^+$ transition of ^{16}C for 110.18°. The upper part shows the results from the Geant4 simulations with Equation 6.24 as a fit-function. The lower part shows this fit-function scaled with $C_{\mathrm{Moving,Exp}}$, which represents $C_{\mathrm{Stopped,Sim}}(\tau_{\mathrm{Sim}})$. The blue band around the function shows its uncertainty including the uncertainty from $C_{\mathrm{Moving,Exp}}$ as well as the fit uncertainties. Also $C_{\mathrm{Stopped,Exp}}=1(1)$ counts is plotted in orange for which the uncertainty is shown as a yellow band (cf. Tab. 6.3).

was fitted. This function is now multiplied with $C^{130°}_{\mathrm{Moving,Exp}}$ to obtain $C_{\mathrm{Stopped,Sim}}(\tau_{\mathrm{Sim}})$ as stated in Equation 6.23. The result of this is shown as a black function in the lower plot of Figure 6.27. The blue band around the function shows its uncertainty including the uncertainty from $C^{130°}_{\mathrm{Moving,Exp}}$ as well as the fit uncertainties. The orange line with yellow band shows the experimental result for the stopped peak component of $C_{\mathrm{Stopped,Exp}}=1(1)$ counts. Here, the mean value from $C_{\mathrm{Stopped,Exp}}$ plus its uncertainty $u(C_{\mathrm{Stopped,Exp}})$ can be seen as an upper limit for the number of counts in the stopped peak component which is still compatible with the experimental data. Hence, all lifetimes for which the blue and yellow area are overlapping are compatible with the experimental data. Due to this, an upper lifetime limit is obtained by determining the intersection between $C_{\mathrm{Stopped,Sim}}(\tau_{\mathrm{Sim}})+u\left[C_{\mathrm{Stopped,Sim}}(\tau_{\mathrm{Sim}})\right]$ (right end of the blue uncertainty band) and $C_{\mathrm{Stopped,Exp}}+u[C_{\mathrm{Stopped,Exp}}]$ (upper border of the yellow uncertainty band). In the here shown example this leads to 409 fs for ICRU73 stopping powers and to 473 fs for SRIM stopping powers as an upper lifetime limit for the 2_2^+ state.

Table 6.4: Results the upper lifetime limit of the 2_2^+ state in ^{16}C using the count ratio method. The Geant4 simulations were performed for $\overline{\beta}_{\mathrm{TO}}$=0.04527(44). The estimated minimum lifetime $\tilde{\tau}_{\mathrm{Min}}$ is obtained from the fits in Figure 6.26. The upper limit τ_{Max} for the lifetime is obtained with the experimental count ratios from Table 6.3. Target thickness uncertainties are included as systematic uncertainties.

	ICRU73		SRIM	
Energy Range in keV	$\tilde{\tau}_{\mathrm{Min}}$ in fs	τ_{Max} in fs	$\tilde{\tau}_{\mathrm{Min}}$ in fs	τ_{Max} in fs
2209.0 to 2213.5	319	$291^{+36}_{-0}\left(\mathrm{syst}_{\mathrm{target}}\right)$	244	$341^{+35}_{-0}\left(\mathrm{syst}_{\mathrm{target}}\right)$
2213.5 to 2217.0	319	$350^{+40}_{-0}\left(\mathrm{syst}_{\mathrm{target}}\right)$	244	$407^{+39}_{-0}\left(\mathrm{syst}_{\mathrm{target}}\right)$

For all other combinations of angles and number of counts in the stopped peak component, the analysis and results were akin and are not discussed in detail. The results for both angles are then combined by calculating the corresponding mean value. The analysis was also repeated for the extreme target thicknesses to include the target thickness uncertainties in the results. The achieved lifetimes are always the largest for the thickest possible target (+10 % thickness). Hence, these results are used as a systematic uncertainty for the upper lifetime limit. The final values from this analysis are summarised in Table 6.4 and discussed now. For the ICRU73 stopping powers and the lower energy region the estimated minimum lifetime is larger than the upper lifetime limit from the count ratio method but it is still valid by considering the upper uncertainty. The results for the SRIM stopping powers are more consistent. Here, the estimated lower lifetime limit is clearly below the upper limit from the count ratio method. The change in the results when switching from ICRU73 to SRIM stopping powers is clearly more pronounced for the case of ^{16}C and lifetimes in the lower femtosecond range, than for the other nuclei which were investigated before. This dependency on the stopping powers and the fact that the results for ^{16}C are more reliable if SRIM stopping powers are used, was also investigated and shown in [Hei15]. Due to this the results for the SRIM stopping powers will be used for the further discussions. Using SRIM stopping powers and take the systematic uncertainties into account, the lifetime can be expected in a range from 244 fs to 376 fs for a center-of-mass transition energy between 2209.0 keV and 2213.5 KeV and the lifetime can be expected in a range from 244 fs to 446 fs for a center-of-mass transition energy between 2213.5 keV and 2217.0 KeV.

The results for SRIM stopping powers are shown in Figure 6.28 and compared to the most recent measurement from Ciemała et al. [CZC$^+$20]. The figure shows the upper lifetime limit (black dashed horizontal line) from the count ratio method and the most likely lifetime range (blue boxes) using the estimated lower lifetime from the mean decay beta method. The results from Ciemała et al. are marked by the red dots. They used the reaction ^{18}O(7.0 MeV/u)+^{181}Ta

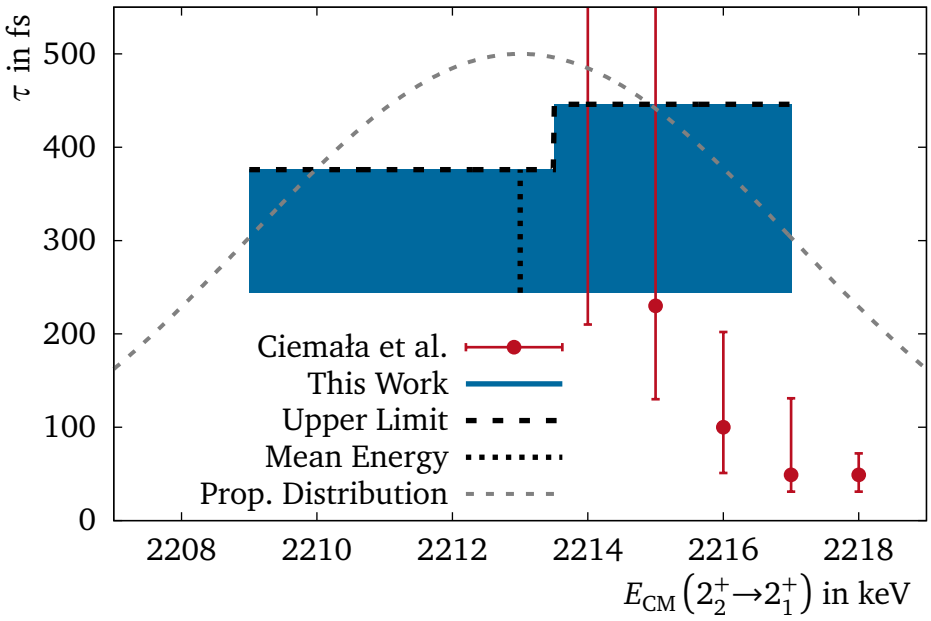

Figure 6.28: Results for the lifetime range of the 2_2^+ state in ^{16}C using the count ratio method and SRIM stopping powers. The values from this work are taken from Table 6.4 and shown as black dashed lines and blue boxes. The horizontal black dashed lines mark the upper lifetime limit while the vertical black dashed line marks the mean gamma-ray energy for the $2_2^+ \rightarrow 2_1^+$ transition as measured in this work. The blue boxes mark the most likely lifetime range. The external values shown as red dots are the most recent measurements from Ciemała et al. [CZC+20]. The gray dashed function shows the relative probability distribution as a function of the transition energy for the here obtained results. It follows a Gaussian distribution with a mean of 2213 keV and a sigma of 4 KeV.

to produce ^{16}C. Then Ciemała et al. extracted the lifetime and the transition energy by comparing the Doppler-shifted gamma-ray line shapes with Monte Carlo simulations. They could not achieve a fixed pair of transition energy and lifetime for which the simulation fits best, but they could obtain a domain for different pairs of lifetimes and transition energies for which the simulation matches the experimental spectrum well. According to Ciemała et al. the transition energy should be located between 2214 keV and 2218 keV for a one sigma confidence, while the lifetime depends strongly on this energy as it can be seen in Figure 6.28. Comparing both results, this work suggests a transition energy which is slightly lower than the energy measured by Ciemała et al. But they are in agreement if the statistical uncertainty is taken into account. In terms of lifetimes, the data points from 2214 keV and 2215 keV are in agreement with the most likely lifetime range from this work. The other data points from Ciemała et al. are lower than the most likely lifetime range from this work. Here, it should be stated again that the results from this work should not be interpreted as a hard limit for the lifetime towards smaller values.

Overall, the agreement is still acceptable by taking into account that in both experiments the number of counts was low and close to the detection limit. In the work from Ciemała et al. the number of counts in the peak is at the lower limit for which a pronounced line shape is developed which is sensitive to the lifetime and the transition energy at the same time.

Focusing on the lifetime of the 2_2^+ state, the comparison with theory, as done in the next section, is a complex case. Here, the lifetime of the state is defined by several different transition strengths. Hence, by knowing the lifetime it is not known how much each transition strength contributes to the total transition rate. Therefore, the different transition strengths will be constrained now. Looking at the level scheme in Figure 1.1 one can see that the 2_2^+ state can decay via the $2_2^+ \rightarrow 0^+$ and the $2_2^+ \rightarrow 2_1^+$ transition. For the $2_2^+ \rightarrow 0^+$ transition only an $E2$ part is possible. For the $2_2^+ \rightarrow 2_1^+$ transition $M1$, $E2$, $M3$, and $E4$ decay modes are available. Here, $M1$ and $E2$ will dominate strongly and higher orders can be neglected (cf. Sec. 2.1). Hence, the total transition rate $\lambda_{\text{Total}}\left(2_2^+\right)$ of the 2_2^+ state is given by

$$\lambda_{\text{Total}}\left(2_2^+\right) = \lambda\left(E2; 2_2^+ \rightarrow 0^+\right) + \lambda\left(E2; 2_2^+ \rightarrow 2_1^+\right) + \lambda\left(M1; 2_2^+ \rightarrow 2_1^+\right) \tag{6.25}$$

theoretically. The most likely lifetime range for the mean transition energy from this work yields

$$\lambda_{\text{Total}}\left(2_2^+\right) = \frac{1}{\tau\left(2_2^+\right)} = \frac{1}{376\,\text{fs}} \text{ to } \frac{1}{244\,\text{fs}} = 2.66 \cdot 10^{12}\,\frac{1}{\text{s}} \text{ to } 4.10 \cdot 10^{12}\,\frac{1}{\text{s}} \tag{6.26}$$

for the total transition rate. With this information alone nothing can be said about the three different transition rates/strengths. But by using the results from Petri et al. [PPC+12] it is also known that the branching ratio for the $2_2^+ \rightarrow 0^+$ transition is limited to

$$\text{BR}\left(\frac{2_2^+ \rightarrow 0^+}{2_2^+ \rightarrow *}\right) = \frac{\lambda\left(E2; 2_2^+ \rightarrow 0^+\right)}{\lambda_{\text{Total}}\left(2_2^+\right)} < 8.8\,\%. \tag{6.27}$$

Combining the results from Equation 6.26 and 6.27 a limit for the $E2$ transition strength of the $2_2^+ \rightarrow 0^+$ transition is given by

$$\lambda\left(E2; 2_2^+ \rightarrow 0^+\right) < 8.8\,\% \cdot \lambda_{\text{Total}}\left(2_2^+\right) \tag{6.28}$$

$$1.22 \cdot 10^9\,\frac{1}{\text{s}} \cdot \left(\frac{E_\gamma(2_2^+ \rightarrow 0^+)}{\text{MeV}}\right)^5 \cdot \frac{B\left(E2; 2_2^+ \rightarrow 0^+\right)}{\text{e}^2\text{fm}^4} < 0.23 \cdot 10^{12}\,\frac{1}{\text{s}} \text{ to } 0.36 \cdot 10^{12}\,\frac{1}{\text{s}} \tag{6.29}$$

$$\frac{B\left(E2; 2_2^+ \rightarrow 0^+\right)}{\text{e}^2\text{fm}^4} < 0.19 \text{ to } 0.30, \tag{6.30}$$

where in the second step the $E2$ transition rate is converted into a $E2$ transition strength following Equations 2.14. For the gamma-ray energy the experimental value from this work of 3973 keV is

used. The uncertainty of the gamma-ray energy can be neglected because the overall uncertainty is completely dominated by the uncertainty of the experimental transition rate. Taking the higher possible experimental value, the transition strength can be finally constrained to

$$B\left(E2; 2_2^+ \rightarrow 0^+\right) < 0.30\,\mathrm{e}^2\mathrm{fm}^4. \tag{6.31}$$

Next, the transition rates in Equation 6.25 will be translated into transition strengths using the conversions from Equations 2.14, which leads to

$$\begin{aligned}\lambda_{\mathrm{Total}}\left(2_2^+\right) = {} & 1.22 \cdot 10^9 \frac{1}{\mathrm{s}} \cdot \left(\frac{E_\gamma(2_2^+ \rightarrow 0^+)}{\mathrm{MeV}}\right)^5 \cdot \frac{B\left(E2; 2_2^+ \rightarrow 0_1^+\right)}{\mathrm{e}^2\mathrm{fm}^4} \\ & + 1.22 \cdot 10^9 \frac{1}{\mathrm{s}} \cdot \left(\frac{E_\gamma(2_2^+ \rightarrow 2_1^+)}{\mathrm{MeV}}\right)^5 \cdot \frac{B\left(E2; 2_2^+ \rightarrow 2_1^+\right)}{\mathrm{e}^2\mathrm{fm}^4} \\ & + 1.76 \cdot 10^{13} \frac{1}{\mathrm{s}} \cdot \left(\frac{E_\gamma(2_2^+ \rightarrow 2_1^+)}{\mathrm{MeV}}\right)^3 \cdot \frac{B\left(M1; 2_2^+ \rightarrow 2_1^+\right)}{\mu_{\mathrm{N}}^2}.\end{aligned} \tag{6.32}$$

By using the experimental results from this work for the total transition rate and the transition energies, this equation can be modified to

$$1.21 \cdot \frac{B\left(E2; 2_2^+ \rightarrow 0^+\right)}{\mathrm{e}^2\mathrm{fm}^4} = \Lambda\left(2_2^+\right) - 0.0648 \cdot \frac{B\left(E2; 2_2^+ \rightarrow 2_1^+\right)}{\mathrm{e}^2\mathrm{fm}^4} - 191 \cdot \frac{B\left(M1; 2_2^+ \rightarrow 2_1^+\right)}{\mu_{\mathrm{N}}^2}, \tag{6.33}$$

where $\Lambda\left(2_2^+\right)$ is the normalized transition rate of the 2_2^+ state given by

$$\Lambda\left(2_2^+\right) = \frac{\lambda_{\mathrm{Total}}\left(2_2^+\right)}{10^{12}\,\frac{1}{\mathrm{s}}} = 2.66 \;\text{ to }\; 4.10. \tag{6.34}$$

By combining the results from Equation 6.31 as well as Equation 6.33 and using the fact that all transition strengths can not obtain negative values, one can deduce explicit constraints for the three transition strengths. To visualize valid combinations for the three transition strengths, these constraints are shown in Figure 6.29 for fixed values of $\Lambda\left(2_2^+\right)$. Part (a) shows the constraints for the two extreme values of $\Lambda\left(2_2^+\right)$, namely 2.66 and 4.10. The two axes define the value of $B\left(E2; 2_2^+ \rightarrow 2_1^+\right)$ and $B\left(M1; 2_2^+ \rightarrow 2_1^+\right)$, while the colour code defines the value of $B\left(E2; 2_2^+ \rightarrow 0^+\right)$. For a given $\Lambda\left(2_2^+\right)$, a valid transition strength triple can only occur inside the coloured areas. Outside of the coloured areas the $B\left(E2; 2_2^+ \rightarrow 0^+\right)$ strength would be negative (above the purple border) or larger than $0.30\,\mathrm{e}^2\mathrm{fm}^4$ (below the red border) which is not inside the limits from this work. It can be seen that the amount of possible transition strength combinations is limited strongly if $\Lambda\left(2_2^+\right)$ is known precisely. With this the validity of theoretical predictions can be tested, which is discussed in the next Section 6.5.4. For this, Part (b) of Figure 6.29 shows the same constraints as Part (a) and the results for different theoretical approaches

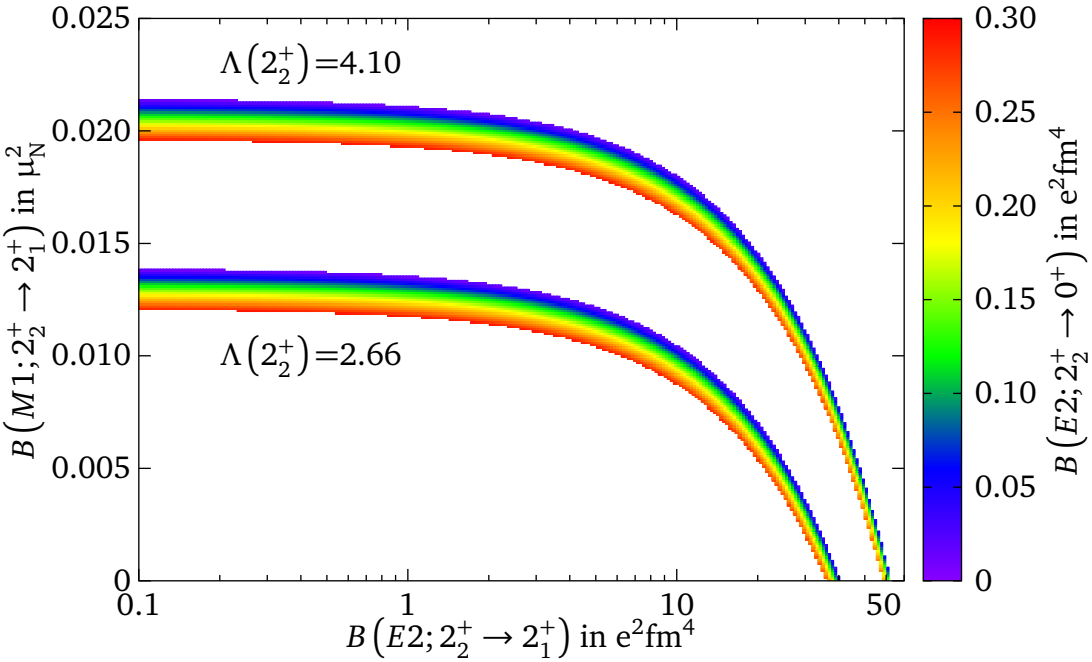

(a) Constraints for the extreme values of $\Lambda\left(2_2^+\right)$

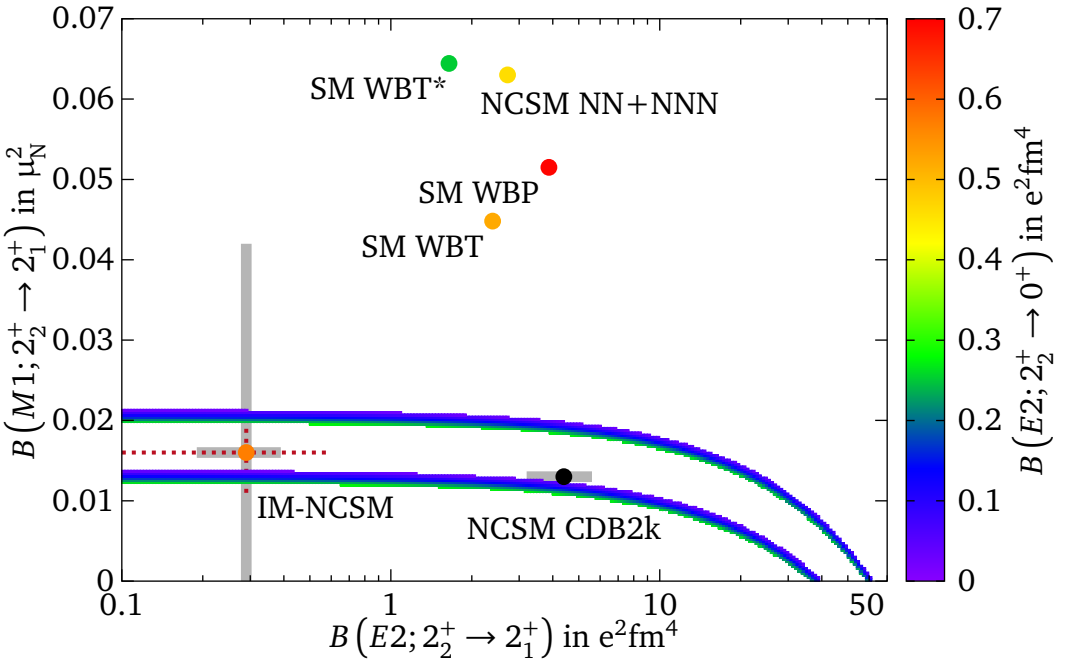

(b) Comparison to theoretical predictions

Figure 6.29: Constraints for the three transition strengths which define the total transition rate $\lambda_{\text{Total}}\left(2_2^+\right)$ in ^{16}C for a fixed $\Lambda\left(2_2^+\right)$. The constraints are defined by Equation 6.31 and 6.33. Part (a) shows the constraints for the two extreme values of $\Lambda\left(2_2^+\right)$. Part (b) shows the same constraints as well as results for different theoretical approaches, which are discussed elaborately in Section 6.5.4. The red dashed line marks the uncertainty due to many-body parts, while the gray band marks the interaction uncertainty for the IM-NCSM calculations. The color of the data points reflects the $B\left(E2;2_2^+ \to 0_1^+\right)$ color code. This is not applied to the data point of the NCSM CDB2k calculations for a better visibility.

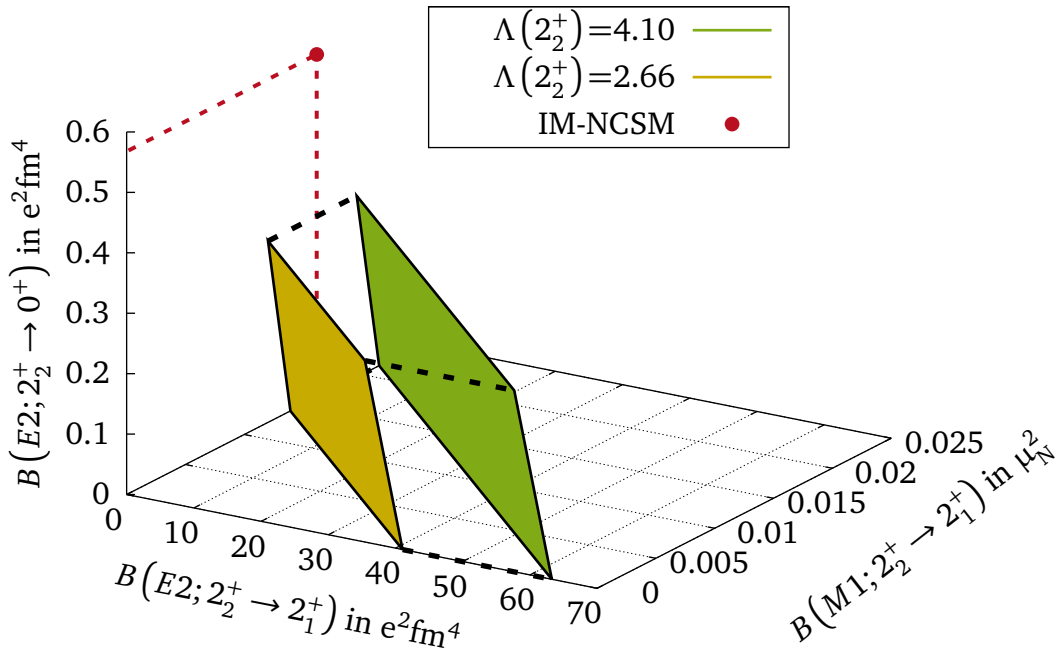

(a) View 1

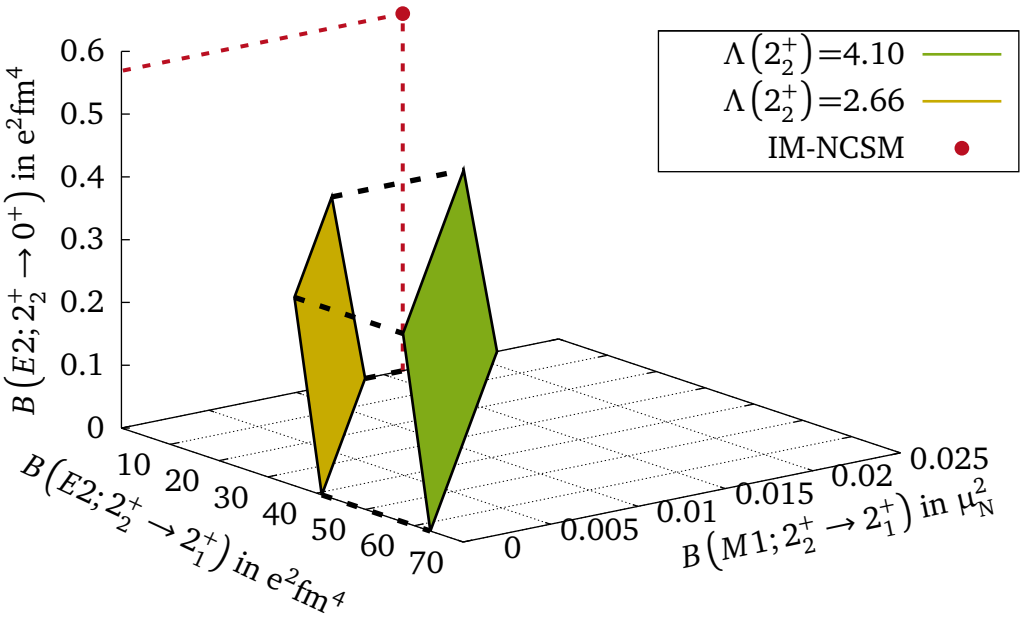

(b) View 2

Figure 6.30: Constraints for the three transition strengths which define the total transition rate $\lambda_{\text{Total}}\left(2_2^+\right)$ of the 2_2^+ state in ^{16}C. The constraints are defined by Equation 6.31 and 6.33. A possible triple of transition strengths has to be placed inside the hexahedron which is defined by the yellow and green plane as well as by the black dashed lines. The shown data point reflects recent theoretical IM-NCSM calculations, which are discussed in Section 6.5.4.

are added. The theoretical approaches are discussed in detail in Section 6.5.4.

Furthermore, Figure 6.30 shows the constraints for the full possible range in terms of $\Lambda\left(2_2^+\right)$. Here, $\Lambda\left(2_2^+\right)$ can vary between $\Lambda\left(2_2^+\right)$=2.66 and $\Lambda\left(2_2^+\right)$=4.10 and the value of $B\left(E2; 2_2^+ \rightarrow 0_1^+\right)$ is projected along the z-axis. The two coloured planes mark the constraints for the two extreme values of $\Lambda\left(2_2^+\right)$ which were also already shown in Figure 6.29. A possible triple of transition strengths has to be placed inside the hexahedron which is defined by the yellow and green plane as well as by the black dashed lines.

6.5.4 Comparison with Theory

Finally, the experimental results for ^{16}C will be compared elaborately to four different theoretical approaches in the following.

The first approach are p–sd shell model calculations using the `OXBASH` shell model code [BERGed], which was applied for three different empirical two-body nucleon-nucleon effective interactions, namely WBP [WB92], WBT [WB92], and WBT* [SSS$^+$08]. These calculations were performed by A. Brown [Bro20, PPC$^+$12]. A motivation and description of these calculations can be found in Section 2.6 and 2.9, as well as in [PPC$^+$12, BERGed].

The second approach are NCSM calculations which were performed by Forssén et al. [FRN13]. It will be focused on their results which were obtained for the CDB2k potential and effective chiral NN+NNN interactions. The basic concept of NCSM calculations are explained in the beginning of Section 2.8. In [FRN13], Forssén et al. used the CDB2k potential to represent pure NN interactions. The CDB2k potential developed in [Mac01] is based on the charge-dependent one-boson exchange theory. It is fitted to the world proton-proton data below 350 MeV as well as to the complete neutron-proton data, which were available in 2000. To apply the NCSM calculations for the CDB2k potential, Forssén et al. used effective interactions to speed up the convergence. To do so, they computed two-body effective interactions, which correspond to a low-energy basis truncation using a unitary transformation in the two-nucleon HO basis. These are also known as Ôkubo–Lee–Suzuki effective interactions [NVB00, Ôk54, FRN13]. To obtain the $B\left(E2;2_1^+\rightarrow 0^+\right)$ strength, they performed a constrained-fit to the strength for different combinations of N_{Max} and $\hbar\Omega$. Hence, the extracted $B\left(E2;2_1^+\rightarrow 0^+\right)$ strength has an uncertainty stemming from this fit. This uncertainty is considered in the following evaluation and is propagated to the strengths of the higher-lying states for which the $B(E2)$ strengths are given relative to the $B\left(E2;2_1^+\rightarrow 0^+\right)$ strength. The used effective chiral NN+NNN interactions are a combination of chiral N^{3}LO two-body forces [EM03] and chiral N^{2}LO three-body forces [GQN09] with a cutoff of 500 MeV. For the NN+NNN interactions the convergence speed is reduced dramatically. Hence, an absolute $B\left(E2;2_1^+\rightarrow 0^+\right)$ strength could not be obtained theoretically and for the higher-lying states the $B(E2)$ strengths could only be obtained relative to the $B\left(E2;2_1^+\rightarrow 0^+\right)$ strength. To calculate all $B(E2)$ strengths in this case, the $B\left(E2;2_1^+\rightarrow 0^+\right)$ is scaled to match the uncertainty weighted mean of $B(E2;2_1^+\rightarrow 0^+)$=4.18(53) e^{2}fm^4 measured in [WFM$^+$08, PPC$^+$12]. The experimental uncertainty is propagated to all other strengths.

The third approach are recent NCSM$^\Diamond$ calculations performed by Roth et al. [Rot20] with advanced chiral effective NN+$NNN^\Diamond$ interactions. The NCSM$^\Diamond$ calculations are set up with harmonic oscillator bases for different values of $\hbar\Omega$, while for the NN+$NNN^\Diamond$ interactions most recent effective chiral two-nucleon plus three-nucleon interactions from Hüther et al. [HVH$^+$20] are used. Hüther et al. constructed these chiral NN+$NNN^\Diamond$ interactions for the NLO, the NNLO, and the N^{3}LO with non-local regulators and a cutoff of 500 MeV. These interactions are based on

a set of chiral NN interactions by Entem, Machleidt and Nosyk [EMN17]. Hüther et al. used the ^{16}O ground-state energy to constrain the one-pion two-nucleon-contact constant and they used the triton ground-state energy to fix the three-nucleon contact parameter. These interactions were able to accurately reproduce two-body phase shifts, ground-states energies and radii at the same time for nuclei up to the medium-mass regime. The problem for the new NCSM$^{\Diamond}$ calculations with chiral effective NN+$NNN^{\Diamond}$ interactions is again that the observables do not fully converge in the case of ^{16}C. Hence, only trends can be concluded for some strengths so far. Nevertheless, these trends are from great interest because they differ significantly from the prediction of the next discussed approach, the IM-NCSM.

The fourth approach avoids the problem of the slow convergence by applying the framework of the IM-NCSM onto the most recent chiral effective NN+$NNN^{\Diamond}$ interactions from Hüther et al. [HVH^{+}20]. These IM-NCSM calculations were carried out by Roth et al. [Rot20], while the framework was developed by Gebrerufael et al. [GVHR17]. The idea of the IM-NCSM was already briefly introduced in the end of Section 2.8 and an elaborated explanation can be found in [GVHR17]. The cutoff for the chiral effective NN+$NNN^{\Diamond}$ interactions was chosen to be 500 MeV and the model space was limited by $N_{\mathrm{Max}}^{\mathrm{Ref}}$=2 and N_{Max}=4. The calculations were performed for the NLO, the NNLO, and the N^{3}LO. By looking at the order-by-order convergence, interaction uncertainties for the results can be estimated. Additionally, many-body uncertainties can be estimated by analysing the $N_{\mathrm{Max}}/N_{\mathrm{Max}}^{\mathrm{Ref}}$ convergence. In the following, the many-body uncertainties of the results are given in the first bracket and the interaction uncertainties in the second bracket. Here, it should be noted that the analysis of the IM-NCSM calculations is still ongoing and the values as well as their uncertainties are preliminary.

The level energies, transition strengths and branching ratios for all the before mentioned theoretical approaches as well as the experimental results are summarized in Table 6.5. The $B(E2)$ strengths for the p–sd shell model were calculated with the effective charges (cf. Sec. 2.1) e_{p}=1.16 and e_{n}=0.33 following the $\propto 1/A$ parametrisation from [SZZS04]. In the work from Petri et al. [PPC^{+}12] it could be already shown that this adjustment results in a better description of the $B\left(E2; 2_2^+ \rightarrow 0_1^+\right)$ strength. The experimental results are given for SRIM stopping powers. In the following the theoretical predictions for the strengths and branching ratios are compared to the experimental results for each state. The level energies and lifetimes are shown as a level scheme in Figure 6.31. They are discussed later in this section.

The results for the 2_1^+ state are for the most part already discussed in [PPC^{+}12]. While the shell model calculations reproduce the $B\left(E2; 2_1^+ \rightarrow 0^+\right)$ strength well, the NCSM calculations with CDB2k interactions predict a too small strength. The strength for the IM-NCSM calculations is suppressed by a factor of ≈3.3 which corresponds to a deviation of ≈–5.5 sigma compared to the experimental results. The NCSM calculations with NN+NNN interactions were not able to calculate the $B\left(E2; 2_1^+ \rightarrow 0^+\right)$ strength due to the slow convergence and, as discussed before, the

strength is substituted by the experimental value to calculate the strengths of the higher-lying states.

For the 2_2^+ state the situation is more complex because three transition types are available. As discussed in Section 6.5.3 these three transition types can be constrained with Equation 6.31 and 6.33. In the following the theoretical approaches will be compared to the most likely lifetime range for the mean transition energy as it was discussed and defined in the end of Section 6.5.3. According to the experimental results including their uncertainties, the $B\left(E2; 2_2^+ \rightarrow 0^+\right)$ strength is most likely to be smaller than $0.30\,\mathrm{e}^2\mathrm{fm}^4$, which is only reflected by the shell model calculations using the WBT* potential. All other approaches provide significantly larger $B\left(E2; 2_2^+ \rightarrow 0^+\right)$ strengths. Especially, the NCSM calculations with CDB2k interactions give a much larger $B\left(E2; 2_2^+ \rightarrow 0^+\right)$ strength of $4.48(1.32)\,\mathrm{e}^2\mathrm{fm}^4$. To check the reliability of the $B\left(E2; 2_2^+ \rightarrow 2_1^+\right)$ and the $B\left(M1; 2_2^+ \rightarrow 2_1^+\right)$ strengths, Part (b) of Figure 6.29 and Figure 6.30 can be used. Focusing on Part (b) of Figure 6.29, it can be seen that the shell model calculations and the NCSM calculations with NN+NNN interactions can not fulfill the constraints in terms of $B\left(E2; 2_2^+ \rightarrow 2_1^+\right)$ and $B\left(M1; 2_2^+ \rightarrow 2_1^+\right)$ strengths. For a given value of $B\left(E2; 2_2^+ \rightarrow 2_1^+\right)$ their predicted $B\left(M1; 2_2^+ \rightarrow 2_1^+\right)$ strengths are too large. For the IM-NCSM calculations and the NCSM calculations with CDB2k interactions a valid combination of $B\left(E2; 2_2^+ \rightarrow 2_1^+\right)$ and $B\left(M1; 2_2^+ \rightarrow 2_1^+\right)$ strengths is predicted but for both the $B\left(E2; 2_2^+ \rightarrow 0^+\right)$ strength is larger than the experimentally estimated limit. Note, the data point for the NCSM calculations with CDB2k interactions does not follow the color code in Figure 6.29 and is completely out of scope in Figure 6.30. Focusing on the branching ratio, the experimental results favour the $2_2^+ \rightarrow 2_1^+$ transition with at least 91.2 % [PPC+12]. This is reproduced well by the shell model calculations and the NCSM calculations with NN+NNN interactions. The IM-NCSM calculations on the other hand, slightly underestimate the branching ratio for the $2_2^+ \rightarrow 2_1^+$ transition which is in conflict with the experimental results from Petri et al. [PPC+12]. The NCSM calculations with CDB2k interactions predict the branching ratio completely wrong, which can be explained with the much too large $B\left(E2; 2_2^+ \rightarrow 0^+\right)$ strength. Hence, for all theoretical approaches except the NCSM calculations with CDB2k interactions the $2_2^+ \rightarrow 2_1^+$ transition dominates strongly. When the partial transition rates are calculated and compared to the total transition rate of the 2_2^+ state, it can be further seen that for the $2_2^+ \rightarrow 2_1^+$ transition the $M1$ part is dominant and the $E2$ part can be neglected. So for all theoretical approaches except the NCSM calculations with CDB2k interactions, the lifetime of the 2_2^+ state is mainly defined by the $B\left(M1; 2_2^+ \rightarrow 2_1^+\right)$ strength.

For the 3_1^+ state nothing detailed can be said about the transition strengths from the experimental side. So far, only the $3_1^+ \rightarrow 2_1^+$ transition could be observed experimentally [PPC+12, WFM+08] which implies a branching ratio for this transition of 100 %. This is also reflected by all theories. But it has to be noted that the $3_1^+ \rightarrow 2_1^+$ transition was observed very weakly, which means that the 3_1^+ state was populated weakly in the experiments. Hence, other transitions with a low branching ratio could be completely missed. Additionally, one has to keep in mind that maybe also

Table 6.5: Level energies, transition strengths and branching ratios for ^{16}C. The values represent the results of several different theoretical approaches and the experiment. The experimental results for the 2_1^+ state, the 3_1^+ state and the BR$\left(2_2^+ \rightarrow 2_1^+\right)$ are taken from [WFM$^+$08, PPC$^+$12]. The $B\left(E2; 2_1^+ \rightarrow 0_1^+\right)$ which is marked with † was not calculated theoretically, but was scaled to the result from [WFM$^+$08, PPC$^+$12]. The branching ratios printed in black are calculated for theoretical transition energies, while the gray ones are calculated for experimental transition energies. For details see Section 6.5.4.

State	Observable	Exp.	IM-NCSM NN+$NNN^\Diamond$ [Rot20]	NCSM NN+NNN [FRN13]	NCSM CDB2k [FRN13]	p–sd Shell Model WBT* [Bro20, PPC$^+$12]	p–sd Shell Model WBT [Bro20, PPC$^+$12]	p–sd Shell Model WBP [Bro20, PPC$^+$12]	Unit
2_1^+	$E(2_1^+)$	1.7596(1)	1.43(89)(5)	1.38	2.43	1.871	2.368	2.385	MeV
	$B\left(E2; 2_1^+ \rightarrow 0^+\right)$	4.18(53)	1.26(1)(8)	4.18(53)†	2.2(6)	3.94	4.21	4.67	e^2fm^4
2_2^+	$E(2_2^+)$	3.973(4)	4.18(1.39)(13)	3.93	4.90	3.861	4.934	4.814	MeV
	$B\left(E2; 2_2^+ \rightarrow 2_1^+\right)$	Eq. 6.33	0.29(29)(10)	2.72(34)	4.4(1.2)	1.644	2.389	3.873	e^2fm^4
	$B\left(M1; 2_2^+ \rightarrow 2_1^+\right)$	Eq. 6.33	0.016(5)(26)	0.063	0.013	0.064	0.045	0.052	μ_N^2
	$B\left(E2; 2_2^+ \rightarrow 0^+\right)$	< 0.30	0.57(43)(8)	0.46(6)	4.48(1.32)	0.252	0.521	0.696	e^2fm^4
	BR$\left(2_2^+ \rightarrow 2_1^+\right)$	>91.2	87(37)(186)	97.3	19.1	97.2	88	85.9	%
			82(35)(170)	95.6	31.8	97.6	93.2	92.2	%
3_1^+	$E(3_1^+)$	4.068(3)	3.0(1.1)(2)	4.34	4.74	4.239	5.691	5.857	MeV
	$B\left(E2; 3_1^+ \rightarrow 2_2^+\right)$	N/A	0.0	0.0	0.0	0.749	0.728	0.801	e^2fm^4
	$B\left(M1; 3_1^+ \rightarrow 2_2^+\right)$	N/A	0.0	0.0	0.0	0.165	0.124	0.128	μ_N^2
	$B\left(E2; 3_1^+ \rightarrow 2_1^+\right)$	N/A	N/A	0.084(11)	0.79(22)	0.058	0.045	0.024	e^2fm^4
	$B\left(M1; 3_1^+ \rightarrow 2_1^+\right)$	N/A	0.003(40)(20)	0.17	0.17	0.167	0.097	0.085	μ_N^2
	BR$\left(3_1^+ \rightarrow 2_1^+\right)$	≈100	100	100	100	99.6	98.3	95.5	%
			100	100	100	100	100	100	%
4_1^+	$E(4_1^+)$	4.1289(2)	N/A	4.01	6.17	4.053	5.036	4.915	MeV
	$B\left(E2; 4_1^+ \rightarrow 2_1^+\right)$	2.74 to $5.78^{+0.32}_{-0.00}$	N/A	3.34(42)	1.96(53)	2.985	3.203	3.413	e^2fm^4

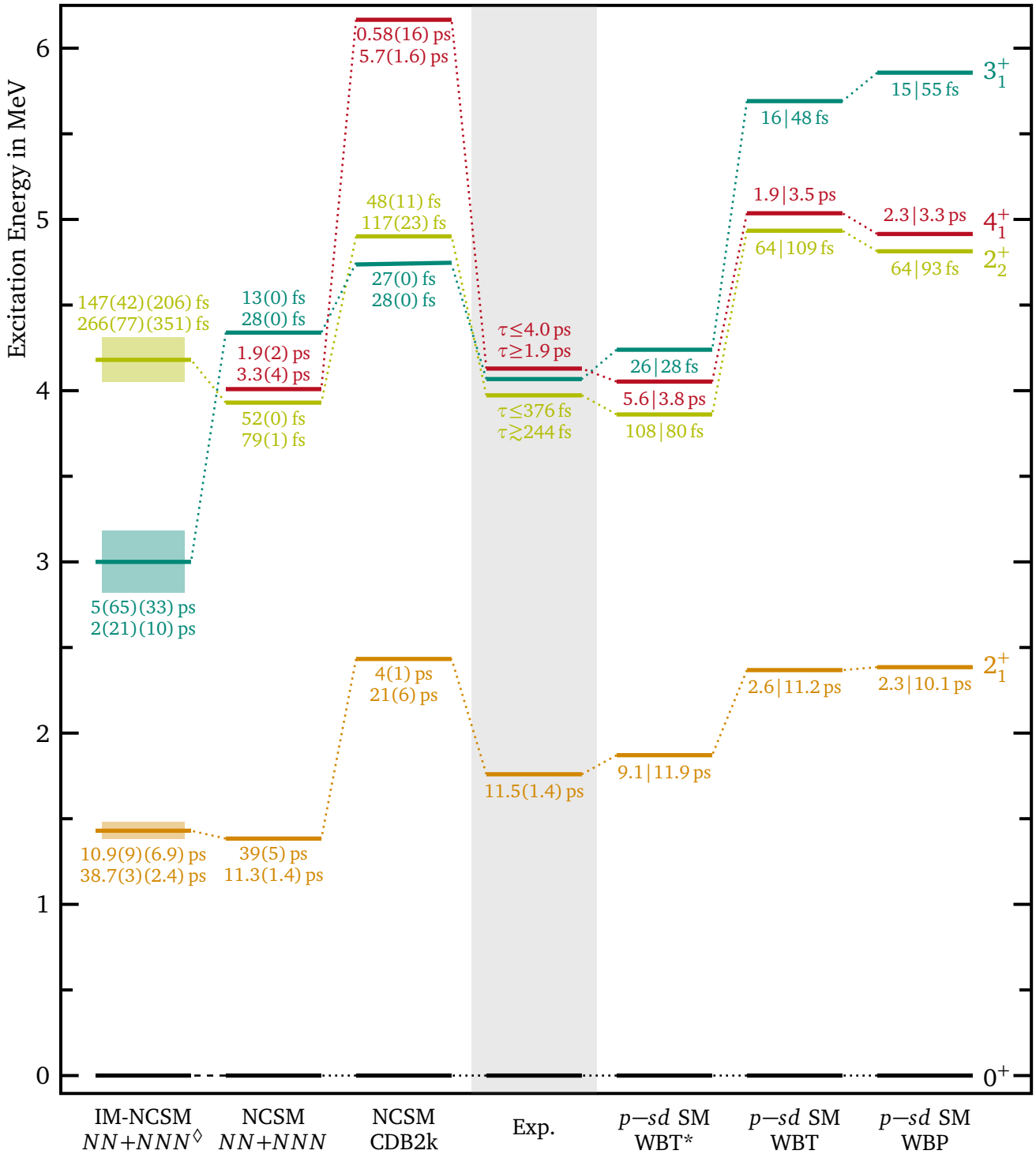

Figure 6.31: Comparison of several theoretical approaches and experimental results for the level scheme of ^{16}C. The experimental results for the 2^+_1 state are from [WFM$^+$08, PPC$^+$12]. The NCSM calculations are from [FRN13], the IM-NCSM calculations are from [Rot20] and the p–sd shell model calculations are from [Bro20, PPC$^+$12]. The left/top printed lifetimes are calculated for the theoretical transition energies, while the right/bottom printed lifetimes are calculated for the experimental transition energies. The $B(E2)$ strengths of the shell model were calculated with effective charges following [SZZS04]. For details see Section 6.5.4 and Table 6.5.

Wiedeking et al. [WFM+08] had ^{15}N contaminations in the $3_1^+ \rightarrow 2_1^+$ transition as it was discussed in Section 6.5.2.

The experimentally obtained range for the $B\left(E2; 4_1^+ \rightarrow 2_1^+\right)$ strength and the theoretical predictions are shown in Figure 6.32. The experimental range represents the results for SRIM stopping powers including the systematic uncertainties as calculated in Section 6.5.1. It can be seen that for the most theoretical approaches a proper strength is predicted. Only the NCSM calculations with CDB2k potential produce a too small transition strength. For the IM-NCSM calculations no results are obtained for the $B\left(E2; 4_1^+ \rightarrow 2_1^+\right)$ strength so far.

All results in terms of lifetimes are summarized in a level scheme which is shown in Figure 6.31. The lifetimes are calculated for the transition strengths from Table 6.5 using Equations 2.14. The uncertainties for the lifetimes for the IM-NCSM calculations do not include uncertainties concerning the theoretical transition energies. The experimental results are shown for SRIM stopping powers. For the 2_2^+ state the most likely lifetime range is shown as it is discussed and defined in the end of Section 6.5.3.

In terms of level energies the situation is sobering. For many predictions the absolute level energies and relative energy gaps between the levels differ strongly from the experiment. So e.g. the *p—sd* shell model calculations with WBT/WBP interactions overestimate the energies of all states. Further, for all theoretical approaches the ordering of the 3_1^+ state and the 4_1^+ state is interchanged compared to the experimental results. Only the *p—sd* shell model calculations with WBT* interactions and the NCSM calculations with *NN+NNN* interactions show a quite reasonable agreement with the experiment in terms of absolute level energies and relative energy gaps between the levels, but the 3_1^+ state and the 4_1^+ state are still swapped. For the recent IM-NCSM calculations the situation is interesting. Here, the level energy of the 2_2^+ state is reproduced very well and the level energy of the 2_1^+ state is slightly too low, while the level energy of the 3_1^+ state is reduced drastically compared to the experimental results and the other theoretical predictions. So the results for the level energy of the 3_1^+ state are worse compared to the NCSM calculations with *NN+NNN* interactions.

Focusing on the lifetimes, the *p—sd* shell model calculations reproduce the experimental value for the 2_1^+ state well, if the experimental transition energies are used. The NCSM calculations with CDB2k interactions overestimate the lifetime by a factor of two. For the *NN+NNN* interactions the lifetime is produced well which is obvious because, as stated earlier, the $B(E2)$ strength was scaled to the experimental results. The IM-NCSM calculations reproduce the lifetime of the 2_1^+ state well if the theoretical transition energies are used, otherwise the lifetime is overestimated by a factor of three. The experimental most likely lifetime range for the 2_2^+ state is underestimated significantly by all theoretical approaches except for the IM-NCSM calculations. For this case, the value is in good agreement with the experimental result if experimental transition energies are considered in the transtion rate calculations. Here one should note that the

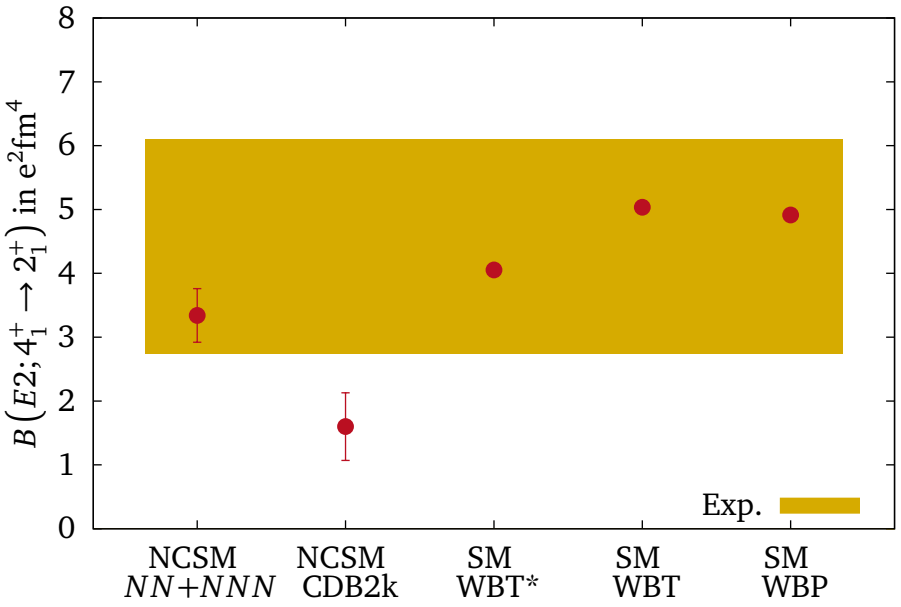

Figure 6.32: Results for the $B\left(E2; 4_1^+ \rightarrow 2_1^+\right)$ strength in ^{16}C. The yellow area represents the experimental limits which are obtained in Section 6.5.1 for SRIM stopping powers. The NCSM calculations are from [FRN13] and the p–sd shell model calculations are from [Bro20, PPC$^+$12]. The strengths of the shell model were calculated with effective charges following [SZZS04]. For details see Section 6.5.4 and Table 6.5.

theoretical uncertainties are very huge, but as stated earlier these are preliminary values. For the 3_1^+ state no final conclusion for the lifetime can be drawn. Assuming the $3_1^+ \rightarrow 2_1^+$ transition should occur in the spectra of this work with approximately the same intensity Wiedeking et al. [Fal08, WFM$^+$08] estimated, the lifetime should be in the femtosecond range (cf. Sec 6.5.2). This is reflected by all theoretical calculations except for the IM-NCSM calculations. But for this case no $B\left(E2; 3_1^+ \rightarrow 2_1^+\right)$ value could be obtained so far and hence the lifetime is strongly overestimated. If a $B\left(E2; 3_1^+ \rightarrow 2_1^+\right)$ value can be calculated in the future this should bring the lifetime down significantly. The lifetime of the 4_1^+ state is experimentally limited between 1.9 ps and 4.0 ps. This is successfully reproduced by the p–sd shell model calculations expect for WBT* interactions in combination with theoretical transition energies, for which the lifetime is deduced to 5.6 ps. The NCSM calculations using NN+NNN interactions also obtained lifetimes which are in agreement with the experimental results. If CDB2k interactions are used the lifetime is given by 5.7(1.6) ps (not shown in Fig. 6.31) for experimental transition energies. This is also in agreement with the experimental value considering the theoretical uncertainty stemming from the constraint-fit. In the IM-NCSM approach the 4_1^+ state is not calculated successfully yet.

Further, the IM-NCSM calculations are now compared to the recent NCSM$^\Diamond$ calculations, which also used the advanced chiral effective NN+$NNN^\Diamond$ interactions. As stated earlier, the NCSM$^\Diamond$ calculations do not finally converge for all strengths in ^{16}C but trends can be clearly deduced. Figure 6.33 shows the final transition strengths for the IM-NCSM calculations (red band) and

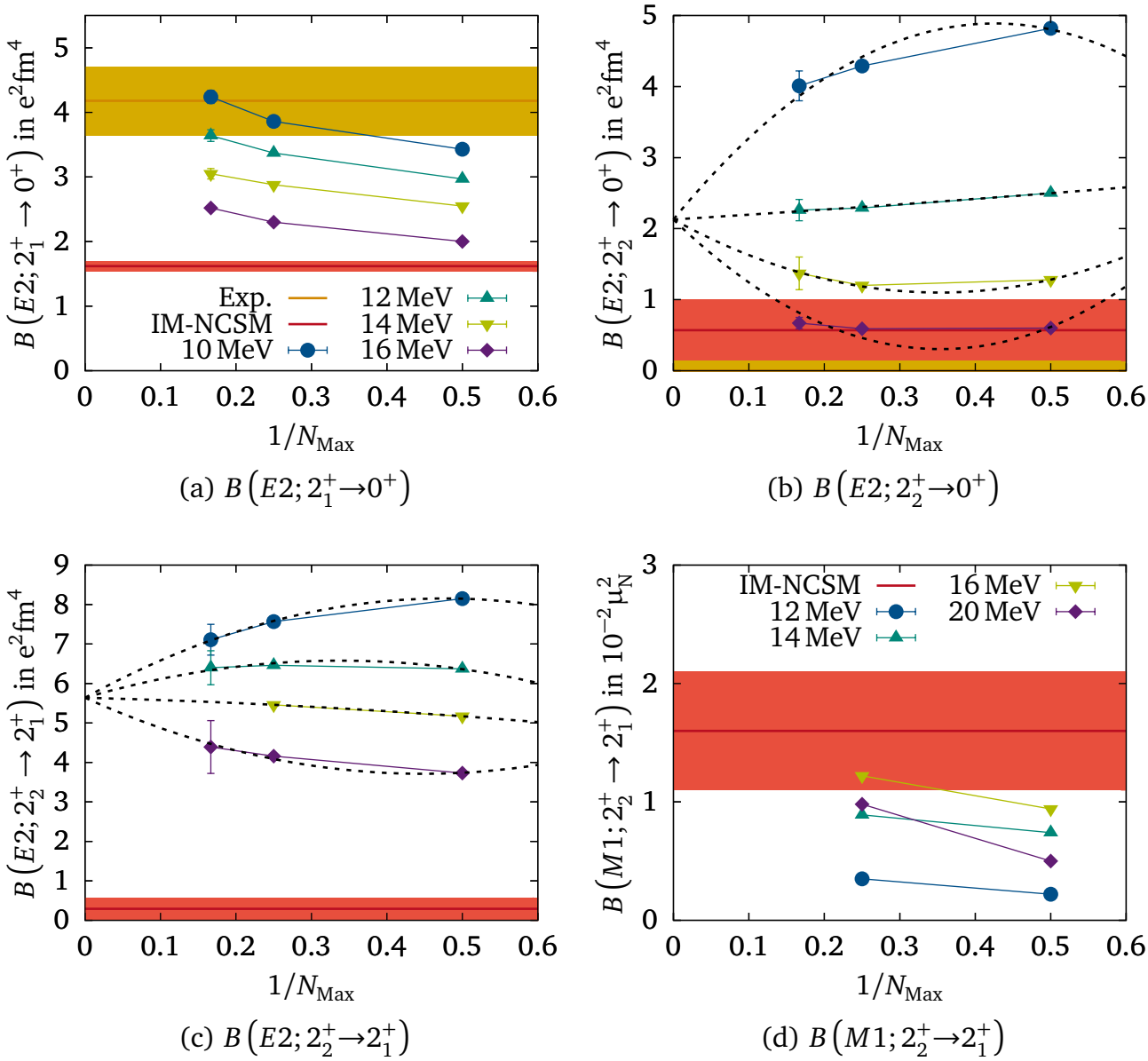

Figure 6.33: Transition strengths in ^{16}C for NCSM$^{\Diamond}$ calculations [Rot20] using advanced chiral effective NN+$NNN^{\Diamond}$ interactions [HVH$^+$20]. The transition strengths are shown as a function of $1/N_{\mathrm{Max}}$ for different sets of $\hbar\Omega$. The black dashed lines are constrained-fits which are described by Equation 6.35. The experimental value for the $B\left(E2;2_1^+\rightarrow 0^+\right)$ strength is the uncertainty weighted mean from [PPC$^+$12, WFM$^+$08]. For comparison the results for the IM-NCSM calculations [Rot20] are shown as a red band. Part (a), (b), and (c) use the same color code for the shown data points which is stated in Part (a). For details see Section 6.5.4 and Table 6.5.

the figure shows the transition strengths for the NCSM$^{\Diamond}$ calculations as a function of $1/N_{\mathrm{Max}}$ for different sets of $\hbar\Omega$. The NCSM$^{\Diamond}$ strengths were calculated for N_{Max}=2, 4, 6. For N_{Max}=6 the importance truncation method was applied to the calculations to speed up convergence.

Due to this, uncertainties are available for these data points. A final predicted strength for the NCSM$^{\Diamond}$ calculations is given by the extrapolation of the data points towards $1/N_{\mathrm{Max}} \rightarrow 0$. Here, the converged strengths at $1/N_{\mathrm{Max}} \rightarrow 0$ should be independent of the choice of $\hbar\Omega$ and hence the extrapolations for different $\hbar\Omega$ should intersect in one point at $1/N_{\mathrm{Max}} \rightarrow 0$. This behaviour can not be obtained for all strengths with the data available so far. A convincing extrapolation is possible for the $B\left(E2; 2_2^+ \rightarrow 0^+\right)$ and the $B\left(E2; 2_2^+ \rightarrow 2_1^+\right)$ strength as it can be seen in Figure 6.33 Part (b) and (c). The black dashed lines mark constrained-fits which are described by

$$q\left(N_{\mathrm{Max}}, \hbar\Omega\right) = q_0 + \frac{c_0(\hbar\Omega)}{N_{\mathrm{Max}}} + \frac{c_1(\hbar\Omega)}{N_{\mathrm{Max}}^2}, \tag{6.35}$$

for which the parameters c_0 and c_1 vary for each $\hbar\Omega$-sequence [FRN13]. The parameter q_0 reflects the final result interpolated to $1/N_{\mathrm{Max}} \rightarrow 0$ and it should be independent of the choice of $\hbar\Omega$. This results in 2.1(5) e^{2}fm^4 for the $B\left(E2; 2_2^+ \rightarrow 0^+\right)$ strength and in 5.6(3) e^{2}fm^4 for the $B\left(E2; 2_2^+ \rightarrow 2_1^+\right)$ strength. Hence, for both strengths much larger values are predicted by the NCSM$^{\Diamond}$ calculations compared to the IM-NCSM calculations. Further, the $B\left(E2; 2_2^+ \rightarrow 2_1^+\right)$ strength is larger than the $B\left(E2; 2_2^+ \rightarrow 0^+\right)$ strength for the NCSM$^{\Diamond}$ calculations. This could be in agreement with the experiment for which the $2_2^+ \rightarrow 2_1^+$ transition is strongly dominant. For the $B\left(E2; 2_1^+ \rightarrow 0^+\right)$ and the $B\left(M1; 2_2^+ \rightarrow 2_1^+\right)$ strength no convincing constrained-fits can be given. For the $B\left(M1; 2_2^+ \rightarrow 2_1^+\right)$ strength too few data points are available. For the $B\left(E2; 2_1^+ \rightarrow 0^+\right)$ strength a convincing extrapolation to one final value at $1/N_{\mathrm{Max}} \rightarrow 0$ for all $\hbar\Omega$-sequence at the same time is not clearly observed so far. Anyhow, large differences to the IM-NCSM calculations can be seen. For the $B\left(E2; 2_1^+ \rightarrow 0^+\right)$ strength the NCSM$^{\Diamond}$ calculations show a trend towards a much larger value which would be in agreement with the experimental value of $B(E2; 2_1^+ \rightarrow 0^+)$=4.18(53) e^{2}fm^4 [PPC$^+$12, WFM$^+$08]. Hence, for this case the NCSM$^{\Diamond}$ calculations give a much better result. For the $B\left(M1; 2_2^+ \rightarrow 2_1^+\right)$ strength the NCSM$^{\Diamond}$ calculations could lead to similar results as the IM-NCSM calculations ($0.016\,\mu_{\mathrm{N}}^2$). This is interesting, because the NCSM calculations with NN+NNN interactions from Forssén et al. [FRN13] predict a much larger $B(M1)$ strength of $0.063\,\mu_{\mathrm{N}}^2$, which was necessary to reproduce the experimental branching ratios of the 2_2^+ state.

All in all, the theoretical calculations still have to be improved to give a proper description of ^{16}C. Especially the ab initio NCSM and IM-NCSM calculations have to be revised to describe the higher-lying states. These results demonstrate how challenging it is to describe neutron-rich nuclei with ab inito approaches. Further, it is remarkably that the results for the IM-NCSM calculations differ significantly from the NCSM/NCSM$^{\Diamond}$ calculations with NN+NNN/NN+$NNN^{\Diamond}$ interactions, since the IM-NCSM framework truncates the NCSM model space, while it should retain the underlying physics. But as state earlier the IM-NCSM calculation results are preliminary and the deviation between the two approaches will be investigated further. From the experimental point of view it is recommended to further investigate the 2_2^+ state and achieve results with

better statistics. The results from this work as well as from Ciemała et al. [CZC+20] are both close to the detection limit and the results depend on the chosen E_{cm} of the investigate $2_2^+ \rightarrow 2_1^+$ transition. It is necessary to get a more precise result for the lifetime of the 2_2^+ state and to pin down the branching ratios more certain. Also the 3_1^+ state should be investigated again because no lifetime could be deduced so far and the 3_1^+ state was only observed for a small number of counts in the past [PPC+12, WFM+08].

7 Conclusion and Outlook

In the scope of this work measurements of electromagnetic properties of ^{16}C and ^{23}Ne were performed and analysed. To measure the lifetimes of excited states in ^{16}C, the reaction ^{9}Be(^{9}Be,2p)^{16}C* was combined with the DSAM at the ANL. For this, a target and degrader setup made of beryllium and gold was used. The emitted gamma rays were measured with Gammasphere, while the emitted particles were detected with μ-Ball. Combining the results from both detectors, gamma-ray spectra could be deduced for which the detected gamma rays were in coincidence with two protons. By analysing the gamma-ray spectra for different detection angles, the mean decay beta of the excited isotopes inside the gold degrader could be deduced. In the next step, predictions for this mean decay beta stemming from Geant4 simulations for two sets of stopping powers were compared to the experimental results to get access to the lifetimes of the states. The Geant4 simulations used experimental results from target-only-runs as an input, to fix the initial kinematic of the excited isotopes of interest. With this, experimental biases and the full influence of the reaction kinematics are reflected in the simulations at the same time. During the analysis it was discovered that the ^{9}Be target was oxidized which opened more reaction channels, such as ^{9}Be(^{16}O,2p1n)^{22}Ne*. Due to this, the well known lifetime of the 4_1^+ state of ^{22}Ne could be used as a benchmark for the here applied analysis. The result of this work with $\tau(4_1^+)$=328(14) fs for SRIM stopping powers is in very good agreement with the previous measurements and so it could be shown that the here used methods lead to reasonable results.

Furthermore, the reaction ^{9}Be(^{16}O,2p)^{23}Ne* occurred during the experiment. Therefore, the lifetimes of two higher-lying states in ^{23}Ne could be measured for the first time. The lifetime of the $(5/2^+, 7/2^+)_2$ state at 2517 keV was calculated to $641(79)\,\mathrm{fs}^{+16\,\mathrm{fs}}_{-6\,\mathrm{fs}}\left(\mathrm{syst}_{\mathrm{target}}\right)$ for SRIM stopping powers, while the lifetime of the $(5/2^+, 7/2^+)_1$ state at 1702 keV was calculated to $168(55)\,\mathrm{fs}^{+8\,\mathrm{fs}}_{-1\,\mathrm{fs}}\left(\mathrm{syst}_{\mathrm{target}}\right)^{+72\,\mathrm{fs}}_{-80\,\mathrm{fs}}\left(\mathrm{syst}_{\mathrm{feeding}}\right)$. For the lower lying $(5/2^+, 7/2^+)_1$ state, feeding from the higher-lying $(5/2^+, 7/2^+)_2$ state has to be taken into account. To deal with this problem a proper excitation ratio between both states was included in the Geant4 simulations. This ratio was extracted from the experimental data under the assumption that the angular distribution is the same for both observed transitions. The obtained experimental results were compared to USDB calculations done by A. Brown [Bro19] using effective charges following the $\propto 1/A$ parametrisation from Sagawa et al. [SZZS04]. While the level energies are reproduced well by the USDB calculations, the lifetimes are significantly underestimated by the USDB calculations. Further, it should be emphasized that this experiment was originally not designed to investigate ^{23}Ne* and so for the target-only-runs analysis only four peaks of the 2517 keV→1702 keV transition close to the detection limit could be used. This enables the possibility for large systematic

uncertainties for the simulated kinematics, which are maybe not reflected in the uncertainties of the here given results. Hence, it is recommended to remeasure the here given lifetimes for clarity. If the same method is used, it should be focused to gain more statistics. Especially for the target-only-runs analysis more statistic is necessary to get a better control over the isotope kinematics in the simulations.

For ^{16}C a lifetime range for the 2_2^+ state could be measured and a lower lifetime limit for the 4_1^+ state of τ_{Min}=$1.9^{+0.0}_{-0.1}\left(\mathrm{syst}_{\mathrm{target}}\right)$ ps could be obtained for SRIM stopping powers. Combined with the results from Wiedeking et al. [WFM$^+$08] the lifetime of the 4_1^+ state has to be between τ_{Min}=$1.9^{+0.0}_{-0.1}\left(\mathrm{syst}_{\mathrm{target}}\right)$ ps and 4 ps. This corresponds to a transition strength limit of $2.74\,\mathrm{e}^2\mathrm{fm}^4 \leq B\left(E2; 4_1^+ \rightarrow 2_1^+\right) \leq 5.78^{+0.32}_{-0.00}\left(\mathrm{syst}_{\mathrm{target}}\right)\,\mathrm{e}^2\mathrm{fm}^4$. Theoretical predictions from NCSM calculations with *NN+NNN* interactions [FRN13] and *p–sd* shell model calculations for several effective two body interactions [Bro20, PPC$^+$12] fulfill this constraint. For the 2_2^+ state the analysis was more challenging due to a very low number of counts close to the detection limit in the peak of interests. The most likely lifetime range for the 2_2^+ state is given by 244 fs to 376 fs for the mean transition energy and SRIM stopping powers. In combination with the upper branching ratio limit of 8.8 % for the $2_2^+ \rightarrow 0^+$ transition measured by Petri et al. [PPC$^+$12], it is possible to constrain the three transition strengths which are involved in the lifetime of the 2_2^+ state. It could be shown that *p–sd* shell model calculations [Bro20, PPC$^+$12] and NCSM calculations using *NN+NNN* interactions [FRN13] can not fulfill the constraints in terms of $B\left(E2; 2_2^+ \rightarrow 2_1^+\right)$, $B\left(M1; 2_2^+ \rightarrow 2_1^+\right)$, and $B\left(E2; 2_2^+ \rightarrow 0^+\right)$ strengths. For IM-NCSM calculations [Rot20] and NCSM calculations with CDB2k interactions [FRN13] a valid combination of $B\left(E2; 2_2^+ \rightarrow 2_1^+\right)$ and $B\left(M1; 2_2^+ \rightarrow 2_1^+\right)$ strengths is predicted but for both the $B\left(E2; 2_2^+ \rightarrow 0^+\right)$ strength seems too large. In terms of the 2_2^+ state lifetime only the IM-NCSM calculations [Rot20] agree with the experimental results, while the other theoretical approaches predict a too small value. Here, it is noticeable that for all investigated theories expect NCSM calculations with CDB2k interactions, the lifetime of the 2_2^+ state is mainly dominated by the $B\left(M1; 2_2^+ \rightarrow 2_1^+\right)$ strength and the other transition types are negligible. The 3_1^+ state of ^{16}C could not be investigated because the $3_1^+ \rightarrow 2_1^+$ transition peaks are contaminated by events from the $7/2_1^+ \rightarrow 5/2_1^+$ transition of ^{15}N.

Overall, it can be concluded from this work that the theoretical descriptions for ^{16}C have to be improved. Especially for ab initio NCSM and IM-NCSM calculations it is still challenging to predict the level energies and transition strengths correctly at the same time. From the experimental point of view it is important to further investigate the 2_2^+ state and achieve measurements with better statistics to limit the lifetime of the 2_2^+ state more precisely. Also the 3_1^+ state should be investigated again because no lifetime could be deduced so far and the 3_1^+ state was only observed with very limited statistics in the past [PPC$^+$12, WFM$^+$08]. For this it is recommended to use a different reaction than the here used ^{9}Be(^{9}Be,2p)^{16}C* reaction, to avoid possible contaminations from ^{15}N.

Part II

Conceptual Design of a Carbon-14 Electron Scattering Experiment at the QCLAM Spectrometer

8 Introduction

As stated in Part I of this thesis, electromagnetic properties of carbon isotopes are of special interest. Here, the ^{14}C isotope plays also an important role. Due to its number of protons and neutrons ^{14}C can be interpreted as a coupling of three alpha particles with two valence neutrons [YKH$^+$17, SKE10, FBNS$^+$16]. As a result of this complex cluster structure, it is rather difficult to describe ^{14}C theoretically by ab initio methods. Also the excited states are complex multi-particle-hole structures. This is similar to the structure in ^{12}C. In this case many states can be described by the clustering of three alpha particles. NCSM calculations fail completely to reproduce the first excited states [MVC$^+$14]. However, modern Lattice Effective-Field-Theory calculations give promising results in first attempts. But they suffer by implementing interactions of higher order like chiral N^{3}LO interactions [EKL$^+$12, EKLM11]. Facing these problems, it is rather interesting how they evolve for ^{14}C. But unfortunately not much about the electromagnetic properties for ^{14}C is known so far. This is due to the fact that experiments with a radioactive ^{14}C target are quite challenging. The only known electron scattering data available for ^{14}C are from 1972/76 measured by Crannell et al. [CHO$^+$72, CFH$^+$77]. They call for a more accurate remeasuring. Because of this, an electron scattering experiment on ^{14}C is planned at the QCLAM spectrometer at the S-DALINAC. The goal of this experiment is to provide key electromagnetic observables of excited states of ^{14}C. They can be used to test and refine different ab initio calculations.

The ^{14}C isotope, well known through the radiocarbon dating method [Lib52], decays with a half-life of 5730 years via a β^- decay [AS91b]. There the end-point energy is 156.5 keV while the mean beta energy is 49.5 keV [AS91b]. The ^{14}C target which is available for this experiment has a total activity of around 8 TBq [Edw08]. Due to the fact that the ^{14}C target is highly radioactive and long-lived, several safety measures have to be applied to prevent the contamination of the experimental equipment or the staff. Seeing that, a new scattering chamber and a new target chamber, which is mounted on top of the scattering chamber, will be designed in this thesis. They will allow to seal the target off from the remaining vacuum system of the QCLAM spectrometer during maintenance work or potential critical situations. For this, also a new valve system will be planned. This system includes three fast valves which seal the scattering chamber off in a few microseconds. This is necessary if a vacuum foil on top of the QCLAM rips apart and thus an air shock wave enters the QCLAM vacuum system. Furthermore, the consequence of such a shock wave will be analysed and discussed. Additionally, the energy deposited inside the ^{14}C target and the following heat up are discussed as well. Also some count rate estimations for a possible experiment at the QCLAM spectrometer will be done in the following part of the thesis.

9 Theory and Physical Background

In this chapter, an introduction to nuclear structure theory of the ^{14}C isotope is given. Also a short overview over the theory of electron scattering is given.

9.1 The Case of Carbon-14

The ^{14}C isotope, consisting of six protons and eight neutrons, is an interesting candidate for complex alpha cluster structures [YKH$^+$17, SKE10, FBNS$^+$16]. Due to this, it is rather difficult to describe ^{14}C theoretically by ab initio methods such as NCSM calculations. Additionally, with $T_{1/2}$=5730 a the ^{14}C isotope has an anomalously long lifetime compared to the lifetimes of other light nuclei which have the same decay channel. Astonishingly, it is nevertheless possible to describe the extraordinary long half-life with NCSM calculations [BNV13, MVN$^+$11]. This was established using chiral NN+NNN interactions. The investigations showed that the very long lifetime for ^{14}C stems from a cancellation between 0p-shell NN interactions and the three body interactions. Hence, the properties of the ^{14}C isotope are influenced strongly by applying three body interactions to the underlying Hamiltonian. Due to its properties, ^{14}C is an interesting candidate to check for influences and the importance of three body forces. Unfortunately ab initio methods have still problems to describe the properties of excited states in ^{14}C. Also from the experimental point of view not much about the electromagnetic properties of excited states in ^{14}C is known. The only known electron scattering data available for ^{14}C are from 1972/76 measured by Crannell et al. [CHO$^+$72, CFH$^+$77].

In the first work, Crannell et al. measured the scattered electrons for nine different incident electron energies between 60 MeV and 120 MeV at laboratory scattering angles of 92.5°, 127.5°, and 145° [CHO$^+$72]. This corresponds to a momentum transfer range from 0.45 fm^{-1} to 0.90 fm^{-1}. The focus was set on the first two 2^+ excited states. For these two states, they were able to extract the form factors, the reduced Coulomb matrix elements for an electric quadrupole excitation, the transition radii and the transition strengths. The results for the reduced matrix elements, the transition radii and the transition strengths can be found in Table 9.1 while the form factors can be found in Table 11.2 and Table A.10. The strength of the 2^+_1 state is 4.6 times larger than the strength of the 2^+_2. A sufficient theoretical interpretation of this is still missing. Additionally, it can be seen that especially for the 2^+_2 state the uncertainties are rather large (e.g. 23 % for the radius). Because [CHO$^+$72] is the only measurement of electron scattering on ^{14}C for angles different than 180° a remeasurement of the two first 2^+ states is urgent. It would be

Table 9.1: The reduced Coulomb matrix elements for an electric quadrupole excitation $\sqrt{B(E2,0)}\uparrow$, the transition radii R, and the transition strengths M^2 for the first two 2^+ states in ^{14}C. The values were measured by Crannell et al. [CHO$^+$72].

E_x in MeV	$\sqrt{B(E2,0)}\uparrow$ in $e$fm^2	R in fm	M^2 in W. U.
7.01	4.32(29)	3.22(22)	1.79(24)
8.32	2.02(38)	3.05(69)	0.39(15)

also of special interest to measure electromagnetic properties of other states additionally to the already investigated first two 2^+ states.

Furthermore, Crannell et al. measured electron scattering at ^{14}C under 180° [CFH$^+$77]. Here they used beam energies of 37 MeV, 50 MeV, and 60 MeV. With this measurement they found eight states in ^{14}C with an excitation energy less than 16 MeV. Because electron scattering under 180° favours strongly magnetic M1 transitions, the $B(M1)$ strength can be estimated very well with this experiment. It could be concluded that clearly the most $B(M1)$ strength is located in one transition at 11.31 MeV which could be identified as a 1^+ state. Here the cross section for E_i=37 MeV is with $12.0(1.2)\cdot10^{-33}$ cm^2/sr extraordinary large compared to the other states. This is different to many other light nuclei like ^{11}B or ^{13}C where the $B(M1)$ strength is fragmented more or less equally into several states [CFH$^+$77]. However, the measured statistics for the weak transitions in [CFH$^+$77] was so small that no multipolarity or transition strength could be deduced from the data. Maybe some $B(M1)$ strength was missed due to too low sensitivity of the experiment. But the extraction of the total $B(M1)$ strength is important due to the still not fully understood phenomena of the quenching of the $B(M1)$ strength in light and medium mass nuclei [Ric85, vNCPRR98]. The quenching of the total $B(M1)$ strength in light and medium mass nuclei is an important case because it contributes to the long-standing problem of quenching of the spin-isospin response in nuclei [Ost92, HvNCR10]. Hence, it would also be very interesting to remeasure electron scattering at ^{14}C under 180°, which would be in principle also possible at the QCLAM spectrometer. Furthermore, it is nowadays possible to measure transitions with weak $B(M1)$ strengths applying the unite cross-section method to inelastic proton scattering data which are measured under extreme forward angles. Here the experimental background is neglectable and even states with very small cross sections can be analysed precisely. This method was successfully established in [BMvNC$^+$16, Bir17, MBM$^+$17, Mat14].

Another theoretical approach which tries to describe excitations in ^{14}C isotopes is the so-called Linear-Chain Cluster State (LCCS) in the framework of the AMD method. The idea of a LCCS was already introduced in 1956 by Morinaga [Mor56] to describe the Hoyle state in ^{12}C. Today many LCCSes in several nuclei are predicted using realistic interactions including AMD. For these

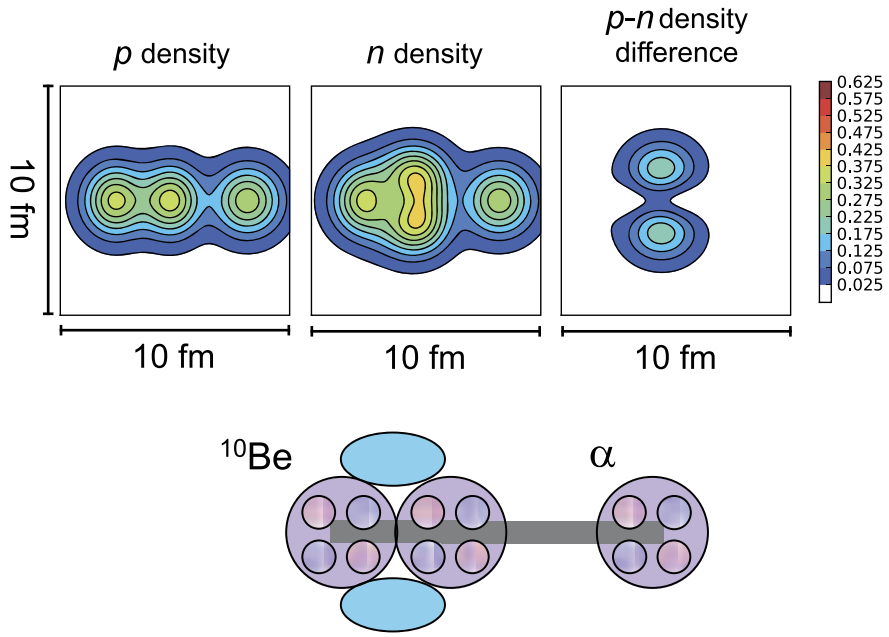

Figure 9.1: Wavefunction in the linear-chaincluster state in ^{14}C as a result of the AMD method [SKE10, SKE11]. The top part shows the proton density ρ_{p}, the neutron density ρ_{n} and the difference between them. The bottom part shows an intuitive picture of the particle alignment which arises from the density distribution above. The figure is modified and reprinted from [YKH$^+$17] with permission from Elsevier.

interactions, linear-chain states can be stable against bending. Looking at the work from Suhara and Kanada-En'yo [SKE10, KEKS13] a prolate band that has a configuration of a LCCS could be predicted for ^{14}C. It could be shown that the LCCS is stabilized by its orthogonality to lower-lying states. The lower-lying states are triaxially deformed cluster states. They are constructed with bended bases. Due to the orthogonality condition the higher-lying LCCSes are prohibited from bending. This is a special case which applies for ^{14}C. In ^{12}C for example no triaxial bands exist and so this mechanism does not apply here. Additional investigations from Suhara and Kanada-En'yo [SKE11] revealed that the wavefunctions stemming from the AMD have a configuration in which two alpha particles and two neutrons are located close to each other, while the remaining alpha particle is further away. This solution is illustrated in Figure 9.1. Here, two equivalent interpretations are possible. In the first interpretation the three alpha particles are aligned in one straight line while the two neutrons can be treated as valence neutrons. Here it could be shown that the two valence neutrons are necessary to stabilize the three alpha chain [FBNS$^+$16]. These two valence neutrons are missing in the case of ^{12}C. This explains why the alpha chains are fragile, bend and collapse for higher excited states in ^{12}C [FBNS$^+$16, KE07]. In the other interpretation for ^{14}C a ^{10}Be core is formed while an additional alpha particle is attached at the outside in such a way that the alpha particles are aligned along a straight line.

Because of the second interpretation, Yamaguchi et al. [YKH$^+$17] used the ^{10}Be+α resonant scattering method in inverse kinematics to investigate LCCSes in ^{14}C. They found several excited

states for which the level energy spacings and the J^π agree perfectly with the theoretical predictions for the LCCSes. Hence, this work can be seen as a proof for LCCSes in ^{14}C. Additionlly, Fritsch et al. [FBNS+16] performed resonant elastic and inelastic alpha scattering of a radioactive ^{10}Be to investigate LCCSes in ^{14}C. They indeed also found two excited states, which can only be explained assuming LCCSes in ^{14}C. Furthermore, they measured a large cross section in the inelastic channel of the 2_1^+ state of ^{10}Be. To describe this theoretically they studied Brink-Bloch wave functions [Bri66]. For this case, they added an alpha particle to an axially deformed ^{10}Be cluster. The alpha particle is placed at the distance d=5 fm under an angle θ relative to the symmetry axis of the ^{10}Be cluster. They could show that the ratio of inelastic interaction to elastic interaction depends strongly on θ and is maximal for θ=0°. To explain the large inelastic channel of the 2_1^+ state a three alpha cluster at which the alpha particles are arranged along a line has to be assumed. This is a second strong indication for LCCSes in ^{14}C.

In summary, the ^{14}C isotope is a rather interesting case and a good candidate to study LCCSes as well as to test how ab initio methods can deal with a pronounced cluster structure. Unfortunately, the experimental knowledge for LCCSes in ^{14}C is rather limited. For example the work from Yuta et al. [YKE16] gives various radii for excited states in ^{14}C calculated with LCCS and AMD approaches, which could be checked in the future experimentally.

9.2 Electron Scattering

During electron scattering, an electron with a relativistic incoming momentum $\vec{k}$ (and energy E_i) hits a nucleus with the charge Ze and transfers the momentum $\vec{q}=\vec{k}-\vec{k}'$ to this nucleus. The scattering of electrons on a nucleus is a process in the quantum regime. The process has to be described by a wave function. This wave function consists of two parts. The first part is an incoming plane wave while, looking from far distance, the second part is a spherical wave function with its center in the position of the scattering center, hence the nucleus. This leads to

$$\Psi(\vec{r}) = \Psi_\mathrm{i}(\vec{r}) + \Psi_\mathrm{f}(\vec{r}) = a\left[\mathrm{e}^{\mathrm{i}\vec{k}\vec{r}} + f(\theta)\frac{\mathrm{e}^{\mathrm{i}k'r}}{r}\right] \tag{9.1}$$

for the total wave function if the electron beam is not polarized. Here $\vec{k}$ is the momentum vector of the incoming electron and k' is the absolute value of the outgoing moment. The factor a is the total wave amplitude and $f(\theta)$ is the so-called scattering amplitude. Furthermore, the particle density can be generally calculated with $P=\Psi(\vec{r})^\dagger\Psi(\vec{r})$. If the electrons have the velocity v, the current densities j are given by

$$j_\mathrm{i} = \Psi_\mathrm{i}^\dagger\Psi_\mathrm{i}v_\mathrm{i} = \left|a\,\mathrm{e}^{\mathrm{i}\vec{k}\vec{r}}\right|^2 v_\mathrm{i} = a^2 v_\mathrm{i} \tag{9.2}$$

$$j_\mathrm{f} = \Psi_\mathrm{f}^\dagger\Psi_\mathrm{f}v_\mathrm{f} = \left|af(\theta)\frac{\mathrm{e}^{\mathrm{i}k'r}}{r}\right|^2 v_\mathrm{f} = a^2\frac{|f(\theta)|^2}{r^2}v_\mathrm{f}. \tag{9.3}$$

where “i” indicates the incoming part and “f” indicates the outgoing part. Using the definition of the cross section this leads directly to

$$\frac{\mathrm{d}\sigma}{\mathrm{d}\Omega}(\theta) = \frac{j_\mathrm{f} dA}{j_\mathrm{i} d\Omega}(\theta) = \frac{v_\mathrm{f}}{v_\mathrm{i}} |f(\theta)|^2 . \tag{9.4}$$

For relativistic electron scattering we have $v_\mathrm{i} \approx v_\mathrm{f} \approx c$ and hence

$$\frac{\mathrm{d}\sigma}{\mathrm{d}\Omega}(\theta) = |f(\theta)|^2 . \tag{9.5}$$

By knowing the scattering amplitude, the cross section can be calculated. To get access to the scattering amplitude, the time-independent Schrödinger equation

$$\nabla^2 \psi(\vec{r}) - U(r)\psi(\vec{r}) = -k^2 \psi(\vec{r}) \tag{9.6}$$

is used. In this equation $U(r)$ is given by $2m/\hbar^2 V(r)$ where $V(r)$ is the scattering potential. It is assumed that the potential $V(r)$ has only a radial dependency. Then equation 9.6 can be solved using the Green’s function formalism to

$$\psi(\vec{r}) = \Phi(\vec{r}) - \frac{m}{2\pi\hbar^2} \int \frac{\mathrm{e}^{\mathrm{i}k|\vec{r}-\vec{r}'|}}{|\vec{r}-\vec{r}'|} V(r')\psi(\vec{r}')\mathrm{d}^3 r'. \tag{9.7}$$

Here $\Phi(\vec{r}) = \mathrm{e}^{\mathrm{i}\vec{k}\vec{r}}$ is the solution of the homogeneous time-independent Schrödinger equation. Equation 9.7 is also called Lippmann-Schwinger-Equation [LS50]. The Lippmann-Schwinger-Equation can be solved approximately using a recursive method. If as a start value $\psi_0(\vec{r})$ is set to $\Phi(\vec{r})$ and one only takes the first step of the recursive method into account, then the so-called first plane wave Born approximation is given by

$$\psi_\mathrm{PWBA}(\vec{r}) = \Phi(\vec{r}) - \frac{m}{2\pi\hbar^2} \int \frac{\mathrm{e}^{\mathrm{i}k|\vec{r}-\vec{r}'|}}{|\vec{r}-\vec{r}'|} V(r')\,\mathrm{e}^{\mathrm{i}\vec{k}\vec{r}'}\,\mathrm{d}^3 r'. \tag{9.8}$$

This approximation is only valid if the distortion of the plane wave by the potential $V(r)$ is small. In the next step, the fact is used that in an experiment the distance of the detector to the scattering center and hence the center of the potential is much larger than the range of the potential. Due to this, $k|\vec{r}-\vec{r}'|$ can be expanded into a Taylor series. By stopping at the first term one gets

$$\psi_\mathrm{PWBA}(\vec{r}) \approx \Phi(\vec{r}) - \frac{m}{2\pi\hbar^2} \frac{\mathrm{e}^{\mathrm{i}k'r}}{r} \int \mathrm{e}^{-\mathrm{i}\vec{k}'\vec{r}'}\, V(r')\,\mathrm{e}^{\mathrm{i}\vec{k}\vec{r}'}\,\mathrm{d}^3 r'. \tag{9.9}$$

By comparing Equation 9.9 with Equation 9.1, the scattering amplitude is expressed by

$$f(\theta) \approx \frac{-m}{2\pi\hbar^2} \int \mathrm{e}^{-\mathrm{i}\vec{k}'\vec{r}'}\, V(r')\,\mathrm{e}^{\mathrm{i}\vec{k}\vec{r}'}\,\mathrm{d}^3 r'. \tag{9.10}$$

For electron scattering the scattering potential on an expanded charge distribution $\rho(r)$ is given by

$$\mathrm{d}V(t) = \frac{Ze^2}{4\pi\epsilon_0 s}\rho(r)\mathrm{d}^3r, \tag{9.11}$$

where s is the distance between the electron and the volume element d^3r. The total potential of the nucleus is given by an integration over the volume of the nucleus and hence

$$V(t) = \frac{Ze^2}{4\pi\epsilon_0}\int \frac{1}{s}\rho(r)\mathrm{d}^3r. \tag{9.12}$$

Plugging this term into Equation 9.10 leads to

$$f(\theta) \approx \frac{Ze^2}{4\pi\epsilon_0}\frac{-mZe^2}{2\pi\hbar^2}\int \mathrm{d}^3r \int \mathrm{d}^3t \frac{\rho(r)}{s}\mathrm{e}^{\frac{\mathrm{i}}{\hbar}\vec{q}(\vec{r}+\vec{s})} \tag{9.13}$$

$$f(\theta) \approx \underbrace{\frac{Ze^2}{4\pi\epsilon_0}\frac{-mZe^2}{2\pi\hbar^2}\int \frac{1}{s}\mathrm{e}^{\frac{\mathrm{i}}{\hbar}\vec{q}\vec{s}}\,\mathrm{d}^3s}_{f_{\mathrm{Rutherford}}(q)} \underbrace{\int \rho(r)\mathrm{e}^{\frac{\mathrm{i}}{\hbar}\vec{q}\vec{r}}\,\mathrm{d}^3r}_{F(\vec{q})} \tag{9.14}$$

for the scattering amplitude. The first part of this equation is the scattering amplitude of the well known Rutherford scattering. The second part is the so-called form factor. It is a Fourier-Bessel transformation of the charge distribution of the nucleus. What was ignored so far is the fact that the electron is a spin 1/2 particle. But because the electrons have a speed of $\beta \approx 1$ the helicity h (which means $h = \vec{k}\vec{s}/(|\vec{k}||\vec{s}|)$) of the electron has to be conserved. Hence, scattering under 180° is strongly suppressed. To implement this into the scattering amplitude, the factor $\sqrt{1-\beta^2\sin^2\theta/2}$ is added to Equation 9.14. Finally, the cross section of relativistic electron scattering is given by

$$\frac{\mathrm{d}\sigma}{\mathrm{d}\Omega} = \left(\frac{Ze^2}{4\pi\epsilon_0}\frac{1}{4E_\mathrm{i}}\frac{1}{\sin^2\frac{\theta}{2}}\right)^2 \cdot (1-\beta^2\sin^2\frac{\theta}{2}) \cdot |F(q)|^2 \tag{9.15}$$

$$\frac{\mathrm{d}\sigma}{\mathrm{d}\Omega} = \frac{\mathrm{d}\sigma}{\mathrm{d}\Omega}_{\mathrm{Rutherford}} \cdot (1-\beta^2\sin^2\frac{\theta}{2}) \cdot |F(q)|^2 \tag{9.16}$$

$$\frac{\mathrm{d}\sigma}{\mathrm{d}\Omega} = \frac{\mathrm{d}\sigma}{\mathrm{d}\Omega}_{\mathrm{Mott}} \cdot |F(q)|^2. \tag{9.17}$$

The first part of the last equation is the so-called Mott cross section. The Mott cross section just depends on the kinematics of the scattering experiment. All the nuclear structure information is given by the form factor $F(q)$. By measuring the experimental cross section for different q values and comparing it to the Mott cross section one gets access to the behaviour of the form factor and thus access to the charge distribution of the nucleus. If the incoming energy E_i is much larger than the rest mass of an electron $m_\mathrm{e}c^2$, then we have $\beta \approx 1$ and the Mott cross section can be rewritten to

$$\frac{\mathrm{d}\sigma}{\mathrm{d}\Omega}_{\mathrm{Mott}} = \left(\frac{Ze^2}{4\pi\epsilon_0}\frac{1}{4E_\mathrm{i}}\frac{\cos\frac{\theta}{2}}{\sin^2\frac{\theta}{2}}\right)^2. \tag{9.18}$$

The momentum transfer q of the electron experienced in the experiment depends on the scattering angle θ, the initial energy E_i and the energy loss of the electron. The energy loss is given by $E_\mathrm{x}{=}E_\mathrm{i} - E_\mathrm{f}$, where E_f is the energy of the electron after the scattering. Then the momentum transfer in units of fm^{-1} can be calculated as

$$q = \frac{1}{\hbar c}\sqrt{\frac{4E_\mathrm{i}(E_\mathrm{i} - E_\mathrm{x})\sin^2\frac{\theta}{2} + E_\mathrm{x}^2}{1 + \frac{2E_\mathrm{i}}{Mc^2}\sin^2\frac{\theta}{2}}}, \tag{9.19}$$

where the recoil of the nucleus is considered and M is the mass of the target nucleus. In the plane wave Born Approximation, it was assumed that the incoming wave is a perfect planar wave before the scattering happens. But this is not true in reality. Due to the electrical potential the plane wave gets distorted before it comes to the scattering. For heavy nuclei this can be considered by applying the distorted plane wave Born approximation. It could be shown that for light and medium mass nuclei the plane wave Born approximation is still valid if this effect is taken into account quantitatively by changing the q dependence of the form factor. Due to the Coulomb force the effective energy of the electron is getting slightly bigger during the scattering. This leads to an increase of the momentum transfer which is corrected using the effective momentum transfer expressed by

$$q_\mathrm{eff} = q\left(1 + \frac{3}{2}\frac{Ze^2}{E_\mathrm{i}R_\mathrm{eq}}\right), \tag{9.20}$$

where R_eq is the radius of the uniform charged sphere. It can be parametrised by

$$R_\mathrm{eq} = \begin{cases} \sqrt{\frac{5}{3}(1.2A^{1/3})^2} & \text{if } A < 20 \\ 1.128A^{1/3} + 2.24A^{-1/3} & \text{if } A \geq 20 \end{cases} \tag{9.21}$$

Then the form factor becomes a function of q_eff and is measured via

$$|F_\mathrm{exp}(q_\mathrm{eff})|^2 = \frac{\frac{\mathrm{d}\sigma}{\mathrm{d}\Omega}\mathrm{exp}}{\frac{\mathrm{d}\sigma}{\mathrm{d}\Omega}\mathrm{Mott}}. \tag{9.22}$$

This section was orientated by [Mac05, Mat14, KBtLC12]. A detailed mathematical description of electron scattering can be found e.g. in [Üb71].

10 Facility and Existing Experimental Setup

The electron scattering experiment on ^{14}C will be performed at the QCLAM setup which is an electron spectrometer at the electron accelerator S-DALINAC at the TU Darmstadt. These setups are explained in the following two sections.

10.1 Electron Accelerator S-DALINAC

The Supraleitende Darmstädter Elektronenbeschleuniger (S-DALINAC) is a superconducting linear electron accelerator at the TU Darmstadt [Pie18, Ric96]. The S-DALINAC started its full operation in 1991 as a two-arch accelerator. In 2015/2016 the accelerator was upgraded by installing a third arch [AHKP16]. With this upgrade, the S-DALINAC can deliver beam energies from 3 to 130 MeV. Furthermore, it is now possible to run the S-DALINAC in an energy-recovery mode. Thus, the S-DALINAC is the first energy-recovery electron linac in Germany [Son17]. The S-DALINAC is able to deliver a continuous-wave beam with electron bunches every 333 ps. The length of one bunch is about 5 ps.

A floor plan of the S-DALINAC is shown in Figure 10.1. At the S-DALINAC the electrons are generated in one of two available guns. The thermionic gun emits electrons into the vacuum by heating a tungsten wire to more than 1,000 K. The spin-polarized electron gun delivers electrons using a photongun. In the photongun, an external laser beam is shot on GaAs photocathodes to cause the photo-electrical effect. The electrons which are set free during the photo-electrical effect are spin-polarized. Polarization degrees up to 86 % have been demonstrated in the past [PEA$^+$11]. After the two guns, the electrons are pre-accelerated electrostatically by high voltage up to 250 keV. Then the electrons pass a normal conducting chopper and a pre-buncher section. They prepare the beam for the main acceleration and can achieve an emittance smaller than 1 mm mrad. In the next step the electrons enter the injector linac. The injector linac consists of a short cryomodule housing a 5-cell niobium capture cavity and of one standard cryomodule housing two 20-cell niobium cavities. All niobium cavities at the S-DALINAC are operated at a frequency of 2.998 GHz. They reach a quality factor of 10^9 while they are operated at 2 K. They can create field gradients of 4-6 MV/m. After the injector linac, the electrons can have energies between 3 and 10 MeV. The electrons can then be guided to the Darmstadt High-Intensity Photon Set-up (DHIPS) or they are bent into the main linac. The main linac consists of four cryomodules. Each module consists of two 20-cell niobium cavities. So the main linac consists of eight 20-cell niobium cavities in total, while the whole S-DALINAC consists of eleven niobium cavities in total. After the electrons passed the main linac, they reach a separation magnet. Here it can be decided,

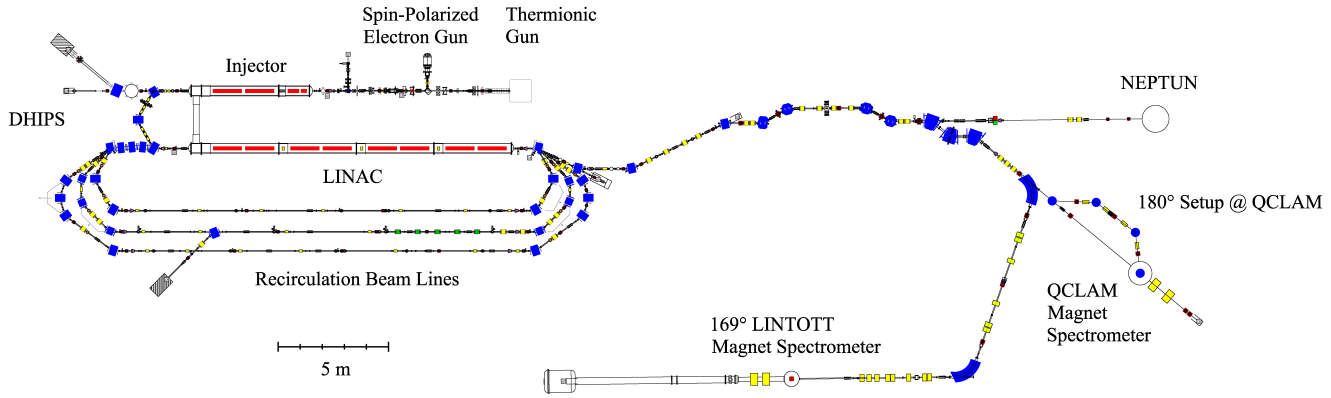

Figure 10.1: Floor plan of the S-DALINAC. Dipole magnets are shown in blue, while quadrupole magnets are shown in yellow. The niobium cavities are marked in red. The figure is taken from [Pie18] with courtesy to M. Arnold.

if the electrons are bent in one of the three recirculation beam lines or if the electrons are extracted into the extraction beam line. The electrons can be recirculated up to three times and hence they pass the main linac up to four times. The number of used recirculation depends on the used mode and the end point energy the beam should have. After the recirculations the electrons are guided into the extraction beam line. In the extraction beam line a highly dispersive chicane with a focus at its dispersion maximum is placed. By using a special slit system at the focal plane point, the chicane works as a high-energy scraper system [JBB+16]. With this scraper it is possible to obtain an halo-free beam with an energy spread $\delta E/E$ better than $2 \cdot 10^{-4}$ [Pie18]. This high quality beam is then guided to one of the three experimental setups in the experimental hall, namely the NEPTUN setup, the QCLAM setup or the LINTOTT magnet spectrometer. Thereby, the beam can be guided via two different beam lines towards the QCLAM setup. One possibility is to use a straight beam line for common scattering experiments with scattering angles between 25° and 155° [Kni91]. The other possibility is to bend the beam through a chicane which allows to perform 180° scattering experiments at the QCLAM spectrometer. Possible energies at the QCLAM spectrometer are 10 to 130 MeV while the current is typically in the range of several µA. The QCLAM spectrometer is explained in the next chapter. This section was orientated by [Pie18].

10.2 The QCLAM Spectrometer

The electron scattering experiment on ^{14}C will be performed at the Quadrupol CLAMshell (QCLAM) spectrometer. The QCLAM was built in 1991 by M. Knirsch [Kni91]. The QCLAM is a large acceptance magnetic spectrometer. It consists of one quadrupole magnet at the entrance and a large bending dipole magnet placed behind the quadrupole. With the quadrupole magnet it is possible to achieve a large horizontal and vertical opening angle of around ±100 mrad, which

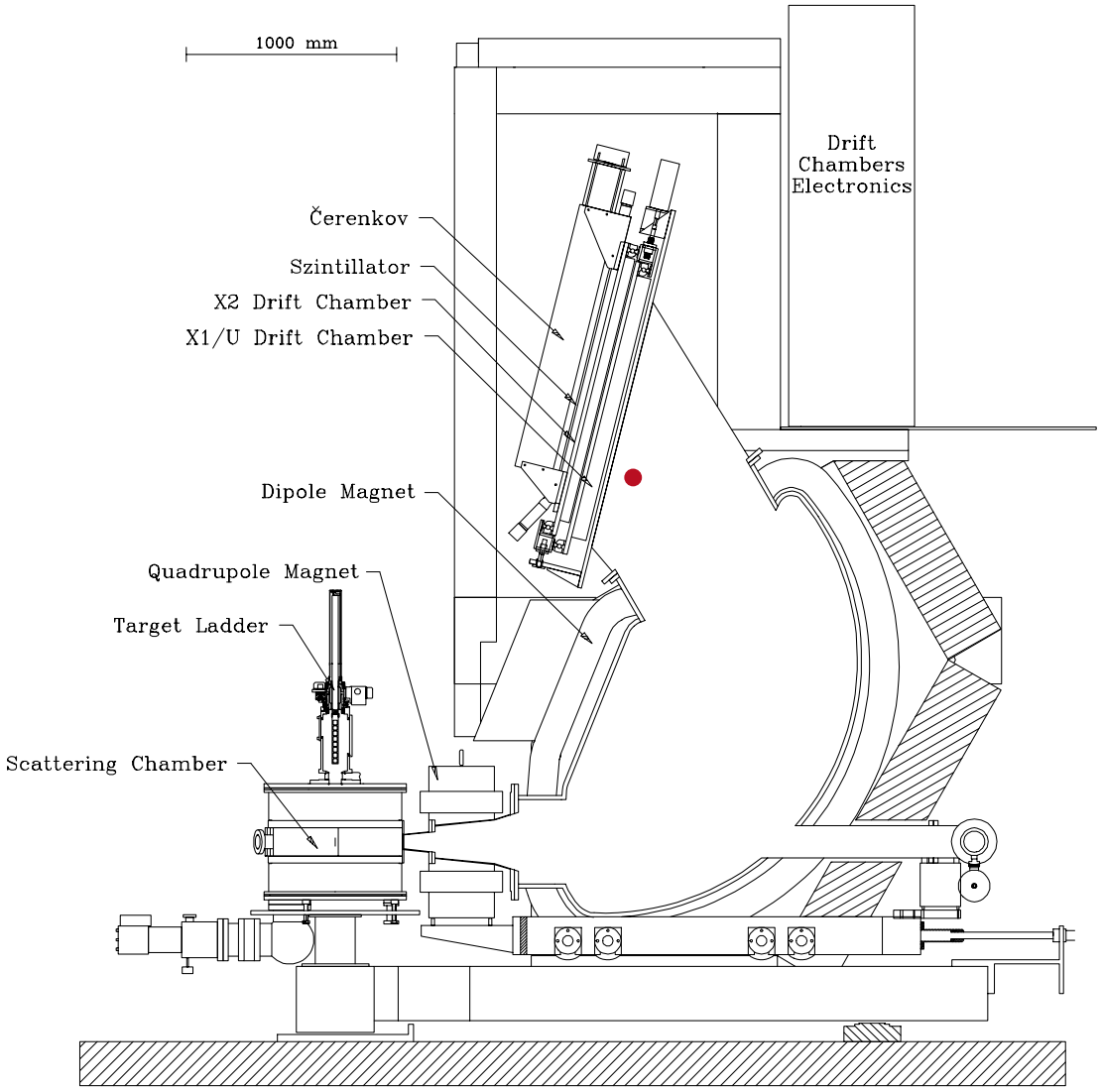

Figure 10.2: Profile of the QCLAM spectrometer given in the plane of symmetry. The red dot indicates the position of two piezoelectric sensors, which are used to measure a possible air shock wave. The figure was modified and taken from [Rei00].

corresponds to a solid angle acceptance of 35 msr. At the same time the momentum acceptance is given by ±10 %.

The profile of the QCLAM is illustrated in Figure 10.2. The electrons coming from the S-DALINAC are hitting the target in the center of the scattering chamber. Most of the electrons will pass the thin targets and be dumped in the Faraday cup. But a small fraction of the electrons will be scattered towards the spectrometer. All electrons which fulfill the solid angle acceptance conditions enter the QCLAM at the quadrupole magnet. The quadrupole magnet focuses the electrons in the horizontal plane before they enter the dipole magnet. In the dipole magnet the electrons are bent. Here the radius of the trajectory of the electrons depends on the momentum of the electrons and thus their kinetic energy. On top of the vacuum chamber of the QCLAM the focal plane is located. It is tilted by 37.97°. Here, the position of the electrons

corresponds to the different kinetic energies the electrons have. Hence, by measuring the position of the electrons one gets the energy the electrons had. But due to the large acceptance of the QCLAM the focal plane is not perfectly planar. It is better described by a focal sphere. To correct for this, it is not sufficient enough to measure the position of the electron. In fact, it is necessary to reconstruct the trajectory the electrons had in the spectrometer. For this, a more complex detector system is used which consists of four different detectors.

The detector system, also shown in Figure 10.2, was firstly designed by K.-D. Hummel [Hum92] and later improved by J. Horn [Hor97] as well as B. Reitz [Rei00]. The scintillator detector is used as a trigger while the Čerenkov detector is used to suppress the background. The two drift chambers are used to measure the position of the electrons and the direction of the momentum vector of the electrons. With this information it is possible to reconstruct the trajectory of the electrons. With the projection of the trajectory into the focal plane one then has the possibility to reconstruct the energy of the scattered electrons. The drift chambers are sensitive detectors which can not be placed inside a vacuum. Due to this reason, the drift chambers are located outside of the vacuum chamber of the QCLAM spectrometer. To seal the QCLAM vacuum chamber against the atmosphere while electrons can still pass the sealing, a thin Mylar foil is mounted at the end of the vacuum chamber. The thickness of the Mylar foil is in the range of 50 μm. Concerning the ^{14}C experiment the worst case would be the breaking of this foil. If this foil rips apart, as happened in the past, a strong air shock wave will enter the QCLAM vacuum system driven by 1 bar pressure difference. By assuming that the shock wave travels by the speed of sound it needs around 7 ms to reach the scattering chamber (cf. Sec. 11.6). It is one of the main challenges to protect the fragile ^{14}C target against a possible shock wave coming from top of the QCLAM. To register such a shock wave additional piezoelectric sensors will be mounted on top of the QCLAM vacuum chamber. The position is marked in Figure 10.2 by the red dot (cf. Sec. 11.4 and Sec. 11.6).

Furthermore, it should be mentioned that at the moment also huge upgrades are ongoing at the QCLAM spectrometer. Under the work of M. Singer [Sin20] the complete electronics are updated to take much larger data rates, which is especially necessary for coincidence experiments. First commissioning runs in 2018 and 2019 were promising. Also a (e,e'γ) coincidence measurement on ^{12}C was successful. In the work from A. D'Alessio new drift chambers for the QCLAM spectrometer will be designed and constructed [D'A20].

11 Carbon-14 Target and New Experimental Setup

In this chapter, the ^{14}C target and a possible energy deposition in the target are described. Then the new experimental setup which is used for the ^{14}C experiment is introduced. At the end, some useful and important estimations concerning the ^{14}C experiment are done.

11.1 Description of the Carbon-14 Target

The ^{14}C target is an item on loan from the ANL. A picture and a schematic side-view of the ^{14}C target can be seen in Figure 11.1. The target is mounted inside an aluminium frame. The frame is shaped rectangular and has a side length of several centimetres. In the center of the frame, a pressed-powdered disc is placed. The disc is composed of ≈54.9 mg of ^{14}C plus 10 mg of polyethylene which serves as a binder. The specific activity of the ^{14}C powder disc is 3.69 mCi/mg=146 GBq/mg. Hence, the total activity of the target sums up to 217.3 mCi=8 TBq. The ^{14}C decays via a β^- decay. There the end-point energy is 156.5 keV, while the mean beta energy is 49.5 keV [AS91b]. The range of this radiation is a few centimetres in air, which is quite short but the total activity is large. Hence, methods have to be applied that one can deal with the target without irradiating body parts i.e. the hands.

The ^{14}C disc has a diameter of ≈0.95 cm. This means that the target thickness is given by 77.45 $\mathrm{mg/cm^2}$ or in other terms by 0.34 mm, if the polyethylene is neglected and the density of the ^{14}C is assumed to be 2.26 $\mathrm{g/cm^3}$. The ^{14}C pressed-powdered disc is trapped between two rings of 19-mm-OD polystyrene with a thickness of 0.5 mm. Window foils are placed in the front and the back of the ^{14}C pressed-powered disc to seal it. The window foils consist of Mylar films (biaxially-oriented polyethylene terephthalate) with a thickness of 0.127 mm which are coated with ≈40 nm of gold. There are three such window foils on both sides, the front and the back side, of the ^{14}C pressed-powered disc. Additionally, a glass frit is placed in one corner of the aluminium frame. It has an internal passageway towards the ^{14}C disc. With this it is possible to achieve a pressure equalisation on both sides of the Mylar windows without rupturing them if the environment of the target is pumped or vented. Furthermore, a mock target is available, which has exactly the same structure as the ^{14}C target but comes without ^{14}C powder inside. This target can be used for background measurements. All these facts are taken from [Edw08]. Later performed wipe tests showed that the ^{14}C target is also contaminated on the outside. This enlarges the safety measures, which have to be carried out to perform the experiment.

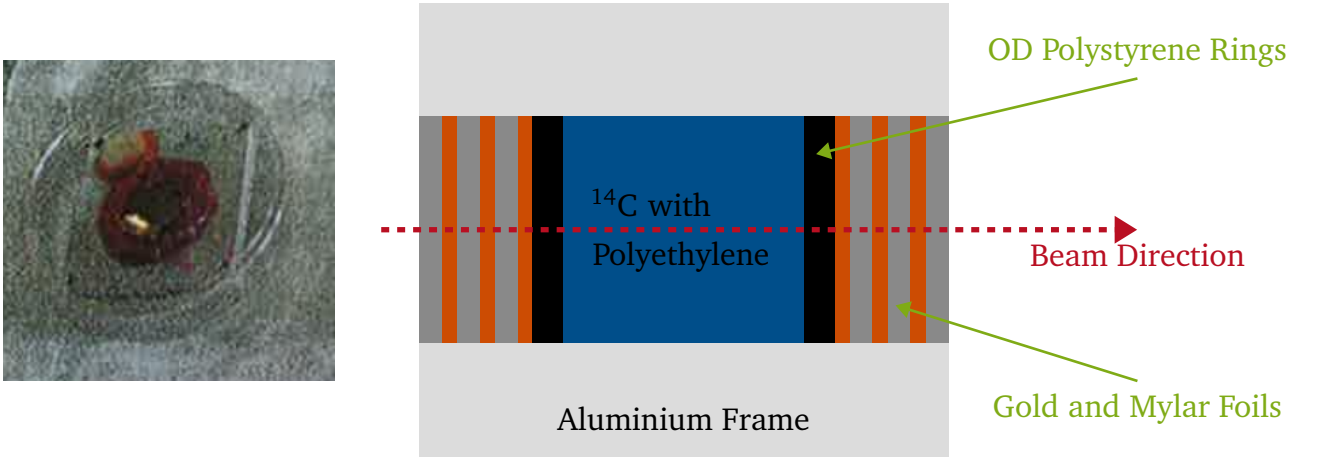

Figure 11.1: A picture (left) and a schematic profile (right) of the ^{14}C target. In the left picture, the target is placed in a Petri dish with a diameter of 60 mm [Edw08].

11.2 Requirements for the new Experimental Setup

For the ^{14}C electron scattering experiment several requirements arise for the new setup and especially for the new scattering chamber which is designed in this thesis. Some account for experimental reasons while the most requirements stem from the fact that the target is highly radioactive. The most important requirements are listed in the following:

- The new scattering chamber should cover as much different scattering angles as possible to cover a large range of q values for a given beam energy.
- The new scattering chamber has to fit to the existing mounting system of QCLAM.
- The lid of the new scattering chamber should be designed in such a way that it is possible to mount the existing target ladder as well as a new one which is constructed for this experiment.
- The distance between the adapter of QCLAM and the center of the new scattering chamber has to be the same distance which is given by the existing system. With this requirement it is ensured that the center of the new scattering chamber is at the pivot point of the QCLAM.
- A new target ladder has to be designed for which it is easy to mount the ^{14}C target fast. For this, one has to take into account that the target is highly radioactive. This means that it should be possible to mount the target without placing parts of the human body, e.g. hands, too close to the target.
- During the experiments some energy will be deposited inside the target. Therefore, it has to be checked how much energy is deposited in the target and the Mylar foils. If the induced temperature rise is too large a cooling system has to be installed.

- It should be possible to seal the target off from the scattering chamber while the target is (dis)mounted in the target chamber. Thus, it should be possible to seal the connection between the scattering and the target chamber.

- It should be possible to separate the target from the scattering chamber, if the scattering angle of the QCLAM is changed. While the scattering angle is changed, the scattering chamber has to be vented and afterwards pumped again. By shutting the target off from the scattering chamber during this process, it is made sure that the atmosphere around the target is not unnecessarily vented and pumped over and over again. Every venting and pumping process is a potential danger for the target.

- It should be possible to seal the target off from the rest of the vacuum setup while it is inside the scattering chamber. Hence, it should be possible to seal the connection between the scattering chamber and all other parts of the vacuum system (Connection to accelerator, Faraday cup and QCLAM).

- It should be possible to evacuate the atmosphere around the target in a very slowly and controlled way. For this, it is foreseen to pump or vent the target chamber separately via needle valves.

- If the Mylar foil at the top of the QCLAM rips apart, there has to be the possibility to detect the air shock wave which is expanding in the vacuum system. Therefore, a pressure sensor has to be installed on top of the QCLAM. The sensor should not be effected by magnetic fields since at this position the magnetic field of QCLAM's dipole magnet is present.

- If the Mylar foil at the top of the QCLAM rips apart there has to be a possibility to seal the scattering chamber off from the rest of the vacuum system. Especially, the QCLAM and the beam line to the accelerator should be sealed off in the microsecond range. For this, fast closing valves are needed at all main ports of the scattering chamber.

- The new scattering chamber has to have a smaller radius than the existing one. This is necessary to place a fast closing valve between the scattering chamber and the QCLAM. The connection between the new scattering chamber and the QCLAM should be design in a way to lose as less solid angle as possible.

- The air which is pumped out of the vacuum system, should be filtered so that no ^{14}C particles are blown into the experimental hall when the ^{14}C target gets damaged somehow. The filters should sit before the fore-vacuum pumps to prevent a possible contamination of them.

- It should be possible to have eye-contact to the ^{14}C target whether it is placed inside the scattering chamber or the target chamber. Hence, both chambers need window flanges.

11.3 Deposited Energy in the Target

A crucial property of the experiment, which has to be checked, is the energy deposition in the target. If too much energy is deposited in the target, than the temperature rise in the target may get into a critical region, in which the target can be damaged. Following [Leo87] two processes are responsible for the energy-loss of electrons in matter: One process is the collision of the electrons with electrons of atoms in the matter. The other process is the so-called Bremsstrahlung. Here the electrons are deflected in the electrical field of the nuclei in the matter. As a consequence of this, the electrons emit some electromagnetic radiation and lose the energy which was converted to the electromagnetic radiation. This part is also called radiation loss. The critical energy E_c at which both effects have roughly the same influence, is reached if the condition

$$E_c \approx \frac{1600 m_e c^2}{Z} \tag{11.1}$$

is fulfilled [Leo87]. For ^{14}C this is the case at $E_c \approx 136$ MeV. If for the first approximation the beam energy is assumed to be $E_{kin} = 100$ MeV, none of the two effects can be neglected. Hence, both effects have to be calculated for all materials which are located in the beam axis.

For the collision part the Bethe-Bloch formalisms can be used [Bet30, Bet32, Blo33]. The Bethe-Bloch formalism was derived for the energy-loss of heavy particles in matter. It describes the collision between incoming heavy particles and the atom electrons in matter. For electrons the equation has to be adjusted due to two reasons. First, the electrons are light compared to heavy particles. Hence, a deflection of the electrons after the collision has to be taken into account. Secondly, if an electron scatters on an electron the indistinguishability of both particles has to be considered in the equation. This leads to

$$-\left(\frac{dE}{dx}\right)_{coll} = 2\pi N_a r_e^2 m_e c^2 \rho \frac{Z}{A}\frac{1}{\beta^2}\left[\ln\frac{\tau^2(\tau+2)}{2(I/m_e c^2)^2} + F(\tau) - \delta - 2\frac{C}{Z}\right] \tag{11.2}$$

for the collision energy-loss [Leo87]. In this equation N_a is the Avogadro constant, r_e is the classical electron radius, m_e is the electron mass, c is the velocity of light, ρ is the density of the absorbing material, Z is the atomic number of absorbing material, A is the atomic weight of the absorbing material, τ is the kinetic energy of the electron in units of $m_e c^2$, I is the mean excitation potential of the absorbing material, δ is the density correction parameter, and C is the shell correction parameter. For electrons the function $F(\tau)$ is given by

$$F(\tau) = 1 - \beta^2 + \frac{\tau^2/8 - (2\tau+1)\ln 2}{(\tau+1)^2}. \tag{11.3}$$

The radiation part describes the energy loss due to deflection of the electrons in the electric fields of the nuclei in the matter. For this process the energy-loss can be expressed via

$$-\left(\frac{dE}{dx}\right)_{rad} = N\int_0^{\nu_0} h\nu \frac{d\sigma}{d\nu}(E_0, \nu)\,d\nu, \tag{11.4}$$

where N is the number of atoms per cubic centimetre ($N = \rho N_a / A$), h is the Planck constant, ν is the frequency of the emitted photon, and $\mathrm{d}\sigma/\mathrm{d}\nu$ is the differential cross section for the radiation of a photon with a given frequency ν. E_0 is the maximum possible energy, which is given by the incoming beam energy. With this, the maximal possible frequency ν_0 is expressed via $\nu_0 = E_0/h$. For relativistic kinetic energies greater than a few MeV, the cross section can be calculated by

$$\mathrm{d}\sigma = 4Z^2 r_e^2 \alpha \frac{\mathrm{d}\nu}{\nu} \left\{ (1+e^2) \left[\frac{\Phi_1(\xi)}{4} - \frac{1}{3}\ln Z - f(Z) \right] - \frac{2}{3} e \left[\frac{\Phi_2(\xi)}{4} - \frac{1}{3}\ln Z - f(Z) \right] \right\}, \quad (11.5)$$

with $\alpha = e^2/4\pi\epsilon_0\hbar c$ (fine-structure constant)[Leo87, KM59]. Because the Bremsstrahlung emission depends a lot on the electric field the electron feels from the nuclei, the amount of screening from the atomic electrons around these nuclei has to be taken into account. In Equation 11.5 this is considered with the screening functions $\Phi_1(\xi)$ and $\Phi_2(\xi)$. For these functions only empirical equations can be given in first approximation. They are expressed in terms of the screening factor

$$\xi = \frac{100 m_e c^2 h \nu}{E_0 E Z^{1/3}}, \quad (11.6)$$

where E is the final total energy of the electron. This factor is derived from the radius of an atom in the Thomas-Fermi model. If ξ is zero, then the electric field of the nucleus is screened completely by the atom electrons. If ξ is much larger than one, then no screening effect occurs. A possible parametrisation of the screening functions is for example given by

$$\Phi_1(\xi) = 20.863 - 2\ln[1 + (0.55856\xi)^2] - 4[1 - 0.6\exp(-0.9\xi) - 0.4\exp(-1.5\xi)] \quad (11.7)$$

$$\Phi_2(\xi) = \Phi_1(\xi) - \frac{2}{3}(1 + 6.5\xi + 6\xi^2)^{-1} \quad (11.8)$$

which has an accuracy of about 0.5 % [Leo87, Tsa74]. The function $f(z)$ in Equation 11.5 is a small correction of the Born approximation. Empirical representations of this function can be found e.g. in [Leo87, DBM54].

The energy-loss is calculated using the ESTAR code [EST19, BCZC17]. For the collision energy-loss it uses the here given Bethe-Bloch formalism with density corrections according to Sternheimer et al. [Ste52, SSB82]. The values for the mean excitation potential I are taken from the ICRU Report 37 [BIA+16]. The Bremsstrahlung part is calculated with theoretical cross section calculations from Seltzer and Berger [SB85].

The results for the energy-loss are listed in Table 11.1. It was assumed that an electron beam with a kinetic energy of 100 MeV hits the target. Then the beam passes the different layers as shown in Figure 11.1 (cf. Sec. 11.1). Because it could not be clearly figured out if parts of the 19-mm-OD polystyrene ring interfere with the beam line, it is assumed that the beam has to pass the whole thickness of the rings two times. The thicknesses of each layer are given by

Table 11.1: Energy-loss for a 100 MeV electron beam hitting the ^{14}C target. The thicknesses of each layer are given by 17.526 $^{mg}/_{cm^2}$ for one Mylar foil, 0.077 $^{mg}/_{cm^2}$ for one gold coating, 52.5 $^{mg}/_{cm^2}$ for one polystyrene ring and 77.45 $^{mg}/_{cm^2}$ for the ^{14}C disc. The beam current was assumed to be 2 μA.

Material	Incident Energy in MeV	Stopping Power Collision in MeV cm^2/g	Stopping Power Radiation in MeV cm^2/g	Stopping Power Total in MeV cm^2/g	Energy Loss Collision in J/s	Energy Loss Radiation in J/s	Energy Loss Total in J/s
Gold	100.00	1.413E+00	1.416E+01	1.557E+01	0.0002	0.0022	0.0024
Mylar	100.00	2.043E+00	2.191E+00	4.235E+00	0.0716	0.0768	0.1485
Gold	99.92	1.413E+00	1.415E+01	1.556E+01	0.0002	0.0022	0.0024
Mylar	99.92	2.043E+00	2.190E+00	4.233E+00	0.0716	0.0768	0.1484
Gold	99.85	1.413E+00	1.414E+01	1.555E+01	0.0002	0.0022	0.0024
Mylar	99.85	2.043E+00	2.188E+00	4.231E+00	0.0716	0.0767	0.1483
Polystyrene	99.77	2.132E+00	1.983E+00	4.115E+00	0.2239	0.2082	0.4321
^{14}C	99.56	1.937E+00	2.036E+00	3.974E+00	**0.3001**	**0.3154**	**0.6156**
Polystyrene	99.25	2.131E+00	1.972E+00	4.103E+00	0.2238	0.2071	0.4309
Mylar	99.03	2.043E+00	2.169E+00	4.211E+00	0.0716	0.0760	0.1476
Gold	99.03	1.412E+00	1.402E+01	1.543E+01	0.0002	0.0022	0.0024
Mylar	98.96	2.043E+00	2.167E+00	4.209E+00	0.0716	0.0760	0.1476
Gold	98.96	1.412E+00	1.401E+01	1.542E+01	0.0002	0.0022	0.0024
Mylar	98.88	2.043E+00	2.165E+00	4.208E+00	0.0716	0.0759	0.1475
Gold	98.88	1.412E+00	1.399E+01	1.541E+01	0.0002	0.0022	0.0024
Sum					**1.179**	**1.202**	**2.381**

17.526 $^{mg}/_{cm^2}$ for one Mylar foil, 0.077 $^{mg}/_{cm^2}$ for one gold coating, 52.5 $^{mg}/_{cm^2}$ for one polystyrene ring and 77.45 $^{mg}/_{cm^2}$ for the ^{14}C disc. In the left part of Table 11.1 the stopping power, which means the energy loss per cm^2/g, for each layer is given. There, the total value is listed as well as its collisions and radiation ratio. In the right part of the table the energy-loss is given for an electron beam with an incident energy of 100 MeV and a beam current of 2 μA. That is an upper limit which can be delivered from the S-DALINAC to the QCLAM. A 2 μA beam corresponds to $1.248 \cdot 10^{13}$ electrons per second. In Table 11.1 it can be seen that the total energy loss in the complete target device sums up to 2.381 J/s. Thereof 1.179 J/s stem from the collision energy-loss and 1.202 J/s stem from the radiation energy-loss. The energy loss scales are linear with respect to the beam current. For further planning the energy loss can just be scaled accordingly.

For the energy-loss due to collision the whole energy will be deposited inside the material. In Table 11.1 it can be seen that for the ^{14}C disc the ratio of energy loss due to collision and due to radiation is more or less the same. For the energy loss due to radiation, not all energy has to be deposited in the material, because it can irradiate out of the target. But for an upper limit it is assumed that also the whole radiated energy is absorbed by the surrounding material. Then the total energy deposition in the ^{14}C disc is given by 0.6156 J/s for the 100 MeV at 2 μA beam. Assuming that the effective heat capacity for the ^{14}C disc is 709 J/(Kg·K), the ^{14}C disc underlies a maximum temperature rise of 15.8 K/s. It seems that it should be thought about cooling possibilities for the target to prevent damage. A solution for this problem is not yet adduced.

For comparison, the temperature rise in a Mylar foil is calculated next. The largest energy deposit arises in the first Mylar foil with 0.1485 J/s. The effective heat capacity depends on the exact type of Mylar foil but as a first approximation the value 1171.52 J/(Kg·K) can be chosen [Fil19]. The mass of the Mylar foil is roughly given by $17.526\,^{mg}/_{cm^2} \cdot \pi(0.95\,\text{cm})^2 = 49.691$ mg. Then the maximum temperature rise for the Mylar foil is calculated to be 2.6 K/s.

11.4 New Experimental Setup

For the ^{14}C experiment, a new vacuum setup has to be installed at the QCLAM. It includes a new scattering chamber, a new target chamber with target ladder, fast closing valves and piezoelectric sensors to trigger them. The new target chamber and target ladder will be explained in Section 11.5. The whole setup has to fulfill four main purposes. First of all, and quite obviously, it has to fit to the existing vacuum and mounting system of the QCLAM. Secondly, it should be possible to seal the new scattering chamber and the target chamber and thus the target off from the rest of the vacuum system. This should enable the possibility to vent or pump the surrounding volume of the target, while the target is separated from other parts of the vacuum system. Additionally, there should be the possibility to vent and pump the surrounding volume of the target very slowly and in a very controlled way to prevent damage at the sealing foils of the target. Finally,

there should be the possibility to separate the target from the remaining vacuum system fast if the foil at the top of the QCLAM rips apart (cf. Sec. 10.2). In this context, fast means in the order of a few milliseconds.

The system which comes as a result of this thesis, fulfills all of the above mentioned criteria. First, the overall vacuum system of the QCLAM is discussed. The vacuum system as it can be used for the ^{14}C experiment is sketched in Figure 11.2. In the orange coloured pipes fore-vacuum ($\approx 10^{-1}$-10^{-3} mbar) is present, while in the blue coloured pipes high-vacuum ($\approx 10^{-5}$-10^{-6} mbar) is present. The scattering chamber has vacuum connections to the accelerator, to the Faraday cup, to the QCLAM, to the fore-vacuum pipes, and to the target chamber. The target camber is not shown in the plan, because it sits on top of the scattering chamber. The target chamber can store the complete target ladder and thus the target. It can be connected to a mobile pumping unit to vent and pump the target chamber separately. It can be separated from the rest of the vacuum system by a manually operated valve labelled with "G". All the valves except the fast closing valves and valve "G" are already existing and installed. The fast closing valves have been bought newly by *VAT* [Dre17]. They are pneumatically closing and will be installed with DN40 CF flanges. Their mechanical closing time is stated and tested by the company to be 9 ms, while the electronics need up to 2 ms to process the signal. The fast valves are marked black in the figure. Fast valve 1 is placed as far as possible towards the accelerator so that the time till a possible shock wave coming from QCLAM hits the valve is maximised. The valve is placed 2.4 m upstream from the scattering chamber. Assuming the shock wave travels with the speed of sound, this gains additional 7 ms until the shock wave hits the fast valve 1. Assuming further that the shock wave needs 7 ms towards the scattering chamber (cf. Sec. 10.2 and Sec. 11.6), the total time till the shock wave hits the fast valve 1 is 14 ms (neglecting the time the wave needs to expand inside the scattering chamber). Fast valve 2 is placed between the QCLAM and the new scattering chamber. It should prevent most of the shock wave to enter the target chamber (cf. Sec. 11.6). Fast valve 3 is located downstream towards the Faraday cup to prevent a possible contamination of it. While the whole setup is pumped or vent, all three fast valves can be closed remotely to seal the scattering chamber off from the remaining vacuum system of the facility. If the foil on top of the QCLAM rips apart piezoelectric sensors which are mounted at top of the QCLAM vacuum chamber trigger the fast valves. The position of the sensors is marked in Figure 10.2. To install them an additional DN40 CF flange was welded on the side of the QCLAM vacuum chamber. The sensors are positioned as close as possible to the foil. The reaction time of a piezoelectric sensor is in the range of µs (rise time of the signal 1 µs). Two piezoelectric sensors with the serial number *113B28* manufactured by *PCB Synotech* [Hü17] are used. The sensitivity of the sensors is about 14.5 mV/kPa. If a shock wave stemming from a breaking foil hits the sensors, the pressure rises by 101 kPa and the signal rises by 1.47 V. Setting a threshold e.g. around 0.5 V it is possible to create a 24 V trigger signal, which is sent to the control unit of the fast closing valves. Then all three fast valves are closed. Two piezoelectric sensors are used

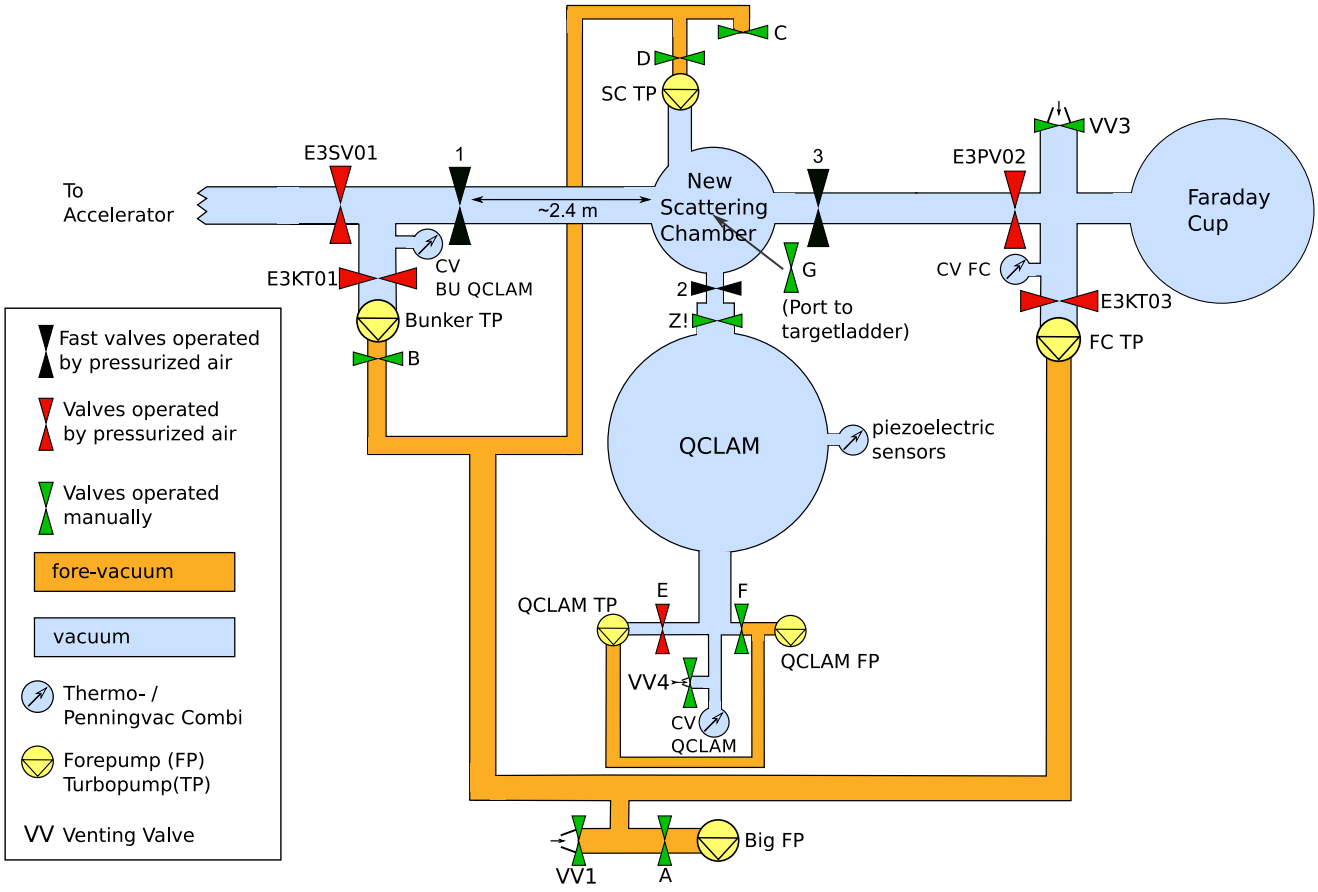

Figure 11.2: Sketch of the QCLAM vacuum system. The scattering chamber and the fast closing valves (shown in black) are new for the ^{14}C experiment. The other shown parts represent the already existing vacuum system.

for redundancy. As soon as one piezoelectric sensor registers a signal the trigger should be send towards the valves.

CAD sketches of the new scattering chamber can be seen in Figure 11.3. The dimension of the ground plate, the height of the beam axis, and the distance between the center of the chamber and the connection to the QCLAM (327 mm, cf. drawings in Sec. B.1) are orientated by the existing scattering chamber designed by M. Kuss [Kus90]. This ensures on the one hand that the scattering chamber can be simply installed on the existing mounting port. On the other hand it is ensured that the target sits in the pivot point of the spectrometer which is important for the imaging properties of the spectrometer.

On the side which faces the QCLAM five ports are installed at the height of the beam axis. This allows to connect the QCLAM to five different scattering angles, namely 38°, 66°, 95°, 123°, and 152°. These ports can be sealed with blind flanges and o-ring sealings (for the dimensions cf. drawings in Sec. B.1). On one port, the connection to the QCLAM is mounted. Between the port and the existing port at the QCLAM the fast valve 2 (cf. Fig. 11.2) can be placed. It is connected to the two ports via two adapters.

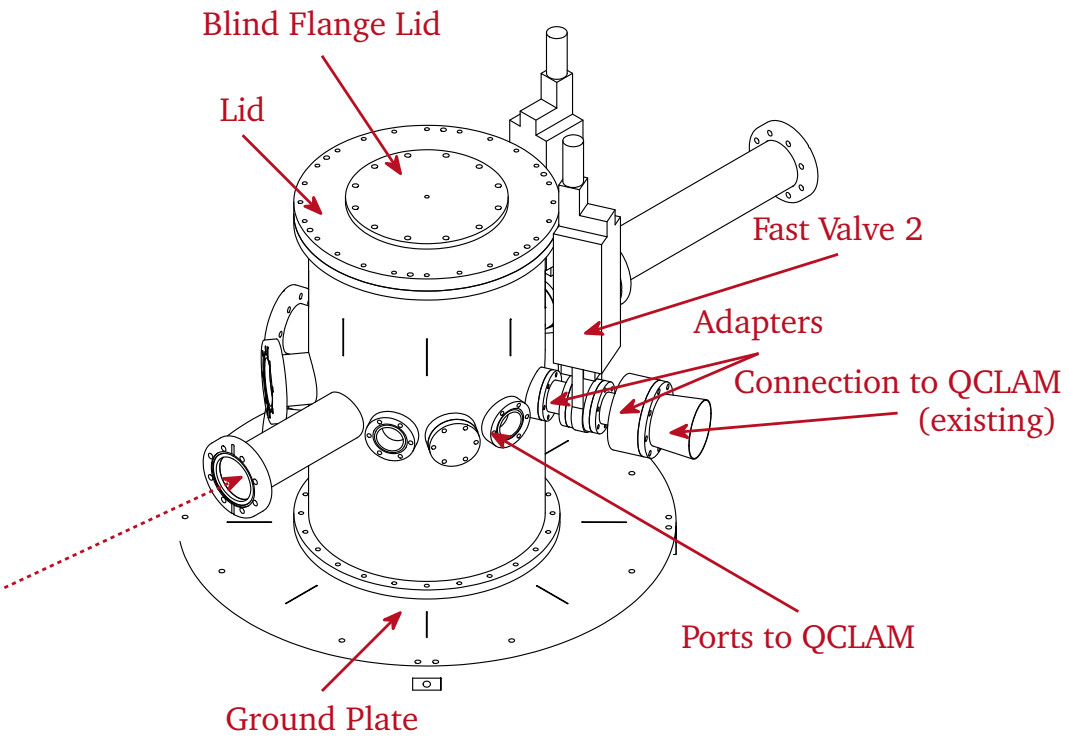

(a) View 1

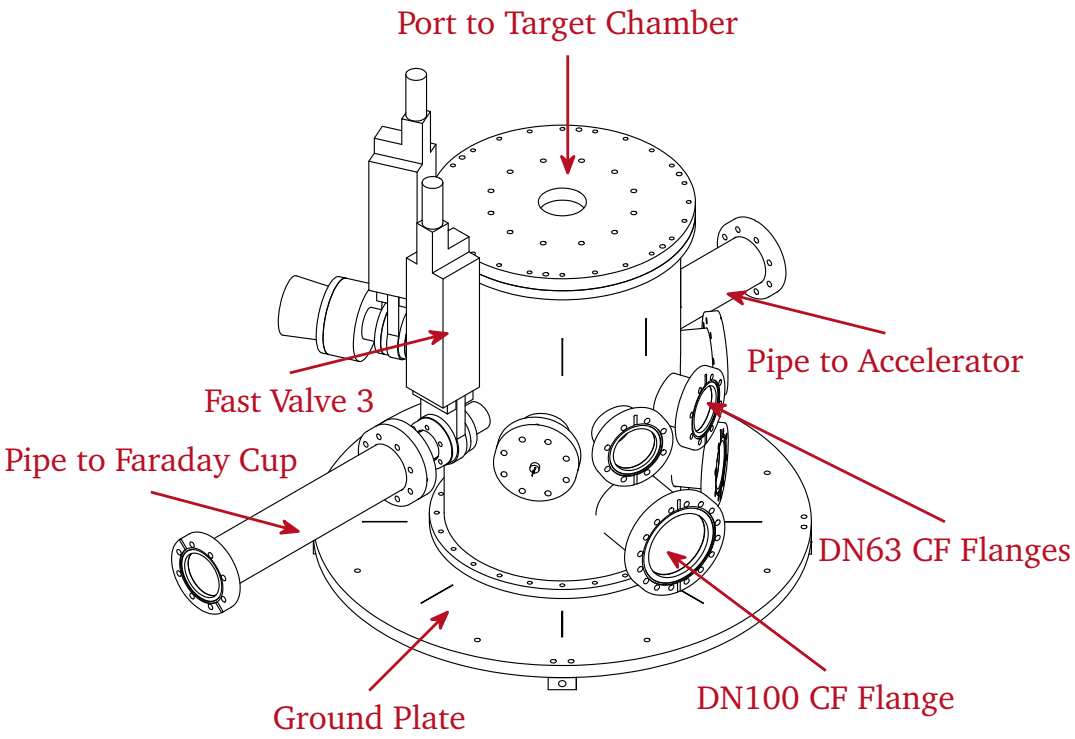

(b) View 2

Figure 11.3: CAD sketches of the new scattering chamber. View 2 is rotated by 180° compared to view 1 around the pivot point of the scattering chamber, which is also the pivot point of the QCLAM. The red dashed arrow indicates the beam axis and its direction. The dimensions of all parts can be found in Section B.1.

On the side which does not face the QCLAM, five DN63 CF flanges and one DN100 CF flange are installed. The DN100 CF flange can be used to install a turbopump. The DN63 CF flanges are for different purposes. Here pressure sensors, window flanges and an electrical feedthrough to power a light source insight the chamber can be mounted.

The lid of the scattering chamber is also sealed to the chamber by o-ring sealings (for the dimensions cf. drawings in Sec. B.1). The lid can be closed with a blind flange or the port on top of the lid can be used to install a target chamber. The port is designed in a way that the existing target chamber can be mounted as well as the new one, which is explained in Section 11.5. Along the beam axis two pipes with DN63 CF flanges are installed, which can be connected to the existing vacuum setup of the QCLAM. Between the chamber and the beam pipe towards the Faraday cup the fast valve 3 (cf. Fig. 11.2) is placed.

The scattering chamber is already built, tested and ready to use. All dimensions can be found in the technical drawings of the scattering chamber, which are presented in the Appendix in Section B.1.

11.5 Target Chamber and Target Ladder

A CAD sketch of the target chamber mounted on top of the scattering chamber can be seen in Figure 11.4. The target chamber can store the complete target ladder and thus the target. The target chamber will be mounted on top of the lid of the scattering chamber. Between the target chamber and the lid of the scattering chamber a DN100 CF manual vent can be placed (valve “G” in Fig. 11.2). With this, it is possible to seal the target off from the rest of the vacuum setup if the target ladder is moved upwards as far as possible. During maintenance work, the target ladder can be moved upwards and then the target is separated from the remaining setup using valve “G”. This should always be done if the scattering has to be vented or pumped (for example if the scattering angle of QCLAM is changed). This improves the safety concerning unwanted contamination of the setup. The target chamber itself is a rectangular box made from aluminium to spare weight. It has a removable door, which is sealed by an o-ring sealing (for the dimensions cf. drawings in Sec. B.2). The door is made from stainless steal and two flanges are welded onto it. One is a DN63 CF flange which is used to install a window flange to always have visible access to the target. The other one is a DN25 KF flange. This flange will be connected to a needle valve and a mobile pumping unit. With this setup, it is possible to vent and pump the target chamber slowly and controlled while it is sealed off from the scattering chamber and thus from the remaining vacuum setup. On top of the target chamber, a port to a DN40 CF flange is installed. On this flange it is possible to mount a linear and rotational feedthrough. For this mechanical feedthrough for example the model *LD40-700 S2+PD40-700 S2* from *Vakuum Anlagenbau* [Elm18] can be used. A sketch of this model can be found in the Appendix B.2. To this device the target ladder will be mounted. Then it is possible to move the target ladder up and down and rotate the target as wanted by using a stepping motor.

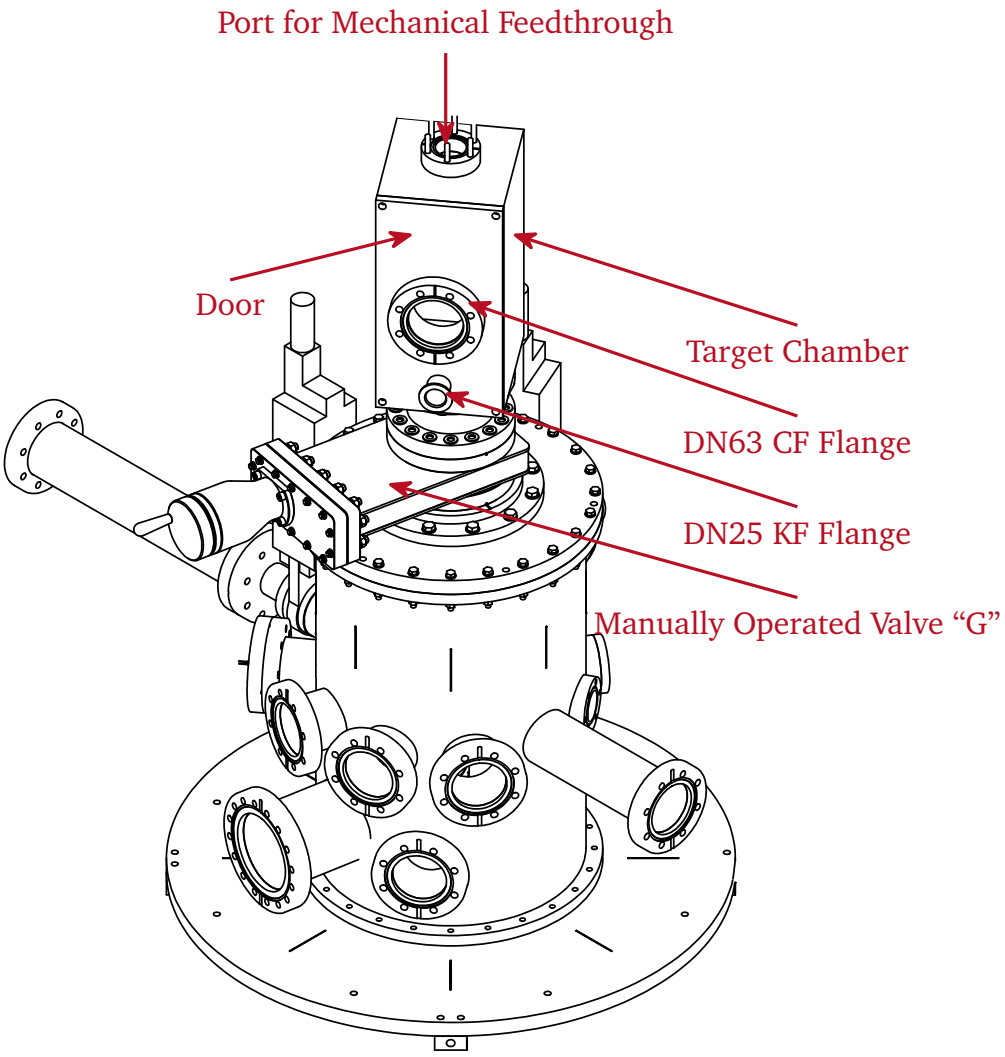

Figure 11.4: CAD sketch of the new target chamber placed on top of the new scattering chamber (cf. Fig. 11.3). The dimensions of all parts can be found in Section B.2.

The target chamber is not built yet but all technical drawings, which can be found in the Appendix B.2, are finished.

11.6 Possible Air Inrush Volume

In this section, the effects of a possible air inrush coming from top of the QCLAM are discussed. As explained before in the worst case the foil on top of the QCLAM can rip apart. Then an air shock wave with 1 bar pressure difference will expand into to vacuum chamber of QCLAM. This shock wave will then travel further into the scattering chamber and all the other connected vacuum parts. To prevent this, the fast valves (cf. Sec. 11.4) are used. As mentioned before, the electronic processing time of the fast valves is up to 2 ms, while the total mechanical closing time is 9 ms. Hence, the complete closing time is 11 ms. This is not enough time for the fast valve 2 to be closed completely before the shock wave appears at the scattering chamber entrance.

Looking at Figure A.7 the profile of QCLAM is shown. The dimensions are given in millimetres and taken from the original construction drawings. To get the time the shock wave needs to reach the fast valve 2 the expansion of the air inside the QCLAM vacuum chamber has to be understood. This is a complex process which could only be taken fully into account if simulations are carried out. But for first approximations a few simple assumptions are made to get a range limit for the travelling time, which should be realistic. Figure A.8 shows the shortest distance the air can travel from the foil to the entry of the scattering chamber. The way is 2097 mm long which is covered after 6.1 ms if the air expands with the speed of sound. Hence, 6.1 ms is the shortest time after a part of the shock wave passes fast valve 2. By assuming a shock wave, which is driven by a 1 bar pressure difference travelling with the speed of sound, the way sketched in Figure A.8 seems very unrealistic. It is more likely that the main part of the shock wave first travels along a straight line into the vacuum chamber of the QCLAM. Due to these reasons, two other possible travelling paths are also calculated. Figure A.9 shows one of the longest paths one can imagine. Here it is assumed that the main part of the shock wave expands in the same way as a light ray would do. It travels along a straight line until it gets reflected at the inner surface of the vacuum chamber. This leads to a path length of 3509 mm which corresponds to a travelling time of 10.2 ms. This path should give an upper limit how long it will take until the shock wave arrives. Finally, Figure A.10 shows a compromise between the two paths mentioned before. Here the length of the path is 2608 mm which corresponds to a travelling time of 7.6 ms.

As a summary of these estimations, one can conclude that the shock wave will not arrive earlier than 6.1 ms, while the main part of the shock waves reaches the fast valve 2 after around 7 ms but not later than 10 ms. Let's assume the earliest time at which a significant amount of the air reaches the fast valve is given by t_{min}=7 ms. Because fast valve 2 needs about 11 ms to close after the trigger signal was measured by the piezoelectric sensors two important questions arise:

1. How much air gets into the scattering chamber while the fast valve 2 is still closing?

2. Is it possible that some air is reflected from the scattering chamber wall so that it gets back into QCLAM?

To answer these questions some calculations are done in the following. All calculations underline the same assumptions: The air always travels at the speed of sound with v_s=343.2 m/s. The volume of the new scattering chamber without any pipes or connections (assume perfect cylinder) is given by V_C=34.6 l. The diameter of the aperture of the fast valves (DN40) is D=40 mm. The total mechanical closing time of the fast valves is measured and certificated by *VAT* to be t_C=9 ms. Thereby, it is estimated by *VAT* that the valve needs t_S=3 ms before it starts to move after it received the signal. The expected processing time of the valve electronics is about 1 ms-2 ms. The maximum value should be smaller than 2 ms. The processing time for the piezoelectric sensor should be in the range of µs and is negligible.

In the first step, the distances and travel times for the air shock wave which is eventually reflected inside the scattering chamber are calculated. The distance from the fast valve to the center of the new chamber is 215 mm. The distance from the chamber center to the chamber wall is 150 mm (cf. drawings in Section B.1). Assuming that the air rushes from the fast valve along a straight line across the chamber, gets then reflected perfectly at the chamber wall and travels back along a straight line to the valve again: The additionally covered distance is $2\cdot(215+150)$ mm =0.73 m. (Note: This assumption is extremely pessimistic, because the air will distribute itself into the whole chamber which leads to a larger travelling time and a huge decrease in the amount of air which rushes back into the direction of the valve). Assuming that the reflected air also travels constantly at the speed of sound v_s, then the time the air needs to get back to the valve is given by $0.73\,\text{m}/v_s \approx 2$ ms. (Note: This assumption is again very pessimistic, because air is still rushing incoming from QCLAM pushed by a pressure difference of nearly 1 bar. So the velocity back to the valve could be smaller if some air gets back at all). The conclusions for these estimations are the following: 7 ms after the piez beforeoelectric sensors are triggered, the shock wave coming from QCLAM passes the valve for the first time ($t_{\text{min},1}$=7 ms). The reflected air reaches the valve not earlier than 9 ms after the piezoelectric sensors are triggered ($t_{\text{min},2}$=9 ms).

In the next step an analytical equation which describes the air flow through a closing valve is derived. If the valve is opened completely, the maximum aperture area is given by $A_{\text{max}}=\pi\cdot D^2/4=1.257\cdot 10^{-3}\,\text{m}^2$. The piezoelectric sensors are triggered at t=0 and the processing time of the valve electronics is given by t_E=2 ms. Then the valve needs additional t_S=3 ms to start its movements. Hence, the total reaction time of the valve is given by $t_R=t_E+t_S$=5 ms. If we assume that the aperture of the valve is closed with constant speed and the profile of the aperture is a rectangle, then the aperture area which is still open at time t can be expressed by

$$A(t)=\begin{cases} A_{\text{max}} & \text{if } 0\le t\le t_R \\ A_{\text{max}}-\frac{A_{\text{max}}}{t_{\text{max}}-t_R}\cdot(t-t_R) & \text{if } t_R<t\le t_{\text{max}} \\ 0 & \text{if } t_{\text{max}}<t \end{cases} \tag{11.9}$$

Here t_{max} is the total time which the valve needs to be closed completely (signal processing time + total mechanical closing time). So we have $t_{\text{max}}=t_E$+9 ms=t_R+6 ms and $A(0)=A(t_R)=A_{\text{max}}$

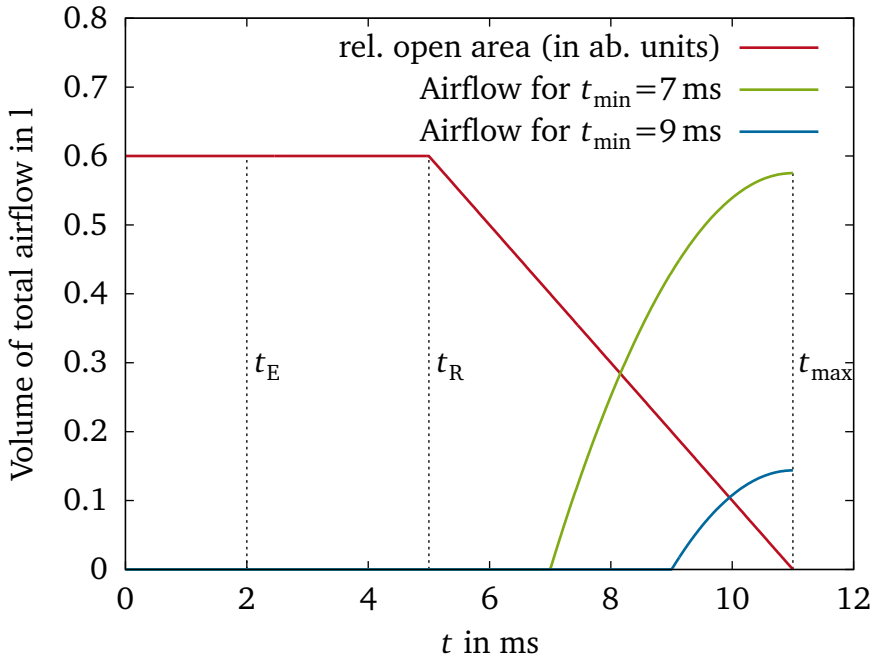

Figure 11.5: Total airflow through a fast closing DN40 CF valve for the worst case with t_E=2 ms and t_{max}=t_E+9 ms =11 ms (calculated with Eq. 11.11). The green curve shows the volume of the inrushed air which has passed the valve before complete closing. The blue curve shows an upper limit of the volume for the reflected air which can flow back to QCLAM. The purple curve shows the relative open aperture area of the valve while it is closing in arbitrary units.

as well as $A(t_{max})$=0. The air volume V which moves through the open aperture area can be calculated with

$$V(t) = v_s \int_{t_{min}}^{t} A(t')\mathrm{d}t', \tag{11.10}$$

where t_{min} is the time at which the air reaches the valve for the first time. Assuming $t_{min} \geq t_R$ and $t_{min} < t_{max}$, then the integral solves to

$$V(t) = -v_s A_{max} \cdot \begin{cases} \frac{(t-t_{min})(t-2t_{max}+t_{min})}{2(t_{max}-t_R)} & \text{if } t_R \leq t \leq t_{max} \\ \frac{(t_{max}-t_{min})(t_{min}-t_{max})}{2(t_{max}-t_R)} & \text{if } t > t_{max} \end{cases} \tag{11.11}$$

With this equation the total volume of the air which passes the closing valve between t_{min} and t_{max} can be calculated.

Let's assume the worst case with t_E=2 ms and t_S=3 ms, which also means t_{max}=t_E+9 ms =11 ms and assume that the air which rushes into the QCLAM reaches the valve at $t_{min,1}$=7 ms. Then the reflected shock wave reaches the valve 2 again at $t_{min,2}$=9 ms. The results for this

assumptions are shown in Figure 11.5. The purple curve shows the relative open aperture area of the valve while it is closing in arbitrary units (cf. Equation 11.9). The air volume which rushes from QCLAM into the chamber while the valve is closing is drawn in green. After t_{max}=11 ms in total 0.58 l air are inside the chamber. As stated earlier, the reflected part of the air starts to pass the valve again after $t_{\mathrm{min,2}}$=9 ms. The volume of air which can pass the valve under perfect conditions after $t_{\mathrm{min,2}}$=9 ms is shown in blue. After t_{max}=11 ms this part sums up to 0.14 l. This is 25.9 % of the total inrushed air volume. But as stated before, most parts of the inrushed air will spread into all directions into the chamber and not be reflected to the valve. Also some amount of this air will go into the beam-pipes and flanges and pumps which means that even less air will have the chance to travel back to the valve. Furthermore, the main argument against a large back-flow of air into the QCLAM is the pressure difference. After t_{max}=11 ms air of a volume of 0.58 l is spread inside a volume, which is larger than $V_{\mathrm{C}}\approx$35 l (volume of scattering chamber). Due to this the maximum pressure inside the chamber in an equilibrium would be in the range of 17 mbar. While at the same time the air which still enters the QCLAM gets pushed by 1000 mbar. For comparisons: If the valve is opened all the time, it would take more than 80 ms to fill the complete volume V_{C} of the scattering chamber.

11.7 Count Rate Estimations for Carbon-14

In this section, count rates for the ^{14}C experiment are estimated. For this the experimental results from Crannell et al. [CHO$^+$72] are used. They give the square of the form factor $F^2(q)$ and the scattering angle θ for several q values for the 2_1^+ state and the 2_2^+ state. These values are listed in Table 11.2 left side for the 2_1^+ state in ^{14}C. In [CHO$^+$72] the square of the form factor $F^2(q)$ was calculated by

$$F^2(q) = \frac{\frac{\mathrm{d}\sigma}{\mathrm{d}\Omega}_{\mathrm{Exp}}}{\frac{\mathrm{d}\sigma}{\mathrm{d}\Omega}_{\mathrm{Mott}}} \tag{11.12}$$

with

$$\frac{\mathrm{d}\sigma}{\mathrm{d}\Omega}_{\mathrm{Mott}}\left[\frac{\mathrm{fm}^2}{\mathrm{sr}}\right] = \left(\frac{Ze^2}{2E_{\mathrm{i}}}\right)^2 \cdot \frac{\cos^2\theta/2}{\sin^4\theta/2} \cdot \frac{1}{1+\frac{2E_{\mathrm{i}}}{Mc^2}\sin^2\theta/2}. \tag{11.13}$$

This equation corresponds to Equation 9.18, where the additional factor corrects for the recoil of the nucleus and e^2 is given as 1.44 MeVfm. The recoil correction is necessary due to the low mass of ^{14}C. With these two equations it is possible to recalculate the measured cross section, while with Equation 9.19 it is possible to calculate E_{i} of the data points given by Crannell et al. [CHO$^+$72]. These values are also listed in Table 11.2 right side for the 2_1^+ state.

With the cross section values it is now possible to estimate count rates which will be measured at the QCLAM spectrometer. The count rates $\dot{N}$ can by calculated via

$$\dot{N}\left[\mathrm{s}^{-1}\right] = \frac{\mathrm{d}\sigma}{\mathrm{d}\Omega}_{\mathrm{exp}}\left[\frac{\mathrm{cm}^2}{\mathrm{sr}}\right] \cdot \frac{N_{\mathrm{A}}[1/\mathrm{mol}]}{M[\mathrm{g/mol}]} \cdot t_{\mathrm{eff}}[\mathrm{g/cm}^2] \cdot \frac{I[\mathrm{A}]}{e[\mathrm{C}]} \cdot \Delta\Omega[\mathrm{sr}], \tag{11.14}$$

Table 11.2: Measured form factors for the 2_1^+ state in ^{14}C. The measured data are taken from Crannell et al. [CHO+72]. E_i is calculated using Equation 9.19, while $d\sigma/d\Omega_{Mott}$ is calculated with Equation 11.13 and $d\sigma/d\Omega_{Exp}$ is calculated via Equation 11.12.

From [CHO+72]			Calculated		
q	θ	$F^2(q)$	E_i	$\frac{d\sigma}{d\Omega}_{Mott}$	$\frac{d\sigma}{d\Omega}_{exp}$
in fm^{-1}	in °	unitless	in MeV	in mb/sr	in mb/sr
0.445	92.9	0.00071	64.15	0.07762	0.00005511
0.671	93.2	0.00273	94.91	0.03483	0.00009507
0.742	92.9	0.00468	104.89	0.02894	0.00013544
0.750	127.6	0.00454	86.40	0.00744	0.00003378
0.754	145.9	0.00542	81.76	0.00284	0.00001540
0.790	145.6	0.00452	85.58	0.00264	0.00001195
0.888	93.2	0.00501	124.65	0.02014	0.00010091
0.905	127.6	0.00679	103.64	0.00516	0.00003503
0.906	145.9	0.00650	97.64	0.00199	0.00001292

where I is the beam current and t_{eff} is the effective target thickness, which is given by

$$t_{eff} = t \cdot \begin{cases} \frac{1}{\cos\theta/2} & \text{if } \theta \lesssim 130° \\ \frac{1}{\sin\theta/2} & \text{if } \theta \gtrsim 130° \end{cases} \tag{11.15}$$

For the beam current I=1 µA was assumed and the maximum possible covered solid angle $\Delta\Omega$ by the QCLAM spectrometer is 35 msr. Due to the new scattering chamber, the maximum solid angle is reduced to $\Delta\Omega \approx 2/3 \cdot 35$ msr=23 msr. The new scattering angle θ_{New} at QCLAM is calculated using Equation 9.19 assuming E_i=85 MeV (realistic value for a experiment at the QCLAM spectrometer). The results are listed in Table 11.3. One can see that the count rates will be relatively high with values between 6 s^{-1} and up to 153 s^{-1}. This is due to the very thick target and the high current which was assumed. But it should be kept in mind that due to the thick target the energy straggling and hence the peak broadening will be large. Also due to the many different materials in the beam axis the background will be relatively high and complex.

In the Appendix in Table A.10 and Table A.11 one can find the same calculations and results for the 2_2^+ state at 8318 keV. It can be seen that the count rates are lower compared to the count rates for the 2_1^+ state. They are in a range between 2 s^{-1} and 20 s^{-1}.

Table 11.3: Count rate estimations for the 2_1^+ state in ^{14}C for a beam energy of E_i=85 MeV. The count rates are calculated with Equation 11.14 while θ_{New} is calculated with Equation 9.19. For q values larger than 0.790 fm^{-1} no setting is possible for E_i=85 MeV.

q in fm^{-1}	θ_{New} in °	t_{eff} in g/cm^2	$\dot{N}$ in s^{-1}
0.445	65.17	0.0919	31.7
0.671	109.28	0.1338	79.7
0.742	129.10	0.1802	152.8
0.750	131.78	0.0849	17.9
0.754	133.18	0.0844	8.1
0.790	148.36	0.0805	6.0
0.888	-	-	-
0.905	-	-	-
0.906	-	-	-

11.8 Possible Q-Values

As mentioned in Section 11.4, five different scattering angles are available with the new scattering chamber. They are 38°, 66°, 95°, 123°, and 152°. This limits the possible q values (cf. Sec. 9.2) at which a measurement can be performed. In Figure 11.6 (a), (b), and (c) possible effective q values for ^{14}C are plotted for all scattering angles versus different beam energies. The effective q values are calculated for the ground state (a), the 2_1^+ state (b) and the 2_2^+ state (c) in ^{14}C. Hence, the energy loss of the electron due to excitation is E_x=0 keV, E_x=7012 keV and E_x=8318 keV, respectively. The effective q values were calculated with Equation 9.20 and 9.19. In Figure 11.6 (a) it can be seen that for the ground state it is possible to cover an effective q value range from 0.04 fm^{-1} to 1.30 fm^{-1}, if the beam energy can be set between 10 MeV and 130 MeV. For 100 MeV beam energy the effective q values 0.341 fm^{-1}, 0.571 fm^{-1}, 0.771 fm^{-1}, 0.918 fm^{-1}, and 1.012 fm^{-1} are possible. In Figure 11.6 (b) it can be seen that for the 2_1^+ state it is possible to cover an effective q value range from 0.05 fm^{-1} to 1.26 fm^{-1}, if the beam energy can be set between 10 MeV and 130 MeV. For 100 MeV beam energy the effective q values 0.332 fm^{-1}, 0.552 fm^{-1}, 0.745 fm^{-1}, 0.886 fm^{-1}, and 0.977 fm^{-1} are possible. In Figure 11.6 (c) it can be seen that for the 2_2^+ state it is possible to cover an effective q value range from 0.06 fm^{-1} to 1.26 fm^{-1}, if the beam energy can be set between 10 MeV and 130 MeV. For 100 MeV beam energy the effective q values 0.330 fm^{-1}, 0.548 fm^{-1}, 0.740 fm^{-1}, 0.879 fm^{-1}, and 0.969 fm^{-1} are possible. So with this setup it is possible to cover a larger range of q values than Crannell et al. did.

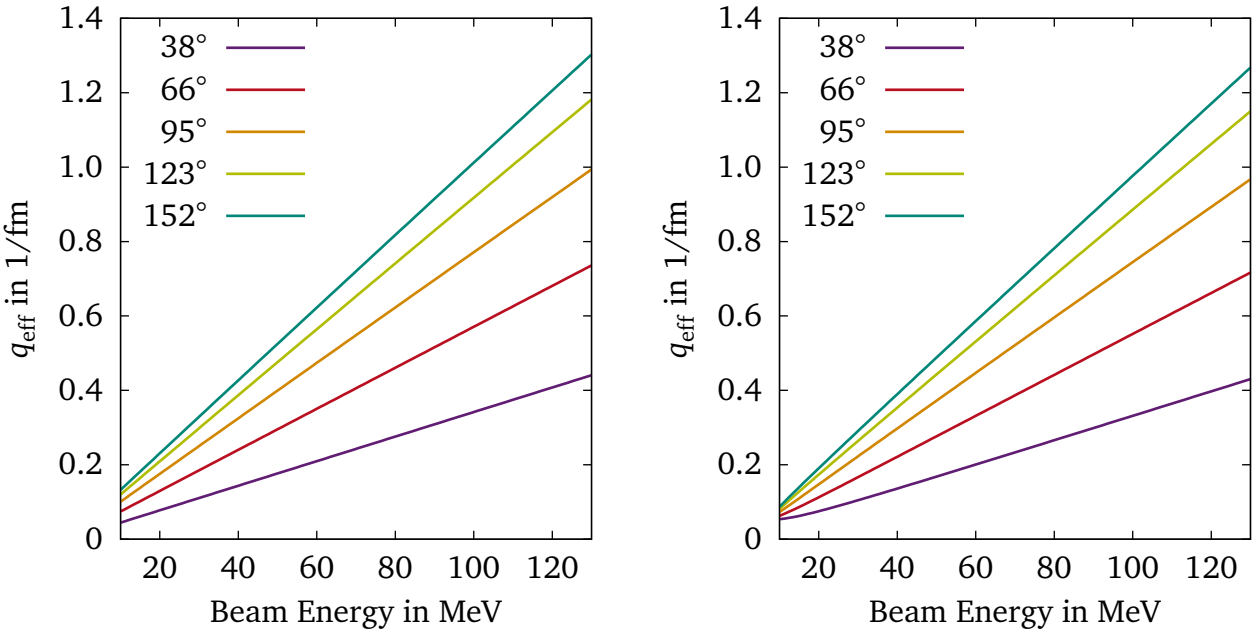

(a) For the ground sate

(b) For the 2_1^+ state

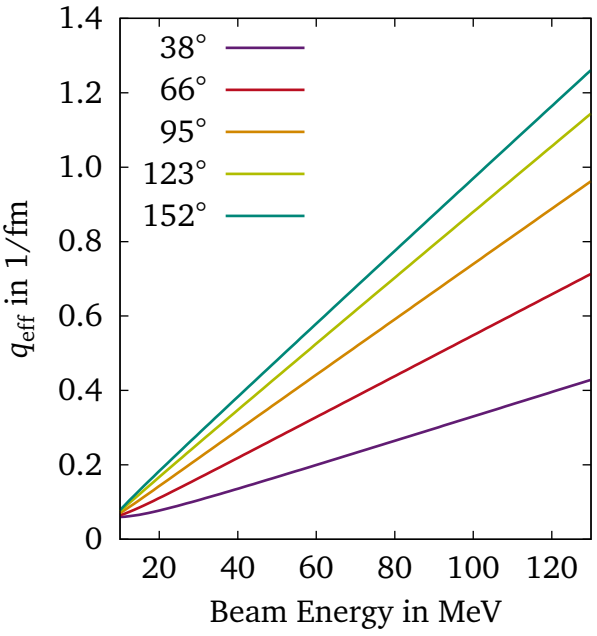

(c) For the 2_2^+ state

Figure 11.6: Possible effective q values for ^{14}C for all scattering angles versus different beam energies. The effective q values were calculated with Equation 9.20 and 9.19.

12 Conclusion and Outlook

In the second part of the thesis, a conceptual design for an electron scattering on ^{14}C at the QCLAM was introduced and prepared. As it could be shown such an experiment could be successfully carried out at the QCLAM spectrometer. For this experiment, a new scattering chamber, a new vacuum system with fast closing valves, and a target chamber were designed. The scattering chamber is already built and tested. The new scattering chamber fits into the existing mounting system of the QCLAM and it is compatible to the existing target chamber. As it could be shown it covers a large range of scattering angles and thus a large range of q values are possible. It is also possible to remeasure the data points from Crannell et al. [CHO$^+$72] with this setup achieving very high count rates due to the thick target and the large solid angle of the QCLAM. The fast closing valves and the piezoelectric sensors to trigger them are bought, tested and are ready to be installed. Also a DN40 CF flange was welded to the vacuum chamber at top of the QCLAM. At this flange the piezoelectric sensors can be installed. The design of the target chamber is finished and it is ready to be built.

To run the experiment in the future, the target chamber has to be built according to the plans given in this thesis. Additionally, a new target ladder has to be designed and built. The target ladder has to be designed in such a way that the target can be easily and quickly mounted without irradiating the laboratory staff. It also has to be thought about a cooling of the ^{14}C target device. Furthermore, the trigger electronic which is implemented between the piezoelectric sensors and the fast valve has to be planned in detail and installed. Also particle filters have to be installed before all involved fore-pumps. Finally, the ^{14}C target has to be shipped to TU Darmstadt and it has to be thought about a possible decontamination of the surface of the target before the experiment is carried out.

Part III

Appendix

A Additional Data and Figures

A.1 Fusion Evaporation Products

The Tables A.1 and A.2 list fusion evaporation products for ^{9}Be shot on ^{9}Be or ^{16}O.

Table A.1: Cross sections for fusion evaporation products for ^{9}Be+^{9}Be with an incoming kinetic energy of 39.8 MeV. The results were achieved with PACE4 [TB08, Gav80]. In total, one million events were calculated. If at least one gamma transition of a residual isotope has been seen in the gamma spectra with a 2p cut, then this is marked in the last column.

Residual Isotope	# Events	Ratio in %	C.S. in mb	Residual Particles	Seen in 2p Cut?
^{18}O	517	0.05	0.4	0p 0n	no
^{17}O	3192	0.32	2.6	0p 1n	no
^{16}O	173930	17.40	142	0p 2n	no
^{15}O	27916	2.79	22.7	0p 3n	no
^{17}N	3976	0.40	3.2	1p 0n	no
^{16}N	3877	0.39	3.2	1p 1n	yes
^{15}N	150878	15.10	123	1p 2n	yes
^{16}C	391	0.04	0.3	2p 0n	yes
^{15}C	462	0.05	0.4	2p 1n	yes
^{14}C	4782	0.48	3.9	2p 2n	yes
^{13}C	329624	33.00	268	2p 3n	yes
^{12}C	196709	19.70	160	2p 4n	no
^{13}B	5840	0.58	4.8	3p 2n	no
^{12}B	35	0.00	0.0	3p 3n	no
^{11}B	103	0.01	0.1	3p 4n	no
^{9}Be	94078	9.41	76.6	4p 4n	no
^{9}Li	33	0.00	0.0	5p 4n	no
^{5}He	63	0.01	0.1	6p 7n	no

Table A.2: Cross sections for fusion evaporation products for ^{9}Be+^{16}O with an incoming kinetic energy of 39.8 MeV. The results were achieved with PACE4 [TB08, Gav80]. In total, one million events were calculated. If at least one gamma transition of a residual isotope has been seen in the gamma spectra with a 2p cut, then this is marked in the last column.

Residual Isotope	# Events	Ratio in %	C.S. in mb	Residual Particles	Seen in 2p Cut?
^{25}Mg	246	0.02	0.2	0p 0n	no
^{24}Mg	2062	0.21	2.0	0p 1n	no
^{23}Mg	18956	1.90	18.0	0p 2n	no
^{23}Na	135907	13.60	129.0	1p 1n	yes
^{22}Na	21165	2.12	20.1	1p 2n	no
^{23}Ne	30135	3.01	28.7	2p 0n	yes
^{22}Ne	16587	1.66	15.8	2p 1n	yes
^{21}Ne	9984	1.00	9.5	2p 2n	yes
^{20}Ne	357704	35.80	340.0	2p 3n	no
^{19}Ne	1833	0.18	1.7	2p 4n	no
^{20}F	23662	2.37	22.5	3p 2n	no
^{19}F	68182	6.82	64.8	3p 3n	no
^{19}O	590	0.06	0.6	4p 2n	no
^{17}O	37125	3.71	35.3	4p 5n	no
^{16}O	254362	25.40	242.0	4p 5n	no
^{16}N	16	0.00	0.0	5p 4n	yes (cf. ^{9}Be+^{9}Be)
^{15}N	1765	0.18	1.7	5p 5n	yes (cf. ^{9}Be+^{9}Be)
^{13}C	19624	1.96	18.7	6p 7n	yes (cf. ^{9}Be+^{9}Be)
^{12}C	5	0.00	0.0	6p 8n	no
^{9}Be	90	0.01	0.1	8p 8n	no

A.2 SRIM Stopping Powers

The Figures A.1 and A.2 show a comparison between the calculated stopping powers from SRIM and experimental results for carbon isotopes.

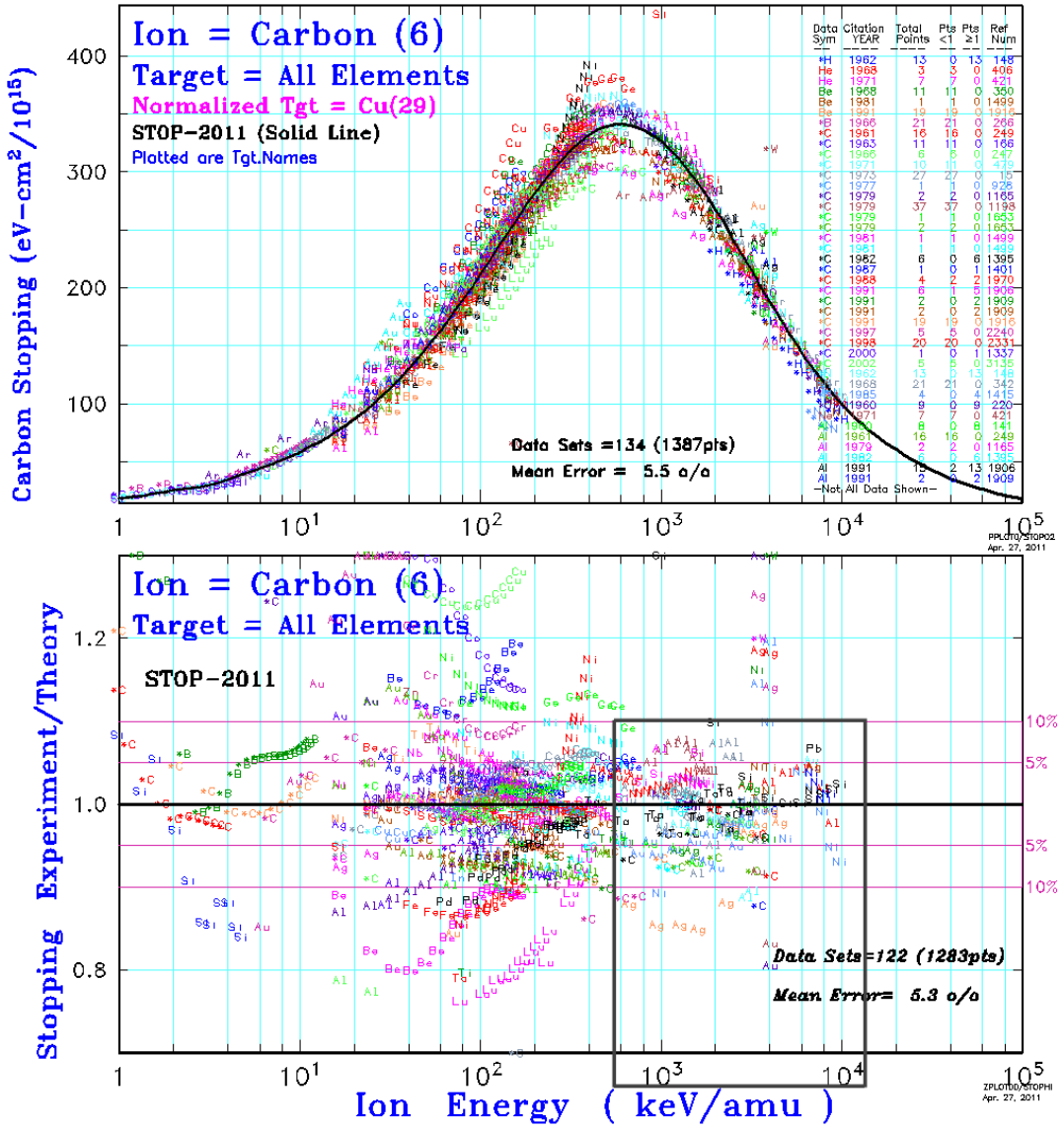

Figure A.1: Comparisons of stopping powers between SRIM and experiments for C isotopes [Zie19, ZZB10]. The dark grey box shows the area of the zoom shown in Figure A.2.

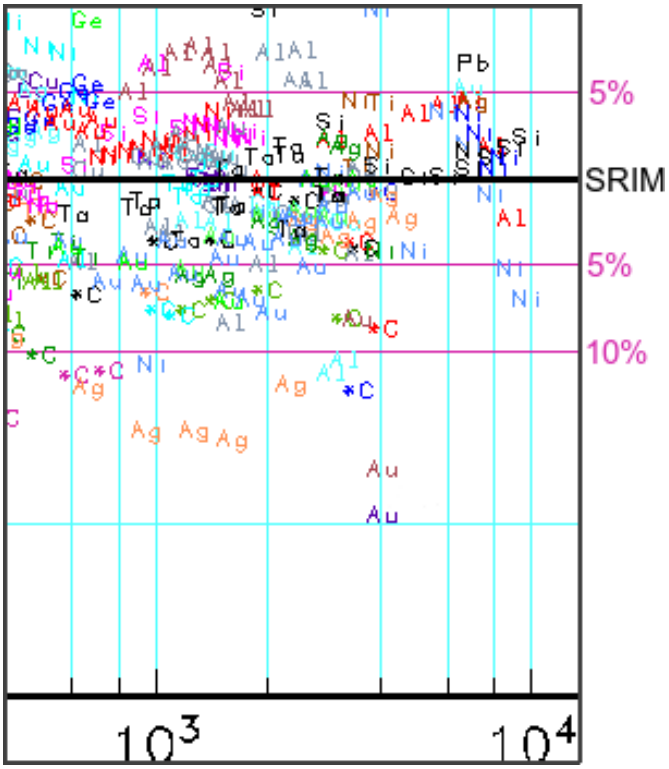

Figure A.2: Zoom in the range of interest which is marked in Figure A.1 bottom with the dark grey box [Zie19, ZZB10]. The experimental values of the stopping power for an Au target are shown in light blue.

A.3 List of Gammasphere Detectors and Calibration Data

Table A.3 shows a list of the used Gammasphere detectors per angle θ. More information about Gammasphere can be found in Section 3.3. The Tables A.4 and A.5 show the offset, the gain and, the pole-zero value for every detector. These values are used to calculate the gamma-ray energy in keV. More information about these topics can be found in Sections 5.1 and 5.2.

Table A.3: Available germanium detectors of Gammasphere for each radiation angle. The second column shows the total number of detectors per angle. The third column shows how many detectors were actually available during the experiment. Furthermore, it should be mentioned that for the angles 50.07°, 69.82°, and 121.72° one detector could not be used because the spectra where non-physical (cf. Sec. 5.2).

Angle θ	Total No. of Detectors	No. of Detectors Available
17.27°	5	0
31.72°	5	3
37.38°	5	1
50.07°	10	8
58.28°	5	5
69.82°	10	9
79.19°	5	4
80.71°	5	5
90.00°	10	7
99.29°	5	5
100.81°	5	5
110.18°	10	9
121.72°	5	4
129.93°	10	10
142.62°	5	5
148.28°	5	4
162.73°	5	3
Sum	110	87

Table A.4: Calibration data of Gammasphere part I: The offset, the gain, and the pole-zero value for every detector are shown. If the offset and the pole-zero value is zero while the gain is 1.0, then the detector was disabled and was not used. Furthermore, it should be mentioned that the detectors 19, 40, and 79 could not be used because the spectra where non-physical (cf. Sec. 5.2).

Det.	θ in °	Offset in keV	Gain in $\frac{\text{keV}}{\text{Channel}}$	P unitless	Det.	θ in °	Offset in keV	Gain in $\frac{\text{keV}}{\text{Channel}}$	P unitless
1	17.27	0.0000	1.00000	0.0000	29	69.82	-0.4319	0.89258	0.8527
2	17.27	0.0000	1.00000	0.0000	30	58.28	0.5514	0.87468	0.8582
3	17.27	0.0000	1.00000	0.0000	31	69.82	0.5995	0.73360	0.8584
4	17.27	0.0000	1.00000	0.0000	32	58.28	0.1875	0.89113	0.8612
5	31.72	0.0000	1.00000	0.0000	33	69.82	-0.7266	0.89499	0.8577
6	17.27	0.0000	1.00000	0.0000	34	69.82	0.5314	0.63942	0.8520
7	31.72	0.4395	0.77581	0.8525	35	69.82	-0.0504	0.87874	0.8558
8	31.72	-0.9433	0.91868	0.8586	36	69.82	0.0000	1.00000	0.0000
9	31.72	0.5646	0.88637	0.8575	37	69.82	1.0534	0.87130	0.8544
10	31.72	0.0000	1.00000	0.0000	38	69.82	-0.1254	0.88037	0.8531
11	37.38	-0.2122	1.00446	0.8531	39	79.19	-0.0778	0.86112	0.8591
12	37.38	0.0000	1.00000	0.0000	40	69.82	-1.7053	0.87847	0.8531
13	37.38	0.0000	1.00000	0.0000	41	79.19	-0.2539	0.88925	0.8607
14	37.38	0.0000	1.00000	0.0000	42	69.82	-0.1634	0.86421	0.8568
15	50.07	0.8964	0.92656	0.8506	43	80.71	-0.6024	0.89662	0.8603
16	37.38	0.0000	1.00000	0.0000	44	79.19	0.1707	0.86543	0.8538
17	50.07	-0.2052	0.86760	0.8563	45	80.71	0.1082	0.83923	0.8511
18	50.07	0.0000	1.00000	0.0000	46	79.19	0.0000	1.00000	0.0000
19	50.07	-1.2015	0.87670	0.8432	47	80.71	-0.1393	0.87123	0.8508
20	50.07	0.0000	1.00000	0.0000	48	79.19	0.2688	1.68687	0.8533
21	50.07	0.7644	0.72505	0.8588	49	90.00	0.2936	0.85484	0.8594
22	50.07	-0.2848	0.85032	0.8567	50	80.71	-0.0816	0.86870	0.8490
23	50.07	-0.2430	0.72851	0.8586	51	90.00	-1.0168	0.854726	0.8602
24	50.07	-0.1152	0.90611	0.8586	52	80.71	-0.0797	0.85483	0.8547
25	58.28	-1.9430	0.84836	0.8552	53	90.00	0.0000	1.00000	0.0000
26	50.07	-0.3499	0.73708	0.8517	54	90.00	0.0000	1.00000	0.0000
27	58.28	0.8163	0.84157	0.8578	55	90.00	0.1260	0.88976	0.8574
28	58.28	0.2842	0.89722	0.8575					

Table A.5: Calibration data of Gammasphere part II: The offset, the gain, and the pole-zero value for every detector are shown. If the offset and the pole-zero value is zero while the gain is 1.0, then the detector was disabled and was not used. Furthermore, it should be mentioned that the detectors 19, 40, and 79 could not be used because the spectra where non-physical (cf. Sec. 5.2).

Det.	θ in °	Offset in keV	Gain in $\frac{\text{keV}}{\text{Channel}}$	P unitless	Det.	θ in °	Offset in keV	Gain in $\frac{\text{keV}}{\text{Channel}}$	P unitless
56	90.00	0.2325	0.88294	0.8613	84	121.72	0.0000	1.00000	0.0000
57	90.00	0.4096	0.86053	0.8588	85	129.93	-0.0538	0.86188	0.8572
58	90.00	0.0000	1.00000	0.0000	86	121.72	0.4045	0.84206	0.8401
59	99.29	-0.5481	0.84679	0.8574	87	129.93	-0.3615	1.03102	0.8593
60	90.00	0.1166	0.84781	0.8438	88	129.93	-0.5131	0.89132	0.8549
61	99.29	0.0148	0.88218	0.8566	89	129.93	0.0221	1.03592	0.8568
62	90.00	0.1285	0.90596	0.8540	90	129.93	0.1698	0.71683	0.8460
63	100.81	-0.9336	1.06813	0.8573	91	129.93	-0.3383	0.96992	0.8573
64	99.29	-0.0900	0.89630	0.8627	92	129.93	0.8290	0.75612	0.8471
65	100.81	0.5704	0.84726	0.8609	93	129.93	0.0025	0.76959	0.8604
66	99.29	0.6705	0.80494	0.8485	94	129.93	0.8749	0.80162	0.8473
67	100.81	0.2975	0.38754	0.8611	95	142.62	-0.3095	0.81968	0.8581
68	99.29	0.5038	0.83642	0.8578	96	129.93	-0.0047	0.98738	0.8541
69	110.18	0.4052	0.88498	0.8561	97	142.62	0.1924	0.84715	0.8569
70	100.81	0.0176	0.93545	0.8572	98	142.62	0.2771	0.81070	0.8549
71	110.18	0.3061	0.75803	0.8613	99	142.62	-0.0312	1.66527	0.8517
72	100.81	-0.1337	0.89249	0.8506	100	142.62	-3.6470	0.86118	0.8447
73	110.18	-0.0305	0.88960	0.8587	101	148.28	0.0000	1.00000	0.0000
74	110.18	0.7772	0.76954	0.8580	102	148.28	0.1464	0.83918	0.8483
75	110.18	-1.0551	0.88889	0.8544	103	148.28	0.9104	0.94211	0.8436
76	110.18	-0.0056	0.89048	0.8523	104	148.28	-0.1108	0.77929	0.8461
77	110.18	0.0010	0.82919	0.8567	105	162.73	0.0000	1.00000	0.0000
78	110.18	0.0000	1.00000	0.0000	106	148.28	0.2732	0.82088	0.8508
79	121.72	-109.48	0.85966	0.8529	107	162.73	0.3462	0.81766	0.8556
80	110.18	1.2738	0.81639	0.8452	108	162.73	-0.5329	0.82041	0.8525
81	121.72	0.2694	0.84269	0.8594	109	162.73	0.0000	1.00000	0.0000
82	110.18	0.9053	0.67428	0.8554	110	162.73	0.2829	0.81673	0.8416
83	121.72	0.2960	0.85698	0.8596					

A.4 Technical Details of Microball

Table A.6 shows technical and geometry details of the μ-Ball CsI(Tl) detectors. See Section 3.4 for more information about μ-Ball.

Table A.6: Technical and geometry details of the μ-Ball CsI(Tl) detectors [SHD+96, SR16]. In ring six just 13 detectors are available due to the space the target mounting needs.

Ring Number	1	2	3	4	5	6	7	8	9
No. of Detectors	6	10	12	12	14	13	12	10	6
Distance in mm	110	80	60	50	50	50	45	47	50
θ in °	9.0	21.0	36.0	52.0	70.0	90.0	111.5	135.0	159.0
Half θ in °	5.0	7.0	8.0	8.0	10.0	10.0	11.5	12.0	12.0
CsI Thickness in mm	2.7	2.4	2.2	1.9	1.6	1.5	1.5	1.3	1.1
p Energy Range in MeV	24.5	22.8	21.7	19.9	17.9	17.3	17.3	15.8	14.3

A.5 Microball Time Gates

Table A.3 shows a list of the used μ-Ball time gates which are needed to obtain a proper coincidence between Gammasphere and μ-Ball (cf. Sec. 5.4).

Table A.7: μ-Ball time gates for each detector.

Det.	T_{left}	T_{right}	Det.	T_{left}	T_{right}	Det.	T_{left}	T_{right}
1	-	-	33	6350	7150	65	6000	6900
2	-	-	34	6450	7250	66	6000	6900
3	-	-	35	6300	7100	67	5900	6700
4	-	-	36	6100	6900	68	5900	6900
5	-	-	37	6200	7050	69	6000	6900
6	-	-	38	6350	7100	70	6100	6800
7	6200	7050	39	6300	7100	71	6100	6900
8	6215	7000	40	6250	7050	72	5950	6800
9	6200	7025	41	6100	6950	73	6100	6900
10	6100	7000	42	6000	6850	74	6150	6800
11	6230	7000	43	6000	6850	75	6050	6900
12	6100	7000	44	6000	6900	76	6000	6800
13	6200	7040	45	6150	6950	77	6000	6800
14	6300	7000	46	6000	6900	78	5900	6700
15	6200	6950	47	6100	6950	79	5800	6500
16	6100	6900	48	6100	7100	80	5900	6700
17	6100	6850	49	6000	7000	81	6000	6750
18	6000	6950	50	6000	6900	82	6200	6750
19	6000	6900	51	6000	6950	83	6250	6700
20	6150	6890	52	6000	7000	84	6200	6700
21	6050	6900	53	6300	7050	85	6200	6700
22	6100	6900	54	6100	6900	86	6200	6700
23	6300	6950	55	-	-	87	6250	6800
24	6100	6900	56	6100	7000	88	6200	6800
25	6100	6900	57	-	-	89	6150	6750
26	6200	7000	58	5750	6800	90	6100	6600
27	6100	6900	59	6100	7100	91	6000	6600
28	6100	7050	60	5900	6800	92	5900	6500
29	6200	7000	61	6100	7100	93	6300	6650
30	6200	7100	62	-	-	94	6000	6800
31	6100	6950	63	6100	7100	95	6000	6600
32	6100	6950	64	6400	7250	96	6150	6650

A.6 Microball Energy Calibration

In this section all data for the μ-Ball energy calibration are shown. For more information see Section 5.6.

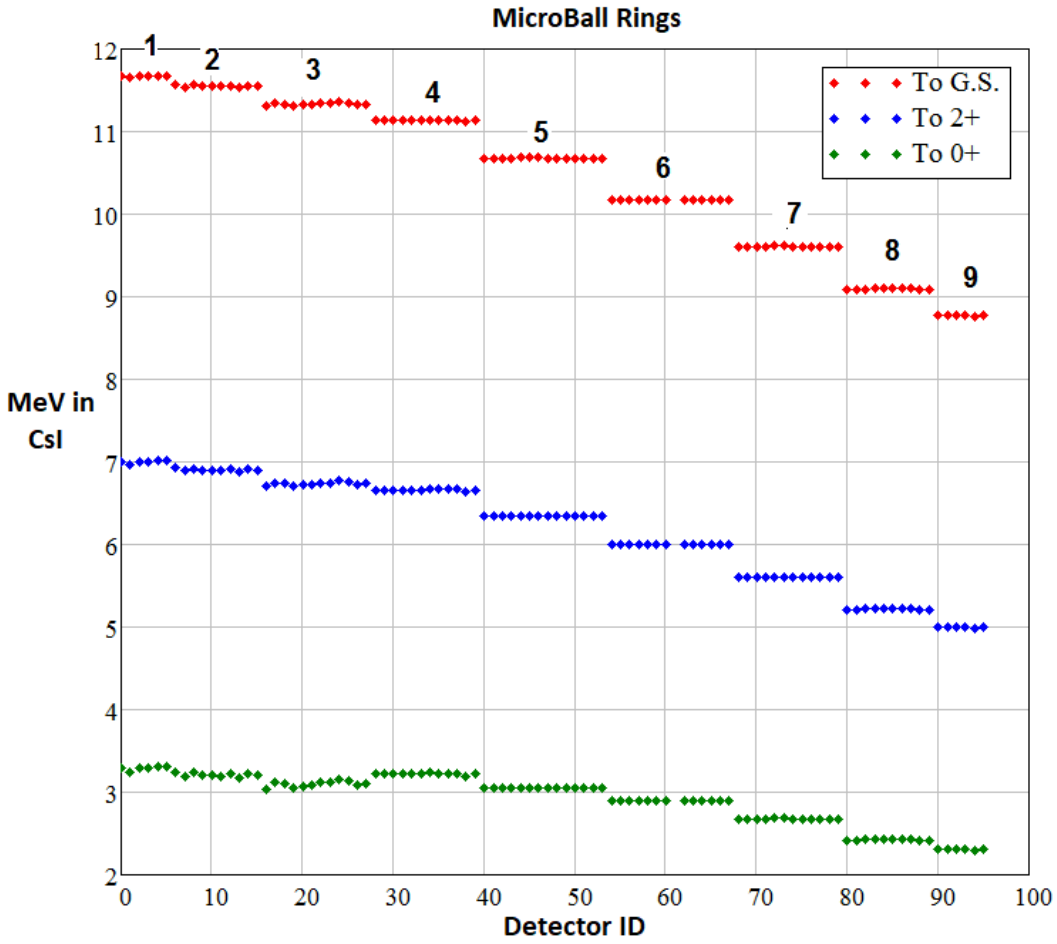

Figure A.3: Calculated proton energy which is deposited in the μ-Ball detectors for the calibration runs shooting a proton beam on ^{12}C. The incoming energy of the proton was 12.24(11) MeV. The three different colors indicates the three different interactions the protons can have with ^{12}C. The figure is taken from [Sar16].

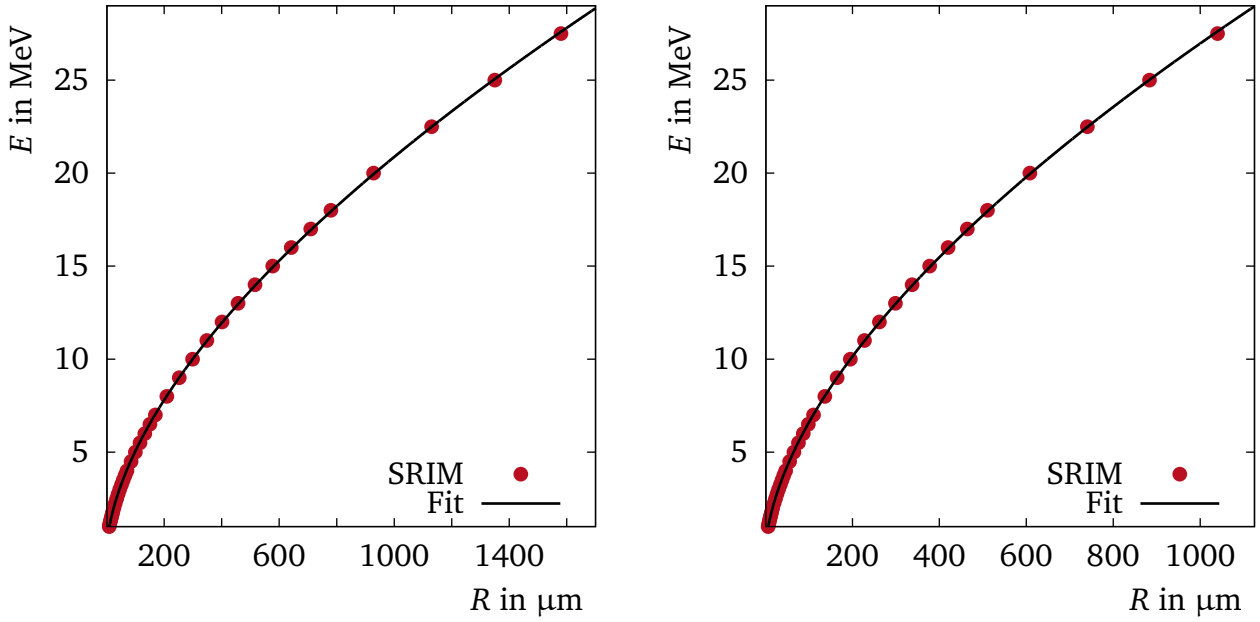

(a) For Pb

(b) For Ta

Figure A.4: Proton range data for Pb and Ta absorbers. The proton range data are obtained from SRIM [Zie19, JFZ15]. The proton energy E in MeV is plotted over the corresponding range R in the material. The shown fit function $E(R)$ can be described by Equation 5.23.

Table A.8: Energy calibration data for μ-Ball. The values of a (slope) and b (intersect) are used to calculate the proton energy in the CsI detectors E_{CsI} according to Eq. 5.22. The values were obtained by the group of D.G. Sarantites et al. [Sar16].

Det.	Gain in $\frac{\mathrm{MeV}}{\mathrm{Channel}}$	Offset in MeV	Det.	Gain in $\frac{\mathrm{MeV}}{\mathrm{Channel}}$	Offset in MeV	Det.	Gain in $\frac{\mathrm{MeV}}{\mathrm{Channel}}$	Offset in MeV
1	-	-	33	0.0034864	0.9014	65	0.0045239	-0.1519
2	0.0067310	-1.4110	34	0.0053370	1.2919	66	0.0037414	0.4443
3	0.0057890	-0.4357	35	0.0038551	1.1448	67	0.0034861	0.1057
4	0.0052210	-0.0858	36	0.0035876	1.5898	68	0.0036865	0.4335
5	0.0051750	-0.1421	37	0.0038177	1.3223	69	0.0032093	0.2311
6	0.0052990	-0.4238	38	0.0040421	1.3948	70	0.0041166	-0.1219
7	0.0045635	0.2270	39	0.0038327	1.4197	71	0.0042156	0.0002
8	0.0044572	0.1806	40	0.0036942	1.6470	72	0.0041641	0.1230
9	0.0051436	0.0782	41	0.0031123	-0.0352	73	0.0041096	0.0195
10	0.0046350	0.1227	42	0.0028751	0.0614	74	0.0037240	-0.0588
11	0.0044204	-0.1660	43	0.0028705	0.0805	75	0.0038558	0.3165
12	0.0054913	-0.2559	44	0.0028887	0.2350	76	0.0036242	0.2835
13	0.0042871	-0.1405	45	0.0030179	0.0395	77	0.0033880	0.2145
14	0.0045862	0.0093	46	0.0026364	-0.0450	78	0.0026277	0.5182
15	0.0049404	-0.0692	47	0.0026168	-0.0438	79	0.0028049	0.0957
16	0.0043552	0.0563	48	0.0027024	-0.0406	80	0.0031284	0.6081
17	0.0042195	-0.0070	49	0.0042201	0.5196	81	0.0037941	-0.0515
18	0.0040451	0.1020	50	0.0031041	0.3342	82	0.0037935	0.0153
19	0.0038537	-0.0320	51	0.0029755	-0.1355	83	0.0039328	0.1750
20	0.0043999	-0.0827	52	0.0026802	0.3069	84	0.0038042	0.1530
21	0.0051013	-0.1266	53	0.0029411	-0.0635	85	0.0033139	0.1821
22	0.0042148	0.0281	54	0.0029684	0.0491	86	0.0034944	0.2794
23	0.0041317	-0.0264	55	0.0044525	0.3996	87	0.0038283	0.0715
24	0.0046435	-0.2516	56	0.0038243	0.3625	88	0.0037564	0.0860
25	0.0042237	0.0496	57	-	-	89	0.0038568	0.2658
26	0.0040674	-0.0522	58	0.0055843	0.3254	90	0.0038883	0.1499
27	0.0040364	-0.0464	59	0.0045217	0.2402	91	0.0036573	0.2159
28	0.0039759	-0.0118	60	0.0048065	0.2518	92	0.0042099	0.2051
29	0.0040219	1.5014	61	0.0043051	0.2248	93	0.0041493	0.1811
30	0.0042733	1.2314	62	-	-	94	0.0032868	0.2504
31	0.0056267	0.9948	63	0.0024481	0.4669	95	0.0034331	0.3772
32	0.0040897	1.0091	64	0.0047993	0.4196	96	0.0044090	-0.1024

A.7 Efficiency Calibration Data

Table A.9 shows the data which where used for the efficiency calibration of Gammasphere. See Section 5.3 for more information about the efficiency calibration. The Figure A.5 illustrates the decay scheme of ^{88}Y.

Table A.9: Efficiency calibration data for ^{56}Co. The table lists the gamma-ray energy E, its relative intensity I_{rel} and the coresponding one sigma uncertainty $u(I_{\mathrm{rel}})$. The relative intensities have been taken from [JSD11].

E in keV	I_{rel} in %	$u(I_{\mathrm{rel}})$ in %
846.770	99.940	0.000
1037.843	14.050	0.040
1238.288	66.460	0.120
1360.212	4.283	0.012
1771.357	15.410	0.060
2034.791	7.770	0.030
2598.500	16.970	0.040
3009.645	1.036	0.013
3202.029	3.209	0.012
3451.232	0.949	0.005
3548.050	0.196	0.002

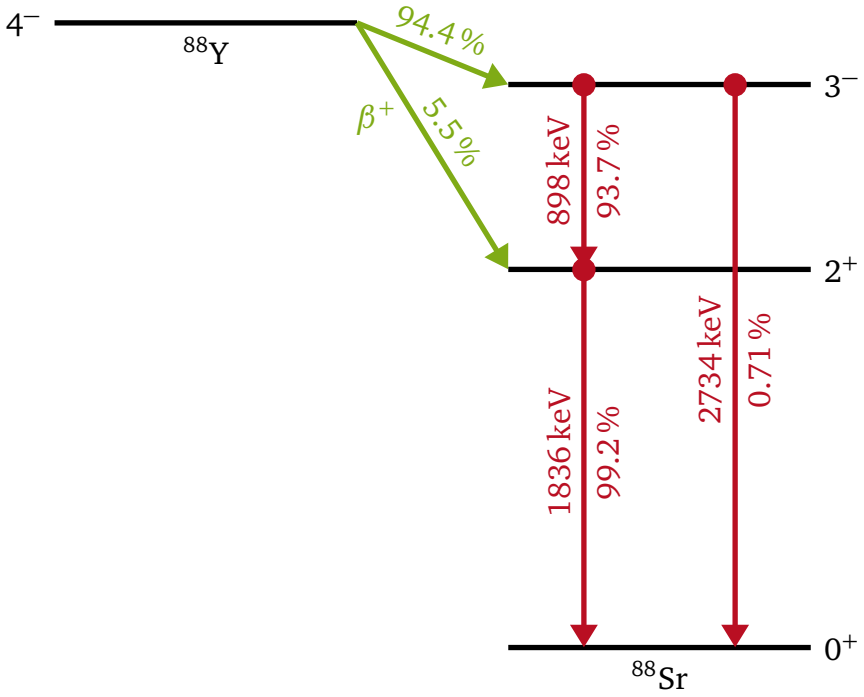

Figure A.5: Simplified decay scheme of ^{88}Y [MS14]. The decay branches are shown in green. Decay branches with a relative intensity smaller 0.03 % are neglected. The percentages at the gamma transitions (illustrated in red) show the relative gamma intensities which are measured after the β^+ decay.

A.8 Level Scheme of Nitrogen-15

Figure A.6 shows the level scheme for ^{15}N.

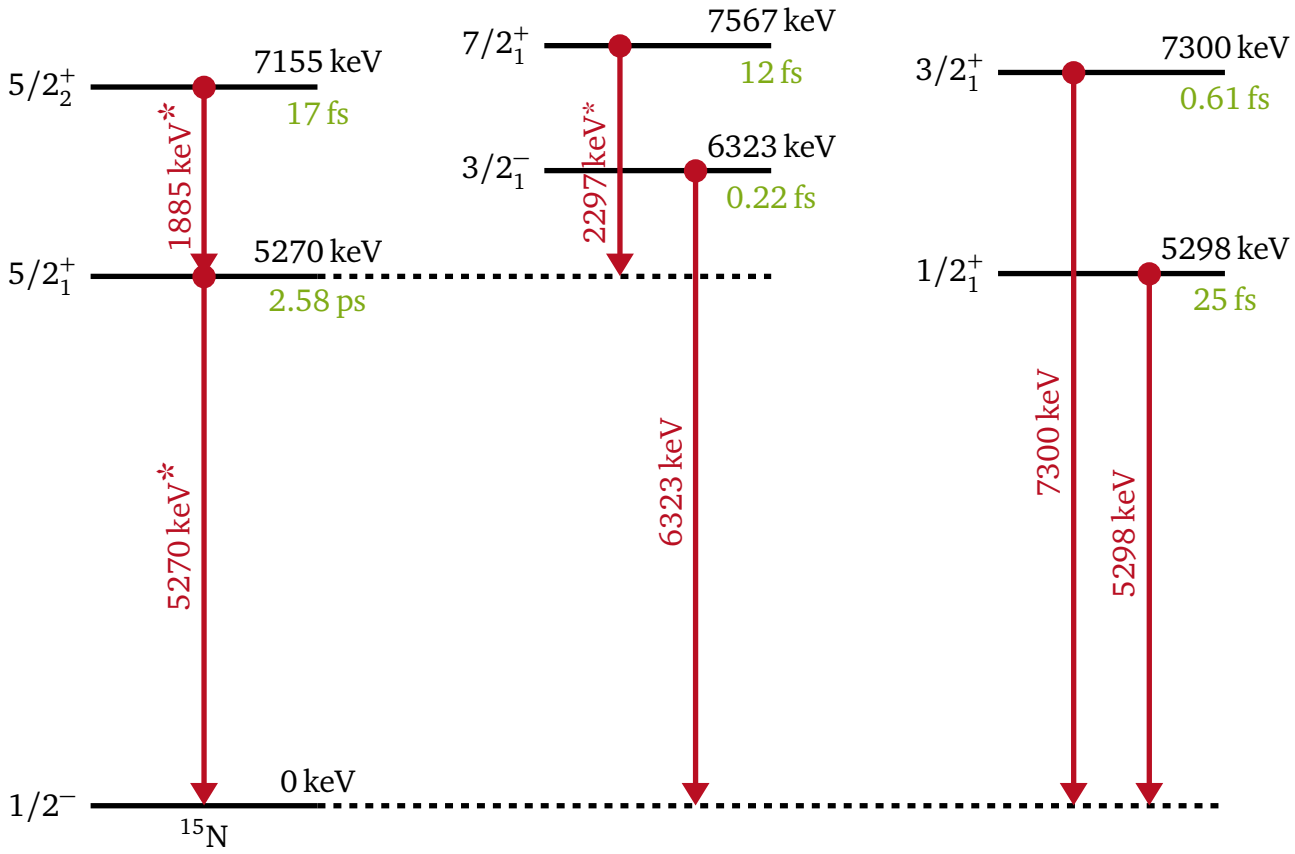

Figure A.6: Level scheme of the six lowest excited states of ^{15}N. The energies printed in black are the energies of the states while the energies printed in red are the transition energies emitted by gamma rays [AS90a]. Only the most dominant transition for each state is shown. The branching ratios of all the other cases are negligible (smaller 4 %) and thus they have not been seen in any spectra. If a gamma-ray energy is marked with a asterisk this transition was seen in the 2p cut spectra. The lifetimes of the states are taken from [AS90a] and shown in green.

A.9 Air Inrush Paths

The following figures show a profile of the QCLAM and possible paths the air shock wave can take. All dimensions are given in millimetres. For more information about a possible air inrush see Section 11.6.

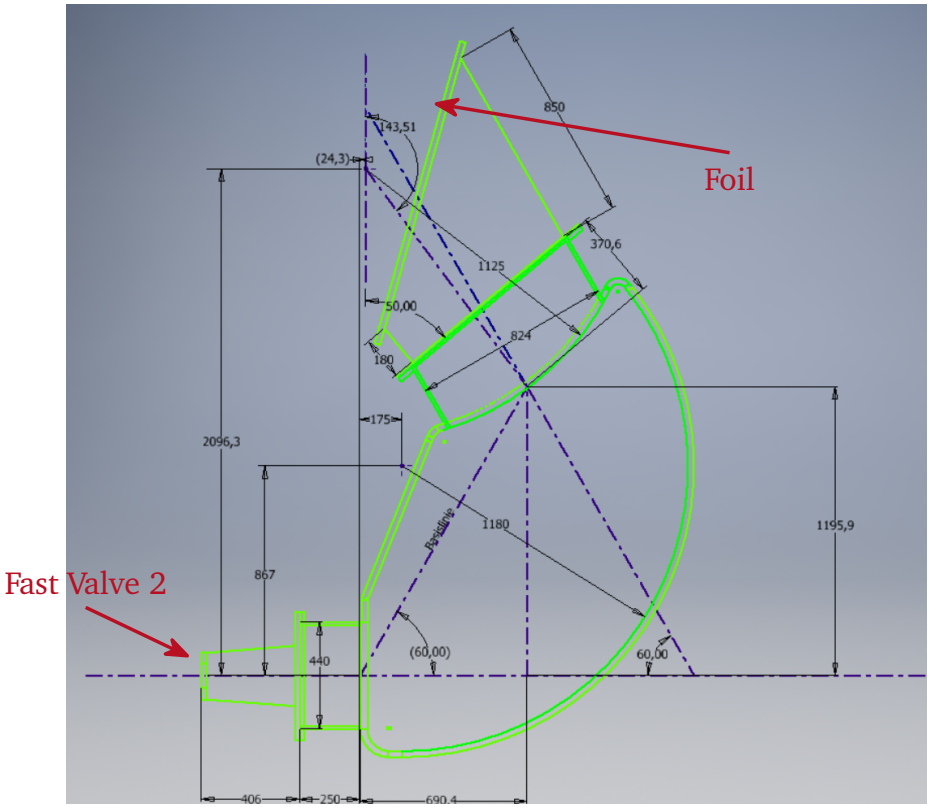

Figure A.7: Profile of the QCLAM spectrometer.The dimensions are given in millimetres and taken from the original construction drawings.

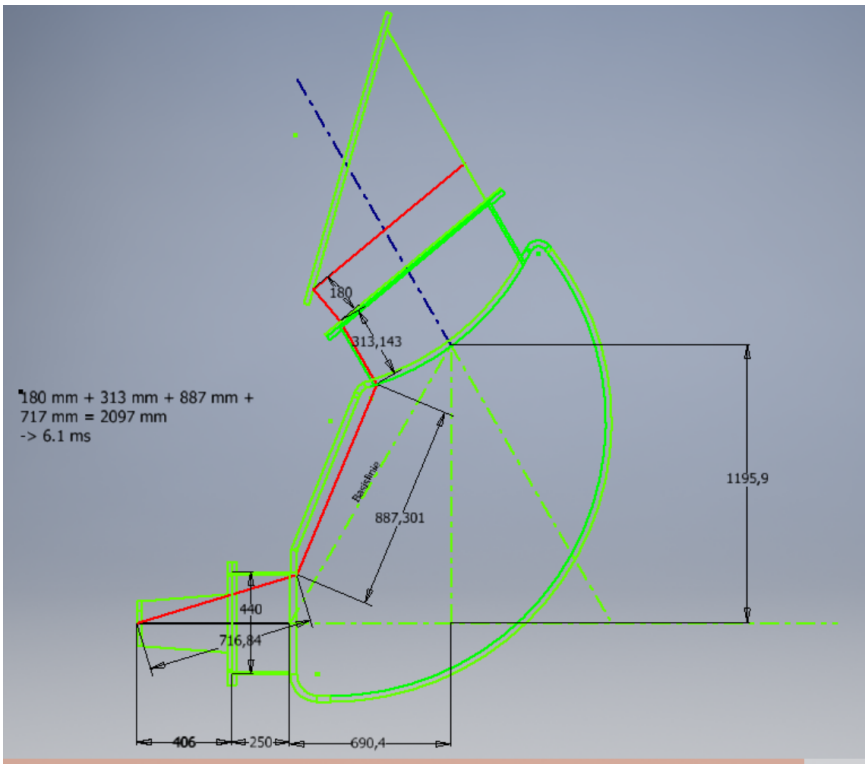

Figure A.8: Profile of the QCLAM spectrometer and the shortest possible air inrush path shown in red.

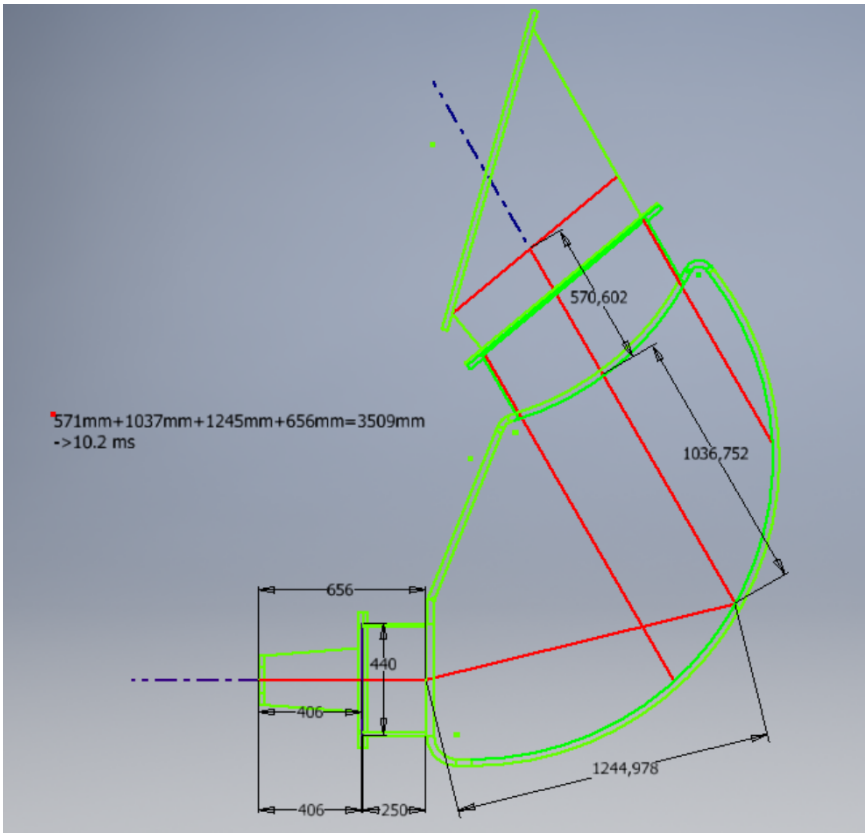

Figure A.9: Profile of the QCLAM spectrometer and the longest possible air inrush path shown in red.

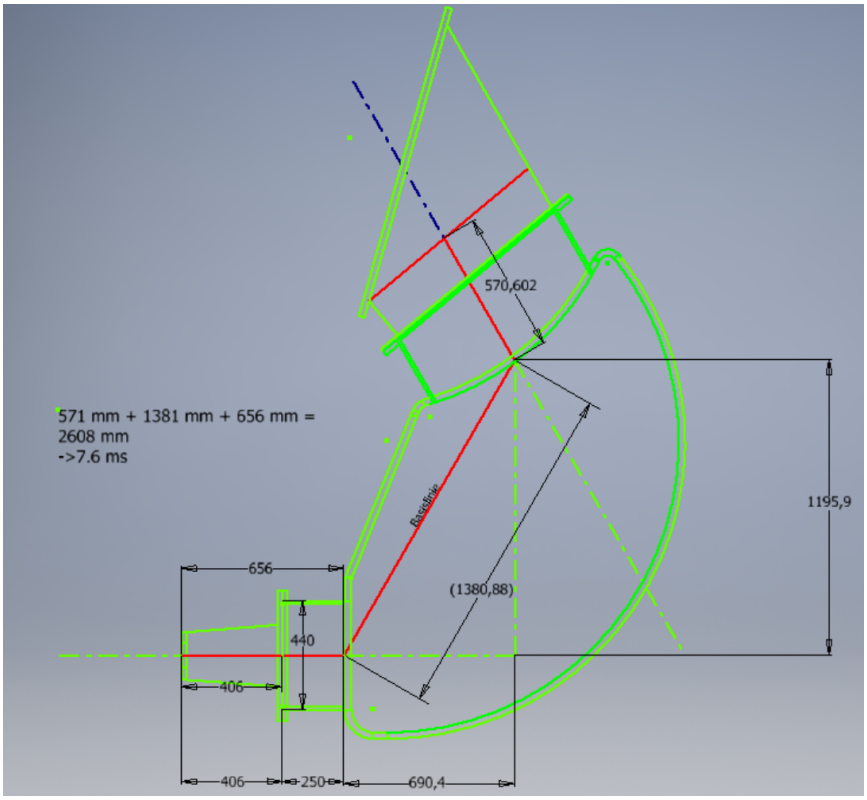

Figure A.10: Profile of the QCLAM spectrometer and an example for a possible air inrush path shown in red.

A.10 Count Rate Estimations for a Carbon-14 Experiment at the QCLAM Spectrometer

Table A.10 shows results for the form factor for the 2_2^+ state in ^{14}C measured by Crannell et al. [CHO$^+$72]. Table A.11 shows the results for the count rate estimations for the 2_2^+ state in ^{14}C. For more information see Section 11.7.

Table A.10: Measured form factors for the 2_2^+ state in ^{14}C. The measured data are taken from Crannell et al. [CHO$^+$72]. E_i is calculated using Equation 9.19 while $\mathrm{d}\sigma/\mathrm{d}\Omega_\mathrm{Mott}$ is calculated with Equation 11.13 and $\mathrm{d}\sigma/\mathrm{d}\Omega_\mathrm{Exp}$ is calculated via Equation 11.12.

From [CHO$^+$72]			Calculated		
q	θ	$F^2(q)$	E_i	$\frac{\mathrm{d}\sigma}{\mathrm{d}\Omega}_\mathrm{Mott}$	$\frac{\mathrm{d}\sigma}{\mathrm{d}\Omega}_\mathrm{exp}$
in fm^{-1}	in °	unitless	in MeV	in mb/sr	in mb/sr
0.671	93.2	0.00069	95.55	0.03446	0.00002357
0.742	92.9	0.00117	105.52	0.02859	0.00003345
0.750	127.6	0.00114	87.05	0.00732	0.00000835
0.754	145.9	0.00164	82.41	0.00280	0.00000458
0.790	145.6	0.00145	86.24	0.00260	0.00000378
0.888	93.2	0.00154	125.29	0.01994	0.00003070
0.906	145.9	0.00171	98.29	0.00196	0.00000335

Table A.11: Count rates estimations for the 2_2^+ state in ^{14}C for a beam energy of E_i=85 MeV. The count rates are calculated with Equation 11.14 while θ_New is calculated with Equation 9.19. For q values larger than 0.790 fm^{-1} no setting is possible for E_i=85 MeV.

q	θ_New	t_eff	$\dot{N}$
in fm^{-1}	in °	in g/cm^2	in s^{-1}
0.671	110.58	0.1360	20.1
0.742	131.08	0.0851	17.8
0.750	133.91	0.0842	4.4
0.754	135.39	0.0837	2.4
0.790	151.86	0.0798	1.9
0.888	-	-	-
0.906	-	-	-

B Technical Drawings

B.1 Technical Drawings of the Scattering Chamber

The following figures show the technical drawings for the scattering chamber. The chamber was build in a German workshop and due to this all labels are given in German as well. All parts are made of stainless steel. All dimensions in the drawings are given in millimetres.

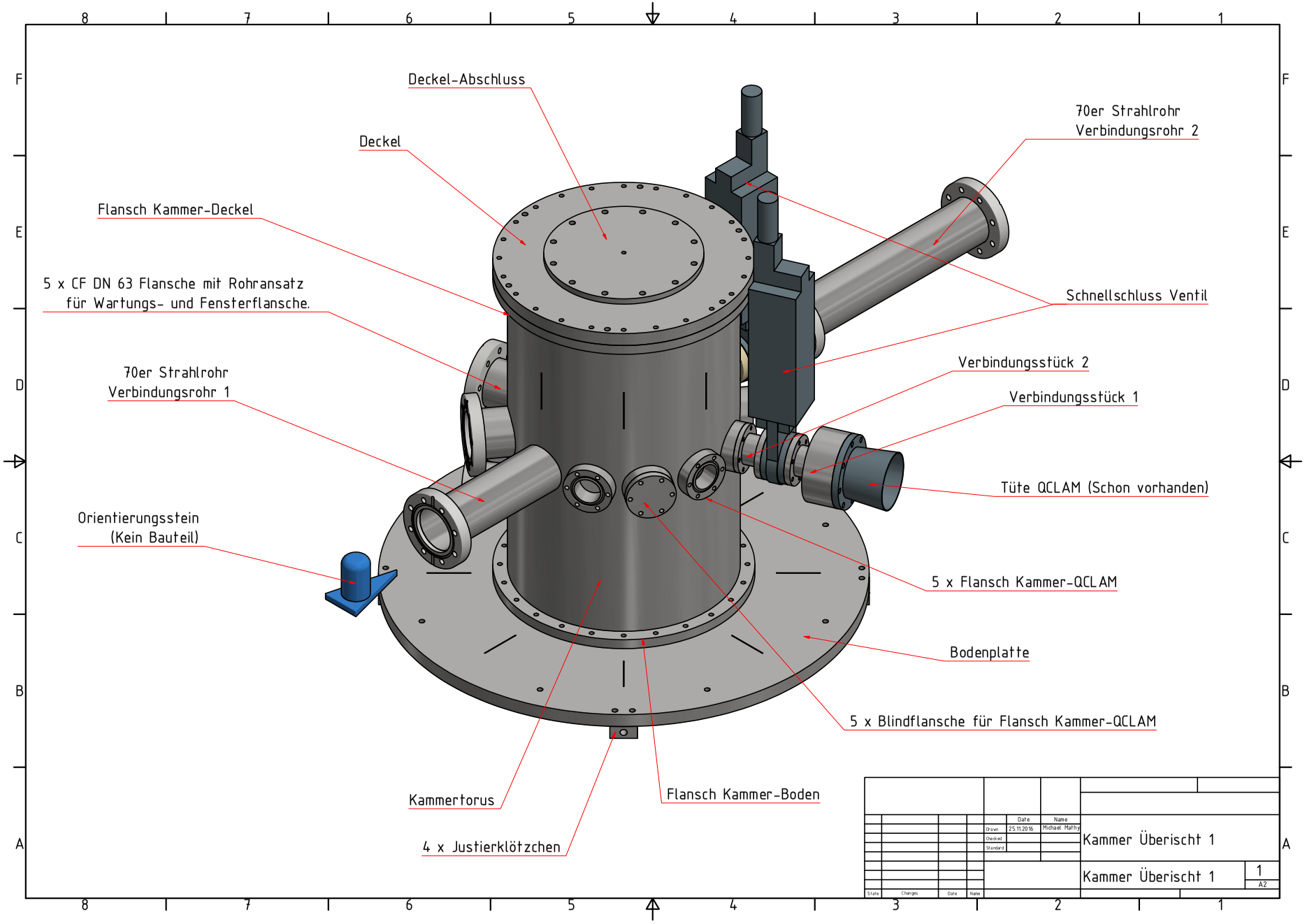
Deckel-Abschluss
Deckel
Flansch Kammer-Deckel
5 x CF DN 63 Flansche mit Rohransatz
für Wartungs- und Fensterflansche.
70er Strahlrohr
Verbindungsrohr 1
Orientierungsstein
(Kein Bauteil)
Kammertorus
4 x Justierklötzchen
Flansch Kammer-Boden
5 x Blindflansche für Flansch Kammer-QCLAM
Bodenplatte
5 x Flansch Kammer-QCLAM
Tüte QCLAM (Schon vorhanden)
Verbindungsstück 1
Verbindungsstück 2
Schnellschluss Ventil
70er Strahlrohr
Verbindungsrohr 2
Date
Name
Drawn
25.11.2016
Michael Mathy
Checked
Standard
Kammer Überischt 1
Kammer Überischt 1
1
A2

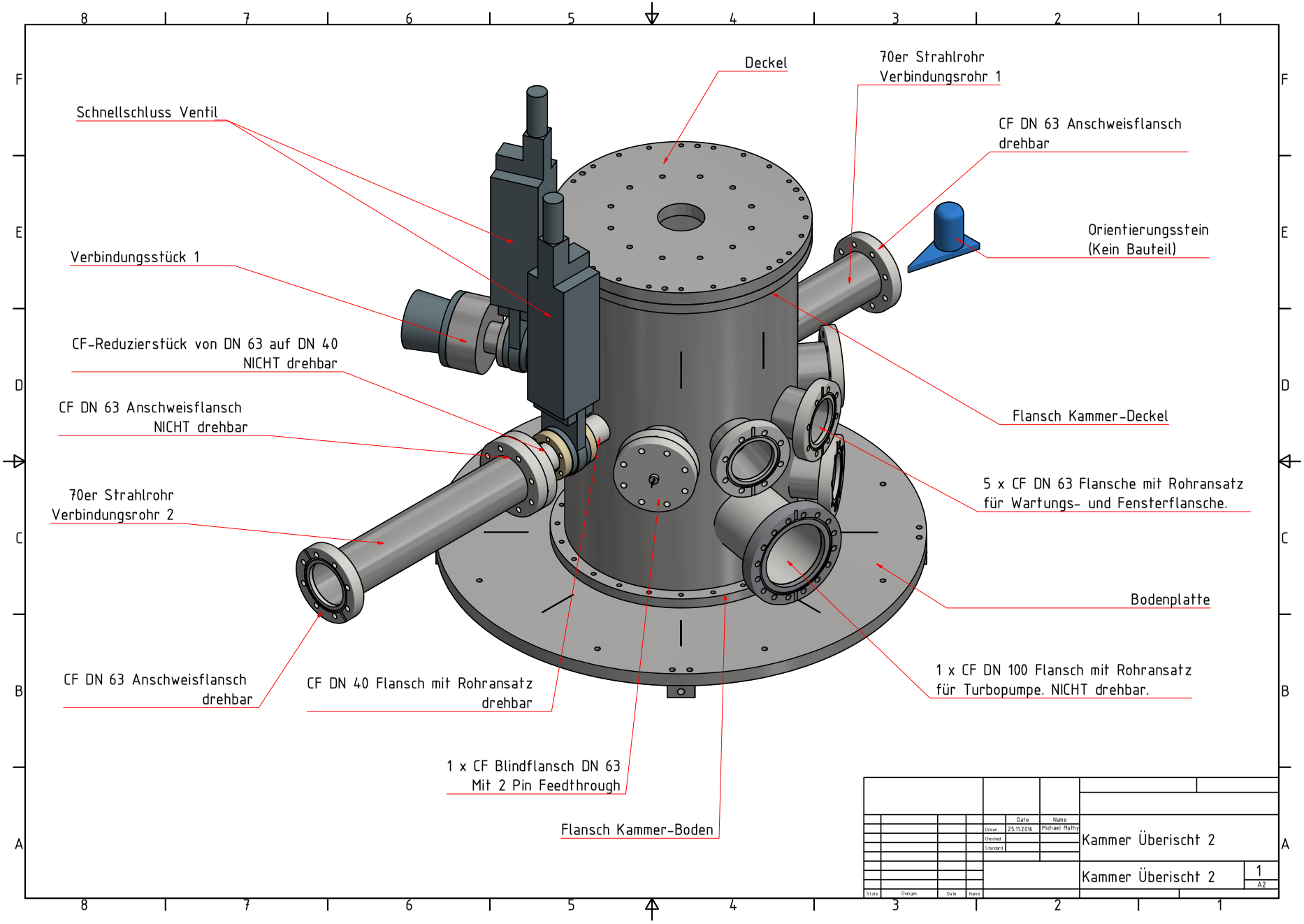
Deckel
70er Strahlrohr
Verbindungsrohr 1
Schnellschluss Ventil
CF DN 63 Anschweisflansch
drehbar
Orientierungsstein
(Kein Bauteil)
Verbindungsstück 1
CF-Reduzierstück von DN 63 auf DN 40
NICHT drehbar
CF DN 63 Anschweisflansch
NICHT drehbar
Flansch Kammer-Deckel
5 x CF DN 63 Flansche mit Rohransatz
für Wartungs- und Fensterflansche.
70er Strahlrohr
Verbindungsrohr 2
Bodenplatte
1 x CF DN 100 Flansch mit Rohransatz
für Turbopumpe. NICHT drehbar.
CF DN 63 Anschweisflansch
drehbar
CF DN 40 Flansch mit Rohransatz
drehbar
1 x CF Blindflansch DN 63
Mit 2 Pin Feedthrough
Flansch Kammer-Boden
Date
Name
Drawn
25.11.2016
Michael Mathy
Checked
Standard
Kammer Überischt 2
Kammer Überischt 2
1
A2
State
Changes
Date
Name

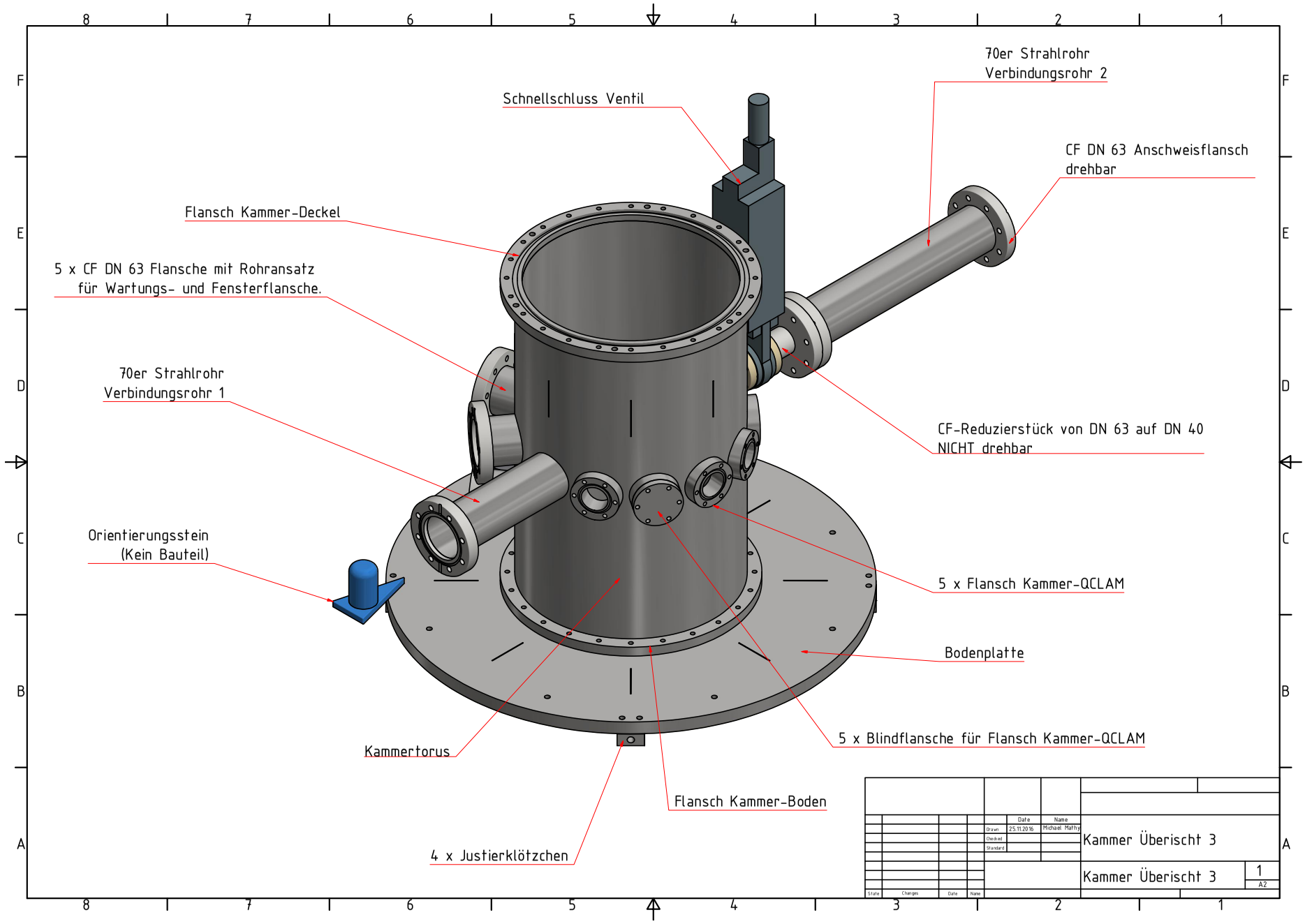
70er Strahlrohr
Verbindungsrohr 2
Schnellschluss Ventil
CF DN 63 Anschweisflansch
drehbar
Flansch Kammer-Deckel
5 x CF DN 63 Flansche mit Rohransatz
für Wartungs- und Fensterflansche.
70er Strahlrohr
Verbindungsrohr 1
CF-Reduzierstück von DN 63 auf DN 40
NICHT drehbar
Orientierungsstein
(Kein Bauteil)
5 x Flansch Kammer-QCLAM
Bodenplatte
5 x Blindflansche für Flansch Kammer-QCLAM
Kammertorus
Flansch Kammer-Boden
4 x Justierklötzchen
Date
Name
Drawn
25.11.2016
Michael Mathy
Checked
Standard
Kammer Überischt 3
Kammer Überischt 3
1
A2
State
Changes
Date
Name

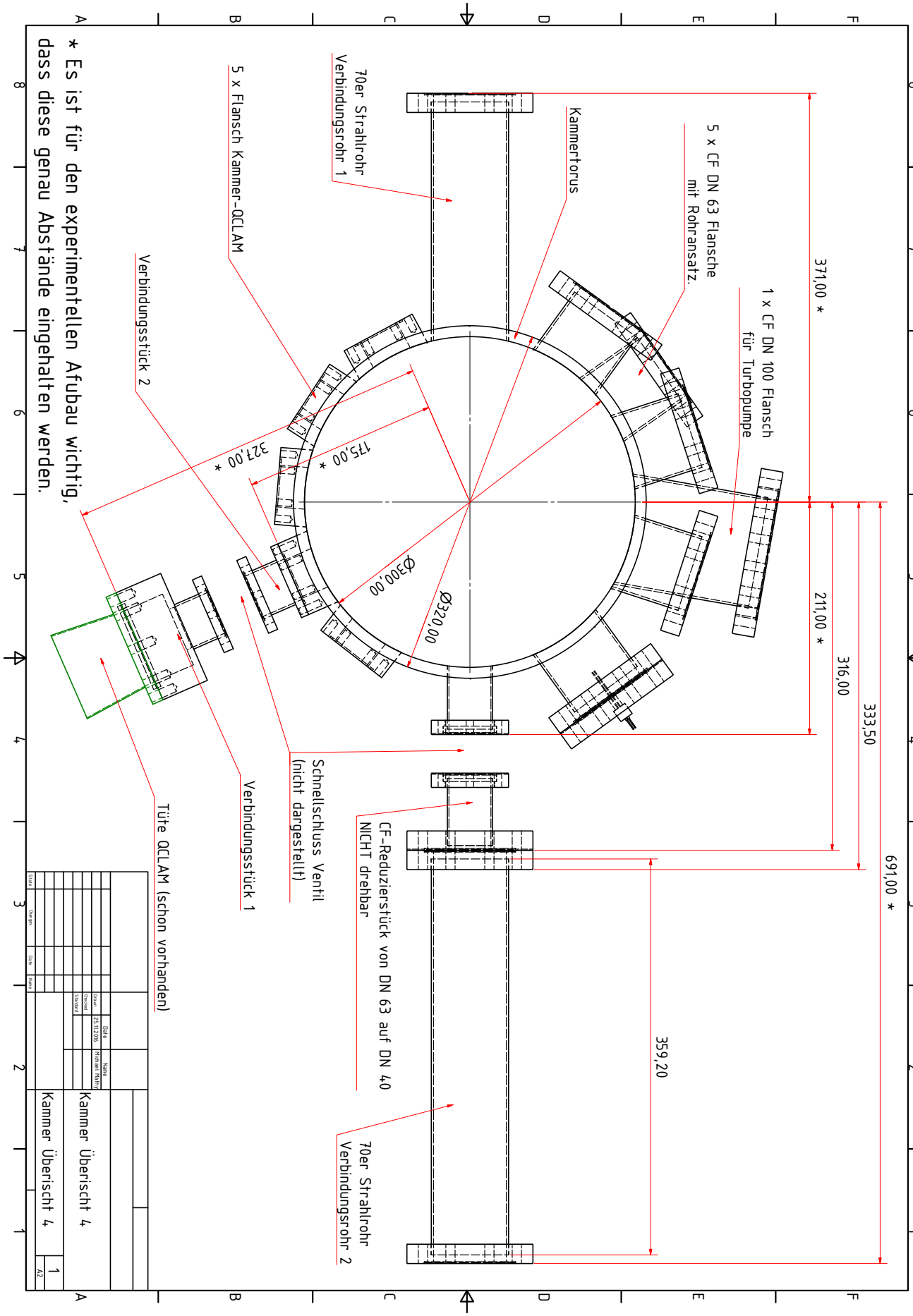
* Es ist für den experimentellen Afubau wichtig, dass diese genau Abstände eingehalten werden.
Kammer Überischt 4
Kammer Überischt 4
A2
1
Name
Datum
25.11.2016
Florian Rothy
Standard
Datum
Name
Zust.
Änderung
Norm
Datum
Name
Maßstab
Gewicht
Blatt
Format
Tüte QCLAM (schon vorhanden)
Verbindungsstück 1
Schnellschluss Ventil (nicht dargestellt)
CF-Reduzierstück von DN 63 auf DN 40 NICHT drehbar
70er Strahlrohr Verbindungsrohr 2
Verbindungsstück 2
5 x Flansch Kammer-QCLAM
70er Strahlrohr Verbindungsrohr 1
Kammertorus
5 x CF DN 63 Flansche mit Rohransatz.
1 x CF DN 100 Flansch für Turbopumpe
371,00 *
691,00 *
333,50
316,00
211,00 *
359,20
Ø320,00
Ø300,00
175,00 *
327,00 *

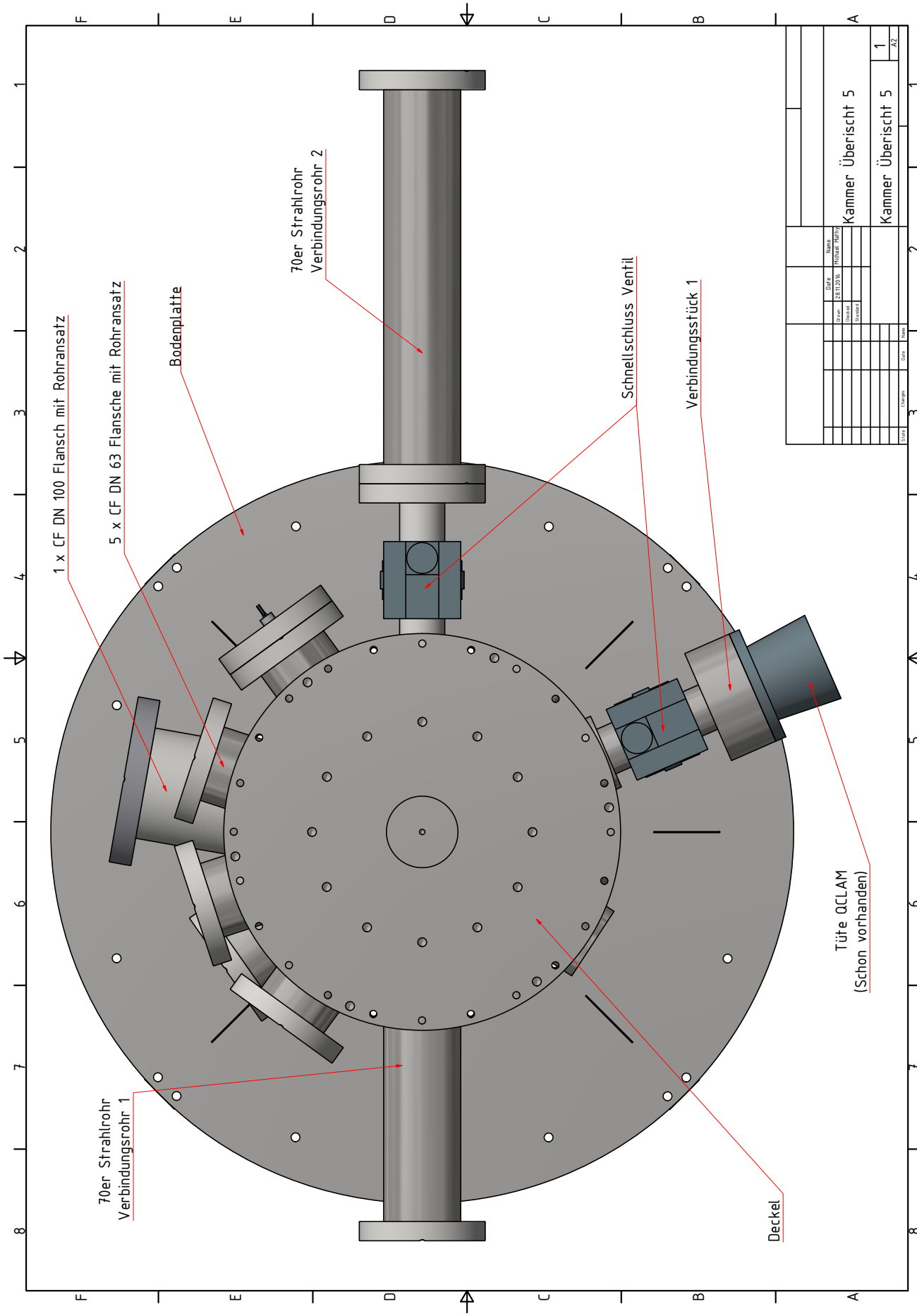
1 x CF DN 100 Flansch mit Rohransatz
5 x CF DN 63 Flansche mit Rohransatz
Bodenplatte
70er Strahlrohr
Verbindungsrohr 2
Schnellschluss Ventil
Verbindungsstück 1
Tüte QCLAM
(Schon vorhanden)
Deckel
70er Strahlrohr
Verbindungsrohr 1
Kammer Überischt 5
Kammer Überischt 5
Name
Michael Raffin
Date
28.11.2016
Drawn
Checked
Standard
Changes
Date
Name
Date
1
A2

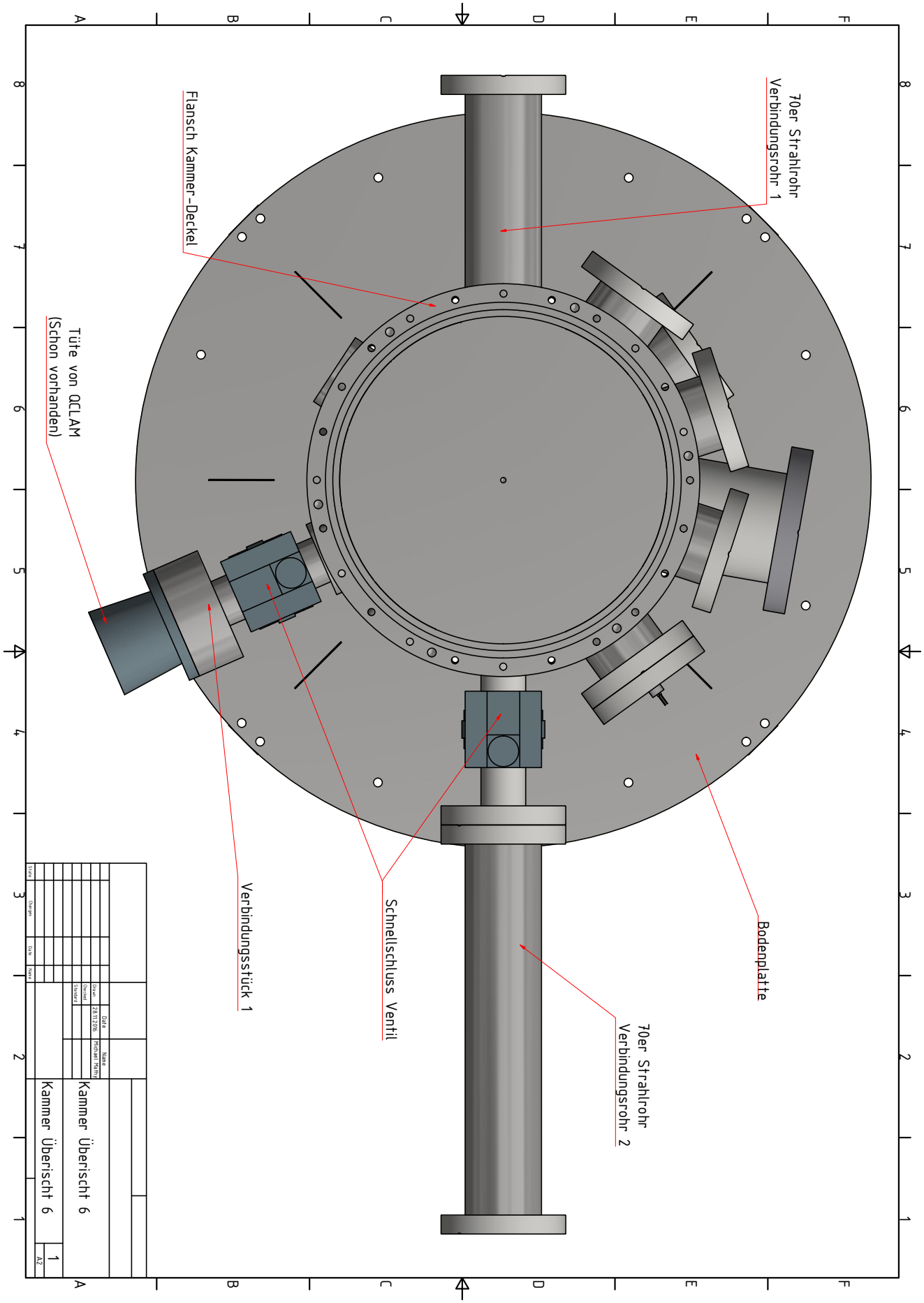
70er Strahlrohr
Verbindungsrohr 1
Flansch Kammer-Deckel
Tüte von QCLAM
(Schon vorhanden)
Verbindungsstück 1
Schnellschluss Ventil
Bodenplatte
70er Strahlrohr
Verbindungsrohr 2
Kammer Überischt 6
Kammer Überischt 6
A2

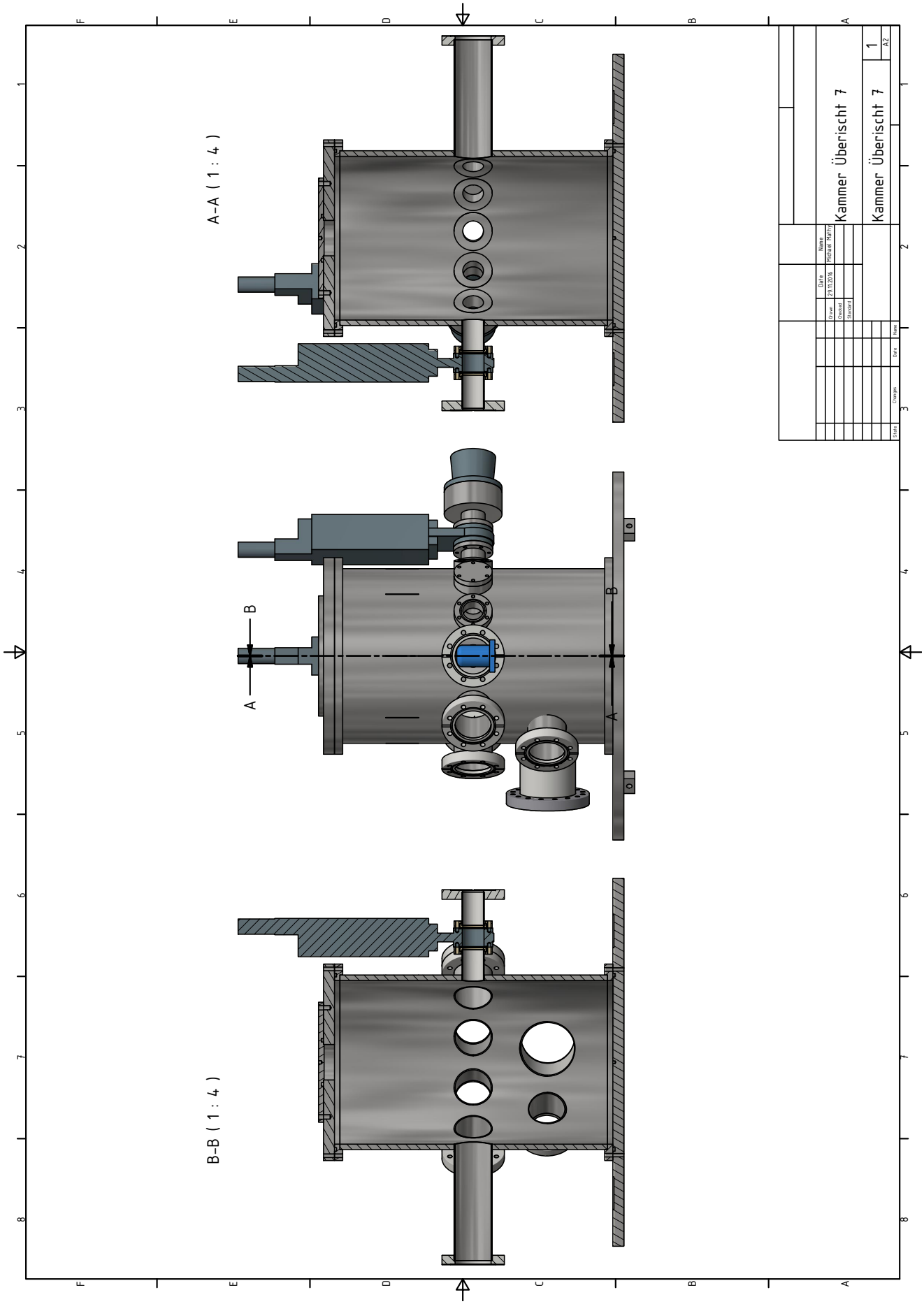
A–A (1 : 4)
B–B (1 : 4)
A
B
Kammer Übersicht 7
Kammer Übersicht 7
Name
Michael Haffke
Date
29.11.2016
Drawn
Checked
Standard
Changes
Date
Name
Date
1
A2

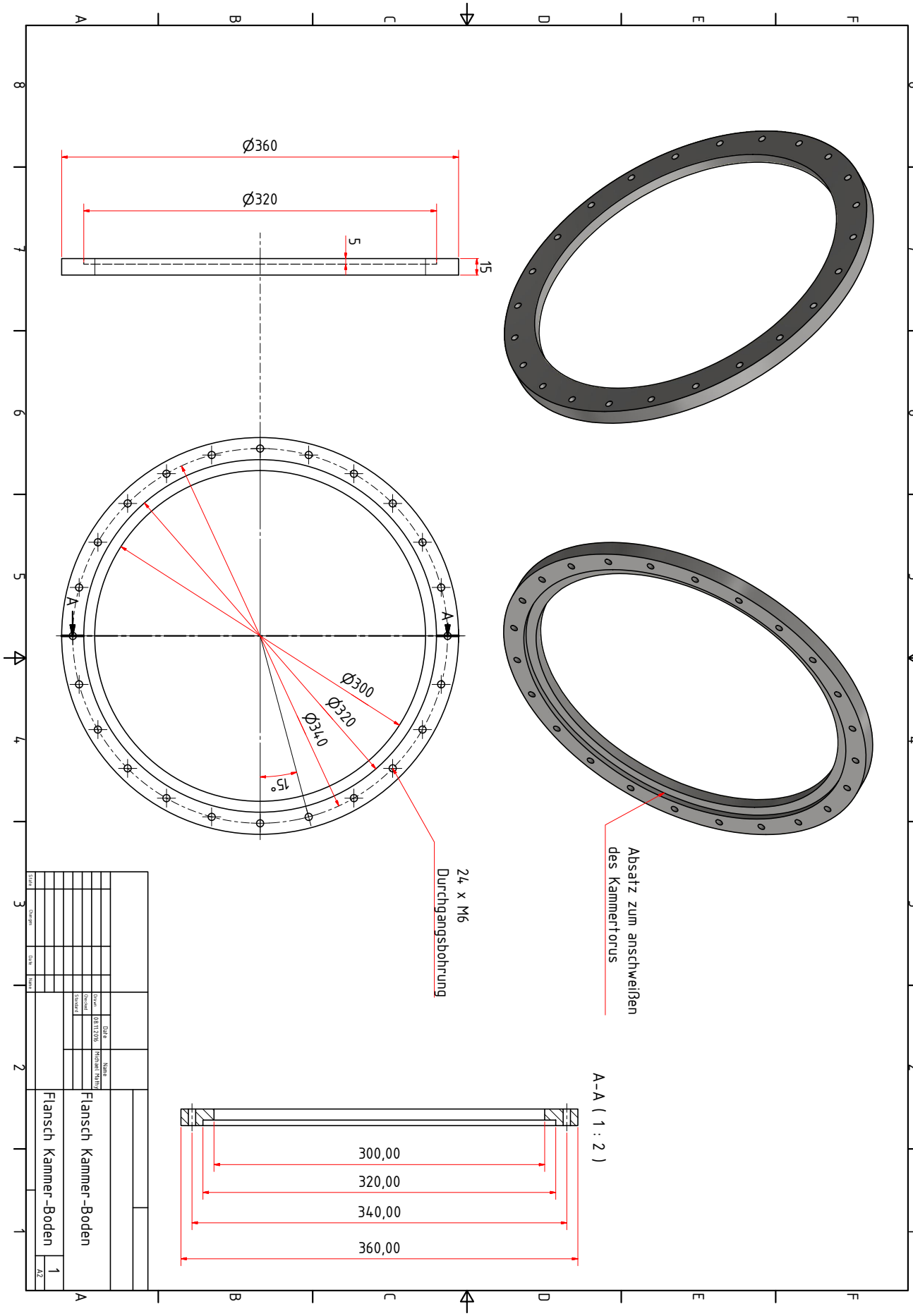
Ø360
Ø320
5
15
Ø300
Ø320
Ø340
15°
A
A
24 x M6
Durchgangsbohrung
Absatz zum anschweißen
des Kammertorus
A–A (1 : 2)
300,00
320,00
340,00
360,00
Flansch Kammer-Boden
Flansch Kammer-Boden
Name
Florian Rothe
Datum
08.11.2016
Maßstab
1
A2

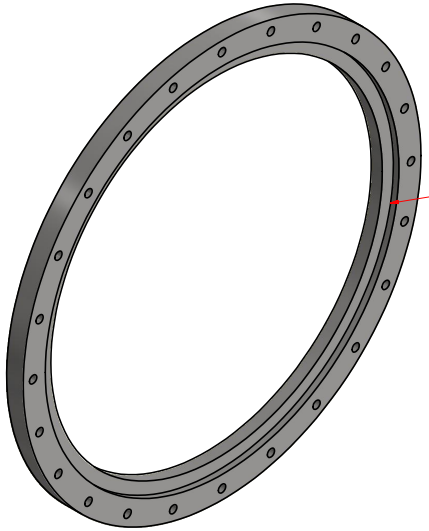

Absatz zum anschweißen
des Kammertorus

Nut für O-Ring. 4,00 mm tief, Kanten abrunden (r=0,20 mm).
(Für O-Ring: 315 mm x 5 mm)

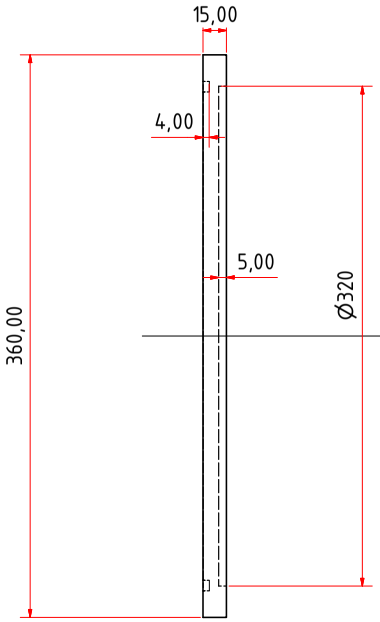

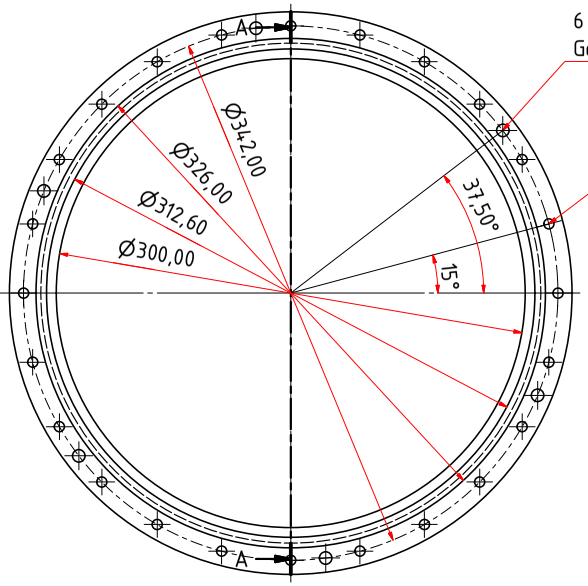

6 x M8
Gewindebohrung 11 mm tief

24 x M6
Durchgangsbohrung

A-A (1 : 2)

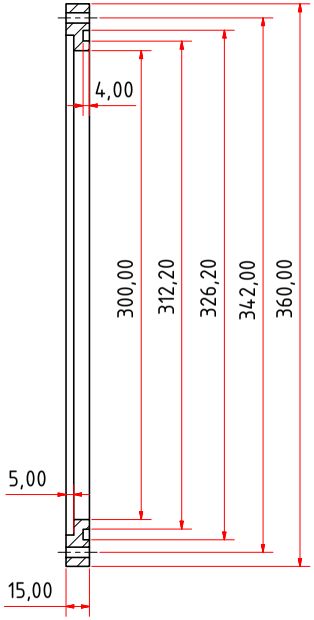

				Date	Name	Flansch Kammer-Deckel
			Drawn	04.11.2016	Michael Mathy	
			Checked			
			Standard			
State	Changes	Date	Name			Flansch Kammer-Deckel 1 A2

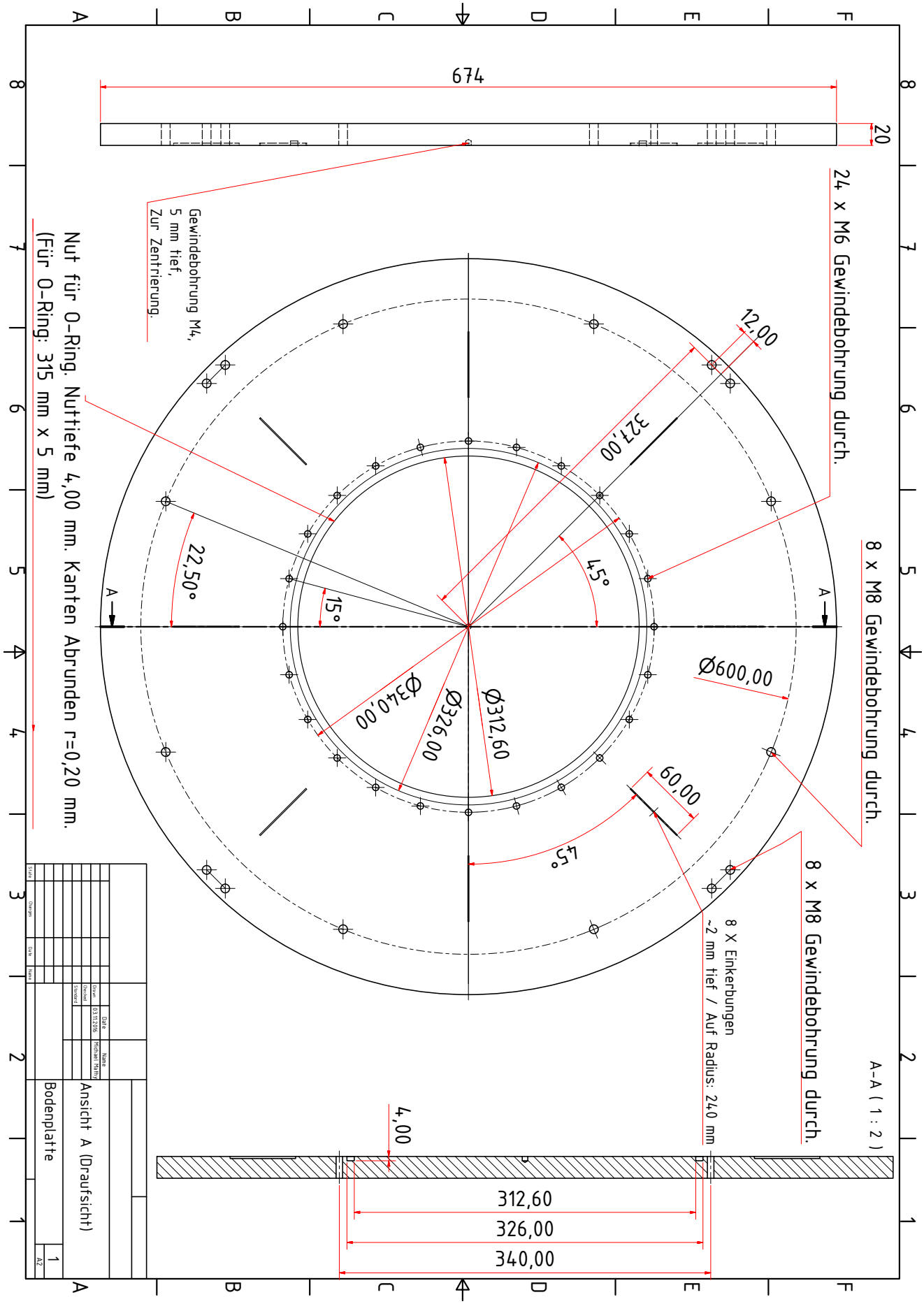
674
20
24 x M6 Gewindebohrung durch.
Gewindebohrung M4,
5 mm tief,
Zur Zentrierung.
Nut für O-Ring. Nuttiefe 4,00 mm. Kanten Abrunden r=0,20 mm.
(Für O-Ring: 315 mm x 5 mm)
12,00
327,00
22,50°
45°
15°
Ø600,00
Ø340,00
Ø326,00
Ø312,60
60,00
45°
8 x M8 Gewindebohrung durch.
8 x M8 Gewindebohrung durch.
8 X Einkerbungen
-2 mm tief / Auf Radius: 240 mm
A–A (1 : 2)
4,00
312,60
326,00
340,00
Ansicht A (Draufsicht)
Bodenplatte
Name
Datum
Maßstab
Blatt
A2

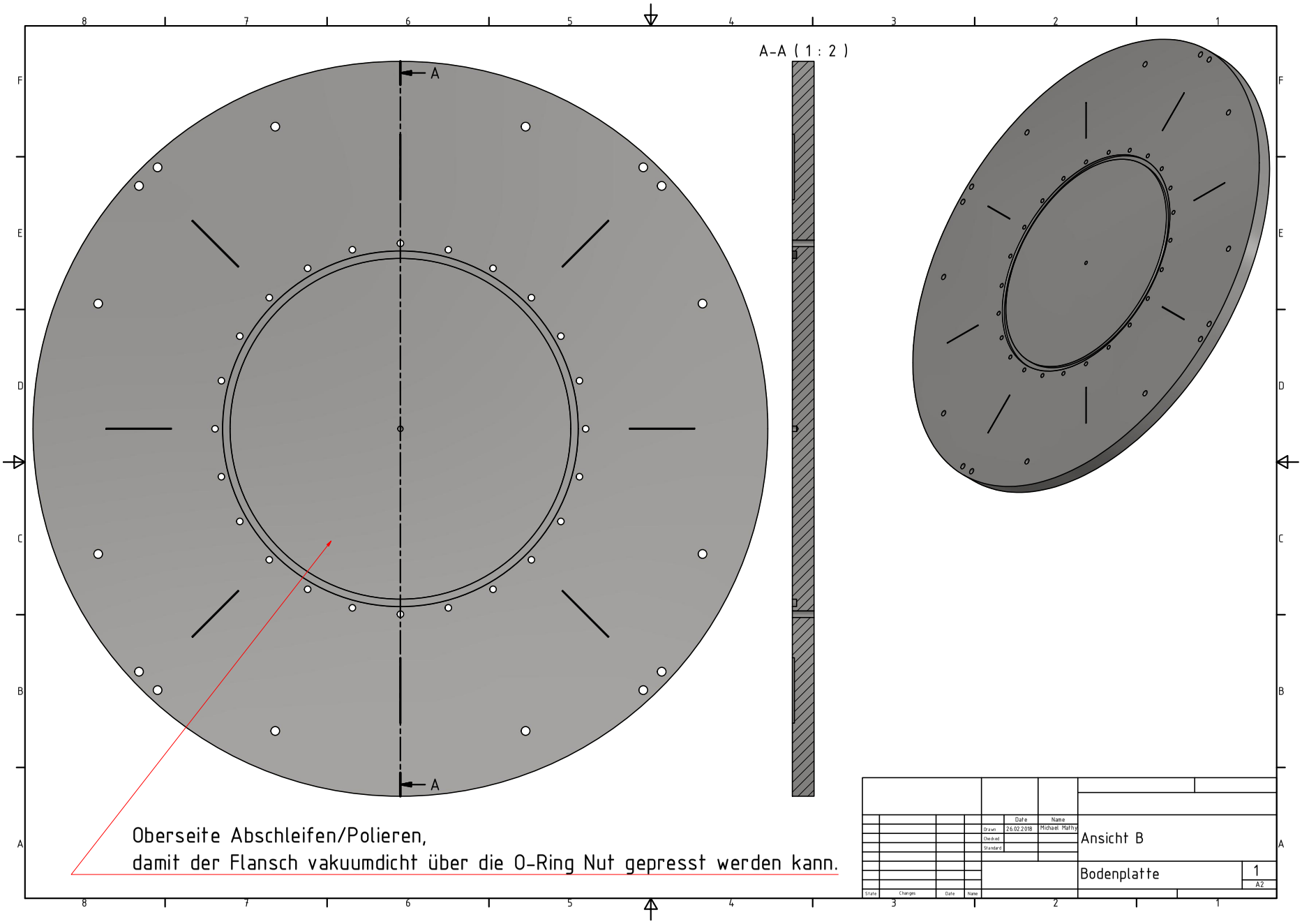
A-A (1 : 2)
A
A
Oberseite Abschleifen/Polieren,
damit der Flansch vakuumdicht über die O-Ring Nut gepresst werden kann.
Date
Name
Drawn
26.02.2018
Michael Mathy
Checked
Standard
Ansicht B
Bodenplatte
1
A2

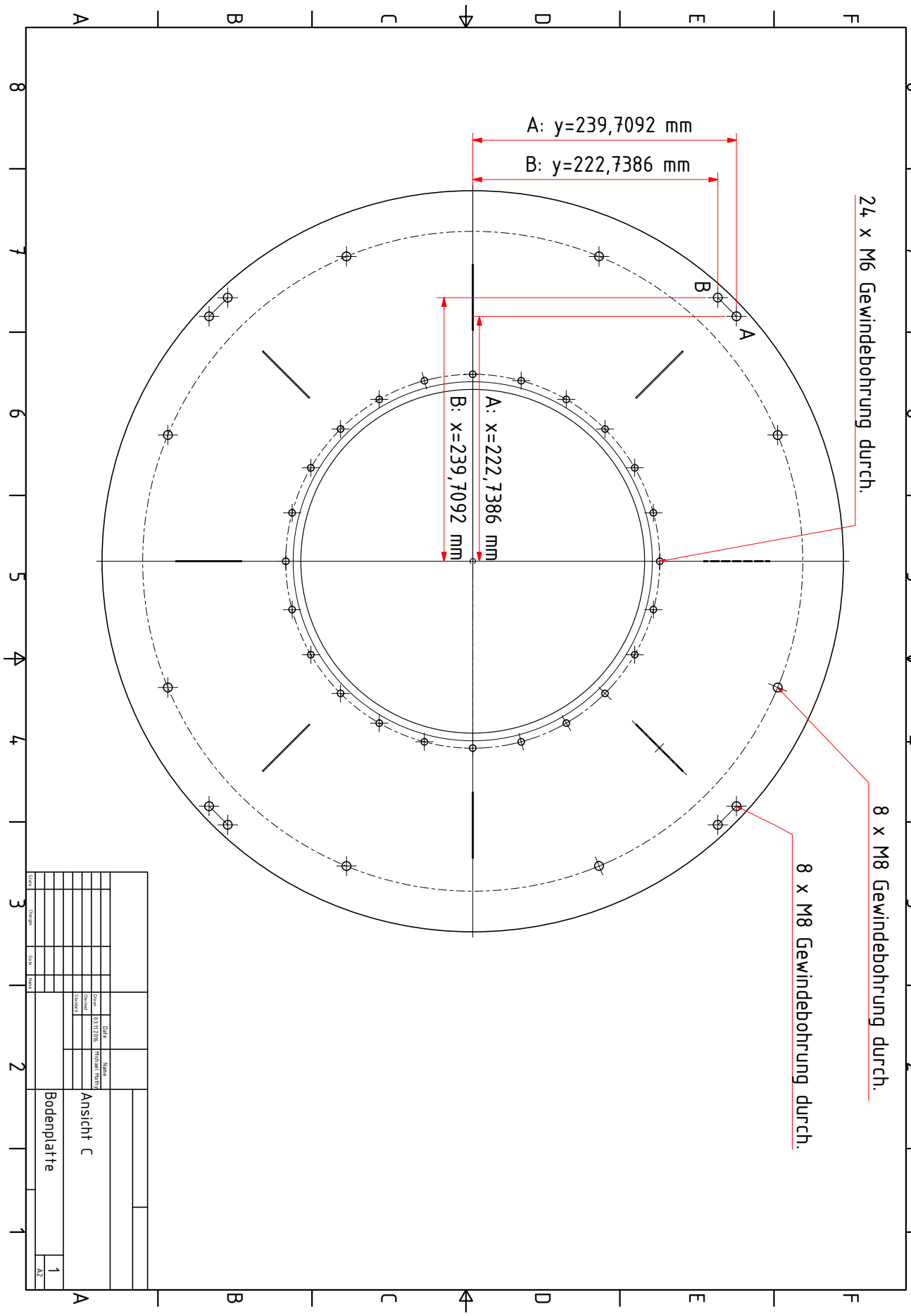
A: y=239,7092 mm
B: y=222,7386 mm
24 x M6 Gewindebohrung durch.
8 x M8 Gewindebohrung durch.
8 x M8 Gewindebohrung durch.
A: x=222,7386 mm
B: x=239,7092 mm
Bodenplatte
Ansicht C

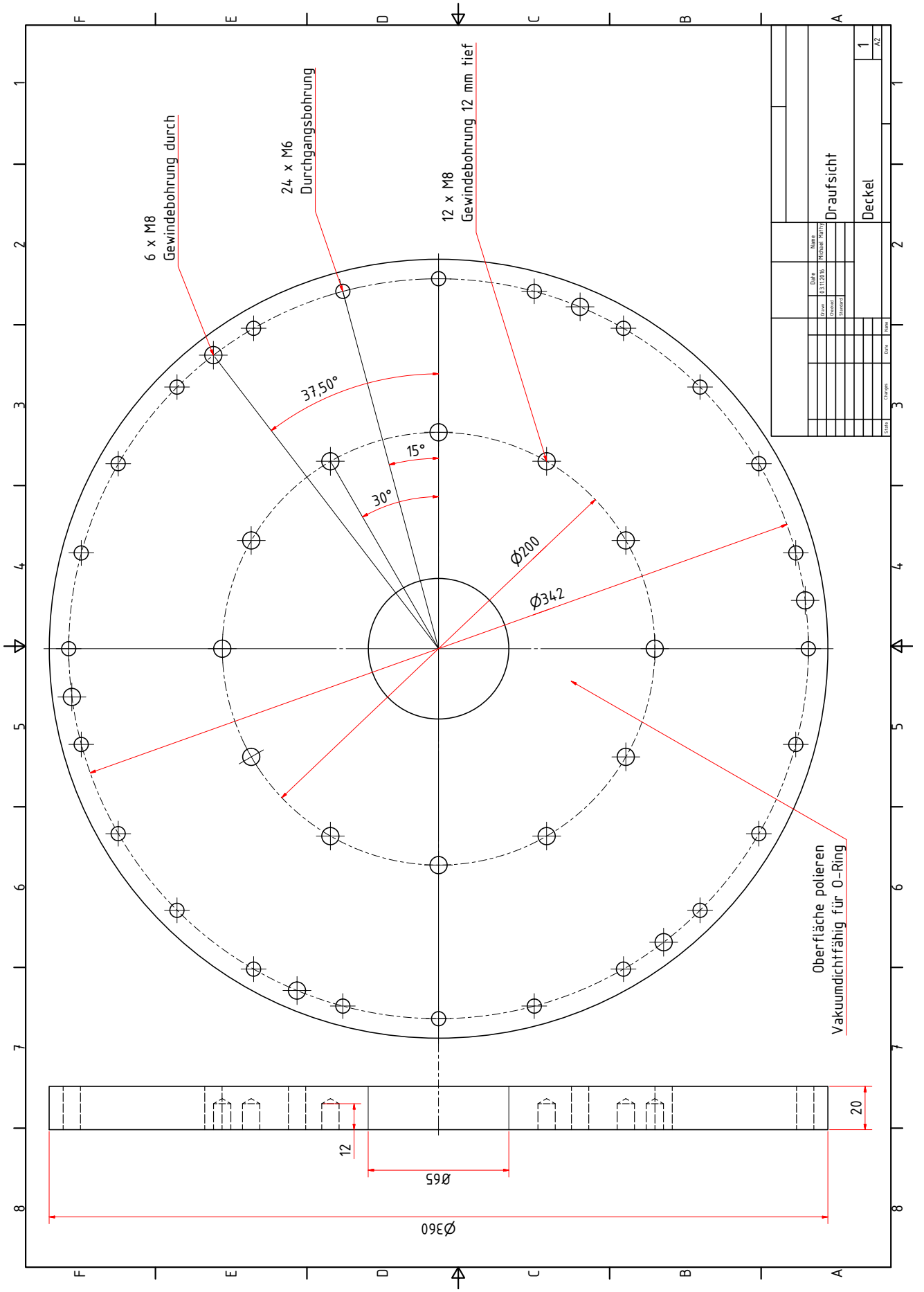
6 x M8
Gewindebohrung durch
24 x M6
Durchgangsbohrung
12 x M8
Gewindebohrung 12 mm tief
37,50°
15°
30°
Ø200
Ø342
Oberfläche polieren
Vakuumdichtfähig für O-Ring
Draufsicht
Deckel
Ø360
Ø65
12
20

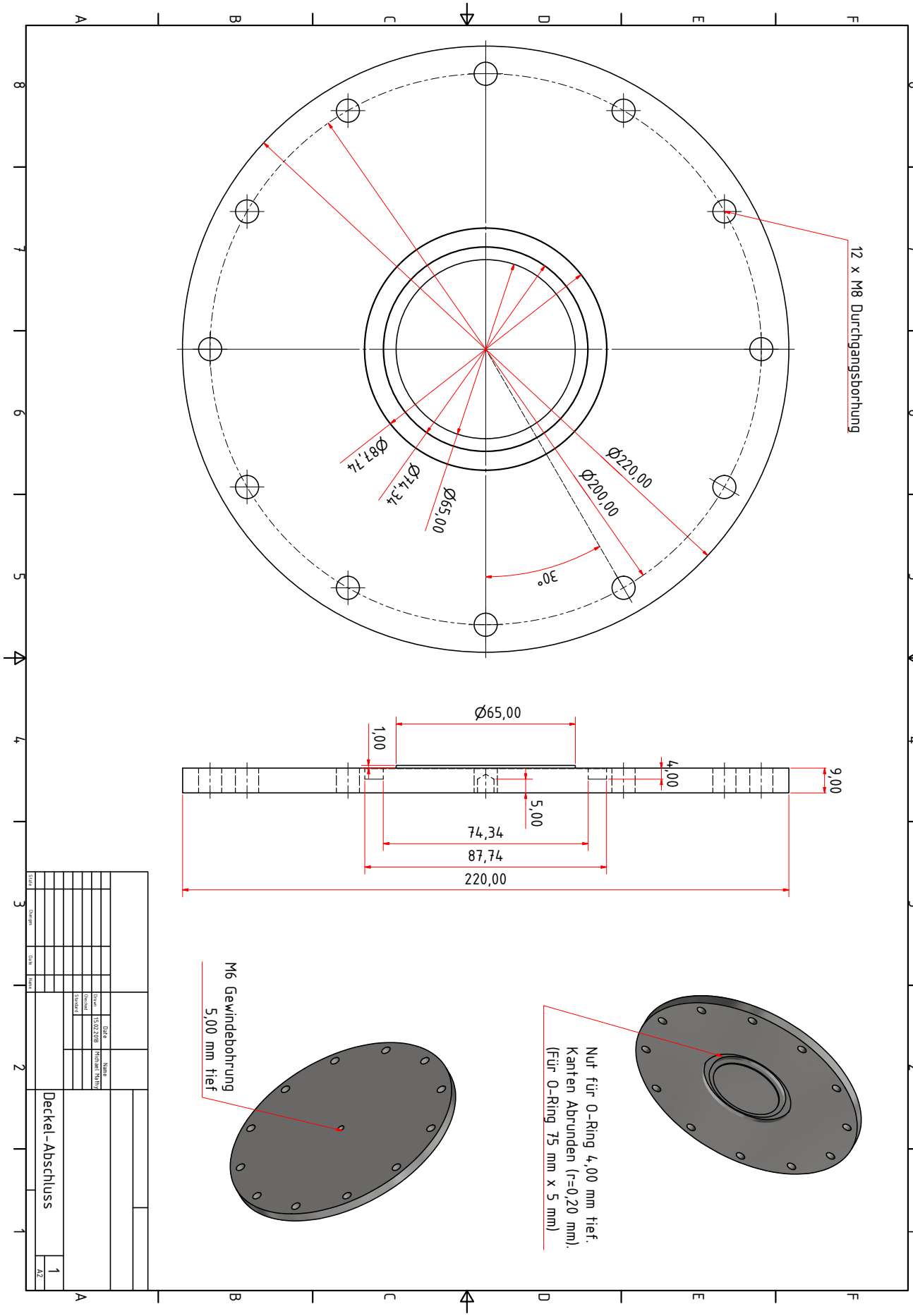
12 x M8 Durchgangsbohrung
Ø87,74
Ø74,34
Ø65,00
Ø200,00
Ø220,00
30°
Ø65,00
1,00
4,00
9,00
5,00
74,34
87,74
220,00
M6 Gewindebohrung
5,00 mm tief
Nut für O-Ring 4,00 mm tief.
Kanten Abrunden (r=0,20 mm).
(Für O-Ring 75 mm x 5 mm)
Deckel-Abschluss
A2
1
15.02.2018
Florian Thürig

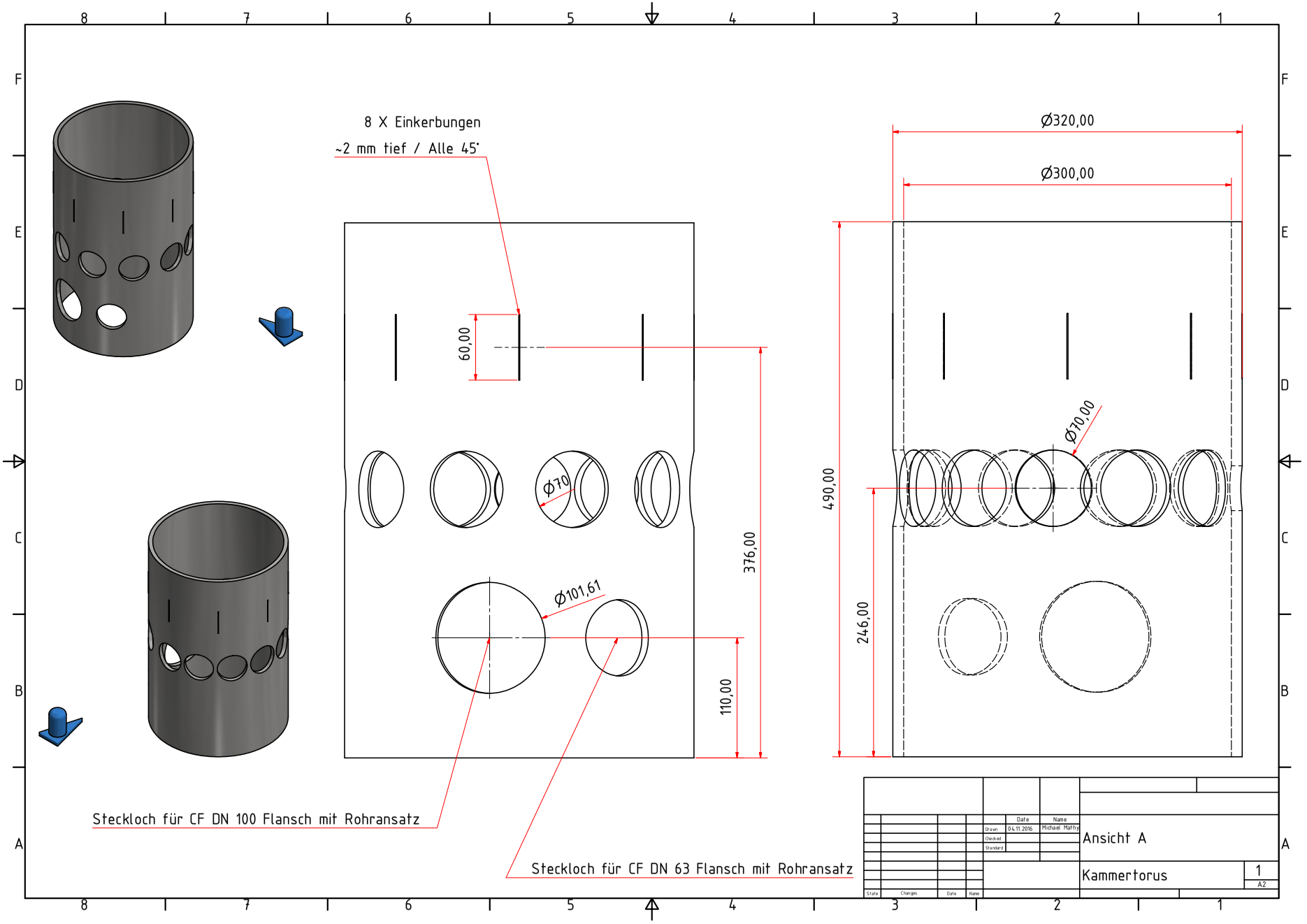
8 X Einkerbungen
~2 mm tief / Alle 45°
60,00
Ø70
Ø101,61
376,00
110,00
Ø320,00
Ø300,00
Ø70,00
490,00
246,00
Steckloch für CF DN 100 Flansch mit Rohransatz
Steckloch für CF DN 63 Flansch mit Rohransatz
Date
Name
Drawn
04.11.2016
Michael Mathy
Checked
Standard
State
Changes
Date
Name
Ansicht A
Kammertorus
1
A2

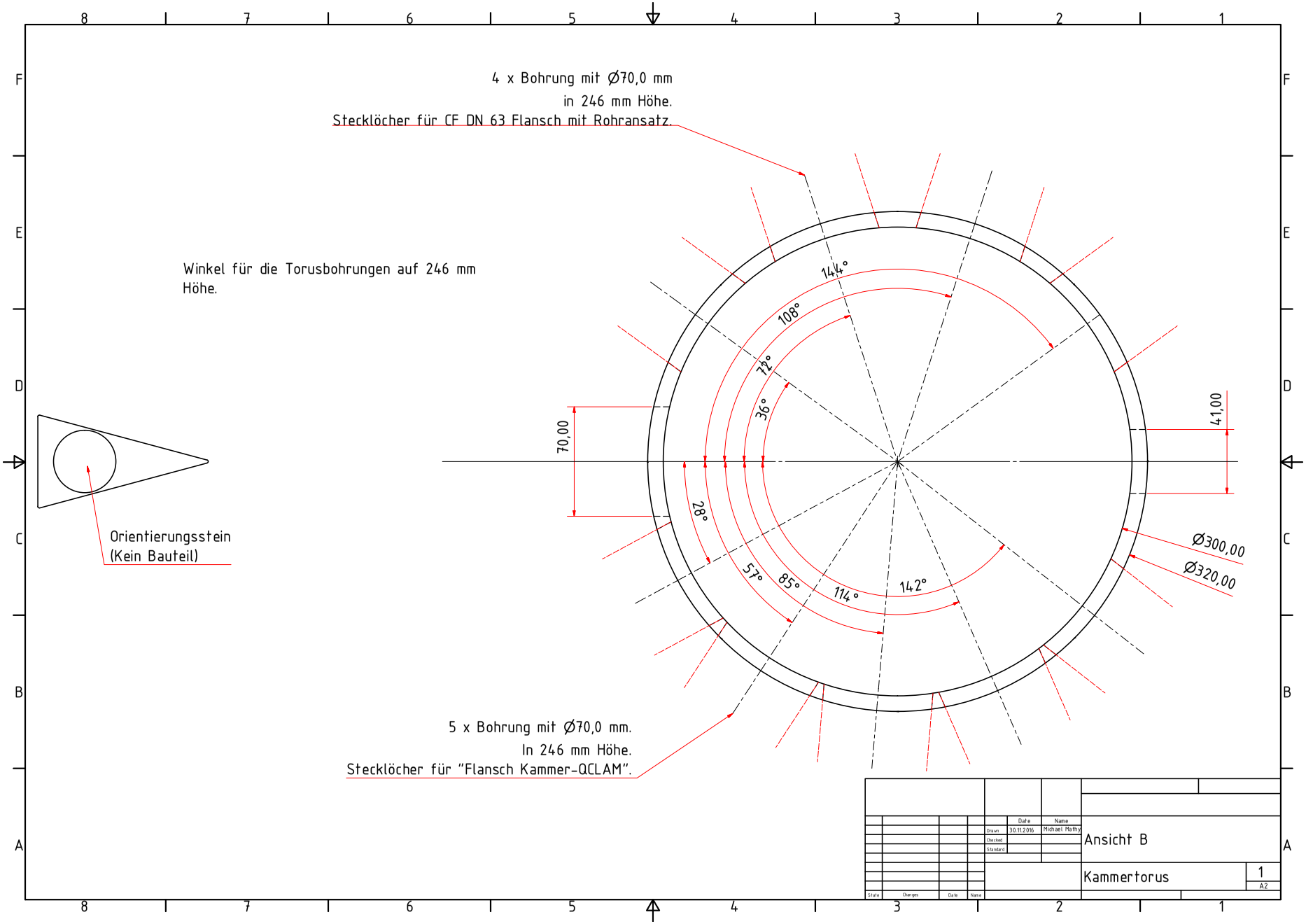
4 x Bohrung mit Ø70,0 mm
in 246 mm Höhe.
Stecklöcher für CF DN 63 Flansch mit Rohransatz.
Winkel für die Torusbohrungen auf 246 mm Höhe.
144°
108°
72°
36°
28°
57°
85°
114°
142°
70,00
41,00
Ø300,00
Ø320,00
Orientierungsstein
(Kein Bauteil)
5 x Bohrung mit Ø70,0 mm.
In 246 mm Höhe.
Stecklöcher für "Flansch Kammer-QCLAM".
Drawn 30.11.2016 Michael Mathy
Checked
Standard
Ansicht B
Kammertorus
1
A2

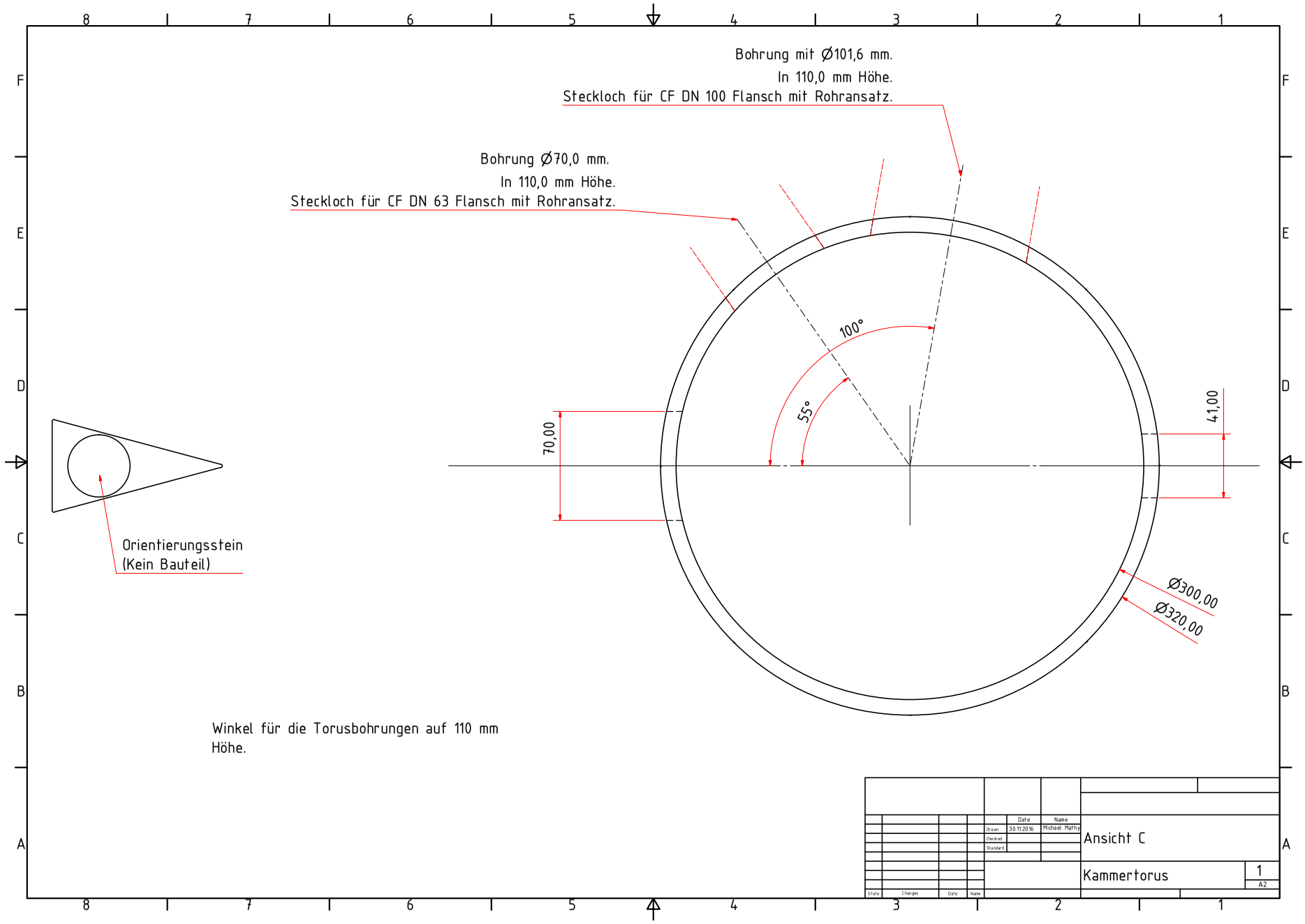
Bohrung mit Ø101,6 mm.
In 110,0 mm Höhe.
Steckloch für CF DN 100 Flansch mit Rohransatz.
Bohrung Ø70,0 mm.
In 110,0 mm Höhe.
Steckloch für CF DN 63 Flansch mit Rohransatz.
100°
55°
70,00
41,00
Ø300,00
Ø320,00
Orientierungsstein
(Kein Bauteil)
Winkel für die Torusbohrungen auf 110 mm
Höhe.
Date
Name
Drawn
30.11.2016
Michael Mathy
Checked
Standard
Ansicht C
Kammertorus
1
A2

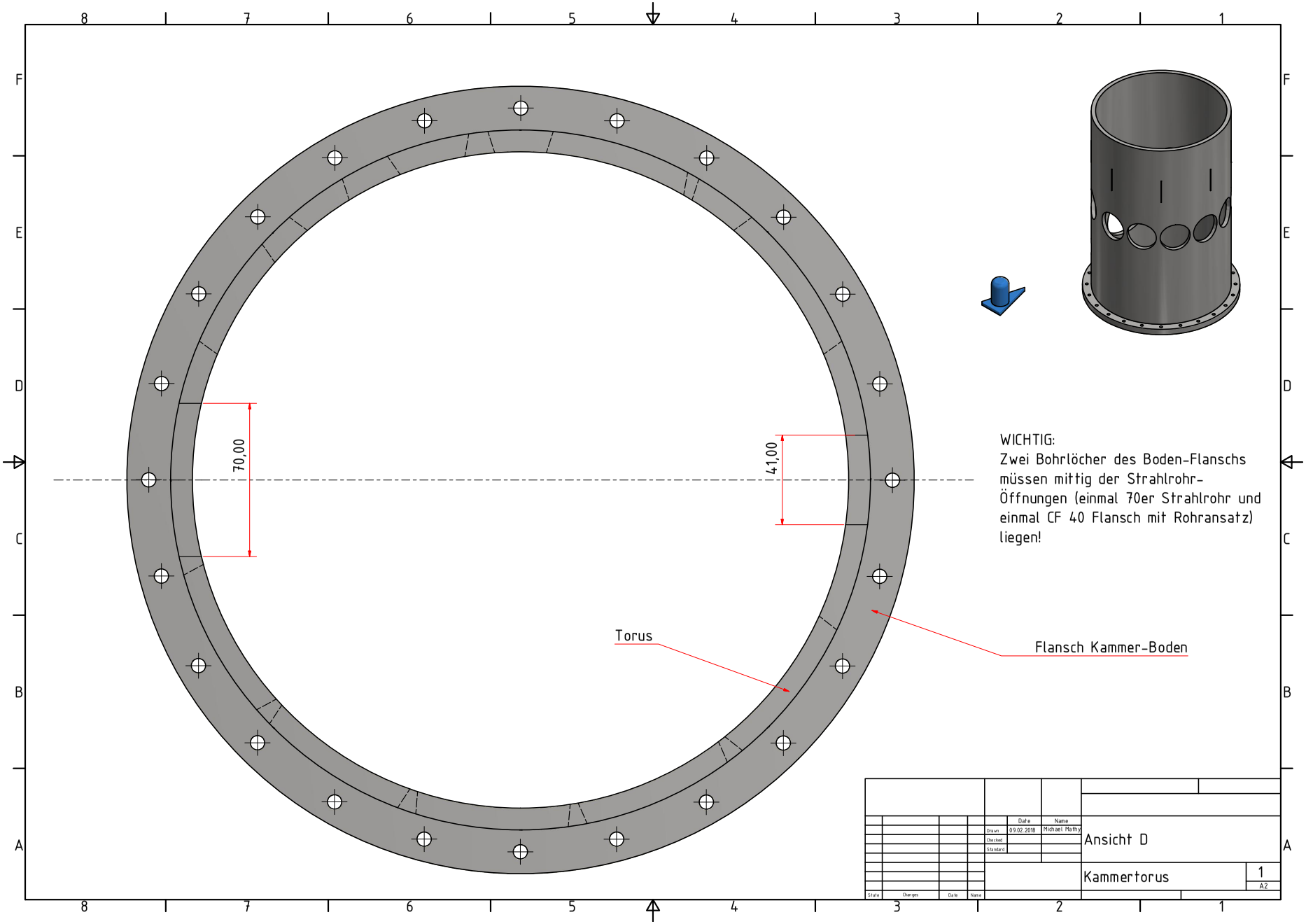
70,00
41,00
WICHTIG:
Zwei Bohrlöcher des Boden-Flanschs müssen mittig der Strahlrohr-Öffnungen (einmal 70er Strahlrohr und einmal CF 40 Flansch mit Rohransatz) liegen!
Torus
Flansch Kammer-Boden
Drawn 09.02.2018 Michael Mathy
Checked
Standard
Ansicht D
Kammertorus
1
A2

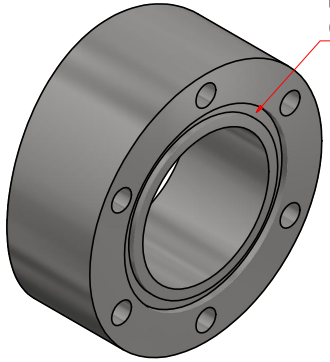

Nut für O-Ring. Nuttiefe 1,50 mm. Kanten Abrunden (r=0,10 mm)!
(Für O-Ring: 44 mm x 2 mm)

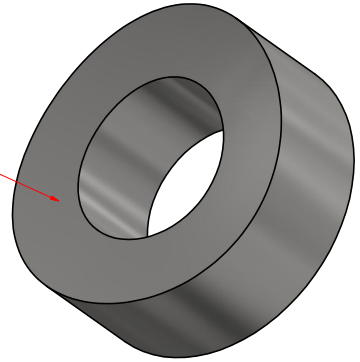

Anpassung an Innenradius
des Kammertorus

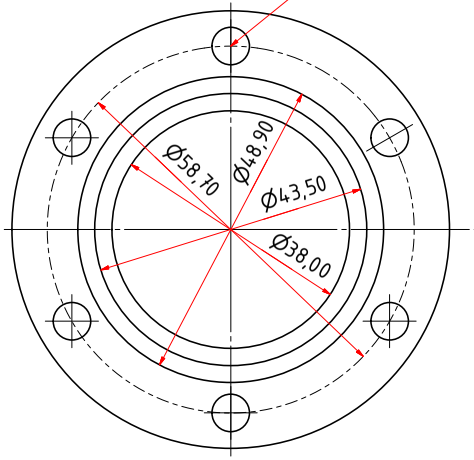

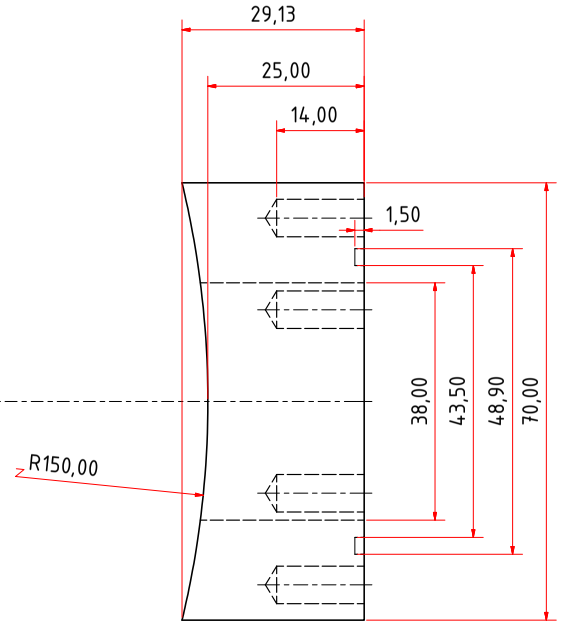

5 Stück benötigt

					Date	Name	Flansch Kammer-QCLAM
				Drawn	04.11.2016	Michael Mathy	
				Checked			
				Standard			
State	Changes	Date	Name				Flansch Kammer-QCLAM 1 A2

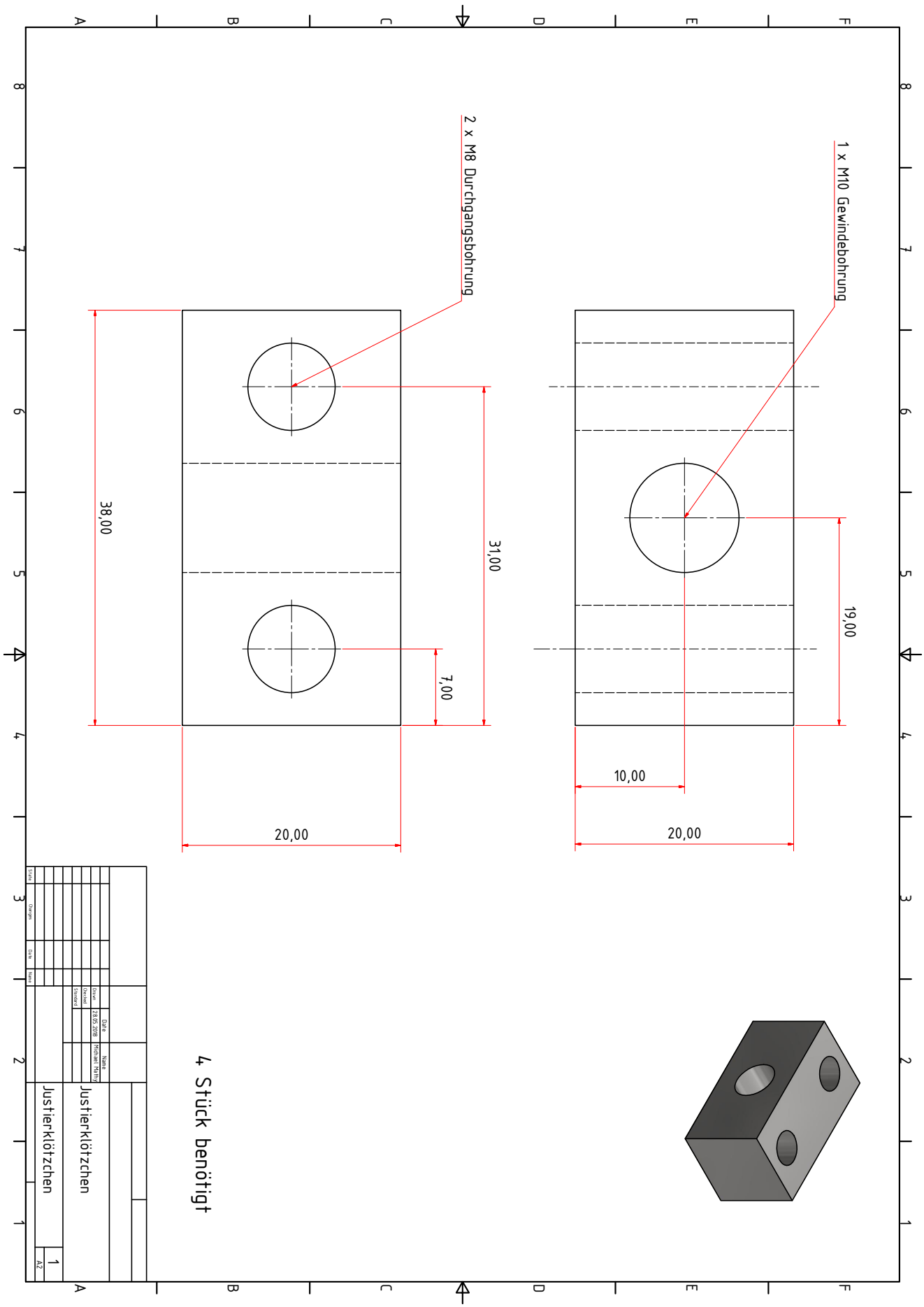
1 x M10 Gewindebohrung
2 x M8 Durchgangsbohrung
38,00
31,00
19,00
7,00
10,00
20,00
20,00
4 Stück benötigt
Justierklötzchen
Justierklötzchen
Justierklötzchen
Name
Datum
Maßstab
Gewicht
Blatt
A2

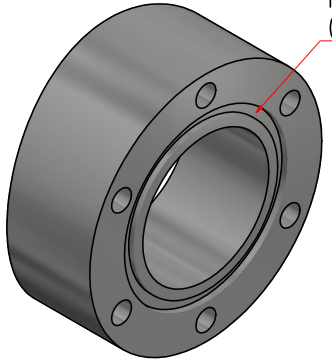

Nut für O-Ring. Nuttiefe 1,50 mm. Kanten Abrunden (r=0,10 mm)!
(Für O-Ring: 44 mm x 2 mm)

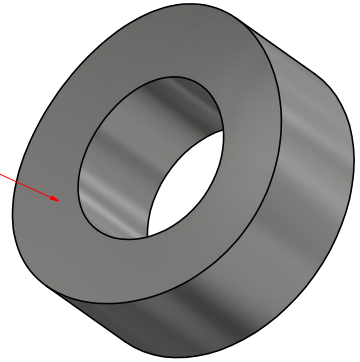

Anpassung an Innenradius
des Kammertorus

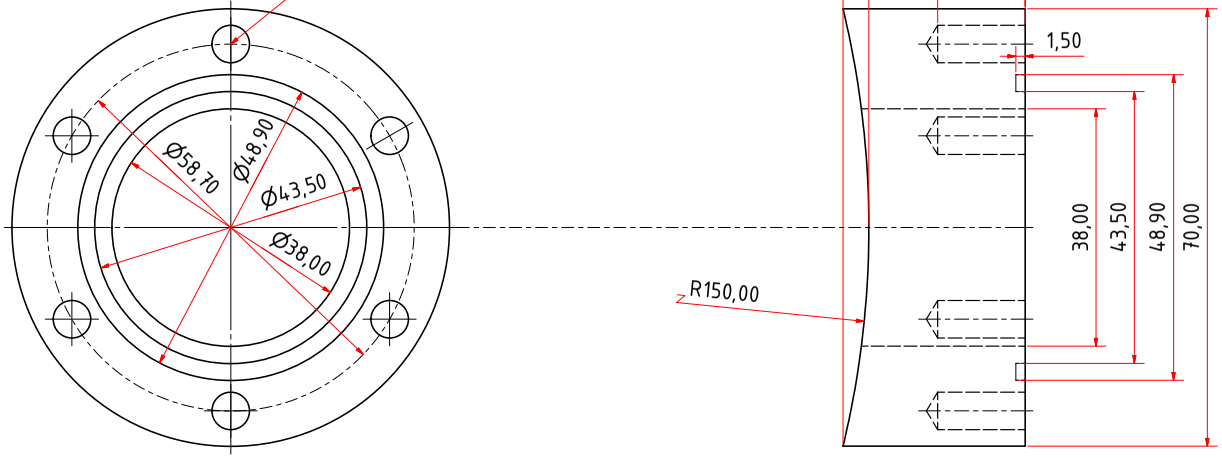

5 Stück benötigt

	Date	Name	
Drawn	04.11.2016	Michael Mathy	Flansch Kammer-QCLAM
Checked			
Standard			Flansch Kammer-QCLAM 1 A2

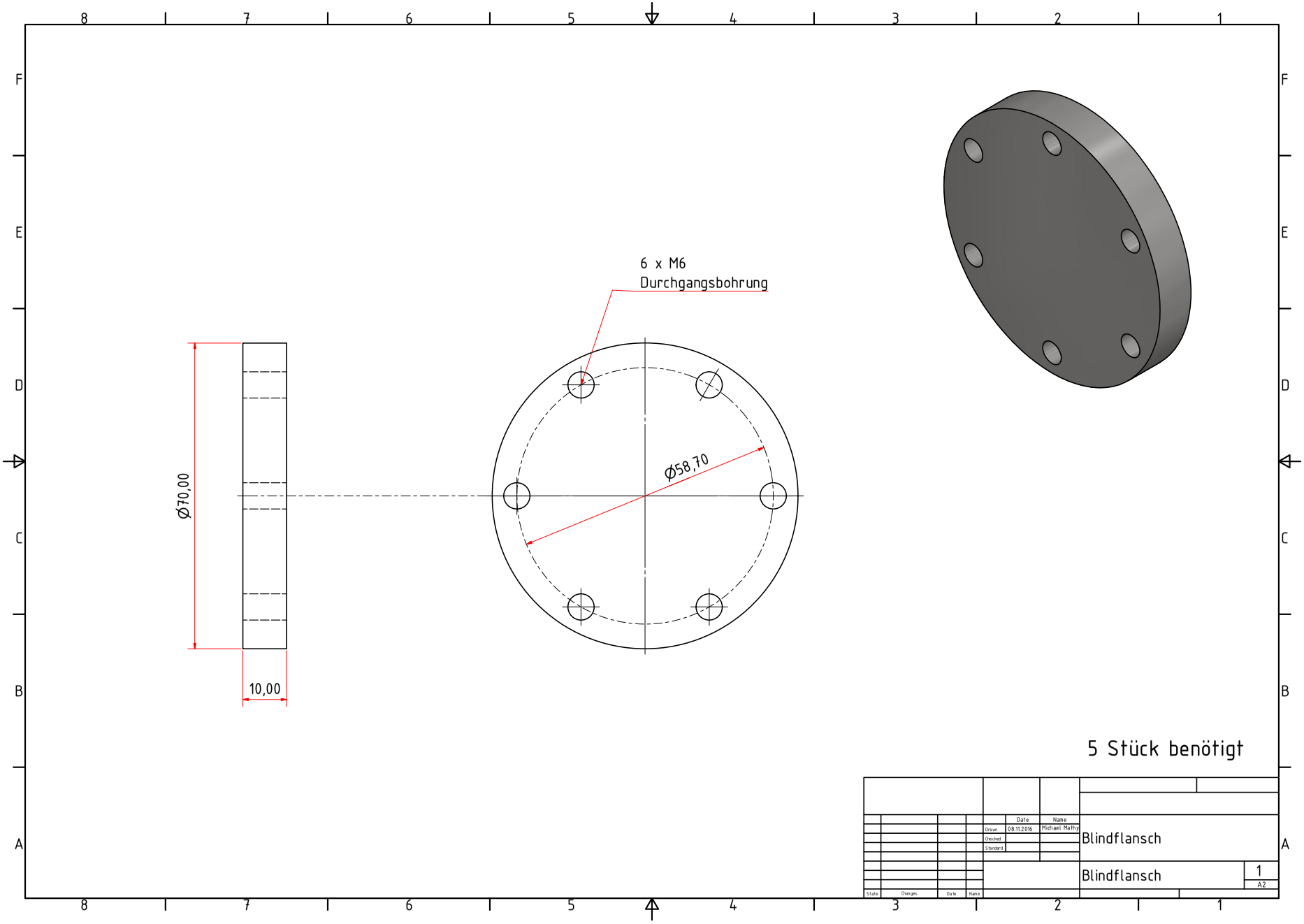
6 x M6
Durchgangsbohrung
Ø58,70
Ø70,00
10,00
5 Stück benötigt
Blindflansch
Blindflansch
1
A2

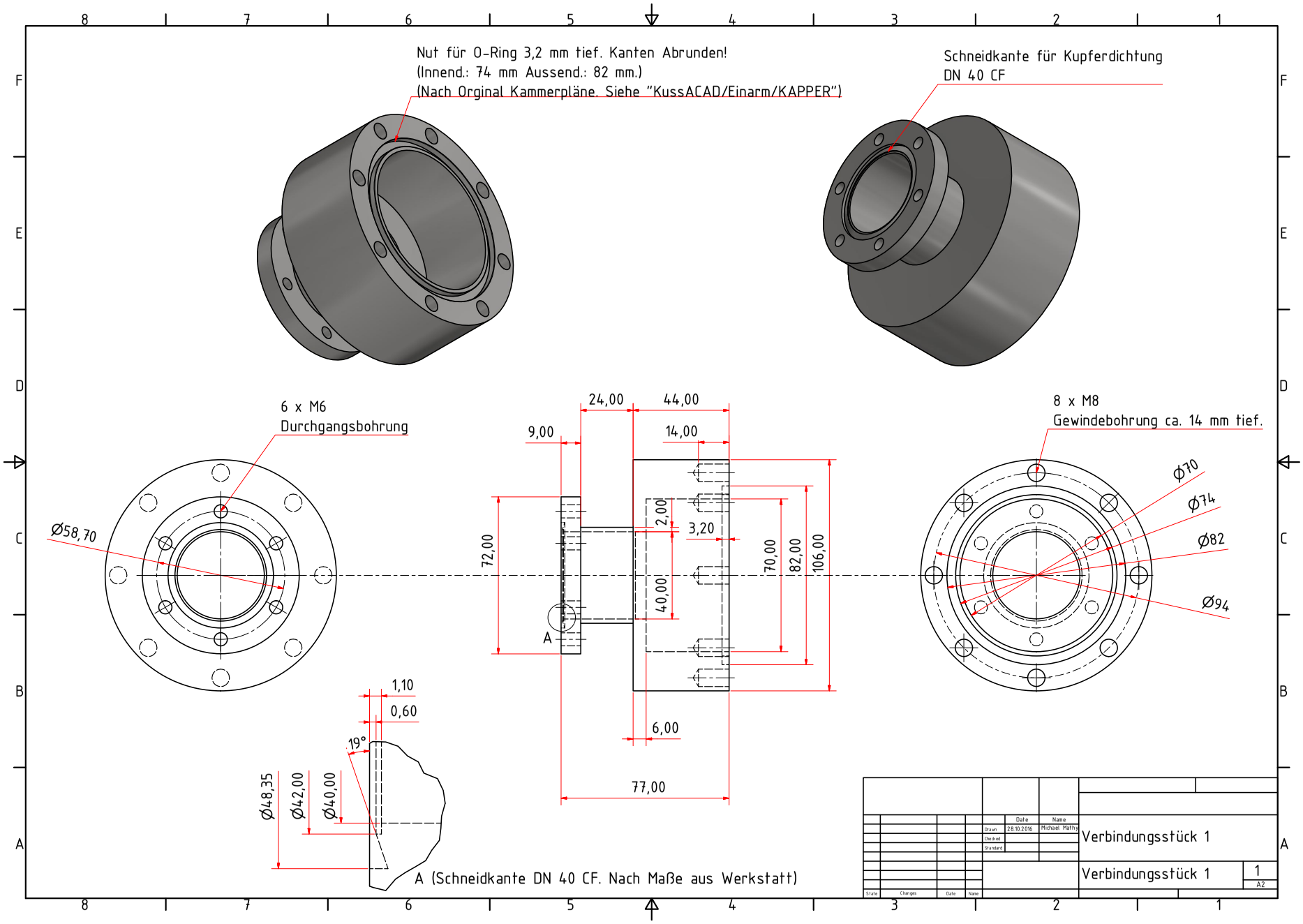
Nut für O-Ring 3,2 mm tief. Kanten Abrunden!
(Innend.: 74 mm Aussend.: 82 mm.)
(Nach Orginal Kammerpläne. Siehe "KussACAD/Einarm/KAPPER")
Schneidkante für Kupferdichtung
DN 40 CF
6 x M6
Durchgangsbohrung
8 x M8
Gewindebohrung ca. 14 mm tief.
Ø58,70
24,00
44,00
9,00
14,00
72,00
2,00
3,20
40,00
70,00
82,00
106,00
6,00
77,00
Ø70
Ø74
Ø82
Ø94
1,10
0,60
19°
Ø48,35
Ø42,00
Ø40,00
A
A (Schneidkante DN 40 CF. Nach Maße aus Werkstatt)
Date
Name
Drawn
28.10.2016
Michael Mathy
Checked
Standard
Verbindungsstück 1
Verbindungsstück 1
1
A2

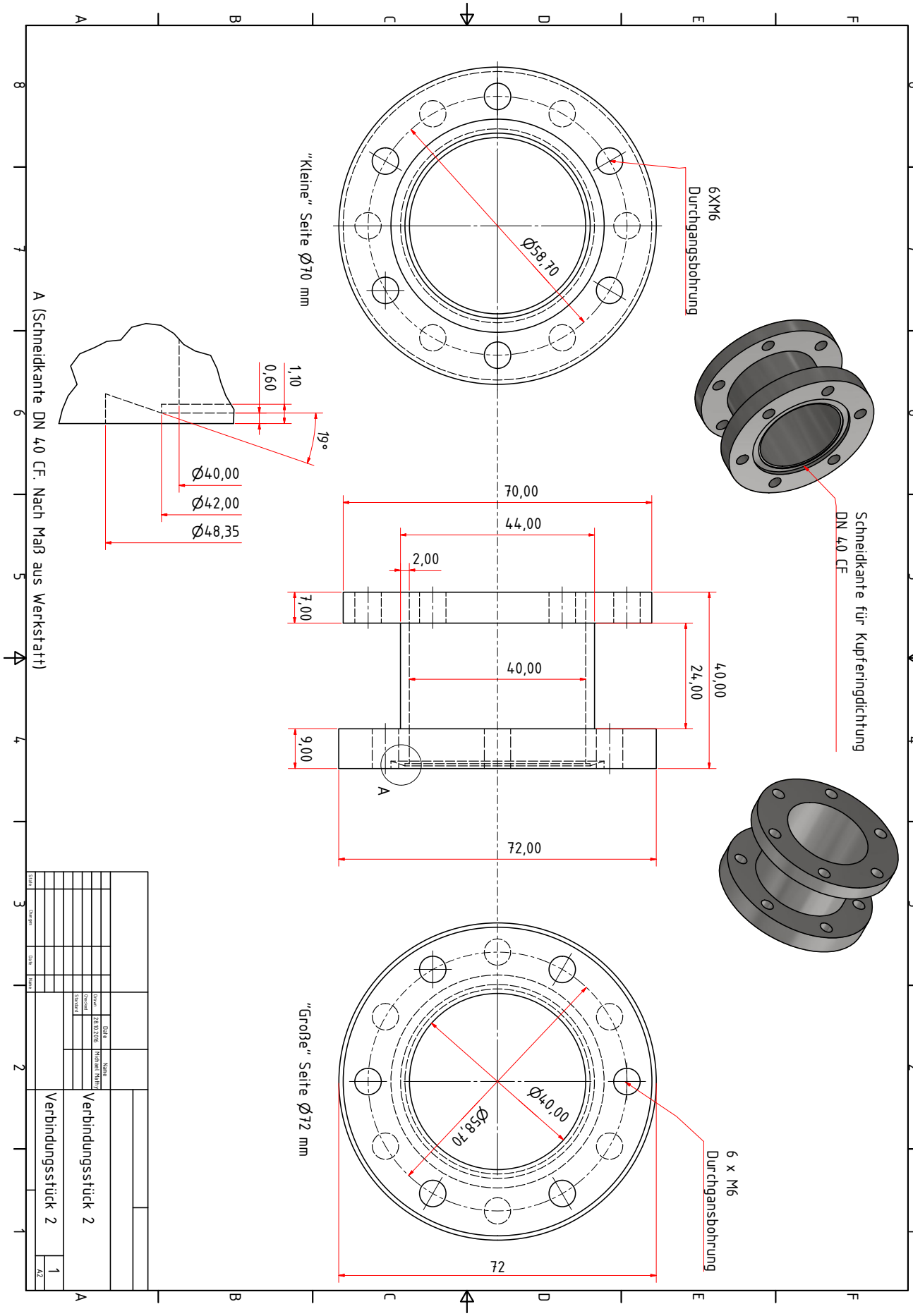
"Kleine" Seite Ø70 mm
6XM6
Durchgangsbohrung
Ø58,70
A (Schneidkante DN 40 CF. Nach Maß aus Werkstatt)
1,10
0,60
19°
Ø40,00
Ø42,00
Ø48,35
Schneidkante für Kupferingdichtung
DN 40 CF
70,00
44,00
2,00
7,00
40,00
24,00
40,00
9,00
A
72,00
"Große" Seite Ø72 mm
Ø40,00
Ø58,70
6 x M6
Durchgansbohrung
72
Verbindungsstück 2
Verbindungsstück 2
Florian Thöny
28.10.2016
1
A2

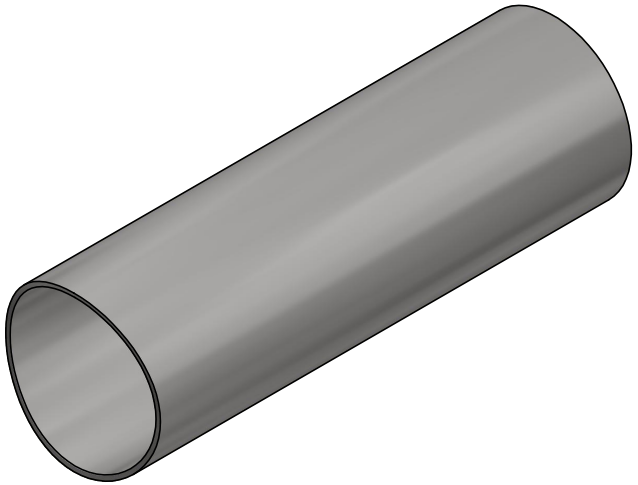

Wurde kommerziell erworben.
Länge und Abbrundung zum Anschweißen muss angepasst werden.

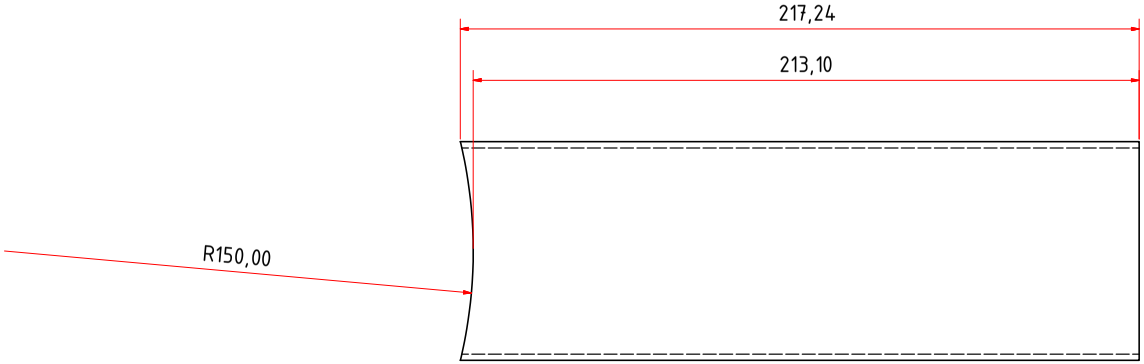

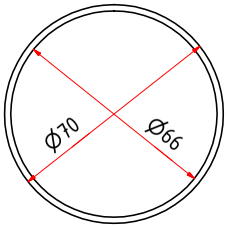

			Date	Name	Verbindungsrohr 1
			Drawn 21112016	Michael Mathy	
			Checked		
			Standard		
State	Changes	Date	Name		Verbindungsrohr 1 — 1 — A2

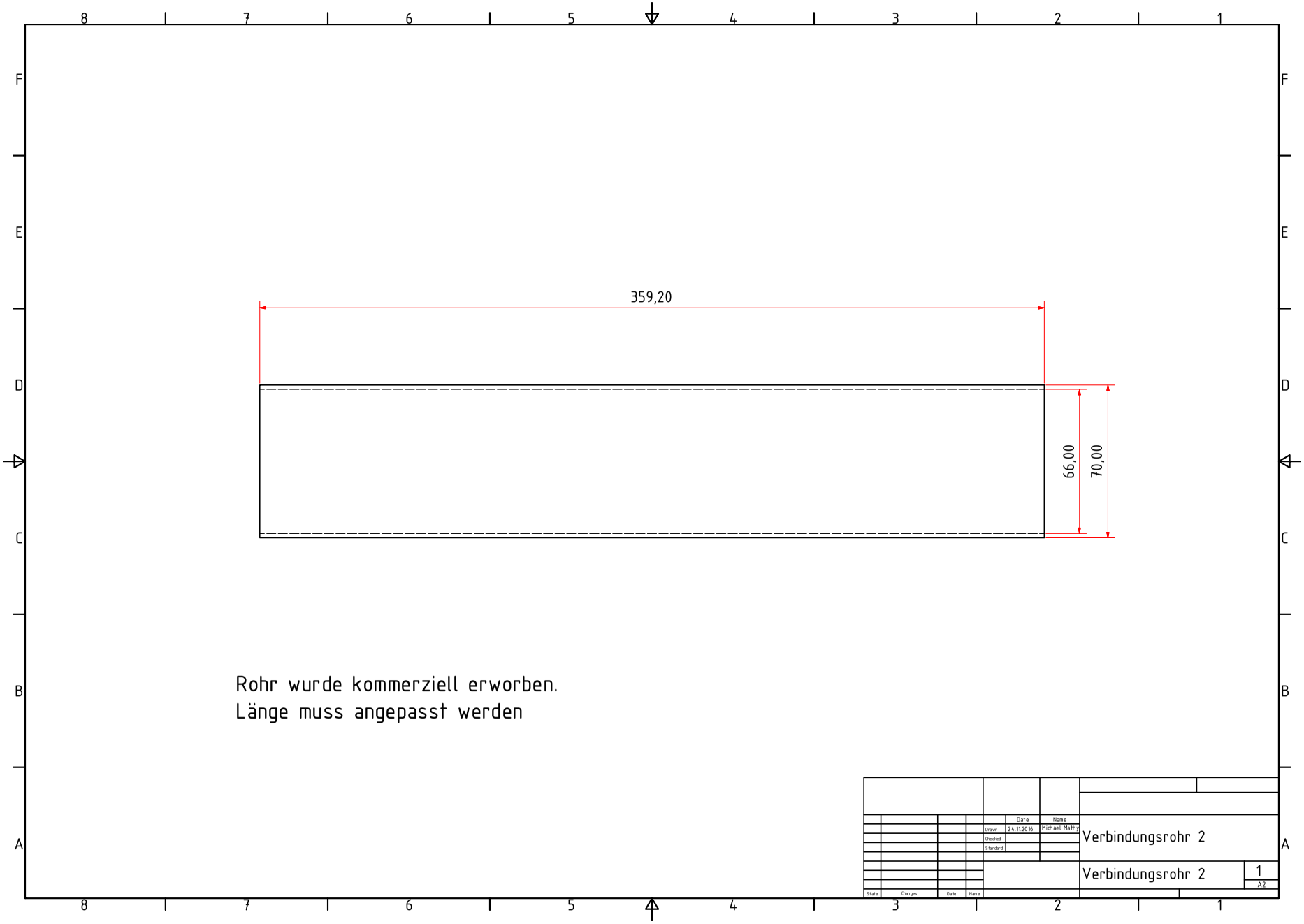
359,20
66,00
70,00
Rohr wurde kommerziell erworben.
Länge muss angepasst werden
Date
Name
Drawn
24.11.2016
Michael Mathy
Checked
Standard
Verbindungsrohr 2
Verbindungsrohr 2
1
A2
State
Changes
Date
Name

CF40 Flansch mit Rohransatz wurde kommerziell erworben.
Abrundung zum Anschweißen muss erstellt werden.
1 mal benötigt.

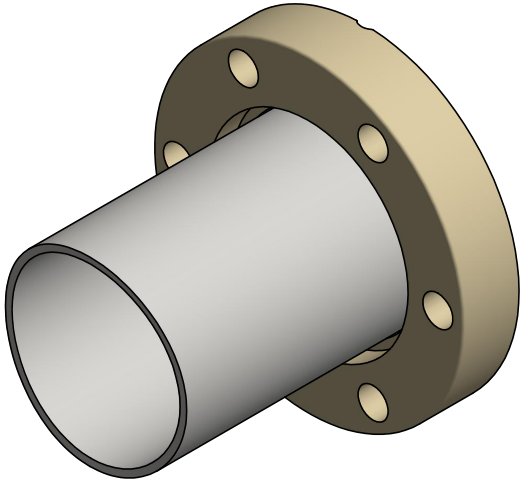

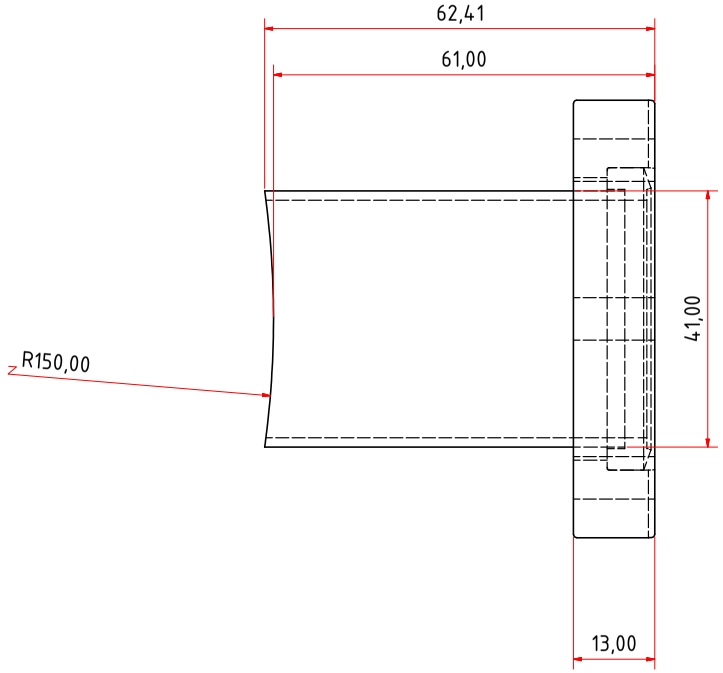

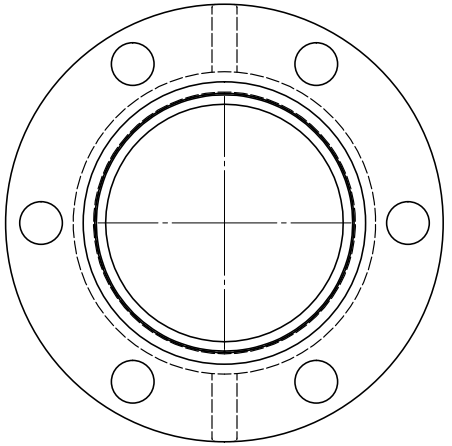

		Date	Name	CF Flansch DN 40 mit R.
		Drawn 28.11.2016	Michael Mathy	
		Checked		
		Standard		
State	Changes	Date	Name	CF Flansch DN 40 mit R. 1 A2

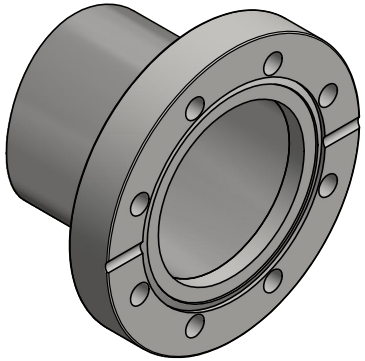

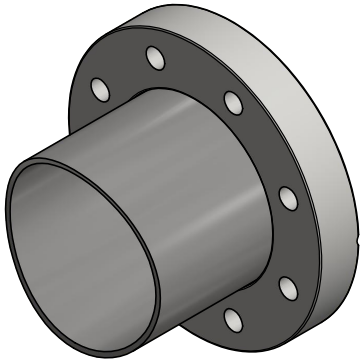

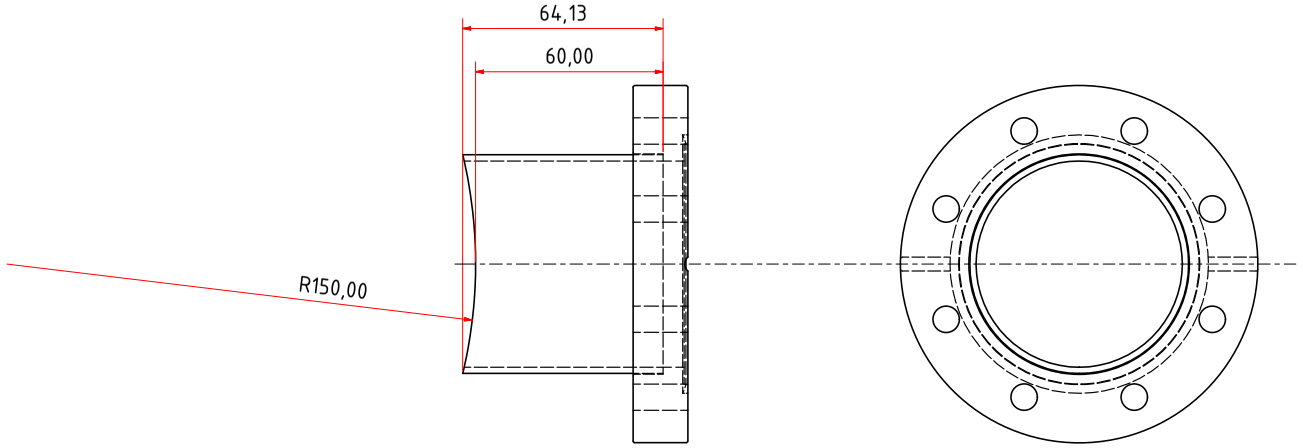

70er Strahlrohr wurde kommerziell erworben.
Die Länge muss angepasst werden.
Abbrundung zum Anschweißen an den Kammertorus muss angepasst werden.
CF DN 63 Flansch (ebefalls kommerziell erworben) muss angeschweißt werden.
Es werden 5 Stück benötigt.

	Date	Name
Drawn	20.02.2018	Michael Mathy
Checked		
Standard		

CF DN 63 Wartungsflansch

CF DN 63 Wartungsflansch 1 A2

DN CF 100 Flansch mit Rohransatz wurde kommerziell erworben..
Abrundung zum Anschweißen muss erstellt werden.
1 mal benötigt.

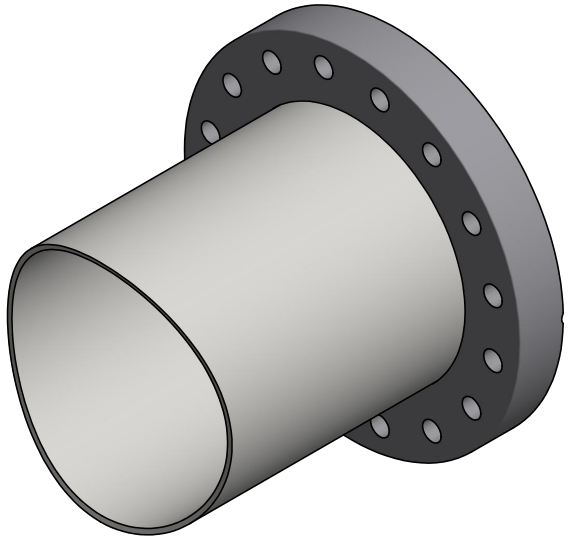

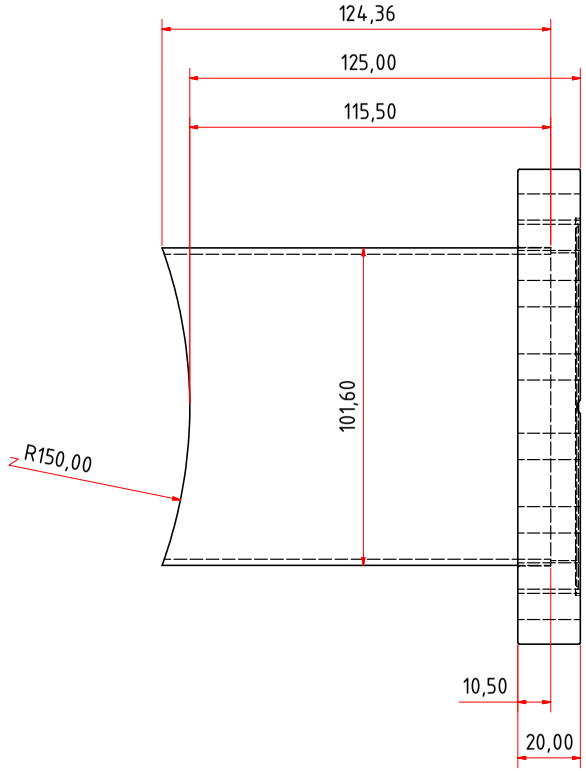

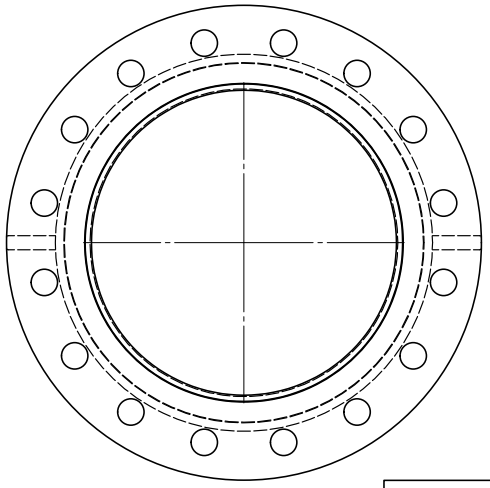

				Date	Name
			Drawn	28.11.2016	Michael Mathy
			Checked		
			Standard		
State	Changes	Date	Name		

CF Flansch DN 100 mit R.

CF Flansch DN 100 mit R. 1 A2

CF Blindflansch DN 63 wurde kommerziell erworben.
Bohrung für 2 Pin-Feedthrough (ebenfalls kommerziell erworben) muss angebracht und der Feedthrough angeschweißt werden.
1 mal benötigt.

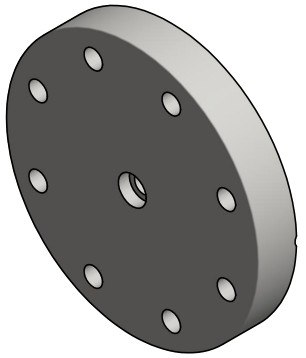

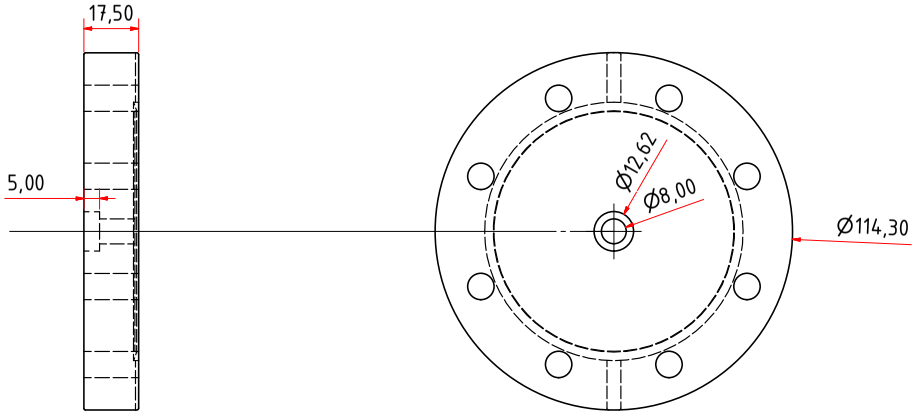

				Date	Name
			Drawn	02.12.2016	Michael Mathy
			Checked		
			Standard		
State	Changes	Date	Name	CF-BLindfl. DN63 m. Bohrung	
				CF-BLindfl. DN63 m. Bohrung	1 A2

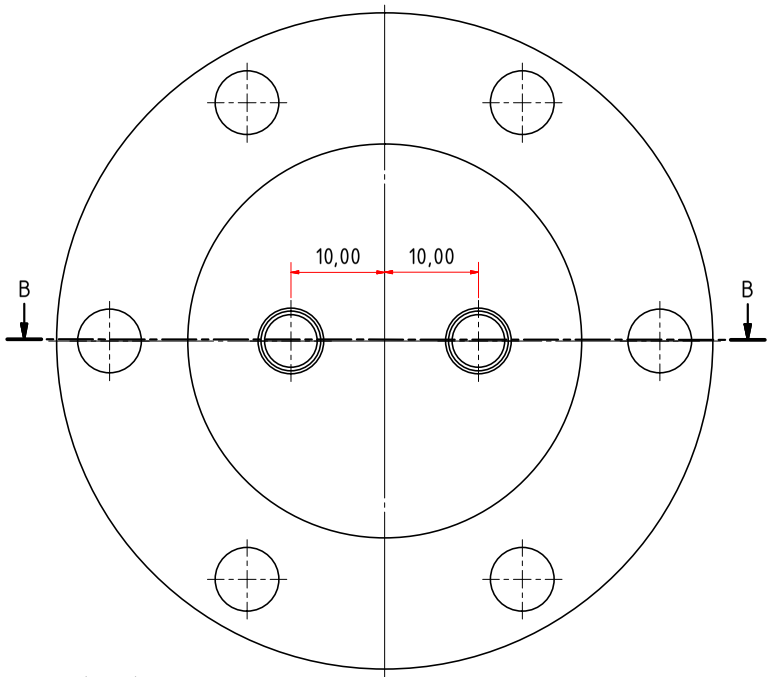

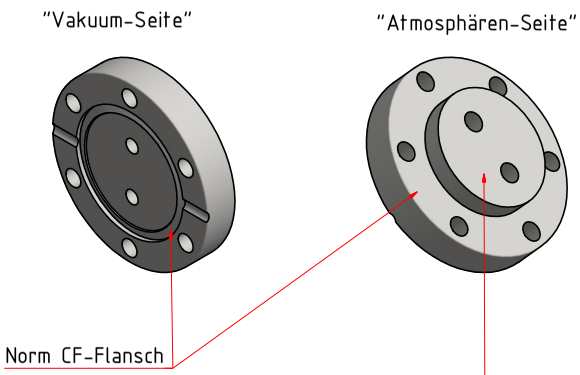

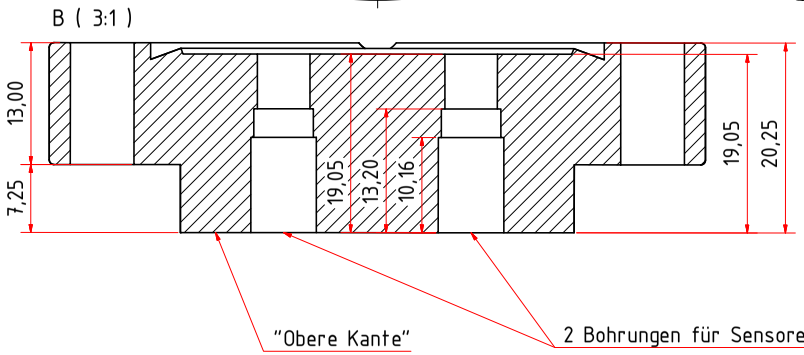

Abfolge der Borhungen:
(Alle Tiefen relativ zu "obere Kante")

1) Ø5,60 mm Bohrung druchgehend.

2) Ø6,40 mm Bohrung 13.20 mm tief.

3) M7 Gewindebohrung 10.16 mm tief.

CF 40 Blindflansch mit Bohrungen für Piezo-Sensoren:

Es wird ein NICHT magnetischer CF 40 Blindflansch aus dem Material 316l verwendet!

Dann muss ein Metallzylinder (Ø42 mm) so angeschweißt werden, dass er 7.25 mm an der "Nicht-Vakuum-Seite" übersteht.
Dann werden die beiden Bohrungen wie links erläutert vorgenommen.

			Date	Name	CF40 BF für Sensoren
			Drawn 05.03.2018	Michael Mathy	
			Checked		
			Standard		
State	Changes	Date	Name		CF40 BF Für Sensoren 1 A2

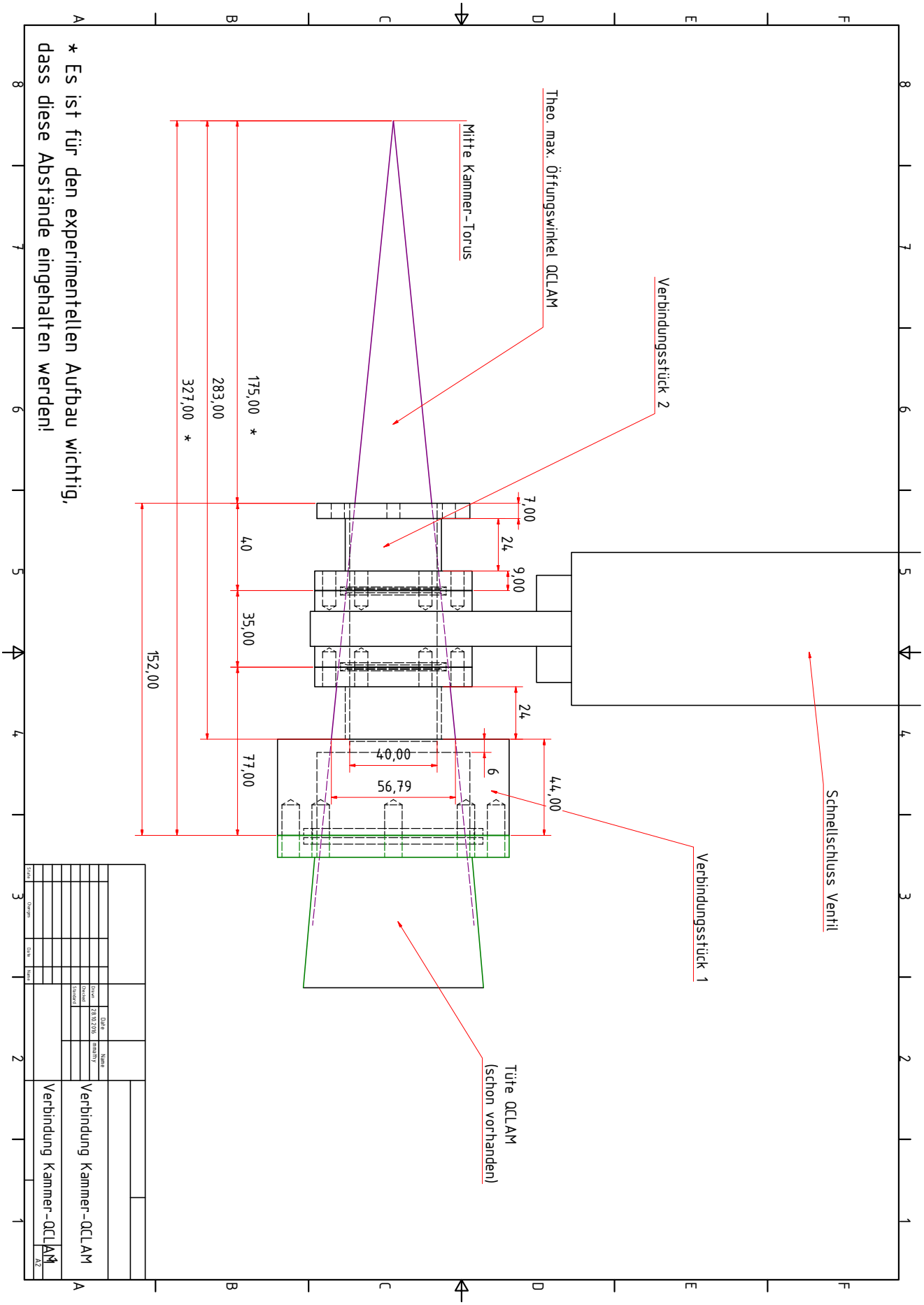
* Es ist für den experimentellen Aufbau wichtig, dass diese Abstände eingehalten werden!
Theo. max. Öffungswinkel QCLAM
Mitte Kammer-Torus
Verbindungsstück 2
Schnellschluss Ventil
Verbindungsstück 1
Tüte QCLAM (schon vorhanden)
175,00 *
283,00
327,00 *
152,00
7,00
24
9,00
4,0
35,00
24
40,00
56,79
6
44,00
77,00
Verbindung Kammer-QCLAM
Verbindung Kammer-QCLAM
A2

B.2 Technical Drawings of the Target Chamber

The following figures show the technical drawings for the target chamber. The chamber will be build in a German workshop and due to this all labels are given in German as well. The parts are made of stainless steel if not stated otherwise. All dimensions in the drawings are given in millimetres.

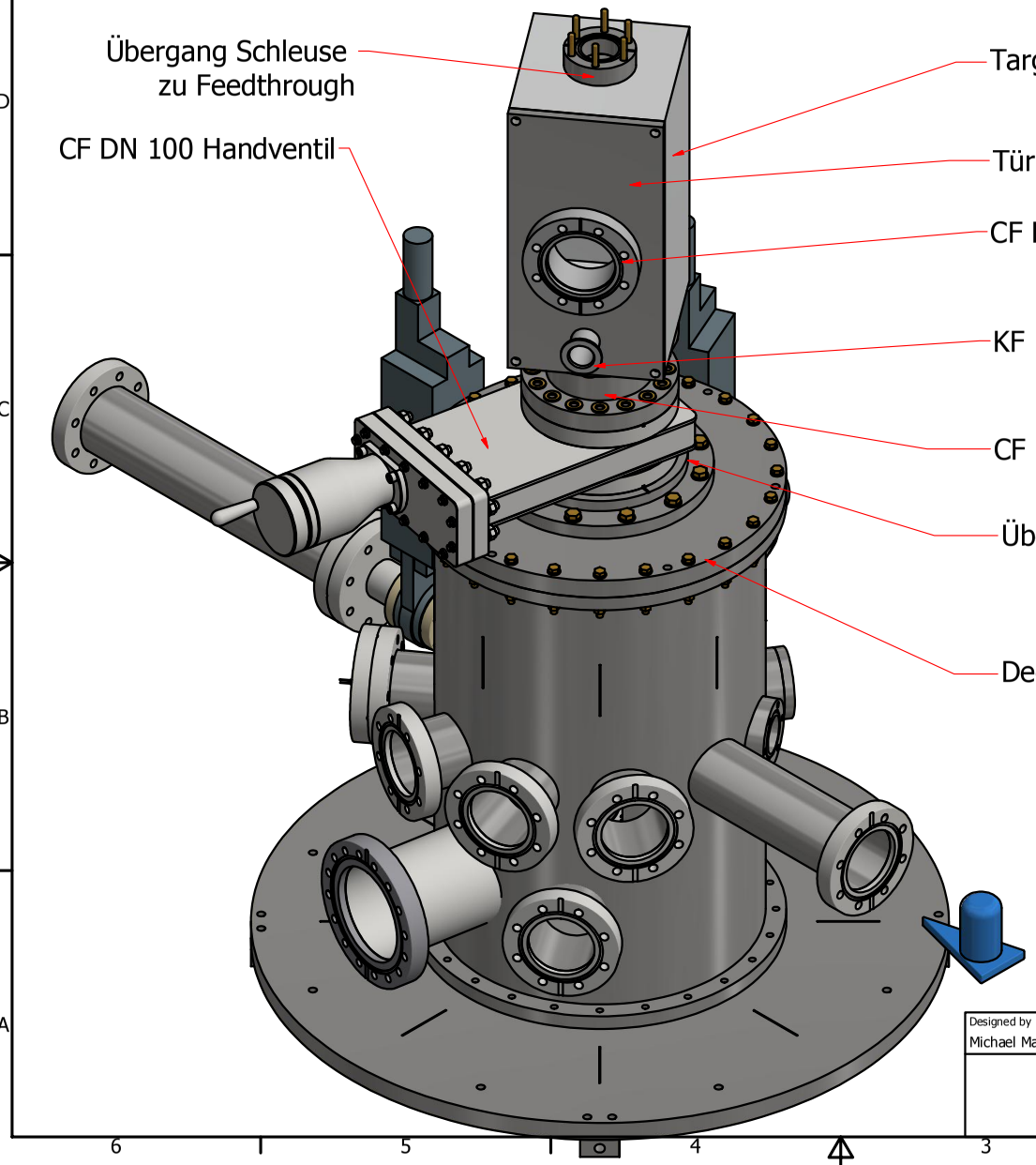

Designed by	Checked by	Approved by	Date		Date	
Michael Mathy					18.07.2018	

TL Übersicht 1

Edition	Sheet
	1 / 1

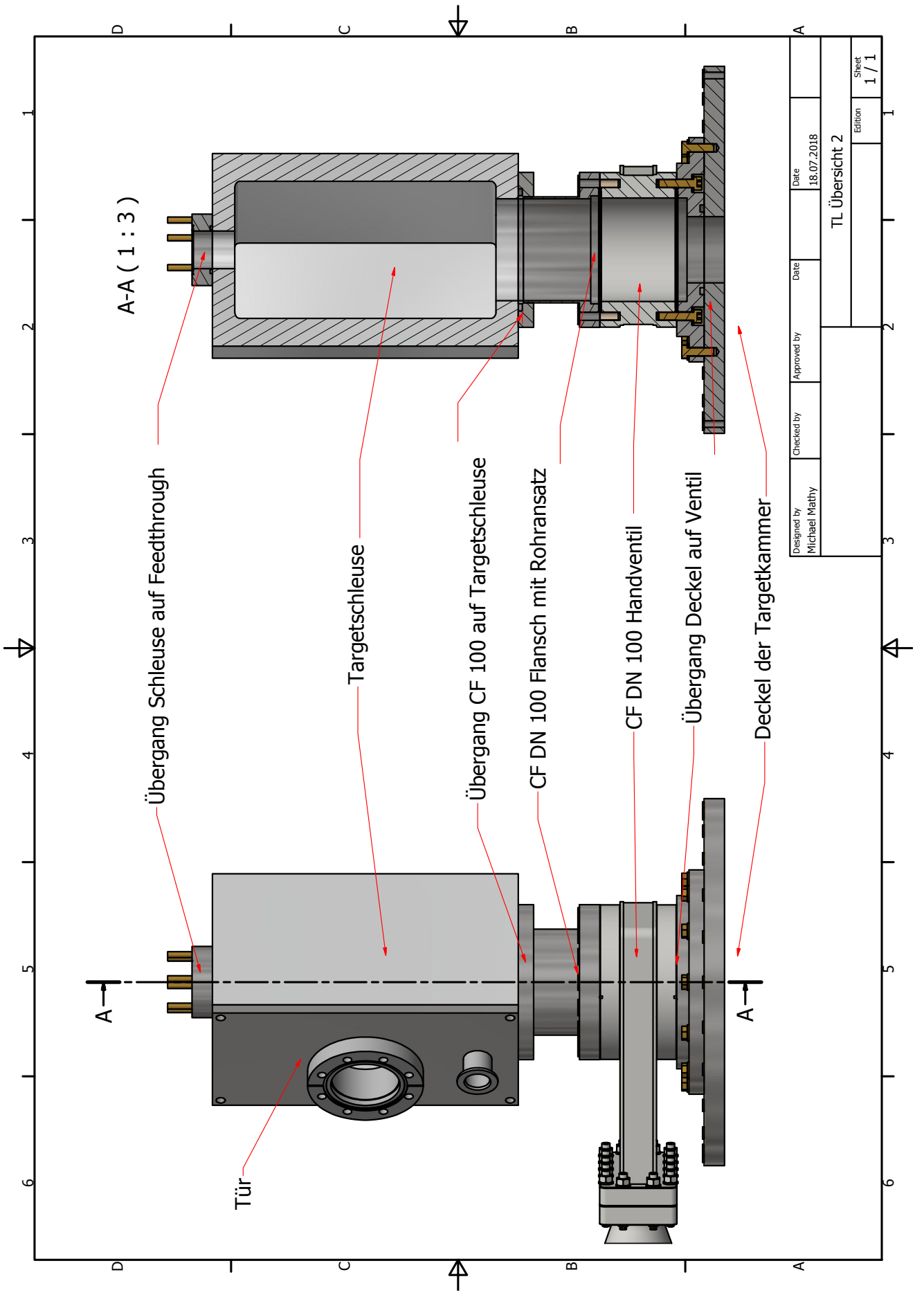
A-A (1 : 3)
Übergang Schleuse auf Feedthrough
Targetschleuse
Übergang CF 100 auf Targetschleuse
CF DN 100 Flansch mit Rohransatz
CF DN 100 Handventil
Übergang Deckel auf Ventil
Deckel der Targetkammer
Tür
A
A
TL Übersicht 2
Designed by
Michael Mathy
Checked by
Approved by
Date
18.07.2018
Edition
Sheet
1 / 1

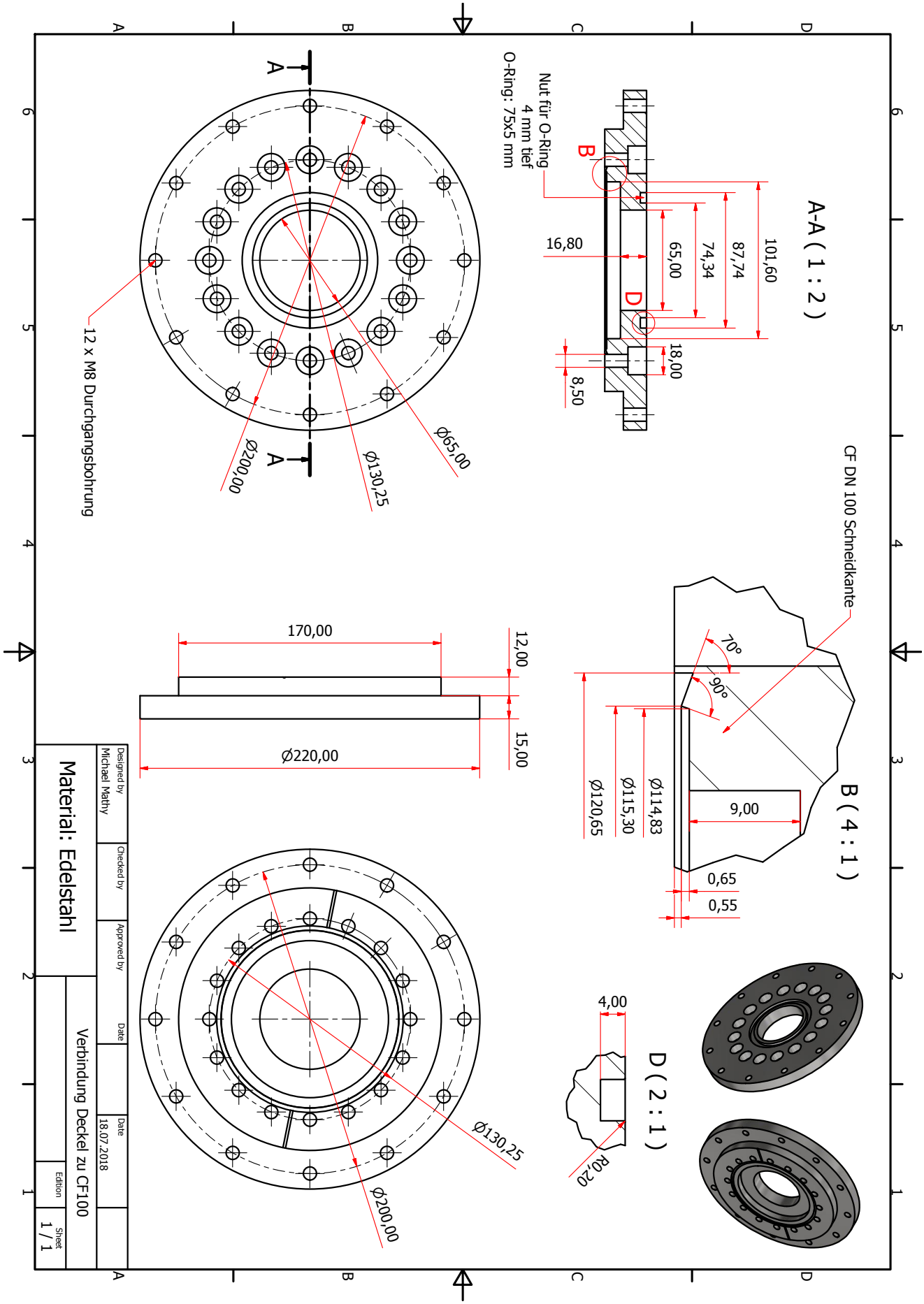
A-A (1 : 2)
Nut für O-Ring
4 mm tief
O-Ring: 75x5 mm
101,60
87,74
74,34
65,00
16,80
18,00
8,50
12 x M8 Durchgangsbohrung
Ø200,00
Ø130,25
Ø65,00
CF DN 100 Schneidkante
B (4 : 1)
70°
90°
Ø120,65
Ø115,30
Ø114,83
9,00
0,65
0,55
170,00
12,00
15,00
Ø220,00
D (2 : 1)
4,00
R0,20
Ø130,25
Ø200,00
Material: Edelstahl
Verbindung Deckel zu CF100
Designed by
Michael Mathy
Checked by
Approved by
Date
Date
18.07.2018
Edition
Sheet
1 / 1

Standard CF DN 100 Flansch mit Rohransatz.
Wird von einer externen Firma erworben.
Länge muss angepasst werden.

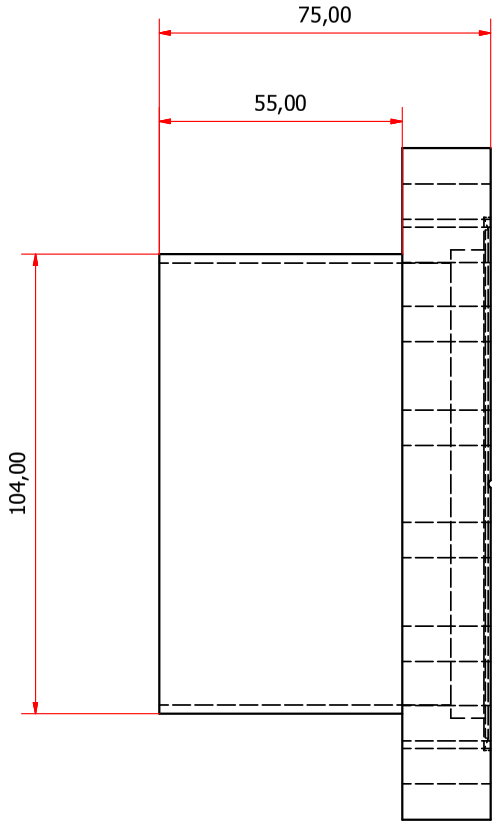

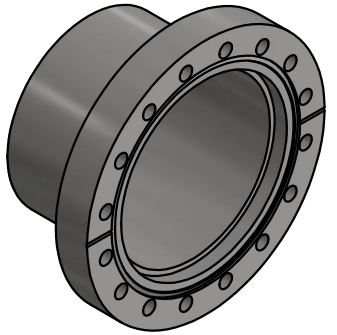

Designed by	Checked by	Approved by	Date		Date	
Michael Mathy					18.07.2018	

Material: Edelstahl	CF DN 100 Fl. mit Rohra.	
	Edition	Sheet 1 / 1

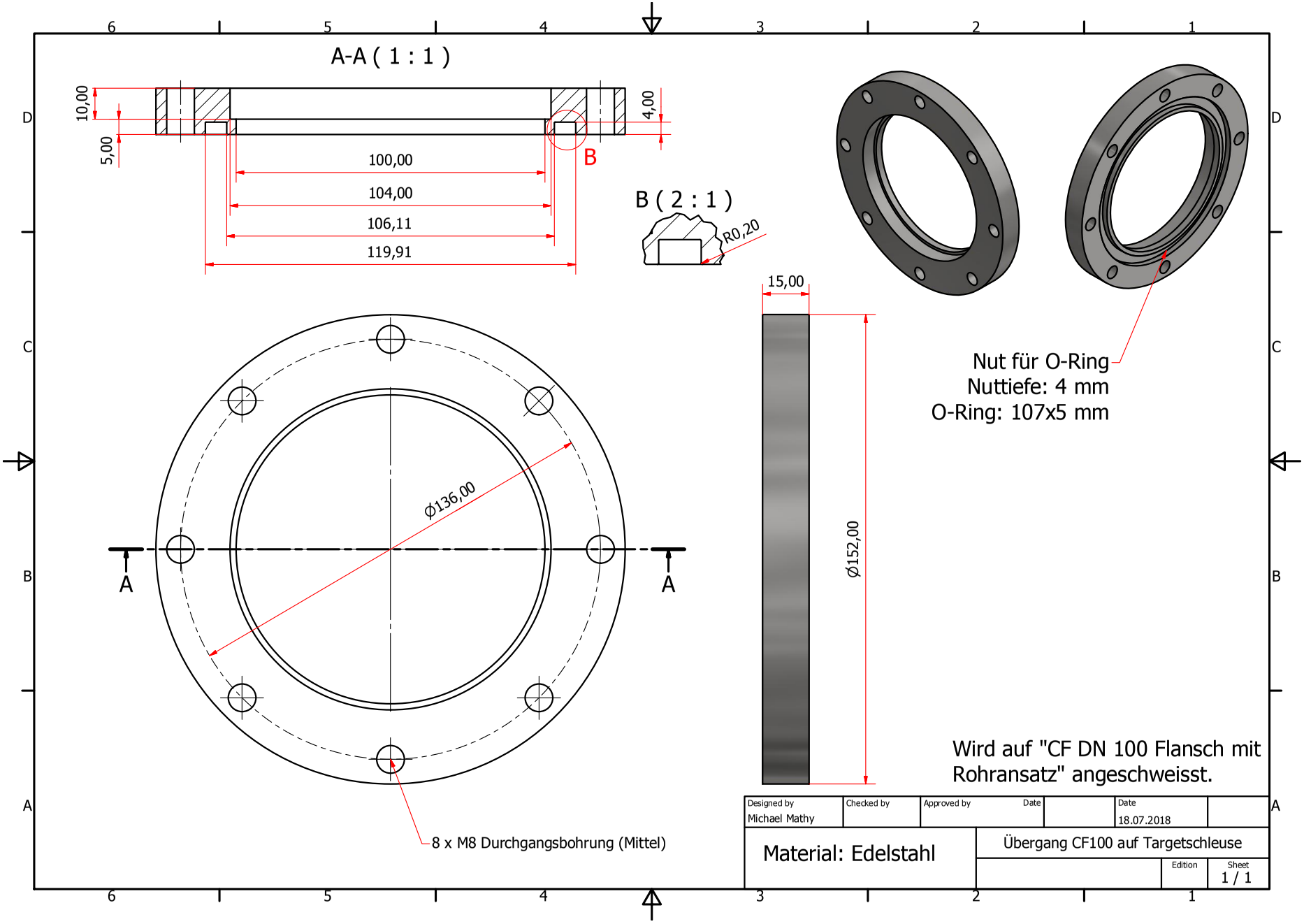
A-A (1 : 1)
10,00
5,00
4,00
100,00
104,00
106,11
119,91
B
B (2 : 1)
R0,20
15,00
Ø152,00
Ø136,00
A
A
Nut für O-Ring
Nuttiefe: 4 mm
O-Ring: 107x5 mm
8 x M8 Durchgangsbohrung (Mittel)
Wird auf "CF DN 100 Flansch mit Rohransatz" angeschweisst.
Designed by
Michael Mathy
Checked by
Approved by
Date
Date
18.07.2018
Material: Edelstahl
Übergang CF100 auf Targetschleuse
Edition
Sheet
1 / 1

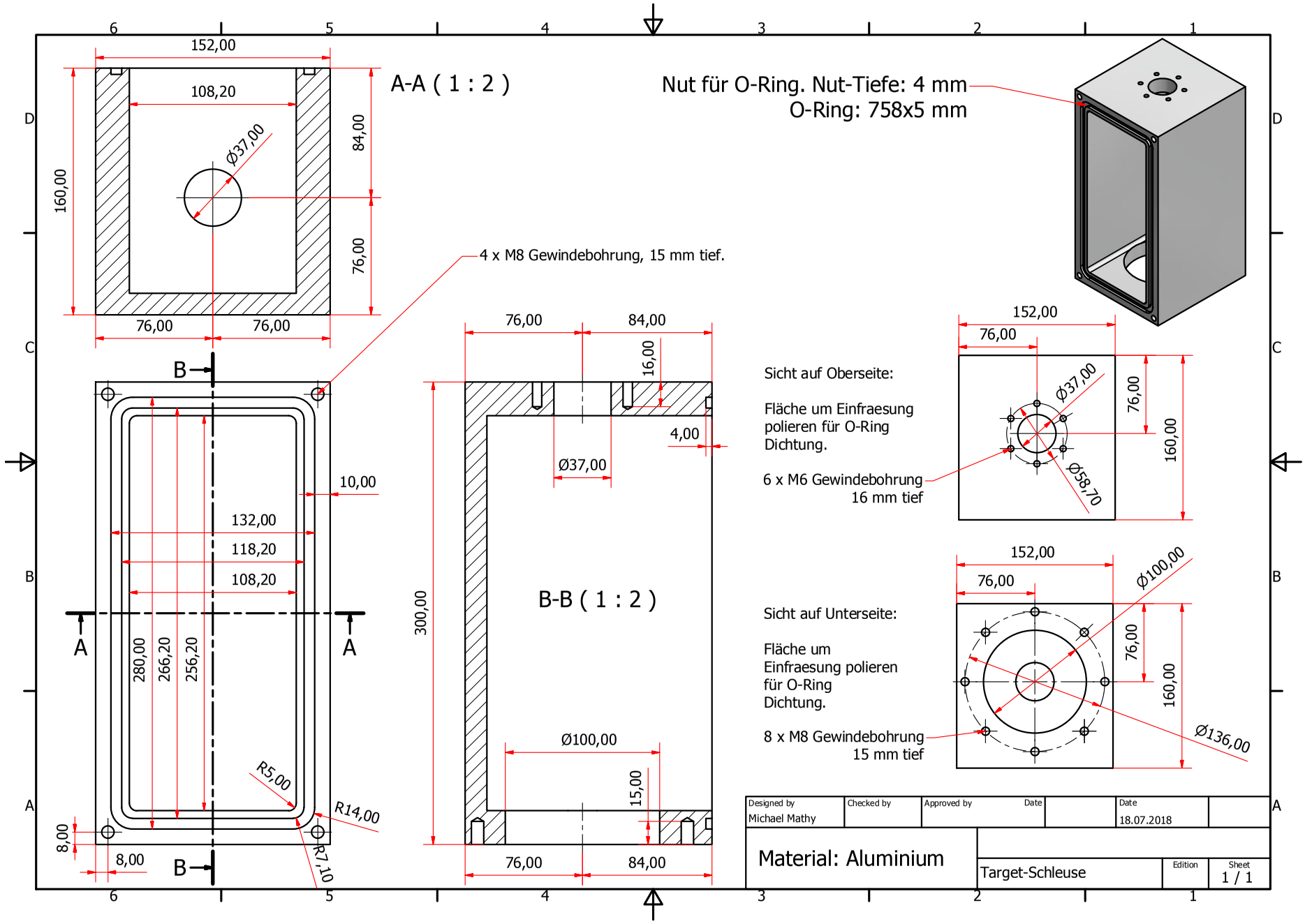
A-A (1 : 2)
152,00
108,20
Ø37,00
160,00
84,00
76,00
76,00
76,00
4 x M8 Gewindebohrung, 15 mm tief.
B
A
A
B
10,00
132,00
118,20
108,20
280,00
266,20
256,20
R5,00
R14,00
R7,10
8,00
8,00
B-B (1 : 2)
76,00
84,00
16,00
4,00
Ø37,00
300,00
Ø100,00
15,00
76,00
84,00
Nut für O-Ring. Nut-Tiefe: 4 mm
O-Ring: 758x5 mm
Sicht auf Oberseite:
Fläche um Einfraesung polieren für O-Ring Dichtung.
6 x M6 Gewindebohrung 16 mm tief
152,00
76,00
Ø37,00
76,00
160,00
Ø58,70
Sicht auf Unterseite:
Fläche um Einfraesung polieren für O-Ring Dichtung.
8 x M8 Gewindebohrung 15 mm tief
152,00
76,00
Ø100,00
76,00
160,00
Ø136,00
Designed by
Michael Mathy
Checked by
Approved by
Date
Date
18.07.2018
Material: Aluminium
Target-Schleuse
Edition
Sheet
1 / 1

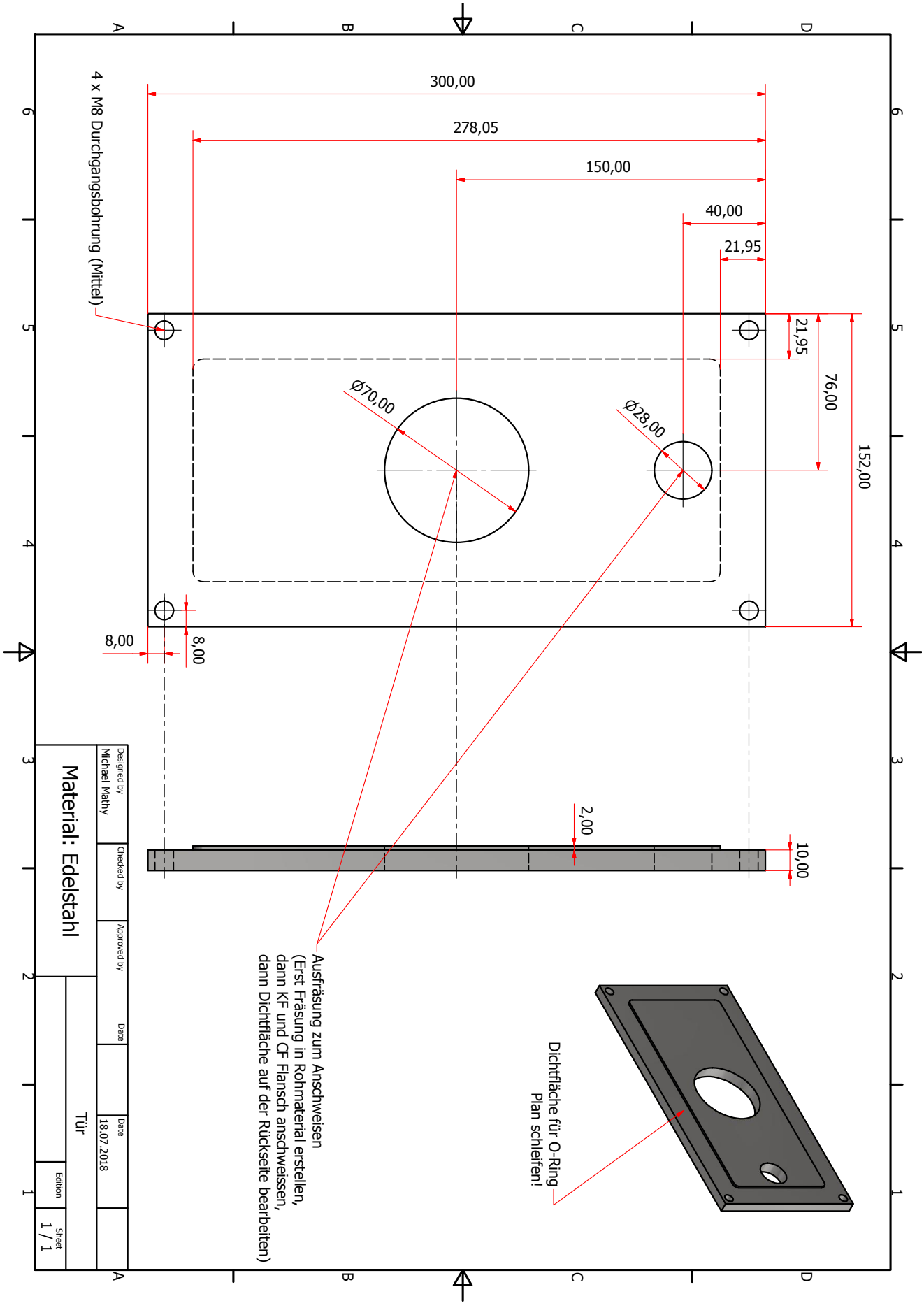
4 x M8 Durchgangsbohrung (Mittel)
300,00
278,05
150,00
40,00
21,95
21,95
76,00
152,00
ø70,00
ø28,00
8,00
8,00
2,00
10,00
Ausfräsung zum Anschweisen
(Erst Fräsung in Rohmaterial erstellen,
dann KF und CF Flansch anschweissen,
dann Dichtfläche auf der Rückseite bearbeiten)
Dichtfläche für O-Ring
Plan schleifen!
Material: Edelstahl
Designed by
Michael Mathy
Checked by
Approved by
Date
Date
18.07.2018
Tür
Edition
Sheet
1 / 1

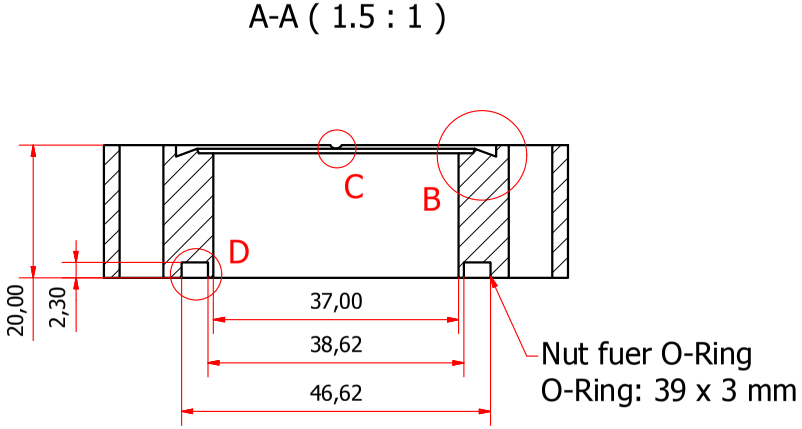

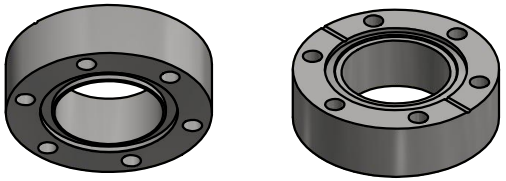

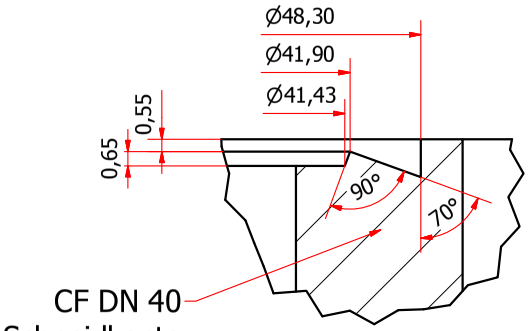

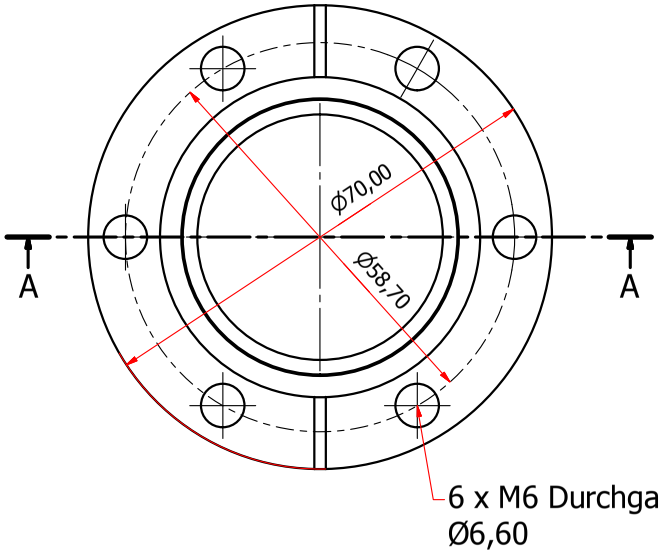

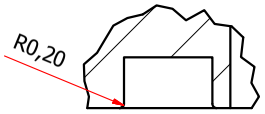

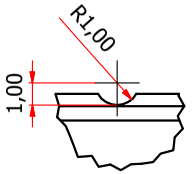

Designed by	Checked by	Approved by	Date		Date	
Michael Mathy					23.07.2018	
Material: Edelstahl		Verbindung Schleuse zu Feedthrough				
					Edition	Sheet 1 / 1

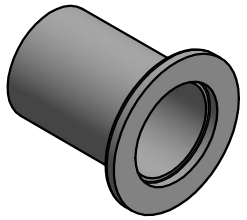

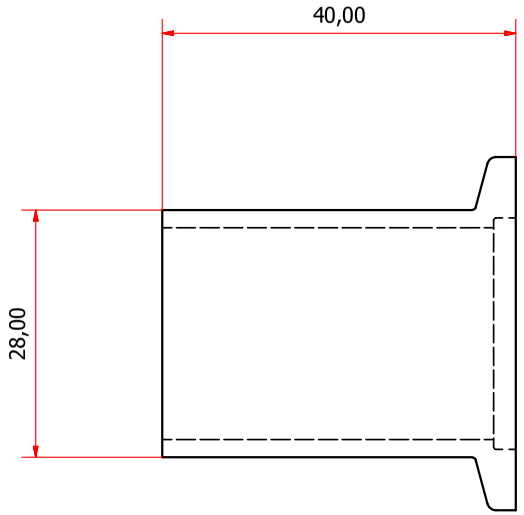

Standard KF DN 25 Flansch mit Rohransatz.
Wird von einer externen Firma erworben.
Länge muss angepasst werden.

Designed by	Checked by	Approved by	Date		Date	
Michael Mathy					18.07.2018	

Material: Edelstahl	KF DN 25 Fl. mit Rohransatz	
	Edition	Sheet 1 / 1

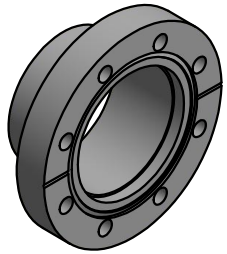

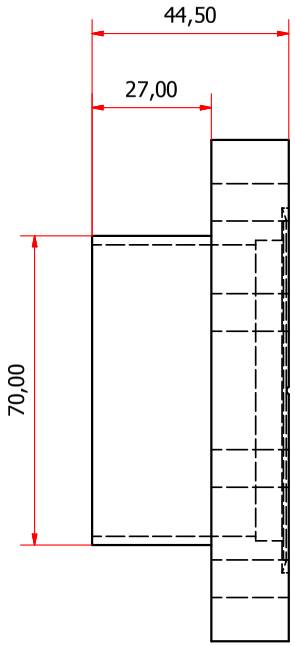

Standard CF DN 63 Flansch mit Rohransatz.
Wird von einer externen Firma erworben.
Länge muss angepasst werden.

Designed by	Checked by	Approved by	Date		Date	
Michael Mathy					18.07.2018	

Material: Edelstahl	CF DN 63 Fl. mit Rohransatz	
	Edition	Sheet 1 / 1

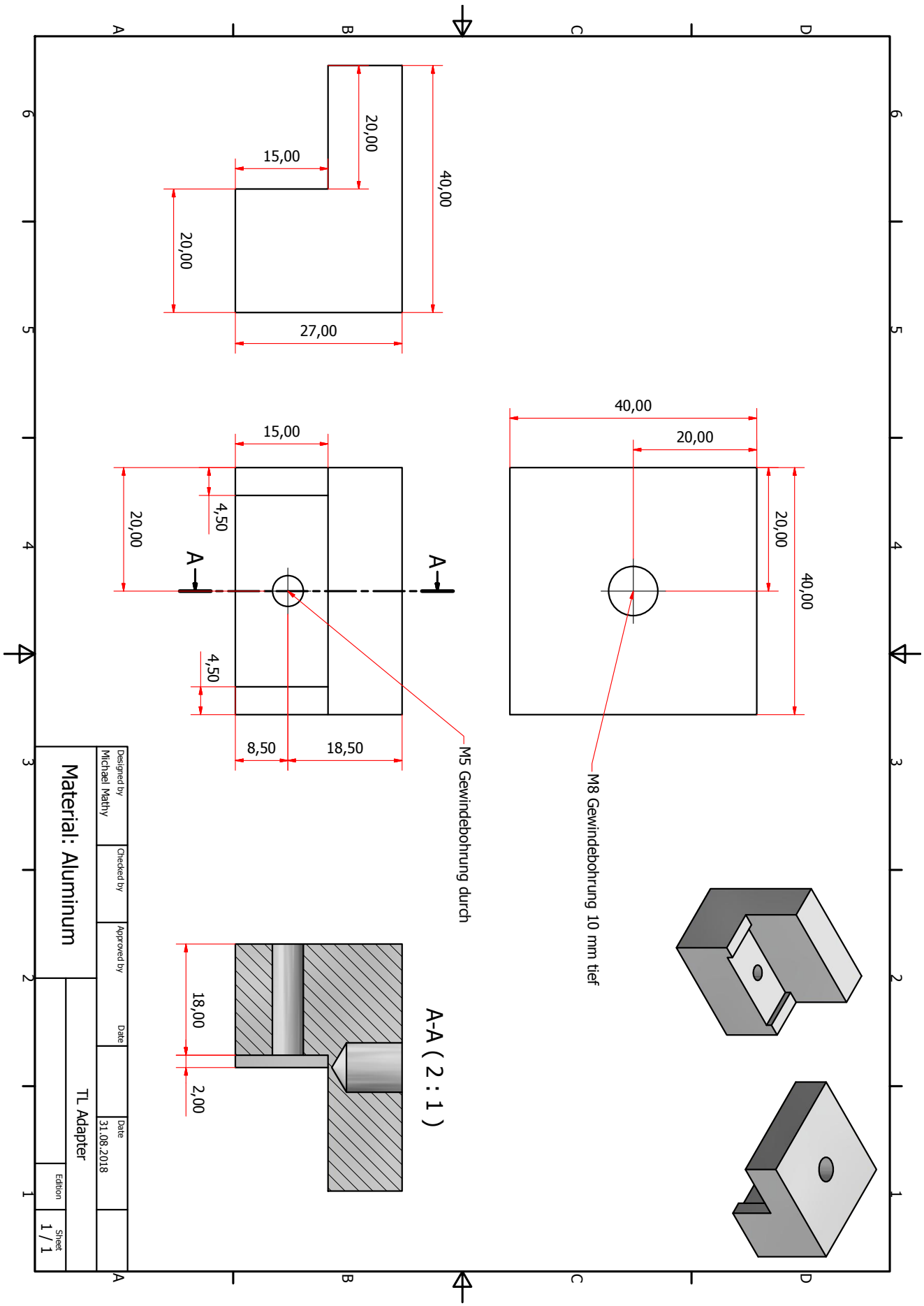
15,00
20,00
40,00
20,00
27,00
40,00
20,00
20,00
40,00
15,00
20,00
4,50
A
A
4,50
8,50
18,50
M5 Gewindebohrung durch
M8 Gewindebohrung 10 mm tief
18,00
2,00
A-A (2 : 1)
Material: Aluminum
TL Adapter
Designed by
Michael Mathy
Checked by
Approved by
Date
Date
31.08.2018
Edition
Sheet
1 / 1

Bibliography

[AAA+12] S. Akkoyun, A. Algora, B. Alikhani, et al. AGATA-Advanced GAmma Tracking Array. *Nucl. Instr. Meth. A*, 668:26–58, 2012. doi:10.1016/j.nima.2011.11.081.

[AHKP16] M. Arnold, F. Hug, T. Kürzeder, and N. Pietralla. Final Design and Status of the Third Recirculation for the S-DALINAC*. In *Proceedings, 7th International Particle Accelerator Conference (IPAC 2016): Busan, Korea, May 8-13, 2016*, page TUPOR026, 2016. doi:10.18429/JACoW-IPAC2016-TUPOR026.

[AS87] F. Ajzenberg-Selove. Energy levels of light nuclei A=18—20. *Nucl. Phys. A*, 475(1):1 – 198, 1987. doi:10.1016/0375-9474(87)90205-3.

[AS90a] F. Ajzenberg-Selove. Nucl. Phys. A523,1 (1991). `https://www.nndc.bnl.gov/nudat2/getdataset.jsp?nucleus=15N&unc=nds`, 1990. [Online; accessed 24th Jun 2019].

[AS90b] F. Ajzenberg-Selove. Nucl. Phys. A523,1 (1991). `https://www.nndc.bnl.gov/nudat2/getdataset.jsp?nucleus=15C&unc=nds`, 1990. [Online; accessed 17th Sep 2019].

[AS90c] F. Ajzenberg-Sselove. Nucl. Phys. A523,1 (1991). `https://www.nndc.bnl.gov/nudat2/getdataset.jsp?nucleus=14C&unc=nds`, 1990. [Online; accessed 17th Sep 2019].

[AS91a] F. Ajzenberg-Selove. Energy levels of light nuclei A=13—15. *Nucl. Phys. A*, 523(1):1 – 196, 1991. doi:10.1016/0375-9474(91)90446-D.

[AS91b] F. Ajzenberg-Selove. Nucl. Phys. A523,1 (1991). `https://www.nndc.bnl.gov/nudat2/decaysearchdirect.jsp?nuc=14C&unc=nds`, 1991. [Online; accessed 28th Oct 2019].

[ASKN91] F. Ajzenberg-Selove, J.H. Kelley, and C.D. Nesaraja. Nucl. Phys. A523,1 (1991). `https://www.nndc.bnl.gov/nudat2/getdatasetClassic.jsp?nucleus=13C&unc=nds`, 1991. [Online; accessed 23th Jan 2020].

[ATL19] ATLAS. Argonne Tandem Linear Accelerator System - ATLAS. `https://www.anl.gov/atlas`, 2019. [Online; accessed 3er July 2019].

[AW76] D. E. Alburger and D. H. Wilkinson. Beta decay of ^{16}C and ^{17}N. *Phys. Rev. C*, 13:835–846, February 1976. doi:10.1103/PhysRevC.13.835.

[BCZC17] M. J. Berger, J. S. Coursey, M. A. Zucker, and J. Chang. Stopping-Power & Range Tables for Electrons, Protons, and Helium Ions. *NIST Standard Reference Database*, 124, July 2017. doi:10.18434/T4NC7P.

[BEPT72] C. Broude, P. Engelstein, M. Popp, and P.N. Tandon. Dependence of the Doppler shift lifetime method on slowing environment. *Phys. Lett. B*, 39(2):185 – 187, 1972. doi:10.1016/0370-2693(72)90769-1.

[Ber07] C. A. Bertulani. *Nuclear Physics in a Nutshell*. Princeton University Press, Princeton, first edition, 2007.

[BERGed] B. A. Brown, A. Etchegoyen, W. D. M. Rae, and N. S. Godwin. MSU-NSCL Report No. 524. Technical report, NSCL, Michigan State University, (unpublished).

[Bet30] H. Bethe. Zur Theorie des Durchgangs schneller Korpuskularstrahlen durch Materie. *Ann. Phys.*, 397(3):325–400, 1930. doi:10.1002/andp.19303970303.

[Bet32] H. Bethe. Bremsformel für Elektronen relativistischer Geschwindigkeit. *Z. Phys.*, 76:293, 1932. doi:10.1007/BF01342532.

[BFP07] S. K. Bogner, R. J. Furnstahl, and R. J. Perry. Similarity renormalization group for nucleon-nucleon interactions. *Phys. Rev. C*, 75:061001, June 2007. doi:10.1103/PhysRevC.75.061001.

[BIA+16] M. J. Berger, M. Inokuti, H. H. Anderson, et al. Report 37. *Journal of the International Commission on Radiation Units and Measurements*, os19(2):NP–NP, 2016. doi:10.1093/jicru/os19.2.Report37.

[Bir17] J. Birkhan. *Elektrische Dipol-Polarisierbarkeit und Spin-M1-Stärke aus ^{48}Ca(p,p')-Daten unter 0°*. PhD thesis, Technische Unversität Darmstadt, 2017.

[Blo33] F. Bloch. Zur Bremsung rasch bewegter Teilchen beim Durchgang durch Materie. *Ann. Phys.*, 408(3):285–320, 1933. doi:10.1002/andp.19334080303.

[BM69] A. Bohr and B. R. Mottelson. *Nuclear Structure, Volume 1: Singe-particle Motion*. World Scientific Publishing Co. Pte. Ltd., Reprinted 1998, Singapore, 1969.

[BM75] A. Bohr and B. R. Mottelson. *Nuclear Structure, Volume 2: Nuclear Deformations*. World Scientific Publishing Co. Pte. Ltd., Reprinted 1999, Singapore, 1975.

[BMvNC+16] J. Birkhan, H. Matsubara, P. von Neumann-Cosel, et al. Electromagnetic $M1$ transition strengths from inelastic proton scattering: The cases of ^{48}Ca and ^{208}Pb. *Phys. Rev. C*, 93:041302, 2016. doi:10.1103/PhysRevC.93.041302.

[BNV13] B. R. Barrett, P. Navrátil, and J. P. Vary. Ab initio no core shell model. *Prog. Part. Nucl. Phys.*, 69:131 – 181, 2013. doi:10.1016/j.ppnp.2012.10.003.

[BR06] B. A. Brown and W. A. Richter. New "USD" Hamiltonians for the *sd* shell. *Phys. Rev. C*, 74:034315, September 2006. doi:10.1103/PhysRevC.74.034315.

[Bri66] D. M. Brink. Course XXXVI. In C. L. Bloch, editor, *Proceedings of the International School of Physics "Enrico Fermi,"*, page 247. Academic Press, New York, 1966.

[Bro19] B. A. Brown. NSCL, Michigan State University, Private Communication, September 2019.

[Bro20] B. A. Brown. NSCL, Michigan State University, Private Communication, February 2020.

[Bru97] Brun, R. and Fons Rademakers. ROOT - An Object Oriented Data Analysis Framework. Proceedings AIHENP'96 Workshop, Lausanne, September 1996. *Nucl. Instr. Meth. Phys. Res. A*, 389:81–86, 1997.

[BW88] B. A. Brown and B. H. Wildenthal. Status of the Nuclear Shell Model. *Annu. Rev. Nucl. Part. Sci.*, 38(1):29–66, 1988. doi:10.1146/annurev.ns.38.120188.000333.

[CFH+77] H. Crannell, J.M. Finn, P. Hallowell, et al. Inelastic electron scattering at 180° from 14C. *Nucl. Phys. A*, 278(2):253 – 260, 1977. doi:10.1016/0375-9474(77)90238-X.

[CHO+72] H. Crannell, P.L. Hallowell, J.T. OBrien, J.M. Finn, and F.J. Kline. Electron scattering from low lying 2^+ states in ^{14}C. In *Proc. Int. Conf. Nucl. Struct. Studies Using Electron Scattering and Photoreaction, Sendai, Japan, K. Shoda, H. Ui, Eds., Res. Rep. Lab. Nucl. Sci. Tohoku Univ. 5, Suppl. 375*, 1972.

[CZC+20] M. Ciemała, S. Ziliani, F. C. L. Crespi, et al. Testing ab initio nuclear structure in neutron-rich nuclei: Lifetime measurements of second 2^+ state in ^{16}C and ^{20}O. *Phys. Rev. C*, 101:021303, February 2020. doi:10.1103/PhysRevC.101.021303.

[D'A20] A. D'Alessio. *In preperation*. PhD thesis, Technische Universität Darmstadt, 2020.

[Dav13] H. M. David. *Study of the N=Z nucleus ^{62}Ga using a new fast beta-decay tagging system*. PhD thesis, The University of Edinburgh, June 2013.

[DBM54] H. Davies, H. A. Bethe, and L. C. Maximon. Theory of Bremsstrahlung and Pair Production. II. Integral Cross Section for Pair Production. *Phys. Rev.*, 93:788–795, 1954. doi:10.1103/PhysRev.93.788.

[DLV+99] M.A. Deleplanque, I.Y. Lee, K. Vetter, et al. GRETA: utilizing new concepts in γ-ray detection. *Nucl. Instr. Meth. Phys. Res. A*, 430(2):292 – 310, 1999. doi:10.1016/S0168-9002(99)00187-4.

[DMP12] A. Dewald, O. Möller, and P. Petkov. Developing the Recoil Distance Doppler-Shift technique towards a versatile tool for lifetime measurements of excited nuclear states. *Prog. Part. Nucl. Phys.*, 67(3):786 – 839, 2012. doi:10.1016/j.ppnp.2012.03.003.

[Dre17] VAT Valves (01109 Dresden). Schnellschlussventil. Serial Number: 75232-CE44. `http://www.vatvalve.com/de/business/valves/catalog/F/750_1_V` [Online; accessed 9th October 2019], 2017.

[dS59] A. de Shalit. Effective Charge of Neutrons in Nuclei. *Phys. Rev.*, 113:547–551, Janurary 1959. doi:10.1103/PhysRev.113.547.

[EB48] L. G. Elliott and R. E. Bell. Experimental Upper Limit for the Mean Life of the 478.5-Kev Excited State of Li^7. *Phys. Rev.*, 74:1869–1870, 1948. doi:10.1103/PhysRev.74.1869.

[EB64] M. A. Eswaran and C. Broude. Lifetime Measurements of States in O^{18} and Ne^{22}. *Can. J. Phys.*, 42:1311, 1964.

[EDQ+89] A. K. Entwistle, C. S. Dyer, J. J. Quenby, A. J. Evans, and M. Joshi. Measurement of neutron and proton-induced background in germanium gamma-ray spectrometers for use in a space environment. *J. Phys. E: Sci. Instrum.*, 22(8):601–611, 1989. doi:10.1088/0022-3735/22/8/013.

[Edw08] A. Edwards. Private Communication, May 2008.

[EKL+12] E. Epelbaum, H. Krebs, T. A. Lähde, D. Lee, and U.-G. Meißner. Structure and Rotations of the Hoyle State. *Phys. Rev. Lett.*, 109:252501, 2012. doi:10.1103/PhysRevLett.109.252501.

[EKLM11] E. Epelbaum, H. Krebs, D. Lee, and U.-G. Meißner. Ab Initio Calculation of the Hoyle State. *Phys. Rev. Lett.*, 106:192501, 2011. doi:10.1103/PhysRevLett.106.192501.

[Elm18] VAKUUM Anlagenbau GmbH (25337 Elmshorn). Lineardurchführung mit Schrittmotorantrieb und Drehdurchführung. Serial Number: LD40-700 S2+PD40-700 S2. `https://www.vab-vakuum.com/` [Online; accessed 9th October 2019], 2018.

[EM03] D. R. Entem and R. Machleidt. Accurate charge-dependent nucleon-nucleon potential at fourth order of chiral perturbation theory. *Phys. Rev. C*, 68:041001, October 2003. doi:10.1103/PhysRevC.68.041001.

[EMN17] D. R. Entem, R. Machleidt, and Y. Nosyk. High-quality two-nucleon potentials up to fifth order of the chiral expansion. *Phys. Rev. C*, 96:024004, August 2017. doi:10.1103/PhysRevC.96.024004.

[ES08] J. Eberth and J. Simpson. From Ge(Li) detectors to gamma-ray tracking arrays – 50 years of gamma spectroscopy with germanium detectors. *Prog. Part. Nucl. Phys.*, 60:283–337, 2008. doi:10.1016/j.ppnp.2007.09.001.

[ESE+78] L.P. Ekström, D.E.C. Scherpenzeel, G.A.P. Engelbertink, H.J.M. Aarts, and H.H. Eggenhuisen. Lifetime measurement of ^{22}Ne(4_1^+) with the high-velocity coincidence DSA method. *Nucl.Phys. A*, 295(3):525 – 531, 1978. doi:10.1016/0375-9474(78)90190-2.

[EST19] ESTAR. ESTAR - Stopping-power and range tables for electrons. `https://physics.nist.gov/PhysRefData/Star/Text/ESTAR.html`, 2019. [Online; accessed 1st October 2019].

[FAB+79] J.S. Forster, T.K. Alexander, G.C. Ball, et al. Lifetime measurements in ^{22}Ne, ^{28}Si and ^{31}P relevant to the interpretation of the Z_2 variation in low velocity DSAM results. *Nucl.Phys. A*, 313(3):397 – 424, 1979. doi:10.1016/0375-9474(79)90509-8.

[Fal08] P. Fallon. Neutron-proton coupling in light neutron-rich nuclei. Presentation, May 2008.

[FAP78] L. K. Fifield, J. Asher, and A. R. Poletti. A precise measurement of the lifetime of the lowest 4^+ state in ^{22}Ne. *J. Phys. G Nucl. Part. Phys.*, 4(3):L65–L69, 1978. doi:10.1088/0305-4616/4/3/005.

[FBNS+16] A. Fritsch, S. Beceiro-Novo, D. Suzuki, et al. One-dimensionality in atomic nuclei: A candidate for linear-chain α clustering in ^{14}C. *Phys. Rev. C*, 93:014321, 2016. doi:10.1103/PhysRevC.93.014321.

[Fil19] DuPont Teijin Films. Physical-Thermal Properties of Mylar. `http://usa.dupontteijinfilms.com/wp-content/uploads/2017/01/Mylar_Physical_Properties.pdf`, 2019. [Online; accessed 2nd October 2019].

[Fir06] R. B. Firestone. Nucl. Data Sheets 108, 1 (2007). `https://www.nndc.bnl.gov/nudat2/getdataset.jsp?nucleus=23NE&unc=nds`, 2006. [Online; accessed 26th June 2019].

[Fir07] R.B. Firestone. Nucl. Data Sheets 108, 1 (2007). `https://www.nndc.bnl.gov/nudat2/getdataset.jsp?nucleus=23NA&unc=nds`, 2007. [Online; accessed 17th Sep 2019].

[Fir15] R. B. Firestone. Nucl. Data Sheets 127, 1 (2015). https://www.nndc.bnl.gov/nudat2/getdatasetClassic.jsp?nucleus=21NE&unc=nds, 2015. [Online; accessed 23th Jan 2020].

[FMC66] D. B. Fossan, R. E. McDonald, and L. F. Chase. Lifetimes of the 1.02-MeV State in Ne^{23}. *Phys. Rev.*, 141:1018–1020, 1966. doi:10.1103/PhysRev.141.1018.

[FMO+07] S. Fujii, T. Mizusaki, T. Otsuka, T. Sebe, and A. Arima. Microscopic shell-model description of the exotic nucleus ^{16}C. *Phys. Lett. B*, 650(1):9 – 14, 2007. doi:10.1016/j.physletb.2007.04.067.

[FRN13] C. Forssén, R. Roth, and P. Navrátil. Systematics of 2^+ states in C isotopes from the no-core shell model. *J. Phys. G Nucl. Part. Phys.*, 40(5):055105, March 2013. doi:10.1088/0954-3899/40/5/055105.

[FZB74] L. K. Fifield, R. W. Zurmühle, and D. P. Balamuth. Identification and lifetime determination of the 6^+ member of the ground-state rotational band in ^{22}Ne. *Phys. Rev. C*, 10:1785–1791, 1974. doi:10.1103/PhysRevC.10.1785.

[Gav80] A. Gavron. Statistical model calculations in heavy ion reactions. *Phys. Rev. C*, 21:230–236, 1980. doi:10.1103/PhysRevC.21.230.

[Gea14] Geant4 Collaboration. Geant4 User's Guide for Application Developers. https://geant4.web.cern.ch/support/user_documentation, 2014. [Online; accessed 22th August 2019].

[Gil08] G. Gilmorel. *Practical Gamma-ray Spectroscopy*. John Wiley & Son, New York, second edition, 2008.

[GQN09] D. Gazit, S. Quaglioni, and P. Navrátil. Three-Nucleon Low-Energy Constants from the Consistency of Interactions and Currents in Chiral Effective Field Theory. *Phys. Rev. Lett.*, 103:102502, September 2009. doi:10.1103/PhysRevLett.103.102502.

[GVHR17] E. Gebrerufael, K. Vobig, H. Hergert, and R. Roth. Ab Initio Description of Open-Shell Nuclei: Merging No-Core Shell Model and In-Medium Similarity Renormalization Group. *Phys. Rev. Lett.*, 118:152503, April 2017. doi:10.1103/PhysRevLett.118.152503.

[HBM+16] H. Hergert, S.K. Bogner, T.D. Morris, A. Schwenk, and K. Tsukiyama. The In-Medium Similarity Renormalization Group: A novel ab initio method for nuclei. *Phys. Rep.*, 621:165 – 222, 2016. doi:10.1016/j.physrep.2015.12.007.

[HCFR89] Mark D. Hoover, Bryan T. Castorina, Greorgy L. Finch, and Simon J. Rothenberg. Determination of the Oxide Layer Thickness on Beryllium Metal Particles. *Am. Ind.*

Hyg. Assoc. J., 50(10):550–553, 1989. doi:10.1080/15298668991375146. PMID: 2801503.

[Hei15] S. Heil. Simulation of gamma-ray detector arrays for nuclear physics experiments. Master's thesis, Technische Universität Darmstadt, February 2015.

[Hei19] S. Heil. *Electromagnetic Properties of ^{21}O and the Self-Calibration of Compton Tracking Arrays*. PhD thesis, Technische Universität Darmstadt, February 2019.

[Hor97] J. Horn. *Entwicklung und Integration eines schnellen Kontrollsystems für den S-DALINAC und Weiterentwicklung der Vieldrahtdriftkammern im QCLAM-Spektrometer*. PhD thesis, Technischen Universität Darmstadt, 1997.

[HPV+20] S. Heil, M. Petri, K. Vobig, et al. Electromagnetic properties of 21O for benchmarking nuclear Hamiltonians. *Phys. Lett. B*, 809:135678, 2020. doi:10.1016/j.physletb.2020.135678.

[HS06] W. Horiuchi and Y. Suzuki. Structure of and $E2$ transition in ^{16}C in a ^{14}C + n + n model. *Phys. Rev. C*, 73:037304, March 2006. doi:10.1103/PhysRevC.73.037304.

[HS07] K. Hagino and H. Sagawa. Three-body model calculations for the ^{16}C nucleus. *Phys. Rev. C*, 75:021301, February 2007. doi:10.1103/PhysRevC.75.021301.

[Hum92] K.-D. Hummel. *Entwicklung, Aufbau und Inbetriebnahme eines Vieldrahtdriftkammer-Detektorsystems für das QCLAM-Spektrometer am supraleitenden Darmstädter Elektronenbeschleuniger S-DALINAC*. PhD thesis, Technische Universität Darmstadt, 1992.

[HVH+20] T. Hüther, K. Vobig, K. Hebeler, R. Machleidt, and R. Roth. Family of chiral two-plus three-nucleon interactions for accurate nuclear structure studies. *Phys. Lett. B*, 808:135651, 2020. doi:10.1016/j.physletb.2020.135651.

[HvNCR10] K. Heyde, P. von Neumann-Cosel, and A. Richter. Magnetic dipole excitations in nuclei: Elementary modes of nucleonic motion. *Rev. Mod. Phys.*, 82:2365–2419, 2010. doi:10.1103/RevModPhys.82.2365.

[Hü17] PCB Synotech GmbH (41836 Hückelhoven). Pressure Sensor. Serial Number: 113B28. `https://www.synotech.de/produkte/datenblatt/?h=PCB&m=113B28` [Online; accessed 9th October 2019], 2017.

[ICR05] ICRU. Stopping of ions Heavier than Helium. *Journal of the International Commission on Radiation Units and Measurements*, 5(1):iii–viii, 2005. doi:10.1093/jicru/ndi002.

[IOA+04] N. Imai, H. J. Ong, N. Aoi, et al. Anomalously Hindered $E2$ Strength $B(E2; 2_1^+ \rightarrow 0^+)$ in ^{16}C. *Phys. Rev. Lett.*, 92:062501, February 2004. doi:10.1103/PhysRevLett.92.062501.

[Jac62] J.D. Jackson. *Classical Electrodynamics*. John Wily & Sons, New York, London, Sydney, first edition, 1962.

[JBB+16] L. Jürgensen, T. Bahlo, C. Burandt, et al. A High-Energy-Scrapersystem for the S-DALINAC Extraction - Design and Installation. In *Proceedings, 7th International Particle Accelerator Conference (IPAC 2016): Busan, Korea, May 8-13, 2016*, page MOPMB012, 2016. doi:10.18429/JACoW-IPAC2016-MOPMB012.

[JFZ15] M.D. Ziegler J. F. Ziegler, J. P. Biersack. *SRIM - The Stopping and Range of Ions in Matter*. Ion Implantation Press, 2015.

[JKC90] H.R. Weller J.H. Kelley, D.R. Tilley and C.M. Cheves. Nucl. Phys. A564, 1 (1993). `https://www.nndc.bnl.gov/nudat2/getdataset.jsp?nucleus=16N&unc=nds`, 1990. [Online; accessed 17th Sep 2019].

[JSD11] H. Junde, H. Su, and Y. Dong. Nucl. Data Sheets 112, 1513 (2011). `https://www.nndc.bnl.gov/nudat2/decaysearchdirect.jsp?nuc=56C0&unc=nds`, 2011. [Online; accessed 8th August 2019].

[KBtLC12] A. Krugmann, O. Burda, and the Lintott-Crew. *Performing Electron Scattering Experiments with the LINTOTT Spectrometer at the S-DALINAC*. TU Darmstadt, Darmstadt, 2012.

[KE05] Y. Kanada-En'yo. Deformation of C isotopes. *Phys. Rev. C*, 71:014310, January 2005. doi:10.1103/PhysRevC.71.014310.

[KE07] Y. Kanada-En'yo. The Structure of Ground and Excited States of ^{12}C. *Prog. of Theo. Phys.*, 117(4):655–680, 2007. doi:10.1143/PTP.117.655.

[KEKS13] Y Kanada-En'yo, F Kobayashi, and T Suhara. Structures of ground and excited states in C isotopes. *Jour. Phys.: Conference Series*, 445:012037, July 2013. doi:10.1088/1742-6596/445/1/012037.

[KM59] H. W. Koch and J. W. Motz. Bremsstrahlung Cross-Section Formulas and Related Data. *Rev. Mod. Phys.*, 31:920–955, 1959. doi:10.1103/RevModPhys.31.920.

[Kni91] M. Knirsch. *Konzeption, Aufbau und Erprobung eines hochauflösenden QCLAM-Elektronenespektrometers mit großem Raumwinkel und hoher Impulsakzeptanz am Elektronenbeschleuniger S-DALINAC*. PhD thesis, Technische Universität Darmstadt, 1991.

[Kno00] G.F. Knoll. *Radiation Detection and Measurement*. John Wiley & Son, New York, Chichester, Weinheim, Brisbane, Toronto, Singapore, third edition, 1999/2000.

[KPS68] W. Kutschera, D. Pelte, and G. Schrieder. Angular correlation and lifetime measurements in ^{22}Ne. *Nucl. Phys. A*, 111(3):529 – 550, 1968. doi:10.1016/0375-9474(68)90237-6.

[Kus90] M. W. Kuss. Konstruktion und Aufbau einer Streukammer mit gleitender Abdichtung für das Q-CLAM Spektrometer am neuen supraleitenden Darmstätder Elektronen-Linearbeschleuniger S-DALINAC. Diplomarbeit, Technische Universität Darmstadt, 1990.

[LCC+04] I.Y. Lee, R.M. Clark, M. Cromaz, et al. GRETINA: A gamma ray energy tracking array. *Nucl. Phys. A*, 746:255 – 259, 2004. doi:10.1016/j.nuclphysa.2004.09.038. Proceedings of the Sixth International Conference on Radioactive Nuclear Beams (RNB6).

[Lee90] I-Y. Lee. Nuclear Structure in the Nineties: The GAMMASPHERE. *Nucl. Phys. A*, 520:c641–c655, 1990. doi:10.1016/0375-9474(90)91181-P.

[Leo87] W. R. Leo. *Techniques for Nuclear and Particle Physics Experiments*. Springer Verlag, Berlin, Heidelberg, New York, first edition, 1987.

[Lib52] W. F. Libby. *Radiocarbon Dating*. University of Chicago Press, Chicago, 1952.

[Loe17] C. Loelius. *Electromagnetic transition strengths studied with Doppler-shift techniques across the contours of the valley of stability*. PhD thesis, Michigan State University, February 2017.

[LS50] B. A. Lippmann and J. Schwinger. Variational Principles for Scattering Processes. I. *Phys. Rev. Lett.*, 79:469–480, 1950.

[LS69] D. Lister and A. B. Smith. Fast-Neutron Scattering from Germanium. *Phys. Rev.*, 183:954–963, 1969. doi:10.1103/PhysRev.183.954.

[Mac01] R. Machleidt. High-precision, charge-dependent Bonn nucleon-nucleon potential. *Phys. Rev. C*, 63:024001, January 2001. doi:10.1103/PhysRevC.63.024001.

[Mac05] H. Macher. *Einführung in die Kern- und Elementarteilchenphysik*. WILEY-VCH, Weinheim, 2005.

[Mat14] M. Mathy. M1 Stärke in ^{48}Ca aus inelastischer Protonenstreuung. Bachelor thesis, Technische Universität Darmstadt, March 2014.

[Mat16] M. Mathy. In-Flight Lifetime Measurement via Decay Position Reconstruction. Master's thesis, Technische Universität Darmstadt, May 2016.

[MBM+17] M. Mathy, J. Birkhan, H. Matsubara, et al. Search for weak $M1$ transitions in ^{48}Ca with inelastic proton scattering. *Phys. Rev. C*, 95:054316, 2017. doi:10.1103/PhysRevC.95.054316.

[ME11] R. Machleidt and D.R. Entem. Chiral effective field theory and nuclear forces. *Phys. Rep.*, 503(1):1 – 75, 2011. doi:10.1016/j.physrep.2011.02.001.

[MK92] T. Mayer-Kuckuk. *Kernphysik: Eine Einführung*. Vieweg+Teubner Verlag, Wiesbaden, fifth edition, 1992.

[Mor56] H. Morinaga. Interpretation of Some of the Excited States of $4n$ Self-Conjugate Nuclei. *Phys. Rev.*, 101:254–258, 1956. doi:10.1103/PhysRev.101.254.

[MPF+14] A. O. Macchiavelli, M. Petri, P. Fallon, et al. Phenomenological analysis of $B(E2)$ transition strengths in neutron-rich carbon isotopes. *Phys. Rev. C*, 90:067305, December 2014. doi:10.1103/PhysRevC.90.067305.

[MS14] E.A. Mccutchan and A.A. Sonzogni. Nucl. Data Sheets 115, 135 (2014) . `https://www.nndc.bnl.gov/nudat2/decaysearchdirect.jsp?nuc=88Y&unc=nds`, 2014. [Online; accessed 9th August 2019].

[MVC+14] P. Maris, J. P. Vary, A. Calci, et al. ^{12}C properties with evolved chiral three-nucleon interactions. *Phys. Rev. C*, 90:014314, 2014. doi:10.1103/PhysRevC.90.014314.

[MVN+11] P. Maris, J. P. Vary, P. Navrátil, et al. Origin of the Anomalous Long Lifetime of ^{14}C. *Phys. Rev. Lett.*, 106:202502, 2011. doi:10.1103/PhysRevLett.106.202502.

[NS12] N. Nica and B. Singh. Nucl. Data Sheets 113, 1563 (2012). `https://www.nndc.bnl.gov/nudat2/getdataset.jsp?nucleus=34S&unc=nds`, 2012. [Online; accessed 1. Nov 2019].

[NSS79] P. J. Nolan and J. F. Sharpey-Schafer. The measurement of the lifetimes of excited nuclear states. *Rep. Prog. Phys.*, 42(1):1–86, 1979. doi:10.1088/0034-4885/42/1/001.

[NVB00] P. Navrátil, J. P. Vary, and B. R. Barrett. Properties of ^{12}C in the Ab Initio Nuclear Shell Model. *Phys. Rev. Lett.*, 84:5728–5731, June 2000. doi:10.1103/PhysRevLett.84.5728.

[OIS+08] H. J. Ong, N. Imai, D. Suzuki, et al. Lifetime measurements of first excited states in ^{16,18}C. *Phys. Rev. C*, 78:014308, July 2008. doi:10.1103/PhysRevC.78.014308.

[Ost92] F. Osterfeld. Nuclear spin and isospin excitations. *Rev. Mod. Phys.*, 64:491–557, 1992. doi:10.1103/RevModPhys.64.491.

[PEA+11] Y. Poltoratska, C. Eckardt, W. Ackermann, et al. Status and recent developments at the polarized-electron injector of the superconducting Darmstadt electron linear accelerator S-DALINAC. *Journal of Physics: Conference Series*, 298:012002, May 2011. doi:10.1088/1742-6596/298/1/012002.

[PFM+11] M. Petri, P. Fallon, A. O. Macchiavelli, et al. Lifetime Measurement of the 2_1^+ State in ^{20}**C**. *Phys. Rev. Lett.*, 107:102501, August 2011. doi:10.1103/PhysRevLett.107.102501.

[PHP+16] M. Petri, S. Heil, S. Paschalis, et al. Lifetime measurement of excited states in ^{16}C. *Experiment Proposal E1548*, 2016.

[Pie18] N. Pietralla. The Institute of Nuclear Physics at the TU Darmstadt. *Nucl. Phys. News*, 28(2):4–11, 2018. doi:10.1080/10619127.2018.1463013.

[PLM+13] S. Paschalis, I.Y. Lee, A.O. Macchiavelli, et al. The performance of the Gamma-Ray Energy Tracking In-beam Nuclear Array GRETINA. *Nucl. Instr. Meth. Phys. Res. A*, 709:44 – 55, 2013. doi:10.1016/j.nima.2013.01.009.

[PPC+12] M. Petri, S. Paschalis, R. M. Clark, et al. Structure of ^{16}C: Testing shell model and ab initio approaches. *Phys. Rev. C*, 86:044329, 2012. doi:10.1103/PhysRevC.86.044329.

[PRS+14] B. Povh, K. Rith, C. Scholz, F. Zetsche, and W. Rodejohann. *Teilchen und Kerne*. Spinger Verlag, Berlin, Heidelberg, ninth edition, 2014.

[Rei00] B. Reitz. *Weiterentwicklung des Detektorsystems am QCLAM–Spektrometer des S–DALINAC und Untersuchung der Reaktionen 48-Ca(e,e') und 58-Ni(e,e') unter 180*. PhD thesis, Technischen Universität Darmstadt, 2000.

[Ric85] A. Richter. Low energy electron scattering and nuclear structure: a few selected examples of elementary electric and magnetic excitations. *Prog. Part. Nucl. Phys.*, 13:1 – 62, 1985. doi:10.1016/0146-6410(85)90003-1.

[Ric96] A. Richter. Operational Experience at the S-DALINAC. In *Epac 96: Proceedings of the Fifth European Particle Accelerator Conference, Sitges (Barcelona)*, 1996.

[RMB08] W. A. Richter, S. Mkhize, and B. A. Brown. *sd*-shell observables for the USDA and USDB Hamiltonians. *Phys. Rev. C*, 78:064302, December 2008. doi:10.1103/PhysRevC.78.064302.

[RMM+87] S. Raman, C.H. Malarkey, W.T. Milner, C.W. Nestor, and P.H. Stelson. Transition probability, $B(E2)\uparrow$, from the ground to the first-excited 2^+ state of even-even nuclides. *Atomic Data and Nuclear Data Tables*, 36(1):1 – 96, 1987. doi:10.1016/0092-640X(87)90016-7.

[Rot20] R. Roth. Technische Universität Darmstadt, Private Communication, September/Oktober 2020.

[Sar16] D.G. Sarantites. Washington University, Private Communication, August 2016.

[SB85] S. M. Seltzer and M. J. Berger. Bremsstrahlung spectra from electron interactions with screened atomic nuclei and orbital electrons. *Nucl. Instrum. Methods Phys. Res. B*, 12(1):95 – 134, 1985. doi:10.1016/0168-583X(85)90707-4.

[SB15] M. Shamsuzzoha Basunia. Nucl. Data Sheets 127, 69(2015). `https://www.nndc.bnl.gov/nudat2/getdataset.jsp?nucleus=22NE&unc=nds`, 2015. [Online; accessed 31th July 2020].

[SH15] H. Sagawa and K. Hagino. Theoretical models for exotic nuclei. *Eur. Phys. J. A*, 51:102, 2015. doi:10.1140/epja/i2015-15102-4.

[SHD+96] D.G. Sarantites, P.-F. Hua, M. Devlin, et al. "The microball" Design, instrumentation and response characteristics of a 4π-multidetector exit channel-selection device for spectroscopic and reaction mechanism studies with Gammasphere. *Nucl. Instr. Meth. Phys. Res. A*, 381(2):418 – 432, 1996. doi:10.1016/S0168-9002(96)00785-1.

[Sin20] M. Singer. *Entwicklung und Inbetriebnahme eines neuen Datenaufnahmesystems am QCLAM-Spektrometer*. PhD thesis, Technische Universität Darmstadt, 2020.

[SKE10] T. Suhara and Y. Kanada-En'yo. Cluster structures of excited states in ^{14}C. *Phys. Rev. C*, 82:044301, 2010. doi:10.1103/PhysRevC.82.044301.

[SKE11] T. Suhara and Y. Kanada-En'yo. Be-α correlations in the linear-chain structure of C isotopes. *Phys. Rev. C*, 84:024328, 2011. doi:10.1103/PhysRevC.84.024328.

[Son17] K. Sonnabend. S-DALINAC: Energie erfolreich zurückgewonnen. *Physik Journal*, 10:7, October 2017.

[SP08] O. Sorlin and M.-G. Porquet. Nuclear magic numbers: New features far from stability. *Prog. Part. Nucl. Phys.*, 61(2):602 – 673, 2008. doi:10.1016/j.ppnp.2008.05.001.

[SPM+20] I. Syndikus, M. Petri, A.O. Macchiavelli, et al. Probing the Z=6 spin-orbit shell gap with (p,2p) quasi-free scattering reactions. *Phys. Lett. B*, 809:135748, 2020. doi:10.1016/j.physletb.2020.135748.

[SR16] D.G. Sarantites and W. Reviol. Washington University, Private Communication, July 2016.

[Sri06] B.B. Srivastava. *Fundamentals of nuclear physics*. Rastogi Publications, Meerut, India, first edition, 2006.

[SSB82] R. M. Sternheimer, S. M. Seltzer, and M. J. Berger. Density effect for the ionization loss of charged particles in various substances. *Phys. Rev. B*, 26:6067–6076, 1982. doi:10.1103/PhysRevB.26.6067.

[SSS+08] M. Stanoiu, D. Sohler, O. Sorlin, et al. Disappearance of the N=14 shell gap in the carbon isotopic chain. *Phys. Rev. C*, 78:034315, Septemper 2008. doi:10.1103/PhysRevC.78.034315.

[Sta11] C. Stahl. Continuous-Angle DSAM: A new quality of lifetime measurements. Master's thesis, Technische Universität Darmstadt, October 2011.

[Sta15] C. Stahl. *New methods for the γ-ray spectroscopy with position-sensitive detector systems*. PhD thesis, Technische Universität Darmstadt, July 2015.

[Ste52] R. M. Sternheimer. The Density Effect for the Ionization Loss in Various Materials. *Phys. Rev.*, 88:851–859, 1952. doi:10.1103/PhysRev.88.851.

[Syn18] I. Syndikus. *Proton-Knockout Reactions from Neutron-Rich N Isotopes at R^3B*. PhD thesis, Technische Universität Darmstadt, November 2018.

[SZZS04] H. Sagawa, X. R. Zhou, X. Z. Zhang, and Toshio Suzuki. Deformations and electromagnetic moments in carbon and neon isotopes. *Phys. Rev. C*, 70:054316, November 2004. doi:10.1103/PhysRevC.70.054316.

[TB08] O.B. Tarasov and D. Bazin. LISE++: Radioactive beam production with in-flight separators. *Nucl. Instrum. Methods Phys. Res. B*, 266(19):4657 – 4664, 2008. Proceedings of the XVth International Conference on Electromagnetic Isotope Separators and Techniques Related to their Applications.

[TBS11] K. Tsukiyama, S. K. Bogner, and A. Schwenk. In-Medium Similarity Renormalization Group For Nuclei. *Phys. Rev. Lett.*, 106:222502, June 2011. doi:10.1103/PhysRevLett.106.222502.

[TBS12] K. Tsukiyama, S. K. Bogner, and A. Schwenk. In-medium similarity renormalization group for open-shell nuclei. *Phys. Rev. C*, 85:061304, June 2012. doi:10.1103/PhysRevC.85.061304.

[Thi11] R. Thies. Prototype tests and pilot experiments for the R3B scintillator-baseddetection systems. Master's thesis, Chalmers University of Technology Göteborg, 2011.

[Tsa74] Yung-Su Tsai. Pair production and bremsstrahlung of charged leptons. *Rev. Mod. Phys.*, 46:815–851, 1974. doi:10.1103/RevModPhys.46.815.

[VBB+12] P. Voss, T. Baugher, D. Bazin, et al. Excited-state transition-rate measurements in ^{18}C. *Phys. Rev. C*, 86:011303, July 2012. doi:10.1103/PhysRevC.86.011303.

[vNCPRR98] P. von Neumann-Cosel, A. Poves, J. Retamosa, and A. Richter. Magnetic dipole response in nuclei at the N=28 shell closure: a new look. *Phys. Lett. B*, 443(1):1 – 6, 1998. doi:10.1016/S0370-2693(98)01298-2.

[Wam11] F. Wamers. *Quasi-free Knockout Reactions with the Proton-dripline Nucleus ^{17}Ne*. PhD thesis, Technische Universität Darmstadt, 2011.

[WB92] E. K. Warburton and B. A. Brown. Effective interactions for the 0*p*1*s*0*d* nuclear shell-model space. *Phys. Rev. C*, 46:923–944, September 1992. doi:10.1103/PhysRevC.46.923.

[WBB+10] A. H. Wuosmaa, B. B. Back, S. Baker, et al. ^{15}C(d,p)^{16}C Reaction and Exotic Behavior in ^{16}C. *Phys. Rev. Lett.*, 105:132501, September 2010. doi:10.1103/PhysRevLett.105.132501.

[WFM+08] M. Wiedeking, P. Fallon, A. O. Macchiavelli, et al. Lifetime Measurement of the First Excited 2^+ State in ^{16}C. *Phys. Rev. Lett.*, 100:152501, 2008. doi:10.1103/PhysRevLett.100.152501.

[WOP67] E. K. Warburton, J. W. Olness, and A. R. Poletti. Nuclear Structure of Na^{22}.I. Gamma-Ray Correlations and Lifetime Measurements for Levels of $E_{ex} < 3.1$ MeV. *Phys. Rev.*, 160:938–963, 1967. doi:10.1103/PhysRev.160.938.

[YKE16] Y. Yuta and Y. Kanada-En'yo. 3α cluster structure and monopole transition in ^{12}C and ^{14}C. *Prog. of Theor. Exp. Phys.*, 2016(12), 2016. doi:10.1093/ptep/ptw178.123D04.

[YKH+17] H. Yamaguchi, D. Kahl, S. Hayakawa, et al. Experimental investigation of a linear-chain structure in the nucleus 14C. *Phys. Lett. B*, 766:11 – 16, 2017. doi:10.1016/j.physletb.2016.12.050.

[Zhu16] S. Zhu. Argonne National Laboratory, Private Communication, 2016.

[Zie19] J. F. Ziegler. SRIM - The Stopping and Range of Ions in Matter. `http://www.srim.org/`, 2019. [Online; accessed 23th May 2019].

[ZZB10] J. F. Ziegler, M.D. Ziegler, and J.P. Biersack. SRIM – The stopping and range of ions in matter (2010). *Nucl. Instr. Meth. Phys. Res. B*, 268(11):1818 – 1823, 2010.

doi:10.1016/j.nimb.2010.02.091. 19th International Conference on Ion Beam Analysis.

[Ôk54] S. Ôkubo. Diagonalization of Hamiltonian and Tamm-Dancoff Equation. *Prog. Theor. Phys.*, 12(5):603–622, 11 1954. doi:10.1143/PTP.12.603.

[Üb71] H. Überall. *Electron Scattering from Complex Nuclei (Part A)*. Academic Press, New York, London, 1971.

List of Figures

List of Tables

Acronyms

AMD Antisymmetrized Molecular Dynamics

ANL Argonne National Laboratory

ATLAS Argonne Tandem Linac Accelerator System

BGO Bismuth Germanate

CDB2k CD-Bonn 2000

DGS Digital Gammasphere

DSAM Doppler-Shift Attenuation Method

EFT Effective Field Theory

FWHM Full Width at Half Maximum

Geant4 Geometry and Tracking Toolkit

HO Harmonic-Oscillator

HPGe High Purity Germanium

ICRU International Commission on Radiation Units and measurements

IM In-Medium

IM-NCSM In-Medium No-Core Shell Model

LCCS Linear-Chain Cluster State

linac Linear Accelerator

μ-Ball Microball

NCSM No-Core Shell Model

PID Particle Identification

PII Positive Ion Injector

QCD Quantum Chromodynamics

QCLAM Quadrupol CLAMshell

RDM Recoil Distance Method

RMS Root Mean Square

S-DALINAC Supraleitende Darmstädter Elektronenbeschleuniger

SRG Similarity Renormalization Group

SRIM The Stopping and Range of Ions in Matter

USD Universal sd Shell

Acknowledgement

This work would not have been possible without a lot of help from many people. Thank you all!

First of all, I would like to thank my supervisor Marina Petri for giving me the opportunity to work on this interesting topic. Thanks for all the support and interest in my work. Thanks for the opportunity to participate in experiments at fascinating accelerator facilities around the world. Thanks for the productive visits at the University of York. Thanks that you never let me down. Thanks that you gave me enough time, when I needed it the most. Due to all of this I learned so much about physics and life itself. Ευχαριστώ!

Further, I want to thank Heiko Scheit for being my second supervisor. Your expertise helped a lot. Thanks for your support on my work as well as with administrative challenges. Also, I want to thank Robert Roth very much for being the second referee even on such a short notice.

In addition, I want to thank Tom Aumann for welcoming me as part of his group and of course I also want to thank all group members a lot. It was a pleasure to work with all of you and you were always a great help concerning any topic. We had a lot of fun on all the summer schools, conferences, and iFridge parties. Also our game nights were hilarious. Therefore, I want to express my special thanks to Sebastian Heil (Team Petri!), Ina Syndikus (Team Petri!), Christopher Lehr (My room buddy :)), Patrick van Beek (My office buddy :)), Sonja Storck-Dutine (Nice new surname, congratulations!), Ashton Falduto (Or is it Fashton Aalduto?), Philipp Kuchenbrod (Hope all Kerbels are fine!), Paulina Müller (Do I still have your muffin box?), Martin Baumann (Rockets, rockets, rockets), Andrea Horvat (Now I also can play the Witcher again :)), Vadim Wagner, Marco Knösel, Dmytro Symochko, Marc Duchêne, Fabia Schindler, Julian Kahlbow, and Diego Semmler.

I also want to thank all members of the spectrometer group. It was always nice to work with you and it was exciting to participate in so many different and challenging experiments. Special thanks to Gerhart Steinhilber and Antonio D'Alessio for the support on the vacuum infrastructure of QCLAM and the design of new vacuum chambers. There are no leaks, just too few pumps.

Further, I thank the μ-Ball group members for their support during the experiment. Especially, I have to give a lot of thanks to Demetrios Sarantites and Walter Reviol for the fruitful discussions about the μ-Ball data analysis.

Thanks for the proof reading to Ashton Falduto, Patrick van Beek, Gerhart Steinhilber, Diana Jahn, Tamara Breimhorst, and Sebastian Heil. Without you my thesis would be adventurous...too adventurous.

Außerdem bedanke ich mich hiermit bei Herrn Opperman und allen seinen Werkstattmitarbeitern. Ihre Expertise, Geduld, Einfallsreichtum und Spontanität waren eine sehr große Hilfe für die Umsetzung all unserer Infrastrukturprojekte am QCLAM.

Schließlich bedanke ich mich herzlich bei allen Personen, die mich seelisch und moralisch im Verlauf der Arbeit und meines gesamten Studiums unterstützt haben. Hierzu zählt meine Familie und besonders meine Eltern, welche mir immer den Rücken freigehalten haben und niemals an meinen Fähigkeiten gezweifelt haben. Weiter danke ich in besonderem Maße meinen Freunden und Kommilitonen, besonders denjenigen, die auch in den dunkelsten Zeiten jede Sekunde für mich da waren. Ihr habt mit dem nötigen Spaß am Leben dafür gesorgt den Arbeitsstress und jede Krise zu überstehen. Außerdem möchte ich mich bei allen meinen Rettern in der tiefsten Not bedanken!

Besonders bedanken möchte ich mich bei Christian und Frederike Ott für all die unzähligen, schönen Erlebnissen und die Unterstützung an hellen und dunklen Tagen. Danke an die kleine Alma Ott für das viele Lachen:) Danke an Christine Grimm. Egal wo du bist, du bist für mich da. Danke an Sarah Christmann, besonders für die vielen Stunden mit Supernatural. Vielen Dank an alle meine wichtigen Wegbegleiter der letzten Jahre: Marion Giegerich (Immer schön weiter joggen!), Jana Schulz, Hannah Hiefner, Erik Wagner, Tamara Rehak, Liesa Greifenstein, Alexander Hufnagel, Nils Haase, Maximilian Schmitt, Sarah Schneider, Diana Jahn und Clara Reichwein. Ohne euch alle wäre meine Welt während dem gesamten Studium nicht so toll gewesen, wie sie es war.

Vielen Dank an die 4/10 Community für die unzähligen schönen, spannenden, verrückten und lustigen Stunden. Mit euch macht es immer Spaß die Zeit zu verbringen, egal ob real oder virtuell. Besonderen Dank an Sina Ankenbrand, Justin Smith und Stefan Schrock. Mid2B!

Vielen Dank an die Boulder-Gang für all die Unterstützung an den vielen grünen Routen: Tamara Breimhorst, Marion Giegerich, Jannick von der Lühe, Anne Höfling und Jan Sittig. Was man nicht schafft, macht man mit Schwung!

Zu guter Letzt: Danke Tami. Danke für alles! Möge das ChiChu immer an deiner Seite sein! Bamben für alle!

This work was funded by the Deutsche Forschungsgemeinschaft (DFG, German Research Foundation) under Grant No. SFB 1245 (project ID 279384907).

Erklärung zur Dissertation

Hiermit versichere ich, dass ich die vorliegende Dissertation selbstständig angefertigt und keine anderen als die angegebenen Quellen und Hilfsmittel verwendet habe. Alle wörtlichen und paraphrasierten Zitate wurden angemessen kenntlich gemacht. Die Arbeit hat bisher noch nicht zu Prüfungszwecken gedient.

Darmstadt, den 2. März 2021

(Michael Bernhard Mathy aus Dieburg)